Toward Ultrafast Detection of Quantum Emitters at a High Repetition Rate

Dissertation
zur Erlangung des Grades eines Doktors
der Naturwissenschaften



vorgelegt von
Amr Farrag

eingereicht bei der Naturwissenschaflich-Technischen Fakultät
der Universität Siegen

Gutachter der Dissertation:	Prof. Dr. Mario Agio Prof. Dr. Giancarlo Soavi
Zusammensetzung der Prüfungskommission:	Prof. Dr. Mario Agio Prof. Dr. Giancarlo Soavi Prof. Dr. Carsten Busse Prof. Dr. Stefan Nimmrichter
Datum der Disputation:	12.05.2026

Abstract

The modern information era is built upon technologies such as telecommunications, cryptography, high-performance computing, and, more recently, artificial intelligence (AI). At the core of all these systems are electronic circuits, whose performance is fundamentally limited by the physical speed of electrons. Photonic technologies, by contrast, rely on light quanta—single photons—that propagate orders of magnitude faster and offer intrinsically higher bandwidth and enhanced security. Replacing electronic components with optical counterparts promises major advances in communication speed, data transfer, secure information processing, and quantum technologies. Central to these developments are ultrabright single-photon sources (SPSs), including quantum dots and color centers in solid-state hosts. However, the brightest SPSs currently require cryogenic temperatures, limiting their practicality in real-world applications.

This dissertation proposes an alternative route toward achieving bright, room-temperature single-photon emission by exploiting high-repetition-rate excitation. Advances in laser technology now allow solid-state lasers to operate at gigahertz repetition rates. By combining such excitation with hybrid quantum systems—where a quantum emitter is coupled to a nanophotonic structure to enhance its radiative emission through the Purcell effect—ultrabright SPSs can, in principle, be realized at room temperature. At these high radiative rates, however, the fluorescence lifetime becomes extremely short, well below the temporal resolution of conventional single-photon detectors, which are further constrained by cost, cryogenic requirements, bulkiness, and limited synchronization capabilities at gigahertz rates.

To address this limitation, this dissertation demonstrates an optical Kerr gate (OKG) operating at a 1-GHz repetition rate with sub-picosecond temporal resolution. The OKG is a third-order ($\chi^{(3)}$) nonlinear optical process that does not require phase-matching conditions and is therefore suitable for broadband fluorescence detection. Kerr gating was achieved using two distinct Kerr media: bulk bismuth-borosilicate (BBS) glass and two-dimensional thin graphite films. In both cases, OKG signals were generated using sub-nanojoule gate-pulse energies—remarkably low compared

with traditional OKG implementations that rely on millijoule-level amplified pulses, more than six orders of magnitude higher. The temporal resolution achieved was 175 $\pm$ 1 fs with BBS glass ($\sim$ 3% gating efficiency) and 141 $\pm$ 6 fs with thin graphite films ($\sim$ 10% efficiency). This compact, room-temperature technique requires no cryocooler, vacuum system, or bulky amplification stages. The demonstrated OKG platform can be directly integrated into a standard confocal fluorescence microscope, enabling ultrafast fluorescence measurements from quantum emitters and paving the way for practical room-temperature ultrabright SPSs.

Zusammenfassung

Diese Dissertation schlägt eine neue Strategie zur Erhöhung der Helligkeit einzelner Quanteneinzelphotonenquellen bei Raumtemperatur vor, indem Festkörperemitter mit Laserpulsen hoher Wiederholrate (1 GHz) angeregt werden. Gleichzeitig wird die dafür notwendige ultraschnelle Nachweistechnologie experimentell entwickelt. Viele Festkörper-Einzelphotonenquellen – etwa Quantenpunkte oder Farbzentren – erreichen ihre höchste Helligkeit nur bei Kryotemperaturen. Eine vielversprechende Alternative besteht darin, diese Systeme mit Gigahertz-Laserraten anzupumpen, wodurch die Photonenzahl pro Sekunde stark erhöht werden kann, ohne auf kryogene oder komplexe nanophotonische Strukturen angewiesen zu sein. In hybriden Quantensystemen, bei denen ein Emitter an eine Nanokavität gekoppelt ist, kann der Purcell-Effekt jedoch zu sub-pikosekundenschnellen Fluoreszenzlebensdauern führen. Solche schnellen Dynamiken können mit herkömmlichen Einzelphotonendetektoren, deren zeitliche Auflösung auf einige Pikosekunden begrenzt ist, nicht mehr gemessen werden.

Um diese Einschränkung zu überwinden, wird in dieser Arbeit ein optisches Kerr-Gate (OKG) mit einer Wiederholrate von 1 GHz und einer zeitlichen Auflösung im Sub-Pikosekunden-Bereich demonstriert. Das OKG basiert auf einem $\chi^{(3)}$-Prozess, erfordert keine strengen Phasenanpassungsbedingungen und kann in unterschiedlichen Kerr-Medien realisiert werden. Zwei Medien wurden untersucht: Borosilikatglas (BBS-Glas) als volumetrisches Kerr-Material sowie dünne Graphitfilme als zweidimensionales Kerr-Medium. In beiden Fällen konnten OKG-Signale mit Gate-Pulsenergien im Sub-Nanojoule-Bereich erzeugt werden – über sechs Größenordnungen unterhalb der Millijoule-Pulse, die in herkömmlichen OKG-Experimenten üblich sind. Mit BBS-Glas wurde eine zeitliche Auflösung von 175 ± 1 fs und eine Gating-Effizienz von etwa 3 % erreicht; dünne Graphitfilme ermöglichten eine noch kürzere Antwortzeit von 141 ± 6 fs bei einer Effizienz von rund 10 %.

Diese Ergebnisse zeigen, dass effizientes Kerr-Gating auch mit moderaten Leistungen gigahertz-basierter Festkörperlaser realisierbar ist – ohne Kryokühler, Vakuumsysteme oder sperrige Verstärker. Das demonstrierte OKG kann direkt in ein konfokales

Fluoreszenzmikroskop integriert werden und ermöglicht die zeitliche Auflösung ultraschneller Fluoreszenzlebensdauern zukünftiger hybrider Quantensysteme, die mit Gigahertz-Pulsraten angeregt werden. Damit liefert diese Arbeit eine entscheidende Basistechnologie für ultrahelle Einzelphotonenquellen bei Raumtemperatur und für kompakte ultraschnelle Messsysteme in der Quantenphotonik.

Acknowledgments

Throughout every PhD journey there are ups and downs, and mine was no exception—though it certainly had more downs before the ups finally arrived. As the first student working on an ultrafast nonlinear optics project within a nano-optics group, I had to navigate countless challenges. The success of this research would not have been possible without the support of several people, and I would like to take this opportunity to express my sincere gratitude to them.

First and foremost, I would like to express my profound gratitude to my PhD supervisor, Prof. Mario Agio, for admitting me to the Nano-Optics group and helping me fulfill my childhood dream of becoming a physics researcher. I am truly grateful for his understanding, patience, and appreciation of the challenging nature of this research topic. I consider myself extremely fortunate to have had such a wonderful supervisor. Thank you, Mario, for your supervision, insightful discussions, support with data analysis, your trust in my abilities, and for providing me with the opportunity to push the frontier in my field of research.

I am also thankful to Dr. Assegid M. Flatae for his co-supervision of this demanding PhD project and for sharing his experience—especially his expertise in building optical setups.

A special thanks goes to Mrs. Sharon Harvey, our secretary, for her constant readiness to help members of the group overcome administrative hurdles. I am particularly indebted to her support at the beginning of my stay, when I could not yet speak German and felt completely lost in the bureaucratic world of Germany.

Within the Nano-Optics group, I would like to thank Navid and Haritha for sharing the office and for the many discussions and conversations we enjoyed. I am grateful to Philip for helping me settle in Germany during a time when adapting to the system felt difficult. My thanks go again to Philip, as well as to Lukas Strauch, for taking care of the coffee supply and ensuring the smooth “coffee management” of the group. I also appreciate the engaging discussions with Lukas Hunold and Joel Strohmann, and I am especially thankful to Joel for his mathematical insight, which helped me revisit and clarify some of my older calculations and codes. A special

thanks go to Maik Lütticke, whose high-quality LabVIEW program he created in our group, was a source of knowledge and inspiration for me, when I was learning LabVIEW programming. In addition to that, I would like to thank Dr. Nemanja Markešević for visiting Greenhorn meeting 2024, I co-organized. And of course, I cannot forget to thank Tofianme, with whom I still enjoy talking to this day.

I would also like to thank our collaborators, without whom the results of this dissertation would not have been possible. My thanks go to Dr. Duncan England for his initial advice on the project and for co-authoring a book chapter with us. I am grateful to Lenorah Stott and Prof. Doris Möncke for preparing the BBS glass specimens, and to Mauro Pucci for polishing the samples. My thanks also go to Alessandro Lagatti and Prof. Andrea Lapini for performing the absorbance measurements. I am deeply indebted to Stephan Schäfer for the initial training in graphene fabrication and for providing the graphite mesa. I am also thankful to Prof. Thomas Lenzer, Prof. Kawon Oum, and Prof. Giancarlo Soavi for their helpful discussions.

Last, but certainly not least, I am deeply grateful to my family in Egypt and to my friends in Egypt, Finland, and Germany for their constant emotional and social support, which helped me persevere through the many challenges along the way.

Declaration on oath

I, Amr Farrag declare that this thesis and work presented in it are my own and has been generated by me as the result of my own original scientific work. I confirm that, to the best of my knowledge, my thesis does not infringe upon anyone's copyright nor violate any proprietary rights. Any ideas, techniques, quotations, or any other material from the work of other people included in my thesis, published or otherwise, are fully acknowledged in accordance with the standard referencing practices.

Siegen, June 2, 2026 Author : Amr Farrag

Table of Contents

Abstract **i**

Zusammenfassung **iii**

Acknowledgments **v**

Declaration on oath **vii**

Acronyms **ix**

1 Introduction **1**

1.1 Quantum emitters for science and technology 1

1.2 Time-resolved fluorescence of quantum emitters 5

1.3 Ultrafast fluorescence of quantum emitters 8

1.4 Detection of ultrafast fluorescence emission 10

1.5 Research objective 12

1.6 Dissertation outline 15

2 Quantum emitters and ultrafast fluorescence detection techniques 17

2.1 Fundamentals of fluorescence and fluorescence enhancement 17

2.1.1 Perrin-Jablonski diagram 18

2.1.2 Characteristics of fluorescence emission 20

2.1.3 Fluorescence lifetime and quantum yield 22

2.1.4 Second-order intensity correlation function 26

2.1.5 Purcell effect and optical nanoantennas 28

2.2 Common quantum emitters 40
2.2.1 Quantum dots 40
2.2.2 Color centers in diamond 47
2.2.3 Ultrafast fluorescent dyes 54
2.2.4 Hybrid quantum systems 56
2.3 Fluorescence microscopy and spectroscopy 61
2.3.1 Scheme of confocal fluorescence microscope 61
2.3.2 Excitation light source 64
2.3.3 Imaging system 65
2.3.4 Spectral characterization 67
2.3.5 Photodetectors 68
2.3.6 Fluorescence lifetime measurement systems 75
2.4 Ultrafast fluorescence detection 79
2.4.1 Streak camera 79
2.4.2 Femtosecond fluorescence measurement by two-photon interference 82
2.4.3 Double-pulse excitation photon anti-bunching for single-molecules 85
2.4.4 Photon counting by time magnification 88
2.4.5 Fluorescence lifetime Hong-Ou-Mandel sensing 90
2.4.6 Frequency up-conversion 93
2.4.7 Optical Kerr gate 97

3 Nonlinear optical sampling via optical Kerr gate 101
3.1 Introduction to nonlinear optics 101
3.2 Third-order nonlinear optical susceptibility processes 102
3.3 Intensity-dependent refractive index 105
3.3.1 Tensor nature of third-order susceptibility 106
3.3.2 Optical Kerr effect 107
3.3.3 Self-phase modulation 110
3.3.4 Cross-phase modulation 113

3.3.5 Two-photon absorption 114
3.4 Optical Kerr effect and self-phase modulation under focusing 115

4 Experimental realization of optical Kerr gate 123
4.1 Experimental setup configuration 123
4.1.1 Ti:sapphire (Ti:sa) GHz repetition rate laser 123
4.1.2 Polarizers 124
4.1.3 Detection scheme using photon counting 128
4.1.4 Linear translation stage 128
4.2 Characterization of optical Kerr gate with carbon disulfide 130
4.2.1 Introduction 130
4.2.2 Tensor nature of material response function 131
4.2.3 Origin of fast and slow responses 132
4.2.4 Experimental Results 136
4.3 Otical Kerr gate with single-mode fiber 148
4.3.1 Introduction 148
4.3.2 Setup configuration 150
4.3.3 Experimental results and discussion 151
4.3.4 Practical considerations for enhanced Kerr signal 153

5 Bismuth oxide-containing glass as a Kerr medium 158
5.1 Introduction 158
5.2 Glass structure and sample preparation 159
5.3 Third-order nonlinearity in glass 162
5.3.1 Two-photon absorption of bismuth-borosilicate glass 164
5.3.2 Self-phase modulation of bismuth-borosilicate glass 168
5.3.3 Kerr effect in glass 169

6 Graphene and thin graphite films as a Kerr medium 189
6.1 Introduction to properties of graphene 189
6.2 Structure of graphene 191

6.2.1 Crystal structure . . . 191
6.2.2 Band structure . . . 193
6.2.3 Stacking order of graphene layers . . . 195
6.2.4 Raman spectrum of graphene . . . 198
6.3 Sample preparation . . . 204
6.3.1 Overview . . . 204
6.3.2 Chemical vapor deposition . . . 206
6.3.3 Mechanical exfoliation . . . 207
6.4 Identification of number of layers . . . 211
6.4.1 Optical microscopy . . . 211
6.4.2 Raman spectrum of graphene layers . . . 217
6.4.3 Atomic force microscopy . . . 219
6.5 Thermal transport and laser damage of Graphene . . . 221
6.5.1 Overview of graphene's thermal properties . . . 221
6.5.2 Thermal conductivity of graphene . . . 224
6.5.3 Mechanisms of laser-induced damage of graphene . . . 226
6.5.4 Experimental setup and results . . . 233
6.6 Nonlinear optical properties of graphene . . . 240
6.6.1 Overview . . . 240
6.6.2 Self-phase modulation of graphene . . . 242
6.6.3 Kerr nonlinearity of Graphene . . . 247

7 Summary and Outlook **264**

A Determination of temporal overlap without Kerr medium **268**

B OKG experiment with CW laser as a probe **272**

List of Publications **278**

Acronyms

APD Avalanche Photodiode

AFM Atomic Force Microscope

BBS Bismuth-borosilicate

BZ Brillouin Zone

CVD Chemical Vapor Deposition

DCR Dark Count Rate

DW Debye-Waller factor

FeDEx Femtosecond Double-Excitation

FWM Four-Wave Mixing

FLG Few-layer Graphene

HBT Hanbury Brown and Twiss

HOM Hong-Ou-Mandel

HOPG Highly Oriented Pyrolytic Graphite

IRF Instrument Response Function

LITG Laser-Induced Transient Grating

ME Mechanical Exfoliation

NV Nitrogen Vacancy

OKG Optical Kerr Gate

OKE Optical Kerr Effect

OPO Optical Parametric Oscillator

PMT Photomultiplier Tube

PD Photodiode

QD Quantum Dot

SiV Silicon Vacancy

SPM Self-Phase Modulation

SLG Single-layer Graphene

SFG Sum-Frequency Generation

SPCR Saturable Photoexcited-Carrier Refraction

SPAD Single-Photon Avalanche Diode

SNSPD Superconducting Nanowire Single-Photon Detector

TCSPC Time-correlated Single-photon Counting

THG Third Harmonic Generation

TPA Two-Photon Absorption

XPM Cross-Phase Modulation

ZPL Zero Phonon Line

Chapter 1

Introduction

1.1 Quantum emitters for science and technology

This dissertation proposes a novel approach for increasing the fluorescence emission rate from quantum emitters at room temperature. This approach relies on pulsed excitation from a solid-state laser operating at 1 GHz repetition rate. The emission rate of these quantum emitters can be further controlled and enhanced via coupling to a nanophotonic structure, i.e., nanocone-forming a hybrid system. The fluorescence enhancement in such a case is achieved by enhancing Purcell factor. When the rate of radiative decay of a quantum emitter is drastically increased, its fluorescence lifetime is shortened, beyond the capabilities of current detector technology. In this dissertation, an optical gating technique is demonstrated that is capable of resolving such ultrashort fluorescence lifetime at room temperature. The significance of such optical gating technique is evident when a laser at very high repetition rate, i.e., 1 GHz is used for exciting the quantum emitter, which is coupled to nanophotonic structures, leading to ultrabright single-photon sources. In this chapter, the first section introduces the quantum emitters, the second section elaborates the standard technique of time-resolved fluorescence spectroscopy. The third section provides some examples of the ultrafast dynamical processes that require high temporal resolution for studying them. The fourth section discusses the current detection schemes, highlighting their advantages and limitations. The last two sections are dedicated for explaining the research project objective, and the dissertation outline, respectively.

Quantum emitters are nanoscale objects with discrete energy levels, which can emit light on demand that cannot be explained by classical theories, and can be excited by an optical or electrical pulse. Common examples of quantum emitters are atoms, ions, semiconductor quantum dots, organic molecules, color centers in wide band-gap materials, and entangled photon pairs. They are interfaces between light and matter

in quantum technologies, enabling single-photon generation, spin-based quantum memories, and coherent spin-photon interfaces. Unlike isolated atoms, which require complex trapping or cooling systems, solid-state quantum emitters are embedded in stable hosts, e.g., color centers in diamond, which leverage nanofabrication for integration into devices. With the benefit of integrability comes other challenges. For instance, solid emitters exhibit variation in the emission wavelength and lifetime because of material inhomogeneities, and crystal defects that can quench or broaden their emission. However, quantum emitters have proven to be promising platforms for various applications, such as quantum computing, quantum communication, and quantum sensing. The research of quantum emitters began with the work of Kimble et al. [1] in 1977, where fluorescence photons emitted by a single atom of sodium within an atomic beam were collected. This was the first observation of photon anti-bunching behavior. Following this work, early experiments of photon anti-bunching detection focused on gaseous systems. Isolating single-emitters that act effectively as individual solid-state atoms, for observing quantum effects was achieved almost 15 years later. Photon anti-bunching in the fluorescence of single dye molecules embedded within a crystal was detected in 1992 [2]. Eight years later, photon anti-bunching from a single quantum dot (QD) at room-temperature was reported [3], and in the same year from fluorescence emitted by single nitrogen-vacancy (NV) in diamond was demonstrated [4]. These pioneering findings paved the way for other researchers to explore the capabilities and challenges of quantum emitters. Since then, research on quantum emitters has expanded to include other color centers in diamond, i.e., germanium-vacancy centers (GeV) [5], tin-vacancy centers (SnV) [6], and silicon-vacancy (SiV) centers [7]; and also extended to defect centers in other solid-state platforms, like silicon carbide (SiC) [8]. Other QDs, such as III-V epitaxial semiconductor QDs, e.g., InAs/GaAs have been investigated, due to their ability to achieve near-unity quantum efficiency, as well as their emission of high purity, indistinguishable single-photons [9]. Recently, quantum emitters hosted within atomically thin materials, i.e., hexagonal boron nitride (hBN) and transition metal dichalcogenide (TMD) monolayers have been reported [10, 11]. Arguably, the fluorescence emitted by defect centers in their host 2D materials may originate from residual organic molecules trapped beneath the atomically thin layers [12].

Several key metrics are commonly used to characterize the performance of a single-photon source (SPS), such as a single quantum emitter [13, 14]. One important parameter is the radiative emission rate, which describes how quickly a photon is emitted. This rate is inversely proportional to the radiative lifetime. Ideally, a bright SPS should emit fluorescence at megahertz, or preferably gigahertz, repetition rates. Another crucial metric concerns the emitted spectrum and linewidth. The coherent component of the fluorescence is represented by the zero-phonon line (ZPL). The

emission spectrum is often affected by thermal, charge, and spin noise. Thermal noise, for example, couples phonons into the emission process, broadening the spectral profile. The ZPL corresponds to the portion of the emission that occurs without phonon involvement, while the remaining incoherent emission forms the phonon sideband. Ideally, the ZPL fraction should approach unity, and its linewidth should be narrow. The minimal achievable ZPL linewidth is set by the inverse of the radiative lifetime—known as the Fourier-transform limit—and is reached when decoherence is negligible. The intrinsic quantum efficiency is another important figure of merit. It is defined as the ratio of the radiative decay rate to the total decay rate (radiative plus non-radiative). An ideal SPS has unit quantum efficiency, meaning that photon generation is deterministic. Single-photon purity is also essential. It is typically quantified by the second-order correlation function at zero time delay, $g^{(2)}(0)$, measured using a Hanbury Brown–Twiss (HBT) interferometer. The purity is given by 1 - $g^{(2)}(0)$; an ideal SPS has $g^{(2)}(0) = 0$, indicating that it emits exactly one photon per excitation event. Another metric is indistinguishability, which measures how quantum-mechanically identical the emitted photons are. This is evaluated through Hong-Ou-Mandel (HOM) interference. Identical photons entering a beamsplitter will bunch and exit through the same output port, while distinguishable photons exit different ports with a 50% probability. Ideally, the HOM interference visibility reaches unity. For entangled photon sources, the entanglement fidelity quantifies how closely the generated quantum state matches an ideal entangled state; high fidelity indicates low noise and minimal decoherence. A metric particularly relevant to this dissertation is the brightness of the quantum emitter. Since quantum efficiency determines whether the emitter generates a photon upon excitation, brightness is closely tied to collection efficiency. In principle, a single emitter should produce one photon every time it is excited by a source such as a pulsed laser. In practice, however, low quantum yield often prevents deterministic photon generation. Moreover, several factors limit the collection efficiency of the generated photons. First, while an emitter radiates into a full 4π solid angle, its host material typically has a high refractive index—for instance, diamond has an index of 2.4. As a result, a significant fraction of photons is trapped inside the medium due to total internal reflection. Second, typical fluorescence microscopes collect only about 5–10% of emitted photons because of scattering and absorption losses in the optical components. Third, the detection process is constrained by the dead time of single-photon detectors, typically on the order of tens of nanoseconds. During this period, the detector cannot register additional photons, further reducing the maximum count rate. For example, photomultiplier tubes (PMTs) have a maximum count rate of 20 MHz, single-photon avalanche diodes (SPAD) can reach up to 30 MHz (e.g., Excelitas, SPCM series), superconducting nanowire single-photon detectors (SNSPD) are up to 200 MHz (e.g.,

ID Quantique, ID281), while the timing electronics for example, modern TCSPC electronics (e.g., MultiHarp 150, PicoQuant GmbH) can reach count rates above 150 MHz. The brightness and the lifetime of major single-photon sources are presented in table 1.1.

Table 1.1: Major single-photon sources, their lifetime and brightness, without coupling to photonic structures

Single-photon sources	**Lifetime (ns)**	**Brightness (Mcps)**
Organic molecules	1–10	∼50
Color centers in diamond	1–10	∼1
Semiconductor QDs	0.1–1	∼10

Two main strategies have been pursued to enhance the brightness of quantum emitters by increasing the collection efficiency of their emitted photons. The first strategy focuses on controlling the directionality of the emitted fluorescence from quantum emitters, by shaping its omnidirectional spatial distribution into a narrow, targeted beam, allowing its collection efficiency to be maximized into a certain direction. The second centers on modifying the fundamental emission rate and the intrinsic quantum efficiency of the emitter itself via enhancing Purcell factor. Both strategies are enabled by optical nanoantennas and microcavities, thanks to recent advances in nano and microfabrication techniques. An optical nanoantenna is a nanoscale device designed to efficiently manipulate and control electromagnetic radiation (light) at optical frequencies. They are the nanoscale analogue of radio-frequency (RF) or microwave antennas, but operate using principles of nanophotonics and plasmonics, often overcoming the classical diffraction limit. These two strategies are, in fact, intertwined: optical antennas primarily used for tailoring the quantum emitter dipole's radiation pattern, affect the fundamental emission rate of the quantum emitter; while microcavities and photonic structures aimed essentially to increase the emission rate, shapes the far-field radiation pattern directionality.

In the first strategy, an optical nanoantenna converts the near-field localized energy of the dipole of the quantum emitter to a specific far-field radiation pattern. The different elements of the optical nanoantenna are precisely spaced, so that the dipole's radiation experiences destructive interference in one direction, while experiencing constructive interference in another, thereby tailoring the isotropic fluorescence emission into a specific direction. For this purpose, several approaches have been developed to control the directionality of fluorescence emission through various designs of nanoantennas. For example, planar Yagi–Uda antennas have been applied to ensembles of fluorescent nanobeads and shown to direct fluorescence into a narrow cone, enabling more efficient detection [15]. Other implementations rely on coupling

the emitter's dipole to a tunable microcavity to improve photon collection efficiency and, consequently, brightness. Tomm et al. [16], for instance, coupled an electrically excited single InGaAs quantum dot to a tunable microcavity, producing a coherent single-photon source delivering thousands of photons in a 1-GHz pulse train. A similar approach was demonstrated by coupling a SnV color center in a diamond membrane to a fiber-based Fabry–Pérot tunable microcavity [17]. A major limitation of such cavity-based systems, however, is that they typically require cryogenic temperatures, restricting their practicality in real-world applications.

The second strategy depends on modifying the decay rate of a quantum emitter. When a quantum emitter is placed inside, or in the vicinity of a nanostructured cavity, and the cavity resonance is tuned, the local density of optical states (LDOS) at the emitter's position is drastically increased. Such hybrid quantum systems require perfectly fabricated nanocavities and precise positioning control between the emitter's location and the nanocavity, otherwise the same optical nanoantenna would inhibit the quantum emitter's emission. An example of those hybrid systems is a gold nanocavity—is coupled to the emitter to control its local density of optical states and enhance its emission rate. This approach is particularly promising because it enables bright photon sources at room temperature. For example, Flatae et al. [18] reported substantial Purcell enhancement of bare core CdTe quantum dots, achieving 1460-fold and 613-fold increases in emission rates for exciton and biexciton states, respectively, at room temperature. Room-temperature coupling of SiV centers in diamond membranes has also been demonstrated, although only for ensembles thus far [19]. Because an increased radiative decay rate corresponds to faster emission, high-temporal-resolution fluorescence techniques capable of resolving such ultrafast fluorescence emission from the quantum emitters, which will help us grasp deeper understanding about their emission dynamics.

1.2 Time-resolved fluorescence of quantum emitters

Time-resolved fluorescence spectroscopy is a powerful technique for measuring how the emission intensity of a quantum emitter decays as a function of time after excitation. The fluorescence lifetime is important because it represents the characteristic time over which the excited state relaxes radiatively. High-resolution lifetime measurements provide insight into radiative and non-radiative decay channels, quenching mechanisms, and the emitter's local environment. Since the fluorescence lifetime τ is inversely proportional to the radiative transition rate and quantum efficiency, a

short lifetime indicates a high radiative rate and, therefore, a brighter photon source. In contrast, a longer lifetime may signal low radiative efficiency or the involvement of metastable states that temporarily trap the excitation. When radiative decay is the dominant relaxation pathway, the fluorescence decay follows a single-exponential profile corresponding to a single characteristic lifetime. However, many emitters exhibit multi-exponential decay, indicating multiple relaxation routes or more complex fluorescence dynamics. For example, the presence of metastable shelving states in color centers can lead to bi-exponential decay.

Depending on the local environment, the fluorescence lifetimes of quantum emitters can vary widely, ranging from a few hundred picoseconds to several microseconds. For example, single colloidal CdSe quantum dots exhibit exciton lifetimes of around 10 ns at room temperature. By adjusting the quantum dot size and the dielectric constant of the surrounding medium, the emission lifetime can be reduced to the sub-nanosecond regime [20]. Even faster emission—on the order of 100 ps has been achieved with single GaAs quantum dots at cryogenic temperatures (5 K) under strong confinement [21]. Nitrogen–vacancy centers also show characteristic lifetimes: NV^- centers in nanodiamonds typically exhibit lifetimes of $\sim$ 22 ns, while NV^0 centers show lifetimes of $\sim$ 29 ns under 540 nm excitation. Shorter lifetimes are observed in bulk diamond [22].

Among the various approaches, time-correlated single-photon counting (TCSPC) is considered the gold standard in time-resolved fluorescence measurements [23]. In TCSPC, quantum emitters are excited by a pulsed light source—typically picosecond or femtosecond lasers—and the arrival times of individual fluorescence photons are recorded by the TCSPC electronics. Simultaneously, the device registers a radiofrequency (RF) signal corresponding to each excitation pulse. By calculating the time difference between the excitation pulse (RF signal) and the detected fluorescence photon, the TCSPC system constructs a histogram of photon arrival times. Fitting this histogram yields the fluorescence decay curve. A schematic illustration of this concept is shown in Fig. 1.1.

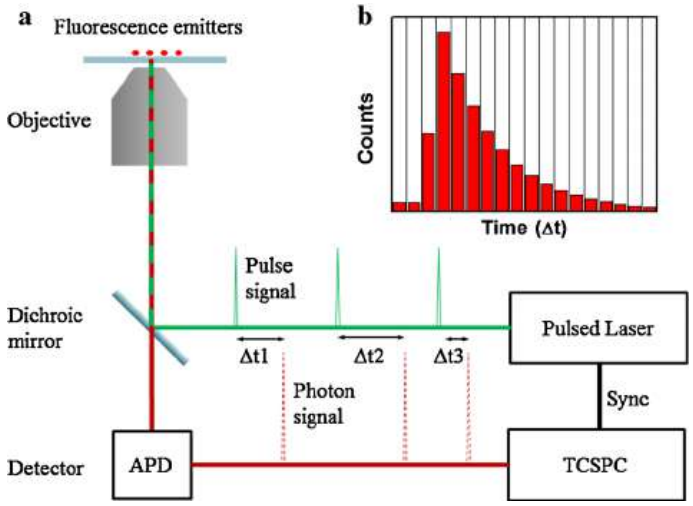


Figure 1.1: Scheme of TCSPC operation principle. [24].

Although the TCSPC electronics themselves are capable of providing a temporal resolution of a few picoseconds, in time-resolved fluorescence experiments, the actual temporal resolution is determined by the instrument response function (IRF). The IRF is mainly a convolution of the pulse width of the excitation laser, and the time jitter of the single-photon detector. The time jitter (known also as temporal resolution) describes the precision and uncertainty of registering the exact arrival times of photons. It is defined by the statistical variations in the measured time difference between the true arrival time of the photon and the time the detector registers the event. Depending on the type of single-photon detector, the time jitter can range between a few hundred picoseconds to microseconds. Nowadays commercial lasers with < 100 fs pulse widths are available. Therefore, the excitation pulse width does not play a significant role in the IRF. The time jitter, though, still remains an essential obstacle, in particular for ultrafast fluorescence emission, like from hybrid quantum systems. There are different types of single-photon detectors, each of which varies in quantum efficiency, temporal resolution, and dark count rate (DCR). Quantum efficiency is defined as the number of charge carriers generated relative to the number of incident photons on the sensor's active area. Dark count rate refers to the charge carriers generated without optical photons, due to thermal excitation. Each of these figures of merit affects the measurements in a distinct manner. While the time jitter can distort the temporal information, especially for ultrafast emission processes, photodetectors with low detection efficiency adversely reduce the maximum count rate, as they produce insufficient charge carriers. This effect becomes especially critical in photon-starving applications, such as SPSs. In contrast, photodetectors with high DCR can artificially inflate the detected count rate in ensemble measurements; or oppositely bury the number of detected photons in case of SPSs. The most commonly used single-photon detectors are photomultiplier

tube (PMT), single-photon avalanche photodiode (SPAD), superconducting nanowire single-photon detector (SNSPD), and quantum-dot field-effect transistor (QD-FET). A comparison between these detectors is provided in table 1.2.

Table 1.2: Comparison of single-photon detectors.

Single-photon det.	**Det. efficiency (%)**	**Time jitter (FWHM, ps)**	**Dark counts (cps)**
PMT	10–50	300	100–200 k
SPAD	40–80	35–500	0.008–30 k
SNSPD	50–90	30–150	1–16 k
QD-FET	2–12	10^5–10^6	0.002–150

In the following section, examples of ultrafast fluorescence emission processes will be provided, showing how the low temporal resolution of the above single-photon detectors limits their ultrafast dynamics.

1.3 Ultrafast fluorescence of quantum emitters

Time-resolved fluorescence spectroscopy is typically used to study emission processes in quantum emitters whose fluorescence decays on nanosecond timescales. However, many fundamental dynamical processes are considerably faster, occurring on picosecond (10^{-12} s) or femtosecond (10^{-15} s) timescales. These ultrafast fluorescence processes include carrier thermalization, exciton–phonon interactions, intervalley scattering, and Auger recombination. Since the radiative and non-radiative decay rates of quantum emitters can be significantly influenced by their local environment, developing time-resolved techniques that operate at such high temporal resolution is essential for gaining insight into these rapid processes.

Early studies that attempted to characterize exciton recombination dynamics in monolayer transition metal dichalcogenides (TMDs), such as WSe_2 and $MoSe_2$, were limited by the modest temporal resolution of conventional time-resolved photoluminescence systems, which typically offer timing resolutions on the order of several tens of picoseconds. With the advent of modern ultrafast methods, temporal resolutions approaching 100 fs have become accessible, enabling the observation of very fast emission decay times of approximately 3–5 ps in monolayer MoS_2, $MoSe_2$, and WSe_2 at low temperature ($T \leq 10$ K) [25]. Ultrafast fluorescence measurements have also allowed the investigation of intervalley dynamics—processes occurring on a few-picosecond timescales that determine the decay of spin and valley polarization in 2D semiconductors [26].

In semiconductor quantum dots, the presence of multi-exciton states leads to fast non-radiative recombination through Auger processes, typically occurring below the nanosecond timescale [27]. Strongly confined QDs, such as individual GaAs quantum dots embedded in quantum structures, exhibit radiative lifetimes as short as $\sim$ 100 ps, as mentioned previously [21]. Ultrafast charge-carrier dynamics in $CuInS_2$ QDs have been shown to occur on sub-nanosecond timescales [28, 29, 30]. Furthermore, time-resolved photoluminescence studies of multi-exciton CdSe QDs have demonstrated that biexcitons emit their photons within a sub-nanosecond Auger lifetime, substantially shorter than the radiative lifetime associated with their single-exciton state [31]. These examples highlight the importance of ultrafast fluorescence techniques in distinguishing between the radiative lifetimes of excitons and multicharged states, such as biexcitons.

Although optical transitions in color centers like NV and SiV centers in diamond occur on the nanosecond scale, certain internal processes are ultrafast. A notable example is the intersystem crossing (ISC) in NV^- centers—a partially non-radiative transition from the excited triplet state into a metastable singlet manifold—which takes place on picosecond timescales and contributes to the overall fluorescence decay [32, 33].

Single organic molecules have also emerged as promising platforms for photonic quantum technologies due to their narrow emission linewidths [34]. Recently, ultrafast fluorescence studies of individual terrylene bisimide (TBI) molecules embedded in a PMMA matrix have been demonstrated using a newly developed technique that integrates a wavelength-tunable ultrafast laser with a confocal scanning microscope. With sub-100-fs temporal resolution and micrometer-scale spatial precision, this approach has enabled direct probing of the femtosecond transient behavior of single molecules, revealing substantial deviations from ensemble-averaged dynamics due to variations in their local environment [35].

Hybrid quantum systems constitute another promising platform for studying light–matter interactions and developing bright single-photon sources. These systems typically consist of a single quantum emitter—such as a quantum dot or a SiV center in a diamond membrane—coupled to a nanophotonic structure, for example a gold nanocone. Proper nanocavity design enables strong confinement of the electromagnetic field, and by adjusting the emitter–cavity separation, the local photonic density of states can be controlled in a way that significantly enhances the radiative decay rate [36]. As a result, the fluorescence lifetime can be reduced to the picosecond range, in accordance with the inverse dependence of lifetime on radiative decay rate [37, 18, 38].

Throughout this review, it has become evident that conventional time-resolved

fluorescence methods relying on techniques such as TCSPC and current single-photon detectors are inherently limited by their electronic timing resolution, typically restricted to picosecond timescale. Hence, different detection techniques have been developed, in order to overcome the low IRF barrier.

1.4 Detection of ultrafast fluorescence emission

The endeavor to overcome the time resolution challenge has led to significant advances, in both, single-photon detector electronics, and optical-based ultrafast techniques. For example, SPADs with time jitter of about 35 ps have been commercially available [39]. The progress of research and development of SNSPDs has rapidly evolved, where sub-3 ps has been recently demonstrated [40]. Such advancement of SNSPD enabled reaching an IRF of 4.4 ps [41]. However, such single-photon detectors require sophisticated fabrication of the meander structure of the nanowire utilized for single photons detection. Moreover, this type of detectors demands a cryocooler, which is costly and renders the entire device bulky. Streak camera is an ultrafast optical detector that converts incident photons into photoelectrons ejected from its cathode, and swept via electrodes before being converted back into photons on a phosphor screen. It has been already employed for fluorescence emission detection [42]. In spite of its ability to reach sub-ps time resolution, streak cameras operate under vacuum. This, in turn, requires periodic maintenance, and makes the device also bulky. Also, this camera has a low signal-to-noise (S/N) ratio at IR regime, and it is difficult to synchronize with high repetition rate lasers, i.e., 1 GHz.

Recent advances in optical measurement have led to the development of several time-resolved ultrafast techniques, some relying on nonlinear sampling and others operating without nonlinear media. Among these is the femtosecond fluorescence measurement method based on two-photon interference, which combines a Mach–Zehnder interferometer with two-photon coincidence detection [43, 44]. This approach enables independent measurement of fluorescence coherence time and ultrafast pulse envelope width. Its key strengths include the absence of nonlinear crystals—allowing operation in spectral regions not covered by $\chi^{(2)}$ media—as well as low power requirements and suitability for weak fluorescence signals. Its temporal resolution is determined mainly by the precision of the delay line. However, the technique suffers from several limitations: it is highly sensitive to dark counts, requires long integration times for weak emitters, and its extraction of fluorescence lifetime depends on deconvolving an autocorrelation curve—an ill-posed problem in which multiple decay functions can produce the same autocorrelation. Consequently, it is not well suited for single-photon emitters.

Another method, designed specifically for single emitters, is the femtosecond double-excitation photon antibunching technique (FeDEx) [45]. This approach exploits the photon antibunching behavior of single-photon sources, using double femtosecond excitation pulses and analyzing coincidence ratios to determine ultrafast fluorescence dynamics. FeDEx does not require nonlinear media or intense lasers and has demonstrated sensitivity down to tens of picoseconds, with applications including measuring ultrafast energy transfer and Purcell-enhanced emission. Its major limitation is that it applies only to single emitters, since antibunching does not occur in ensembles. Additionally, the technique requires precise control of the double-pulse delay and sufficient photon counts per excitation cycle.

A more technologically involved technique is photon counting by time magnification (the time-lens or TM-TCSPC approach), which uses four-wave mixing Bragg scattering in highly nonlinear fibers to stretch ultrashort fluorescence signals into longer temporal profiles that can be resolved with standard SPAD and TCSPC systems [46]. This method provides sub-picosecond intrinsic resolution ($\sim$ 550 fs), high sensitivity down to $\sim$0.03 photons/pulse, and high conversion efficiency exceeding 97%. However, it requires a complex arrangement of synchronized pump lasers, dispersion-compensating fibers, and nonlinear components. Temporal distortions introduced by fiber dispersion must be corrected, and the system is limited by the gate pulse width and noise contributions such as spontaneous Raman scattering.

Fluorescence-lifetime Hong–Ou–Mandel (FL-HOM) sensing presents another alternative based on two-photon interference [47]. In this technique, an attenuated reference pulse interferes with fluorescence photons, and the depth and decay of the HOM dip reveal the fluorescence lifetime. FL-HOM operates at low photon numbers, requires no nonlinear media or high-power lasers, and has demonstrated picosecond-scale lifetime measurements for several dye systems. Its limitations include reliance on interferometric stability, difficulty coupling faint fluorescence into single-mode fibers, and sensitivity to the spectral bandwidth of filters, which affects both temporal resolution and interference visibility.

Frequency up-conversion, a well-established $\chi^{(2)}$ nonlinear sampling technique, mixes fluorescence with a strong gate pulse inside a nonlinear crystal to generate a sum-frequency signal that is free from background fluorescence. This method achieves sub-100-fs temporal resolution and can detect even single-photon fluorescence after upconversion [48, 49]. It is widely applicable to biophysics, mid-IR imaging, and quantum optics. However, its implementation is technically demanding because it requires satisfying stringent phase-matching conditions, which become challenging for broadband fluorescence. Thin crystals allow broader bandwidths but require high gate-pulse energies, and nonlinear crystals are expensive and susceptible to optical

damage. The setup is therefore complex and sensitive to alignment.

Finally, the optical Kerr gate (OKG) is a $\chi^{(3)}$-based technique that uses an intense laser pulse to induce ultrafast birefringence in a Kerr medium placed between crossed polarizers, thereby opening a temporal "gate" through which fluorescence can be sampled [50]. OKG offers sub-picosecond temporal resolution without requiring phase matching, and it is compatible with a wide range of Kerr media, including liquids, solids, fibers, and 2D materials. It has been used in ultrafast spectroscopy, microscopy, and even single-photon waveform measurement. Its primary disadvantage is its reliance on high-intensity gate pulses, typically produced by amplified lasers operating at low repetition rates. Achieving spatial and temporal overlap between pump and probe beams can also be sometimes experimentally demanding.

In summary, while substantial progress has been made toward achieving ultrafast fluorescence detection, the existing techniques often require cryogenic detectors, nonlinear crystals, high-power lasers, or precise interferometric stability, limiting their practicality for compact, robust, and high-repetition-rate measurements at room temperature. These constraints underline a clear need for an alternative approach, which is the focus of the following section.

1.5 Research objective

The goal of this dissertation is to propose an alternative approach for enhancing the brightness of quantum emitters through high-repetition-rate pulsed excitation. To pursue this idea, a solid-state Ti:Sa femtosecond laser operating at a 1-GHz repetition rate (producing one billion pulses per second, each of which is temporally separated with 1 ns from the consective one) will be used to increase the emission rate of quantum emitters at room temperature. This method avoids the complexity of cryogenic instrumentation and eliminates the need for intricate micro- and nanocavity structures typically used to enhance emission. Moreover, it remains compatible with realistic experimental conditions and constraints, such as the low quantum yield of many quantum emitters, the limited collection efficiency of standard confocal fluorescence microscopes, and the maximum count rate of single-photon detectors.

A key motivation for employing a gigahertz excitation source is its ability to deliver a substantially higher number of excitation events per unit time than conventional MHz lasers, thereby enabling significantly higher fluorescence count rates and improved S/N ratio. This becomes particularly important for low-quantum-yield emitters, where only a small fraction of excitation pulses result in detectable photons. To quantify this advantage more rigorously, we consider the expected fluorescence counts

per time bin in a Kerr-gated detection scheme. Assuming a fluorescence lifetime of 1 ns and a gate time resolution of 100 fs, the probability of detecting a single photon in a given time bin is on the order of 10^{-4}. This probability is further reduced by the collection efficiency of the microscope, the gating efficiency of the OKG, and the detection efficiency of the single-photon detector, but it increases directly with the repetition rate of the excitation laser. For instance, assuming a fluorescence lifetime of 10 ps, a collection efficiency of 10%, a gate efficiency of 10%, and a detector efficiency of 50%, the overall probability per bin becomes approximately 5×10^{-5}. When multiplied by a 1-GHz repetition rate, this yields an expected signal of about 10^3 counts per second (cps) per time bin, which is sufficient for reliable detection. Under identical conditions, an 80-MHz laser would yield fewer than 10^2 cps, a level comparable to the dark-count rate of avalanche photodiodes (typically 25–100 cps), making accurate measurements significantly more challenging. Thus, gigahertz excitation is essential for achieving adequate S/N in Kerr-gated ultrafast fluorescence measurements.

Ultrabright single-photon sources (SPSs) can therefore be realized when a 1-GHz excitation laser is combined with a hybrid quantum system, in which a quantum emitter—for example, a SiV center in diamond—is coupled to a nanocavity such as a gold nanocone. With an intrinsic emission lifetime of approximately 1 ns, such a system can exhibit radiative lifetime shortening down to a few hundred picoseconds through Purcell enhancement. Given the rapid timescales involved and the limitations of current detector technology, an ultrafast measurement technique capable of resolving such events is required.

Considering the advantages and drawbacks of existing ultrafast techniques, the optical Kerr gate (OKG) nonlinear sampling method has been selected for this work. Its primary advantage is that it does not require the stringent phase-matching conditions associated with $\chi^{(2)}$ processes. Although ideal quantum emitters possess narrow zero-phonon lines (ZPLs), real emitters often exhibit comparatively broad spectral bandwidths; $\chi^{(3)}$-based Kerr media impose no symmetry or phase-matching constraints and, in principle, nearly any transparent medium can serve as a Kerr medium. Nevertheless, specific requirements must be met to maximize gating efficiency. First, the Kerr medium must possess a high nonlinear refractive index n_2. Second, the medium thickness must be sufficient to accumulate a meaningful nonlinear phase shift, yet not so large that group-velocity dispersion reduces the gate-pulse intensity. Third, the gate-pulse intensity must be high but not excessive, as overly intense pulses may induce self-phase modulation and generate spectral broadening that overlaps with the probe or fluorescence signal, thereby degrading the S/N ratio. Additionally, the Kerr medium must be transparent at both the

fluorescence and gate wavelengths, and its damage threshold must exceed the applied gate-pulse intensity.

In this dissertation, an OKG operating at a 1-GHz repetition rate with sub-picosecond time resolution is demonstrated using bismuth-borosilicate (BBS) glass and thin graphite films as Kerr media, following characterization of the setup using carbon disulfide (CS_2). Each Kerr medium was chosen for specific reasons. BBS glass offers a relatively high n_2 value of approximately 10^{-18} m^2/W and a sub-picosecond response time arising from bound-electron hyperpolarizability [51, 52]. Thin graphite films, composed of several graphene layers, were selected because a single graphene layer exhibits an exceptionally large n_2, several orders of magnitude higher than in bulk materials [53]. Moreover, their minimal thickness greatly reduces sensitivity to spatial-overlap mismatch and group-velocity mismatch between pump and probe beams. The OKG signals obtained in each experiment were generated using sub-nanojoule gate-pulse energies—six orders of magnitude lower than the energies typically required in conventional OKG implementations that rely on amplified laser systems. To the best of the author's knowledge, this work demonstrates the lowest gate-pulse energies ever reported for achieving a measurable OKG signal, marking a substantial reduction compared with conventional implementations.

A distinguishing feature of this work is that, unlike conventional OKG experiments—which typically use moderate-power lasers followed by amplifiers that generate millijoule-level pulses at low repetition rates—here, the Kerr gate is driven by a high-repetition-rate (1-GHz), moderate-power Ti:sa laser. Consequently, the peak gate-pulse intensity is modest compared to that used in typical $\chi^{(3)}$ experiments. To compensate, the OKG is implemented under tightly focused illumination, guided by a semi-analytical model developed in the Nano-Optics group for maximizing Kerr-gate efficiency through careful optimization of pump and probe beam waists [54]. Furthermore, the high repetition rate increases the risk of heat accumulation in the Kerr medium, potentially leading to thermal lensing. To mitigate this, the gate wavelength must be chosen to minimize both linear and nonlinear absorption, while remaining sufficiently close to the probe wavelength to avoid excessive group-velocity mismatch. This issue is significant for relatively thick Kerr media such as BBS glass, but negligible for atomically thin media like graphene or thin graphite films. In this work, the OKG experiments were primarily performed in a degenerate configuration (same wavelength for pump and probe) and mostly in a counter-propagating geometry.

1.6 Dissertation outline

The objective of this dissertation, together with a brief state of the art of modern quantum emitters—i.e., hybrid quantum systems—and time-resolved ultrafast fluorescence techniques, has been presented here. Chapter 2 introduces the basic concepts related to fluorescence emission and the enhancement of fluorescence via increasing the Purcell factor, particularly by means of optical nanoantennas. It also presents common quantum emitters, such as QDs, color centers in diamond, ultrafast fluorescent dyes, and hybrid quantum systems. Then, the essential components of conventional confocal fluorescence microscopes, including the excitation light source, imaging systems, spectrometer, etc., are discussed. Afterwards, a detailed state-of-the-art overview of time-resolved ultrafast fluorescence techniques is provided.

Chapter 3 is dedicated to the theoretical foundation of nonlinear optical sampling. It begins with an introduction to nonlinear optics, then discusses third-order nonlinear optical susceptibility processes, and subsequently examines the theoretical aspects of various intensity-dependent refractive index phenomena, such as the optical Kerr effect and self-phase modulation. Finally, it presents a semi-analytical model for calculating optical Kerr gate efficiencies and self-phase modulation when they occur under focused illumination in a nonlinear medium.

Chapter 4 provides the experimental details involved in constructing an OKG setup. It begins with the necessary optical and electronic components, followed by the importance of CS_2, an explanation of its tensor nature, and the origin of its fast and slow nonlinear responses. The experimental results and their analysis are then presented. At the end, the results of a former M.Sc. project in the Nano-Optics group, which attempted to achieve OKG at a 1-GHz repetition rate using a single-mode fiber as a Kerr medium, are discussed, and several practical considerations for future implementations are provided.

Chapter 5 focuses on bismuth oxide–containing glasses, such as BBS glass, as Kerr media. After the introduction, the glass structure is described, and the sample preparation method is presented. The relevant third-order nonlinear optical processes—such as two-photon absorption, self-phase modulation, and the Kerr effect—are then discussed, followed by the experimental results and their analysis.

Chapter 6 is dedicated to graphene and thin graphite films. It begins with an introduction to the unique properties of graphene, followed by its crystal and band structure, the various stacking orders of graphene layers, and the Raman spectrum of graphene. An overview of sample preparation techniques is then given, with emphasis on the two widely used approaches: chemical vapor deposition and mechanical

exfoliation. Afterwards, methods for identifying the number of graphene layers in a sample—such as optical microscopy, Raman spectroscopy, and atomic force microscopy—are discussed. The chapter then covers the thermal properties and mechanisms of laser-induced damage in graphene, ending with our experimental investigation of laser-induced damage at a 1-GHz repetition rate. Finally, a literature review on self-phase modulation in graphene and optical Kerr experiments is provided, along with our corresponding experimental results.

In Chapter 7, the results obtained throughout this dissertation are summarized and discussed, followed by an outlook on future work.

Chapter 2

Quantum emitters and ultrafast fluorescence detection techniques

Studying fluorescence emission from fluorescent molecules and quantum emitters requires understanding some of the underlying basic physical concepts, which are presented in the first section. Physical properties of commonly studied quantum emitters are discussed in the second section, as well as naturally ultrafast fluorescence dyes, and emission-rate-controlled quantum emitters coupled to plasmonic nanostructures. The third section introduces the typically utilized experimental setup for the characterization of various physical properties of quantum emitters, enabling us to determine their spectra, fluorescence lifetimes, and the correlations among their emitted photons. The experimental setups discussed in this section are limited to room-temperature measurements; cryogenic and vacuum systems, which suppress phonon effects on the fluorescence spectrum, are excluded. This is because measurements at room temperature are more viable for real-life applications, i.e., quantum-based technologies. The fourth section reviews the state-of-the-art of ultrafast detection of fluorescence emission, discussing the pros and cons of each presented technique.

2.1 Fundamentals of fluorescence and fluorescence enhancement

Molecular systems vary in their configurations and in the chemical bonds that connect their constituent atoms. Substances that have rigid conjugated π-electron systems are often capable of emitting fluorescence. In conjugated π-electron systems, the electrons are typically delocalized across several atoms, thereby reducing the

energy gaps between molecular orbitals and increasing stability, which allows efficient absorption in the visible and UV. Furthermore, the rigidity of their chemical structure often favors radiative pathways for dissipating the absorbed energy.

The principles of energy absorption and subsequent light emission are also central to a wider class of systems known as quantum emitters. These nanoscale or atomic-scale systems, which include colloidal quantum dots (QDs), color centers in solids (like the nitrogen-vacancy (NV) center in diamond), and localized excitons in 2D materials (such as hexagonal boron nitride), exhibit quantized electronic energy levels. This quantization enables highly efficient, bright fluorescence, often resulting in single-photon emission—a key requirement for quantum technologies. Unlike the π-electron system, the emission energy (color) in QDs is determined by their size (quantum confinement), while in color centers, it is dictated by a point defect within a crystal lattice.

2.1.1 Perrin-Jablonski diagram

The energy diagram describing the absorption and energy dissipation pathways is referred to as Jablonski diagram, named after the Polish physicist Aleksander Jablonski, who is well known for his contributions to fluorescence spectroscopy and who developed this diagram to explain the fluorescence mechanism and kinetics [55]. Less commonly, the diagram is referred to as the Perrin–Jablonski diagram, acknowledging the significant contributions of the two French physicists Jean Perrin and his son Francis Perrin.. Jean Perrin introduced resonant energy transfer between molecules via dipole–dipole interactions [56]. His ideas were later developed by Theodor Förster between two molecules, a donor and acceptor, so called Förster Resonance Energy Transfer (FRET). Furthermore, he was the first to use molecular energy diagrams to describe the absorption and emission of light, based on which he illustrated the thermally-activated delayed fluorescence. Francis Perrin - in his PhD dissertation [57] - developed the active sphere model for fluorescence quenching.

A typical Jablonski diagram is illustrated in Fig. 2.1, in which the energy levels are classified according to their spin multiplicity, given by $2S + 1$, where S is the total spin of an energy level, and it is the sum of the electron quantum spin numbers m_{s}, where m_{s} is the quantum spin number of a single electron that takes the values $+\frac{1}{2}$ or $-\frac{1}{2}$. Accordingly, each electronic state can either be a singlet, in which $2S + 1$ is 1, when $S = 0$ (one electron has $m_{\mathrm{s}} = +\frac{1}{2}$, the other one has $m_{\mathrm{s}} = -\frac{1}{2}$); or a triplet in which $2S + 1$ is 3, occurring when $S = 1$ (e.g. one electron spin $m_s = +\frac{1}{2}$, and the other spin is $m_{\mathrm{s}} = +\frac{1}{2}$). The singlet electronic ground, first, second excited states are depicted as S_0, S_1, S_2, respectively. The first triplet state is depicted as T_1, and

each electronic excited state, S or T has vibrational energy states.

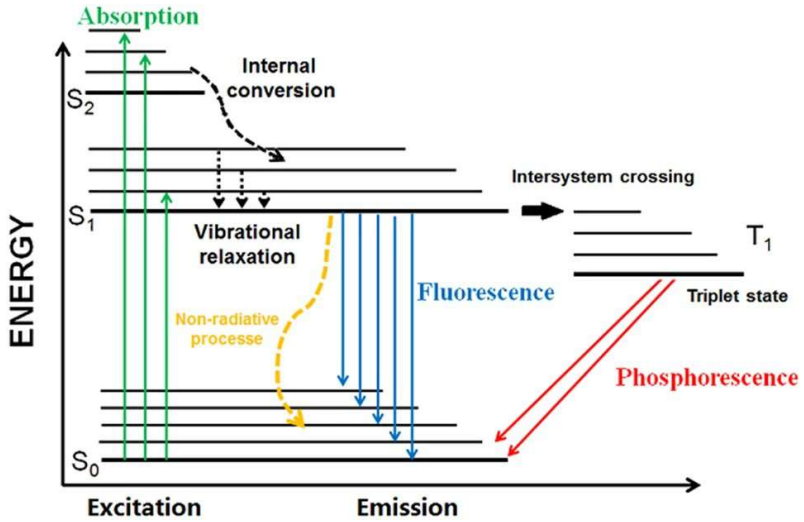


Figure 2.1: Perrin-Jablonski diagram, showing radiative and non-radiative transitions [58].

The fluorescent molecules reside typically at the lowest vibrational energy state of the ground electronic singlet state S_0. When a photon is absorbed by a molecule, an electron is promoted to one of the high vibrational energy states of the first excited singlet state S_1, or the second excited singlet state S_2. The absorption from $S_0 \rightarrow S_1$, or from $S_0 \rightarrow S_2$ occurs on a very fast timescale $\sim 10^{-15}$ s, due to the fact that electrons are much faster to respond to electromagnetic (EM) radiation, relative to the nucleus, which is assumed to be fixed in position, according to the Franck-Condon principle. The energy absorbed by a photon can be dissipated through various possible transitions. One such possible transition is internal conversion, in which the electron can cross over between energy levels of the same spin multiplicity, e.g. singlet-to-singlet, or triplet-to-triplet. Another possible transition is vibrational relaxation, where the electron in the higher vibrational energy state undergoes non-radiative decay to the lowest vibrational energy state of the excited electronic singlet state to which it was excited by the absorbed photon. In non-radiative decay, the electron loses its energy in the form of heat. At the lowest vibrational energy state of e.g., S_1, other possibilities for further transitions emerge. For instance, the electron can continue its non-radiative decay to one of the vibrational energy states of the ground singlet electronic state S_0. Alternatively, the electron undergoes a radiative transition to one of the vibrational energy states of S_0, whereas a photon at a longer wavelength is emitted from the molecule. This process is called fluorescence. Instead of fluorescing, the electron can undergo the so-called intersystem crossing, in which the electron crosses over between electronic states of different spin multiplicities, e.g., $S_1 \rightarrow T_1$. Theoretically speaking, the transition from T_1 to S_0 is spin-forbidden, nonetheless, the radiative decay can still take place, which is called in this case phosphorescence.

The time scale of this process is much longer than that of fluorescence, typically ranging from microseconds to seconds (and in some systems up to minutes).

2.1.2 Characteristics of fluorescence emission

Fluorophores or fluorescent materials emit EM radiation typically at longer wavelengths than their absorption spectra, as illustrated in Fig. 2.1, and mentioned earlier. That was first observed by Sir G. G. Stokes, who noticed that quinine solution emits blue fluorescence and absorbs UV radiation from sunlight. This is why the shift between the fluorophore's absorption spectrum and its emission spectrum is named after him. As shown in Fig. 2.2, the two spectra partially overlap, with the emission spectrum shifted toward longer wavelengths. However, a region of overlap remains that one should avoid upon selection of the excitation wavelength, otherwise, the emitted photons would be re-absorbed by the fluorophores. The reason for Stokes shift is that when the electron is promoted to one of the high vibrational energy states of the singlet excited state, it dissipates part of its energy non-radiatively as a heat. Such loss of energy leads to reduction of the emitted fluorescence photon, thereby having longer wavelength. Moreover, when the electron reaches the lowest vibrational energy level of e.g. S_1, it can undergo non-radiative transition to one of S_0 higher vibrational energy states, then loses its energy even further.

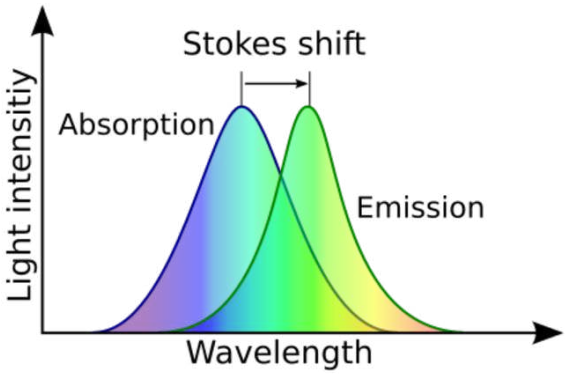


Figure 2.2: Stokes shift between the absorption and emission spectrum [59].

Another aspect of the fluorescence emission spectrum is that it is independent of the absorption spectrum. This is in accordance with Kasha's rule [60], which states that the fluorescence emission occurs from the lowest electronic energy singlet state, namely, S_1. That implies even when a high energy photon (shorter wavelength) is absorbed, and excites the electron to one of the highest electronic singlet states S_n, where $n > 1$, the electron will often relax non-radiatively till it reaches to S_1. The reason underlying this that the vibrational relaxation takes place over short timescale 10^{-12} s, as opposed to fluorescence, which ranges between several hundreds of ps

to dozens of ns. Also, there is strong overlap among different vibrational energy transitions, facilitating the fast transitions among them. Direct relaxation from higher electronic singlet states, though, happens, but rarely.

For most fluorophores, the spectrum from $S_0 \rightarrow S_1$ is a mirror image of the spectrum from $S_1 \rightarrow S_0$, due to the similarity among the transitions occurring between one singlet state of them to the other, and also to the similarity of the vibrational energy levels each singlet state possesses. An example of the mirror-image rule of absorption and emission spectrum of anthracene is provided in Fig. 2.3. Several possible transitions from the lowest vibrational energy state in S_0 to the highest vibrational energy state in S_1 yield the absorption spectrum. After the electron undergoes non-radiative transition to the lowest vibrational energy state in S_1, the electron can relax back to any vibrational energy state in S_0, thereby creating the fluorescence spectrum. Since the energy gaps among vibrational energy states in S_1 are similar to their counterparts in S_0, thus the spacing among the absorption spectrum peaks, are similar to the spacing among the fluorescence spectrum peaks. Based upon, Franck-Condon principle, the nuclei of the fluorophores are presumably fixed in position, the electron transitions are vertical, meaning no displacement from the nucleus during those transitions, as illustrated in Fig. 2.4. Accordingly, if a transition from a certain vibrational energy state in S_0 to another vibrational energy state in S_1 singlet state is likely to occur, determined by the Franck-Condon factor, the reciprocal transition to S_0 is most probable to happen.

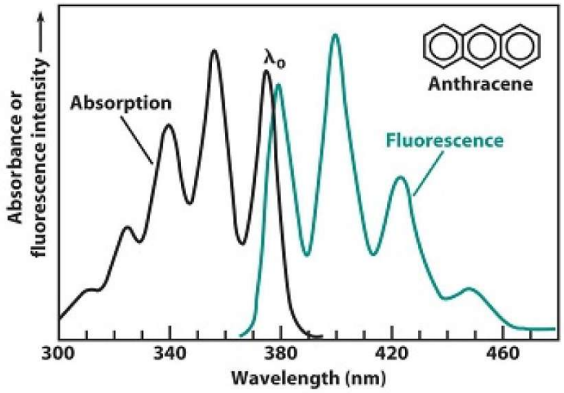


Figure 2.3: Mirror-image rule of absorption and fluorescence of Anthracene spectrum [61].

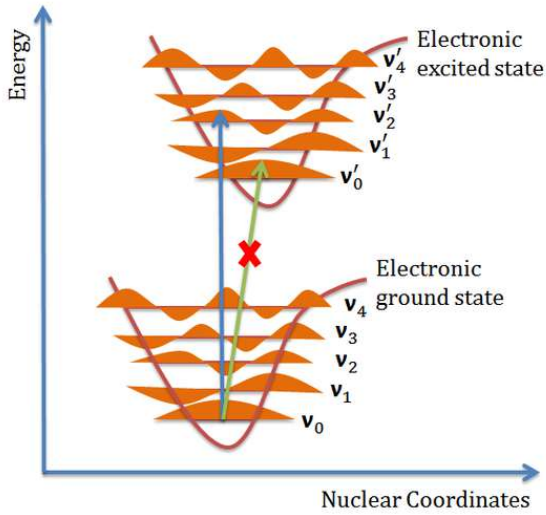


Figure 2.4: Vertical transitions following Franck-Condon principle [62].

2.1.3 Fluorescence lifetime and quantum yield

Steady-state fluorescence spectroscopy was, for many years, frequently employed to study the properties of fluorophores. Thus, the scope was to study the absorption and emission spectrum and the Stokes shift and the mirror-image between them. Later on, there has been a growing interest to study fluorescence kinetics, in particular fluorescence decay.

Basically when a fluorophore absorbs EM radiation, the electron gets excited from the lowest vibrational energy state in S_0 to one of the highest vibrational energy states in, i.e., S_1, it rapidly decays some energy in the form of heat, over $\sim 10^{-12}$ s timescale to the lowest vibrational energy state at the electronic singlet excited state S_1, as described earlier. The average time the molecule stays in the excited state before fluorescence emission is called fluorescence lifetime τ [63]. This lifetime determines the temporal window within which the fluorophore will interact with, or diffuse into its environment [55]. Having a very long fluorescence lifetime is not favorable for some applications, such as imaging. This is because the collected fluorescence intensity will not be high enough, as the number of excitation-emission cycles will not be large. The most distinct feature of fluorescence lifetime τ is that it is independent of the fluorophore concentration. Nevertheless, the local environment surrounding the fluorescent molecules, e.g., pH, or temperature could affect their fluorescence lifetimes.

In the simplest case, when the fluorophores are not interacting with each other - in contrast to the case where, e.g., two dimers are interacting with each other to form excimer, the relaxation of a fluorescent molecule residing at the excited state

happens via spontaneous, mutually independent decay mechanisms, each of which is characterized by a specific rate constant k. This is because fluorescence decay is not the only mechanism responsible for the depopulation of the excited molecules present at the first singlet electronic state S_1. Often, other processes, such as non-radiative decay and/or quenching are competing against fluorescence decay. Quenching is a mechanism, often undesirable, by which the excited fluorescent molecule favorably loses its energy via other relaxation pathways than fluorescence, thereby reducing the emitted fluorescence intensity, and its lifetime. One example of quenching effect is depicted in Fig. 2.5, in which the thioamide (quencher) decreases the fluorescence signal collected from a fluorescein dye (fluorophore), commonly used in biomedical imaging [64]. Because each decay mechanism is a spontaneous, mutually independent process, each decay mechanism occurs at a different rate constant. The fluorescence decay rate constant is called k_{f}, while the non-radiative decay rate constant is called k_{nr}. Quenching decay rate constant is called k_{Q}. Therefore, the total decay rate constant $k = k_{\mathrm{f}} + k_{\mathrm{nr}} + k_{\mathrm{Q}}$. Fig. 2.6 depicts a simplified Perrin-Jablonski diagram, in which the aforementioned decay constants are represented, including the unavoidable quenching rate of the fluorophore via its environment.

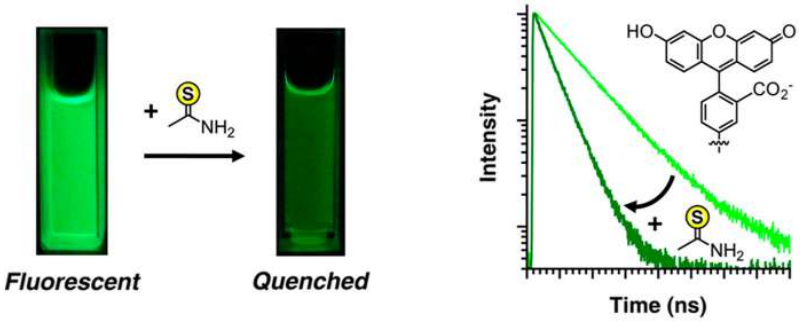


Figure 2.5: Effect of quenching of thioamide on a fluorophore, fluorescein dye [63].

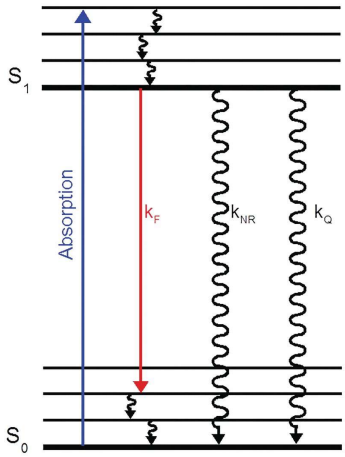


Figure 2.6: Simplified Perrin-Jablonski diagram showing various decay processes [64].

Without consideration of the process of quenching, the fluorescence decay process

can be described by first-order kinetics. This is because the rate of fluorescence is directly depends on a single reactant, that is the concentration of the fluorescent molecules [A*] at the excited state, through this first-order rate equation:

$$\text{Rate} = k[\text{A}^*], \tag{2.1}$$

where $k = k_\text{f} + k_\text{nr}$. That implies the molecule at excited state has the same probability to emit a photon, at any given instant of time. In other words, the probability of a molecule emitting a photon is independent of time. This probability holds, given the assumption that the different decay processes are spontaneous. In existence of a quencher, the decay process is truly described by second-order kinetics [65], where the rate equation becomes:

$$\text{Rate} = k[\text{A}^*] + k_q[\text{A}^*][\text{Q}], \tag{2.2}$$

where $[Q]$ is the concentration of the quencher. The kinetics is described now by a second-order rate equation, as the rate of fluorescence decay depends on two reactants, as opposed to one reactant in Eq. 2.1. In this case, it is assumed that the concentration of each reactant is comparable to the other, which gives rise to the rate of decay depending on both of them, thereby complicating the analysis of the decay process. Nevertheless, if the quencher concentration $[Q]$ is much higher, as mostly the case, than the concentration of fluorescent molecules at the excited state [A*], then one can assume that the rate constant k_q is roughly constant. Therefore, the kinetics of decay process can be approximately considered as a pseudo-first order, which simplifies the analysis, so the rate equation becomes:

$$\text{Rate} = k'[\text{A}^*], \tag{2.3}$$

whereas $k' = k_\text{f} + k_\text{nr} + k'_\text{q}$, where $k'_\text{q} = k_\text{q}[Q]$. In this case, the rate equation for excited-state decay would be:

$$\frac{dN(t)}{dt} = -kN(t), \tag{2.4}$$

where $N(t)$ is the number of excited fluorophores at time t, and k is the total decay rate constant. The solution to this rate equation gives the exponential decay rate function:

$$N(t) = N_0 e^{-kt}, \tag{2.5}$$

where N_0 is the initial number of excited fluorophores. Therefore, fluorescence

intensity $I(t)$ also follows exponential decay rate:

$$I(t) = I_0 e^{-t/\tau}, \tag{2.6}$$

where $\tau = 1/k$. If fluorescence decay is the only depopulation mechanism at S_1, then τ in Eq. 2.6 equals the radiative lifetime τ_{f}, hence the total decay rate constant k will be reduced to the radiative decay rate constant k_{f}. It is noteworthy to mention that the radiative lifetime is a unique parameter for each fluorophore, and it is independent of the fluorophore concentration. Furthermore, it is very difficult to determine τ_{f} directly from the fluorescence intensity curve, due to the presence of other competing mechanisms alongside fluorescence decay, as pointed out before.

Another important concept in fluorescence spectroscopy is the quantum yield Φ_{f}. This is basically the ratio between the number of fluorescence photons emitted by a fluorophore to the number which that fluorophore absorbed from the excitation EM radiation. If all absorbed photons were converted into fluorescence, the quantum yield Φ_{f} will be 1. On the other hand, if the fluorophore at the excited state relaxes all its energy through other pathways than fluorescence, then Φ_{f} will be 0. Typically, Φ_{f} of fluorophores vary between 0 and 1. The quantum yield can be calculated via the relevant decay rate constants of the decay mechanisms involved in the relaxation process, such that Φ_{f} can be expressed as:

$$\Phi_f = \frac{k_f}{k_f + k_{nr} + k_Q} = \frac{\tau_{total}}{\tau_f} \tag{2.7}$$

In this sense, we can see how the quantum yield is related to the fluorescence lifetime. With rearrangement of Eq. 2.7, one can express the radiative lifetime in terms of the total decay rate and the quantum yield, such that Eq. 2.7 become:

$$\tau_f = \frac{\tau_{\mathrm{total}}}{\Phi_f}. \tag{2.8}$$

Note that the total decay rate τ_{total}, as well as the quantum yield Φ_{f} must be experimentally measured in order to calculate the radiative lifetime τ_{f}. Usually a mono-exponential decay function is adequate to represent the fluorescence decay curve. Some complex cases necessitate usage of multiple-exponential decay functions for more accurate fitting of the fluorescence intensity curve behavior. Commonly utilized fluorescence lifetime measurements approaches will be presented in subsection 2.3.6. Also, a discussion of the state-of-the-art of ultrafast fluorescence detection techniques will be provided in section 2.4.

2.1.4 Second-order intensity correlation function

The quantum theory of photodetection presents a powerful tool for characterising the statistical nature of various light sources, which is particularly effective for identifying single-photon quantum emitters through the second-order intensity correlation function, $g^{(2)}(\tau)$ [66], and it is defined as follows:

$$g^{(2)}(\tau) = \frac{\left\langle \hat{E}^{(-)}(t)\hat{E}^{(-)}(t+\tau)\hat{E}^{(+)}(t+\tau)\hat{E}^{(+)}(t)\right\rangle}{\left\langle \hat{E}^{(-)}(t)\hat{E}^{(+)}(t)\right\rangle \left\langle \hat{E}^{(-)}(t+\tau)\hat{E}^{(+)}(t+\tau)\right\rangle}, \tag{2.9}$$

which quantifies the correlation between the probability of detecting a photon at time t and that of detecting another photon at a later time $t+\tau$. The numerator of this function is a joint detection probability of two photons at time t and $t+\tau$, such that it calculates the expectation-value of firstly annihilating photons $\hat{E}^{(+)}(t)\hat{E}^{(+)}(t+\tau)$ at time t and $t+\tau$, then creating photons $\hat{E}^{(-)}(t+\tau)\hat{E}^{(-)}(t)$ again to establish measurable photon correlations. The brackets $\langle\rangle$ indicate that the correlation function is measured over an ensemble of many photons. The join detection probability is normalized by the denominator consisting of the product of individual detection probabilities $\left\langle \hat{E}^{(-)}(t)\hat{E}^{(+)}(t)\right\rangle \left\langle \hat{E}^{(-)}(t+\tau)\hat{E}^{(+)}(t+\tau)\right\rangle$ at t and later at $t+\tau$, which in turn renders $g^{(2)}(\tau)$ dimensionless quantity for comparing various light sources. The function $g^{(2)}(\tau)$ can be expressed in a more compact form using the intensity quantity such that,

$$g^{(2)}(\tau) = \frac{\left\langle \hat{I}(t)\hat{I}(t+\tau)\right\rangle}{\left\langle \hat{I}(t)\right\rangle^2}, \tag{2.10}$$

whereas $\hat{I}(t) = \hat{E}^{(-)}(t)\hat{E}^{(+)}(t)$.

The most crucial value of $g^{(2)}$ is when $\tau = 0$, which represents the probability of simultaneously detecting two photons at the same time. For instance, if $g^{(2)}(0) = 1$ this would indicate that the light source is coherent, e.g, lasers, and that its statistical behavior can be expressed via Poissonian statistics, where the arrival times of photons exhibit no correlation. On the other hand, if $g^{(2)}(0) = 2$, it means the photons from the light source possess chaotic arrival times, often called photon-bunching, because photons arrive together in bunches. An example of such a light source is any thermal light source, like blackbody radiation. The photon statistics in this case is expressed by super-Poissonian statistics. Non-classical light sources exhibit correlation less than one, $g^{(2)}(0) < 1$, in which case the statistical behavior is represented by sub-Poissonian statistics and the photons' arrival times show anti-bunching behavior. Ideally, a single-photon source has $g^{(2)}(0) = 0$, nonetheless, due to other noise sources it could be slightly higher. It is a convention in the single-photon source community that a quantum emitter is considered a true single-photon source if $g^{(2)}(0) < 0.5$.

The aforementioned expression of $g^{(2)}$ function used a classical notation of the electric fields and intensity of photons. However, a quantum formulation can be used, expressed directly in terms of annihilation and creation operators in $g^{(2)}$ function, which reads

$$g^{(2)}(\tau) = \frac{\left\langle \hat{a}^\dagger(t)\hat{a}^\dagger(t+\tau)\hat{a}(t+\tau)\hat{a}(t) \right\rangle}{\left\langle \hat{a}^\dagger(t)\hat{a}(t) \right\rangle^2}, \tag{2.11}$$

where $\hat{a}$ and $\hat{a}^\dagger$ are the annihilation and creation operators, respectively. Hanbury Brown-Twiss (HBT) interferometers have been pivotal for measurement of $g^{(2)}(\tau)$ to characterize light sources, particularly single-photon sources. This type of interferometry was developed in 1954 by Hanbury Brown and Twiss for initially measuring the angular diameter of radio stars [67]. Two years later, they adapted their technique to measure correlations between photons in two coherent light beams [68], which is a paradigm shift for the study of the nature light sources based on their correlation statistics. The HBT interferometer consists of a 50/50 beam splitter (BS), two photodetectors and a time-correlator to record the time-delay between detection events. When a stream of photons impinge onto the BS, 50% of it would be reflected, while the other 50% would be transmitted, and the two photodetectors (e.g., avalanche photodiodes) lie at the output ports of the BS to detect the photons they receive. Typically, a histogram of coincidence events (number of detected photon pairs) versus time delay τ, showing how likely photons arrive together. For obtaining the $g^{(2)}(\tau)$, the coincidence counts $C(\tau)$ vs. the delay are divided by the average counts at long τ, away from $\tau = 0$.

Provided the difference between continuous laser sources (CW) that gives stable intensity over time, and the pulsed laser sources whose intensity is localized in time, the measured $g^{(2)}(\tau)$ curve will be different, depending upon which laser source is used for exciting the single quantum emitter. Whereas the CW lasers exhibit constant correlation at longer τ, with an observed dip at $\tau = 0$, while with pulsed lasers the $g^{(2)}$ curve will have peaks around arrival times that correspond to the laser repetition rate, with ideally no peak at the location where $\tau = 0$. In practice, there shall be a tiny peak at $\tau = 0$, as we pointed out before. An example illustrating the difference between $g^{(2)}$ measured with CW and pulsed excitation is provided in Fig. 2.7 for a single InAs quantum dot embedded in GaAs [69].

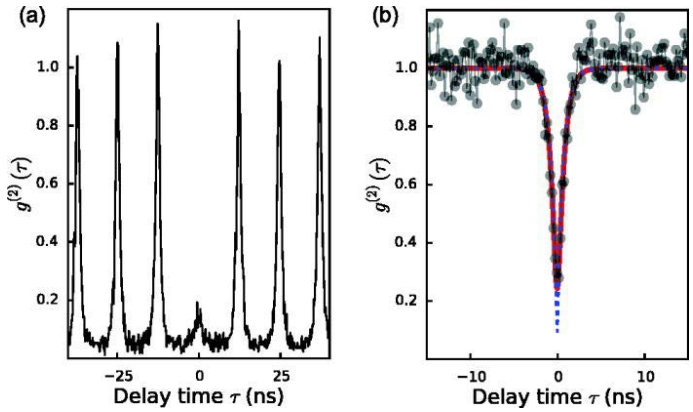


Figure 2.7: (a) Second order correlation function under pulsed excitation, (b) Second order correlation function under CW excitation [69].

2.1.5 Purcell effect and optical nanoantennas

We remember from our previous discussion that fluorescence lifetime is the average time, during which the excited fluorescent molecule stays at the first excited singlet state S_1 before decaying back to the ground singlet state S_0. And that when a fluorophore emits photons, the radiative decay - spontaneous emission - is predominantly the mechanism by which the molecule relaxes back to S_0. The spontaneous emission rate, hence the natural lifetime of an emitter is, in fact, not an absolute number. We mentioned earlier that the local environment in which the emitter is situated can enhance or suppress the spontaneous emission rate. Thus, the natural lifetime can be either shorter or longer, depending on the surrounding environment of the fluorescence emitter. Placing a fluorescent emitter into a cavity is one of the effective ways in order to control its spontaneous emission rate.

Let's consider the fluorescent emitter, for simplicity, as a two-level system and placed into a single-mode cavity of volume V_0. Single-mode cavity means that there is only one resonant cavity mode that is matched with the emission frequency of the emitter. In the weak coupling regime, which we consider here, the two-level system emitter can be treated using the perturbative approach, similar to the case in free space. The spontaneous emission rate can be obtained via Fermi's golden rule:

$$W = \frac{2\pi}{\hbar^2}|M_{12}|^2 g(\omega), \tag{2.12}$$

where M_{12} is the transition matrix element, and $g(\omega)$ is the density of states. We

can consider now that the single-mode cavity has an angular frequency ω_c with a half-width $\Delta\omega_c$, as shown in Fig. 2.8, determined by the quality factor Q, where $Q = \omega_c/\Delta\omega_c$ [70]. The quality factor Q, as the name indicates, is a factor to characterize the quality of a cavity, such that the higher the Q-factor, the longer the photon time inside the cavity, and the better that cavity can store the energy. Furthermore, the narrower the linewidth $\Delta\omega_c$, the sharper is the single-mode of the cavity.

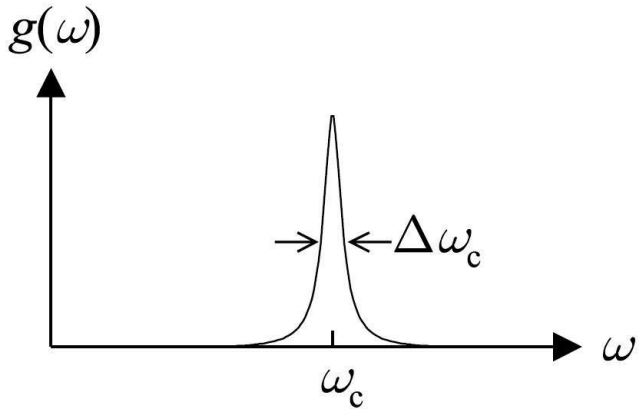


Figure 2.8: Density of states $g(\omega)$, cavity mode ω_c and its linewidth $\Delta\omega_c$ [70].

For a single mode, we have the following condition, that is:

$$\int_0^\infty g(\omega)\, d\omega = 1, \tag{2.13}$$

which is satisfied when a normalized Lorentzian function for $g(\omega)$ is used:

$$g(\omega) = \frac{2}{\pi\Delta\omega_c}\frac{\Delta\omega_c^2}{4(\omega-\omega_c)^2+\Delta\omega_c^2}. \tag{2.14}$$

When $\omega = \omega_0$, where ω_0 is the angular frequency of the atomic transition, and at the exact resonance between the cavity mode and the atomic transition, Eq. 2.14 reduces to:

$$g(\omega_0) = \frac{2}{\pi\Delta\omega_c} = \frac{2Q}{\pi\omega_0}, \tag{2.15}$$

where the quality factor relation $Q = \omega_c/\Delta\omega_c$ was used to obtain $g(\omega)$. The transition matrix element of an emitter in free space is given by:

$$M_{12}^2 = \frac{1}{3}\mu_{12}^2\mathcal{E}_{\text{vac}}^2 = \frac{\mu_{12}^2\hbar\omega}{6\epsilon_0 V_0}. \tag{2.16}$$

By substitution in Eq. 2.12, the spontaneous emission rate W for an emitter at free

space would be:

$$W \equiv \frac{1}{\tau_R} = \frac{\mu_{12}^2 \omega^3}{3\pi\epsilon_0 \hbar c^3} \tag{2.17}$$

where τ_{R} is the radiative lifetime.

By analogy to free space emission, one can define a transition matrix element M_{12} to be:

$$M_{12}^2 = \xi^2 \mu_{12}^2 \mathcal{E}_{\mathrm{vac}}^2 = \xi^2 \frac{\mu_{12}^2 \hbar\omega}{2\epsilon_0 V_0}, \tag{2.18}$$

here we define the normalized dipole orientation factor ξ, such that it is:

$$\xi = \frac{|\mathbf{p} \cdot \mathcal{E}|}{|\mathbf{p}||\mathcal{E}|}. \tag{2.19}$$

With substitution of Eq. 2.14 at ω_0 and Eq. 2.16 into Fermi's golden rule, we get the emission transition rate into cavity W as:

$$W^{\mathrm{cav}} = \frac{2Q\mu_{12}^2}{\hbar\epsilon_0 V_0} \xi^2 \frac{\Delta\omega_c^2}{4(\omega_0 - \omega_c)^2 + \Delta\omega_c^2}. \tag{2.20}$$

At this moment, Purcell factor F_{p} can be introduced, which is defined by:

$$F_{\mathrm{P}} = \frac{W^{\mathrm{cav}}}{W^{\mathrm{free}}} \equiv \frac{\tau_R^{\mathrm{free}}}{\tau_R^{\mathrm{cav}}}. \tag{2.21}$$

On substituting Eq. 2.17 and Eq. 2.20 into Eq. 2.21, we get:

$$F_{\mathrm{P}} = \frac{3Q(\lambda/n)^3}{4\pi^2 V_0} \xi^2 \frac{\Delta\omega_c^2}{4(\omega_0 - \omega_c)^2 + \Delta\omega_c^2}. \tag{2.22}$$

Note that c/ω has been replaced by $(\lambda/n)/2\pi$, where λ is the wavelength in free-space, and n is the refractive index of the medium in the cavity. If the dipole axis is fully aligned with the electric field direction at the exact resonance, Eq. 2.22 is reduced to popular Purcell factor expression:

$$F_{\mathrm{P}} = \frac{3Q(\lambda/n)^3}{4\pi^2 V_0}. \tag{2.23}$$

Purcell factor F_{p} can be used as a parameter to characterize the effect of a cavity on spontaneous emission rate of an emitter, such that F_{p} greater than 1 indicates an enhancement of emission, whilst F_{p} smaller than 1 indicates an inhibition of emission. In view of Eq. 2.22 and Eq. 2.23, we can see that the enhancement of spontaneous emission rate (i.e., radiative decay rate) dictates certain requirements to be attained. For instance, the quality factor Q of the cavity should be high, additionally, the cavity mode volume should be small. Moreover, the cavity mode should be as close

as possible to the angular frequency atomic transition, and equally important to ensure that the electric field direction is fully aligned with the dipole axis. When the cavity mode frequency is at resonance with the atomic transition frequency, the enhancement of spontaneous emission rate is caused by the relative increase of the density of states at the cavity mode frequency into which the emitter releases radiatively its energy. On the contrary, the inhibition is caused by the decrease of the density of states to which the emitter can radiate.

Antennas are ubiquitous, as telecommunication towers, as miniaturized antennas in our mobile phones, and on top of our buildings for radio and TV broadcasting. The main function of antennas is to convert the free-propagating electromagnetic radiation into localized energy and vice versa. Technically, it is a device consisting of metal rods and wires that converts electric current into EM radiation for transmission into free-space, or converting EM radiation into electric currents for receiving signals. Antennas are commonly used in the radiofrequency (RF) or microwave frequency range [71]. Besides transistors, antennas revolutionized our life, leading to the giant leap humanity undertook to advance our world through effective communications. The word "Antenna" stems from Italian language, and translates into "Aerial" in English. The word antenna was first used by Guglielmo Marconi - the inventor of radio - in the context of radio wave, when he was carrying out his first radio wireless communication. About a decade later, the word has been incorporated into English, and currently used to refer to transmission or reception of electromagnetic waves. A classical example of an antenna is the Yagi-Uda antenna, as shown in Fig. 2.9 (a), is often used for radio and TV broadcasting. Its essential function is to send and receive radio and TV signals along a certain direction, wherein the signal is strengthened due to the antenna structure. Yagi-Uda antenna consists of a driven dipole that emits and receives signals, preceded by a bit longer metallic rod than the driven dipole component called reflector to prevent the propagation of EM radiation in the backward direction via destructive interference in that direction. On the contrary, the driven dipole component is followed by a series of metallic rods a bit shorter than the driven component called directors, which constructively interfere with the EM signals in the forward direction, hence enhancing the radiation directionality into the forward direction. Owing to the directionality of radiation propagating along the antenna, the radiation has a unique pattern, indicated in Fig. 2.9 (b).



Figure 2.9: (a) Yagi-Uda antenna, (b) Radiation pattern transmitted by Yagi-Uda antenna [72].

Optical antenna is analogous to radiowave and microwave antenna but within the optical regime. However, rather than converting the EM radiation into an electrical current, it converts a freely propagating optical radiation into localized energy and vice versa between two transducers, namely the transmitter and the receiver [73]. The typical size of the transducer is smaller than the radiation wavelength λ and of the order of $\lambda/100$, i.e., an optical radiation at 500 nm, would have an antenna size on $\sim$ 5 nm, therefore optical antennas are also referred to as optical nanoantennas. In fact, fabrication of optical nanoantennas were enabled by the development of nanofabrication techniques, often by top-down approach, in particular electron-beam lithography and focused ion beam milling. Common antenna structures in radio and micro frequencies have equivalent counterparts in the optical regime. For example, the optical Yagi-Uda antenna provided in Fig. 2.10 (a) was fabricated by electron-beam lithography, and in Fig. 2.10 (b) a bow-tie antenna, fabricated by focused ion beam milling is provided. Contrary to a classical antenna, given the nanoscale of the optical antenna, the transmitter is often a quantum object, e.g., an atom, ion or a quantum dot.

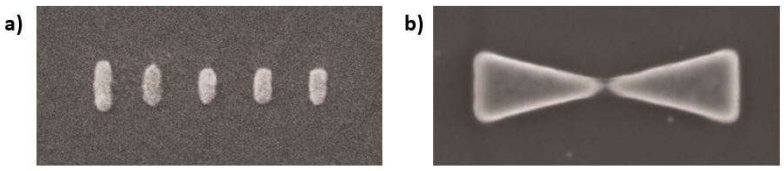


Figure 2.10: (a) Optical Yagi-Uda antenna fabricated by electron-beam lithography, (b) optical bow-tie antenna fabricated by focused ion beam milling [73].

The antenna is commonly characterized by certain parameters, such as antenna efficiency and directivity and antenna aperture. If we look at Fig. 2.11, the transmitter and receiver are modelled as dipoles, and the antenna enhances the efficiency from the transmitter to a receiver. This is achieved by increasing the radiated power P_{rad} relative to the total power dissipated by heat and other channels P_{loss} [74]. The

antenna efficiency ϵ_{rad} reads:

$$\epsilon_{\text{rad}} = \frac{P_{\text{rad}}}{P_{\text{rad}} + P_{\text{loss}}}. \tag{2.24}$$

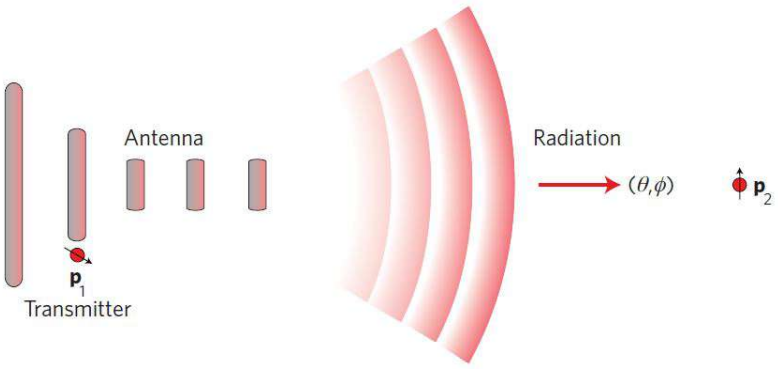


Figure 2.11: Scheme of Yagi-Uda antenna for enhancing the signal. The transmitter and receiver are modelled as dipoles [74].

To distinguish between the antenna and the transmitter, we can define the intrinsic quantum yield of an emitter as

$$\eta_i = \frac{P^0_{\text{rad}}}{P^0_{\text{rad}} + P^0_{\text{intrinsic loss}}}, \tag{2.25}$$

where the symbol 0 denotes the case when there is no antenna. Given Eq. 2.25, we can now rewrite Eq. 2.24 so that it becomes

$$\epsilon_{\text{rad}} = \frac{P_{\text{rad}}/P^0_{\text{rad}}}{P_{\text{rad}}/P^0_{\text{rad}} + P_{\text{antenna loss}}/P^0_{\text{rad}} + [1-\eta_i]/\eta_i}. \tag{2.26}$$

From Eq. 2.25 and Eq. 2.26 we can see that if the quantum emitter has no intrinsic losses, its intrinsic quantum yield η_{i} will be equal to 1, which implies that the existence of the antenna will result in reducing the transmission efficiency. Nonetheless, if $\eta_{\text{i}} \neq 1$ like in most emitters, the antenna can boost the efficiency, featuring the importance of using optical antennas for quantum-based devices. The radiated power by an antenna has distribution into specific directions, and the parameter which measures the ability of an antenna to emit radiation into certain direction is called directivity $D(\theta, \phi)$ defined as follows:

$$D(\theta,\phi) = \frac{4\pi}{P_{\text{rad}}} p(\theta,\phi), \tag{2.27}$$

where $p(\theta, \phi)$ is the angular power density. In the definition of directivity, the angular power density is normalized by an isotropic antenna, in which the power transmitted

is uniform in all directions. The efficiency of an antenna can be enhanced further by concentrating the light into a certain direction, thereby increasing the emission directivity. Combining the antenna efficiency ϵ_{rad} and the directivity $D(\theta, \phi)$, the gain G of an antenna will be $G = \mathcal{E}_{\text{rad}} D$.

The antenna has a distinct aspect, that is reciprocity. By virtue of that reciprocity, the electric field $\mathbf{E}_1$ of a dipole $\mathbf{p}_1$ (transmitter) - affects the other dipole $\mathbf{p}_2$ (receiver) and similarly the electric field $\mathbf{E}_2$ of the dipole $\mathbf{p}_2$ affects the dipole $\mathbf{p}_1$. In this regard, the antenna which is good as a transmitter is also a good receiver, and vice versa. One can write the electric fields and the dipole moments interchangeably

$$\mathbf{p}_1 \cdot \mathbf{E}_2 = \mathbf{p}_2 \cdot \mathbf{E}_1. \tag{2.28}$$

For the case in which a two-level system quantum emitter, the reciprocity gives rise to a relationship between the excitation rate Γ_{exc} and the spontaneous emission rate Γ_{rad}

$$\frac{\Gamma_{\text{exc},\theta}(\theta, \phi)}{\Gamma^0_{\text{exc},\theta}(\theta, \phi)} = \frac{\Gamma_{\text{rad}}}{\Gamma^0_{\text{rad}}} \frac{D_\theta(\theta, \phi)}{D^0_\theta(\theta, \phi)}. \tag{2.29}$$

Another important parameter to consider about antennas is the antenna aperture. It describes the effective area with which the incident radiation falls onto the antenna's dipole. For a two-level quantum emitter, the dipole's ability to absorb electromagnetic radiation is typically determined by its intrinsic absorption cross-section $\sigma_0 = 3\lambda^2/(2\pi)^2$ which sets the maximum absorption limit in the absence of an optical antenna. When an optical antenna exists, the antenna aperture is related to the absorption cross-section of the dipole and that relationship can be represented as

$$\sigma = \sigma_0 \frac{|\mathbf{n}_p \cdot \mathbf{E}|^2}{|\mathbf{n}_p \cdot \mathbf{E}_0|^2}, \tag{2.30}$$

with $\mathbf{n}_{\text{p}}$ the unit vector along the absorption emitter's dipole axis, $\mathbf{E}$ is the electric field at the detector position, σ_0 and $\mathbf{E}_0$ are the absorption cross-section and the electric field without the antenna, respectively. Note that both σ_0 and σ rely upon the direction of incidence of the electric field and the polarization direction $\mathbf{n}_{\text{p}}$. From Eq. 2.30, we see that the absorption cross-section of a quantum emitter can be significantly enhanced when placed in the vicinity of an optical antenna, provided that the dipole polarization axis $\mathbf{n}_{\text{p}}$ and the incident amplified electric field $\mathbf{E}$ are well-aligned.

The role of an optical antenna is not solely limited to enhancing the absorption of a quantum emitter via amplification of the incident electric field, improving the directivity and increasing the absorption cross-section, etc. In fact, it can also enhance the quantum emitter's emission via increasing the spontaneous emission

rate of its dipole by several orders of magnitudes. In this context, it is useful to express the optical antenna parameters in terms of optical cavity parameters, e.g., Purcell factor, quality factor and mode volume. It was pointed out earlier, that the main two relaxation mechanisms, through which a two-level quantum emitter can dissipate its excited-state energy, namely radiative Γ_{rad} and non-radiative Γ_{nr} decays. For simplicity, we shall set $\Gamma_{\mathrm{nr}} = 0$, thus the total decay rate $\Gamma_{\mathrm{tot}} = \Gamma_{\mathrm{rad}}$. Using Fermi's Golden rule, the decay rate can be expressed [75] as

$$\Gamma = \frac{2\pi}{\hbar} \sum_{\mu} \frac{\hbar\omega_{\mu}}{2\epsilon_0} \left| \mathbf{d} \cdot \boldsymbol{\alpha}_{\mu}(\mathbf{r}_0) \right|^2 \delta(\hbar\omega - \hbar\omega_{\mu}). \tag{2.31}$$

Here, it is assumed that the transition frequency ω is in resonance with only one mode $\boldsymbol{\alpha}_{\mu}(\mathbf{r}_0)$, and the dipole vector $\mathbf{d}$ is parallel to the incident electric field. After considering the optical density of states $G(\omega)$, the mode volume V_{μ} and the quality factor Q, Eq. 2.31 can be expressed as

$$\Gamma = \frac{2d^2 Q}{\epsilon_0 \hbar V_{\mu}} = F\Gamma_o, \tag{2.32}$$

where F denotes the Purcell factor. If we replace the Purcell factor F, with the local density of states (LDOS) defined as $\rho(\mathbf{r}_0, \omega) = g(\omega)|\alpha(\mathbf{r}_0)|^2$, the spontaneous emission rate would be

$$\Gamma = \frac{\pi d^2 \omega}{\varepsilon_0} \rho(\mathbf{r}_0, \omega) = \frac{\rho(\mathbf{r}_0, \omega)}{\rho_0(\mathbf{r}_0, \omega)} \Gamma_0. \tag{2.33}$$

For metal nanoparticle antenna, the field electric field near the apex of the tip of the antenna E_{tip} reads

$$E_{\mathrm{tip}} = \xi E_{\mathrm{dip}} + \mathbf{E}_0 \approx (1 - L)\chi \mathbf{E}_0, \tag{2.34}$$

where ξ denotes the so called lighting rod effect, E_{dip} is the near field due to the electric dipole induced in the antenna, χ is antenna susceptibility and L is a geometrical factor related to the antenna shape. Since the radiative decay rate $\Gamma_{\mathrm{rad}} = \eta_{\mathrm{a}}\Gamma_{\mathrm{tot}}$, the change of spontaneous emission rate would be

$$\frac{\Gamma_{\mathrm{t}}}{\Gamma_0} \simeq \left| \frac{\mathbf{E}_{\mathrm{tip}}}{\mathbf{E}_0} \right|^2 \frac{1}{\eta_{\mathrm{a}}}. \tag{2.35}$$

For better understanding of the optical properties of the antenna when coupled to a quantum emitter, we can use the polarizability model with radiative corrections [75]

$$\alpha \simeq \frac{2\pi a b^2}{3L} \frac{\omega_0}{\omega_0 - \omega - i\Gamma_a/2}, \tag{2.36}$$

here $\omega_0 = \omega_\mathrm{p}\sqrt{L/\varepsilon_\mathrm{b}}$ is the resonance frequency of the antenna, in which ω_p is the plasma frequency and $\Gamma_\mathrm{a} = \gamma + 2k^3ab^2\omega_0/9L$ is linewidth. Note that a geometrical factor L was introduced, which is related to the aspect ratio $AR = a/b$ of the antenna shape. For example, for a sphere $AR = 1$, $L = 1/3$, while for a prolate spheroid when $AR \gg 1$, L tends to 0.

The antenna efficiency can be calculated from Eq. 2.36,

$$\eta_\mathrm{a} = \frac{1}{1 + \frac{\gamma}{\omega_\mathrm{p}} \frac{9\sqrt{\varepsilon_\mathrm{b}} L \mathrm{AR}^2}{2(ka)^3}}, \tag{2.37}$$

where the term γ/ω_b represents the efficiency dependence on the material losses. From $Q = \frac{\omega_0}{\Gamma_a}$, after substitution by the antenna efficiency η_a, the quality factor can be defined as

$$Q = \eta_\mathrm{a} \frac{9L\mathrm{AR}^2}{2(ka)^3}. \tag{2.38}$$

For more direct comparison between optical antennas and nanoscale resonators, the active volume V_ph of the device, used in units of $(\lambda/n_\mathrm{b})^3$ must be included. For instance, the antenna efficiency will be expressed as

$$\eta_\mathrm{a} = \frac{1}{1 + \frac{\gamma}{\omega_\mathrm{p}} \frac{3}{4\pi^2} \frac{\sqrt{\varepsilon_\mathrm{b}} L}{V_\mathrm{ph}}}. \tag{2.39}$$

It is clear from Eq. 2.39 that the antenna efficiency drops when the physical volume V_ph decreases below 10^{-4} cubic wavelength, which is illustrated in Fig. 2.12, where the circles represent molecules, optical antennas, and resonators, respectively. Each colored circle of those optical antennas belongs to a different shape, i.e., nanospheroids (green), nanorods (red) and nanorod pairs (blue). Besides, Γ_a is heavily influenced by γ/ω_b, which is indicative of the losses in the metal of the optical antenna.

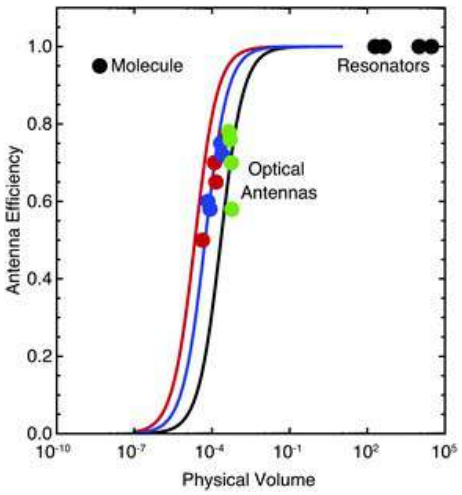


Figure 2.12: Comparison of the antenna efficiency of optical antennas versus molecules and resonators as a function of V_{ph}. The curves represent the antenna model: $AR = 1$, $\gamma/\omega_{\mathrm{b}} = 0.005$ (black), $AR = 10$, $\gamma/\omega_{\mathrm{b}} = 0.005$ (blue), $AR = 1$, $\gamma/\omega_{\mathrm{b}} = 0.005$ (red). The circles refer to resonators, a molecule and optical antennas: nanospheroids (green), nanorods (red), and nanorod pairs (blue)[75].

Another figure of merit that we express in terms of the physical volume V_{ph} of the optical antenna is the quality factor Q, where

$$Q = \eta_{\mathrm{a}} \frac{3}{4\pi^2} \frac{L}{V_{\mathrm{ph}}}. \tag{2.40}$$

Let us remember that increasing Purcell factor demands having a high quality factor Q and small volume V_{m}. As one can see in Eq. 2.40, the quality factor is inversely proportional to the physical volume V_{ph}. Fig. 2.13 shows the relationship between Q and V_{ph}. It is evident from the figure also that shrinking V_{ph} below 10^{-4} cubic wavelength does not increase the quality factor of the optical antenna further, thereby setting an upper-limit for the enhancement of spontaneous emission rate.

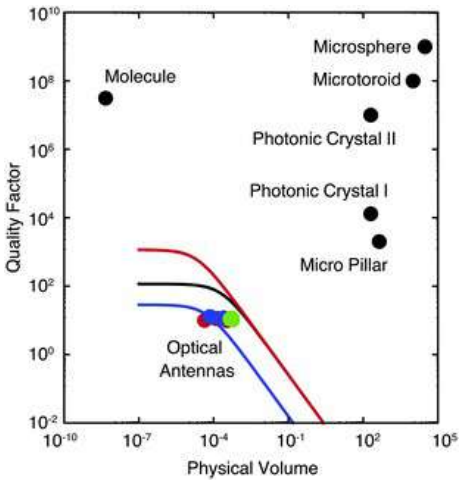


Figure 2.13: The Q factor as a function of Vph in comparison to other physical systems. The curves represent the antenna model: $AR = 1$, $\gamma/\omega_{\mathrm{b}} = 0.005$ (black), $AR = 10$, $\gamma/\omega_{\mathrm{b}} = 0.005$ (blue), $AR = 1$, $\gamma/\omega_{\mathrm{b}} = 0.005$ (red). The circles refer to resonators, a molecule and optical antennas: nanospheroids (green), nanorods (red), and nanorod pairs (blue)[75].

We can now calculate the enhancement of spontaneous emission rate by replacing $K = \left|\frac{E_{\mathrm{tip}}}{E_0}\right|^2$ in Eq. 2.35 by it is equivalent definition

$$K = \left(\frac{9}{2}\eta_{\mathrm{a}}\frac{\mathrm{AR}^2}{(ka)^3}\right)^2 (1-L)^2, \tag{2.41}$$

which eventually results in the following expression

$$\frac{\Gamma_{\mathrm{t}}}{\Gamma_0} = \eta_{\mathrm{a}}\frac{9}{16\pi^4}\frac{(1-L)^2}{V_{\mathrm{ph}}^2}. \tag{2.42}$$

The relationship between the enhancement of spontaneous emission rate $\frac{\Gamma_t}{\Gamma_0}$ as a function of the optical antenna physical volume V_{ph} is depicted in Fig. 2.14. We see that using optical antennas, a similar order of magnitude enhancement of spontaneous emission rate as in optical resonators can be attained.

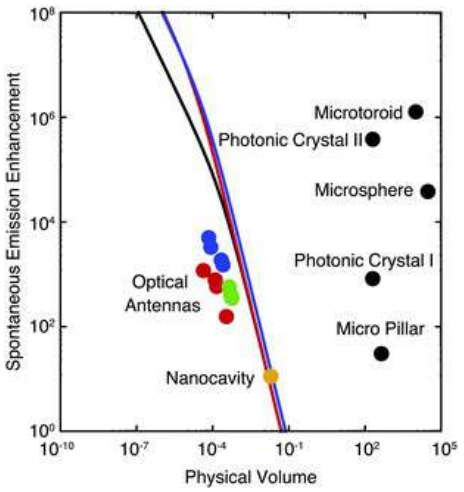


Figure 2.14: Comparison between optical antennas and nanocavities, in terms of the enhancement of the SE rate as a function of V_{ph}. The curves represent the antenna model: $AR = 1$, $\gamma/\omega_{\mathrm{b}} = 0.005$ (black), $AR = 10$, $\gamma/\omega_{\mathrm{b}} = 0.005$ (blue), $AR = 1$, $\gamma/\omega_{\mathrm{b}} = 0.005$ (red). The circles refer to resonators, a molecule and optical antennas: nanospheroids (green), nanorods (red), and nanorod pairs (blue)[75].

Mode volume V_{m} can be expressed in terms of the quality factor Q and the enhancement of spontaneous emission rate $\frac{\Gamma_t}{\Gamma}$, with the following relationship

$$V_{\mathrm{m}} = \frac{3}{4\pi^2} Q \left(\frac{\Gamma_{\mathrm{t}}}{\Gamma_0} \right)^{-1}. \tag{2.43}$$

Substituting Eq. 2.40 and Eq. 2.42 in the equation of V_{m}, we obtain

$$V_{\mathrm{m}} = \frac{L}{(1-L)^2} V_{\mathrm{ph}}, \tag{2.44}$$

which gives us a direct relationship between the mode volume of the optical antenna and its physical volume.

Based on what has been discussed so far, one can see that optical antennas-i.e., metal nanostructures such as Au or Ag-with appropriate geometrical shape and physical volume can considerably enhance the spontaneous emission rate of a two-level system quantum emitter. We recall that the faster an emitter is, the shorter the time it stays in the excited state. For slow fluorescence emission from commonly used quantum emitters, there are well-established approaches for their lifetime measurements, that shall be discussed in subsection 2.3.6 of section 2.3. This is actually because their long lifetimes corresponding to their slow emission are longer than the electronic response time of the electronic detectors often utilized in fluorescence microscopy and spectroscopy laboratories. Consequently, the instrument response function (IRF) is fairly adequate for temporally resolving their fluorescence decay. The difficulty arises when the fluorescence emission rate approaches the limit of IRF, which in turn

leads to temporal distortion of the measured lifetime signal due to the low temporal resolution enabled in that case by the IRF. Several techniques have been developed in order to overcome such limitation, each of which offer some advantages and suffer from some drawbacks (cf. Section 2.4).

2.2 Common quantum emitters

Fluorescent quantum emitters are at the core of quantum-based systems for both fundamential research and applications. This is because they can be considered as two-level atoms, which enables not only grasping deeper understanding of the foundations of quantum mechanics, but also for their promising applications that can harness the unique properties of quantum systems. Common types of fluorescence quantum emitters can be man-made solid-state systems, such as color-centers in diamond, or quantum dots; or natural systems, such as fluorescent dyes. Particular interest is devoted to ultrafast fluorescence quantum emitters, especially single-photon emitters, as they hold the promise to be the future of quantum-based applications, i.e., quantum communication, quantum information processing, that often require bright light sources at high repetition rate. This ultrafast emission can be achieved by manipulating the surrounding environment of the quantum emitter, e.g., through coupling to optical nanoantenna, forming a hybrid system with the quantum emitter.

2.2.1 Quantum dots

Quantum dots (QDs), initially named semiconductor nanocrystals (NC), are most heavily studied semiconductors at the nanoscale. Most famous of those and widely used in various applications are cadmium selenide (CdSe), cadmium sulfide (CdS), indium phosphide (InP), lead sulfide and selenide (PbS) and (PbSe), in addition to the perovskite $CsPbBr_3$ and $CsPbI_3$, notably utilized in solar cells. In the 1980s, Alexei Ekimov and Alexander Efros were investigating semiconductor-doped glasses while developing theories to explain their properties in the formerly Soviet Union, simultaneously but half a world away geographically, Louis Brus in the USA was studying semiconductor particles in liquid colloids. This led to the onset of quantum dots research and the associated theoretical studies for the interpretation of their size-dependent properties [76]. Later in 2023, both Ekimov and Brus, along with Bawendi were awarded nobel prize in Chemistry for their discovery and developments of quantum dots [77]. Size-dependent absorption of quantum dots and their luminescence spectra have been realized to be determined by the spatial confinement of their carriers, namely electrons, holes and excitons in three

dimensions (3D), which results in dramatic modification of their energy spectra. When the size of the quantum dot decreases, the lowest quantum confinement levels of electrons and holes increases, and the bandgap of optical transitions is increased [78, 79, 80, 81]. This behavior is distinct in comparison to their parental bulk solids. Owing to their quantum confinement in 3D, semiconductor quantum dots are considered having 0D, and because their electrons and holes exhibit discrete atomic-like density of states, they can be considered as artificial atoms. Such unique properties, in particular, strong absorption and narrow-band emission across the visible and infrared wavelengths, allow the design of materials with tunable chemical and physical properties [82]. The concept of quantum confinement and its effect on the energy bandgap is illustrated in Fig. 2.15.

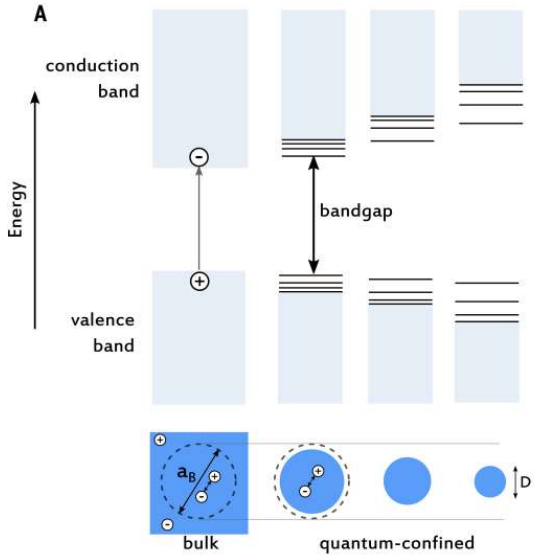


Figure 2.15: Effect of quantum confinement on size-dependent properties of QDs [82].

From Fig. 2.15, we see that as the QDs become smaller, namely experience more quantum confinement, the effective bandgap E_g increases, which leads to blue shift of the absorption and emission spectrum. Such distinct behavior particularly occurs when the spatial extent of the electronic wavefunction, determined by the QD diameter denoted by D is smaller than the Bohr exciton diameter a_B. A simple quantum particle in a box model, developed by Louis Brus, predicts the size-dependent contribution to the bulk energy gap [79], for a spherical QD with radius R, found that it is proportional to $1/R^2$, and is expressed as:

$$E_g(\mathrm{QD}) = E_{g0} + \frac{\hbar^2 \pi^2}{2 m_{eh} R^2}, \tag{2.45}$$

where E_{g0} is the bulk semiconductor bandgap energy, $m_{eh} = m_e m_h/(m_e + m_h)$ in

which m_e and m_h are the effective mass of the electron and hole, respectively; R is the radius of the spherical QD.

When an electron is excited across the wide bandgap, it experiences strong interaction with its corresponding hole in the valence band, which takes place owing to Coulomb attraction and spin-exchange coupling that produce strongly confined exciton (electron-hole pair). Multiple electron-hole pairs (multiexcitons) can be created under intense excitation of QDs, which gives rise to enhanced many-body phenomena. Typically, a single exciton is neutral in its charge state, this is because an exciton consists of an electron, which is negatively charged, and a hole, which is positively charged. Also, charged exciton states commonly occur in spectroscopic studies or during the operation of QD-based devices. Charged exciton states are formed by addition of an extra charge to the neutral exciton, and called *Trion*, given that it consists of three electric charge carriers. Based upon the type of this extra charge, a trion can be a positive trion, if the excess charge is positive; or it can be a negative trion, if the excess charge is negative. This modifies the neutral exciton's radiative decay and creates a non-radiative pathway, associated with the so-called Auger process, in which the energy of an excited exciton is not emitted as a photon, instead, that energy is imparted to the excess charge [83]. Auger recombination is a non-radiative multicarrier Auger process, where the exciton decays by transferring its energy to a third charge carrier, promoting this charge to higher energy level. This excess charge quickly loses its energy non-radiatively. Such process sometimes is called Auger decay, and it is a very efficient process in QDs and leads to ultrafast dynamics from a few to hundreds of picoseconds, depending on the size of the QDs. The high efficiency of the Auger decay process is attributed to the close proximity of the charge carriers that leads to strong Coulomb interaction, besides the relaxation of the momentum conservation. Note that the momentum conservation condition is relaxed in QDs as a consequence of the quantum confinement, because when material is confined in 3D this breaks already the crystal structure symmetry, hence the momentum does not have well-defined quantum number. A scheme for different trion's energy diagrams and their Auger recombination processes is presented in Fig. 2.16.

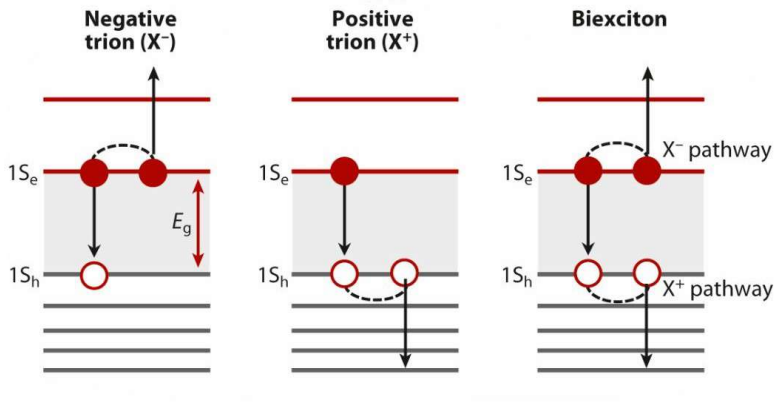


Figure 2.16: Non-radiative Auger recombination of negative trion (X^-), positive trion (X^+) and a biexciton (X^-X^+), respectively. Adapted from [84].

After excitation from the valence band, the non-radiative Auger recombination process of a negative trion (X^-) can be described by Coulomb scattering between two electrons in the conduction band, as observed in Fig. 2.16, where the decay rate of this process is k_{-1A}, hence Auger lifetime $\tau_{X^-} = 1/k_{-1A}$. The same can be realized for a positive trion (X^+) but between two holes in the valence band, where the decay rate of this process is k_{+1A}, and the associated Auger lifetime $\tau_{X^+} = 1/k_{+1A}$. Auger recombination of bi-excitons can be perceived as a superposition between two independent pathways of a negative trion X^-, and positive trion X^+. More specifically, given that a biexciton consists of two electrons and two holes, the recombination process involves re-excitation of either another electron, or another hole. The Auger decay rate of this process is $k_{2A} = 2(k_{-1A} + k_{+1A})$, and an Auger lifetime $\tau_{2A} = 1/k_{2A}$. The Auger lifetime of a biexciton is actually four times faster than the lifetime of either a positive or a negative trion alone.

QDs show superior optoelectronic properties, such as their wide tunability, narrow emission bandwidths, high brightness and high efficiency, which attracted much attention for a plethora of applications, for example, photovoltaic cells [85], display [86], biomedical imaging [87], quantum information technology [88], and many others. Fig. 2.17 displays graphically multiple quantum-dots-based applications in various fields.

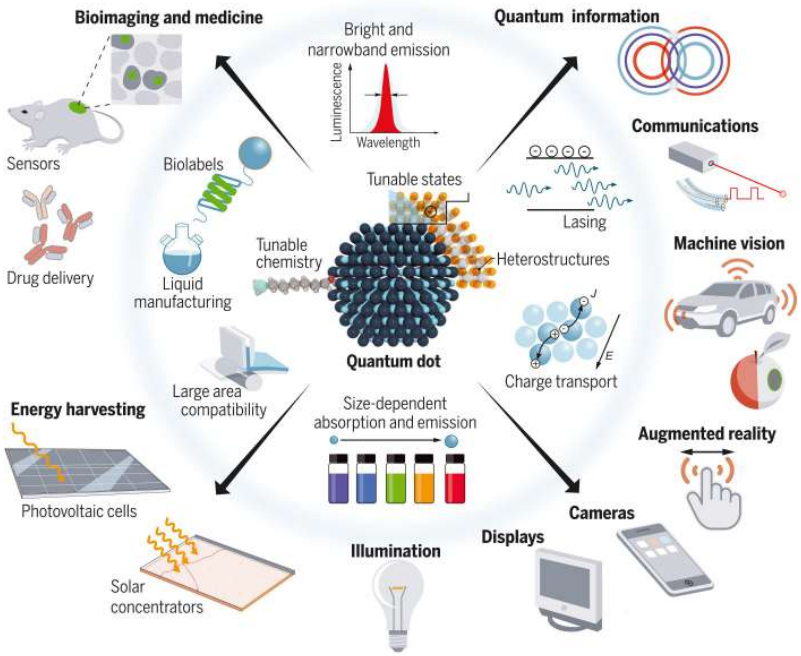


Figure 2.17: Graphical display of numerous quantum-based applications [82].

One particular application of QDs of interest for us, and aligned with the scope of this dissertation is the usage of QDs as a single-photon source. Usually, fluorescence quantum emitters are limited by their structure, whereby the fluorescence emission is often well specified at a particular wavelength, with certain bandwidth. Nonetheless, QDs can be fabricated in a controllable manner, such that their absorption and emission spectra are tuned, as mentioned previously, according to the desired application. Moreover, their emission process can be initiated either by electrical excitation, or via optical excitation. The former aspect, particularly, lured the scientific community to investigate QDs for potential optoelectronic devices, where quantum dots-based single-photon sources could be feasibly integrated and provide wide spectral coverage. By analogy to electrical bits, when a single QD emits a photon, this is equivalent to "On" state, and the QD represents "1", on the contrary, when no photon is emitted, this is equivalent to "Off" state, and the QD represents "0". Under continuous excitation of a single QD, a stream of photons will be emanating from the QD, provided that its quantum yield is maximal. Nevertheless, single QDs can sometimes exhibit blinking of their emitted fluorescence, sometimes also referred to as fluorescence intermittency, where for certain time intervals the single QD is at "On" state, whilst at some other time intervals it is at "Off" state. This phenomenon occurs exclusively in single QDs and was first reported for CdSe QDs [89], as shown in Fig. 2.18, in which fluorescence photon counts from a single 0.2 nm radius nanocrystals of CdSe, coated with 4 layers of ZnS were measured with 40 ms sampling interval, and excitation intensity of $\simeq$ 520 W/cm^2.

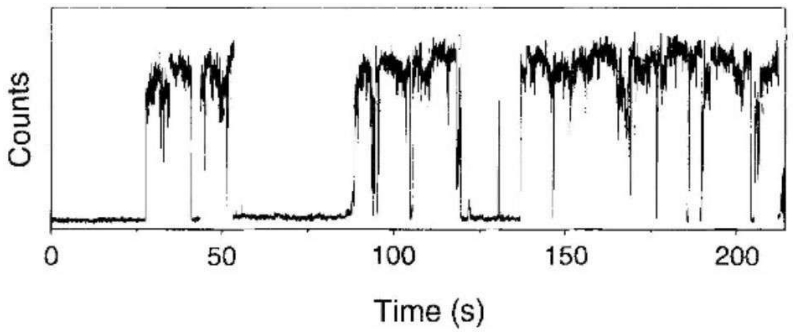


Figure 2.18: Fluorescence intermittency of single CdSe nanocrystals [89].

Fluorescence intermittency is attributed primarily to two main mechanisms, one is by surface-trap mediated non-radiative recombination, and second is by Auger recombination. QDs acquire a large surface-to-volume ratio, and their surface could have some defects, or dangling bonds, in which a charge carrier electron/hole might be trapped. In this case, this charge carrier will recombine but its energy will be dissipated as heat (non-radiative decay). In Auger recombination, as discussed above, when an exciton is created upon excitation, after some time, the electron-hole pair rather than recombining by emitting a fluorescence photon, the energy of the exciton is imparted to a third charge, which later dissipates it non-radiatively. Therefore, when a single QD is at the "On" state, the electron-hole pair loses its energy by emitting fluorescence photons, whilst when it is at the "Off" state, the energy is dissipated non-radiatively [90]. Fluorescence blinking is unfavorable considering a single QD used as a single-photon source, since this source will be unstable, rendering it considerably inefficient, especially for some applications like quantum communications. There are already some approaches that attempt to mitigate the effect of blinking. For instance, through chemical routes by adding a shell to the core structure of the QD, preventing the charge carriers from reaching the surface of the QD [91]. An alternative approach, recently developed [92], to control fluorescence blinking of CdSe/CdS in which ultrafast mid-Infrared (MIR) $\simeq 5.5$ μm laser pulses are employed to generate strong electric fields that stimulate (quantum) tunneling of the excess charge, leaving only the exciton. The advantage of using MIR pulses with moderate E-field strengths is that they enable stimulation of quantum tunneling of the extra charge of the trion, without creating new excitons.

Single-photon sources from QDs have achieved rapid progress. For example, Bounouar (2012), et al. [93] demonstrated a single-photon source at room temperature from an epitaxially-grown ZnSe/CdSe QD positioned on a ZnSe nanowire, whereas they found out that the biexciton is more appropriate transition for single-photon emission, with intrinsically short radiative decay time of 300 ps, owing to the large non-radiative decay of the excitons to the dark states. This SPS has the potential for

GHz rate emission, which renders it potentially suitable for quantum information and communications. A single-photon emission, nearly blink-free, from a colloidal InP/ZnSe QDs was achieved by Chandrasekaran (2017) et al. [94], where the QDs exhibited photostability at strong optical excitation. An investigation of an ensemble of 25 QDs showed that the PL lifetime of those QDs are 22.5 ns on average. Additionally, it has been proven that those QDs exhibit photon antibunching when irradiated with a CW laser at 445 nm, as well as a picosecond at 10 MHz pulsed laser also at 445 nm. Recently, colloidal perovskite QDs have emerged as promising SPSs for quantum information applications. For example, a weakly confined hybrid organic-inorganic perovskite (HOIP) QD was synthesized and used at room temperature. In particular, this HOIP was an 11 nm $FAPbBr_3$ QDs that showed superior single-photon emission with $g^{(2)}(0) < 0.07 \pm 0.03$ in the work of Wang et al. [95], with nearly blink-free emission. For scalable photonics devices capable of emitting single photons, electrically-driven single-photon sources from QDs have been pursued. For example, in Lin et al. [96], a device for generating single photons was reported, where isolated colloidal CdSe/CdS core/shell QDs (10 nm in diameter) were buried in an insulating Poly(methyl methacrylate) (PMMA) layer, sandwiched between an electron-transport layer and a polymeric hole-transport layer, see Fig. 2.19. According to their claim, their device can generate single photons with near-optimal antibunching at room temperature, with $g^{(2)}(0) < 0.05$ without spectral filtering or background correction.

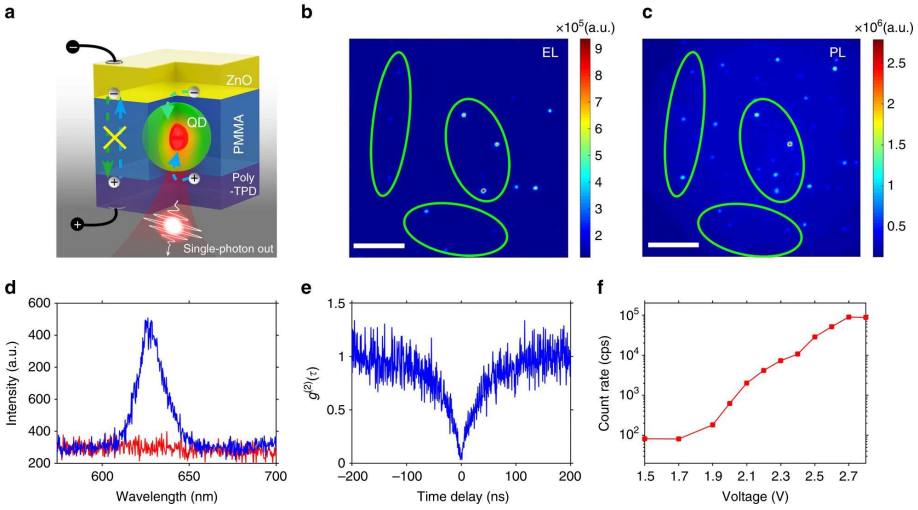


Figure 2.19: (a) Schematic diagram of the device, (b) Electroluminescence driven at 2.4 eV of QDs, (c) Corresponding photoluminescence excited by CW laser at 450 nm. (d) Electroluminescence spectrum [blue curve] (driven at 2.8 V) and detector's noise counts [red]. (e) $g^{(2)}(\tau)$ of QD driven at 2.6 V. (f) Average electroluminescence counts of single QD driven at different voltages [96].

That work in particular represents significant achievement as the electrically-driven

QD SPS operates at room temperature. Previous works with QDs as SPSs were achieved at cryogenic temperatures [97, 98, 99, 100]. For a very recent coverage about the current advances, challenges and future direction of single-photon generation from QDs, we refer the reader to ref. [101].

2.2.2 Color centers in diamond

Natural diamond is a mineral extracted from underground mines and is well-known in layman culture as a glamorous gemstone. Besides, it is favorably used as a cutting tool, since diamond is the hardest material ever known. Under certain conditions, synthetic diamonds can be fabricated and used for other purposes, too. Diamond is essentially a carbon allotrope, and is a highly crystalline material. It has some unique physical and chemical properties, e.g., optical transparency, high thermal conductivity, high refractive index, and surface inertness at room temperature. The crystal structure of diamond is formed as tetrahedral sp^3-covalent bonding of carbon atoms with four nearest neighbours in a cubic lattice, as shown in Fig. 2.20. This structure allows for forming {111}, {110}, {100} facets in a single crystal.

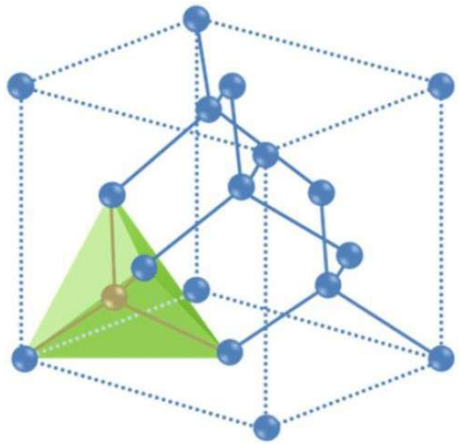


Figure 2.20: Cubic lattice crystal structure of diamond [102].

Diamond is one of the wide-bandgap semiconductor materials with 5.5 eV bandgap (corresponding to 225 nm deep-UV). It is optically transparent within the range 400-750 nm wavelengths. The coloration often observed with natural diamonds is associated with the impurities (defects) in the diamond [102].

Color centers are defects/impurities embedded in diamond and are a promising platform for quantum science and applications. In particular, they can be good candidates for achieving on-demand single-photon sources at room temperature [103]. The origin of color centers in diamond stems from various resources, for example, they can exist due to dislocations or stacking faults in the diamond crystal lattice,

or point defects, i.e., intrinsic impurities, extrinsic dopants, or vacancies [104]. Due to its unique physical and chemical properties, diamond is, in fact, an excellent host for color centers. Consequently, there are around 500 color centers lying within the spectral range between 170 up to 20000 nm, which cover wide spectral regions from vacuum UV to mid-IR. Some examples of those color centers in diamond are H, He, Ni, Co, N, Si, Li, B,.. just to name a few [105]. Those elements alone do not form color centers in diamond. Instead, they are bound to adjacent vacancies existing in the diamond crystal lattice.

The wide-bandgap of diamond allows accessible large energy ranges for discrete, impurity-induced energy-levels to be formed into diamond's bandgap. This enables fluorescence emission from optically active impurities over a large spectral range. Ideally, fluorescence emission is considered purely between electronic energy states, where phonons, which are quantized crystal vibrations, do not contribute to fluorescence emission, *zero-phonon-line* (ZPL). As a matter of fact, at cryogenic temperatures, where the phonons are mostly suppressed, pure emission from ZPL can be achieved. At room temperature, though, low-energy contributions from density of states of phonons influences the fluorescence emission linewidth from the electronic transitions. As a result, fluorescence emission from ZPL is not sharp, since the phonon sidebands broaden the emission bandwidth, especially when the phonon coupling with the impurity in diamond is strong. Most of the phonons in diamond are high energy phonons due to the stiffness of its crystal lattice, and those are not easily thermally populated. This implies that low-energy phonons play a minor role, meaning sharp fluorescence at room temperature remains possible [106]. Measurement of the electron-phonon coupling can be carried out with one of two interrelated ways. One, by Debye-Waller factor (DW), which is defined as the integrated luminescence intensity from ZPL, $\mathrm{I_{ZPL}}$, divided by the integrated total luminescence of the color center I_{tot}, such that $\mathrm{DW} = \mathrm{I_{ZPL}}/\mathrm{I_{tot}}$. The $\mathrm{I_{tot}}$ refers to the total integrated luminescence intensity from ZPL and phonon sidebands, and DW factor informs how much of fluorescence emission stays in ZPL, indicative of the purity of the optical transition. Second, through Huang-Rhys factor (S), defined as $\mathrm{I_{ZPL}}/\mathrm{I_{tot}} = \exp(-\mathrm{S})$, alternatively $\mathrm{S} = -\ln(\mathrm{DW})$. Evidently, the left-hand side represents the DW factor. The S factor is, in fact, a measure of the coupling between the electronic transitions and phonons. It informs about how much luminescence/fluorescence is spread into phonon sidebands.

Among the plethora of color centers in diamond, two color centers in particular, have been intriguing for detailed study and rapidly become the focus for tangible solid-state quantum systems. Those are the nitrogen-vacancy (NV) color center and silicon-vacancy (SiV) color centers. Nitrogen-vacancy (NV) was identified, for the

first time, as a major impurity in Type I diamond by Kaiser et al. [107]. Diamond crystals are commonly classified by Type I, which represent the majority of diamond crystals ($\approx$ 95% of diamonds), and Type II, which are rare, according to their differences in infrared and ultraviolet transmission. The rare Type II diamond has absorption bands between 3000 and 6000 nm only and a sharp absorption edge in UV below 225 nm. In addition to acquiring similar absorption band of Type II, Type I diamond crystals exhibit an additional absorption band between 6000 nm and 13000 nm, and a tail on the absorption edge, which vary from specimen to specimen. Thirty-eight years later, single NV defect centers were observed for the first time by Gruber et al. [108], at room temperature. The emission spectrum of single NV centers is shown in Fig. 2.21.

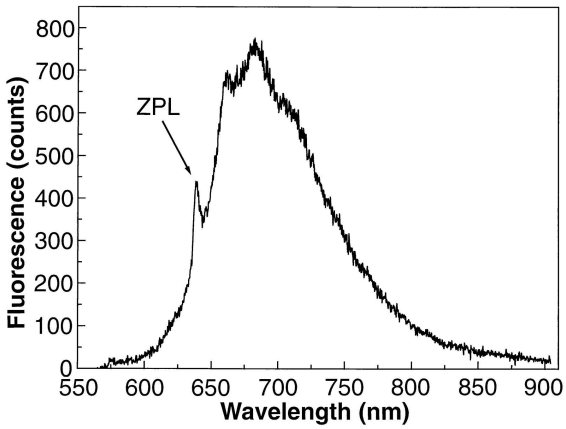


Figure 2.21: Fluorescence emission spectrum of individual NV centers [108].

The individual NV centers in diamond were excited at 514 nm, and fluorescence was emitted from ZPL at 637 nm. The single NV defect centers exhibited photostability and optical detection of magnetic resonance (ODMR) was feasible. In the year of 2000, two groups [109, 4] demonstrated single-photon sources at room temperature from single NV centers in diamond. The photon antibunching nature of the individual NV color centers was confirmed in both works via the measurement of second-order correlation $g^{(2)}$ function. The NV color center in diamond consists of a nitrogen ion and one adjacent vacancy, see the inset of Fig. 2.22, and mostly known with two charge states, negatively-charged nitrogen vacancy NV^-, and neutrally-charged nitrogen vacancy NV^0, each of which has a distinct fluorescence spectrum, see Fig. 2.22 [110].

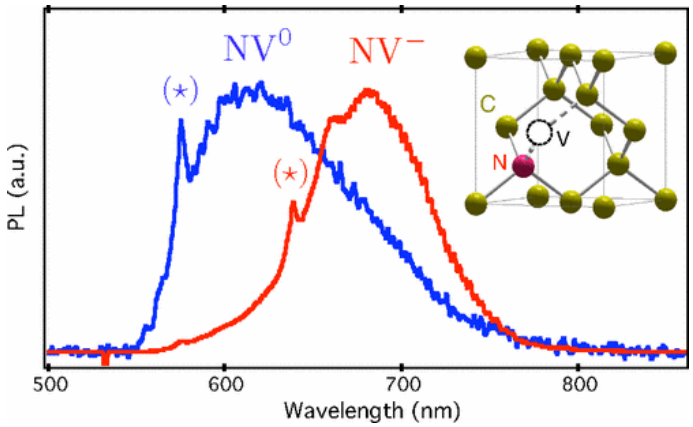


Figure 2.22: Normalized PL spectra of single NV^0 center (blue) and single NV^- center(red). Location of ZPL of each charge state is marked with $(*)$, NV^0 at 575 nm and NV^- at 637 nm, respectively [110].

The NV^- center has been employed for most of the single-photon source experiments with a ZPL at 637 nm. It has been demonstrated that the charge state of single NV^- centers temporarily changes to NV^0 with a ZPL at 575 nm, which is known as photochromism [111].

Because NV centers have strong electron-phonon coupling, the emission band spans roughly 100 nm, and only 4 % of emission is emitted at ZPL, the rest is spread into phonon sideband [112], and this is considered disadvantageous for single-photon sources. Nevertheless, NV color centers are still vital for quantum applications as qubits due to their very long coherence time, as demonstrated here [113, 114]. The lifetime of the NV center in bulk diamond is 11.6 ns, and can roughly be doubled in nanodiamond [115] due to the modified local density of states.

Silicon vacancy (SiV) is another attractive color center in diamond, which holds great promise for quantum-based applications. Unlike NV centers, the SiV color center consists of a Si ion situated between two adjacent vacant carbon lattice sites, see the inset of Fig. 2.23 (a). In total, 10 electrons are associated with this color center, which has neutral charge SiV^0. The SiV^0 can capture an extra electron, to be associated eventually with 11 electrons, and become negatively charged SiV^- complex. This extra electron remains unpaired resulting in an effective spin of $\frac{1}{2}$ [116]. The SiV^- center emits its fluorescence at 737 nm, while SiV^0 has much weaker fluorescence at 940 nm [117].

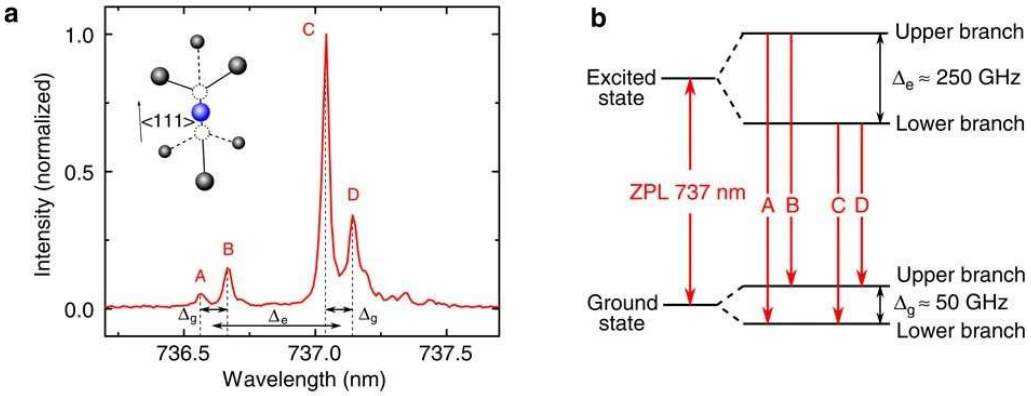


Figure 2.23: (a) fluorescence spectrum of SiV^- at 4 K, and its atomic structure in the inset, (b) energy-diagram with four fine structure transitions [116].

At cryogenic temperature, the ZPL of SiV^- splits into four fine-structure transitions, labeled from A to D, due to the split of the ground and excited states, caused by spin-orbit coupling. Note that the splitting in the excited state Δ_e is 5 times the splitting in the ground state Δ_g, and that each of the four fine structure transitions has different intensity, with C transition having the highest intensity. It is clearly indicated in Fig. 2.23 (b) that this transition, in particular, occurs between the lower branch of the ground state and the lower branch of the excited state.

At room temperature, SiV^- color center has low electron-phonon coupling with the diamond lattice, so as a result more than 70% of the fluorescence emission is concentrated in its narrow ZPL with 0.7 nm bandwidth, shown in Fig. 2.24, at 738 nm. In fact, the ZPL emission line can vary between 730-750 nm, affected by the mechanical stress in the host matrix, i.e., nanodiamond, and the emitted fluorescence is fully linearly polarized [118].

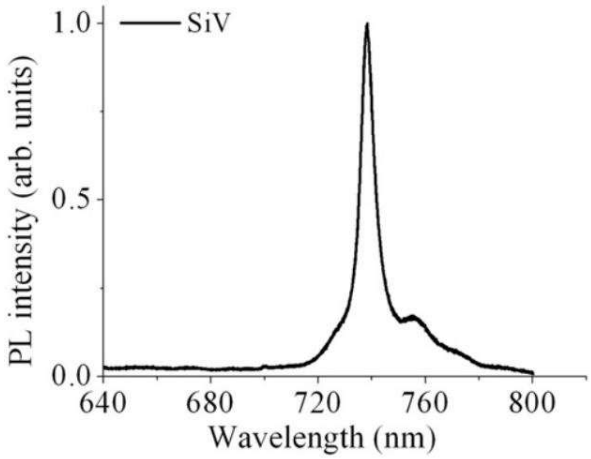


Figure 2.24: Photoluminescence intensity of ZPL of SiV at 738 nm with phonon sidebands at room temperature [119].

An important figure of merit for single-photon sources is their photon count rates upon saturation by excitation light. Fluorescence count rate, I, depends on the excitation power P, as expressed by the following relationship:

$$I = I_{\infty} \frac{P}{P + P_{\text{sat}}} \tag{2.46}$$

where the fitting parameters are I_{∞}, which is the maximum obtainable count rate, and P_{sat} is the saturation power, respectively. Achieving saturation at low excitation power for a certain emitter indicates a very efficient excitation path [120]. Another aspect quite related to the photon count rates, hence the single-photon source brightness, is the fluorescence lifetime. The shorter the fluorescence lifetime, the more photon counts one can get from the single-photon source. SiV^{-} color centers exhibit short lifetime in comparison to NV centers, where SiV^{-} centers show $\approx$ 1.55 ns fluorescence lifetime at T= 0 K, while this value gets down to $\approx$ 1 ns at room temperature [121]. The lifetime of quantum emitters can be shortened so that they exhibit ultrafast fluorescence emission, brighter single-photon source, as will be discussed in subsection 2.2.4.

Despite diamond material contains intrinsically (as-grown) color centers embedded into its crystalline structure, on-demand fabrication of specific color centers is also possible using various fabrication techniques, most commonly used are high-pressure high-temperature (HPHT) method, ion implantation, chemical vapor deposition (CVD), and less commonly followed fabrication approaches but rapidly growing are detonation and laser writing and activation of color centers. The HPHT technique mimics in fact the natural synthesis process of diamond, by artificially exposing a carbon-rich precursor to high pressure, up to 20 GPa and high temperature, up to 3000 K, whereas the amorphous carbon precursor is turned into crystalline nanodiamond [122], or single crystal diamond [123]. During the synthesis process, a dopant precursor for the color center to be created, e.g., silane-functionalized adamantane [124] for SiV creation, or from substitutional nitrogen atoms as N_s defect contained in a nitrogen-rich carbon aerogel precursor [125], or doped via infiltration of atmospheric air [126] present into the HPHT fabrication device, which is so-called diamond anvil cell (DAC). Inside the DAC, a high pressure is exerted on the carbon precursor and dopants, and high temperature is achieved via laser heating. The HPHT technique cannot grow thin diamond membranes or finely control the structure of diamond. Here, CVD technique comes into play, which enables fabrication of high-quality diamond samples that can be spin-free [113]. Typically in CVD method, a gaseous precursor like hydrogen H_2 and carbon source, e.g., methane CH_4 are mixed into a low-pressure reactor. A microwave or hot-filament creates a plasma, which dissociates the gases into reactive species, and the diamond is created

onto a substrate, such as single-crystal diamond wafer. For incorporating a color center into the diamond, either a silicon-containing gas precursor such as silane can be introduced during the diamond growth [127], or by using a quartz or silicon substrate, which are sometimes used for growing the diamond. Alternatively, Si ions can be incorporated via irradiation, often called ion implantation technique, which is widely utilized for fabrication of color centers in diamond, in particular NV and SiV centers. In this technique, the target diamond material is bombarded by a focused beam of ions or electrons, creating vacancies by knocking out some carbon atoms from their lattice sites in the diamond crystal. This procedure alone is not sufficient for creation of active color centers, where the bombarded ions bond with some vacancies in their vicinity. That's why annealing at high temperatures, e.g., $\sim$ 900 °C is required for efficient color center formation [105]. It is crucial for some quantum-based applications, in particular those of single-photon sources to fabricate color centers in a controllable manner, so that scalability of quantum devices could be attained. Precise fabrication of NV and SiV have been achieved via ion implantation, as shown in Fig. 2.25 (a) for NV centers [128], and in Fig. 2.25 (b) for SiV centers [129].

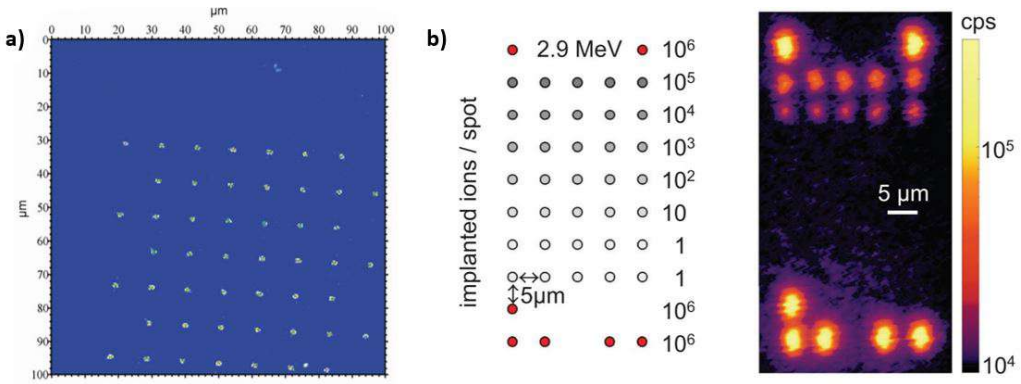


Figure 2.25: Fluorescence image of NV implanted at 2 MeV [128], (b) Fluorescence image of implanted matrix of SiV color centers [129].

For a comprehensive review about the fabrication techniques of color centers, the reader is referred to the following articles: for CVD diamond fabrication [130], for fabrication of single color centers in general [131], and for fabrication techniques of SiV in particular [132].

2.2.3 Ultrafast fluorescent dyes

Ultrafast fluorescence emission is not exclusive to QDs or color centers in diamond. Some dyes, either natural or synthetic exhibit ultrafast emission, as well, at picosecond timescales. They are used for some applications, however, they also serve as a testbed

for newly developed ultrafast time-resolved techniques. In turn, those new techniques could serve for the fundamental study of those dyes, in order to grasp a better understanding of them. For instance, Allura red AC is a synthetic dye approved to be used as food colorant and in pharmaceutical products in the US, and also used as a fluorescence probe of microviscosity [133]. In low-viscosity media, this dye has weak fluorescence that is often negligible, or undetectable. Nonetheless, as the viscosity of the medium increases, the quantum yield of Allura red AC dye increases, along with the emission intensity and the lifetime. The emission wavelength of Allura red AC dye is 590 nm [134]. Some studies have revealed that Allura red AC exhibits molecular rotor behavior, which is why its fluorescence is sensitive to the viscosity of the environment. A hallmark of molecular rotors is that the excited state can undergo intramolecular twisting, which opens non-radiative decay pathways and quenches fluorescence [135]. When Allura red AC is in low viscous fluid, e.g., water, such twisting of the excited-state takes place readily quickly. As a result, Allura red AC has ultrashort fluorescence lifetime $\sim$ 12 ps , see Fig. 2.26 (a). On the other hand, if it is in a high viscous fluid, like glycerol, the intramolecular twisting is considerably hindered, leading to slower, yet picosecond, ultrafast emission $\sim$ 231 ps, see Fig. 2.26 (b).

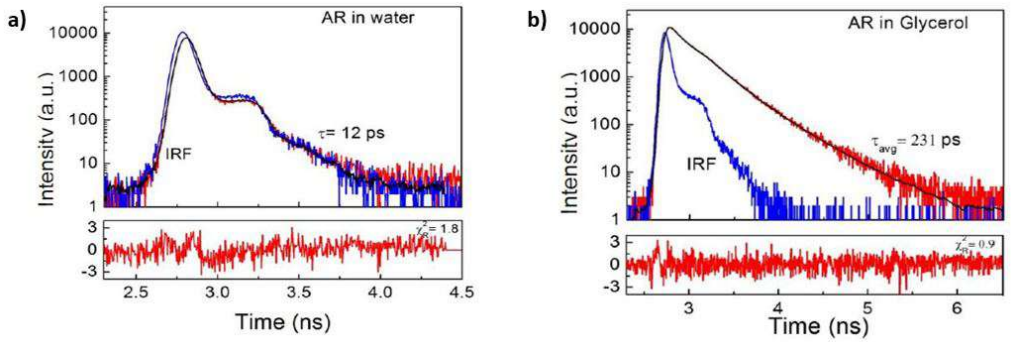


Figure 2.26: Fluorescence lifetime of Allura Red AC in (a) water and (b) in glycerol [135].

β-carotene is another pigment but natural, and it is important for the photosynthesis process. It plays the role of light-harvesting pigment in plants due to its large oscillator strength in the visible range, and its efficient singlet energy transfer to chlorophyll [136]. The fluorescence emission spectrum of β-carotene was reported and its peak emission is at 513 nm. The fluorescence lifetime of β-carotene was measured in different studies and under different conditions. One can notice a disparity among the reported results, which can be attributed to using different solvents, measuring under different temperatures, as well as carrying out the measurement via different techniques. For example, it was found that the lifetime decay from S_2 to S_1 state is 195 fs across all emission wavelengths [136], and the lifetime of S_1 state is 10 ps.

By contrast, Bachilo and Gillbro reported S_1 state lifetimes of 10 ps at 293 K and 20 ps at 77 K, respectively [137]. Anderson et al. [138] found that based on the number "N" of conjugated C = C bonds in the β-carotene, the lifetime of S_1 state can vary, for example, they revealed that for mini-8-β-carotene ($N = 8$) the S_1 state lifetime was 100 ps at 293 K and 280 ps at 77 K, and found it to be 60 ps at 293 K in toluene and 130 ps at 77 K in 3-methylpentane for mini-9-β-carotene ($N = 9$). In stark contrast to measured S_1 lifetime values, Dalinger et al. [139] reported < 1ps lifetime for β-carotene, measured by resonance-enhanced Raman spectroscopy and transmittance studies.

Another dye known with its ultrafast fluorescence emission is the photoexcited hemicyanine dye, trans-4-[4-(dimethylamino)styryl]-1-methylpyridinium iodide, commonly abbreviated 4-DASPI. The structure of 4-DASPI consists of an electron-donating group, an electron-accepting group connected via a conjugated vinylene bridge, which is illustrated in Fig. 2.27.

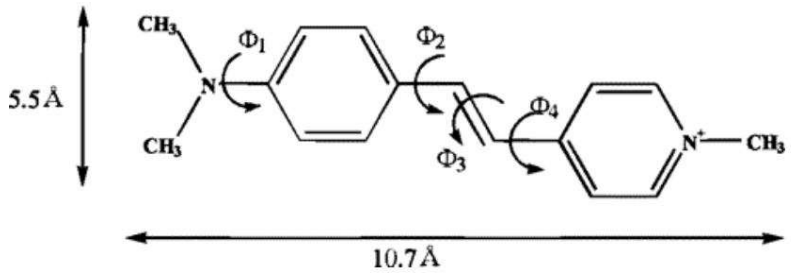


Figure 2.27: Molecular structure of 4-DASPI [140].

The peak of the absorption spectrum of 4-DASPI in water is 452 nm and its peak emission spectrum is at 613 nm, and the fluorescence lifetime was found to be 11 ps [140]. The interaction of 4-DASPI with excitation light resembles to some extent the interaction of the Allura Red AC dye. Upon photoexcitation, it can happen that the 4-DASPI, the molecule can twist around a single bond leading to ultrashort decay due to activation of non-radiative decay pathways. This behavior also depends upon the viscosity of the solvent in which the 4-DASPI exists. Lyons et al. [47], also measured fluorescence lifetime of 4-DASPI in water and recovered from their developed technique - will be discussed in section 2.4.5 - to be 7.22 ps. They attributed the difference between the 11 ps reported earlier in literature to the 7.22 ps they measured to differences in the temperature, pH, and chosen emission wavelength. In the same work, the lifetime of 4-DASPI was measured in ethanol and found to be 65 ps, which is in good agreement with the previously reported value of 62 ps in [141].

2.2.4 Hybrid quantum systems

The pursuit of SPSs that are highly efficient, ultrabright with GHz emission rate, and offer room temperature operation for quantum-based applications, has fueled strong interest to overcome the challenges associated with single quantum emitters, such as low quantum-yield and non-radiative energy pathways, which limit the efficiency of current SPSs. To address those problems, coupling quantum emitters into a cavity has been extensively studied. Proper selection of the cavity and tuning it appropriately ensures an enhanced Purcell factor increases the photonic density of states at the emitter frequency, thereby increasing the spontaneous emission rate and source brightness. For example, the intrinsic radiative lifetime of CdSe/ZnS core/shell single QDs is typically $\sim$ 10 ns, which severely limits the maximum single-photon counts from such SPS. In 2015, Hoang et al. [142], obtained an ultrafast room temperature single-photon emission from single colloidal QDs via coupling to a plasmonic nanocavity. Due to a 540-fold reduction of the emission lifetime, the single QDs exhibit 10 ps lifetime, and a 1900-fold increase in the total emission intensity. The structure of the hybrid system of the single QD and the plasmonic nanocavity is shown in Fig. 2.28.

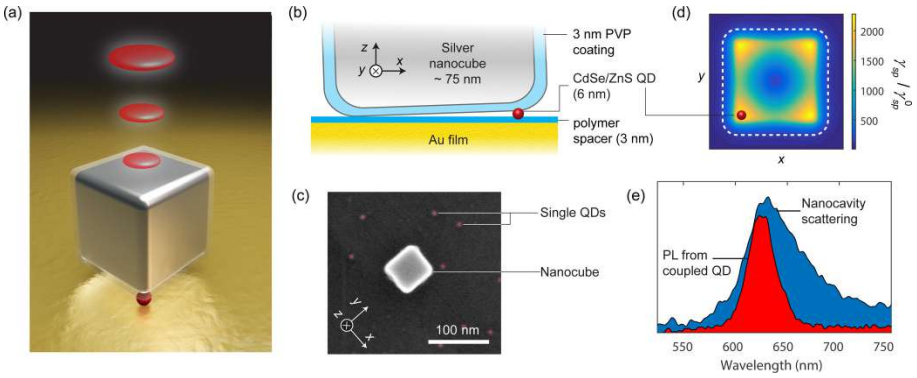


Figure 2.28: Hybrid single QD/plasmonic cavity system. (a) Graphical representation of the hybrid system, (b) Illustration of single colloidal CdSe/ZnS QD embedded into the nanocavity, (c) SEM image of single QDs and the nanocube, (d) Simulated enhancement of spontaneous emission rate, (e) Scattering spectrum of Nanocube (blue) and PL of single QD coupled to nanocube [142].

The nanocavity in their work consisted of a silver (Ag) nanocube, as seen in Fig. 2.28 (b), coated with 3 nm polymer adhesion layer surrounding its structure, a gold-film also coated ith 3 nm polymer as spacer, and a 6 nm single CdSe/ZnS QD was placed in between. In Fig. 2.28 (d), a simulation was carried out showing the concentrated regions of E-fields, and as observed a single QD placed at highly concentrated E-field shows Purcell enhancement $F_{\mathrm{p}} \simeq 2000$-fold. The same research group has followed similar approach, 2016, [143], where they coupled an Ag nanocube to PbS colloidal

quantum dots, which resulted in 1100-fold increase in radiative decay rate, and achieved a reduction of emission lifetime from milliseconds to nanoseconds.

Coupling of a single fluorescent quantum emitter to a plasmonic cavity can also enhance the radiative emission of a bare core QD, enabling a high control of the photophysics, while eliminating the need for chemical engineering of the QD structure by adding a shell layer to its core. For instance, Flatae et al. [18], in 2019, coupled a bare core CdTe QD, placed at the tip of an atomic force microscope (AFM) to a gold (Au) nanocone. In their work, it was reported a Purcell enhancement of emission rates of 1460-fold and 613-fold for excitons and bi-excitons, respectively. Consequently, the radiative lifetime of excitons was reduced from $\tau_X = 189.3$ ns to $\tau_X = 0.82$ ns, and the radiative lifetime of biexcitons was reduced from $\tau_{XX} = 172$ ns to $\tau_{XX} = 0.59$ ns. The overall reduction of excited-state lifetime as a function of the coupling strength between the single QD and the nanocone, and the change of the QD's emission spectrum is shown in Fig. 2.29.

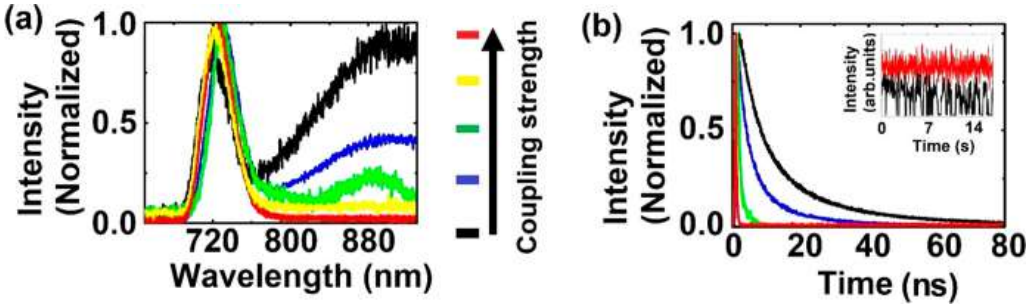


Figure 2.29: Fluorescence emission of single bare core CdTe QDs coupled to Au nanocone. (a) Emission spectrum as function of coupling strength, (b) Normalized intensity decay as a function of time, inset: fluorescence blinking before and after coupling [18].

It is obvious from Fig. 2.29 (a), particularly the black curve that, besides the emission of the CdTe QD, there is also trap-state emission, arising from delayed emission from trapped electron-hole pairs, whenever the bare QD is not coupled to a plasmonic cavity. The coupling strength between a single bare QD and a plasmonic cavity is characterized in terms of and can be modified by the distance between the QD and the Au nanocone, the polarization direction of the excitation laser and dipole orientation of the QD. Since the localized surface plasmon-polariton resonance is well-aligned with the QD emission, and the coupling strength is optimized, the Purcell enhancement introduced leads to efficient radiative decay pathway for the created electron-hole pairs, thereby increasing fluorescence emission at the emission wavelength ~ 720 nm, while simultaneously suppresses the long-wavelength trap-state emission, as indicated in Fig. 2.29 (a). Consequently, this gives rise to reduction of the radiative decay time, as the coupling strength increases, as shown in Fig.

2.29 (b). One can see in the inset of Fig. 2.29 (b) that, not only the fluorescence lifetime of the single QD is reduced, but due to the efficient radiative decay caused by the Purcell enhancement, the blinking has been drastically minimized, due to the coupling to the plasmonic nanocavity.

Coupling QDs to microcavities can also enhance the brightness and speed of a single-photon QD source. Tomm et al. [16] (2021), used an InGaAs QDs embedded in a semiconductor heterostructure of n- and p-layers coupled to a tunable Fabry-Pérot cavity to obtain on-demand single photons from the single QDs. The advantage of their structure is that it allows electrical control of the charge state of the single QDs via Coulomb blockade. Maintaining the charge state of the QDs is vital because it prevents creation of any extra charge states, which could possibly decay throughout non-radiative decay pathways.

Given that color centers in diamond offer a more stable platform for quantum science studies and applications, such as high photon count rates, brightness and high photostability, improving their fluorescence emission via coupling to micro- & nano-cavities has been intriguing, especially at room temperature. For instance, Kumar et al. [144] (2013), coupled a single NV center in nanodiamond to two chemically-grown Ag nanowires. The coupling between the two systems was achieved via an AFM tip, which attached these two systems together, depicted in Fig. 2.30. Enhancement of spontaneous emission decay rate by a factor of 8.3 was reported.

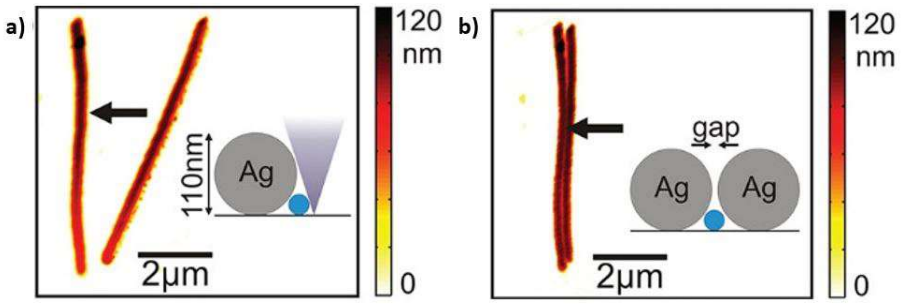


Figure 2.30: (a) Single NV center coupled to single Ag nanowire, (b) Single NV center placed between two Ag nanowires [144].

Without coupling the single NV center to the Ag nanowires, the fluorescence lifetime of this center in the nanodiamond was measured to be $\sim$ 45.2 ns. When such a single color center is coupled to one Ag nanowire its fluorescence decay reduces to $\sim$ 11.9 ns, while coupling the same emitter between two Ag nanowires, having a gap between them, reduces the fluorescence decay curve even further to $\sim$ 5.4 ns.

It was pointed out earlier that single NV color centers in diamond are not ideal SPSs, one approach to overcome this limitation is by nanofabrication of diamond structures,

e.g., optical cavities, or waveguides, which can enhance single-photons extraction from the single NV therein. Processing of diamond samples inevitably degrades the NV centers embedded in its crystalline structure. To preserve the quality of diamond, Riedel et al. [145] (2017), used a thin diamond membrane, and designed a tunable Fabry-Pérot cavity, made from one flat mirror and one curved mirror, and the thin diamond membrane was coupled to the microcavity. In 2017, too, a similar idea was implemented but for SiV in nanodiamond by Benedikter et al. [146], where the tunable microcavity consists of a flat mirror, but the curved mirror was deposited on a tip of fiber. Typically, the photon count rate from a quantum emitter reaches maximally 10^5 counts per second (cts). However, ultrabright photon emission ($\approx 35\times10^6$ cts) from single NV centers in nanodiamond was reported in 2018, by Bogdanov et al. [147], using Nanopatch antenna made out of silver, see Fig. 2.31, which has a nanogap, and achieves a reduction of NV lifetime to sub-nanosecond timescale at room temperature.

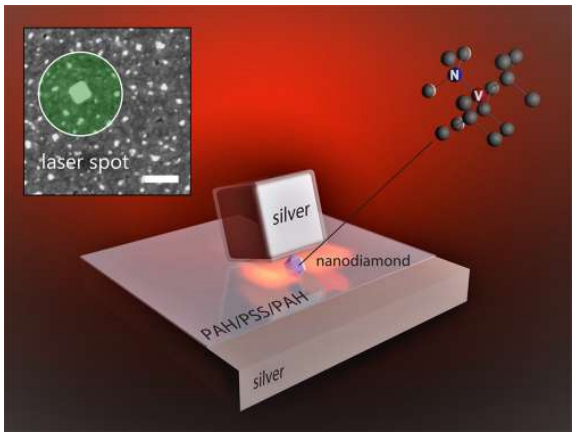


Figure 2.31: Structure of Nanopatch antenna, consisting of Ag substrate and Ag cube, where the single NV center in nanodiamond is placed in the gap between the cube and substrate [147].

The Purcell enhancement of SiV color centers embedded in diamond membranes, coupled to plasmonic nanocavity has been theoretically studied in 2019 by Kambalathmana et al. [148], and a design of an optical nanoantenna composed of gold nanocone coupled to SiV color centers in thin diamond membranes has been proposed. For practical realization of such systems, appropriate fabrication techniques and the optimized design parameters have been investigated for the gold nanocones used in plasmonic antenna structure for the sake of enhancing the radiative decay rate of single SiV color centers, see Kambalathmana et al. [36]. With an ensemble of SiV^- color centers implanted at 5 and 10 nm depths in ultrathin diamond membrane, coupled to plasmonic gold nanocavity, see Fig. 2.32, has been reported, by Boyce et al. [149] (2024), of a 135-fold enhancement of spontaneous emission rate and < 8 ps fluorescence lifetime has been achieved.

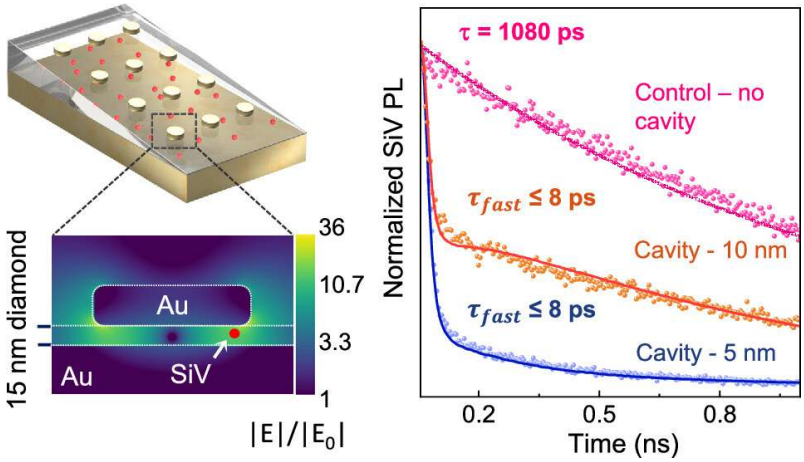


Figure 2.32: (a) Wedged diamond membrane implanted with SiV^- centers enclosed by Au cavity, (b) Reduction of fluorescence lifetime for those SiV^- centers implanted at 5 and 10 nm, respectively [149].

In their work, the diamond membrane was etched creating a wedge structure and was implanted with SiV^- color centers, and the diamond wedge structure was enclosed by a Au nanocavity consisting of Au nanodisk fabricated on top, and Au substrate underneath. Although a control sample of such diamond implanted with SiV^- centers for comparison with those enclosed by the Au nanocavity, the fluorescence lifetime reduction proclaimed in their work cannot be decisively verified. One of the reasons is that in reality an ensemble of SiV^- under a Au nanodisk cannot be implanted at exactly the same depth, this would expose them to different values of E-field intensity under the Au nanodisk, hence the lifetime reduction would be non-uniform. Another reason is comparison between different SiV^- ensembles on the same diamond membrane that vary in thickness, is not valid, given that each emitter experiences a different surrounding. For proper comparison, firstly the quantum yield should be taken into account upon comparing quantum emitters to ensure that the lifetime reduction is caused by enhancement of spontaneous emission rate; secondly, a single SiV^- color center embedded into the diamond membrane at certain depth with and without the nanocavity, should be compared. The same research group has very recently reported enhanced radiative decay rate, leading to ultrabright emission from a single SiV^- with 362 Mcps at room temperature, see [150].

2.3 Fluorescence microscopy and spectroscopy

In the previous section we discussed various types of quantum emitters and how they differ from each other. The gold standard for studying fluorescence emission is the confocal fluorescence microscope. In the following subsections, we shall provide details about each fundamental component of such a microscope.

2.3.1 Scheme of confocal fluorescence microscope

A traditional confocal fluorescence microscope consists of various components, each of which enables us to obtain specific information about the fluorescent emitters under study. Generally, an imaging system e.g. camera is used to image the location of fluorescent quantum emitters in the sample. An excitation laser source is essential in order to excite them. This could be a pulsed or continuous wave (CW) laser. In spite of referring to confocal fluorescence setups as microscopes, attaching a spectrometer to them allows to perform spectral characterization of the fluorescence source. Measurement of fluorescence lifetime requires the use of very sensitive photodetectors down to a single-photon level. When two of such photodetectors are used with a 50/50 beam splitter, one can form the so-called Hanbury Brown-Twiss (HBT) interferometer, which reveals the second-order coherence properties of the fluorescence source via the second-order intensity correlation function $g^{(2)}$, discussed earlier. This is essential for distinguishing between a truly single-photon quantum emitter and an ensemble. A general scheme of a traditional confocal microscope is indicated in Fig. 2.33

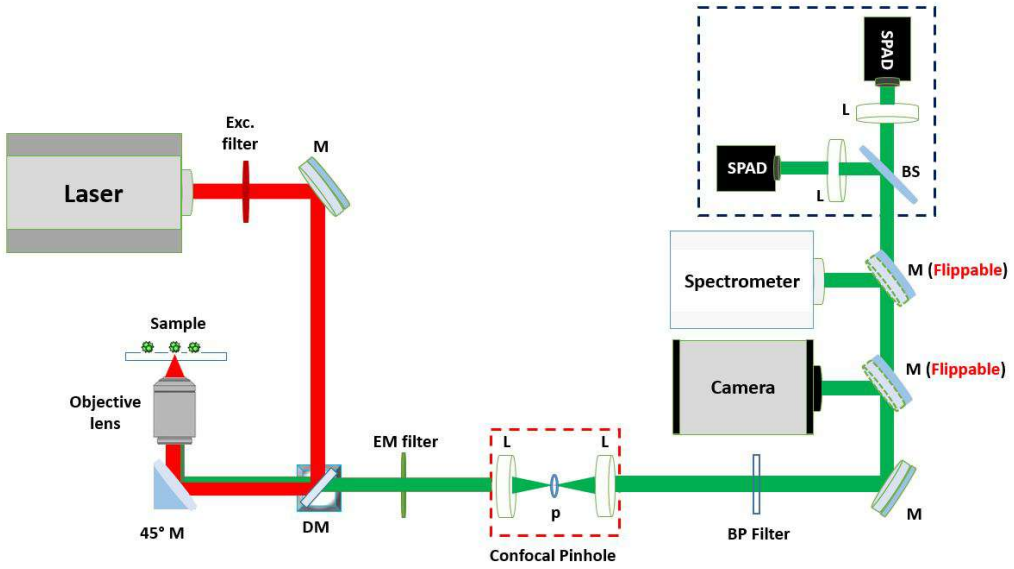


Figure 2.33: Standard confocal fluorescence microscope. M: Mirror, L: lens, Exc.: Excitation, DM: Dichroic Mirror, EM.: Emission, and BP: Bandpass.

Typically in a confocal fluorescence microscope, and shown in Fig. 2.33, the laser light is emitted from the laser source and reflected off a dichroic mirror (DM), then reflected upward and focused tightly via an objective lens to excite the quantum fluorescence emitter(s) of interest. The emitted fluorescence is generally emitted uniformly in all directions, covering a 4π solid-angle. However, there are some limitations when it comes to fluorescence collection. For instance, for high-index samples (e.g., diamond), much of the emission is trapped by total internal reflection.

Furthermore, the objective lens which collects fluorescence is limited by its inherent ability, characterized by its numerical aperture NA $= n \sin\theta$, where n is the refractive index of the surrounding medium of the objective lens, and θ is the half the solid-angle of the collection cone.

Selection of an objective lens with a high collection angle θ - high NA - ensures better collection of the emitted fluorescence. Also, increasing the refractive index of the surrounding medium helps to maximize the collection of fluorescence emitted from the sample. Usually when the medium interfacing the objective lens surface and the sample is air, this objective lens is suitable for collecting fluorescence from ensembles of quantum emitters. For ensembles of fluorescence emitters, an objective lens of, e.g., 63× magnification and 0.75 NA is sufficient for fluorescence collection. Nonetheless, such objective lenses are not adequate for single-photon emitter fluorescence detection. Instead, oil-immersion objective lenses are preferable, as oil has a higher refractive index than air. Such objective lenses have larger magnification and > 1 NA. Collected fluorescence is then reflected by a mirror and transmitted through the dichroic mirror (long-pass filter, cutoff frequency 650 nm, AHF Analysen Technik AG) while blocking most of the back reflected excitation laser. In this regard, the reflection and transmission wavelength range of the DM should be carefully chosen, so that the reflection of the incident excitation laser onto the sample and the transmission of the emitted fluorescence are maximized. Since the DM cannot completely block the back reflected excitation laser, additional filters to eliminate the residual laser light are often used.

After the DM comes another essential part, which is the confocal pinhole. This part is not merely a pinhole, but consists of one lens which focuses fluorescence light into a tiny spot at which the confocal pinhole is placed, and another lens after the confocal pinhole in order to collimate the fluorescence light beam. The name of confocal fluorescence microscopes stems from the fact that such types of microscopes have two focal points; one onto the sample at the location of the emitter(s) of interest, and another one at the pinhole position, hence the name “confocal” for the fluorescence microscope. In fact, the confocal pinhole is a vital part of the fluorescence microscope, in particular when single-photon quantum fluorescence emitters are studied. When the excitation laser is focused onto a particular focal plane at which the quantum emitters of interest are located, not only the fluorescence of those is emitters is collected, but also fluorescence signal from neighbour ensembles located at different planes of the sample will be collected as well, which in turn will blur the information gathered from the target quantum emitters, i.e., their image will look blurry on the camera, due to the background noise. The role that the confocal pinhole plays here is that it permits collection of fluorescence signals from the target focal plane, whilst

blocking the fluorescence signal emanated from other planes of the sample. Hence, it enhances the signal-to-noise ratio.

For collimating the fluorescence beam after the confocal pinhole part, it should be considered that the two lenses be placed far apart at a distance equal to the sum of their focal distances. Moreover, it is recommended that the pinhole size to be roughly 30% larger than its diffraction-limited spot size, which can be calculated from the relationship:

$$D = \frac{\lambda f}{r} \tag{2.47}$$

where λ is the wavelength of fluorescence light, f is the focal lens of the focusing lens, and r is the beam radius. Our fluorescence microscope was initially characterized via laser light from an optical parametric oscillator (OPO) emitting at 650 nm of a beam of 0.35 mm radius, focused by the first confocal lens, whose focal length is 25 mm has a diffraction-limited spot (diameter) of 46.42 μm, according to Eq. 2.47. Considering the 30 % extra diameter, this means that out confocal pinhole should be ideally 60.35 μm. Such precise pinhole diameter cannot be matched exactly with existing commercially available pinholes. Thus, in our case one should either use a 50 μm or 75 μm.

Fluorescence light can be ultimately directed toward the remaining part of the setup by means of a reflecting mirror. Along the reflection path, some flippable mirrors will be used, and each one of these then direct the fluorescence toward the imaging system, spectrometer, as seen in Fig. 2.33. When both mirrors are unflipped, fluorescence light will propagate through a straight line and would be split via a 50/50 beam splitter, followed by a focusing lens along each optical path in order to focus the collected fluorescence onto the sensor area of the photodetectors for lifetime measurements and the $g^{(2)}$ correlation function.

2.3.2 Excitation light source

For exciting the fluorescent quantum emitters from the ground state to the excited state, a monochromatic light source with photon energy matching the energy difference between the two states must be used. Generally, laser sources due to their coherence are better for excitation than incoherent light sources. CW lasers [151, 152, 129, 109] and pulsed lasers [153, 154, 155, 16, 156, 157], and sometimes both [158, 159, 160, 161] have been used to excite various quantum emitters, such as quantum dots and different color centers in diamond. In principle, both types of lasers give the same kind of information, though, the $g^{(2)}$ function looks different when CW laser is used in excitation in contrast to the one obtained via pulsed laser excitation,

as mentioned earlier in subsection 2.1.5. For the measurement of a single-photon quantum emitter, the type of laser utilized for excitation is not significant, since in either case, we care about the $g^{(2)}$ value at zero. The common issue that is often encountered with fluorescent quantum emitters of low photostability, irrespective of which type of laser excitation is used, is the photobleaching. For that, quantum emitters should be excited at low-to-moderate laser energy. However, pulsed laser sources can lead to faster photobleaching for single QDs than CW laser [162]. A significant difference between usage of CW or pulsed laser for excitation lies in the fluorescence lifetime measurement technique being utilized. For instance, it is possible to gain information about the lifetime, when CW laser is used for excitation via frequency domain (e.g. phasor diagrams) measurement. However, that is not the case when the lifetime is measured via the temporal domain measurement, such as time-correlated single-photon counting (TCSPC) technique, which requires pulsed excitation of the sample. Brief discussion about phasor diagrams and further details about TCSPC measurement technique will be provided in subsection 2.3.6. In this work, we adopt the TCSPC technique, hence we use a pulsed laser source.

For this work we use a tunable Titanium:sapphire (Ti:sa) laser (Taccor Tune 10 - Novanta) with 1 GHz repetition rate laser, output power $>$ 1.8 W ($\sim$ 2 W) at 800 nm, pulse duration $<$ 80 fs and wavelength range 730-910 nm. Since the emitted laser is in the infrared (IR) range, part of its energy is split to pump a tunable fs optical parametric oscillator (OPO) capable of synchronized operation at 1 GHz repetition rate (APE GmbH). The OPO has two outputs, idler with a wavelength range 1750-4000 nm, which is optionally blocked and signal with a wavelength range 505-740 nm. Initially, the OPO signal in the visible range at 650-670 nm was used for excitation of our samples, and also as a probe for the optical Kerr gate (OKG). Because it was noticed that the chosen wavelength of the OPO was drifting, and because of high pump power portion required to run the OPO split from Ti:sa laser, which could be otherwise used to increase the gate (pump) beam for the OKG, the OPO is no longer used. Instead, we rely fully on Ti:sa (Taccor Tune 10) to perform all experiments presented in this dissertation. Further details about OKS experiments will be discussed in Chapter 4. Now, the output full power of the Ti:sa IR laser will be split by a 90/10 beam splitter into two parts. The major part - 90 % of the laser power ($\sim$ 1800 mW) - will be used as a gate (pump) beam for the OKS experiment, while the remaining 10 % (200 mW) will be exploited initially as a probe for the same experiment and later as an excitation source for the quantum fluorescence emitters. In the latter case, the emitted fluorescence will be the probe beam in the OKS.

2.3.3 Imaging system

For measuring any physical property of an ensemble of fluorescence quantum emitters, or a specific single emitter, the first step is to image the emitter(s) to determine their locations. Scientific cameras are often used to achieve this goal. In particular, two semiconductor technologies, i.e., the scientific complementary metal-oxide-semiconductor (sCMOS) camera, or sometimes electron-multiplying coupled-charged detector (EMCCD) cameras are commonly utilized in fluorescence microscopes.

In fact, scientific cameras have greatly advanced fluorescence microscopy, which consequently gave rise to pushing the frontier of imaging of biological samples, as well as fluorescence quantum emitters. This is due to the advantages such kinds of cameras can offer. For instance, they provide high sensitivity as they are designed to capture low light signals, which is beneficial for detecting materials of low quantum yield, as well as capturing images of single fluorescence quantum emitters, and that is helpful for quantum science and quantum-based applications. In this regard, EMCCD cameras are capable of providing higher sensitivity than sCMOS cameras, and that allows single fluorescence quantum emitters in a relatively feasible manner than sCMOS cameras. Another aspect provided by scientific cameras, equally important to the high sensitivity is the high resolution. At high resolution, images of small biological cells, or single emitters can be clearly captured, within the diffraction limit of the fluorescence microscope. In addition to those advantages, scientific cameras are supplied by cooling systems to reduce the thermal noise of the camera's sensor, and also software for data acquisition and analysis.

Regardless of the designed signal readout architecture of the scientific camera sensor employed for a certain application, the underlying physical concept governing the photodetection process is the same, that is the photoelectric effect. So, depending upon the incident photon energy, and the work function of the sensor's material, the incident photons on a certain pixel impart their energy to electrons, providing them with an adequate kinetic energy. Subsequently, those photoelectrons are collected from each pixel according to the designed signal readout architecture by which we can image the region of interest of the sample. Both sCMOS and CCD camera sensors differ essentially in the signal readout architecture.

For imaging of fluorescence quantum emitters presented in this work, we use an air-cooled sCMOS camera (Andor Zyla 4.2). The model Zyla 4.2 uses a front illuminated sCMOS sensor type, with a 13 $\times$ 13 mm sensor size and the number of active pixels (W $\times$ H) is 2048 $\times$ 2048 (4.2 Megapixel). Each pixel is 6.5 $\times$ 6.5 μm, and has a well depth (e^-) 30000. The rate of pixel readout varies based on the speed of reading the signal, e.g., the slow read has 216 MHz pixel readout rate, while the fast read has 540

MHz rate. The pixel readout rate affects the read noise (e^-) median, for example, at 216 MHz (slow read) the read noise median [rms] is 0.90 but at 540 MHz (fast read), the read noise (e^-) median [rms] is 1.1. The overall maximum quantum efficiency of the Zyla 4.2 model is 82 %, and the dark count rate, which is the number of electrons per pixel per second at minimum temperature, is 0.10 for air-cooled cameras.

Some examples of images of fluorescence emitters from the characterization of our home-built confocal fluorescence microscope are provided in Fig. 2.34, in which the sCMOS camera was characterized by capturing images of individual CdTe quantum dots (PlasmaChem GmbH), shown in Fig. 2.34 (a), and ensembles of SiV color centers in diamond, shown in Fig. 2.34 (b)

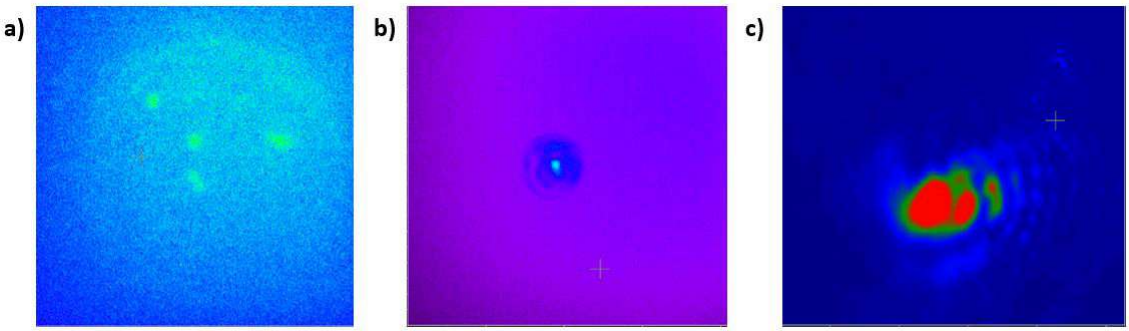


Figure 2.34: Imaging of fluorescence emitters. (a) Ensemble of CdTe quantum dots, (b) Single CdTe quantum dot, (c) Ensemble of SiV color centers in diamond

.

2.3.4 Spectral characterization

Each type of fluorescence quantum emitter has a characteristic emission spectrum that acts as its optical fingerprint. We mentioned earlier in subsection 2.2.2, that the charge state of color centers in diamond, e.g., NV centers, results in having a distinct spectrum for the same type of color centers, whereby one can distinguish two charge states via spectral characterization.

For studying the spectral properties of fluorescence quantum emitters, typically a spectrometer is attached to the confocal fluorescence microscope. Since the emitted fluorescence at the ZPL is often small, some residual excitation laser and other background radiation can obscure the signal. Thus, it is important to select the appropriate set of filters, i.e., long-pass filter and bandpass filter to improve the signal-to-noise ratio (SNR) of the fluorescence signal of interest.

In this work, we used in most of the measurements a portable high-sensitive spectrometer (Ocean-Optics - Model: QE Pro), provided with a TE cooled CCD detector. The Model QE Pro works in the Vis-IR spectral range, in particular within the

wavelength range ∼ 586-965 nm, and its optical resolution (FWHM) ∼ 1.2 nm. It also has signal-to-noise ratio (single scan) of 1000:1, and a dynamic range 85000:1 (single scan). Moreover, its integration time ranges between 8 ms up to 60 minutes. With such characteristics, it was quite suitable for most of the measurements performed here. However, for experiments that require higher spectral resolution and higher sensitivity such as self-phase modulation (SPM) experiments, another spectrometer was utilized, which was Andor spectrograph - model: Shamrock 500i-D2. This is an imaging spectrometer based upon Czerny-Turner optical design, and acquires a high resolution down to 0.03 nm. The model we use is Shamrock-500i and such optical design can offer excellent optical performance, however, to ensure the best performance the appropriate grating groove density (number of lines per mm - l/mm) should be selected for an aberration-free operation. Another important consideration related to the grating is the grating efficiency. It describes the ability of the diffraction grating to disperse the detected wavelength range. The QE Pro spectrometer was used to characterize the emission spectrum of the CdTe quantum dots, see Fig. 2.35 (a), whose image was presented in Fig. 2.34 (a), and for the characterization of the SiV center in diamond, see Fig. 2.35 (b), where the SiV spectrum was filtered via a long-pass and bandpass filters.

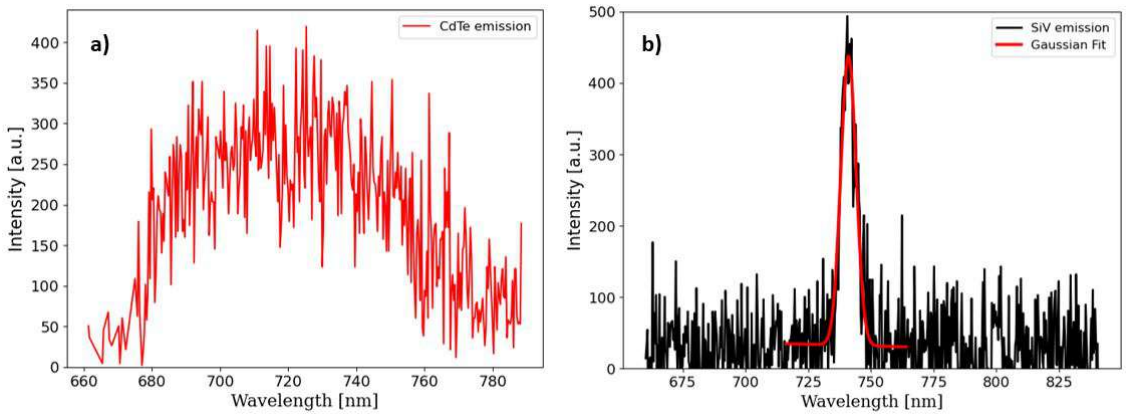


Figure 2.35: Spectral characterization of quantum emitters. (a) Spectrum of an ensemble of CdTe quantum dots, (b) Spectrum of an ensemble of SiV color centers in diamond (black), and fitting of its ZPL linewidth (red)

2.3.5 Photodetectors

Photodetectors are a vital component for any fluorescence microscope. Without them, the average excited-state lifetime of a fluorescence emitter cannot be measured, as shall be explained in the next subsection. Furthermore, the $g^{(2)}$ function by which we can determine the nature of the fluorescence light source, whether it is a single emitter or an ensemble, cannot be unveiled.

The sensors of the photodetectors used for the measurement of fluorescence lifetime and $g^{(2)}$ function are sensitive down to a single-photon level. This is why they are called single-photon detectors (SPDs). The underlying physical concept by which a photon is detected is again the photoelectric effect, where the target photon to detect is converted into a single electron. Though, this photoelectron is not sufficient for the electronic circuit of the photodetector's sensor to feasibly read it out. Thus, a multiplication process for the photo-generated electrons is strictly needed for single-photon detection.

It is crucial to mention that the type of single-photon detectors (SPDs) frequently used in confocal fluorescence microscopes are not photon-number resolved (PNR) detectors. Meaning, they are not capable of counting the number of individual single-photons incident on them. Such photon detectors work fundamentally with a binary system, whereas a click refers to a detection event of a single or more photons incident onto the detector's sensor, while no click indicates no photons are being detected. Resolving the number of incident photons is required for some applications such as quantum metrology, quantum computing and photon statistics. For that purpose, some photon-number resolved detectors, e.g., transition-edge sensors (TES), visible light photon counters (VLPCs), and arrays of single-photon detectors (pseudo-PNR vial spatial or temporal multiplexing) are used. In general, PNR detectors are complex and work at slow speed, and often operate at cryogenic temperatures. Further details about those detectors can be found in [163, 164, 165].

The spectral range of the operation of an SPD and its corresponding detection sensitivity is dictated by its sensor's material, which determines whether or not a certain SPD is suitable for a certain application [166]. A single-photon detector is considered ideal if it has the following characteristics [167]: The detection efficiency is 100%. It is the probability that the incident photon onto the sensor is detected. The dark count rate (DCR) is zero. Dark count rate refers to the detected e^- counts per second in absence of incident photons. Such e^- signals arise due to thermal excitation. The dead time is zero. It is the time during which the SPD cannot process any incident photons. Basically, when a photon impinges on a photodetector, this photon is being processed further until its corresponding signal is being read out. For some time, which is the dead time, any other photon that hits the detector's sensor is not read out. Once that dead time has elapsed, the photodetector will be ready to receive another photon. Another aspect of the ideal SPD is that its time jitter is zero. By time jitter we mean, the variation of the time interval Δt between the moment at which a detector absorbs a photon and the moment at which that photodetector generates an output electric pulse corresponding to the absorbed photon. It is a crucial parameter for timing measurement, as large time jitters can

blur the timing information corresponding to the lifetime decay, an effect that has particular influence in the case of ultrafast fluorescence emission.

In practice, there is no such a thing as an ideal detector, or ideal detection parameters. As a matter of fact, the aforementioned parameters vary considerably depending upon the type of used detector and the materials it is made from. Some types of photodetectors exhibit superior performance in some aspects than the others. The most common single-photon detectors that have been used in the scientific community are photomultiplier tube (PMT), single-photon avalanche photodiode (SPAD), and superconducting nanowire single-photon detector (SNSPD).

Historically, one of the first used photodetectors was photomultiplier tubes (PMT), where it was initially employed in scintillation counters for radiation detection [168], then later on it had been applied as photon detectors [169]. PMTs are devices for obtaining large electrical signals from few individual photons [170], and they offer large active areas (diameter $>$ 10 mm, and wide spectral range 115-1700 nm [166]. A basic PMT consists of a vacuum tube with a photocathode, which absorbs light and converts it into primary electrons. As we know from photoelectric effect, the energy of the incident photons onto the photocathode materials must exceed the work function corresponding to the photocathode material, in order to liberate electrons. Those primary photoelectrons subsequently strike a series of electrodes called dynodes, each of which is biased at a larger voltage than the previous electrode (dynode) generating a cascade of secondary electrons, whose electrical signal is proportional to the incident light photons. This is basically the mechanism by which the initial low signal is multiplied. The entire photo multiplication process is illustrated in Fig. 2.36.

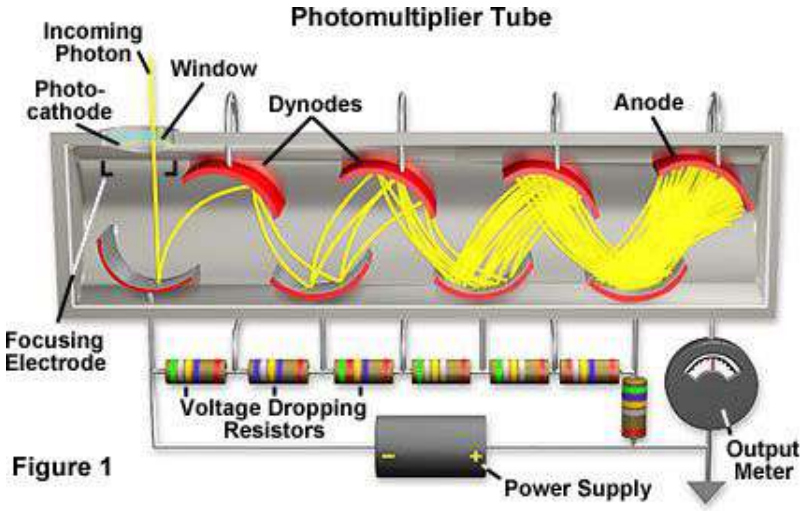


Figure 2.36: Scheme of photomultiplier tube [171].

PMTs are very sensitive to low-light, down to single-photon level, and have fast

response time $\sim$ ns, low dark counts at ambient temperature, in addition to wide dynamic range [171]. However, it is often bulk, fragile, expensive and requires high voltage up to few kilovolts for operation. PMTs having GaAsP photocathodes suffer from low quantum efficiency 40% at 500 nm. PMT with as low as 100 Hz dark counts, and as high as 10 MHz are commercially available, with a time jitter of 300 ps (FWHM). Beside PMTs working in the visible wavelengths, there exist PMTs at telecommunication wavelengths, e.g., by cooling InP/InGaAs photocathode up to 200 K. Unlike their modest performance in the visible range, such PMTs perform poorly at 1550 nm with detection efficiency of 2%, dark count 200 kHz, and a time jitter of 300 ps (FWHM).

Superconducting nanowire single-photon detector (SNSPD) is another type of single-photon detectors, which rapidly emerged due to their high detection efficiency ranging from UV to IR, i.e., $> 90\%$ at telecom wavelength 1550 nm [172], low dark counts 10^{-4} Hz [173], small timing jitter < 3 ps [40], very fast reset time [174] down to a few hundred ps and excellent time resolution, i.e., IRF 4.4 ps [41]. Due to those unique properties, SNSPDs have found their way through various applications, such as quantum-based applications, e.g., quantum information [175], light detection and ranging (LIDAR) [176], mass spectrometry [177], and diffuse correlation spectroscopy [178]. Commonly used materials as SNSPDs are nitride-based materials, e.g., niobium nitride (NbN), niobium titanium nitride (NbTiN); silicon-based materials, such as tungsten silicide (WSi) and molybdenum silicide (MoSi); or rare-earth cuprate oxides like $YBa_2Cu_3O_{6+x}$ (YBCO) and $Bi_2Sr_2Ca_2Cu_3O_{10}$ (BSCCO). For a comparative study of different superconducting materials and their applications for single-photon nanowire detectors, the reader is referred to Ref. [179]. In addition, for a comprehensive overview about the physics, evolution and state-of-the-art and challenges of SNSPDs, we refer to the following review articles Refs. [180, 181, 182].

The structure of an SNSPD encompasses a nanowire patterned onto a thin film with nano dimensions. This nanowire is cooled via a cryocooler below a critical temperature T_c, thus enabling a superconducting state, and biased with a current I_b which flows without resistance due to the superconductivity. The bias current I_b is carefully set slightly below the critical current I_c, above which the superconductivity state is lost. At the edges of the thin film, the nanowire is connected to an electronic circuit so that the induced voltage signal when a photon arrives is measured.

The photon detection mechanism of SNSPDs, in particular for moderate to high energy photons is explained by the hotspot model [183]. Basically, when a photon impinges onto a certain location of the nanowire, the energy of that photon creates a hotspot, which raises the local temperature at that location beyond the critical temperature T_c, hence the superconductivity state is lost. As the energy deposited

by the photon breaks some Cooper pairs, in this case the electrons flowing locally along the nanowire will experience resistance, leading to a voltage signal, which can be detected by the attached electronic circuitry after being amplified. Given that the superconducting nanowire is cooled, after some time "reset time" the superconductivity state will be retrieved again. Despite a single-photon at 1.5 μm has an energy of 0.83 eV, which is very small, this is sufficient to break the superconductivity state locally where the photon hits the nanowire, thus inducing a measurable voltage signal [184]. In Fig. 2.37, an entire SNSPD system is shown (a), where the major part of the detector is the cryocooler while on top the thin film (the enlarged view) attached to the circuit is placed (b), and an SEM image of that nanowire is shown (c) that has a meander structure to increase the sensor area, which in turn enhances the nanowire detection's sensitivity, and in (d) the operating principle is illustrated.

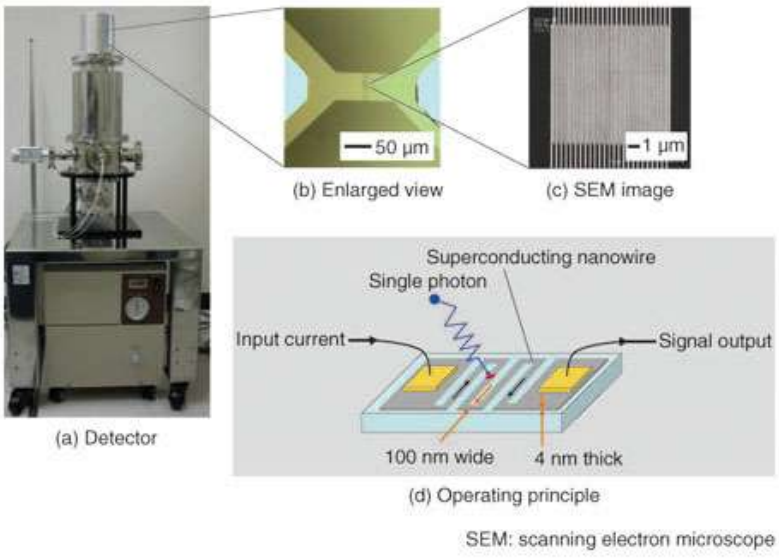


Figure 2.37: Superconducting nanowire single-photon detection system [184].

Although SNSPDs exhibit superior performance in terms of the above-mentioned metrics, they are bulky systems, which necessitates usage of costly cryocoolers for operation down to few kelvins. Furthermore, their detection efficiency drops in the near-IR to $\leq 50\%$, particularly below 1000 nm. However, SNSPDs are still under development and find new pathways toward further applications, for example, for tissue imaging using fluorescent dye indocyanine green (ICG), where the SNSPD was integrated into a confocal fluorescence microscope forming a portable system, with the aim to enable deep tissue imaging with safe laser power range [185].

Semiconductor-based photodetectors are another type of single-photon detectors often called single-photon avalanche diodes (SPADs) and utilized in various applications, particularly in fluorescence detection and single-molecule spectroscopy. Unlike other

photodetectors, they are compact, enabling their integration into table-top setups, or commercial devices; they work at less power consumption, and they possess more ruggedness, meaning that they are less vulnerable to mechanical shocks, magnetic fields and environmental conditions. These altogether ensure operational durability for such kinds of detectors. More importantly, they operate under ambient conditions, which eliminate the need for either vacuum systems or cryocoolers as opposed to PMTs and SNSPDs, respectively. The semiconductor materials often used for SPADs are silicon (Si) and InGaAs/InP ($\sim$ 1.0-1.70 μm).

A SPAD essentially consists of a p-n junction diode, which is reverse-biased at a voltage V_a above the breakdown voltage V_{BD}, and this corresponds to the "OFF" state in which no current flows. The electric field in the depletion region of the p-n junction is high, nonetheless, there are no free carriers. This mode of operation is analogous to gas counters for ionizing radiation, that is why this mode of operation is sometimes called "Geiger mode". When a single-photon is absorbed in the depletion region of the p-n junction, it creates a single electron-hole pair via photoelectric effect, as referred to earlier, and this single charge carrier is accelerated due to the strong field in this region, and gain adequate kinetic energy to trigger an avalanche of secondary charge carriers via impact ionization, which is a self-sustaining multiplication process. This process allows detection of weak signals. In spite of the exponential growth of the current due to the generated avalanche of charge carriers, the space-charge effect limits that current to a constant level, which is proportional to the excess bias voltage $V_E = V_a - V_{BD}$. Upon certain value of avalanche current 1 mA, the diode turns into an "ON" state [66]. This avalanche process does not remain indefinitely and it is quenched by an external voltage (quenching circuit) that sets the voltage V_E to below V_{BD}, or $\approx V_{BD}$, then after some time it sets the voltage to above V_{BD}. In other words, the circuit is reset to the original "OFF" state, thus ready to receive another single-photon. A simple diagram of the I-V curve of the SPAD operation depicting the reset process is in Fig. 2.38. It is vital to elaborate that since reception of the single-photon till the circuit of the p-n junction is reset, the SPAD will not be able to detect another photon, which is why this time is referred to as dead time.

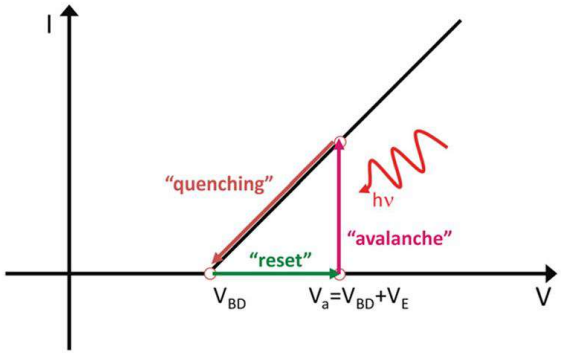


Figure 2.38: I-V curve of quenching and reset of SPAD p-n junction [66].

It is worth pointing out a distinct difference between the three types of diodes, namely the photodiode (PD), avalanche photodiode(APD) and the single-photon avalanche diode (SPAD) in terms of the voltage range selected for their operation. This difference is pictorially clarified in Fig. 2.39 [186]. As can be seen in the I-V curve, the three diodes operate commonly in the reverse bias voltage region, however, the PD operates at a smooth current output when a signal is detected. On the contrary, the APD current increases more sharply than in PD as the reverse bias voltage goes toward the breakdown voltage V_{BD}. Although the APD operation principle relies also on avalanche generation of charge carriers, the real distinction between APDs and SPADs appears in the Geiger mode, namely when the detector is set at a voltage above the V_{BD}. The current rises sharply in that particular region of the I-V curve. As a matter of fact, this is necessary for detection of very weak signals such as single-photons, in the sense that an adequate high electrical signal is generated when a single-photon is absorbed.

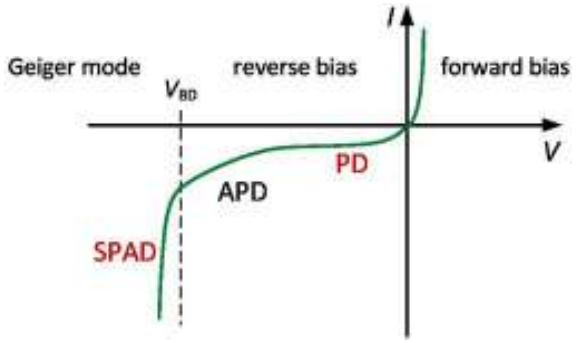


Figure 2.39: I-V curve showing the difference between PD, APD and SPAD [186].

One might have noticed the discrepancy between the I-V curve in Fig. 2.38 and Fig. 2.39, in terms of the location of the reverse bias voltage region. Given that each of them is taken from a different reference, each figure is suitable to clarify a certain concept. For instance, Fig. 2.38 is suitable to show clearly the concept of resetting the detector circuit after which the detector is ready for a new detection

event. Nevertheless, Fig. 2.38 mistakenly shows the voltage region of operation in the forward bias region, although a SPAD operates actually in the reverse bias region, which is typically located at the left-side of the I-V curve. On the contrary, Fig. 2.39 shows rightfully that the photodiodes generally and SPADs particularly work at voltages in the reverse bias region, which is at the left-side of the I-V curve.

High DCR is one of the fundamental noise sources that can reduce the S/N ratio of the photon detection process. Another source of noise is the so-called "Afterpulsing". This effect occurs by deep energy levels with the bandgap of the semiconductor material of the sensor, i.e., from defects/impurities, which trap few charge carriers for some time, then release them when the detector is reset and ready for a new avalanche detection event.

Time jitter is another parameter that has an influence on the accuracy of the time measurement process. It is the uncertainty between the arrival time of photons, and the output electric pulses of the SPAD, typically defined by the FWHM of the timing diagram of the SPAD connected to the time-correlator. Ideally, if the time jitter is zero, when photons hit the detector, after a certain time, those photons would generate charge carriers at the same time and be detected as an output voltage pulse. In reality, though, the avalanche process is in fact probabilistic, which in turn leads to statistical fluctuations between the actual arrival time of the photons to the detector, and the release of an output electric pulses. Moreover, the electronic circuit of the detector introduces some uncertainty in the time measurement, thus contributing to the time jitter.

Throughout this work, two identical Si-SPADs were purchased from Micro Photon devices (MPD), with the ultimate aim to use them for fluorescence photon detection and $g^{(2)}$ function measurement to identify single-photon quantum emitters. Besides, they were fundamentally utilized to detect the Kerr-rotated signal from the probe laser beam, as will be explained in chapter 4, in optical Kerr gate experiments. Such SPADs offer maximally up to 50% photon detection efficiency at 550 nm, and slightly lower than 30% photon detection efficiency at the SiV emission at 738 nm.

In spite of the DCR of the two SPADs (few tenths of cts) we use in this work from MPD can have DCR down to 1 c/s, according to the company's specifications, they have practically few dozens of counts per second (c/s) [39]. Further, the time resolution of such SPADs is < 50 ps.

2.3.6 Fluorescence lifetime measurement systems

Determination of fluorescence lifetime of a quantum emitter cannot be determined solely by a photon detector. The reason for that is that photon detectors are only capable of detecting photons, yet they cannot count how many photons are incident onto them. Here, the need for a photon counting system arises in order to be able to measure the fluorescence lifetime. There are two commonly used approaches for the determination of the lifetime, one that relies on the frequency-domain, while the other one is on the time-domain.

In the frequency-domain the main technique is called the phasor approach, whose potential and importance has not initially been well perceived, yet is gaining more recognition recently for its vitality, in particular in biological applications, more specifically for the application of fluorescence lifetime imaging (FLIM). In phasor approach, the excitation laser source is modulated at a certain frequency, hence the emission is also modulated at the same frequency. Though, since the fluorescence emission is delayed in time with respect to the excitation process, there will be a phase shift between the excitation and the emission curves, from which we can determine the fluorescence lifetime.

The fundamental technique in the time-domain approach is the time correlated single-photon counting (TCSPC) technique, sometimes called time-tagging, and it is a powerful technique for fluorescence decay measurements being sensitive for low-light signals at picosecond time scale and highly precise for time-tagging of the electronic signals, commonly used in various applications. TCSPC technique is based upon designating a timestamp (thus the name time-tagging) for the arrival of photons from both the excitation laser and fluorescence photons detected via photon detectors. Then, by calculating the time difference Δt between the exciting photon and the detected fluorescence photon, and statistically repeating this process for multiple times, a histogram can be constructed, thereby a fit for the fluorescence decay curve can be performed. The feasibility of this technique stems from modern advances in laser and timing electronics. For instance, pulsed laser sources are capable of emitting a train of pulses at high repetition rates. This enables such a statistical process to be attained with a large statistical ensemble of counts. Furthermore, the advancement of the current electronics allows for a precise tagging of the arrival of photons in time.

The technique is used via a compact electronic module named time-correlated single photon counter (TCSPC). It has been an effective tool to measure low-light signals in various fields such as life science, material science, quantum optics and metrology. In particular, it plays a crucial role in various applications, some examples are time-

resolved fluorescence, single molecule detection, Förster resonance energy transfer (FRET), and fluorescence lifetime imaging (FLIM).

TCSPC is based generally upon detection of arrival times from periodic light sources used in exciting the quantum emitter of interest, detection of the arrival times of single-photons emitted, and reconstruction of the decay signal from the individual time measurements [187, 188]. It relies on the high-repetition rate (e.g. 80 MHz) of the light source used for excitation, and that the signal is low enough at the detector such that the probability that it would detect more than one photon per signal at the detector is negligible [23]. The process of fluorescence detection is stochastic, in the sense that not every exciting pulse for a quantum emitter yields a fluorescence photon at the detector. The excitation light source emits a train of pulses regulated by a constant separation in time, which is inverse of its repetition rate. When the exciting laser pulse is emitted from the laser source, an equivalent radio-frequency (RF) is emanated from it and sent to the TCSPC module, and considered as a 'start' click, in other words, a time tag is assigned for the onset of excitation moment. Similarly, if a fluorescence photon is being detected by a photon detector, i.e., SPAD, a signal will be also sent to the TCSPC and considered as a 'stop' click. The difference in time between these two clicks, Δt, is calculated. For every exciting pulse this process is repeated over and over again until a histogram is built up forming the trend of the fluorescence decay. The entire process and the distribution of photons after time t from the excitation laser is illustrated in Fig. 2.40. The produced histogram can be subsequently fitted commonly with an exponential decay function, from which the lifetime of a fluorescence emitter τ can be extracted.

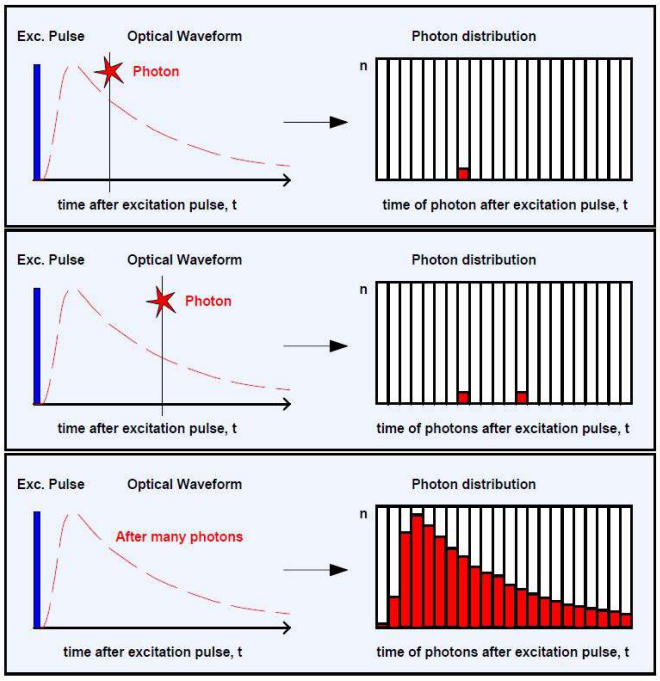


Figure 2.40: Scheme for illustration of TCSPC operation principle [23].

Analog signal recording techniques are evidently limited by the detector bandwidth. Thus, the width of the instrument response function (IRF) cannot be shorter than the single-photon response. TCSPCs offer extremely high time resolution, much better than photon detectors, this is due to their ability to accurately record the exact arrival time of a pulse signal, not its pulse width. The IRF in TCSPCs is typically characterized by the r.m.s error (standard deviation), or the FWHM of the time distribution, and is limited in this regard to the transit time spread (TTS), which is the time charge carriers take to travel through the detector, and this time can be 10 times narrower than a single-photon response of a detector. Fig. 2.41 shows how the IRF of a TCSPC is affected by the TTS in response to infinitely short light pulses.

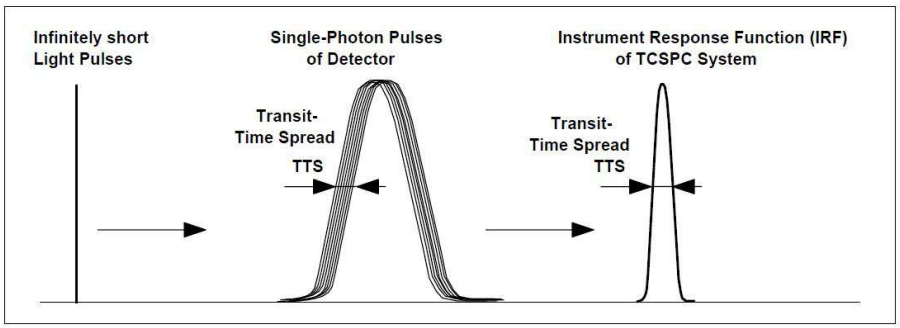


Figure 2.41: Single-photon response of a detector and the IRF of a TCSPC to infinitely short light pulses [23].

In addition to the effect of TTS, another source of timing error is the time jitter introduced by the electronic components of the TCSPC and is caused by the finite rise/fall time of the electric signals, where the amplitude noise emanated from thermal noise or interference is transformed into corresponding time error (phase noise). The total IRF of a TCSPC strongly depends on the relative magnitude of its individual sources of time uncertainties, and can be obtained by the following geometric sum [189]:

$$e_{\text{IRF total}} = \sqrt{\sum e^2_{\text{component}}}. \tag{2.48}$$

In this work, the commercial brand PicoHarp 300 TCSPC module (PicoQuant) was used. PicoHarp 300 has two identical synchronized but input independent channels, and possesses 65536 histogram time bins, with a minimum of 4 ps bin width, which defines the maximum obtainable time resolution that can be achieved using this TCSPC device. It can count up to 10 million counts per second. The acquisition time of this module ranges between 1 ms to 100 hours, and it has < 95 ns dead time.

For proper detection of fluorescence photons, it is significant to emphasize the importance of maintaining the number of detected fluorescence photons per excitation cycle does not exceed 1, the reason for that is when more than one fluorescence photon is emitted, the early photon will be detected while the later photons would not be registered during the detector's dead time. Over multiple cycles, the early arriving fluorescence photons will be over-represented, and this effect is the pile-up. On the contrary, the late arriving photons would be under-represented, which will artificially shorten the fluorescence decay curve upon high photons emission [190], indicated in Fig. 2.42.

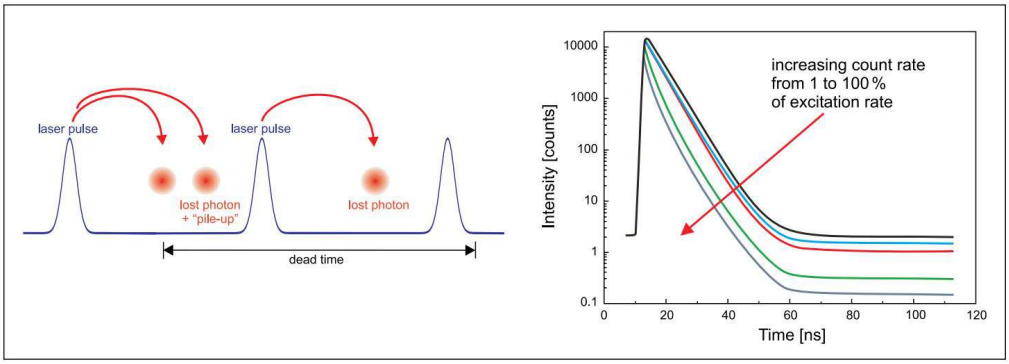


Figure 2.42: Illustration of pile-up effect and its impact on lifetime measurement [190].

The pile-up effect is not significant when the fluorescent source is a single-photon quantum emitter, as they exhibit inherently photon antibunching, meaning that by default no more than one photon is emitted per excitation cycle. The significance

of the pile-up effect manifests itself with fluorescence ensembles. In this case, high excitation increases the probability of having more than detected fluorescence photons at once. The recommended photon count rates at the detector for maintaining single-photon statistics is 1-5% of the excitation rate.

2.4 Ultrafast fluorescence detection

Rapid progress in electronics has led to incredibly fast electronics circuits that are used in numerous applications on a daily basis. Yet, those fast electronics are slow compared to the timescale of ultrafast fluorescence emission, usually a few tens of picoseconds or a few hundred of femtoseconds. Thus, they lack the sufficient temporal resolution to resolve the dynamics of quantum emitters. Several optical-based techniques have been developed to overcome this hurdle. Some of them rely on nonlinear materials using second-order and third-order nonlinear optical processes. Other techniques avoid nonlinear materials and instead exploit the statistical properties of fluorescence from quantum emitters (bunching or antibunching) to reveal their ultrafast emission. Some others exploit innovative concepts to magnify the ultrashort signal in time, so that it becomes measurable.

2.4.1 Streak camera

The era of high-speed photography of ultrafast transient phenomena, especially for studying ultrafast natural processes and new light sources, began with the invention of a mechanical version of the streak camera (streak records), wherein a simple drum camera with a photographic film was rotated at a certain speed, for imaging fast event and was capable of resolving two events separated by 10^{-5} s in time [191]. After further developments, a faster streak camera system was developed in 1949, using photoelectronics [192], and was capable of resolving time events down to 10-100 ps. This camera was used to characterize ultrafast pulses from mode-locked lasers [193]. Ever since streak cameras have been used as a tool for resolving ultrafast events in different applications across different spectral regions, e.g., sub-ps X-ray emission from laser-induced plasma [194], study beam dynamics from accelerator [195], spectral evolution of fluorescence [196], and study of ultrafast solvent dynamics [197]. The concept of streak cameras has been pushed to its frontiers by breaking the time resolution down to attosecond timescale [198, 199].

A streak camera is an ultrafast optical detector designed for capturing extremely short time events. It offers 2D information, i.e., light intensity vs. time vs. position, or it can be vs. wavelength. The operation principle is as follows: light is passed

through a slit and focused onto a photocathode inside the streak tube. Then, the photocathode converts the incident light into electrons, directly proportional to its intensity. High speed sweep electrodes accelerate and deflect the photoelectrons, which then strike a phosphor screen, converting them back to light, which represents temporal and spatial light intensity variations. Earlier optical pulses arriving at the phosphor screen are displayed at the top corner, while later pulses are displayed below. The key advantages of a streak camera are the capability to perform simultaneous measurements of light intensity on spatial (or wavelength) and temporal axes, it has a superb temporal resolution, down to sub-ps, in addition to having a wide dynamic range from detecting a single event up to high-repetition phenomena (e.g. GHz). Further, it covers a broad spectral detection range, from X-rays to near IR [200]. Streak cameras also possess ultra-high sensitivity, down to a single photoelectron, and a real-time readout system, for image processing without any delay because of film processing.

One of the major applications in which streak cameras play a pivotal role is fluorescence spectroscopy and microscopy. In this application, fluorescence emission from a target specimen is collected and sent to the streak camera, which works according to the operation principle elaborated earlier. Spectral information can as well be gathered about the specimen, if a grating is used for dispersing the emitted fluorescence. This fluorescence measurement system provides a 2D image that contains spatial, spectral and temporal information. A schematic representation of a typical setup to study fluorescence emission, showcasing the various components involved in a streak camera is presented in Fig. 2.43.

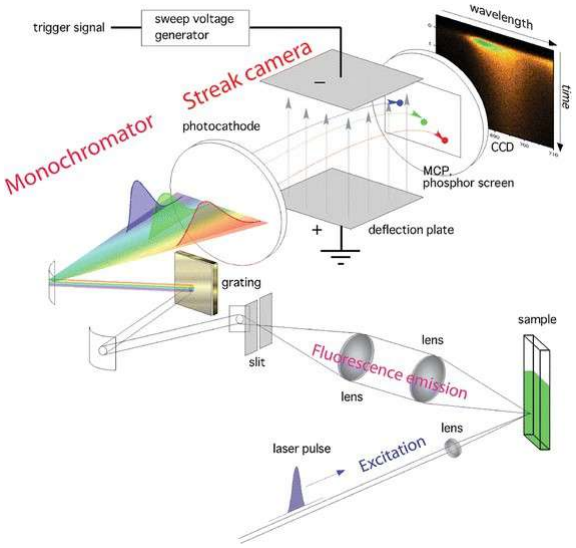


Figure 2.43: Scheme of a setup for studying fluorescence emission, showcasing the different elements of a typical streak camera [201].

Biomedical applications, such as probing protein targeting and mutations in a specific

protein sequence, are not obtainable with conventional intensity-based fluorescence lifetime microscopy (FLIM). Combining fluorescence lifetime microscopes with a streak camera, so-called streakFLIM, can circumvent this barrier that ultimately enables probing of fluorescence dynamics, as demonstrated by Krishnan et al. [42]. Measurement of single quantum emitters, i.e., GaAs QDs has been demonstrated by Hours et al. [21] (2005), where the radiative lifetime of an exciton, as short as 100 ps was measured via a streak camera with 20 ps temporal resolution. Streak cameras have been proven to be a powerful tool for feeble signal measurements, even at single-photon level. For example, single-photons from a parametric down-conversion photon source in the telecom wavelength range have been measured by a streak camera, as reported by Allgaier et al. [202] (2018). Typically, streak cameras have low signal-to-noise ratio in the IR regime, which hinders efficient photodetection at this regime. To overcome this challenge, they utilized up-conversion technique in a periodically-poled Lithium niobate waveguide, to convert the telecom single-photons into visible regime, which can be harnessed with commercially available streak cameras with maximum detection efficiency. For extensive reviews of fluorescence measurements by a streak camera, Ref. [201] and Ref. [203] are good references.

In spite of the key advantages that streak cameras have, they also have some drawbacks letting them not always be an ideal choice for ultrashort light phenomena. For example, streak cameras are sophisticated large-sized devices with different photoelectronic components for resolving ultrafast time events, and they are sensitive to environmental factors such as temperature and vibration. This demands frequent calibration for reliable measurements. In addition, the cost of a streak camera is very high, in the range of a few hundred thousand dollars, which is not an affordable budget. Technically, the space-charge effect of the photoelectrons poses considerable challenge for ultrashort time resolution, in particular on sub-ps time scale, despite the efforts to overcome this obstacle [204]. Moreover, the high speed sweep electrodes have a trigger jitter upon sweep initiation, which makes streak cameras difficult to synchronize them with e.g., GHz repetition rate lasers. Although streak cameras have overall high-sensitivity, this is not the case over wide spectral range, as we pointed out, where their signal-to-noise ratio is not sufficiently high in the IR regime. Given their ability to acquire 2D images with spatial, temporal or wavelength information, the large data volume also poses storage and processing challenges. This issue besides the slow readout system of the camera make them not ideal choice for GHz repetition detection events.

2.4.2 Femtosecond fluorescence measurement by two-photon interference

This is a technique developed for measuring fluorescence emitted on ultrafast timescales, i.e., fs, which employs two-photon interference. It is established based on the principle of intensity interference, akin to two-photon correlation technique developed by Hanbury Brown-Twiss [67, 68], explained earlier in section 2.1.5, aiming at overcoming the limitation associated with the time resolution, often determined by the detector response time. This is actually attained by merging a Mach-Zehnder interferometer with the two-photon correlation technique. That combination demonstrated the ability to measure the coherence time of light [205], as well as the beat frequency between light beams of different frequencies [206]. The idea was extended by Miyamoto et al. [207] to measure the temporal variation of the field intensity, and successfully measured the ultrafast pulse widths and the coherence time from a coherent light source, a mode-locked dye laser in that case. As known, unlike lasers that are coherent light sources, fluorescence emitters are incoherent sources. Meaning that each fluorescence emission has a random phase in comparison to other emissions from the same sample.

The application of the aforementioned technique has been extended further by Baba et al. [43] from the same research group to include incoherent light sources, e.g., fluorescence emission. Further, this technique has been applied so that it can separately measure the coherence time and the ultrafast fluorescence pulse widths (envelope widths), which are otherwise superimposed together. The bottleneck of the original two-photon intensity interference in terms of the slow response time of the photodetectors is overcome by employing a scheme in which the two-photon interference is measured by two-photon detectors at the output ports of the two arms of the Mach-Zehnder interferometer, which can be delayed in time using, e.g., a delay line, as shown in Fig. 2.44. In such a scheme, the time resolution of the coincidence photon detection is merely limited by the minimal possible displacement of the delay line and the accuracy of the positions.

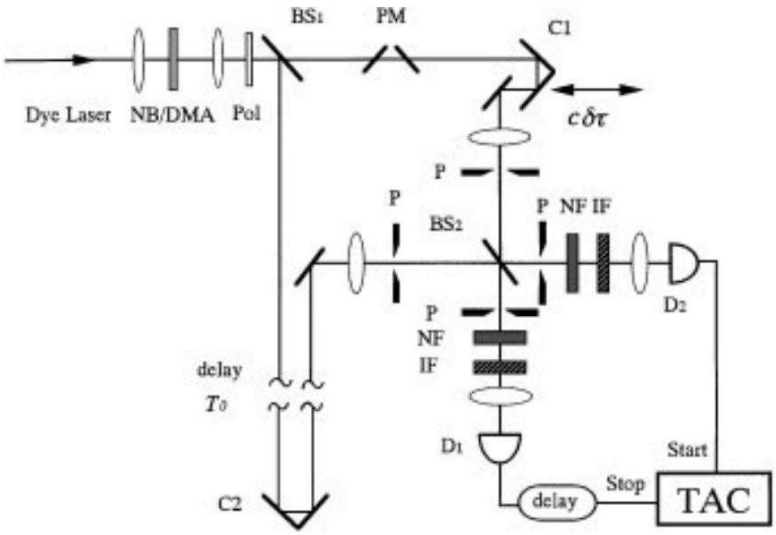


Figure 2.44: Scheme for separately measuring the coherence time and the pulse envelope of ultrafast fluorescence pulses, combining two-photon intensity detection with a Mach-Zehnder interferometer. As seen the emitted fluorescence is split via BS_1 and has fixed time delay T_0 in one arm, and controllable time delay c $\delta\tau$ in the other arm [43].

The key idea to separate the coherence time τ_c from the pulse envelope width τ_L of two incoherent fluorescence pulses is to introduce a fixed delay of one pulse repetition T_0 in time between the two arms of the Mach-Zehnder interferometer to measure solely the pulse envelope τ_L; or to introduce a fixed time delay T_0 electronically between the two detectors to measure only the coherence time τ_c. In the case of delaying the two adjoining fluorescence pulses between the two arms of the interferometer, what is being measured is the coincidence photon counts between the two detectors as a function of a variable delay c $\delta\tau$ between the two arms of the interferometer. The fixed time delay T_0 plays the role of destroying the phase coherence between the fluorescence pulses in each arm, and the two detectors measure the coincidence counts of two different pulses, however the intensity correlation does not vanish, which enables measuring only τ_L but the coherence dip τ_c has already vanished. By allowing equal time arrival between the two arms but introducing an electronic offset T_0 between the two photodetectors, the measurement is carried out using the same fluorescence burst but the photodetectors measures delayed version, in which case the envelope profile is wiped out but the indistinguishability between the two coincident photons causes a dip that belongs only to the coherence dip, which allows measuring its time width τ_c separately. This method has been successfully applied to measure the ultrafast fluorescence emission from a dye solution of Nile blue dissolved in a neat N-dimethylaniline (DMA). Based on the measurements, the deconvolved τ_L from the autocorrelation curve, shown in Fig. 2.45, was found to be 90 fs, which is close to the 100 fs decay time, reported in [208] of the same dye solution. The

coherence time τ_c was obtained by extending the delay cable between BS_2 and the TAC for introducing a pulse repetition delay T_0 and found it to be 370 fs.

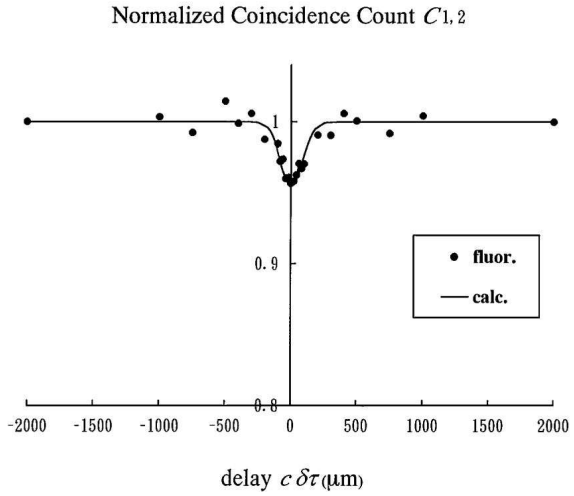


Figure 2.45: Normalized coincidence counts of ultrafast fluorescence pulse (dots) as a function of the delay $\delta\tau$, and the calculated curve (line). The dip represents the autocorrelation function of the fluorescence envelope, separated from the coherence dip [43].

This technique offers significant advantages such as the lack of need to use nonlinear crystals, which enable the application of it for some spectral regions where there are no nonlinear crystals covering their spectral range. Moreover, the technique does not require high power lasers, and it can detect relatively weak signals like fluorescence emission. Also, the temporal resolution offered by this technique is limited by the minimal movement increment of the linear translation stage. However, the technique suffers from some critical disadvantages. For instance, for very weak signals, e.g., fluorescence of a small ensemble of quantum emitters, the data acquisition becomes a hurdle, whereas a very long time of integration is needed, in order to get recognizable coherence or pulse envelope dips [44]. This demonstrates the inability of this technique to be applied for ultrafast single-photon emitters. Further, the technique is very sensitive to dark counts, which severely affects very weak fluorescence signals. Another major drawback is that, as we have seen, the recovery of the ultrafast fluorescence pulse width (fluorescence lifetime) is obtained from its autocorrelation curve. This requires the solution of an ill-posed problem [209], because of the lack of uniqueness of the solution, that is the fluorescence lifetime in this case. In other words, different fluorescence lifetime decay curves can give the same autocorrelation curves, which imposes a challenge on the recovery of the actual fluorescence lifetime.

2.4.3 Double-pulse excitation photon anti-bunching for single-molecules

Here is another technique, for resolving the ultrafast fluorescence emission devised specifically for single-photon emitters, which relies on femtosecond double-excitation (FeDEx) for interrogating photon correlations, where the degree of photon anti-bunching is measured as a function of the time delay between the two excitation pulses. This technique was introduced by the group of John Lupton [45] with the aim to measure ultrafast fluorescence from single-photon emitters, while circumventing other techniques shortcomings. The core idea of FeDEx technique utilizes the photon statistics of single-photon quantum emitters, that is the photon antibunching, which those emitters exhibit. When a laser pulse excites a fluorescent sample, containing single quantum emitters, given that a single emitter can be considered as a two-level system, the single emitter undergoes a transition from the ground to excited state. After some time, it will relax back to the ground state, emitting a fluorescence photon, which will go through a 50/50 beam splitter of a HBT setup, and reach one of the photodetectors. When the single emitter is still at the excited state, if another laser pulse comes, whose delay in time Δt with respect to the first pulse is much less than the fluorescence lifetime τ_{PL} ($\Delta \mathrm{t} \ll \tau_{\mathrm{PL}}$), that single-photon emitter will not emit any photons. The single-photon quantum emitter can undergo another excitation and emission cycle, provided that the time delay between the two excitation pulses $\Delta \mathrm{t} > \tau_{\mathrm{PL}}$. At time delay $\Delta t = 0$ between the two photodetectors, the HBT will receive one photon at only one of the photodetectors. This means the number of coincidence detection counts at the center of the histogram $\mathrm{N_c}$ will be zero. On the other hand, when $\Delta t \neq 0$, the number of coincidence detection counts at lateral sides of the histogram N_l will be much higher. The operation principle of FeDEx is illustrated in Fig. 2.46.

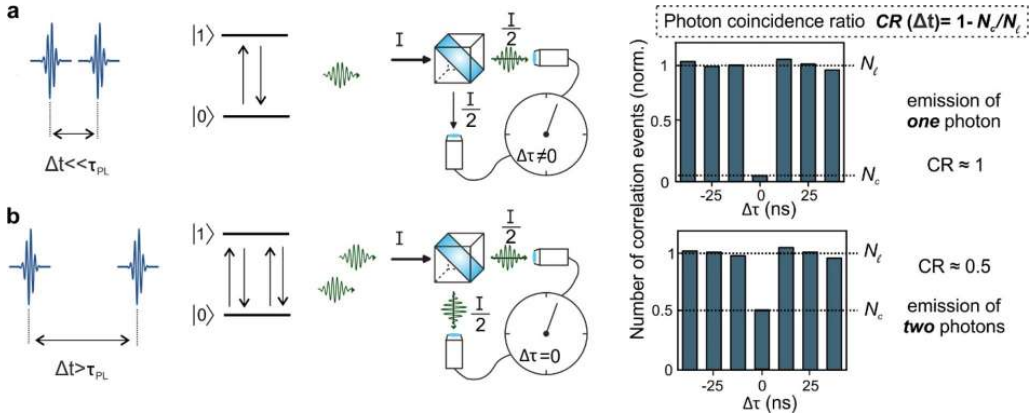


Figure 2.46: FeDEx technique for probing ultrafast dynamics of single-photon emissions. (a) Double excitation pulses separated in time less than fluorescence lifetime, and corresponding photon statistics (upper right), (b) Double pulses are separated in time more than fluorescence lifetime, with the effect on photon statistics (lower right) [45].

In FeDEx technique, the photon coincidence ratio as a function of the delay between the two excitation pulses is defined as $CR(\Delta t) = 1 - N_c/N_l$. Clearly, $CR(\Delta t) = 1$ when $\Delta t \ll \tau_{\mathrm{PL}}$ as $N_{\mathrm{c}} = 0$, while it is equal to 0.5, when $\Delta t > \tau_{\mathrm{PL}}$ because two photons will be excited due to the double-pulse excitation, where the 50/50 BS will typically send one photon at each photodetector. Technically, for implementing FeDEx technique, a fs laser at high repetition rate, i.e., 80 MHz is used for excitation and it is split into two train of pulses, where a linear translation stage is used to control the delay between the two consecutive pulses in time Δt. In spite of the stochastic emission of fluorescence photons, the excitation-emission cycles are initiated periodically at the repetition rate of the laser. For example, if an 80 MHz laser is used, each two consecutive pulses will be separated by a 12.5 ns in time. In turn, the lateral side peaks of the histogram will appear around $\pm$ n (12.5 ns), where n = 1,2,3... etc. In Fig. 2.46, one can see that indeed the locations of $\mathrm{N_l}$ appear at multiples of 12.5 ns.

In order to extract the fluorescence lifetime of the single-photon emitter or single molecule of interest, one counts the number of coincidence photon pairs (occurrence) from the CR curve at $\Delta t = 0$, for each time delay between the double excitation pulses Δt. The histogram of occurrence versus CR is then fitted to a Gaussian curve. This histogram is typically constructed from excitation by many laser pulses of a single molecule, and in this particular case from 100 single molecules to find any trend of the fluorescence lifetime. The single molecules' histograms, indicated in Fig. 2.47 (a) are from a phenyl-substituted ladder-type poly(para-phenylene) (PhLPPP), dispersed in a PMMA matrix, and deposited on a glass slide. The exponential decay curve of fluorescence lifetime can be constructed from the maximum of each Gaussian

curve fitting, each of which corresponds to a CR at a particular delay time Δt. From that data, a single-exponential decay curve can be used to fit the data for the lifetime determination, as shown in Fig. 2.47 (b). Alternatively, it is possible to logarithmically plot the data, in order to extract the fluorescence lifetime, from a straight line, illustrated in Fig. 2.47 (C). From the single-exponential decay curve in Fig. 2.47 (b), the conjugated polymer PhLPPP has a lifetime of 405 $\pm$ 8 ps. The photon coincidence ratio CR(∞), which is the CR value at very large time delay Δt between the double-excitation pulses is subtracted to remove any background from the photon coincidence counts.

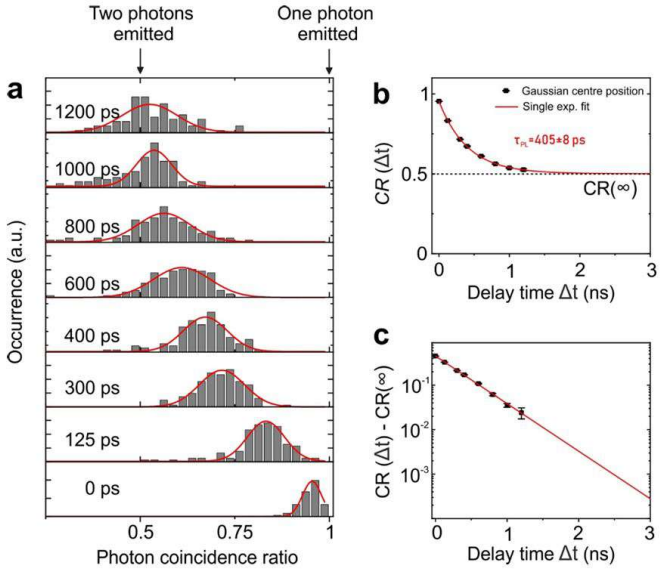


Figure 2.47: Fluorescence decay curve of conjugated polymer PhLPPP. (a) Histogram of number of photon pair coincidence at different delay time t (grey) and Gaussian function for each distribution (red), (b) Gaussian center position for each t (black), single-exponential curve fit (red), (c) Logarithmic plot of the data in (b) [45].

In addition to implementing the FeDEx technique on the conjugated polymer PhLPP, the technique was also successfully applied to measure the energy transfer time between donor-acceptor couples of a single dye-end-capped π-conjugated oligomer that transferred energy to the dye, where by virtue of this technique, the energy transfer measured time was 13.2 $\pm$ 2 ps. Furthermore, the same technique was utilized to measure radiative emission enhancement due to an increase in Purcell factor of a single Cy7 dye molecule, placed between two gold nanoparticles of 100 nm diameter. FeDEx technique was able to temporally resolve a fluorescence lifetime down to 19 ps from such a hybrid system, which significantly demonstrates the capability of resolving ultrafast time events at sub-ps timescale. It has been also used to study the nanoscale exciton diffusion and annihilation dynamics in multichromophoric nanoparticles, such as QD aggregates and conjugated polymers [210].

We have seen that FeDEx technique is based on a clever approach which employs the photon statistics associated with single molecules or single quantum emitters to infer their ultrafast emission dynamics. Moreover, it neither requires a nonlinear medium, nor very intense laser beams, and it is actually limited by the laser pulse duration used for exciting the single molecule of interest. However, the technique is restricted to only single emitters, owing to their photon antibunching behavior, which does not extend its usage beyond single emitters, i.e., ensembles.

2.4.4 Photon counting by time magnification

Time magnification, sometimes referred to as time lens, is an unconventional technique for photon counting. As known, the ultrashort lifetime of, for example, fluorescence cannot be resolved by either a SPAD or TCSPC, because the response time of the electronics used in those devices are slowly responding. The concept of time magnification is that the ultrashort lifetime of the signal under test (SUT) is stretched, or magnified in time, by applying a temporal phase modulation, so that a conventional photodetector would be capable of resolving it. The time lens in this regard is analogous to spatial lenses, which divert the light rays in the spatial domain, and it is achieved via a low-noise high-efficiency parametric time lens. Fig. 2.48 presents a depiction of the concept of time lens and how it works in conjunction with TCSPC systems.

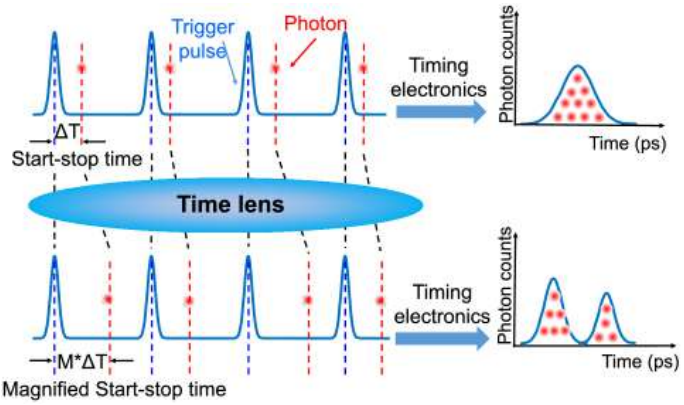


Figure 2.48: Scheme for illustrating the concept of time lens with timing electrons [46].

The time lens is essentially based on a parametric nonlinear optical process, so-called four-wave mixing Bragg scattering (FWM-BS). In FWM-BS, two swept strong pump beams co-propagate down a highly nonlinear fiber and create modulated refractive index gradient (moving grating). Along the two strong pump beams, a signal beam, which is in this case is the SUT interacts with the moving grating via FWM process, and energy is transferred to the SUT converting it into a magnified idler. The FWM

process is a phase-matched process, such that

$$\omega_i = \omega_s + \omega_{p2} - \omega_{p1} \tag{2.49}$$

$$k_i = k_s + k_{p2} - k_{p1} \tag{2.50}$$

where i denotes idler, s is signal, p_1 & p_2 denote pump 1 and pump 2, respectively, and can achieve $> 90\%$ conversion efficiency [211, 212].

Li et al. [46] applied the time lens technique via a spool of 30 m highly nonlinear fiber (HNLF), and two pump lasers. One was a swept pump laser generated by chirping of 100 MHz mode-locked Erbium (Er)-doped fiber through a 680 m of single-mode fiber, so that it introduces dispersion of -15.12 ps^2, then subsequently filtered by 14 nm bandpass filter to get the pump laser at 1540 nm, then amplified via an Er-doped fiber amplifier. This swept pump laser was stretched to 165 ps, which defines the time lens aperture. Second laser was a quasi-CW laser generated from a tunable laser source and emits at 1558 nm, and was modulated by an amplitude modulator synchronized with the swept pump into 360 ps pulses, which were then amplified. These two lasers create the moving grating, which interacts with the SUT. The SUT in their work was a sub-picosecond pulse with 5 nm bandwidth at 1255 nm, obtained through supercontinuum generation, and synchronized with the two pump lasers. It propagated through a 200 m of dispersion compensating fiber (DCF), which provided an input with dispersion 15 ps^2.

Their work demonstrated a temporal magnification ratio (M) of 130 of the SUT, and 97 % photon conversion efficiency, and a detection sensitivity of 0.03 photons/pulse, limited only by spontaneous Raman scattering noise. In order to achieve such high photon conversion efficiency, the swept pump (P_1) and the quasi-CW pump (P_2) were adjusted such that $P_1 = P_2$ and in the HLNF $(P_1 + P_2) \cdot \gamma \cdot L = \pi$, where is the nonlinear coefficient of the HLNF = 24 W^{-1} Km^{-1}. The signal at 1255 nm was converted to an idler at 1244 nm, which was then filtered and propagated through two DCF modules that provide 1958 ps^2 overall dispersion. Following the temporal magnification of the idler, a SPAD at a gated-mode with 5 ns gate-on time and TCSPC were used for the characterization of this SUT (output idler), a scheme of their setup is provided in Fig. 2.49.

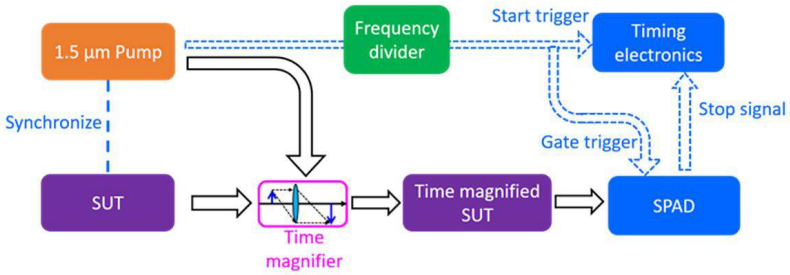


Figure 2.49: Scheme of time-magnified SUT with SPAD and TCSPC (TM-TCSPC) [46].

In order to determine the actual temporal resolution of the TM-TCSPC system, namely, the intrinsic IRF, four input SUT at 790 fs, 920 fs, 1040 fs, 1170 fs were generated, and measured via background-free second-harmonic generation (SHG) intensity autocorrelator (AC), respectively. The FWHM of any of the four pulses is denoted as W_{AC}, and considered the ground truth for the four pulses measurement. Afterwards, those signals were propagated through the TM-TCSPC system, which temporally magnified them. For getting the pulse widths, the resulting output idler for each pulse needs to be demagnified by the temporal magnification ratio, then deconvolved by the IRF of the system. The demagnified FWHM of TM-TCSPC signals $W_{TM\text{-}TCSPC}$ were obtained, and the intrinsic IRF of the system can be determined from $IRF = (W^2_{TM\text{-}TCSPC} - W^2_{AC})^{\frac{1}{2}}$, assuming Gaussian shape for the pulse widths and the IRF. The dispersive fibers used in their work introduced some distortion in the TM-TCSPC histogram, which were corrected by fitting the four pulses and minimizing the r.m.s error, and the intrinsic IRF of the system was found to be 550 fs.

2.4.5 Fluorescence lifetime Hong-Ou-Mandel sensing

This is a recently developed technique which relies mainly on Hong-Ou-Mandel (HOM) interferometry. Hong-Ou-Mandel interferometers use a two-photon interference effect for measuring coincidence count rate changes when the photons in one arm of the interferometer are delayed in time relative to the other arm. When two photons meet at the input port of a beam splitter and they are indistinguishable, due to quantum interference they will go through the same output port to one of the detectors, coincidence count rate measured by $g^{(2)}$ as a function of the relative delay between the two photons will consequently drop when the temporal delay is zero, a characteristic of HOM interferometers, known as HOM dip. In fact, the two-photon interference effect can occur between two independent light sources [213], and this effect can effectively even take place with incoherent light sources [214].

The approach developed by Lyons et al. [47] being discussed here employs this concept, called fluorescence lifetime Hong-Ou-Mandel (FL-HOM) where a reference signal which is in this case an attenuated laser pulse interferes with a fluorescence photon at the same wavelength. With random arrival times of fluorescence photons, and as the reference signal is delayed in time relative to the fluorescence signal, the $g^{(2)}$ function will have the shape of an exponential decay, associated with the fluorescence emission from which the fluorescence lifetime can be estimated. The technique enables detection of ultrafast fluorescence signals and can work at low-photon numbers, without a need for any nonlinear medium or high intensity lasers.

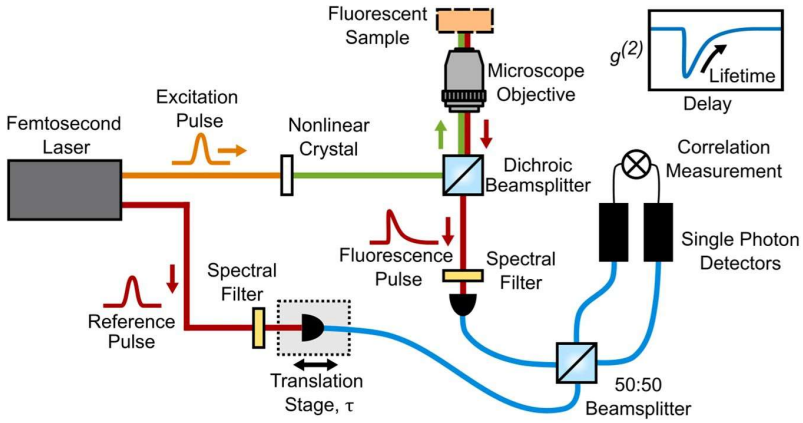


Figure 2.50: Experimental setup of FL-HOM. The top right corner illustrates the $g^{(2)}(\tau)$ from which fluorescence lifetime can be estimated [47].

Technically, the setup consists of a Mach-Zehnder interferometer using two outputs from the same pulsed laser source. One output is called excitation pulse (EP), which is used to excite the fluorescence emitter after being frequency-doubled to obtain a suitable wavelength for excitation of the sample. Fluorescence emitted by the sample is spectrally filtered from excitation pulse residual, and sent to a 50/50 BS through a single-mode fiber for spatial filtration. The second output labeled as reference pulse (RP) is tuned to the fluorescence emission, and synchronized with the EP, and spectrally filtered around fluorescence wavelength, and sent to the 50/50 BS through a single-mode fiber connected to a fiber coupler mounted on a translation stage to control the relative delay between the two light sources, as shown in Fig. 2.50. The two output ports of the 50/50 BS are connected via a pair of single-mode fibers to a pair of SPAD for photon detection, which are connected to a TCSPC unit.

The fluorescence intensity profile is basically a convolution between the temporal intensity profile of the excitation pulse $I_{\mathrm{ex}}(\mathrm{t})$ and the fluorescence lifetime $F_{\mathrm{fl}}(\mathrm{t})$, give

$$I_{\mathrm{FP}}(t) = I_{\mathrm{ex}}(t) * F_{\mathrm{fl}}(t), \tag{2.51}$$

where $F_{\mathrm{fl}}(t) = Ae^{-t/\mu}$ is the single-exponential decay of fluorescence emitted by

the sample, with A is the amplitude and μ is the decay constant. Evidently, this convolution integral reveals the fluorescence lifetime $F_{\text{fl}}(t)$, when $I_{\text{ex}}(t)$ is temporally short adequately with respect to the fluorescence lifetime being measured, so that $I_{\text{FP}}(t) \simeq F_{\text{fl}}(t)$. It is possible from the general form of the second-order intensity correlation function, discussed earlier in section 2.1.5 to calculate the normalized number of coincident photon pair events as a function of the optical delay between the two arms of the interferometer, controlled by the translation stage, which reads

$$C(\tau) \sim 1 - 4C_0(\sigma)e^{-\tau/\mu}, \tag{2.52}$$

where σ is the temporal duration of the reference laser pulse, C_0 is a constant that indicates the interference visibility between the two light sources, depending upon their amplitude, duration, and transmission and reflection constants of the BS.

To demonstrate its capability, the technique has been used to measure the fluorescence decay from three different samples, which are 4-DASPI dye, Allura Red dye that were discussed before in section 2.2.3, and Pinacyanol Iodide. From the measurement analysis the following fluorescence lifetimes were retrieved; 6.23 ps for 4-DASPI, 1.60 ps for Allura Red, and 3.66 ps for Pinacyanol Iodide, as shown in Fig. 2.51 below.

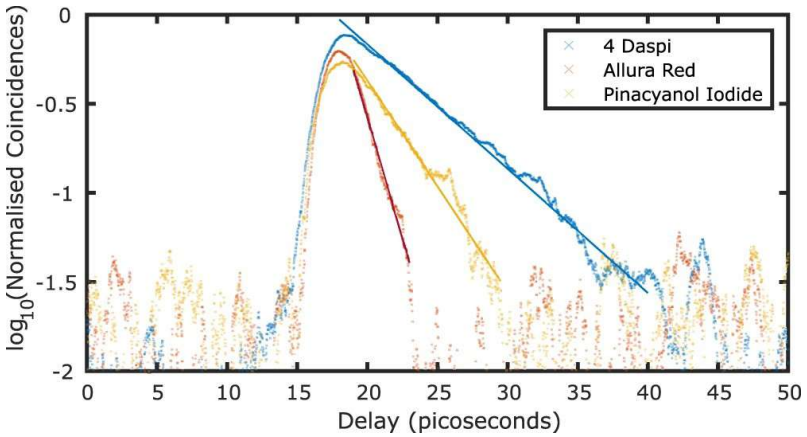


Figure 2.51: Lifetime estimation of different samples. Logarithm of the normalized coincidence counts (inverted) [47].

Although the FL-HOM technique is, fundamentally, limited by the reference pulse width, σ, the temporal resolution measurement is influenced by the spectral filter bandwidth used in the measurement. The wider the bandwidth of the spectral filter, the higher the temporal resolution and undesirably the lower the interference visibility between the RP and fluorescence signal. For optimal interferometric visibility, it has been found out that the reference pulse duration should be about 70% of the fluorescence lifetime. Similar to the previously presented ultrafast emission techniques, FL-HOM does not rely on nonlinear media, which often demand high power lasers.

However, the challenge with this technique, in addition to the aforementioned difficulty, is that it requires an interferometric precision to align the reference pulse and the faint fluorescence signal of interest. Such a task is typically difficult to achieve with moderately intense light sources, and it would be even more difficult to achieve, particularly for single-photons that would be partially lost when they are coupled to single-mode fibers.

2.4.6 Frequency up-conversion

Frequency up-conversion is one of the two widely applied fundamental nonlinear optical sampling techniques for time-resolving the ultrafast fluorescence emission. In this technique, the weak fluorescence signal is sampled via a strong pump beam (sometimes also called Gate beam) in a birefringent nonlinear medium, such as barium borate (BBO) or potassium dihydrogen phosphate (KDP) nonlinear crystals. The nonlinear sampling process occurs because the strong pump beam at ω_{G} is mixed with the weak fluorescence ω_{f} signal into the nonlinear crystal, and the detected signal is the sum of both input frequencies, that is why the detection is often referred to as background-free, as the output has different frequency than the frequency of the two input signals, which are dumped or filtered after the nonlinear crystals. In nonlinear optics jargon, this process is called sum-frequency generation (SFG), and it is a second-order nonlinear optical process $\chi^{(2)}$. Thus, SFG is a more sensitive process than the third-order nonlinear processes $\chi^{(3)}$, thereby it requires less intensity of the pump beam I_{G}.

One strictly necessary requirement to satisfy in SFG is the phase-matching condition, such that:

$$\omega_{SFG} = \omega_G + \omega_f, \tag{2.53}$$

$$k_{SFG} = k_G + k_f. \tag{2.54}$$

This can be attained by changing the crystal's angle θ, or by changing the frequency of the gate beam ω_{G}. It is also possible to satisfy phase matching conditions via changing the temperature of the nonlinear crystal [215]. Notably, in this process, the fluorescence of the frequency signal ω_{f} is up-converted by the gate beam frequency ω_{G}, hence this technique is given the name frequency up-conversion. A scheme of sum-frequency generation into a nonlinear crystal is presented in Fig. 2.52.

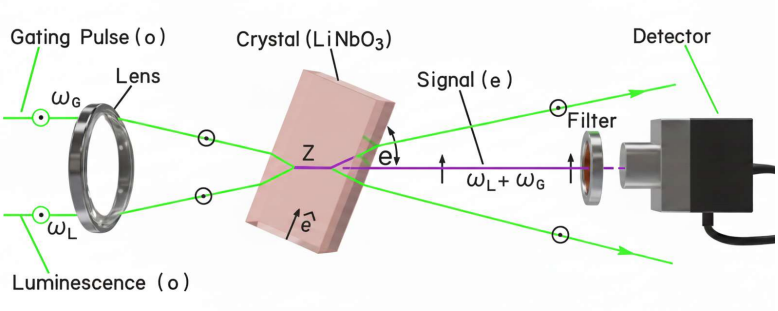


Figure 2.52: Scheme of sum-frequency between the gate pulse and fluorescence signal in a nonlinear crystal. Adapted from [215].

For sampling the ultrafast fluorescence signal, the gate beam is scanned at variable time delay with respect to the fluorescence signal, and the intensity of the sum-frequency generated signal I_{SFG} at any given delay τ is directly proportional to the cross-correlation between the two input beams, namely the gate and the fluorescence, and is given by the following relationship:

$$I_{\mathrm{sum}}(\tau) \approx \int_{-\infty}^{\infty} I_{\mathrm{fl}}(t) I_1(t-\tau)\, dt. \tag{2.55}$$

The above relationship holds under the assumption of a small fluorescence depletion, i.e., $< 10\%$ conversion efficiency [216]. The essence of this sampling scheme and its corresponding fluorescence energy diagram is illustrated in Fig. 2.53.

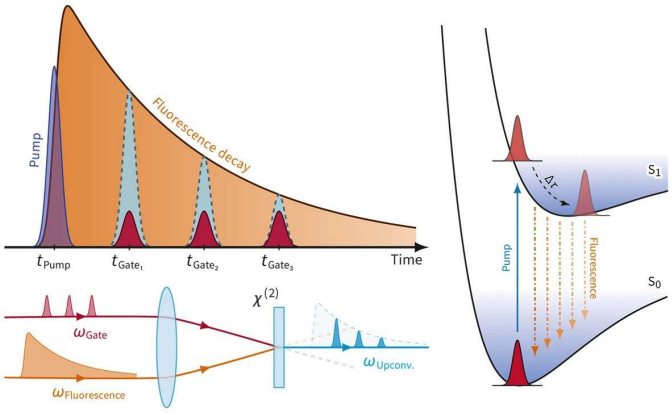


Figure 2.53: Nonlinear sampling of fluorescence signals via SFG and the corresponding energy diagram [217].

The conversion efficiency of SFG nonlinear optical process, which is the ratio between the power of the up-converted signal and the power of input signal is governed by the following relation [218]:

$$\frac{P_3}{P_1} = \frac{2^3 \pi^2 d_{\mathrm{eff}}^2 L^2 P_2}{\epsilon_0 c n_1 n_2 n_3 \lambda_3^2 A} \mathrm{sinc}^2\left(|\Delta k|\, L/2\right), \tag{2.56}$$

where P_3 is power of up-converted signal (SFG signal), P_1 is the power of input wave signal, which is in this case the fluorescence signal, and P_2 is the power of gate signal, respectively. All power values have the unit of Watt [W]. The effective nonlinearity of the crystal in the direction of phase matching is denoted by d_{eff} m/V, L is crystal length in m, $\epsilon_0 = 8.854 \times 10^{-12}$ F/m is the vacuum permittivity, c = $3{\times}10^8$ m/s; n_{i} is the refractive indices of fluorescence, gate and up-converted signal, respectively. The wavelength of up-converted signal is expressed by λ_3 [m], and $A = \pi w_0^2$ is the cross-sectional area in m^2 of the laser beam with a beam radius w_0. In Eq. 2.55, all the units follow the SI system, and the plane-wave fixed field approximation is adopted, which signifies that several restricting factors can be neglected, such as diffraction, anisotropy and group-velocity mismatch, etc. From that equation, one can see that the conversion efficiency can be increased, either by increasing the power of the gate beam P_2, or by increasing the nonlinear crystal length L.

SFG is a parametric process, meaning that the population of electrons at the ground-state do not move to a real excited-state, and the entire process occurs solely up to virtual energy levels. This gives an advantage in terms of the time resolution of the frequency up-conversion technique, as it would be only limited by the gate's pulse width. On the other hand, the necessity to satisfy phase matching condition poses considerable challenge for this technique, as it is often achieved over narrow spectral range. If the fluorescence quantum emitter has a broad fluorescence emission, either the nonlinear crystal must be tuned to maintain phase matching condition, or the gate laser beam be tuned in order to scan the full spectral range of the fluorescence emission, while keeping the ω_{SFG} fixed at which the phase matching condition is met. Nevertheless, increasing the $\chi^{(2)}$ nonlinear crystal length will limit the acceptance bandwidth of weak input signal. Broad phase matching condition can be attained when a thin nonlinear crystal is used, although to compensate for the reduction of the thickness of the nonlinear crystal, higher input power of the strong input signal will be needed for efficient conversion efficiency.

Upconversion of broad fluorescence bandwidth of 7200 cm^{-1} ($\approx$ 1389 nm) from a laser dye Coumarin 153 in acetonitrile, and 4-dimethylamino-4'-cyanostilbene (DCS) in acetonitrile was achieved by using a thin KDP nonlinear crystal (100 μm) and with 100 fs time resolution, without readjustment of the optical elements of the setup [219]. Given the thin thickness of the KDP used in this work, the strong input laser was amplified to adequately high power to obtain good conversion efficiency. Rong et al. [220] demonstrated the detection of fluorescence at single-photon level from SiV color center in diamond at 738 nm by upconverting its frequency to 436 nm in a periodically-poled lithium niobate (PPLN) crystal using sum-frequency generation between the fluorescence emitted at 738 nm and a short (11 ps) pump laser at 1064

nm, with the aim to avoid the time jitter introduced by the APD and TCSPC often used in fluorescence detection. The extracted lifetime of the measured fluorescence was 0.755 ns, which is comparable to the time-jitter from the single-photon detectors.

Some quantum optics applications such as quantum cryptography and quantum communications cannot take full advantage of the low-loss at the telecom wavelength 1550 nm in optical fibers. Single-photon counters often utilized at this wavelength are InGaAs, and they are not fairly efficient, due to their high DCR. To overcome their limitation, sum-frequency generation offers frequency upconversion down to single-photon level at 1550 nm to visible wavelengths, which can be more efficiently detected via Si APDs [48, 221, 222, 49]. For example, M. Albota et al. [48] showed that frequency upconversion of single-photons at 1550 nm to the visible range at 631 nm can be achieved by sum-frequency generation of light at 1550 nm with a pump laser beam at 1064 nm in a PPLN crystal. The power emitted at 1064 nm from the Nd:YAG laser was 400 mW and was not sufficient to obtain good conversion efficiency of the 1550 nm signal. To overcome this limitation, this laser power was circulated in a resonant pump cavity, which raised the input power to 21.6 W. This enabled the conversion efficiency to reach 90 %.

Imaging in mid-IR (e.g. 2-5 μm) wavelength range has attracted interest due to wide-ranging applications, such as cosmic exploration, defect inspection, remote sensing, and medical diagnosis. The camera imagers usually used in mid-IR wavelengths range from narrow bandgap semiconductors, e.g., HgCdTe and InSb. These imagers require an expensive fabrication process based on epitaxial growth methods and cryogenic operation. Significant progress has been achieved for room temperature operation of photodetectors that work in mid-IR range, rather than the conventional sensors, which also possess high DCR. Frequency upconversion has been an alternative, by mid-IR photons can be upconverted to visible frequencies that can be efficiently detected via Si-based photodetectors, as they have superior performance relative to the conventional mid-IR sensors. For example, a wide-field mid-IR single-photon conversion imaging has been recently realized at high-frame-rate and 3D-imaging [223].

The high temporal-resolution (sub-ps) of the frequency upconversion technique, limited by the laser pulse width, has sparked an interest to utilize this technique to study the ultrafast dynamics of biological systems, such as tryptophan, proteins, peptides and nucleic acids, and their interaction with their surrounding environment. Tryptophan, for example, is a pivotal amino acid and its biological significance lies as it is one of the building blocks of proteins. Moreover, it is a precursor for some key molecules such serotonin and melatonin. It often exhibits complex fluorescence decay, i.e., bi-exponential lifetimes, and such behavior arises from microheterogeneity in local

environment and interactions, like charge transfer, solvent relaxation and quenching [224]. For more information about the application of frequency upconversion for study of ultrafast fluorescence emission in biophysics, the reader is referred to refs. [225] and [226].

As we have seen, despite its high temporal resolution, and its need for less intense laser, compared to the so-called optical Kerr gate, as will be discussed in the subsequent subsection; frequency upconversion technique is cumbersome as it requires fulfilling the phase matching condition, which would be difficult to apply with broad spectral fluorescence signal, especially for ultrashort signals, since as we know the shorter a signal in time, the wider it is in the frequency domain. Moreover, it dictates buying expensive nonlinear crystals, and exposing them to highly intense laser fields.

2.4.7 Optical Kerr gate

Optical Kerr gate (OKG), also called optical Kerr gate (OKS) is another technique that belongs to nonlinear optical sampling techniques, and it is based on optical Kerr effect, named after the Scottish physicist John Kerr. Optical Kerr effect describes the modification of the refractive index of a medium due to the high intensity of an optical field I(t), i.e., laser, as indicated in the equation below.

$$n(I) = n_0 + n_2 I(t). \tag{2.57}$$

When a weak laser beam propagates through a medium, it experiences the traditional linear refractive index n_0. But if the laser beam intensity is high, the medium in which this intense beam is propagating will experience a modification of the linear refractive index n_0, thus another term consisting of the so-called nonlinear refractive index n_2 and the laser intensity has to be added, as seen in Eq. 2.57. In other words, the total refractive index experienced by the medium will be a function of the laser intensity. Optical Kerr effect will be explained in more detail in section 3.3.2 of Chapter 3.

Optical Kerr gates consist of a nonlinear medium situated between two crossed polarizers. This nonlinear medium is sometimes also referred to as Kerr medium. In principle, most materials can be Kerr media, and it can be solid, liquid or gas. Typically, the Kerr medium must be isotropic, meaning the linear refractive index n_0 is uniform across all directions in the medium. When a linearly polarized intense laser beam, often called gate or pump beam impinges onto this nonlinear medium, it induces birefringence. Another weaker laser beam passing through the same medium but with different polarization direction can probe such induced birefringence. Such

a weak beam is often called a probe beam. Normally, the probe beam passes through the first polarizer, and the Kerr medium, since the Kerr medium must be chosen to be transparent for the pump and probe wavelengths propagating through it. However, the second polarizer (also called analyzer), which is set at 90° with respect to the first polarizer will block the passage of the probe beam, thereby hindering it from reaching the detector. The birefringence occurs since the nonlinear medium (Kerr medium) along the polarization direction of the intense laser beam experiences a different refractive index than the refractive index n_0 experienced in other directions. Thus, when a linearly polarized probe beam propagates along the Kerr medium at a polarization angle θ, relative to the pump polarization, its projection onto the pump beam will experience $n_0 + n_2 I$, while its projection onto the perpendicular direction will experience n_0. This creates a difference in refractive index Δn, where $\Delta n = n_2 I$, which will eventually lead to a phase shift $\Delta\varphi$. As a result the probe beam polarization will be slightly rotated. The operation principle of an optical Kerr gate resembles to some extent the half-wave plate.

The influence of an intense laser beam on a weaker beam is often called cross-phase modulation, which is described in more detail in section 3.3.4 of the next chapter, and it is considered one of the third-order $\chi^{(3)}$ nonlinear optical processes. This provides a major advantage because the phase matching condition does not need to be fulfilled. Besides, optical Kerr gates can achieve high temporal resolution as it is solely governed by the materials response time. When an electric field (from the intense laser beam) is applied on a Kerr medium, the electron cloud responds nonlinearly to the applied electric field, which is called electron hyperpolarizability, and is often a very fast response like in most solids. In some other materials, e.g., liquids, besides the electron cloud response, the nucleus also contributes to the materials response time. This often arises from the molecular reorientation, and leads usually to slower response since the nucleus is much heavier than its surrounding electrons. Thus, depending on the Kerr medium, sub-picosecond temporal resolution could be attained. The disadvantage of optical Kerr gate technique, though, is that it requires highly intense laser beams, usually obtained via laser amplifiers at low repetition rates, because $\chi^{(3)}$ nonlinear optical processes are less sensitive than their $\chi^{(2)}$ counterparts.

In a standard experimental setup of an optical Kerr gate, the pump beam is sent through Kerr medium to induce a birefringence, and variable time delay $\Delta\tau$ is introduced to the probe beam. As the probe beam propagates along the Z-axis in the medium, it accumulates the induced nonlinear phase shift $\Delta\varphi$. In order to maximize the transmitted probe signal, the two beams must be spatially and temporally overlapped in the Kerr medium.

In addition to achieving spatial and temporal overlap between the pump and probe, the angle of polarization between the pump and probe must be 45° to maximize the transmitted probe signal for a given nonlinear medium. There are other parameters that help to maximize the induced nonlinear phase shift, hence the transmitted probe beam signal. For instance, the intensity of the gate beam I_{gate} should be very high, also the Kerr medium should be carefully chosen such that it possesses the highest possible n_2 value. Furthermore, on one hand, increasing the thickness of the Kerr medium L ensures increasing $\Delta\varphi$; on the other hand, though, after a certain thickness, the group velocity dispersion (GVD) will begin to play a role and will reduce the gate intensity. Therefore, increasing the Kerr medium thickness should be reasonably done, unless the medium is engineered to have zero-dispersion at the gate beam wavelength, like in the case of photonic crystal fibers (PCFs). A scheme of an optical Kerr gate is illustrated in Fig. 2.54.

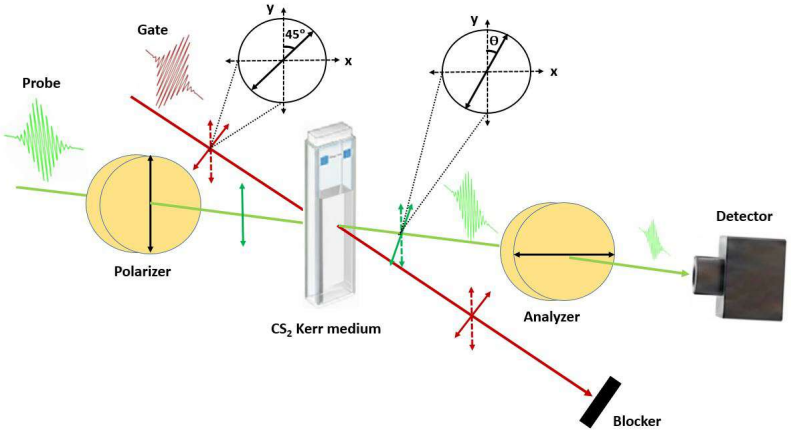


Figure 2.54: Optical Kerr gate.

Since inducing cross-phase modulation requires powerful optical fields, implementing optical Kerr gate was only possible after the invention of lasers in 1960 [227]. The first implementation of an optical Kerr gate was achieved by Duguay and Hansen in 1969 [228]. In their work, a green laser at 530 nm generated via second harmonic generation in a 2 cm KDP crystal was the probe, while the gate beam was an IR laser at 1060 nm. Two liquids were used as Kerr media, one was carbon disulfide (CS_2), whose response time was $\sim$ 1.8 ps, and the second was nitrobenzene, which has a 32 ps response time. A few years later, Sala and Richardson [229] analysed the theoretical aspects of optical Kerr effect induced by ultrashort laser pulses in conjunction with optical Kerr gates. With the onset of femtosecond lasers [230], a direct measurement of sub-picosecond birefringent response in CS_2 became possible [231, 232]. The availability of laser sources enables the study of Kerr effect and optical Kerr gates in various media, such as liquids [233], organic materials [234], optical fibers [235], bulky solids [236], e.g., glasses [237, 238], and 2D materials [239,

240].

Due to the high temporal resolution, the lack of necessity to achieve phase-matching condition, and the feasibility of its implementation, OKS technique has attracted much interest for wide applications, such as optical gating in spectroscopy [241, 50, 242, 243, 244], microscopy [245, 246], imaging of 2D objects [247], 3D imaging [248], or through turbid medium [249], and all-optical ultrafast switches [250], just to name a few. For example in [245], a wide-field Kerr-gate based microscope was developed capable of collecting diffraction-limited 2D fluorescence images with sub-100 fs time resolution. The gate pulse, in their work, was at 790 nm, with relatively high energy of 40 μJ, low repetition rate of 1.25 kHz, and 60 fs pulse duration. The Kerr medium was 0.5 mm of fused silica, and the microscope was tested by firstly studying the ultrafast emission from a cluster of gold nanoparticles, and secondly, 4-dimethylamino–nitrostilbene (DNS) dissolved in tetrahydrofuran (THF) in a 1 mm fused silica cuvette. Later, this microscope was utilized to study the ultrafast carrier dynamics in a single CdSSe nanowire at different excitation fluences [251]. In [246] another version of the Kerr-gate microscope capable of resolving ultrafast fluorescence in the UV region was developed. In our work here, the aim has been to develop a Kerr-gate microscope capable of studying ultrafast fluorescence emission with sub-ps time resolution, low-energy gate laser at high repetition rate. Optical Kerr gates have shown importance for some ultrafast quantum optics applications. For example, recently, using an optical Kerr gate, an ultrafast measurement of a heralded single-photon wave packet at sub-ps time resolution from an entangled single-photon source was performed, where the Kerr medium was a 28 cm PCF placed inside a Sagnac interferometer [252].

Chapter 3

Nonlinear optical sampling via optical Kerr gate

In this chapter we introduce the basic concepts that belong to nonlinear optics, with emphasis on those of particular relevance to our work. We begin the first section, with a brief introduction of nonlinear optics. Then, a brief introduction about third-order $\chi^{(3)}$ nonlinear optical processes will be presented. In the next section, we focus particularly on intensity-dependent refractive index physical phenomena, such as optical Kerr effect, two-photon absorption, etc. The last section presents a semi-analytical model that demonstrates the possibility of ultrafast detection of single-photon emitters at high repetition rates, under the tight focusing of the laser spot sizes of the gate and probe beams.

3.1 Introduction to nonlinear optics

The nonlinear optical sampling technique we are trying to demonstrate in this work, namely optical Kerr gate (OKG) for gating ultrafast fluorescence signals, sometimes called optical Kerr shutter (OKS) relies essentially on the so-called optical Kerr effect (OKE). OKE is a nonlinear, intensity-dependent change in the refractive index, n, of a material in response to an applied electric field. OKE arises from a third-order nonlinear optical process $\chi^{(3)}$. Unlike second-order $\chi^{(2)}$ processes, which require a noncentrosymmetric medium to occur, third-order $\chi^{(3)}$ are not bound by inversion symmetry and occur in centrosymmetric and noncentrosymmetric media provided the field is sufficiently intense.

In linear optics, the induced polarization $\tilde{\mathbf{P}}(t)$ (defined as the dipole moment per unit volume), of a material depends on the strength of the electric field $\tilde{E}(t)$, often

described by

$$\tilde{\mathbf{P}}(t) = \epsilon_0 \chi^{(1)} \tilde{\mathbf{E}}(t), \tag{3.1}$$

where the proportionality constant $\chi^{(1)}$ is the linear susceptibility, and ϵ_0 is the free space permittivity. For description of nonlinear optical responses of a medium, Eq. 3.1 must be generalized, such that the induced polarization $\tilde{\mathbf{P}}(t)$ is expressed as a Taylor-series expanded to be

$$\begin{aligned} \tilde{\mathbf{P}}(t) &= \varepsilon_0 \left[\chi^{(1)} \tilde{\mathbf{E}}(t) + \chi^{(2)} \tilde{\mathbf{E}}^2(t) + \chi^{(3)} \tilde{\mathbf{E}}^3(t) + \cdots \right] \\ &\equiv \tilde{\mathbf{P}}^{(1)}(t) + \tilde{\mathbf{P}}^{(2)}(t) + \tilde{\mathbf{P}}^{(3)}(t) + \cdots . \end{aligned} \tag{3.2}$$

where $\chi^{(2)}$ and $\chi^{(3)}$ are the second-order and third-order nonlinear optical susceptibility, as mentioned earlier, and both $\tilde{\mathbf{E}}(t)$ and $\tilde{\mathbf{P}}(t)$ are considered scalar quantities, so far, for simplicity [253]. In reality, $\tilde{\mathbf{E}}(t)$ and $\tilde{\mathbf{P}}(t)$ are vector quantities, and in this case $\chi^{(1)}$, $\chi^{(2)}$ and $\chi^{(3)}$ are second-, third-, fourth-ranking tensors, respectively. We also assume that the medium responds instantaneously to the applied electric field, and that the medium is lossless and dispersionless. In our treatment of optical Kerr shutter under tight focusing, we took dispersion into account, as will be explained in section 3.4. From, Eq. 3.2 we can see that, the second-order nonlinear optical polarization is $\tilde{\mathbf{P}}^{(2)}(t) = \varepsilon_0 \chi^{(2)} \tilde{\mathbf{E}}(t)^2$, and the third-order nonlinear optical polarization is $\tilde{\mathbf{P}}^{(3)}(t) = \varepsilon_0 \chi^{(3)} \tilde{\mathbf{E}}(t)^3$.

3.2 Third-order nonlinear optical susceptibility processes

There are various nonlinear optical phenomena, wherein the material responds to the cube (third power) of the applied electric field. These processes typically demand higher intensity to occur more than their counterparts of second-order nonlinear $\chi^{(2)}$ processes. Some examples of such third-order nonlinear optical $\chi^{(3)}$ processes include third-harmonic generation (THG), optical Kerr effect (OKE), self- and cross-phase modulation (SPM & XPM), four-wave mixing (FWM), nonlinear absorption.

Third-harmonic generation is a nonlinear optical process, in which three photons with frequency ω are annihilated and one photon at 3ω is created. This process enables the conversion of an electromagnetic field at a certain frequency to a higher frequency. Such a process can be helpful, for example, to access some spectral regions beyond the emission spectrum of a laser crystal. The optical Kerr effect represents a modification of the refractive index Δn of a certain medium's refractive index n_0, often called Kerr medium, in response to an intense light beam, i.e., ultrashort laser,

propagating through that medium, such that $n(I) = n_0 + \Delta n$, where $\Delta n = n_2 I$. This effect has been employed in numerous applications, such as Kerr-lens for mode-locked laser pulses [254, 255, 256], optical light switching [250, 257, 258, 259], fluorescence spectroscopy [241, 243, 244] and microscopy [245, 246], and most recently OKE has extended to new applications, such as biomedical applications [260, 261], even has been used as an underlying mechanism for high-harmonic generation [262] and attosecond pulses [263]. Self-phase modulation (SPM) is another important nonlinear optical phenomenon. It occurs when a laser beam modifies its own phase through the intensity-dependent refractive index. It is considered a self-action phenomenon, because it involves a single beam affecting, or acting upon itself. SPM is the basis of another important phenomenon: supercontinuum generation, during which the spectral band of an ultrafast intense laser beam expands drastically yielding a very broad, even beyond an octave spectral band, covering several spectral regions at once [264, 265]. A counterpart of self-phase modulation is the so-called cross-phase modulation (XPM), which unlike self-phase modulation, involves two beams where one strong laser beam - often called pump beam (sometimes is called gate beam) - affects the phase of another weak laser beam, often called the probe beam. As a matter of fact, this process is the underlying operation principle of optical Kerr shutters, which typically does not allow the probe beam to pass through it, unless the pump beam rotates the polarization of the probe beam via inducing a nonlinear phase change of it [266]. Four-wave mixing (FWM) is a nonlinear optical process that involves three input beams, and one output beam. Besides the demand for high optical intensities, it does require achieving phase-matching. Nonlinear absorption is another $\chi^{(3)}$ process, where under high laser intensity, two or more photons are absorbed at certain ω, promoting an electron to a real energy level, in contrast to, i.e., THG whereby three photons reach a virtual energy state. Nonlinear absorption also includes the so-called saturable absorption. In this case, the ability of a material to absorb energy is reduced under the high intensity laser irradiation. This has been mainly useful for saturable absorbers, for Q-switching or mode-locked lasers.

It is helpful to express the total polarization induced in a medium as a sum of a linear ($\tilde{P}_L(t)$) contribution and a nonlinear contribution ($\tilde{P}_{NL}(t)$) :

$$\tilde{\mathbf{P}}_{TOT}(t) = \tilde{\mathbf{P}}_L(t) + \tilde{\mathbf{P}}_{NL}(t), \tag{3.3}$$

where the nonlinear part ($\tilde{P}_{NL}(t)$) in the case of third-order nonlinear optical processes represents the third-order polarization $\tilde{\mathbf{P}}^{(2)}(t)$. Eq. 3.2, mentioned earlier, neither takes into account the medium absorption, nor its dispersion. Assuming material homogeneity, invariance by time translation and causality principle, the general

expression of linear polarization [267], will be

$$\begin{aligned}\tilde{\mathbf{P}}_L(t) = \mathbf{P}_i^{(1)}(t) &= \varepsilon_0 \int_0^1 R_{ij}^{(1)}(t-t_1)E_j(t_1)\mathrm{d}t_1 \\ &= \varepsilon_0 R_{ij}^{(1)}(t) \otimes E_j(t),\end{aligned} \tag{3.4}$$

where the last expression is a convolution product, which when converted into frequency-domain will yield the following simple product

$$\mathbf{P}_i(\omega) = \varepsilon_0 \chi_{ij}^{(1)}(-\omega_{out};\omega)\mathbf{E}_j(\omega), \tag{3.5}$$

where $\chi_{ij}^{(1)}(-\omega_{out};\omega) = \int_{-\infty}^{+\infty} R_{ij}^{(1)}(t_1)\exp(i\omega t_1)\mathrm{d}t_1$ is the first-order susceptibility of a material, that is a second-rank tensor. In the linear case, $\omega_{out} = \omega$. To express higher-order processes, that encompass all nonlinear optical processes, whose polarization is referred to as $\tilde{\mathbf{P}}_{NL}(t)$; the formula of Eq. 3.4 can be scaled to express quadratic, cubic, or even higher-order polarizations, which will be

$$\begin{aligned}\mathbf{P}_i^{(n)}(t) = \varepsilon_0 \int_0^t \int_0^t \cdots \int_0^t R_{ijk\ldots\eta}^{(n)}(t-t_1, t-t_2, \ldots, t-t_n)\times \\ \mathbf{E}_j(t_1)\cdot\mathbf{E}_k(t_2)\ldots\mathbf{E}_\eta(t_n)\mathrm{d}t_1\mathrm{d}t_2\ldots\mathrm{d}t_n,\end{aligned} \tag{3.6}$$

where $R_{ijk\ldots\eta}^{(n)}$ is the total response function of the material that takes time response into account. Whereas in the generalized form of Eq. 3.6, the nonlinear susceptibility is a complex quantity that relates the complex amplitude and the applied electric field. The nth-order susceptibility $\chi^{(n)}$ can be obtained by Fourier transforming the response function of the material, Eq. 3.6, into frequency-domain

$$\begin{aligned}\chi_{ij\ldots\eta}^{(n)}(-\omega_{out};\omega_1,\omega_2,\ldots,\omega_n) = \int_{-\infty}^{+\infty}\cdots\int R_{ij\ldots\eta}^{(n)}(t_1,t_2,\ldots,t_n) \\ \times\exp[\mathrm{i}(\omega_1 t_1+\omega_2 t_2+\cdots+\omega_n t_n)]\mathrm{d}t_1\mathrm{d}t_2\ldots\mathrm{d}t_n,\end{aligned} \tag{3.7}$$

where $R_{ij\ldots\eta}^{(n)}$ is an $(n+1)$-rank tensor denoted as the nth-order response function of the material.

The third-order polarization expression can be rewritten by expressing the response function and the electric fields with their respective Fourier transforms as

$$\begin{aligned}\mathbf{P}_i^{(3)}(t) = \frac{\varepsilon_0}{(2\pi)^3}\iiint_{-\infty}^{+\infty}\chi_{ijkl}^{(3)}(-\omega_4;\omega_1,\omega_2,\omega_3)\times\mathbf{E}_j(\omega_1)\mathbf{E}_k(\omega_2)\mathbf{E}_l(\omega_3) \\ \times\exp[-\mathrm{i}(\omega_1+\omega_2+\omega_3)t]\mathrm{d}\omega_1\mathrm{d}\omega_2\mathrm{d}\omega_3,\end{aligned} \tag{3.8}$$

where $\chi^{(3)}$ is the 3rd-order susceptibility defined as the Fourier transform of the

response function of the material

$$\chi^{(3)}_{ijkl}(-\omega_4;\omega_1,\omega_2,\omega_3) = \iiint_{-\infty}^{+\infty} R^{(3)}_{ijkl}(t_1,t_2,t_3) \times \exp[\mathrm{i}(\omega_1 t_1+\omega_2 t_2+\omega_3 t_3)]\mathrm{d}t_1\mathrm{d}t_2\mathrm{d}t_3. \tag{3.9}$$

From which we can see that the nonlinear response is time dependent and a function of different wavelengths. Because different nonlinear terms of the tensors can be involved, it is vital to carefully select the laser wavelength, as well as its pulse duration, which both have strong influence on the nonlinear response of the material.

The $\chi^{(3)}$ susceptibility described in Eq. 3.9 expresses four-wave mixing (three excitation wavelengths and one response) and it is a fourth-rank tensor of 3×3×3×3 with 81 terms, and the third-order polarization can be written in frequency-space as

$$P_i(\omega_4) = \varepsilon_0 \sum_p \sum_{jkl} \chi^{(3)}_{ijkl}(\omega_4;\omega_1,\omega_2,\omega_3) E_j(\omega_1) E_k(\omega_2) E_l(\omega_3) \tag{3.10}$$

where i, j, k, l refer to the Cartesian components of the electric fields.

3.3 Intensity-dependent refractive index

The description of refractive index of a nonlinear medium, when an intense optical field is propagating through, is

$$n = n_0 + \bar{n}_2 \langle \tilde{E}^2 \rangle, \tag{3.11}$$

where n_0 is the linear refractive index, often experienced when a weak optical field propagates through the medium, $\bar{n}_2$ is the nonlinear refractive index defined with a bar to avoid confusion with another defined n_2, and $\langle \tilde{E}^2 \rangle$ is the time average of the complex electric field squared. If the optical field is defined as $\tilde{E}(t) = E(\omega)e^{-\mathrm{i}\omega t} + \mathrm{c.c.}$, where c.c. signifies the complex conjugate of the electric field, the time average will be

$$\langle \tilde{E}(t)^2 \rangle = 2E(\omega)E(\omega)^* = 2|E(\omega)|^2, \tag{3.12}$$

We find that

$$n = n_0 + 2\bar{n}_2 |E(\omega)|^2 \tag{3.13}$$

3.3.1 Tensor nature of third-order susceptibility

A full description of the fourth-rank tensor of the third-order susceptibility $\chi^{(3)}_{ijkl}$ requires 81 individual elements. These 81 individual elements can be all independent and nonzero for crystalline solids with low symmetry. This large number of independent elements can be dramatically reduced for materials having higher degree of spatial symmetry. For instance, isotropic materials have only three independent elements. Materials like glasses, liquids, and vapor are often isotropic materials. Considering the general case wherein the applied frequencies of the electric fields are arbitrary, the third-order susceptibility can be represented as $\chi_{ijkl} = \chi^{(3)}_{ijkl}(\omega_4 = \omega_3 + \omega_2 + \omega_1)$, and it means that three input electric fields are incident into a material, each of which has different frequency, and result in observation of the third-order nonlinear optical phenomena of interest, such that the polarization leads to an oscillation at the frequency ω_4. When the medium is isotropic, this implies that the medium has spatial symmetry, meaning if the polarization occurs along a certain axis of the cartesian coordinate, when the coordinate system is rotated, this polarization must be the same after the coordinate rotation. In fact, this symmetry of the isotropic material imposes strong restrictions on which elements of $\chi^{(3)}_{ijkl}$ can be nonzero. Consequently, this isotropy of the nonlinear medium leads to a drastic reduction of the number of $\chi^{(3)}$ tensor elements from 81 down to 21 elements, which are as follows:

$$\chi_{1111} = \chi_{2222} = \chi_{3333}, \tag{3.14}$$

$$\chi_{1122} = \chi_{1133} = \chi_{2211} = \chi_{2233} = \chi_{3311} = \chi_{3322}, \tag{3.15}$$

$$\chi_{1212} = \chi_{1313} = \chi_{2323} = \chi_{2121} = \chi_{3131} = \chi_{3232}, \tag{3.16}$$

$$\chi_{1221} = \chi_{1331} = \chi_{2112} = \chi_{2332} = \chi_{3113} = \chi_{3223}. \tag{3.17}$$

Note that these 21 nonzero elements follow an even-index rule, whereas the indexes 1, 2, 3 must appear an even number of times, otherwise, this will violate the symmetry conditions dictated by the isotropy of the medium. If an index appears an odd number of times, e.g., χ_{1222}, this would mean that the medium responds in $\hat{x}_1$ direction to an electric field applied to a $\hat{x}_2$ direction, which is an unrealistic choice in an isotropic medium, as there is no reason for the response to favor $+\hat{x}_1$ direction, rather than $-\hat{x}_1$. Hence, such a response would vanish if the index appears in an odd-number.

The 21 elements stated in Equs. 3.14 of the $\chi^{(3)}$ tensor are not, actually, independent.

They are related to one another via the equation

$$\chi_{1111} = \chi_{1122} + \chi_{1212} + \chi_{1221}. \tag{3.18}$$

The outcome of Eq. 3.18 arises as a consequence of rotational invariance (due to isotropy) of the coordinate system. This means the predicted nonlinear polarization should remain the same, even if the coordinate system is rotated by a certain degree. Eq. 3.18 represents a particular result from a coordinate system rotation of 45° around the $\hat{x}_3$ axis, and in such a case the nonlinear polarization can be expressed in terms of $\hat{x}_1$ and $\hat{x}_2$ axes.

3.3.2 Optical Kerr effect

The optical Kerr effect is an analogy to the traditional electro-optic Kerr effect that was discovered by the Scottish scientist John Kerr [268, 269]. The electro-optic (EO) Kerr effect relates electricity and light, such that a material changes its refractive index in response to a static applied electric field, often called DC Kerr effect [270]. The EO Kerr effect differs from Pockels effect in that the change in refractive index scales quadratically to the static applied electric field strength in the EO Kerr effect, whilst in Pockel effect the change in refractive index scales linearly with the applied electric field strength. In 1956 [271], Buckingham introduced an AC Kerr effect, which is now known as Optical Kerr Effect (OKE). The OKE in materials stems from fluctuations from the electronic cloud (hyperpolarizability), and from various molecular motions.

The refractive index change can be described either by Eq. 3.11 or Eq. 3.13, which expresses the optical Kerr effect. In the simplest case, when a linearly polarized single beam interacts with a nonlinear medium, the nonlinear polarization that influence the propagation of this beam at frequency ω will be

$$\mathbf{P}^{\mathrm{NL}}(\omega) = 3\varepsilon_0\chi^{(3)}(-\omega;\omega,\omega,-\omega)|E(\omega)|^2E(\omega). \tag{3.19}$$

Then the total polarization of the material will be expressed as

$$P^{\mathrm{TOT}}(\omega) = \varepsilon_0\chi^{(1)}E(\omega) + 3\varepsilon_0\chi^{(3)}|E(\omega)|^2E(\omega) \equiv \varepsilon_0\chi_{\mathrm{eff}}E(\omega), \tag{3.20}$$

The effective susceptibility introduced here is

$$\chi_{\mathrm{eff}} = \chi^{(1)} + 3\chi^{(3)}|E(\omega)|^2. \tag{3.21}$$

Generally the refractive index of a material is related to the susceptibility in this form,

$$n^2 = 1 + \chi_{\text{eff}}. \tag{3.22}$$

The relationship between the nonlinear refractive index n_2 and the third-order nonlinear susceptibility $\chi^{(3)}$ can be found by substituting n, from Eq. 3.13 in Eq. 3.22, and χ_{eff} from Eq. 3.21, such that

$$\left[n_0 + 2\bar{n}_2|E(\omega)|^2\right]^2 = 1 + \chi^{(1)} + 3\chi^{(3)}|E(\omega)|^2. \tag{3.23}$$

When the left-hand side of Eq. 3.23 is equated with the right-hand side of the same equation, it gives $n_0^2 + 4n_0\bar{n}_2|E(\omega)|^2 = (1 + \chi^{(1)}) + [3\chi^{(3)}|E(\omega)|^2]$, where the term $4\bar{n}_2|E(\omega)|^4$ has been neglected, being very small. Comparing the linear and nonlinear parts on both sides together, gives the following relationships

$$n_0 = (1 + \chi^{(1)})^{1/2}, \tag{3.24}$$

and

$$\bar{n}_2 = \frac{3\chi^{(3)}}{4n_0}. \tag{3.25}$$

Throughout the above discussion, a single beam was used to measure the refractive index change, as schematically depicted in Fig. 3.1 (a). Alternatively, two separate beams can be used to measure the intensity-dependent refractive index, as illustrated in Fig. 3.1 (b). In this case, a strong beam of amplitude $E(\omega)$ causes a refractive index modification experienced by a weak probe beam $E(\omega')$. The nonlinear polarization of the probe beam will be

$$P^{\text{NL}}(\omega') = 6\varepsilon_0\chi^{(3)}(\omega' = \omega' + \omega - \omega)|E(\omega)|^2E(\omega'). \tag{3.26}$$

Note the degeneracy factor, 6, in Eq. 3.26 is double the degeneracy factor, 3, in Eq. 3.19 that corresponds to a single beam case. As long as the two beams are physically distinguishable, for instance, by propagation in different directions, in Fig. 3.1 (b), the degeneracy factor, 6, will remain the same, even when both of them have the same frequency, namely $\omega' = \omega$.

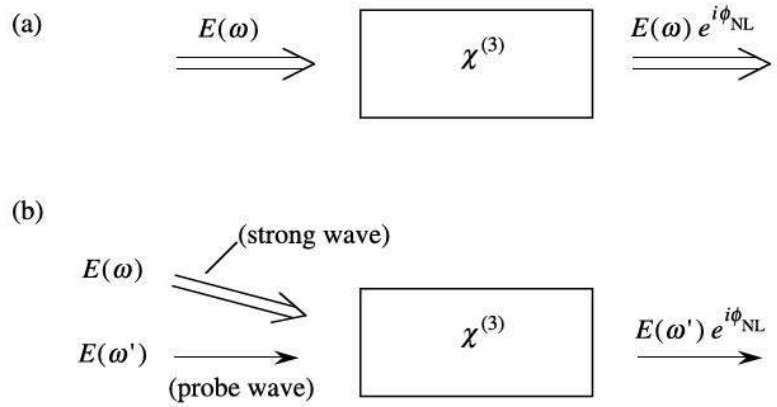


Figure 3.1: Single and two beams for measuring the intensity-dependent refractive index. (a) a strong beam affects its own propagation (SPM), (b) a strong beam affects the propagation of a weaker beam (XPM) [253].

The probe beam experiences a change in refractive index of the medium it propagates through, that is given by

$$n = n_0 + 2\bar{n}_2^{(\text{cross})}|E(\omega)|^2 \tag{3.27}$$

where $\bar{n}_2^{(\text{cross})} = \frac{3\chi^{(3)}}{2n_0}$.

Clearly, the nonlinear coefficient $\bar{n}_2^{(\text{cross})}$ that describes the cross-coupling when a strong beam is affecting a weak probe beam is double the nonlinear coefficient of the single strong beam, expressed in Eq. 3.25. From that we conclude, a strong beam of a frequency ω can affect the phase of a weak beam as twice as it can affect its own phase.

Although $\bar{n}_2$ is helpful for the understanding of the nonlinear optical phenomena, the description of the intensity-dependent refractive index, n, by the alternative quantity n_2 is more convenient, such that

$$n = n_0 + n_2 I, \tag{3.28}$$

where I is the time-averaged intensity of the optical field, that is given by

$$I = 2n_0'\epsilon_0 c|E(\omega)|^2. \tag{3.29}$$

With this convenient expression the refractive index is defined in terms of its real and imaginary parts as $n = n' + in''$, and likewise for n_0 and n_2. As the total refractive index is the same, irrespective of which way is found more convenient to describe the nonlinear contributions, one can see through a comparison between Equs. 3.13

and 3.29 that

$$2\bar{n}_2|E(\omega)|^2 = n_2 I, \tag{3.30}$$

therefore $\bar{n}_2$ and n_2 are related by

$$n_2 = \frac{\bar{n}_2}{n_0' \epsilon_0 c}, \tag{3.31}$$

where Eq. 3.29 is substituted in Eq. 3.30. If the expression of $\bar{n}_2$ in Eq. 3.25 is substituted in Eq. 3.31, one can find that n_2 is related to $\chi^{(3)}$ by

$$n_2 = \frac{3}{4 n_0 n_0' \epsilon_0 c} \chi^{(3)}. \tag{3.32}$$

3.3.3 Self-phase modulation

Self-phase modulation (SPM) occurs when an optical pulse experiences a time-dependent phase shift as it propagates through a medium with an intensity-dependent refractive index. This phase modulation leads to a characteristic spectral broadening of the pulse. It was first observed by Shimizu, in 1967 [272] and used to interpret the frequency broadening often observed in liquids by a self-focusing Q-switched laser. Shortly after that, it was demonstrated by Alfano and Shapiro [273] that this spectral broadening, due to SPM, occurs in almost any transparent medium using a short light laser that can extend over 100,000 cm^{-1}[274]. This represents the first observation of what has been later called, supercontinuum generation. Pure observation of SPM demands maintaining a constant laser beam cross-section during the propagation through the nonlinear medium. This unfortunately cannot be achieved easily in most media, when the self-focusing of the intense laser beam is significant. However, this requirement can be fulfilled in optical fibers and waveguide, as self-focusing is negligible. For comprehensive understanding about the SPM and supercontinuum generation, Ref. [275], is an excellent reference. The origin of this phenomenon can be understood by considering an optical pulse field propagating through a nonlinear medium, which is expressed as

$$\tilde{E}(z,t) = \tilde{A}(z,t) e^{i(k_0 z - \omega_0 t)} + \text{c.c.} \tag{3.33}$$

that has a total refractive index given by

$$n(t) = n_0 + n_2 I(t), \tag{3.34}$$

where $I(t) = 2 n_0 \epsilon_0 c |\tilde{A}(z,t)|^2$. So far, it has been assumed that the medium responds instantaneously to the pulse intensity, and that the optical pulse propagates through

a small thickness medium, such that it does not experience reshaping or dispersion. Such assumptions allow us to consider solely the phase change undergone by the laser pulse intensity, where this phase change of the transmitted optical pulse [253] will be

$$\phi_{\mathrm{NL}}(t) = -n_2 I(t)\omega_0 L/c. \tag{3.35}$$

This time-varying phase of the wave leads to a modification of the transmitted pulse spectrum, which will be typically broader than the incident optical pulse spectrum. There are some cases in which the transmitted spectrum will experience spectral narrowing rather than spectral broadening. The modification of the transmitted optical pulse can be determined from the calculation of its energy spectrum

$$S(\omega) = \left| \int_{-\infty}^{\infty} \tilde{A}(t) e^{-i\omega_0 t - i\phi_{\mathrm{NL}}(t)} e^{i\omega t} dt \right|^2. \tag{3.36}$$

For harnessing the idea of the spectral modification of an input optical pulse propagating through a medium, it is necessary to introduce the concept of instantaneous frequency of a pulse $\omega(t)$, which is defined by

$$\omega(t) = \omega_0 + \delta\omega(t), \tag{3.37}$$

where

$$\delta\omega(t) = -\frac{d}{dt}\phi_{\mathrm{NL}}(t).$$

is the variation of the instantaneous frequency. This definition holds, given that the amplitude $\tilde{A}(t)$ is slowly varying compared to the optical period of the laser pulse.

Assuming that the intensity of the optical pulse has a Gaussian distribution in time, as depicted in Fig. 3.2

$$I(t) = I_0 \exp\left(-4\ln 2 \frac{t^2}{\tau^2}\right), \tag{3.38}$$

where τ is the temporal width of the optical pulse (FWHM), the nonlinear phase shift will then be given by

$$\phi_{\mathrm{NL}}(t) = -\frac{n_2\omega_0 L}{c} I_0 \exp\left(-4\ln 2 \frac{t^2}{\tau^2}\right), \tag{3.39}$$

and accordingly the change in the instantaneous frequency, depicted in Fig. 3.2 (b) will be

$$\delta\omega(t) = \frac{8\ln 2\, n_2\omega_0 L}{c\tau^2} I_0 t \exp\left(-\frac{4\ln 2\, t^2}{\tau^2}\right). \tag{3.40}$$

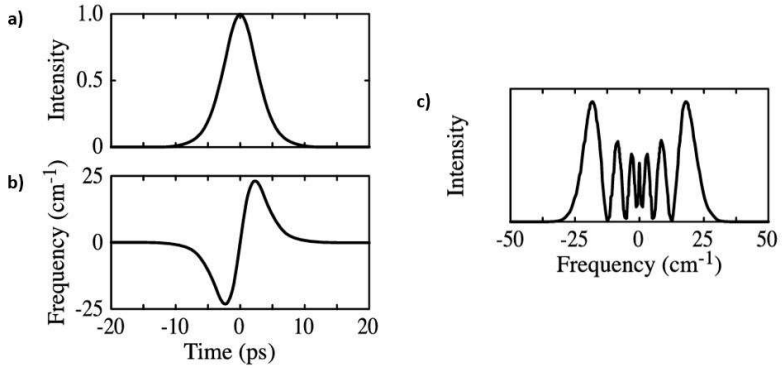


Figure 3.2: (a) Temporal intensity profile of a Gaussian pulse. (b) Change of the instantaneous frequency of a Gaussian pulse. (c) Example of a SPM with a peak nonlinear phase shift $\Delta\phi^{(max)}$ of about 6π [276].

It is evident from Fig. 3.2 (b) that the leading edge of the optical pulse shown in Fig. 3.2 (a) is shifted toward lower frequencies, while the trailing edge of that pulse is shifted toward higher frequencies, provided that the material possesses a positive nonlinear refractive index, $n_2 > 0$. The power spectrum shown in Fig. 3.2 (c) provides an example of a strong SPM having a peak of nonlinear phase shift $\Delta\phi^{(max)}$ of about 6π for an initially unchirped pulse. The characteristic oscillations observed can be understood considering the instantaneous frequency picture [276]. If we look at Fig. 3.2 (b), there are two points t_1' and t_2' on the time axis t that contribute to any specific point of the instantaneous frequency change $\delta\omega$. The exception of this occur at $\delta\omega = 0$, where three points on the time axis contribute to this particular case. The amplitude of the power spectrum (Fig. 3.2 (c)) depends on the interference between these time contributions and their relative phase with respect to each other. If, for example, a peak nonlinear phase shift $\Delta\phi^{(max)} = 2m\pi$ is considered, with m an integer, the power spectrum will show a peak at $\delta\omega = 0$, because the three time contributions, at $t = 0$ (center), and both leading and trailing wings are in phase together, with a $2m\pi$ phase difference. As we move toward the left-hand side of Fig. 3.2 (b) where the $\delta\omega$ is increased, their associated time points t_1 and t_2 will move closer, hence their corresponding phase difference $\Delta\phi(t_1')$ - $\Delta\phi(t_2')$ will be reduced. When this phase difference is decreased by π, a local minima will appear in the power spectrum. If the phase difference decreases with a total 2π, a second peak will occur, and so on. This process continues until the frequency reaches an extremum, where the phase difference is zero and the power spectrum exhibits a peak. Accordingly, the locations of peaks and minima on the power spectrum can be

represented through the following relationship

$$\begin{aligned} \text{number of peaks} &\approx \frac{\Delta\phi_{\max}}{\pi} + 1 \\ \text{number of minima} &\approx \frac{\Delta\phi_{\max}}{\pi} \end{aligned} \tag{3.41}$$

In the last section, it will be explained how Eq. 3.35 can be modified to express the situation in which the optical pulse is tightly focused.

3.3.4 Cross-phase modulation

Cross-phase modulation (XPM) is analogous to SPM but with a significant difference, that is the strong pump (gate) beam modulates the phase of another beam, i.e., the probe, often much weaker than the pump. Basically, when a linearly polarized pump beam propagates through an isotropic medium, due to Kerr effect this beam induces a time-varying birefringence, where along its polarization axis the medium acquires slightly higher or lower total refractive index $n(I)$ - expressed in Eq. 3.34 - depending upon the sign of the n_2 of that medium. The linearly polarized probe beam propagating through the same medium will experience a difference in refractive index between its polarization direction and a projection from the pump beam. This leads to a phase shift $\Delta\varphi(t)$, or retardation in its phase, and eventually its polarization will be rotated. It is important to draw attention to the fact, both SPM and XPM can concurrently take place in a nonlinear medium. In this situation, the strong pump modifies its own phase, while simultaneously modifies the phase of the probe beam. The process of XPM is the essence of optical Kerr shutters. This induced phase change for a weak probe beam by a much stronger pump beam [277], owing to XPM can be expressed as

$$\Delta\varphi(t) = \frac{2\pi L}{\lambda}\Delta n(t) \tag{3.42}$$

where L is the interaction length in the medium, λ probe beam wavelength, $\Delta n(t)$ is a time-dependent Kerr index change under the influence of a linearly polarized strong pump.

In OKG the nonlinear medium is placed between two crossed polarizers, and the probe beam is often delayed with respect to the pump, and the transmitted Kerr signal in a practical experiment will be given by

$$\mathrm{T}(\tau) = \int_{-\infty}^{\infty} I_{\text{probe}}(t-\tau)\sin^2\left(\frac{1}{2}\Delta\varphi(t)\right)dt, \tag{3.43}$$

where $I_{\text{probe}}(t) = I_{0,\text{probe}}e^{-4\ln 2(t/\tau_p)^2}$. This equation implies that the polarization angle θ between the pump and probe pulses is 45°. For different polarization angles,

Eq. 3.43 must be modified to include the term $\sin^2(2\theta)$, which evidently gives the value 1 at $\theta = 45°$.

Similar to the effect of SPM, the XPM caused to the probe beam by the pump beam leads to a spectral broadening of the probe's spectrum. Depending upon how strong the pump beam is, such spectral broadening can be increased or decreased. Albeit, the strong pump beam will be associated with other adverse effects such as SPM, or stimulated Raman scattering. Such adverse effects represent no harm for the detection of signals of interest, provided that the signal is well-filtered spectrally before reaching the single-photon detectors. Nevertheless, they are totally undesirable when they overlap with the spectral bandwidth region of the detected probe beam, particularly when the probe signal is feeble, like from single-photon sources.

3.3.5 Two-photon absorption

This is a nonlinear optical process wherein an atom undergoes a transition from the ground state to the excited state after absorption of two simultaneous photons. Unlike linear absorption, this process demands a strong laser intensity to be undergone. The absorption cross-section describing this process increases linearly with the laser intensity according to the relationship

$$\sigma = \sigma^{(2)} I, \tag{3.44}$$

where $\sigma^{(2)}$ is a coefficient that describes the strength of the two-photon absorption process [253]. In linear optics, the linear absorption cross-section σ is constant, namely it does not rely on the intensity of the laser used for the linear absorption. The atomic transition rate R is generally related to the absorption cross-section through the relationship $R = \sigma I/\hbar\omega$.

For the case of two-photon absorption process, atomic transition rate would be

$$R = \frac{\sigma^{(2)} I^2}{\hbar\omega}, \tag{3.45}$$

whereas R scales quadratically with the laser intensity as seen in this relationship. The study of the two-photon absorption process was enabled by the invention of the ruby laser in 1960. Because shortly after that, the first experimental investigation of it was carried out by Kaiser and Garret [278] in 1961, where they studied the emitted blue fluorescent light around 425 nm upon the irradiation of $CaF_2 : Eu^{2+}$ crystals with a red light at 694.3 nm obtained from a ruby laser source. The two-photon absorption has proven to be an effective spectroscopic tool, especially for

the determination of some energy levels positions that are not directly linked to the atomic ground state via a one photon transition.

Provided that optical Kerr effect experiments demand high intense lasers for the pump beam, the two-photon absorption process should be taken into account for any given Kerr medium, whose energy levels difference between its ground and excited state could be matched by simultaneous absorption of two, or sometimes even more photons at a particular wavelength selected for the pump (gate) beam. This requirement can be relaxed whenever a low repetition rate laser is employed in an optical Kerr gate experiment. However, with high repetition rate lasers, two-photon absorption can be an additional heat source for the Kerr material, in addition to the linear absorption of that material. Therefore, heat can be accumulated in the Kerr medium, giving rise to a formation of a thermal lens that can counteract the optical Kerr effect, if the thermo-optic coefficient dn/dt of the Kerr medium is negative, hence reducing the gating efficiency, or even worse, eliminating it. In case of large heat accumulation in a Kerr medium, a thermal management strategy should be followed, e.g., cooling the Kerr medium, in order to mitigate the heat effect.

3.4 Optical Kerr effect and self-phase modulation under focusing

Third-order nonlinear optical processes characterized by $\chi^{(3)}$ generally demand very high intense laser beams for achieving reasonable detection with modest S/N ratio. Even if this requirement is fulfilled, the detected signals are feeble. For example, OKE induced by the strong pump beam, yields very small nonlinear phase shifts for the probe beam. This very small shift leads to a small polarization rotation of the probe beam's polarization in an OKG. Such very high intense laser pulses are obtained via amplifying the output pulses of a solid-state laser. Due to the limitation of current laser amplifiers to handle high repetition rate lasers, even though the solid-state laser cavity produces a train of pulses at high repetition rates, the amplifier will reduce that rate. Thus, single-photon sources at high emission rates set stringent condition for efficient operation. On one hand, current solid-state lasers that can produce high repetition rates, i.e., 1 GHz, suffer from low average power, so their peak intensity is barely sufficient for OKG operation. On the other hand, tackling the limited laser pulse intensity by using laser amplifiers would give rise to insufficient emission rates from those single-photon sources; first being excited at low-repetition rate, and second, being inherently limited by their low quantum yields. Coming around this bottleneck is possible, by avoiding the usage of laser amplifiers,

which will enable making use of the solid-state laser high repetition rate, provided that the emitted laser pulses are tightly focused. In this case, tight focusing of the laser pulses would help to increase the peak intensity of these pulses, to some extent.

Here, a semi-analytical theoretical model is introduced, originally published by Fattah et al. [54], that investigates the possible detection of ultrafast single-photon sources at 1 GHz repetition rate. In a standard OKG setup, such tight focusing is enabled by the appropriate lenses for both the gate beam and the probe beam. The model developed assumes that both beams are degenerate (same wavelength) and co-propagating in an isotropic Kerr medium. When these two laser beams are spatially and temporally overlapped into the Kerr medium, as we know, under the high intensity of the pump (gate) beam, a birefringence will be induced that will ultimately result in the probe beam polarization rotation, hence leaking through the second polarizer, which otherwise would not allow such beam to pass. Considering the gate intensity propagating through a Kerr medium of thickness, L, in a cylindrical coordinates r, z, and taking dispersion into account, the gate intensity profile will be given by

$$I_{\mathrm{g}}(r,z) = I_{\mathrm{g}}(z)\exp\left[-2\left(\frac{r_0}{w_0(z)}\right)^2\right], \tag{3.46}$$

where $w_0(z) = w_0\sqrt{1+(z/z_{\mathrm{R},0})^2}$, $z_{\mathrm{R},0} = \pi n w_0^2/\lambda$ is the Rayleigh range, w_0 is the beam waist, and n is the linear index of refraction.

This intensity profile will at $r = 0$ take the form

$$I_{\mathrm{g}}(z) = I_0 I_{\mathrm{disp}}(z)\frac{1}{1+(z/z_{\mathrm{R},0})^2}, \tag{3.47}$$

where $I_0 = 2\frac{\sqrt{\ln 2}E}{\pi^{3/2}\tau_0 w_0^2}$ is the pulse peak intensity, and $I_{\mathrm{disp}}(z) = \frac{\tau_0^2}{\sqrt{\tau_0^4+[4\ln 2\phi(z+L/2)]^2}}$ expresses how the gate intensity evolves due to the material dispersion, E is the pulse energy, τ_0 is the pulse duration, and ϕ is the group velocity dispersion (GVD) of the nonlinear crystal.

The nonlinear phase shift of the probe beam induced by the gate beam intensity is given by the following relationship:

$$\mathrm{d}\varphi = \left(\frac{2\pi n_2}{\lambda}\right) I_{\mathrm{g}}(z)\mathrm{d}z, \tag{3.48}$$

where n_2 is the nonlinear index of refraction of the Kerr medium, and λ is the wavelength of the probe pulse in the medium. The infinitesimal phase shift must be numerically integrated to obtain the phase shift $\Delta\varphi(0,L)$ on the optical axis accumulated by the probe beam, when it travels through the nonlinear crystal in the

presence of the gate pulse.

Note that an analytical solution of the accumulated phase shift is not feasible, owing to the inclusion of the dispersion into $I_g(z)$, that is the reason it must be numerically integrated. Also, the Kerr efficiency will be eventually scaled with z as the two beams propagate through the nonlinear medium, as the intensity of these two beams changes as a function of z. The transmitted light through the OKG, along the optical axis is related to the accumulated phase shift accumulated by the formula:

$$T(0, L) = \sin^2 \left[\frac{\Delta\varphi(0, L)}{2} \right]. \tag{3.49}$$

To see how material dispersion affects the gate beam intensity, and in turn the induced nonlinear phase shift, Fig. 3.3 shows the difference in the phase shift in case dispersion is taken into account. This is, in fact, crucial for the proper selection of the thickness of the nonlinear medium (Kerr medium). The Kerr medium thickness, L, is considered for the ideal case, in which both the pump and probe beams are collinear, and assuming that absorption of Kerr medium of the degenerate wavelengths is negligible.

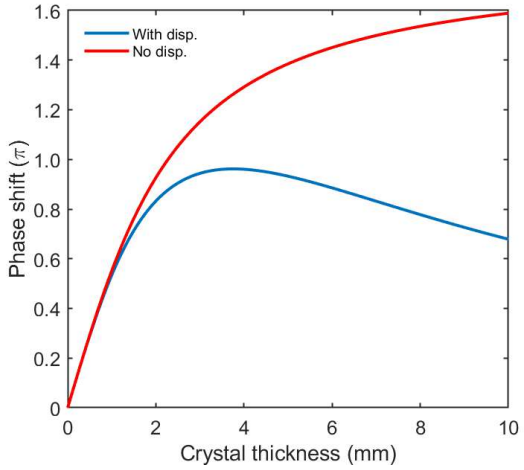


Figure 3.3: Induced phase shift for the probe beam as a function of the nonlinear thickness, with/without considering dispersion. Parameters: $\lambda = 800$ nm, $w_0 = 10$ μm, $E = 4$ nJ, $\tau_0 = 80$ fs, $n = 2.45$, $n_2 = 1.6 \times 10^{-18}$ m^2/W, $\phi = 1057.19$ fs^2/mm.[54].

For calculating the gate efficiency of the OKG, assuming that the photon pulse and the gate pulse has Gaussian profile, under the tight focusing by the used lenses in the OKG, one must consider that each ray of the probe beam experiences a different phase shift. Therefore, the ray trajectory of the probe beam besides the distance z

affects the intensity, whereas the ray trajectory will be defined by

$$r(z) = r_0\sqrt{1 + (z/z_{\mathrm{R}})^2}, \tag{3.50}$$

where r_0 is the distance from the optical axis at the beam waist. Accordingly, the induced phase shift will be defined by

$$\Delta\varphi(r_0, L) = \Delta\varphi(0, L) \exp\left[-2\left(\frac{r_0}{w_0}\right)^2\right], \tag{3.51}$$

where the phase shift $\Delta\varphi(0, L)$ is given by

$$\Delta\varphi(0, L) = \frac{4\pi n_2 z_{\mathrm{R},0} I_0}{\lambda} \arctan\left(\frac{L}{2z_{\mathrm{R},0}}\right), \tag{3.52}$$

where $z_{\mathrm{R},0}$ is the Rayleigh range of the gate beam, and in this equation the effect of dispersion has been neglected to avoid computational complexity. Considering the above equations, now the transmittance of the ray trajectory r_0 through the OKG can be calculated by the following relationship

$$T(r_0, L) = \sin^2\left[\frac{\Delta\varphi(r_0, L)}{2}\right]. \tag{3.53}$$

The transmittance of a ray trajectory $T(r_0, L)$ in Eq. 3.53 assumes already that the polarization angle, θ, between the pump and the probe beam is 45°. Hence, $\sin^2(2\theta) = \sin^2(2 \times 45°) = 1$. If that is not the case, the polarization angle, θ, must be taken into account.

For calculating the transmittance experienced by the whole probe beam, the transmittance of all ray trajectories must be averaged, which is defined by

$$T(w_0, w_1, L) = \frac{\int_0^\infty T(r_0, L) \exp\left(-2r_0^2/w_1^2\right) r_0 \mathrm{d}r_0}{\int_0^\infty \exp\left(-2r_0^2/w_1^2\right) r_0 \mathrm{d}r_0}, \tag{3.54}$$

where the transmittance of the OKG is a function of the gate beam waist, w_0, the probe beam waist, w_1, as well as the Kerr medium thickness, L. The transmittance (gate efficiency), defined in Eq. 3.54, as a function of the pump and probe beam diameters for different values of Kerr medium thicknesses, L, is shown in Fig. 3.4.

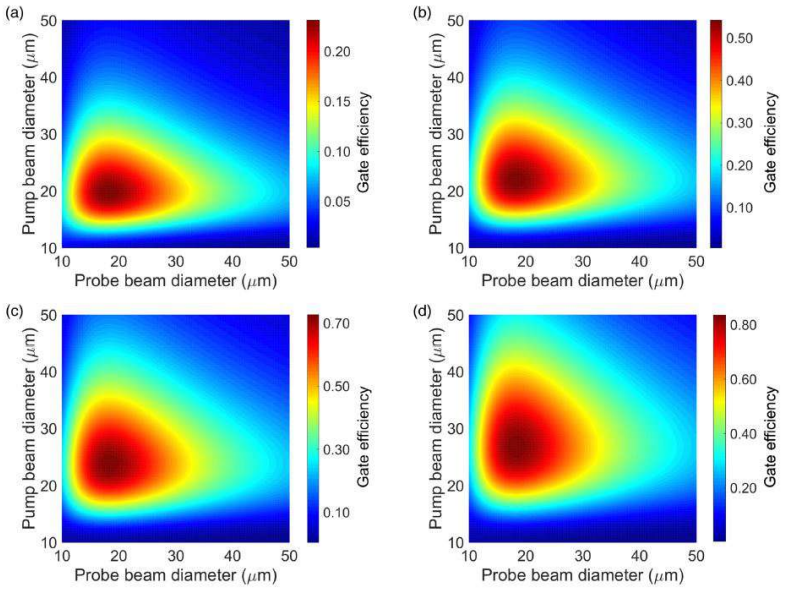


Figure 3.4: Gate efficiency (transmittance of the probe beam) as a function of the pump and probe beam diameters at different thicknesses L. (a) L=1 mm, (b) L=2 mm, (c) L=3 mm, (d) L=5 mm. Parameters: $\lambda = 800$ nm, $w_0 = 10$ μm, $E = 4$ nJ, $\tau_0 = 80$ fs, $n = 2.45$, $n_2 = 1.6 \times 10^{-18}$ m^2/W, $\phi = 1057.19$ fs^2/mm.[54].

It is vital to clarify the difference between the transmittance, as defined in Eq. 3.54, and the transmittance defined in Eq. 3.43. The transmittance of Eq. 3.54 calculates the accumulated nonlinear phase shift experienced by the probe beam, as the latter propagates through a Kerr medium of thickness, L. Eq. 3.54 also considers the beam diameters of the pump and the probe beams. It is quite helpful in the case of operating an OKG under tight focusing of the two beams. Nonetheless, in real OKG experiments the probe beam accumulates the nonlinear phase shift, while the probe beam pulse is delayed relative to the pump beam pulse in time by $\Delta\tau$. Here, comes the role of Eq. 3.43 into play, which integrates the transmitted signal as a function of the time delay, $\Delta\tau$, between the two pulses.

The temporal resolution of an OKG, which determines the instrument response function (IRF), is limited, in principle, by the gate pulse width. Certainly, this assumes that the material responds instantaneously to the external electric field applied on it. With this assumption, where the gate pulse width is the main determinant of the IRF, the gate pulse temporal profile is defined according to the following relationship for Gaussian pulses

$$I_g(t) = I_0 \exp\left[-4\ln 2 \frac{(t-t_0)^2}{\tau_0^2}\right], \tag{3.55}$$

where τ_0 is given by the average of the pulse duration before and after the Kerr medium, and the pump peak intensity, I_0, is considered constant, and corresponds to

the transmittance defined in Eq. 3.54. A plot of the temporal profiles of transmittance as a function of time for different thicknesses of the Kerr medium is shown in Fig. 3.5.

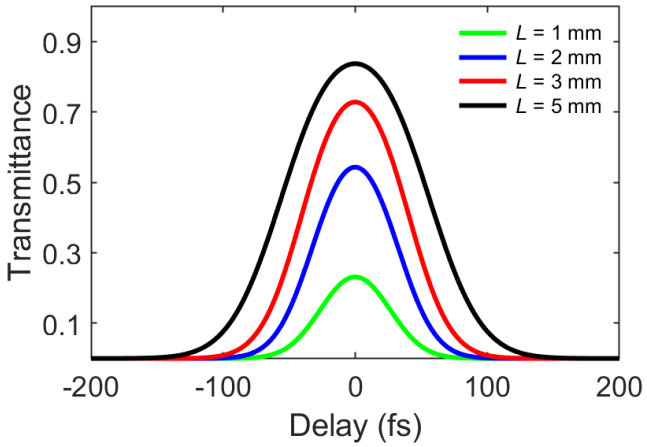


Figure 3.5: Temporal profiles of the transmittance as a function of time for different Kerr medium thickness. Parameters: $\lambda = 800$ nm, $w_0 = 10$ μm, $E = 4$ nJ, $\tau_0 = 80$ fs, $n = 2.45$, $n_2 = 1.6 \times 10^{-18}$ m^2/W, $\phi = 1057.19$ fs^2/mm.[54].

Note from Fig. 3.5 that the thicker a Kerr medium is, the lower the temporal resolution becomes (broader transmittance curve). When dispersion effect is taken into consideration, with thicker Kerr media, the loss of temporal resolution becomes more severe. It is important to emphasize that the instantaneous response is caused by the bound electrons (hyperpolarizability), as referred to previously. As a matter of fact, in reality the IRF of an OKG is determined by the nonlinear response time, which can be longer than the gate pulse duration. A clear example is CS_2, whose nonlinear response time is within the range 1.6-2 ps, due to the nuclear contribution in addition to the hyperpolarizability of bound electrons. Later, a numerical error was found out concerning the results of Fig. 3.4 (d). This numerical error emerges from the algorithm Matlab uses, for calculating integrals involving infinity in one of the integral's limits. As seen in Eq. 3.54, for obtaining the OKG transmittance, one has to integrate the numerator from 0 to ∞. The denominator was analytically calculated, hence it was not an issue. To avoid this numerical error, a new code has been written in Python, and linked to a C script, which independently computes the integral, and sets the border for this integral, in order to prevent this issue from occurring again. Accordingly, the value of the maximum obtainable OKG efficiency, and its associated optimal pump and probe beam diameters has been corrected. For example, for a thickness $L = 5$ mm, and using the same parameters shown in Fig. 3.4, the maximum OKG efficiency would be $\sim 30\%$, and its associated pump beam diameter is ~ 36 μm, and the probe beam diameter is ~ 31 μm, as illustrated in

Fig. 3.6. This is a huge difference in OKG efficiency, given that the earlier OKG efficiency shown in Fig. 3.4 (d) was $\sim 83\%$.

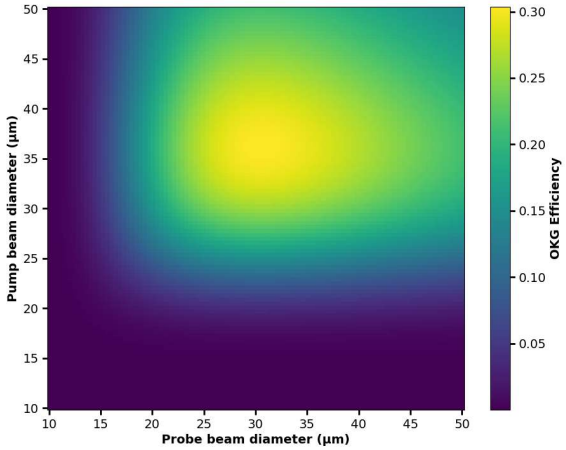


Figure 3.6: Corrected OKG efficiency and pump and probe diameters, for a Kerr medium with $L = 5$ mm, shown in Fig. 3.4 (d), using the same parameters.

So far, the tight focusing of the pump and probe beams and its influence on OKG efficiency, has been considered. That leads to taking into account the phase change experienced by each ray trajectory, and averaging their phase change. Since OKG efficiency stems from the induced nonlinear phase, due to the XPM because of the gate beam, a similar approach can be followed with SPM under tight focusing of the gate beam. The definition of the instantaneous phase introduced above, did not consider the gate pulse intensity variation $I_{\mathrm{g}}(t)$. When it is included the infinitesimal on-axis nonlinear phase change will take the form

$$\mathrm{d}\phi = -\left(\frac{2\pi n_2}{\lambda_{\mathrm{g}}}\right)\frac{I_{\mathrm{g}}(t)}{1+(z/z_{\mathrm{R},0})^2}\mathrm{d}z. \tag{3.56}$$

By integration the Eq. 3.56, the value of of on-axis nonlinear phase change will become

$$\phi(0,L,t) = -\left(\frac{4\pi n_2 z_{\mathrm{R},0}}{\lambda_{\mathrm{g}}}\right) I_{\mathrm{g}}(t)\arctan\left(\frac{L}{2z_{\mathrm{R},0}}\right). \tag{3.57}$$

With considering the different phase shift $\phi(0,L,t)$ experienced by each ray trajectory at r_0, one finds

$$\phi(r_0,L,t) = \phi(0,L,t)\exp\left(-2r_0^2/w_0^2\right), \tag{3.58}$$

and the average phase shift $\overline{\phi}(L,t)$ of all rays will give the following expression

$$\overline{\phi}(L,t) = \phi(0,L,t)\frac{\int_0^\infty \exp(-2r_0^2/w_0^2)\exp(-2r_0^2/w_0^2)r_0\mathrm{d}r_0}{\int_0^\infty \exp(-2r_0^2/w_0^2)r_0\mathrm{d}r_0}. \tag{3.59}$$

Performing the integration of Eq. 3.59 yields $\overline{\phi}(L,t) = \phi(0,L,t)/2$, from which we see that the average of all rays is half of the on-axis value. With excluding the GVD, the average phase $\overline{\phi}(L,t)$ will be expressed with the following relationship

$$\overline{\phi}(L,t) = -\frac{2\pi n_2 z_{\mathrm{R},0}}{\lambda_{\mathrm{p}}} \arctan\left(\frac{L}{2z_{\mathrm{R},0}}\right) I_0 \exp\left[-4\ln 2 \frac{(t-t_0)^2}{\tau_0^2}\right], \tag{3.60}$$

where $Z_{\mathrm{R},0}$ represents the focusing strength, which the above equation depends on. Given this equation, the spectrum of the transmitted gate pulse through a nonlinear medium of thickness L, represented in Eq. 3.36, after the tight focusing consideration will be given by

$$S(\omega) = \left| \int_{-\infty}^{\infty} \tilde{A}(t) \exp(-i\omega_0 t - i\overline{\phi}(L,t)) \exp(i\omega t) \mathrm{d}t \right|^2, \tag{3.61}$$

whereas ω_0 is the pulse carrier frequency, and $\overline{\phi}(L,t)$ is the nonlinear phase as a function of time, as specified by Eq. 3.36. The above-mentioned results have been published in Ref. [279].

Chapter 4

Experimental realization of optical Kerr gate

4.1 Experimental setup configuration

4.1.1 Ti:sapphire (Ti:sa) GHz repetition rate laser

The laser used in the optical Kerr gate experiments, as pump (gate) and probe is a tunable solid-state Ti:sa laser (Taccor Tune, Novanta), with an average output power 1800 mW. The tunability range is between 740-910 nm, with an emission peak at 800 nm and a pulse width < 80 fs at the laser output. This laser has a uniquely high repetition rate, 1 GHz, meaning that each pulse is temporally separated from the consecutive pulse in the pulse train by 1 ns. This actually dictates that the laser must be used for fast processes, such as ultrafast fluorescence emission below 1 ns, or be it a relaxation time from a Kerr medium. Otherwise, the interaction of one particular pulse in the pulse train would be affected by its adjacent pulses in time, which will distort the temporal information, concerning the process under investigation. Besides its main cavity, the laser has a control unit (ULC-16), and a thermoelectric chiller (Tcube edge, Solid State Cooling Systems, USA) for cooling, which is connected via long tubes for exchanging the cooling liquid (e.g. coolant concentrate G4, GLYSANTIN). It is crucial to operate and maintain such a laser at the appropriate temperatures, or else it would fail to operate. Moreover, the control unit has three inherent fans for cooling it down, and is covered with a sheet of pores to prevent dust particles from getting into the control unit. In most of the optical Kerr gate experiments presented here, the Taccor laser was both the pump (gate) beam, and the probe, implying that both pump and probe beams of the optical Kerr gate are degenerate.

4.1.2 Polarizers

Optical Kerr gate experiments typically require two polarizers, where the first polarizer (P_1) allows laser light (or fluorescence signal in the future) with polarization parallel to the polarizer's axis to get into the OKG; the second polarizer (P_2) is often called analyzer. The analyzer must be crossed with respect to the first polarizer, namely rotated at 90°. For that two 1″-diameter economy film polarizers (LPNIRB100, Thorlabs) were used, with 600-1100 nm operating wavelength range, and anti-reflection (AR) coating range 650-1050 nm. Both the transmission wavelength range and the AR coating range should be appropriately selected to ensure maximum transmission for the pump and probe beam.

Another crucial factor in the polarizer type selection is the extinction ratio (ER) of the polarizers, which is defined as the ratio between the maximum to minimum transmission of a linearly polarized input light. The maximum transmission is obtained when the polarization axis of both polarizers are parallel, and the minimum transmission is obtained when their polarization axes are perpendicular to one another. According to the specifications of LPNIRE100-B film polarizers, the ER is $>$ 1000:1 (600-950 nm), and $>$ 400:1 (600-1100 nm). Traditionally, Glan-Taylor, or Glan-Thomson polarizers are preferred in OKG experiments, as they offer quite high ER, i.e., 100,000:1. Such polarizers are made of calcite crystals, which are delicate and should be treated with appropriate care, especially in terms of temperature variations. Both the transmittance and the ER of our film polarizers were measured to verify their match with their specifications. These measurements were carried out where the light source was our Taccor fs at 820 nm. Furthermore, the two polarizers were tested individually for transmittance and together for the ER value; outside the Kerr setup and within the Kerr setup. The transmittance measurement of each polarizer outside Kerr setup shows that both have identical transmittance of $\approx$ 88%, which is nearly 4% higher than Thorlabs specifications value, as shown in Fig. 4.1. Nonetheless, the ER values obtained differ notably from what stated by the specs sheet, as indicated in Fig. 4.2. Whereas the ER of P_1 and P_2 together exhibit more than double the value reported by Thorlabs specs.

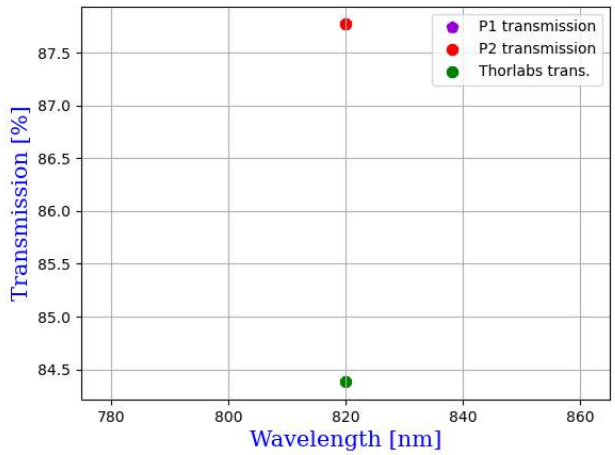


Figure 4.1: Transmittance of the two polarizers (P_1 & P_2) measured individually (outside the optical Kerr setup) with Taccor fs laser at 820 nm, and compared to Thorlabs transmittance value.

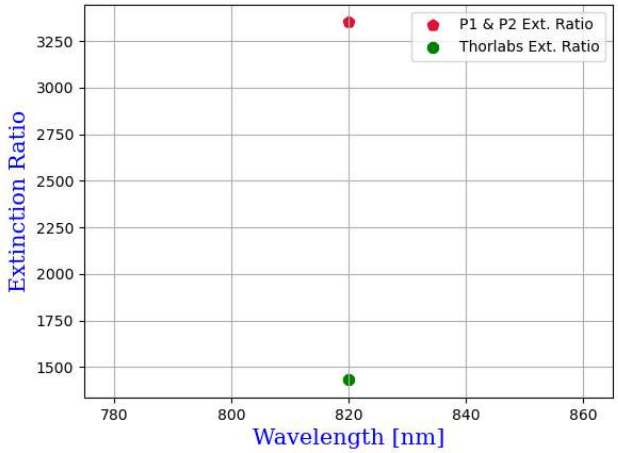


Figure 4.2: Extinction ratio (ER) value of P_1 & P_2 together, measured at 820 nm of Taccor fs laser (outside the optical Kerr setup), showing more than double the ER value reported by Thorlabs.

Another measurement of the two polarizers was performed using also Taccor fs laser but at 810 nm and within the optical Kerr setup shows absurdly different ER value, around two orders of magnitude lower than the measured value with Taccor laser at 820 nm, as indicated in Fig. 4.3. Although it is expected that measuring at a different wavelength would lead to different transmittance and ER value, the expected difference in measurements is huge, compared to just a 10 nm change in the fs laser wavelength from 820 to 810 nm.

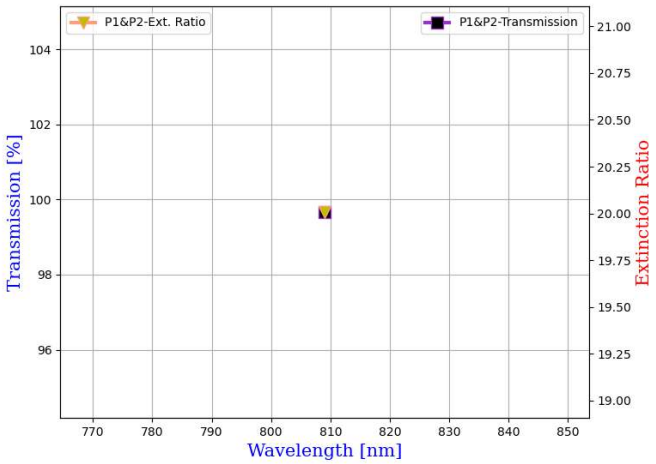


Figure 4.3: Transmittance and ER measurement of P_1 and P_2 polarizers together (within the optical Kerr setup), where Taccor fs laser at 810 nm was the light source.

Another investigation of both transmittance and ER value outside the optical Kerr setup using another fs laser (Toptica FemtoFiber pro) at particularly 650, 660 and 670 nm shows another inconsistency. For instance, the transmittance of P_1 and P_2 individually at 650 nm was approximately higher than Thorlabs value by 2 - 2.5%, which is a reasonable difference, as shown in Fig. 4.4. However, Thorlabs value was higher by $\sim$ 5% than P_1 and P_2 actual transmittance at 660 nm, $\sim$ 4% higher than the actual transmittance at 670 nm.

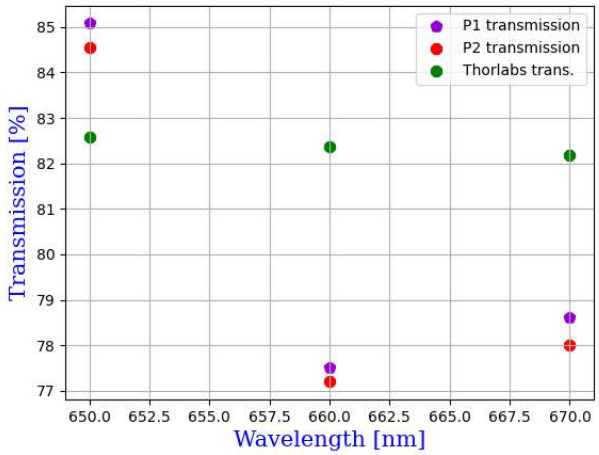


Figure 4.4: Transmittance measurement using Toptica fs laser at 650, 660, 670 nm, respectively. This measurement was performed outside the optical Kerr setup.

The ER values of P_1 and P_2 together at the three fs laser wavelengths were completely lower than Thorlabs reported value in their specifications. For example, at 650 nm, the experimentally measured ER value by our Toptica fs laser is $\approx$ 1300, while

Thorlabs reported value is ≈ 2375, which is around 82% higher than our measured value, as presented in Fig. 4.5. This difference increases even more at 660 nm, and becomes drastically huge at 670 nm, about 200 % for Thorlabs value, as compared to our values.

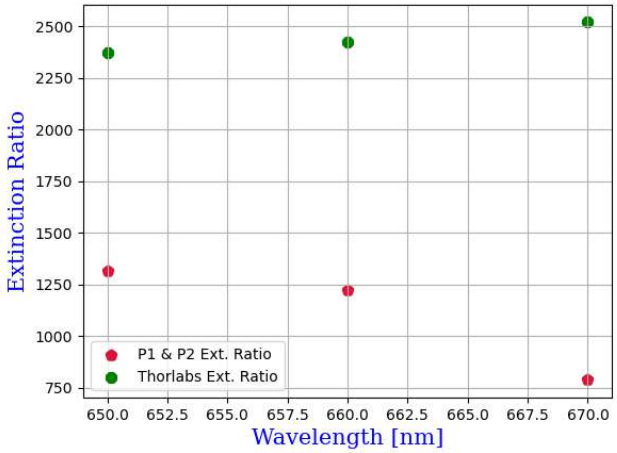


Figure 4.5: ER values of P_1 & P_2 together measured using Toptica fs laser at 650, 660, 670 nm, respectively. These measurements were performed outside the optical Kerr setup, and show an increasing difference in the ER in favor of Thorlabs reported values.

The discrepancy observed between our measured data and Thorlabs reported values can be understood considering that their ER data are theoretically obtained, not experimentally measured. Furthermore, the ER measurements shown above were taken by fs lasers, and as we know, such short laser pulses in time, are wide in terms of their spectral width. In turn, the laser pulse contains multiple frequencies, which ultimately gives an ER value that is an average of them. Despite the discrepancy in these different measurements, either in transmittance or in ER values, the performance of both P_1 and P_2 when P_2 is crossed with respect to P_1 in an actual optical Kerr setup was reasonable, with about 0.1% leakage of the probe beam. Nonetheless, it is still highly recommended to use a pair of polarizers with higher extinction ratio, in particular for an application, such as optical Kerr gating of single-photon sources.

During OKG experiments, it was observed that rotating either the first polarizer (P_1) or the second polarizer (P_2) leads inevitably to a deviation of the probe beam path. For example, when P_2 used in our experiment was rotated at different angles, the probe beam was deviated accordingly, as clarified in Fig. 4.6. Note that both the distance and its direction vary from the original beam spot along with the change of the rotation angles. Similar behavior was observed when P_1 was rotated. Rotating P_1 should supposedly change only the polarization angle between the pump and probe beams, without introducing deviation in the probe optical path. This deviation is

undesirable, and can give rise to misleading results. Provided that the sensor area of the SPAD is very small, any small deviation of the probe beam typically aligned to hit the sensor's center, will lead to detecting a lower signal, as the probe beam moves far away from the sensor area. In this case, changing the polarization angle between the pump and probe from the 45°, corresponding to maximum OKG signal can be misinterpreted as the OKG signal decreases essentially, due to the probe beam deviation.

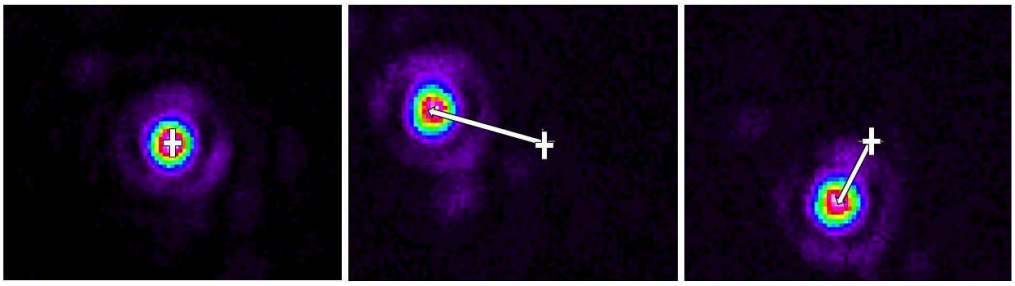


Figure 4.6: Deviation of the probe beam direction when P_2 is rotated. The first photo to the left-side was before P_2 rotation, showing the original spot location, the middle and the right-side photo show the change in the direction and distance from the original location after P_2 was rotated.

4.1.3 Detection scheme using photon counting

The detection of the OKG signal of the probe beam was attained by employing the HBT interferometer configuration, where the 50/50 beam splitter splits the probe beam into two parts, each of which is detected via one SPAD, connected to a TCSPC for photon counting. The first SPAD along the main probe beam path is connected to Ch_0 of the TCSPC, while the second SPAD located perpendicular to the direction of the main probe beam is connected to Ch_1. In principle, one SPAD detector is sufficient for the detection of an OKG signal. Nevertheless, due to the expected small OKG signal, two SPADs were used where their OKG signals can be added together. It serves as further verification about the results. To readout the TCSPC counts obtained at each delay step $\Delta\tau$, for plotting the measured OKG signals, a LabVIEW program was written for interfacing the TCSPC device with the linear translation stage.

4.1.4 Linear translation stage

In order to delay the pump (gate) beam pulses in time relative to the probe beam for resolving its signal, a high precision linear translation (M414.3DG, Physik Instrumente (PI) GmbH) stage was utilized. The M414.3DG linear stage has one active axis,

driven by a DC gearhead motor and has a 300 mm travel range. The minimum incremental motion is 0.1 μm, and it corresponds to 0.66 fs in time that represents the maximum temporal resolution of any pump-probe-based experiment. This comes from the speed of light, c, relationship to distance, d, and time t, where $t = 2d/c$. The factor 2 is sometimes overlooked in the pump-probe spectroscopy and nonlinear optics community, leading to erroneously considering the maximum temporal resolution to be 0.33 fs. The motion of the linear translation stage is controlled via a control unit Mercury servo controller C-863.12, Physik Instrumente (PI) GmbH. The Mercury servo controller is connected to a PC via USB cable and administered by a commercial software PIMikroMove ver. 2.31.2.0.

For determination of the distance range that corresponds to the temporal overlap between the pump and probe pulses, before placing any Kerr medium, the pump beam was initially spatially overlapped with the probe beam on a thin glass coverslip at the Kerr medium location, and both beams were detected using a photodiode (TDA 200 trigger diode assembly, PicoQuant), which was connected to a 1.5 GHz oscilloscope (LeCroy 9362, Teledyne LeCroy) that can handle 10 Giga samples per second to readout the output voltage signal. The pump pulses were delayed using the linear translation stage, over a long range, i.e., 1-295 mm (out of the 300 mm maximum travel range) to find the range of temporal overlap. The detection of either the pump or the probe beam independently showed that the photodiode can resolve well the 1 GHz repetition rate of the Taccor laser, showing as expected, that the temporal separation between each two consecutive pulses is, indeed, 1 ns. To acquire the data in an automated fashion, both the delay line and the oscilloscope were synchronized and interfaced via another LabVIEW program, written specifically for this purpose. Both pump and probe pulses were detected using a single photodiode detector, which was connected only to one channel on the oscilloscope panel. Moving the delay line for distances corresponding to a few femtoseconds between the pump and probe pulses are below the time resolution of the oscilloscope, since typically the electronic response time is slow, which hinders it from resolving such a very short time. For the aforementioned reasons, the temporal overlap manifests itself in the form of constructive interference with maximal amplitude, when the pump and probe pulses are fully overlapped in time; and minimal amplitude, when they are far apart. The details about the determination of the pump and probe pulses can be found in Appendix A.

Ultimately, the OKG setup composed of the above-mentioned components like the one shown previously schematically in Fig. 2.54 is aimed to be incorporated into a conventional confocal fluorescence microscope, similar to the one depicted in Fig. 2.33, where the final optical setup after this incorporation will be as presented in

Fig. 4.7 below.

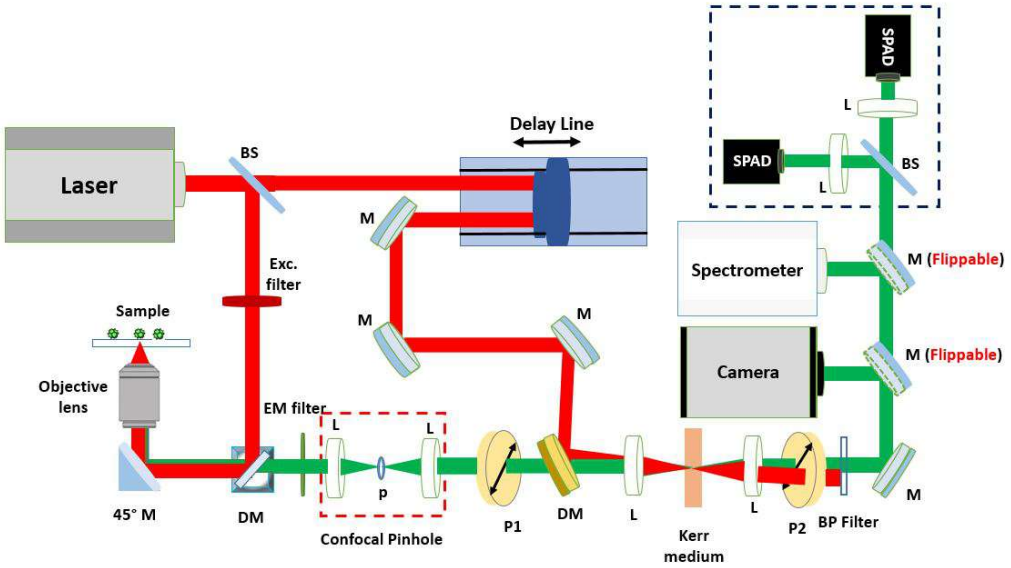


Figure 4.7: Scheme of a confocal fluorescence microscope after incorporating an OKG into it.

4.2 Characterization of optical Kerr gate with carbon disulfide

4.2.1 Introduction

Ensuring a proper performance of an optical Kerr gate experiment after building up the OKG setup necessitates characterizing it with a standard Kerr medium. For this purpose, carbon disulfide has been chosen for the OKG characterization. Carbon disulfide is an inorganic molecule, whose chemical formula is CS_2 and its molecular weight is 76.141 [280]. The chemical structure consists of a carbon atom that is covalently bonded with two sulfur atoms, namely S=C=S. The CS_2 molecule is non-polar, thus it has no permanent dipole moment. It has been extensively studied [277, 281, 282, 283, 284, 285] and it was one of the very first materials, whose nonlinear optical properties were investigated by the so-called z-scan technique, demonstrating its powerfulness for extracting the values of nonlinear refractive index, n_2, nonlinear absorption, β, and thermal nonlinearity [286, 287]. Since then, it has been often used as a standard reference material for the characterization of Z-scan technique setups [234, 288, 289, 290], as well as the characterization of optical Kerr gates [291, 292, 52, 50, 248]. The reason for using a neat liquid of CS_2 as standard material is mainly because it has a large nonlinear refractive index n_2 in comparison to other liquids. Typically, the intensity dependent refractive index change of a medium, Δn

is described by $n_2 I$, where I is the intensity of the laser illuminating the CS_2 sample. The n_2 value is often considered constant, only when the bound electrons of a Kerr medium contribute to the nonlinear response, which responds almost instantaneously. As a matter of fact, this is not the case with a material, such as CS_2, because the nuclei contribute to the nonlinear response. Given that those nuclei are heavier in mass relative to electrons, their response is slow. Thus, the contribution of the nuclear motion to n_2 will be different, depending upon the experimental parameters, e.g., excitation wavelength λ and pulse duration τ, and the applied field polarization. Over decades of research to understand and characterize the nonlinear optical properties of CS_2, still until nowadays the research effort continues to unravel the mysteries of this material. For example, the n_2 of CS_2 has positive sign, when studied over a wide range of wavelengths, however, Kim et al. [293] revealed that the positive sign of n_2 exhibited by CS_2 is only valid over a wavelength range between 600 nm and 1100 nm, which is dictated by the dominance of the third-order self-focusing, due to Kerr effect. At shorter wavelengths, e.g. 500 nm, though, the CS_2 acquires a negative sign of n_2 value, as the fifth-order nonlinearity begins to play a role at shorter wavelengths. Whereas it competes against the third-order nonlinearity, and can even dominate it when the intensity is high sufficiently, because the fifth-order nonlinearity is accompanied by a self-defocusing, which eventually leads to the negative n_2 value. In fact, using short wavelength lasers for the characterization of n_2 of CS_2 is not the only cause for obtaining a negative n_2 value, thermo-optic nonlinear effects, i.e., thermal lens effect can reverse the sign of n_2, even if the laser wavelengths range is between 600 and 1100 nm, provided that the repetition rate of the utilized laser is high [294].

In the following subsections, a discussion about the tensorial nature of the CS_2 response function will be provided. Then, because the response time of CS_2 in the liquid phase can be widely classified into fast and slow response times, an elaboration of the physical origin of each response time will be presented. Lately, the experimental results regarding the use of CS_2 to characterize our OKG will be provided.

4.2.2 Tensor nature of material response function

In considering a light field interacting with a nonlinear medium like CS_2, that light field is often assumed to be linearly polarized. The third-order response function of a nonlinear medium exhibits a strong dependence on the light polarization, owing to being a fourth-rank tensor. Likewise is the magnitude of the nonlinear refraction. However, the rise and decay times of a nonlinear medium are independent of the light field polarization.

In view of the tensor nature of third-order nonlinear optical processes, and because of the isotropy of CS_2 as a nonlinear medium, one can understand that the third-order material response tensor $R^{(3)}_{ijkl}$ can be reduced from 81 elements down to solely four elements, which are $R^{(3)}_{1111}$, $R^{(3)}_{1122}$, $R^{(3)}_{1212}$ and $R^{(3)}_{1221}$, where $1, 2 = x, y$. When the light field illuminates a CS_2 sample, the bound electrons follow the electric field vector almost instantaneously. This actually occurs as a consequence of the medium isotropy, whereas the bound electrons will not have a favorite response direction, and to achieve the least work, they follow the electric field along its oscillation direction. In fact, the instantaneous work is $\mathrm{d}W = F\ \mathrm{d}s$ and the force F depends only on the distance to the nuclei, not on any angle; which explains how bound electrons minimize their work by following the electric field oscillation direction. We can conclude further from this discussion and Eq. 3.14 in chapter 3, that

$$\mathcal{R}^{(3)}_{1111} = \mathcal{R}^{(3)}_{1122} + \mathcal{R}^{(3)}_{1212} + \mathcal{R}^{(3)}_{1221} \tag{4.1}$$

which implies that $\mathcal{R}^{(3)}_{1111}$ can be represented as a sum of three independent tensor components of the third-order response function, which are located at the right-hand side. These elements of the tensor can be even reduced further, if only the nonlinear refraction (Kerr nonlinearity) is considered. That is because the polarization frequency is equal to the oscillation frequency of the external electric field, and in this particular case not all tensor permutations are distinct, and in fact some elements of the tensor will be equal. According to the so-called intrinsic permutation symmetry, the response time of the material does not depend on the polarization of the external light field, so, $\mathcal{R}^{(3)}_{1212}E_2E_1E_2^* = \mathcal{R}^{(3)}_{1122}E_1E_2E_2^*$, where $\mathcal{R}^{(3)}_{1212}$ and $\mathcal{R}^{(3)}_{1122}$ can be considered as one parameter. Thus, in the restricted case of nonlinear refraction, only two independent tensorial components remain.

4.2.3 Origin of fast and slow responses

The atoms and molecules of CS_2 material undergo various types of motions when an intense electric field is applied to them. Such motions include electronic, rotation, vibration, rocking, collision, liberation, molecular redistribution and translation (diffusion). These motions occur on local and non-local spatial range [295], which are schematically depicted in Fig. 4.8.

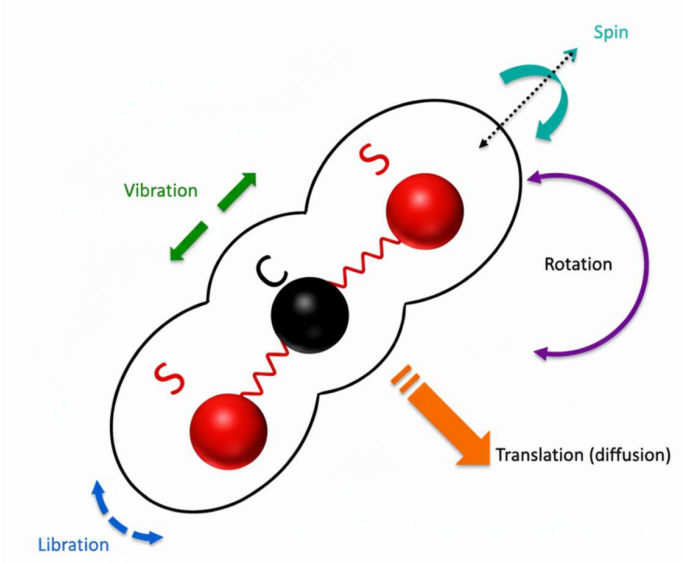


Figure 4.8: Scheme of CS_2 molecule exhibiting different kinds of motions. Adapted from [295].

Each type of motion exhibited by CS_2 atoms and molecules has a relaxation time associated with it. For instance, the electron cloud distortion, sometimes called electron hyperpolarizability, has the fastest relaxation ever, 10^{-17} s. The molecular redistribution is four orders of magnitude slower than the electron cloud distortion, 10^{-13} s. Both the molecular liberation and molecular vibration have similar relaxation time, that is 10^{-13} s. The previous electronic and molecular motions are considered ultrafast and fast response times. Molecular reorientation is considered a slow relaxation mechanism, where its relaxation time is in the range of 10^{-10} - 10^{-12} s. There are other relaxation mechanisms, which are even slower, such as electrorestriction (10^{-8} s) and thermal change (10^{-8}-1 s) [296, 233].

According to the definition of the Kerr effect, discussed in chapter 3, the relationship between the external applied electric field E and the index of refraction is

$$n = n_0 + n_2 E^2(t), \tag{4.2}$$

where n is the resultant local refractive index that arises from adding the linear refractive index n_0, and the change of the refractive index $\Delta n = n_2 E^2(t)$ as a result of the Kerr effect when an external electric field is applied, which consists of the nonlinear refractive index n_2, multiplied by the optical pulse envelope as a function of time. Because the nonlinear index change is proportional to the pump beam intensity, the index change is expressed as $\Delta n(t) = n_2 I(t)$. The nonlinear refractive index n_2 can be expressed as a summation of different nonlinear refractive indexes, each of which relates to independent relaxation mechanisms associated with different

kinetics and have different relaxation times τ

$$n_2 = \sum n_2(\text{electronic}) + n_2(\text{molecular}). \tag{4.3}$$

Accordingly, the change of the temporal Kerr index can be expressed as a summation of independent relaxation mechanisms, and this change will be aligned along the electric field direction and will be affected by various mechanisms taking place, owing to the coherent oscillations of the molecules.

$$\begin{aligned}\Delta n(t) = &\left[\frac{n_2}{\tau}\right]_{\text{electronic}} \int_{-\infty}^{t} I_{\text{pump}}(\tau_D) e^{-(t-\tau_D)/\tau_e} d\tau_D \\ &+ \left[\frac{n_2}{\tau}\right]_{\text{molecular}} \int_{-\infty}^{t} I_{\text{pump}}(\tau_D) e^{-(t-\tau_D)/\tau_m} d\tau_D + \ldots\end{aligned} \tag{4.4}$$

where τ_{D} is the time delay between the pump and probe pulses, τ_{e} is the electronic response time and m is the molecular reorientation relaxation time, which corresponds to molecular orientation, redistribution, collisions, liberation and vibrations; and

$$I_{\text{pump}}(t) = I_{0,\text{pump}} e^{-4\ln 2(t/\tau_p)^2}. \tag{4.5}$$

The transmitted Kerr signal of the probe beam as a function of the time delay between the pump and probe pulses of CS_2 in liquid phase is presented in Fig. 4.9 (blue curve), where this signal is decomposed into its constituents underlying signals corresponding to the electronic (ultrafast), molecular (fast), and translation or rotation (slow) responses [295].

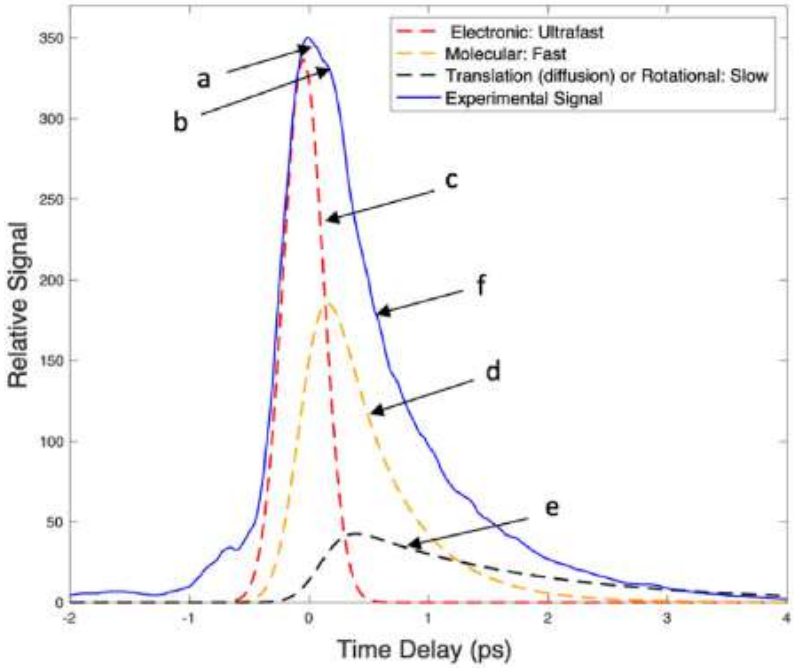


Figure 4.9: Transmitted Kerr signal (Probe) as a function of time delay (ps) of liquid CS_2 and its decomposed time responses. The main exponential decay (blue-f), small bump (blue-a) give rise to ultrafast electronic response (dashed red-c), fast molecular response (dashed orange-d), and slow translation or rotational molecular response (dashed black-e) [295]

.

When the main exponentially decaying OKG signal, curve (f), is decomposed into its elemental components, we find that the electron cloud distortion shows an ultrafast response time $\tau_{\text{ultrafast}} = 50$ as (curve c). This happens because electrons are very light particles, as compared to the nuclei, whose movement can be very fast following the rapid oscillations of the applied electric field. The small bump (b) in the blue curve (f) represents various fast molecular mechanisms such as redistribution, rotation, spin, liberation, and vibration, which are shown in curve (d), that has a relaxation time $\tau_{\text{fast}} = 500$ fs. Such mechanisms contribute also to the intermolecular interactions, because often liquid samples have a large number of molecules, leading to collisions and formation of self-assembled cages arising from the intermolecular forces. The τ_{fast} measured in the work of Ref. [295] is on the same order of a previously performed study to measure the same relaxation time [297]. Diffusive rotational and reorientational processes, curve (e), have a slow response time $\tau_{\text{slow}} =$ 1.5 ps, which is consistent with previous values reported in literature [230, 298]. The response time of CS_2 in gaseous phase, i.e., vapor is much faster than its counterpart of liquid CS_2. The viscosity of the material plays a central role in this difference in the sense that, CS_2 in the liquid phase is much more affected by the intermolecular forces from neighboring molecules. On the contrary, CS_2 vapor has fewer molecules, hence lower interactions with other molecules, whereas its viscosity originates from

the intramolecular forces undergoing ultrafast processes from the neighboring air molecules surrounding each CS_2 molecule. This leads also to obtaining considerably lower Kerr signal, because the n_2 value depends directly on the number of molecules N in the OKE, where $n_2 \propto N\chi^{(3)}$. This difference of the Kerr response time between the CS_2 phases, liquid and vapor is clearly shown in Fig. 4.10.

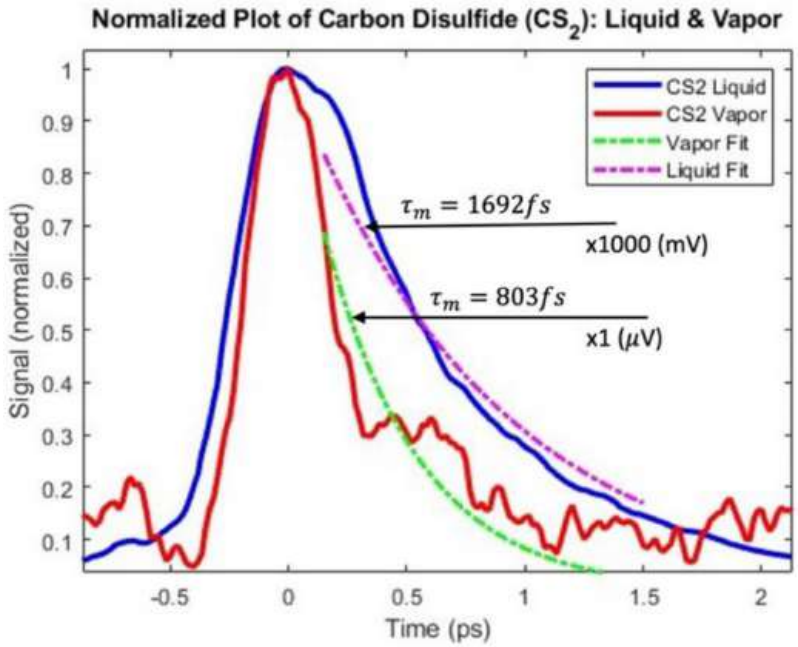


Figure 4.10: Difference of Kerr response time between CS_2 in liquid and gaseous phase [295].

4.2.4 Experimental Results

After building up the optical Kerr gate (shutter) by placing two crossed polarizers and the photodetectors (SPADs), liquid CS_2 was selected for the characterization, as it has higher $n_2 \sim 10^{-19}$-10^{-18} m^2/W than other liquids, and some solids as well. Further, it has a well-known temporal response, which is roughly 1.6-2 ps, as mentioned before. The CS_2 liquid (Sigma Aldrich) was placed into a 5 mm cuvette, made of quartz glass (Thermo Fisher Scientific), which is transparent in the wavelength range used in the experiments. This cuvette was covered with a lid, however, it turned out that having the lid alone does not ensure keeping the liquid for a long time in the curvette, since the CS_2 is volatile. That is why a small piece of a scotch tap was used for stronger sealing. A home-built holder was created to hold the cuvette with the CS_2 it contains. It was important to verify that the pump or the probe beam wavelength are transparent through both the cuvette and the CS_2 liquid. Also, it was important to investigate the possibility of having autofluorescence induced by the wavelength of either the pump or the

probe. Due to the initial plan to use the pump beam at $\lambda_{\text{pump}} = 820$ nm, and the optical parametric oscillator (OPO) as probe at $\lambda_{\text{probe}} = 650$-$670$ nm, the linear transmission and autofluorescence were investigated at these two wavelengths. This initial plan for the OKG was made such that the probe beam from the OPO can be spectrally filtered to achieve signal detection at high S/N ratio. Nonetheless, because of the drift in the OPO wavelength over time, and to afford more laser power for the pump beam, the OPO has not been used anymore. Instead, the output of the Taccor fs laser was split via a 90/10 BS, such that 90 % goes to the OKG, passing by the delay line, and acts as the pump (gate) beam, while the remaining 10% is used as a probe. Both the quartz glass cuvette and the CS_2 liquid showed $> 90\%$ transmission, after considering the scattered light outside the powermeter sensor area. For detecting any autofluorescence, a high resolution spectrometer was used over the wavelength range 383-900 nm to check it but no autofluorescence signal was detected. With the new experimental configuration, both the pump and probe beams are degenerate, namely they possess the same wavelength. This wavelength remained 820 nm, as it ensures high reflectance ($\approx 96.57\%$ for p-polarized light and $\approx 99.60\%$ for s-polarized light) for the short-pass dichroic mirror (DMSP, cutoff 805 nm). It has also been the plan to operate the OKG where the pump and probe beams are counter-propagating with respect to each other. The purpose of this scheme, which is not often followed in standard optical Kerr gate experiments, was to protect the very sensitive photodetectors (SPADs) from damage, due to the high intensity of the pump beam, and to also avoid saturating these detectors under the high intensity. Unfortunately, both the frequency (wavelength) degeneracy, as well as the counter-propagation of the two beams set an enormous challenge for the detection of the OKG signal, as will be elaborated later.

Before beginning the actual characterization of the OKG setup with CS_2, it was important to ensure spatial overlap between the pump and probe beam spots at the center of the cuvette filled with CS_2 liquid, and to find the location that corresponds to the maximum temporal overlap. For attaining the spatial overlap, the cuvette was replaced with a thin glass coverslip at the focal plane of both the pump and probe beams. A lens with focus at 100 mm was selected for tight focusing of the probe beam, while another lens with focus at 50 mm was chosen for the pump beam. Since the lens focusing the pump beam would yield tighter focus than the probe beam, the beam spot size was controlled via a moveable lens situated in between a couple of lenses, set before the 50 mm focusing lens. After careful alignment between the pump and probe spots, each spot size for each beam was measured and controlled, such that the probe beam spot size was ~ 20 μm, and the pump (gate) beam was ~ 30 μm. It is highly recommended in OKG experiments to have a larger beam spot size for the pump than the probe, in order to account for any subtle misalignment

between the two beams. For the temporal overlap, the aforementioned method in subsection 4.1.2 was followed, and the position on the delay line that corresponds to the maximum overlap was determined. However, it is vital to consider that since placing any Kerr medium, after removing the thin glass coverslip will change the optical path for the two overlapped pulses; the delay line should be scanned at a lower distance from the original temporal overlap position. This is because CS_2 has a linear refractive index, $n_0 \approx 1.61$, and the cuvette filled with CS_2 has a thickness of 5 mm, this will lead to slower propagation into the CS_2. In addition to the previous alignments and checks, the gate beam average power was measured, and owing to power losses as the gate beam propagates through various optical components, and the delay line power loss, from the 1.8-2.0 W output of the Taccor fs laser, only ~ 1 W is obtained before the Kerr medium. Provided that the laser has 1 GHz repetition rate, this gives an average pump pulse of 1 nJ. Assuming the Fourier-transform limited pulse width at the laser output is 80 fs, the laser pulse width is estimated to be ~ 100 fs at the optical Kerr gate. Using an autocorrelator device (APE GmbH), it was estimated that a laser pulse width can be increased by $\sim$ 3-4 fs, after passing through a ~ 3 mm lens. From the formalism presented in chapter 3, the pulse peak intensity can be calculated as $I_0 = 2\sqrt{\ln 2}E/\pi^{(3/2)}\tau_0 w_0^2$, where E is the average pulse energy, τ_0 laser pulse width, w_0 is the beam waist, which gives

$$\begin{aligned} I_0 = 2\sqrt{\ln 2} \times (1 \times 10^{-9})/\pi^{(3/2)} \times (100 \times 10^{-15}) \times (15 \times 10^{-6})^2 \\ \approx 1.33 \times 10^{13}\mathrm{W/m^2} \approx 1.33 \times 10^{9}\mathrm{W/cm^2}. \end{aligned} \tag{4.6}$$

In spite of this such pulse peak intensity (≈ 1.33 GW/cm^2), that can be considered relatively high for linear optics applications, it is considered somewhat weak, or at best modest pulse peak intensity, for a $\chi^{(3)}$ nonlinear optical process like optical Kerr gate. Usually, standard OKG experiments use amplified laser pulses, whose peak intensity can reach up to TW/cm^2. To make sure that this peak intensity does not exhibit SPM, the same OKG setup was used, by just blocking the probe beam, and measuring the gate beam laser before and after CS_2. Here, the gate beam does not pass through the two polarizers, too, thus they are not involved in this kind of measurement. The gate beam diameter is ~ 30 μm, and its pulse peak intensity I_0 is ~ 1.33 GW/cm^2 as calculated above. The SPM measurement is in an excellent agreement with the simulation of SPM under focusing for CS_2, considering $n_2 \sim 10^{-19}$ m^2/W, as seen in Fig. 4.11 (a), and indicates that Taccor laser intensity does not lead to a change of its spectral width. This result is in excellent agreement with a simulation for CS_2 using Equ. 3.61 in chapter 3, presented in Fig. 4.11 (b).

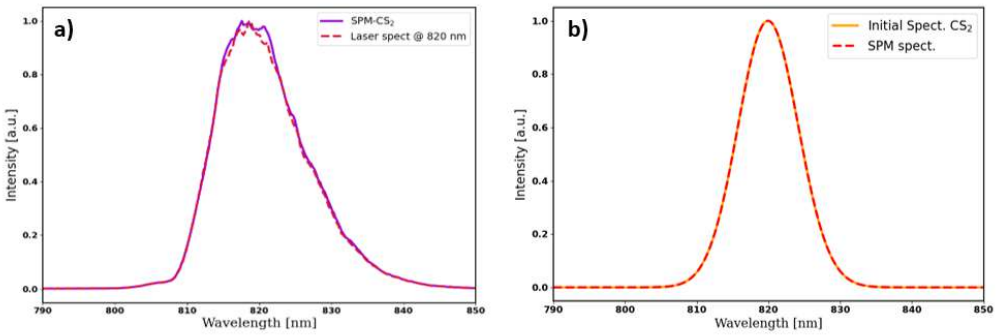


Figure 4.11: SPM of CS_2 liquid. (a) Experimental measurement, (b) Simulation using gate laser at wavelength 820 nm, pulse duration $\sim$ 100 fs, beam spot diameter 30 μm, and pulse peak intensity $\sim$ 1.33 GW/cm^2, $n_0 = 1.61$, pulse energy 1 nJ, n_2 = 3.5$\times 10^{-19}$ m^2/W, for a thickness of 5 mm.

The actual optical Kerr experiment begins with placing the 5 mm thick CS_2 cuvette between the two cross-polarizers, such that the focal planes corresponding to both pump and probe beams are located at the middle of the cuvette. In contrast to standard OKG experiments, in our experimental configuration, the pump beam pulses are the ones, which are delayed at steps of $\Delta\tau$ relative to the probe beam pulses. Therefore, Eq. 3.43 in chapter 3 must be modified to be as follows:

$$\mathrm{T}(\tau) = \int_{-\infty}^{\infty} I_{\mathrm{probe}}(t) \sin^2\left(\frac{1}{2}\Delta\varphi(t-\tau)\right) \sin^2(2\theta) dt, \tag{4.7}$$

where the effect of the polarization angle θ between the pump and probe beams was included, and was ensured in our experiment to be 45°, in order to maximize the collected Kerr signal. After an initial scan of pump beam pulses using the delay line to find their new temporal overlap location with the probe beam pulses, the delay line was scanned for 2 mm distance, in order to collect the Kerr-rotated signal. It was noticed that scanning at large temporal steps yields a different Kerr signal time trace. For example, when the temporal stepsize was 200 fs, the Kerr signal time trace appeared awkwardly inverted, as shown in Fig. 4.12, as opposed to the well-known standard Kerr signal time trace.

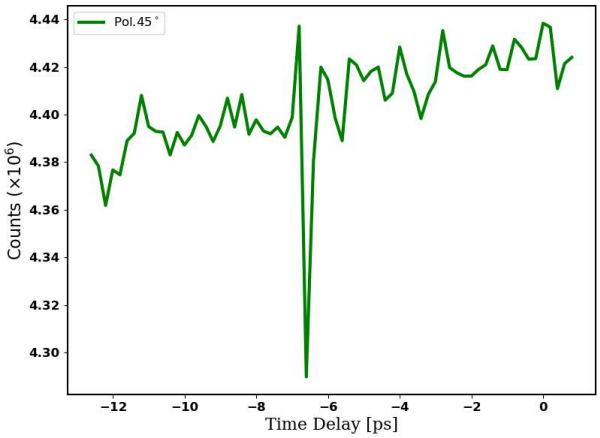


Figure 4.12: Kerr signal time trace obtained at temporal stepsize 200 fs, with integration time of 20 s.

Reducing the temporal stepsize to 100 fs helped to resolve more details in the Kerr signal time trace, yet it is still vague, such that no information about the CS_2 can be extracted, see Fig. 4.13.

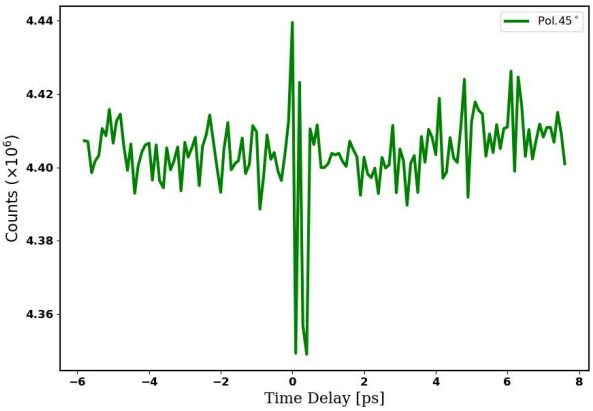


Figure 4.13: Kerr signal time trace obtained at temporal stepsize 100 fs, with integration time of 20 s.

Reducing the temporal stepsize even further, down to 25 fs, presented in Fig. 4.14, maintained the vagueness of the time trace, nonetheless the Kerr time trace at 25 fs begins to reveal a temporal profile that shows more details, yet not fairly good to gain knowledge about the CS_2 response time.

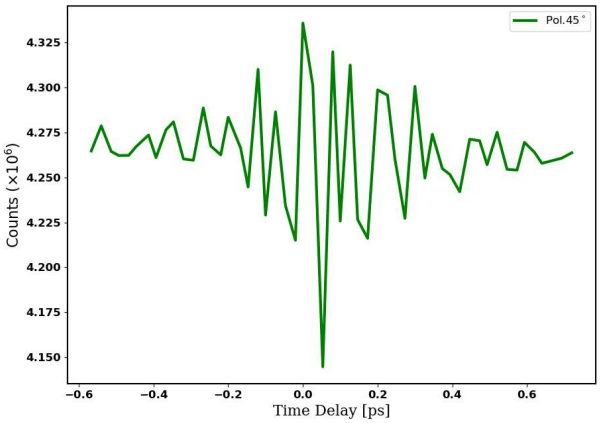


Figure 4.14: Kerr signal time trace obtained at temporal stepsize 25 fs, with integration time of 20 s

In order to extract information about the nonlinear response time of CS_2, the Kerr time trace needs to be fully resolved. Thus, as the minimum temporal stepsize (maximum temporal resolution) enabled by the linear translation stage is 0.66 fs, this stepsize was used to completely resolve any fine details belonging to the Kerr signal time trace, as illustrated in Fig. 4.15, in which the integration time had to be reduced to 1 s, since scanning at such a very small stepsize takes a large amount of time.

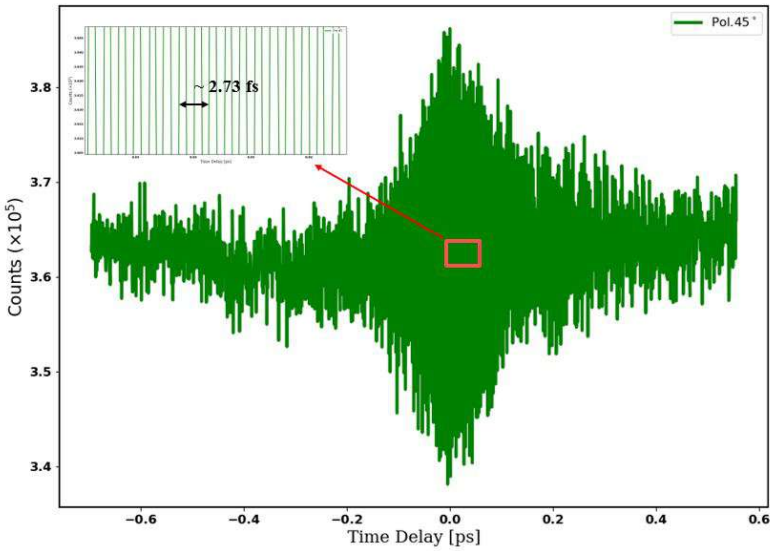


Figure 4.15: Kerr signal time trace obtained at temporal stepsize 0.66 fs, with integration time of 1 s, the inset is a zoom-in on the rectangle (red), showing the fast oscillation with temporal cycle of $\sim$ 2.73 fs.

If we zoom-in on the fringes of Fig. 4.15, located at the center of it, we see that it shows a fast oscillation, with a temporal cycle of $\sim$ 2.73 fs. This temporal cycle

corresponds to the wavelength 820 nm used in this experiment, where the temporal cycle $t = \lambda/c$. This tells us that the fringes seen in Fig. 4.15 are interference fringes that occur, because of the interference between the two beams (pump & probe), which are degenerate in frequency/wavelength. Similar interference fringes were observed in an OKG experiment with CS_2 as Kerr medium [299]. Looking back at Figs. 4.12, 4.13, and 4.14, one can understand that the awkward times traces obtained in these figures were undersampling the fast oscillation that resulted from the interference between the pump and probe beams, as they are propagating across each other. Since CS_2 is a nonlinear medium, such interference between the pump and probe beams might lead to a transient grating, which can scatter both beams, so-called laser-induced transient grating (LITG). This might interpret another interesting observation that at some parts, especially at the tails of the Kerr signal time trace, the oscillation temporal period can be as low as $\sim$ 1.32 fs (corresponds to $\sim$ 396 nm), or becomes as high as $\sim$ 6 fs (corresponds to $\sim$ 1800 nm). One can think, alternatively, that the chirp experienced by each beam could lead to some variation. However, given that each beam passes through few optical elements such that having a chirp will be unavoidable, the small chirp acquired by each beam does not still be adequate to give rise to such oscillation cycle variations. Another possibility could be the degree of accuracy and/or unidirectional repeatability of the delay line stepsize, that contributes to temporal cycle variations. An initial investigation of the delay line accuracy, showed that the average accuracy offset tested for 10 positions is $\sim$ 21 nm, with 279 nm difference between the minimum and maximum offset. Also, it was found that the average offset of unidirectional stepsize repeatability for 5 positions is $\approx$ 135 nm, with a maximum offset of 140 nm. A distinction between the effect of the delay line accuracy/unidirectional step repeatability fluctuation is possible, if a spectral analysis of the transmitted probe signal is carried out, i.e., via a spectrometer.

Before starting the analysis of the Kerr medium nonlinear response time, it is important that the temporal profile of OKG is extracted from the Kerr signal time trace. For this purpose, the fast oscillation must be removed. The strategy to do this is by firstly applying Fourier transform to the Kerr signal time trace, for converting them from the time-domain to the frequency-domain. Then, a low-pass filter is applied to the data, so that the slow component is extracted. By applying an inverse Fourier transform, the filtered envelope in time-domain can be obtained. In our case, an asymmetric Heaviside function must be applied, in the frequency-domain, on one side only of the two-sides of the frequency spectrum, starting from 0 Hz, so that it effectively works. This method enables, not only to get rid of the baseline, seen in all time traces, but also enables to extract the Kerr signal envelope (temporal profile), which can be further analyzed. The envelope of Kerr signal time trace of Fig. 4.15 is

presented in Fig. 4.16, along with the fitting of its nonlinear response components.

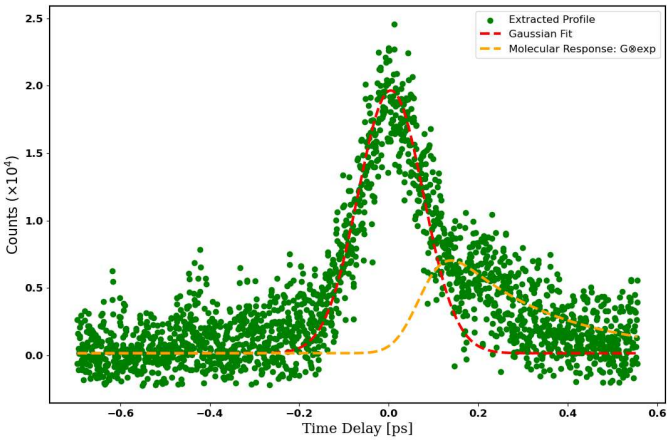


Figure 4.16: Temporal profile (envelope) of the Kerr signal trace of Fig. 4.15, with its fitting parameters of FWHM $\approx 172 \pm 2$ fs (red dashed curve) for the cross-correlation, and with $\tau = 227 \pm 22$ fs for the fast molecular response (orange dashed curve).

As presented earlier in Eq. 4.3, the nonlinear response of CS_2 has mainly two components, electronic, which is an ultrafast time response; and molecular, which is either fast and/or slow, depending on the substance phase (liquid or vapor) and its associated molecular relaxation mechanism. The transmitted Kerr signal measured by the photodetector, expressed in terms of response function is given by

$$S_{\text{measured}}(\tau) = \int \mathrm{d}t\, I_{\text{probe}}(t)\left[(R_{\text{OKE}} * I_{\text{pump}}(t-\tau))\right]^2, \tag{4.8}$$

where $I_{\text{pump}}(t-\tau))$ is the pump intensity envelope, delayed by τ, $I_{\text{probe}}(t)$ is the probe intensity envelope (fixed in time), $R_{\text{OKE}}(t-t')$ is the response function of the Kerr medium. When the convolution $(R_{\text{OKE}} * I_{\text{pump}})(t-\tau)$ is expanded, Eq. 4.8 will become

$$S(\tau) \propto \int |E^{\text{sg}}(t)|^2 \mathrm{d}t \propto \int \mathrm{d}t\, \mathcal{I}_{\text{probe}}(t)\left[\int \mathrm{d}t'\, R_{\text{OKE}}(t-\tau-t')\mathcal{I}_{\text{pump}}(t')\right]^2. \tag{4.9}$$

If only bound electrons (hyperpolarizability) respond to the external applied electric field, and nonlinear response is instantaneous, such that $R_{\text{OKE}} \propto \delta(t)$, then the convolution simplifies to $R_{\text{OKE}} * I_{\text{pump}}(t-\tau) = I_{\text{pump}}(t-\tau)$, thus the signal becomes

$$S_{\text{electronic}}(\tau) \propto \int I_{\text{probe}}(t)[I_{\text{pump}}(t-\tau)]^2 \mathrm{d}t. \tag{4.10}$$

If the temporal intensity profile of the pump and probe beams has the same shape, e.g., Gaussian, like our case, then this integral is the cross-correlation between the

probe and squared pump pulses, namely $S_{\text{electronic}}(\tau) \propto (I_{\text{probe}} * I^2_{\text{pump}})(\tau)$. Due to the contribution of molecules like in CS_2, the total nonlinear response of the Kerr medium will be expressed as

$$R_{\text{OKE}}(t) = R_{\text{elec}}(t) + R_{\text{mol,fast}}(t) + R_{\text{mol,slow}}(t), \tag{4.11}$$

where $R_{\text{elec}}(t) = A_e\delta(t)$ is the instantaneous response of the electrons, $R_{\text{mol,fast}}(t) = A_{\text{f}}e^{-t/\tau_{\text{f}}}H(t)$ is the fast molecular response ($\sim$ 100-600 fs), and $R_{\text{mol,slow}}(t) = A_{\text{s}}e^{-t/\tau_{\text{s}}}H(t)$ is the slow molecular response ($\sim$ 1-2 ps). Let's keep in mind that in reality the exponential decays associated with the fast and slow nonlinear responses are convolved with the Gaussian function arising from the cross-correlation between the pump and probe beams. Thus, each one of them will be mathematically expressed as an ExGaussian function. For example, the fast molecular response will be given by

$$S_{\text{fast}}(t) \propto A_f \exp\left(\frac{\sigma^2}{2\tau_f^2} - \frac{t-t_0}{\tau_f}\right)\left[1 + \text{erf}\left(\frac{t - t_0 - \sigma^2/\tau_f}{\sqrt{2}\sigma}\right)\right], \tag{4.12}$$

while the slow response will be given by

$$S_{\text{slow}}(t) \propto A_s \exp\left(\frac{\sigma^2}{2\tau_s^2} - \frac{t-t_0}{\tau_s}\right)\left[1 + \text{erf}\left(\frac{t - t_0 - \sigma^2/\tau_s}{\sqrt{2}\sigma}\right)\right], \tag{4.13}$$

where A_{f}, τ_{f}, A_{s}, τ_{s} are the amplitudes and the relaxation time constants of the fast and slow components, respectively. And, t_0 is the temporal offset of each response, σ is the Gaussian width obtained from the Gaussian function used for fitting of the cross-correlation between the pump and probe beams. At the end, the total molecular nonlinear response will be expressed by a summation of these two ExGaussian functions, as seen in Fig. 4.9

According to the presented equations, and given that our Kerr medium here is a liquid CS_2, the data points of our temporal profiles should be ideally fitted with the above-mentioned three functions; Gaussian for the cross-correlation, and two ExGaussian functions, one for the fast molecular relaxation, while another for the slow molecular relaxation. However, the decay tail associated with the slow molecular relaxation of liquid CS_2 had a significantly small amplitude, overlapped with noise, which turned their fitting cumbersome. Alternatively, fitting with weighted nonlinear least square was tried out, and it could not resolve, though, the slow relaxation contribution to the nonlinear response. This manifested itself in the form of obtaining a large uncertainty in the slow relaxation decay constant. This might be caused as a consequence of our relatively small gate peak pulse intensity ($\sim$ 1.33 GW/cm^2), which was not sufficient to induce detectable diffusive orientational motions; while it was enough for provoking local molecular redistributions and/or density fluctuations,

which manifest itself in the fast molecular nonlinear response on the scale of $\sim$ 100-600 fs, as mentioned in Ref. [295]. Therefore, in the following data analysis, our temporal profiles are fitted with a Gaussian function for the cross-correlation part, while an ExGaussian function for the fast molecular response. So, the cross-correlation part in Fig. 4.16 was fitted with a Gaussian function (red curve), which shows that its FWHM $\approx 172 \pm 2$ fs that represents the electronic response. With an estimated gate and probe width of $\sim$ 90-100 fs, this result is reasonable. The exponential molecular response modified by the Gaussian function (orange curve), was fitted with the ExGaussian, which give an exponential decay constant $\tau = 227 \pm 22$ fs. As discussed earlier, and as elaborated in Ref. [295], the molecular nonlinear response can be classified into two types: fast which occurs within the time range $\sim$ 100-600 fs, due to local translational anisotropy, caused by molecular redistribution or microscopic collision or density fluctuations; slow taking place within $\sim$ 1.2-1.7 ps, due to diffusive orientational motions. The slow molecular response does not occur in CS_2 vapor, but it does in CS_2 liquid. The result shown in Fig. 4.17 that has an exponential time decay $\tau = 227 \pm 22$ fs lies within the time range of the fast molecular responses. Another measurement taken with 0.66 fs temporal stepsize, and with 1 s integration time, but scanned over longer range, showed that the cross-correlation FWHM $\approx$ 106 ± 2 fs the exponential decay time $\tau = 272 \pm 13$ fs, which also lies within the range associated with molecular fast response, shown in Fig. 4.17.

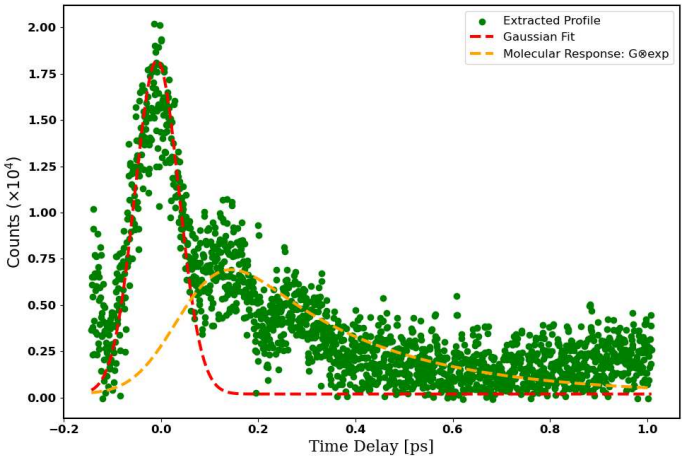


Figure 4.17: Temporal profile (envelope) of a Kerr signal trace (0.66 fs temporal stepsize), with its fitting parameters of FWHM $\approx 106 \pm 2$ fs (red dashed curve) for the cross-correlation, and with $\tau = 272 \pm 13$ fs for the fast molecular response (orange dashed curve).

Other measurements were taken to verify the results, but at larger temporal stepsizes and longer integration times, presented in Fig. 4.18. In Fig. 4.18 (a), the temporal profile of Kerr signal was taken with 25 fs temporal stepsize and 20 s integration time.

The cross-correlation FHWM $\approx 130 \pm 9$ fs, while the exponential decay constant $\tau = 213 \pm 120$ fs. This huge uncertainty arises because of the dominance of noise, as lock-in amplifier was not used. In Fig. 4.18 (b), the temporal profile was taken at finer temporal stepsize of 5 fs, but with 15 s integration time shows that the cross-correlation FWHM $\approx 129 \pm 7$ fs, and the exponential decay constant $\tau = 131 \pm 26$ fs. This result has somewhat reasonable uncertainty, probably because of the larger number of points, the temporal profile has, as compared to 4.18 (a).

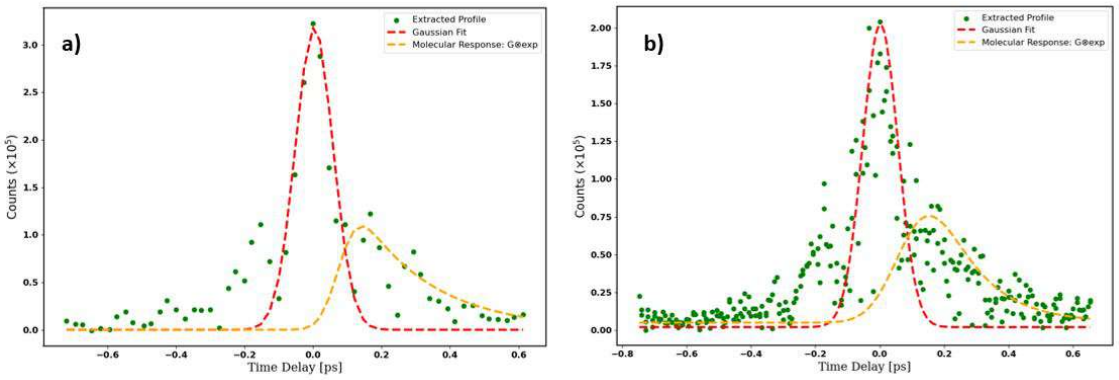


Figure 4.18: Temporal profile of Kerr-rotated signal with (a) 25 fs temporal stepsize and 20 s integration time (FWHM $\approx 130 \pm 9$ fs, $\tau = 213 \pm 120$ fs); (b) 5 fs temporal stepsize and 15 s integration time (FWHM $\approx 129 \pm 7$ fs, $\tau = 131 \pm 26$ fs).

The Kerr-rotated probe signal is very small, hence its detection and collection can be sometimes cumbersome. One of the technical challenges faced to collect the Kerr signals, was that the Kerr signal time trace was prone to deformation, due to any kind of instabilities of the optical setup. For example, when the transmitted Kerr-rotated probe beam was split via the 50/50 beam splitter placed before the two photodetectors, one detector can collect a good signal time trace, while the other one collects a deformed trace, even though they are derived from the same probe beam. An example of such a thing is provided in Fig. 4.19, in which the Kerr signal time trace, whose filtered temporal profile is shown in Fig. 4.18 appears clearly and symmetric when detected with a photodetector, connected to Ch_0 on the TCSPC, while it looks distorted (despite collecting more signal) when it was simultaneously collected via the photodetector, connected to Ch_1 on the TCSPC. The potential reason could be that each photodetector has its own lens, in order to focus the beam signal onto the small active area of the detector. Since each lens is aligned differently to maximize the number of counts readout by the TCSPC, if the probe beam deviates slightly from the optical axis, the spherical surface of the detector's focusing lens can increase this deviation even further. Another reason could be that one photodetector suffers from electrical noise, which distorts the Kerr signal time trace, hence its temporal profile. Careful investigation of this issue will be needed.

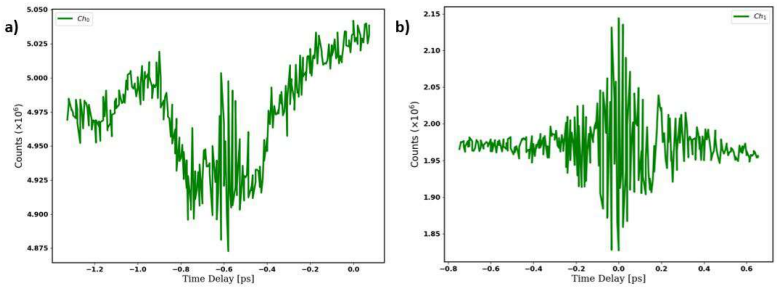


Figure 4.19: Difference between the same Kerr signal time trace (Fig. 4.18 (b)) collected simultaneously by two different photodetectors, one connected to Ch_0 of the TCSPC (a), and another connected to Ch_1 of the TCSPC (b).

Another technical difficulty associated with the detection of time traces of Kerr signals relates to the fluctuation of the Taccor laser wavelength, and the aforementioned fluctuation of the repeatability of the linear stage (delay line) stepsize. These two sources of fluctuations can affect the detected time trace, where one can clearly see that, when the Kerr time trace is undersampled. For example, Fig. 4.20 shows four different time traces of the same Kerr signal, which were obtained by scanning the pump beam across the probe beam over a delay line distance of 2 mm, with the same integration time of 10 s, and the same temporal stepsize of 200 fs; yet, each trace looks fundamentally different from others. This happens because of any small wavelength deviation, and/or fluctuation in the stepsize repeatability.

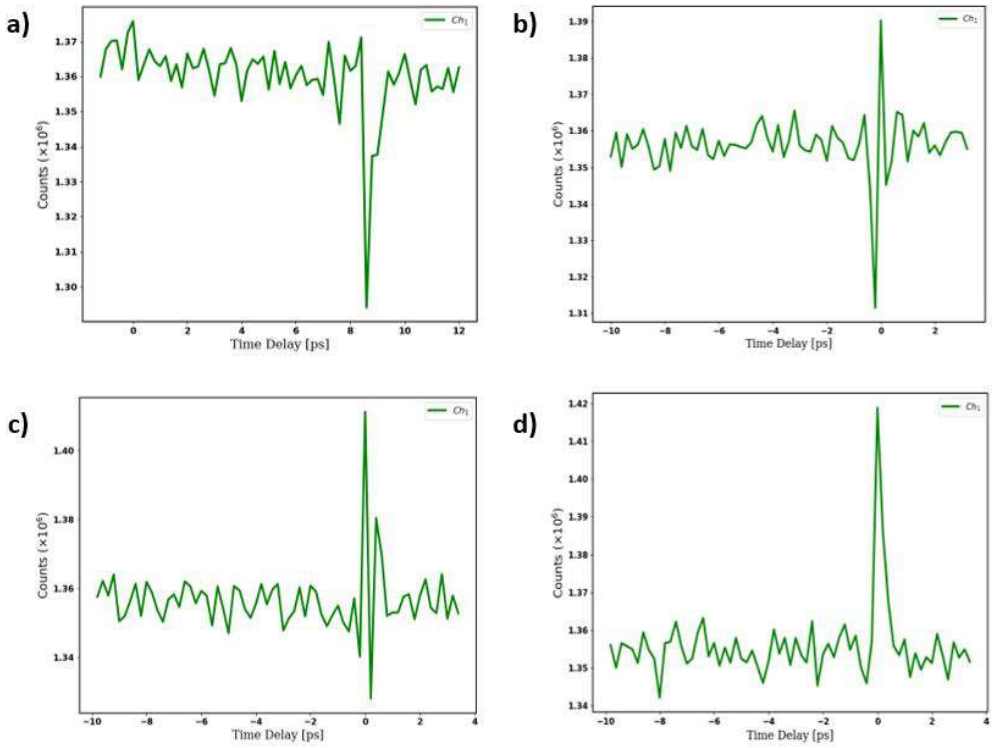


Figure 4.20: Variations of four time traces of the same Kerr signal, obtained with 10 s integration time, with 200 fs temporal timesteps, due to small deviation of the laser wavelength, and/or fluctuation of the delay line accuracy, or stepsize repeatability.

4.3 Otical Kerr gate with single-mode fiber

4.3.1 Introduction

Optical fibers consist generally of a core made of glass with linear refractive index, n_1, surrounded by a cladding layer with linear refractive index, n_c, slightly lower than the core's index. Such type of optical fibers is often referred to as step-index fiber, in order to distinguish it from another type of optical fibers, so-called graded-index fiber. In graded-index fibers, the refractive index decreases gradually along the radial direction from the center toward the core boundary [300]. There are two main parameters by which optical fibers are characterized. The first parameter is the relative core-cladding index difference $\Delta = n_1 - n_c/n_1$, and the second parameter is so-called V-number, defined as $V = k_0 a(n_1^2 - n_c^2)^{1/2}$, where $k_0 = 2\pi/\lambda$, a is the core radius, and λ is the wavelength of light. The V-number indicates the number of modes that an optical fiber can support, and step-index fibers especially designed with $V < 2.405$, are considered single-mode fibers (SMF). The distinct difference between single-mode and multi-mode fibers is that the core radius of multi-mode fibers is relatively large ≈ 25 μm, as compared to single-mode fibers, whose core radius needs

to be < 5 μm, when $\Delta \approx 0.003$. This particular feature of single-mode fibers is quite beneficial for nonlinear optical applications, i.e., third-order $\chi^{(3)}$ nonlinear optical processes, as high laser intensity can be attained using moderate laser powers. This enables the usage of single-mode fibers in a wide range of applications that involve optical Kerr effect, where optical Kerr gates, with single-mode fibers as Kerr media can be utilized. For example, optical Kerr gates can be used for ultrafast all-optical switches in telecommunication using quantum networks, for routing photons at high speed [301], for optical switching of heralded single-photon sources [250], or for quantum information processing [302, 303]. Optical Kerr switching has been also used for carving out configurable ultrafast sub-picosecond pulses from continuous wave lasers [304].

Single-mode fibers are made from fused silica that has low nonlinear refractive index n_2 on the order of $\sim 10^{-20}$ m^2/W, which is as such not adequate for clear observation of nonlinear optical effects, in particular, third-order nonlinear optical $\chi^{(3)}$ effects, unless high intensity lasers are used. Nonetheless, as mentioned before, their small core radius allows for achieving high intensity utilizing modest laser power. Furthermore, optical fibers have the advantage that they can acquire very large lengths, which is not possible to achieve with typical bulky Kerr media thicknesses. However, increasing the length of an optical fiber comes with the cost of dispersion, which lowers the peak intensity of a pump laser beam, hence reducing its ability to induce nonlinear effects.

Here, the results of a master thesis project are presented, in which an optical Kerr gate was constructed with a commercial single-mode fiber as a Kerr medium, and a fs laser pulses at 1 GHz repetition rate as the pump (gate), while the probe was a CW laser. The aim of that project was to demonstrate the ability to obtain optical Kerr signals at 1 GHz repetition rate and sub-picosecond temporal resolution, so that when satisfactory results are obtained, single-mode fibers can be employed as the main Kerr medium for gating ultrafast fluorescence signals. For more details about this project, the reader is referred to the original master's thesis in Ref. [305]. Since there have been significant improvements to be achieved, section 4.3.4 is entirely dedicated to proposing some procedures that should be taken into account, in order to obtain highly transmitted Kerr signals of the probe beam that are consistent with the theoretical expectations.

4.3.2 Setup configuration

The optical Kerr gate consists of a Kerr medium, which is a commercial 10-12 cm single-mode fiber (SM600, 633-780 nm, Thorlabs) placed in between two crossed

linear polarizers. The length of the SMF was chosen to be below the dispersion length L_{D} to avoid dispersion of the pump beam. This L_{D} was calculated given the parameters of the experiment and found to be 25 cm [305]. The pump beam was derived from the 1 GHz repetition rate Taccor Tune fs laser at 750 nm, with a pulse width of roughly 100 fs. The CW laser was a PicoQuant diode laser (PDL-800D) at 656.64 nm, and its output power was drastically reduced, such that only 1.7 mW power was measured at the SMF output. Initially, it was planned to use a photodiode detector connected to an oscilloscope for measuring the transmitted Kerr signals of the probe (CW laser), but the signal was very weak, such that the photodiode detector could not detect the transmitted probe signal. Instead, a spectrometer was utilized for the detection of the transmitted Kerr signal. Similar to the experiment that used CS_2 as a Kerr medium for the characterization of the OKG, the pump and probe beams were counter-propagating, so that the detector is not saturated or damaged, because of the high power of the pump beam. It is important to point out that each type of detection scheme measures the transmitted Kerr signal of the probe differently. For instance, the detection of the Kerr-rotated probe signals via a photodiode detector provides information about the Kerr signal in the time-domain. As the probe beam is initially a CW laser, and the two crossed polarized will have some leakage - even without the presence of the pump beam - it is expected to see a small flat noisy line on the oscilloscope display. Since both the leakage and the transmitted Kerr signal were below the detection sensitivity threshold of the photodiode detector, this scheme of detection did not work out. The second approach, in which a spectrometer was used, relies on the fact that the Kerr rotation, induced due to the high intensity of the pump pulse will lead to a spectral broadening of the spectrum of the probe beam - CW laser in this case. Given that the spectrum used for detection was highly sensitive (QE Pro, Ocean Optics), it was possible to detect the transmitted Kerr-rotated in the frequency-domain following this detection scheme, where a bandpass filter was placed in front of the spectrometer to allow only the CW probe laser to be detected. A scheme of the experimental configuration of this setup is provided in Fig. 4.21.

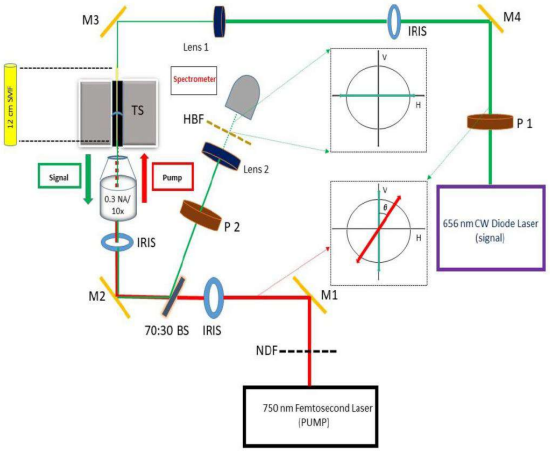


Figure 4.21: A scheme of an OKG using single-mode fiber, where the probe is a CW laser, and the pump is fs laser [305].

4.3.3 Experimental results and discussion

It is always crucial before measurement of transmitted Kerr signal in any OKG experiment that aims ultimately at detecting very weak signals, such as fluorescence to measure initially the self-phase modulation. This is because the high intensity of the pump beam can experience self-spectral-broadening that could partially overlap with the spectral profile of the probe beam - fluorescence emission in this case - thereby reducing the detection S/N ratio, or in the worst case scenario to obscure the probe signal completely. That is why the results concerning SPM are firstly introduced, following that the Kerr-rotated probe signals are presented.

To investigate the SPM, owing to the high intensity of the pump beam, the CW laser was blocked, and only the pump beam was allowed to propagate down the SMF at 11, 65, 150, 250 mW, respectively. These power values were measured at the output of the SMF, where the coupling efficiency between the input and output pump powers were nearly 50%. The results of SPM are shown in Fig. 4.22. As seen in the figure, the pump laser spectrum was independently measured - before coupling it into the SMF - and fitted with Gaussian function to determine its initial FWHM, which was found to be 13.46 nm. Then, the laser was coupled into the SMF at powers formerly mentioned (indicated in the inset of Fig. 4.22 as well) and their spectra were measured and fitted in a similar manner.

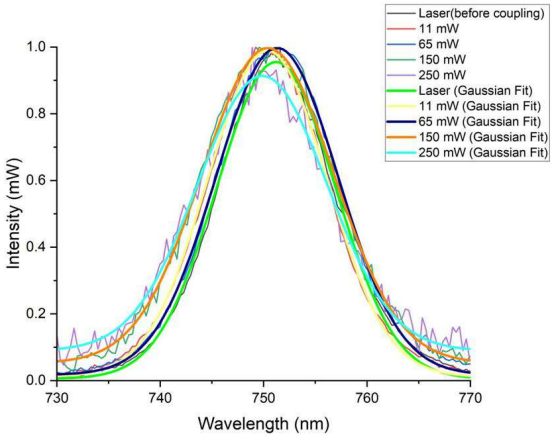


Figure 4.22: SPM of normalized spectral profiles of the pump laser, at different laser powers, fitted with Gaussian function [305].

The FWHM values obtained from the fitting were 13.58, 13.89, 14.72, 14.90 nm, corresponding to pump laser power of 11, 65, 150, 250 mW, respectively. This result shows a consistent trend, where the FWHM of the laser spectral profile was increasing, as a result of the increase of the laser power, as anticipated.

Following the characterization of the SPM of the pump laser into the SMF, the probe beam (CW laser) was unblocked, where its spectral profile was initially obtained while the pump laser was blocked. Then, both beams were allowed to propagate in a counter-direction, as indicated before, for the OKG measurements. Here the set of pump laser powers were 25, 100, 180, 250 mW, respectively. Again, the coupling efficiency achieved was nearly 50%. The OKG results are shown in Fig. 4.23.

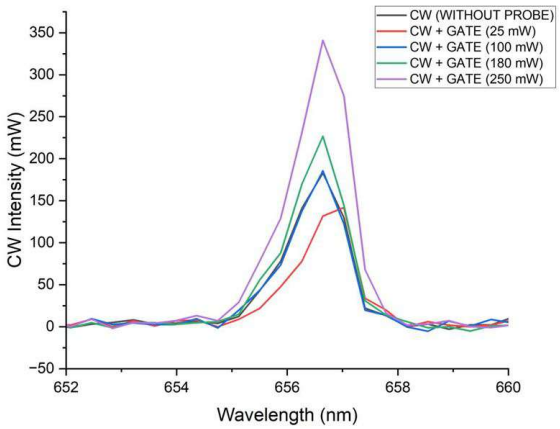


Figure 4.23: Spectral profiles of the transmitted probe signal at the output of SMF at different pump powers [305].

Without the presence of the intense pump beam, the CW laser will be transmitted through the SMF, and only a small portion of it will be leaking through the second polarizer (often called analyzer), as the two crossed polarizers are not perfect. When

the pump beam is allowed to propagate down the SMF, due to Kerr rotation of the probe beam, it is anticipated that the leaked CW laser signal going through the analyzer will be increased, thus both the amplitude and spectral width of the spectrum will be higher, where this increase is directly proportional to the pump beam power. Nonetheless, it is evident from Fig. 4.23, that the data do not follow the expected trend. For example, the CW spectral profile measured at 100 mW pump laser power has similar amplitude and spectral width of the CW laser spectrum without the pump beam. Further, the spectrum of the CW probe laser detected at the presence of 25 mW pump laser power has smaller amplitude and bandwidth than the CW laser spectrum without coupling the pump laser. However, the spectra of the probe taken at 180 mW and 250 mW follow the anticipated trend, whereas their amplitude and spectral width increase with the increase of the pump laser powers. This obviously indicates that there are other physical mechanisms that play a role, leading to different output signals from expected.

Here, the absurd finding will be discussed, while in the next subsection some further improvements would be proposed for attaining more consistent results in the future. First of all, it is well-known that silica from which the SMF is made exhibits ultrafast Kerr response at sub-ps time scale. This is because only electron cloud distortion is the main respondent to the oscillation caused by the electric field of the fs laser. This indicates that the data collection must be adequately fast to harness the fast signal, especially in the case where the probe beam is CW laser. In fact, in traditional OKG experiments, in which pulsed laser sources are used as pump and probe, this is not a critical issue, since the OKG signal is collected when both pulses are temporally overlapped. In contrast, when the probe beam is a CW laser, similar to this experiment discussed here, the probe beam can detect other nonlinear effects that occur on relatively longer time scales, e.g., thermal lensing due to heat accumulation. Although thermal lensing effects in optical fibers are neither rarely reported, nor fully understood [306], it is still possible that the 1 GHz repetition rate laser used as a pump helps in accumulating heat into the SMF, which in turn creates a thermal lens. Typically, thermal lens acts as a self-defocusing lens that drastically reduces the intensity of the pump, giving rise to inconsistent results.

4.3.4 Practical considerations for enhanced Kerr signal

Over the course of this experiment, there had been other issues besides the potential effect of long response time effects, e.g., thermal nonlinearity caused by heat accumulation. Addressing those issues is of paramount importance for attaining consistent OKG signals. For example, the pump (gate) beam coupling efficiency in the SMF

was roughly 50%, this does not enable investigating OKE and polarization rotation of the probe beam effectively, as the detection of a reasonably transmitted Kerr signal demands using as high as possible intense pump laser beams. Therefore, increasing the coupling efficiency for the pump (gate) beam can in principle enable obtaining higher transmitted probe signals. It was noticed throughout this experiment, that the pump beam profile at the output of the SMF was not Gaussian, and it was rather like a stretched oval. For optimal detection of Kerr-rotated probe signals, both the pump and probe beam must be spatially overlapped. This can be achieved if both beams share a similar spatial intensity profile, e.g., Gaussian profile, that are well-overlapped into the SMF. Thus, adjusting the pump beam spatial profile, as well as checking out the spatial overlap can result in better detection of probe signals. The relatively small coupling efficiency also influenced the CW probe laser power getting into the SMF. As previously mentioned, the CW probe power measured at the fiber output was 1.7 mW, which is relatively small power. As known, the OKG efficiency is determined as the ratio between the Kerr-rotated probe power and the input probe power. This implies that increasing the input probe power should lead to increasing the output power, detected due to the Kerr effect. Considering that the CW laser used as a probe was unpolarized before going through the first polarizer, almost 50% of its power was already lost after passing through that polarizer. Hence, it is also possible in this experiment to increase the input CW laser power, without even enhancing the coupling efficiency into the SMF via replacing the probe with another linearly polarized CW laser, which would not experience the same power loss, as a result of passing through the first polarizer. Needless to say, that the input probe power must be reasonably increased and must be kept sufficiently smaller than the pump power, otherwise, the probe beam can induce undesirable nonlinear effects on its own, which must be absolutely avoided. Another issue in this experiment was the small extinction ratio of the two polarizers. As well-known, the two crossed polarizers in any OKG experiment are playing an essential role, for detecting OKG probe signals, with high S/N ratio. This is the case, when the two polarizers possess a very high extinction ratio, which was not fully achieved, where the extinction ratio of the two crossed polarizers was relatively small. Replacing the two crossed polarizers, with a pair of polarizers having much higher extinction ratio, e.g., Glan-Taylor, or Glan-Thomson polarizers, will definitely lead to enhanced S/N ratio. Provided that the silica of the SMF has ultrafast response time, and that other nonlinear effects, i.e., thermal nonlinearity occur over longer time scales; it is vital to ensure that the OKG signal is rapidly harnessed, in order to avoid the influence from other competing effects. This, in principle, can be attained via lock-in amplifier detection, which also effectively serves for dramatically reducing the noise during detection, hence enhancing the S/N ratio. Unfortunately, lock-in amplifiers were not involved

in this experiment, which if it were included, would have enabled the detection of Kerr-rotated signals with unambiguous, conclusive results. For example, the usage of lock-in amplifier detection technique was instrumental in the work of Ref. [307] to unambiguously discriminate between the SPM caused by the pump intensity, the cross-phase modulation (OKG probe signal), background signal, and CW probe beam signal leakthrough - owing to imperfect polarizers. The latter was a fundamental issue, whereas their SMF experienced fluctuations of the leakthrough probe signals, which was attributed to a varying strain occurring in the SMF, caused by air currents and other vibrations in the vicinity of the fiber.

We have seen that achieving reasonable optical Kerr signals requires high-quality polarizers with very high extinction ratios. Characterization of the home-built OKG setup using a standard medium such as CS_2 revealed both the capabilities and the limitations of the system. Although CS_2 is a liquid and typically exhibits a slow decay tail in the temporal Kerr response in standard OKG experiments, the results presented above show that CS_2 behaved as if it were a vapor—despite not being one.

One possible explanation is that the slow component is buried under noise originating from electronic noise in the SPADs and TCSPC modules, stray light reaching the detector, and leakage of the probe beam due to insufficient extinction ratio. Therefore, polarizers with a higher extinction ratio must be used to minimize probe-beam leakage, and a lock-in amplifier should be employed to greatly suppress other types of noise. This could enhance the visibility of the slow decay tail, and provides even better visibility of the fas molecular response.

Another explanation is related to the small pulse-peak intensity used to induce the Kerr effect. Because the electrons in CS_2 are light, even modest peak intensities are sufficient to drive electronic oscillations, contributing to the nonlinear response. However, nuclei are much heavier, and it is possible that the gate-pulse peak intensity used here was insufficient to trigger the slower diffusive orientational motions that normally appear as slow Kerr components. It is worth noting that standard OKG experiments typically use much higher pulse-peak intensities. In this regard, the results presented here may be of interest, as they suggest that liquid CS_2 under weak or modest peak intensities may mimic the Kerr response of its vapor phase.

For conclusive verification, a similar OKG experiment could be performed using another femtosecond laser capable of much higher pulse-peak intensities, which can then be gradually reduced to values comparable to those used in this work. Conducting this experiment at a different repetition rate and/or wavelength poses no limitation, as the primary focus is on the effect of pulse-peak intensity on the Kerr-response dynamics. The anticipated outcome would be that at sufficiently high intensities, liquid CS_2 will exhibit the well-known three nonlinear components—ultrafast elec-

tronic, fast molecular, and slow molecular responses—as reported in the literature. As the peak intensity is reduced toward the level of the Taccor fs laser used here, the slow component should disappear, leaving only the ultrafast electronic and fast molecular responses, provided that our interpretation is correct.

For the OKG experiment performed in a single-mode fiber using a CW laser, we recommend increasing the coupling efficiency of the laser into the fiber and using a linearly polarized probe beam together with polarizers of higher extinction ratio. Additionally, the use of a lock-in amplifier is strongly advised to enable unambiguous detection of the OKG signal.

Chapter 5

Bismuth oxide-containing glass as a Kerr medium

5.1 Introduction

Many photonic innovations rely on nonlinear optical properties, especially for information technology. Significant research has focused on the nonlinear optical behavior of glasses, with an aim to harness their capability and potential of applications. The main driving force behind this interest has been the development of pulsed lasers and optical fibers. Materials with high third-order polarization can be used for applications such as supercontinuum generation and all-optical switches, and so on. The goal in those applications is to attain high nonlinearity with fast response. In contrast to crystals that are responsible for achieving second-order nonlinear effects, e.g. SHG, THG and so forth, glasses are amorphous materials which lack long-range order and therefore exhibit inversion symmetry on average, which forbids second-order nonlinear processes. With the advent of high-power lasers, the nonlinear optical properties of glass have caught even more interest, because of the interesting nonlinear optical phenomena that require high intense laser power. For instance, the Kerr effect (third-order nonlinearity) is responsible for the phenomenon of self-focusing, due to the formation of a light-induced lens, which can eventually, in extreme cases, lead to the destruction of the optical component it is propagating through. Moreover, such an effect can result in distortion of the wavefront of the laser beam [308]. Starting from the last decade in the twentieth century, there has been an ever increasing interest in three particular types of optical glasses; these are oxide glasses, chalcogenide glasses and halide glasses [267]. Particular interest has been devoted to the oxide and chalcogenide glass families, owing to their optical transparency in the near-infrared [309, 310], and high optical nonlinearity [311, 312,

313, 314]. Oxide-containing glass, in particular bismuth-borosilicate glass (BBS) was chosen as the Kerr medium for the optical Kerr gate experiments. This is due to its high nonlinear refraction index n_2, relative feasibility of fabrication, as well as its transparency in the visible and near-IR wavelength range, which suits the emission wavelengths from our light sources. Additionally, unlike liquid CS_2, BBS glass enables obtaining an instrument response function at sub-ps timescale. This is because only bound electrons are the ones that respond to an external applied electric field of the laser beam.

In the following section, the glass structure will be presented and the sample preparation recipe will be introduced. Afterwards, section 5.3, will be devoted to discussing the third-order nonlinearity of glass in general, with special emphasis on two-photon absorption, self-phase modulation and Kerr effect in BBS glass, respectively. In the same section, the results of the carried out measurements related to those nonlinear optical phenomena will be presented and discussed.

5.2 Glass structure and sample preparation

The fundamental constituents of the bismuth borate glass family are composed of bismuth oxide (Bi_2O_3) and boric oxide (B_2O_3). Boric oxide, B_2O_3, in particular, is one of the vital glass formers, where a melt with a high composition of B_2O_3 has high viscosity and tendency to form glass [315]. It also exhibits interesting linear and nonlinear optical properties in its crystalline form. The structural units that the boron atom forms are usually $[BO_3]^{3-}$ and $[BO_4]^{5-}$ by coordinating with three or four oxygen atoms, respectively. These two structural units can also be combined to form different B_xO_y structural groups. In amorphous environments, i.e., glass, the calculations show that the anionic group $[BiO_4]^{5-}$ is thought to strongly influence the linear refractive index. Addition of B_2O_3 to the bismuth oxide Bi_2O_3 enables the tunability of the optical properties of glass over a wide spectral range, depending upon the composition of these two components. It was shown that the content of Bi_2O_3 in bismuth borate glass strongly affects the linear refractive index and the UV absorption edge. As the bismuth oxide content increases, the absorption edge shifts to longer wavelength, and the linear refractive index increases. The bismuth-borate glasses are often prepared by melting the glass raw ingredients into a crucible made of platinum (Pt), or aluminum oxide (Al_2O_3) at elevated temperatures. Afterwards, the melt is poured onto a plate, then annealed for some time before polishing to get the desired thickness. For instance, Sugimoto et al. [51], prepared bismuth-borate glass by mixing the Bi_2O_3 and B_2O_3 with other ingredients, such as SiO_2, TiO_2, Li_2CO_3, Na_2CO_3, CeO_2, and $BaCO_3$. Generally, the extra additives serve certain

purposes, i.e., enhance the thermal stability or increase the mechanical durability, or as network modifier for the glass. For example, CeO_2 is specifically added to the bismuth-borate glass in order to suppress the precipitation of Bi metal under melting. The mixture of the raw ingredients is generally melted in a crucible, and placed in a furnace in air at elevated temperature for a certain duration. The melt is then poured onto plates for annealing, and subsequently cut at the desired thickness, and polished for obtaining smooth surface.

The bismuth-borosilicate glass prepared for our optical Kerr gate experiments is a ternary system composed essentially of Bi_2O_3-B_2O_3-SiO_2 (BBS), in addition to CeO_2 for the aforementioned purpose of using CeO_2 component. For our optical Kerr gate experiments, two BBS glass samples were prepared with the following composition: Bi_2O_3 (60 mol.%), B_2O_3 (20 mol.%), SiO_2 (20 mol.%), but we did not add CeO_2 to our composition. The mol.% denotes the number of moles percentages relative to other ingredients' moles. This composition was based on a study about the third-order nonlinear optical properties of BBS samples reported in Ref. [52]. Besides the exclusion of CeO_2, the glass formation conditions were deliberately altered as opposed to those of Ref. [52] to minimize coloration of glass. Our raw ingredients were melted in an Al_2O_3 crucible at 950 °C for 20 mins. Then, the melt was poured into a graphite mold at room temperature, before annealing it at 395 °C for 1 hr and cooled slowly down to room temperature at a rate of $\sim$ 1 °C/min. Afterwards, each glass sample of the two was cut to have a 3 mm thickness, and polished to 1 μm. Fig. 5.1 shows an image of one of the two BBS glass specimens, mounted into a lens holder.



Figure 5.1: Image of a 3 mm thick BBS glass specimen.

In spite of the external polishing of the BBS glass specimens, one can note in Fig. 5.1 though, that the glass is not internally uniformly cooled down. This, in fact, introduces considerable thickness variations across the specimen area. In turn, such variations influence the light transmission percentage, as well as the nonlinear optical

signal amplitude, which are both thickness-dependent quantities.

Bismuth-containing glasses are transparent in the near-IR spectral region, with roughly 80% transmission in this spectral range. However, this transmission drastically drops below 500 nm, as indicated in Fig. 5.2. The glass composition, in particular, the Bi content in the glass specimen plays a significant role, because the less Bi the glass sample contains, the more its transmission spectrum is shifted toward the UV spectral region, and less polarizability it acquires.

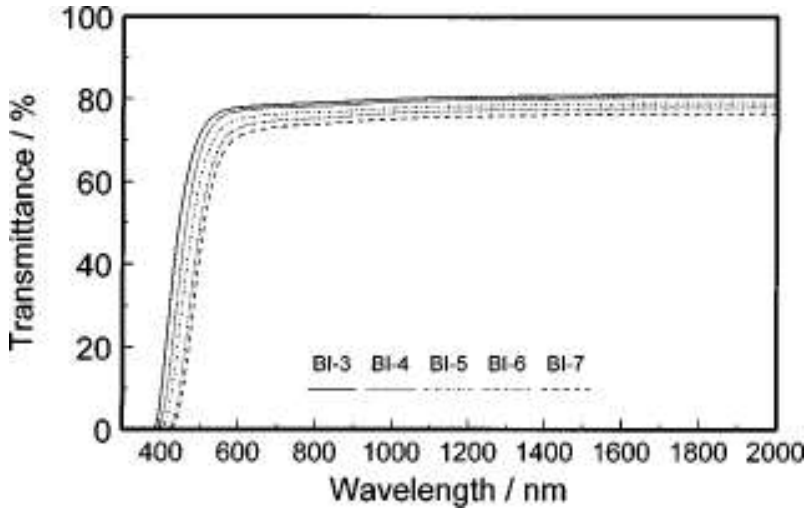


Figure 5.2: Transmission spectrum of BBS glass of different Bi compositions. BI-3 has the least Bi composition, and BI-7 has the highest Bi compositions [52].

To check the linear absorption and transmission of our BBS samples, we measured the absorbance of one of the identical two glass specimens, using a commercial UV-Vis-IR spectrophotometer (Perkin Elmer Inc.), that has different lamps as light source able for covering a spectral range from λ = 320-2500 nm. Then, the absorbance data were converted into transmission measurements, shown in Fig. 5.3.

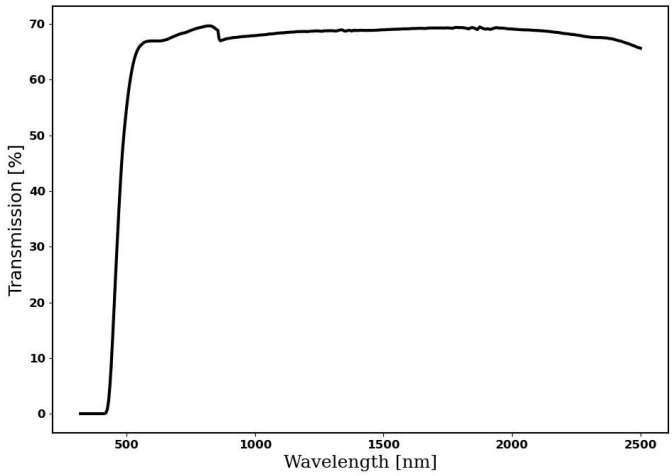


Figure 5.3: Transmission ratio of BBS glass specimen measured via a commercial spectrophotometer, from 350 nm to 2500 nm.

As we can see, within the wavelength range of interest for the OKG experiment, namely 760-820 nm, the transmission ratio is $\sim$ 69-70%. Further measurements were done using a CW laser (PicoQuant) at 656 nm, and a pulsed laser (Taccor tune, Novanta) at 820 nm showed that the transmission ratio is 76-78% at 656 nm, and 75-77% at 820 nm. This implies that the BBS glass absorbs roughly 22-24% of the incident light at 656 nm, while it absorbs nearly 23-25% of the incident light at 820 nm. In comparison to graphene, whose single-layer has an absorption of $\sim$ 2.3%, the absorption ratio of BBS glass is approximately similar to 10 layers of graphene sample.

5.3 Third-order nonlinearity in glass

The physical quantity that expresses third-order nonlinear optical processes is the third-order nonlinear optical susceptibility $\chi^{(3)}$. Estimating this quantity for a certain material, e.g., glass enables proper assessment of that material, in order to determine its suitability for a particular application. Third harmonic generation (THG) measurements have been used to estimate the value of $\chi^{(3)}$. For example, in the work presented in Ref. [52] a 6 ns pump laser at 1900 nm wavelength with near 50 MW/cm^2 peak power density was used for THG measurements, and used the following formula to estimate the $\chi^{(3)}$ value,

$$\chi^{(3)} = \left(\frac{n+1}{n_s+1}\right)^4 \left(\frac{I_{3\omega}}{I_{3\omega,s}}\right)^{1/2} \chi_s^{(3)} \frac{l_{c,s}}{l_c}, \tag{5.1}$$

where l_c is the coherence length over which both ω and 3ω are in phase with each other, when they are propagating through the bismuth-containing glass, $l_{c,s}$ is the coherence length for fused silica. Both $I_{3\omega}$ and $I_{3\omega,s}$ are the measured peak intensity of bismuth-containing glass, and fused silica, respectively. The values of n is for Bi-glass while n_s is for fused silica ($n_s = 1.46$ at 633 nm), and $\chi_s^{(3)}$ is the third-order susceptibility of fused silica. Substituting the corresponding values in the above formula, gives $\chi^{(3)} = 9.3 \times 10^{-12}$ esu ($1.30 \times 10^{-19} \mathrm{m}^2/\mathrm{V}^2$) for the Bi-glass. Reported $\chi^{(3)}$ values of oxide glass was 3.7×10^{-12} esu ($5.18 \times 10^{-20} \mathrm{m}^2/\mathrm{V}^2$) [316] and 1.4×10^{-11} esu (1.96×10^{-19} $\mathrm{m}^2/\mathrm{V}^2$) for chalcogenide glass [317].

To understand the origin of the high third-order nonlinear optical susceptibility $\chi^{(3)}$ and its associated third-order polarization, it is important to consider the molar refractions of materials, described by Lorenz-Lorentz equation:

$$\left(\frac{n^2-1}{n^2+2}\right)\frac{M}{\rho} = \frac{4\pi}{3} N_A \alpha = [R], \tag{5.2}$$

where $[R]$ is the molar refraction of cm^3/mole unit, n refractive index, ρ is the density, M is the molecular weight, N_A is Avogadro's constant, and α is the polarizability of a molecule. The molar refraction is the measure of the total polarizability of a mole of a substance. For a single molecule, akin to single dielectric, the molar refractivity R is proportional to the polarizability of that single molecule. Real materials, though, are affected by nearby molecules. This is because the induced dipole moment of one molecule affects the field felt by other neighbouring molecules, and here comes the density of molecules into play [318, 319]. Since the third-order polarization depends on the polarizability α of a molecule, larger polarizability leads to larger $[R]$, hence larger third-order nonlinear optical susceptibility $\chi^{(3)}$ of a molecule. The number of molecules in the unit volume, i.e., the molar concentration must be taken into account for bulk materials, because third-order nonlinear optical properties depend on it. The molar concentration of materials is given by

$$M_c = \rho/M \tag{5.3}$$

where M_c is the molar concentration. According to this relationship and Lorenz-Lorentz equation, the third optical nonlinearity depends on the product of $[R]$ and M_c. Usually Bi_2O_3-containing glasses have larger $[R]$ than chalcogenide glass and SiO_2 glass. Although the average molecular weight of Bi_2O_3 glasses are larger, hence M_c are smaller, the product of $[R]M_c$ is still bigger in Bi_2O_3-containing glasses, because of large $[R]$ values, which is why they have higher nonlinearity than both chalcogenide and SiO_2 glasses.

5.3.1 Two-photon absorption of bismuth-borosilicate glass

Linear absorption can take place, whenever the light frequency used for excitation is at- or near-resonance with real excited states. In a transparent spectral region far from resonance, two photons can be simultaneously absorbed if high photon density is available, a condition often fulfilled at the focal volume of the laser beam. For consideration of nonlinear optical absorption like two-photon absorption (TPA), the imaginary part of the $\chi^{(3)}$ will be included. Hasegawa et al. [320] used Z-scan technique for measuring the nonlinear two-photon absorption coefficient for a bismuth-containing glass (Bi_2O_3 65.5 mol.%), and reported a value of $\beta = 0.8$ cm/GW at 769 nm. Also, Zhang et al. [321] used the same technique for a ternary system of high content Bi_2O_3, encompassing Bi_2O_3-B_2O_3-WO_3 (BBW) and reported a range of $\beta = 0.254$-0.345 cm/GW for a series of BBW samples of different WO_3 compositions. The higher value of β corresponds to a higher content of WO_3, while the lower value is for the lowest WO_3 content in the glass samples.

There are mainly a couple of reasons of why TPA is important to consider, one, because the high intensity of the laser becomes less effective when this intensity leads to nonlinear absorption, which reduces the intensity required for inducing a modification of refractive index, Δn, where $\Delta n = n_2 I$ as pointed out in chapter 3. Second, nonlinear absorption, e.g., two-photon absorption besides linear absorption of a material (i.e., glass) can be a considerable issue, when high repetition rate lasers are used. This is because, even with small absorption coefficients (linear and nonlinear), heat can be readily accumulated into the medium, resulting in the so-called thermal lensing effect. In this case, the accumulated heat will act as a negative lens (diverging lens), opposing, or sometimes canceling the intensity-dependent self-focusing, caused by Kerr effect, as well as the focusing of the laser intensity into the focal volume. This poses a limitation for any intensity-dependent nonlinear optical phenomena, e.g., optical Kerr gate, often used in applications like optical switching. Given that the fs laser (Taccor Tune, 1 GHz repetition rate) used in this dissertation's work has more than one order of magnitude repetition rate higher than most of other commercial solid-state lasers, it is pivotal to investigate the existence of TPA.

The investigation of possible existence of TPA in any nonlinear medium is typically performed by measuring the TPA directly at the wavelength of interest. There are few techniques that measure TPA, usually in tandem with the ability to also measure n2 of that material. The most common technique often used for such characterization is Z-scan technique. In our case, direct measurement of n_2, TPA characterized by β, or both was not possible, for the following reasons: First, applying the Z-scan technique necessitates building a new setup, and there is no adequate space on the

optical table for it; Second, Z-scan technique needs a higher intense laser beam, much higher than we can obtain from the Taccor fs laser. Alternatively, the investigation of possible existence of TPA would be limited to only estimating whether or not, it is possible for TPA to exist. This can be done by estimating the optical bandgap of the Kerr medium, which in this case is the BBS glass, and checking if this bandgap matches half of the wavelength of the laser used, hence double its photon energy. In other words, through the determination of optical bandgap of the BBS glass, one can infer if two photons of the laser can excite the electrons from the ground state to the excited state, provided that this bandgap matches the energy of these two photons. Tauc plot is a standard method, by which the optical bandgaps of amorphous materials can be estimated. It was developed by Jan Tauc [322, 323], it is based on measuring the linear light absorption, or transmission and from the data to get a curve, whose X-axis is the photon energy $h\nu$ in eV, while its Y-axis is $(\alpha h\nu)^n$, where $n = 2$ for optically allowed direct bandgap, while $n = \frac{1}{2}$ for optically allowed indirect bandgap, which suits our case. From this curve, the optical bandgap can be estimated via linear fitting of the leading edge of this absorption curve, named after Tauc, and from the interception of the straight line fitting with the X-axis, one can determine the optical bandgap of a certain material. This method has been applied to several materials, including glasses for the same goal. For example, Gao et al. [324] used the Tauc plot method to determine the optical bandgap of BBS glass samples, each of which has different Bi_2O_3 content into each sample, as illustrated in Fig. 5.4.

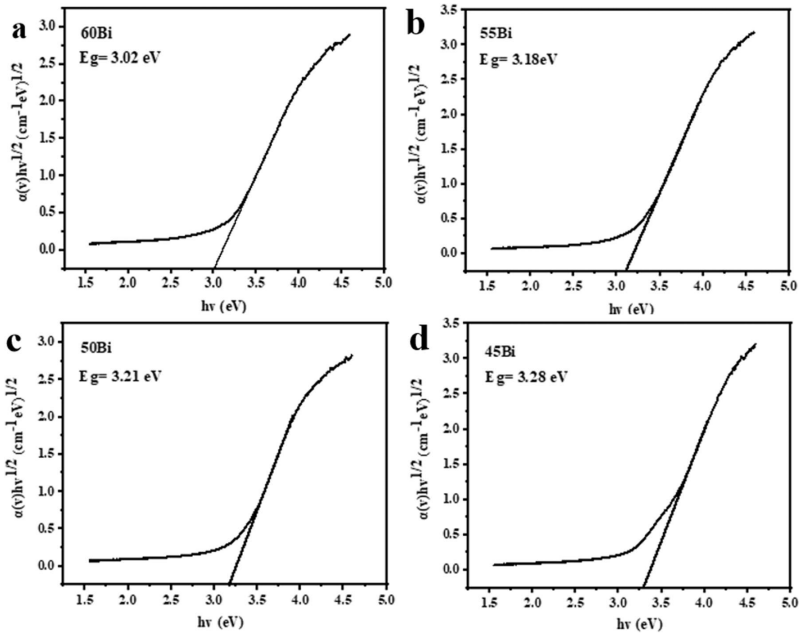


Figure 5.4: Optical bandgap E_g values of four samples, with different Bi content: (a) 60Bi, (b) 55Bi, (c) 50Bi, 45Bi samples [324].

One can note from Fig. 5.4, that increasing the Bi_2O_3 content into a BBS glass sample leads to decreasing the value of its optical bandgap E_g. Following the same method with our BBS glass samples, the measured light absorbance data have been converted into transmittance data via the relationship $A = -\log(T)$, where A is the absorbance and T is the transmittance. Then from the transmittance data the absorption coefficient α as a function of the photon energy, E, is obtained by using the Bouguer-Lambert-Beer absorption law $\alpha(E) = +1/d \ln(1/T)$, where d is the glass thickness [325]. Afterwards, a Tauc plot of the data has been constructed, as seen in Fig. 5.5. Note that between approximately 3.09 eV and 3.54 eV, there is a dip in the Tauc plot, which corresponds to the wavelength range 350-400 nm. If we plot this section from the transmission curve, presented in Fig. 5.5, within that spectral range, we shall find that there is a small peak in this spectral range. This dip arises from this transmittance peak, whereas this small peak is amplified because of the logarithmic equation of $\alpha(E)$, which manifests itself eventually in a large dip within its corresponding photon energy range. Fitting the leading edge of the Tauc plot, with a straight line that intercepts the photon energy axis, as indicated in Fig. 5.6, shows that the optical bandgap of our BBS sample is $E_g = 2.93$ eV, which is slightly lower than the reported $E_g = 3.02$ eV in Fig. 5.4, in the work of Ref. [324], whose sample contains 60 mol.% of Bi_2O_3 like ours.

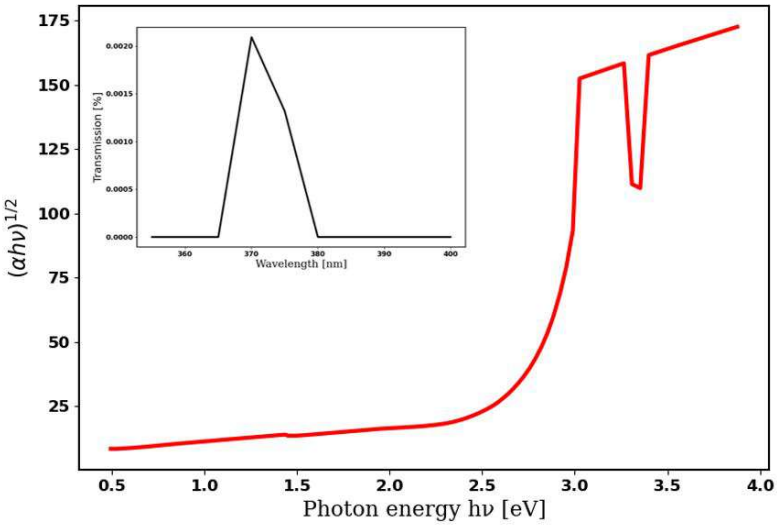


Figure 5.5: Tauc plot of BBS glass sample. The dip observed between 3.09 eV (400 nm) and 3.54 eV (350 nm) is an amplified and reversed transmission peak within this wavelength range, see the inset, as a result of the logarithmic absorption law (α_E).

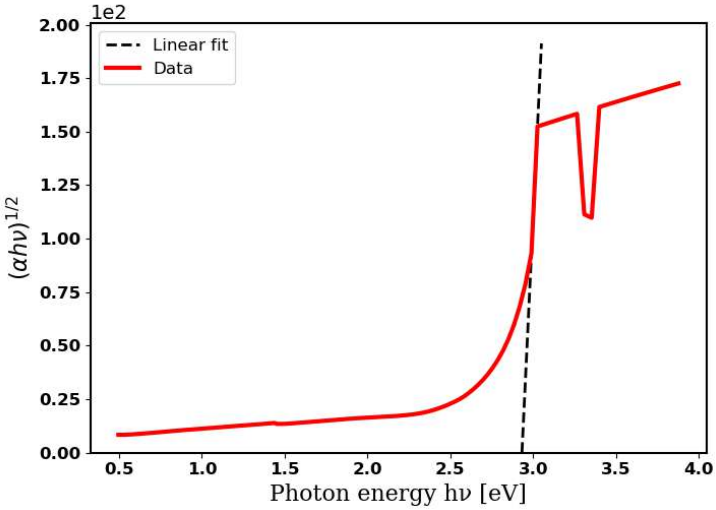


Figure 5.6: Linear fitting of the Tauc plot of the BBS glass sample that contains 60 mol.% Bi_2O_3. This linear fit interception point with X-axis shows that our BBS glass has $E_g = 2.93$ eV.

Since most of the optical Kerr gate measurements—where the pump (gate) and probe beams were counter-propagating—were performed at $\lambda = 820$ nm, with a spectral bandwidth of 15 nm, the effective operating wavelength range was approximately 812.5–827.5 nm. As discussed earlier in Chapter 4, this wavelength was chosen because the dichroic mirror exhibits high reflectivity in this range. For two-photon absorption (TPA) to occur, two photons within 812.5–827.5 nm must be absorbed simultaneously. This corresponds to an effective wavelength range of 406.25–413.75 nm (half the operational wavelength range).

Although the measured optical bandgap of our BBS glass specimen is $E_g = 2.93$ eV, corresponding to $\lambda_g = 422.86$ nm—which lies outside the 406.25–413.75 nm range required for TPA—one cannot entirely rule out the possibility of TPA. There are two main reasons for this.

First, in an ideal glass the intrinsic bandgap is typically at much higher energies (deep UV), but real glasses always contain trace impurities at the ppm level. These impurities introduce strong charge-transfer absorption bands at significantly lower energies (visible or near-IR), thereby shifting the apparent absorption edge [326]. As a result, a Tauc plot often reflects impurity-induced absorption, not the true intrinsic bandgap of the glass. This makes the experimentally extracted λ_g potentially underestimated.

Second, uncertainties in the Bi_2O_3 content (nominally 60%) and errors in the measured absorbance spectrum were not included, both of which could shift the apparent bandgap. For instance, the BBS glass reported in Ref. [324], which contains the same

Bi_2O_3 percentage as our sample, exhibits a slightly larger bandgap of $E_g = 3.02$ eV (corresponding to $\lambda_g = 410.54$ nm). This value already lies within the 406.25–413.75 nm range where TPA would be possible.

Therefore, small fluctuations in Bi_2O_3 concentration or measurement uncertainties from the commercial spectrometer used for absorbance characterization can easily shift λ_g into the 406.25–413.75 nm window. For these reasons, the occurrence of TPA in our BBS glass sample cannot be completely excluded.

5.3.2 Self-phase modulation of bismuth-borosilicate glass

Self-phase modulation is one of the intensity-dependent refractive index phenomena and responsible for the spectral broadening of a high intense laser beam, as discussed earlier in chapter 3. It typically requires high-peak-power lasers to be noticeable, and is usually observed in glass in the form of an optical fiber [320], where optical fibers can provide the adequate length for scaling-up the effect. Investigating SPM is of paramount importance for the application of optical Kerr gates for ultrafast single-photon emitters detection. It is well-known that single photons carry feeble amounts of energy, which render their detection very challenging. For example, a single-photon at 738 nm (SiV fluorescence emission line) carries ~ 0.27 attojoules. The nonlinear phase shift in optical Kerr gates is induced by a very high intensity pump (gate) laser beam, which often has a different wavelength from the one that belongs to the single-photons. Even if the pump (gate) beam propagates at slightly different angle than the probe beam in the Kerr medium, there will be significant light residual at the pump beam wavelength that gets into the optical path of the probe beam, thus spectral filtrating will be required for the detection of the fluorescence single-photon signal. Regardless of how perfect a spectral filter is, and how far the pump wavelength is selected from the single-photons wavelength, SPM when it is strong can lead to spectral broadening of the pump (gate) wavelength, in spectral regions overlapping with the fluorescence wavelength. That is why in designing a confocal fluorescence microscope that incorporates an optical Kerr gate into it, it is crucial to characterize the potential SPM to avoid unwanted noise that can likely obscure the fluorescence signal of interest. As presented in chapter 3, a formulation of SPM under focusing has been developed, which enables us to simulate the effect. Moreover, SPM has been investigated in BBS glass experimentally.

The experimental procedure to measure SPM is rather simple, and to do so the Taccor fs laser spectrum was measured without initially the BBS glass at 820 nm. Then, the BBS glass was placed in the optical path of the fs laser, and then the laser spectrum was measured again for comparison. The laser beam used for SPM

measurements is the gate beam, which has a peak pulse intensity of ≈ 1.33 GW/cm^2, and 30 μm beam diameter, similar to the gate beam parameters presented before for CS_2. For reliable data and to account for the fs laser fluctuations, each set of spectra was measured 10 times with and without the BBS glass, where the data corresponding to the case of with/without BBS glass were averaged for comparison. Needless to say, such gate peak pulse intensity is capable of saturating, or even worse, damaging the spectrometer. Therefore, a neutral density filter, along with a spectral filter must be placed in front of the fiber collimator that collects the signal and sends it to the spectrometer. As seen in Fig. 5.7, the measured spectra of Taccor laser after placing the BBS glass exhibits a subtle spectral broadening, due to SPM. The FWHM of the laser spectrum after passing through the BBS glass is 13.3 $\pm$ 0.05 nm, while the FWHM of the laser spectrum alone is 13.1 $\pm$ 0.03 nm.

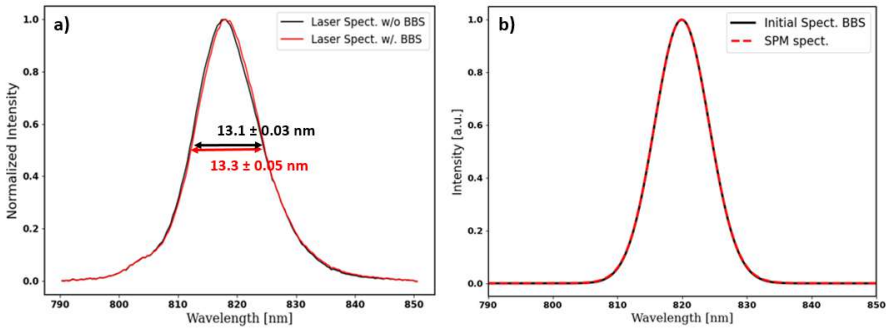


Figure 5.7: SPM of BBS glass. (a) Experimental measurement, (b) Simulation using gate laser at wavelength 820 nm, pulse duration $\sim$ 100 fs, beam spot diameter 30 μm, and pulse peak intensity ~ 1.33 GW/cm^2, $n_0 = 2.45$, pulse energy 1 nJ, $n_2 = 1.6 \times 10^{-18}$ m^2/W, for a thickness of 3 mm.

5.3.3 Kerr effect in glass

The optical Kerr effect has been studied extensively in glass. The nonlinear refractive index change stems from different phenomena, each of which has its origin, as well as its time response. These phenomena can be of thermal, electrostrictive, nuclear, and electronic origin,

$$n_2 = n_2^{\text{electronic}} + n_2^{\text{nuclear}} + n_2^{\text{electrostrictive}} + n_2^{\text{thermal}}. \tag{5.4}$$

The origin of electronic and nuclear response comes from the oscillation of the electron cloud, or vibration of the nucleus. Both can contribute simultaneously, or separately. In more detail, the electronic response results from the spontaneous nonlinear distortion of the distribution of electrons around the nucleus. The nuclear response is often slower, and is caused by optical-field-induced nuclear motion [327].

Hellwarth et al. [328] estimated that the nuclear contribution to the total nonlinear response of a fused quartz is approximately 19-24 %. Despite Raman spectra of most glasses indicating large nuclear polarizabilities, there has been no conclusive evidence for a nuclear contribution in glass. However, Kang et al. [329] showed that only some glasses, e.g., sulfide-containing or heavy-metal oxide glasses have significant nuclear contribution up to 36 % of the total nonlinear response. Speaking about the time response of each contribution, the pure electronic cloud distortion contribution, far from resonance, is the fastest, with characteristic time below 1 fs. The nuclear contribution to $\chi^{(3)}$ arises from the redistribution of the position of nuclei within the excitation period. This redistribution is much slower than the electronic response, it is on the order of a few hundred femtoseconds to a few picoseconds. As a result, the nuclear time response will be considerably correlated to the laser pulse duration. The electrostrictive contribution is related to the material density change when it experiences an electric field, and its time response is often of the order of tens of nanoseconds, like acoustic waves in materials. The thermal response arises owing to the electric field absorption by the material, and dissipating it in the form of heat. Among other contributions, this can be considered the slowest in terms of time response, and it is of the order of tens of microseconds.

The nonlinear optical properties of BBS glass using a degenerate optical Kerr gate of a 30 fs laser at 800 nm and 1 kHz repetition rate was studied by Lin et al. [330], and the nonlinear refractive index was estimated to be $n_2 = 1.6 \times 10^{-14}$ cm^2/W. Moreover, nonlinear response time of BBS glass was measured and found to be $<$ 90 fs, significantly shorter than CS_2. The work reported in Ref. [52] conducted an investigation of BBS glass, using degenerate four-wave mixing (DFWM) with a 200 fs laser at 810 nm and 200 kHz repetition rate, and found that the ultrafast response time is $<$ 200 fs. This result is in excellent agreement with an earlier work from the same research group [51]. This research group also constructed an optical Kerr gate [259] with BBS glass as the Kerr medium, for demonstrating optical switching using a 1.5 THz gate beam. The response time of the OKG switching was reported to be $<$ 150 fs. BBS glass as Kerr medium was used in an optical Kerr gate (nondegenerate) in the work of Tan et al. [242] for gating the spectra from a chirped supercontinuum generated beam from a sapphire plate. The ultrafast response time of BBS glass, reported as $<$ 85 fs, showed that it offers better time resolution than CS_2. Although the optical Kerr gate (also called optical Kerr shutter) arises fundamentally from a photoinduced birefringence in the Kerr medium, in degenerate optical Kerr gate experiments, it is possible that a self-diffraction of the pump (gate) and the probe beams. This self-diffraction takes place, due to the formation of the so-called laser-induced transient grating (LITG), which was briefly discussed in chapter 4, and originally stems also from third-order susceptibility $\chi^{(3)}$.

This effect is maximum, when both pump and probe beams have similar polarization, at $\theta = 0°$, or 180°. This typically occurs as a result of a superposition of two coherent pulses of equal wavelength that yield spatially modulated distribution of energy density. The self-diffraction begins to be critical, when the laser pulse duration is comparable to the response time of the nonlinear medium (Kerr medium), in such a case an exchange of energy between the two beams can happen. It is important to emphasize that the temporal behavior of self-diffraction due to LITG depends solely on the correlation time of the two interfering laser pulses. Meaning, it does not indicate the nonlinear response time of the Kerr medium. In optical Kerr gate experiments on fs timescale, it is crucial to separate photoinduced birefringence and self-diffraction to figure out the time response of the nonlinear medium. Yan et al. [331] identified the pump power and polarization angle dependence of the signal intensity, i.e., Kerr-rotated signal after the analyzer, in both CS_2 and BBS glass, however the findings concerning BBS glass shall only be here discussed, as it is our scope in this chapter. Because of the ultrafast response time due to the electronic cloud distortion, the time response of BBS glass can be shorter than and limited by the laser pulse width, which is usually in fs timescale. Therefore, it is absolutely not possible to separate the OKG signal from the self-diffraction one, as indicated in Fig. 5.8.

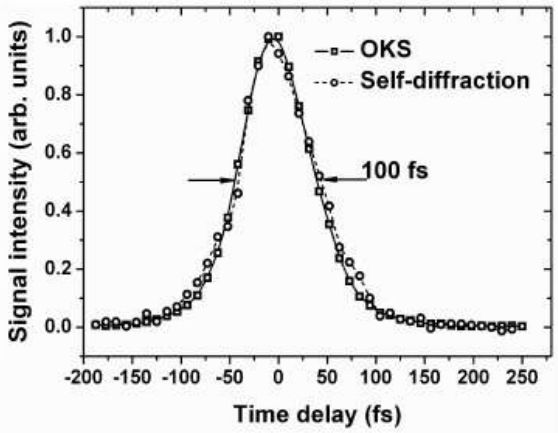


Figure 5.8: Temporal behavior of OKG and self-diffraction signals [331].

The comparable FWHM (estimated to be < 100fs) led to the investigation of the OKG signal dependence on the pump power at different polarization angles. Over a range of pump powers 0.4-5.5 mW, and polarization angles of 20°, 45°, 70°, respectively, the investigation was carried out, shown in Fig. 5.9.

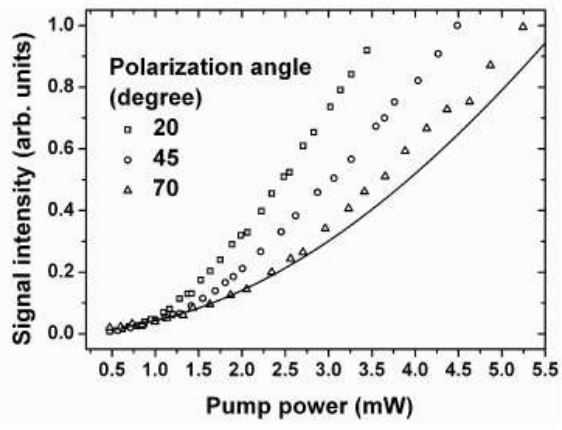


Figure 5.9: Dependence of OKG signals on pump power in BBS glass at different polarization angles [331].

The solid line in Fig. 5.9 is the fitting of OKG data, according to the theoretical equations of OKG, discussed in chapter 3. As seen, the OKG data at 70° (triangles) are well-fitted when the pump power is 2 mW, however, at higher pump powers, the curve begins to deviate from the theoretically anticipated behavior. To further confirm that the deviation of OKG signals data are attributed to self-diffraction, the dependence of OKG signals on the polarization angles between the pump and probe was investigated at 1 mW pump power, for avoiding the influence of self-diffraction, and similar dependence was studied at higher pump power, as shown in Fig. 5.10.

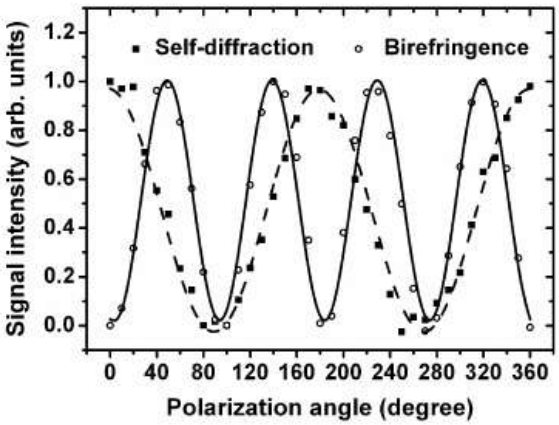


Figure 5.10: OKG signal and self-diffraction dependence on the polarization angle between the pump and probe [331].

As expected the photoinduced birefringence and self-diffraction are both distinct, and depend differently on the polarization angle between the pump and probe. For instance, the locations of peaks and troughs corresponding to self-diffraction occur at $n\pi$ (n = 0,1,2,..) and $\pi/2 + n\pi$ (n = 0,1,2,..), respectively. The OKG signals exhibit different dependency, whereas the maximum values appear at $\pi/4 + n\pi/2$ (n = 0,1,2,..), while the minimum values appear at $\pi/2 + n\pi/2$ (n = 0,1,2,..). Furthermore,

it is clearly shown in Fig. 5.10, that at lower polarization angles than 45°, the self-diffraction signal increases, as opposed to the decreasing OKG signal. Thus, for clear separation between these two signals, it is highly recommended to use relatively low average pump power during femtosecond OKG experiments.

In the following, we present our experimental results obtained with BBS glass as the Kerr medium in a degenerate optical Kerr gate configuration, using the 1-GHz femtosecond laser simultaneously as the gate and probe beam. The measurements were carried out in both counter-propagating and co-propagating geometries.

Similar to the former OKG experiment with CS_2, discussed in the previous chapter, which were performed in order to characterize the OKG setup, the pump and probe beams were counter-propagating one another, in order to avoid damaging, or saturating the very sensitive photodetectors (SPADs). The previous experimental parameters, such as the probe and gate beam spot sizes, as well as the gate beam pulse peak intensity were also used for the OKG experiment with the 3 mm thick BBS glass specimen. Also, the polarization angle between the pump and probe was set at 45°, but here by setting a half-wave ($\lambda/2$) plate in the gate beam path at 22.5°, as a $\lambda/2$ plate rotates the polarization by 2θ, when the plate is rotated by θ. The OKG signal was recorded by measuring the Kerr-rotated probe signal after the second polarizer (analyzer) as a function of the delay $\Delta\tau$ created by delaying the pump beam relative to the probe beam. The linear translation stage was delayed for a total distance corresponding to 1.44×10^{-12} s (~ 1.44 ps) at the highest possible temporal resolution, namely at 0.66 fs, as used before with CS_2. The time trace of this signal is shown in Fig. 5.11, in which the x-axis is the time delay, and its y-axis is the number of counts per second, as the signal of this time trace was integrated for only 1 s.

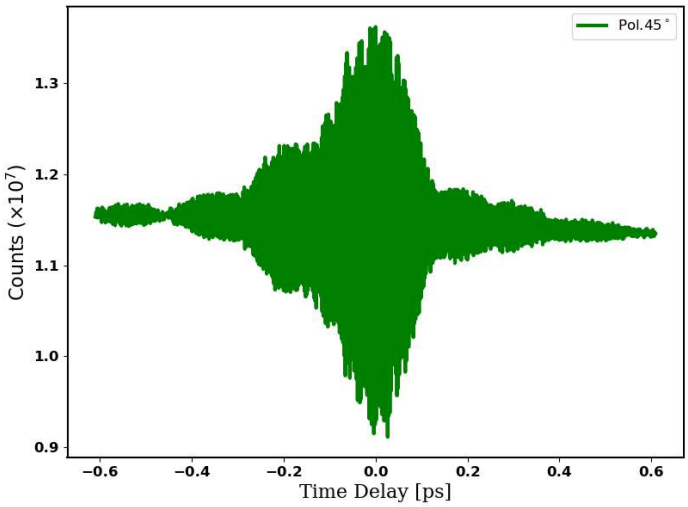


Figure 5.11: Time trace of OKG signal as a function of the time delay $\Delta\tau$ at 0.66 fs temporal resolution between the pump and probe beams, with 1 s integration time.

Note that the Kerr signal time trace in Fig. 5.11 has a base line around 1.15×10^7 counts, and the pump and probe beams interfere with each other, which leads to the LITG effect discussed in chapter 4. Since the degenerate pump and probe beams wavelength is 820 nm, the temporal cycle duration is ~ 2.73 fs, similar to the time trace obtained by CS_2 sample. This temporal cycle duration varies approximately between 2.0 (corresponds to 759 nm) - 2.54 fs (corresponds to 600 nm), for the reasons explained for CS_2 in the previous chapter. The envelope of this signal was obtained by filtering out the fast oscillating part. Following the approach explained in chapter 4 for extracting the temporal profile (envelope) from the time trace, the envelope was fitted with a Gaussian function, whose FWHM $\approx 175 \pm 1$ fs, which is illustrated in Fig. 5.12.

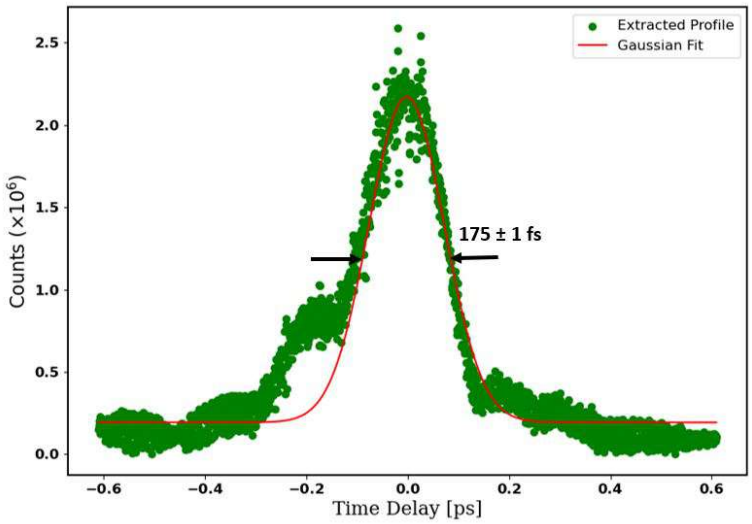


Figure 5.12: Temporal profile of OKG signal of the time trace, fitted with a Gaussian function, whose FWHM $\approx 175 \pm 1$ fs.

The extracted temporal profile shown in Fig. 5.12 is a convolution of a cross-correlation between the gate and probe beams, and the nonlinear response time of the BBS glass. This implies that the nonlinear response time of the BBS glass $<$ 175 fs. A precise determination of the actual nonlinear response time would require measurement of the cross-correlation between the pump and probe beams, and deconvolving the temporal profile of the OKG signal via the cross-correlation value. Scanning the time delay between the pump and probe beams in a nonlinear medium at 0.66 fs temporal resolution is time consuming, especially if an optical Kerr gate would be incorporated into a confocal fluorescence microscope, other measurements at lower temporal resolutions (i.e., 10 fs) have been carried out. For example, the OKG signal was measured at 10 fs temporal stepsize, rather than 0.66 fs, and the obtained time trace of that signal is shown in Fig. 5.13, where the polarization angle is still 45° and the integration time is 1 s.

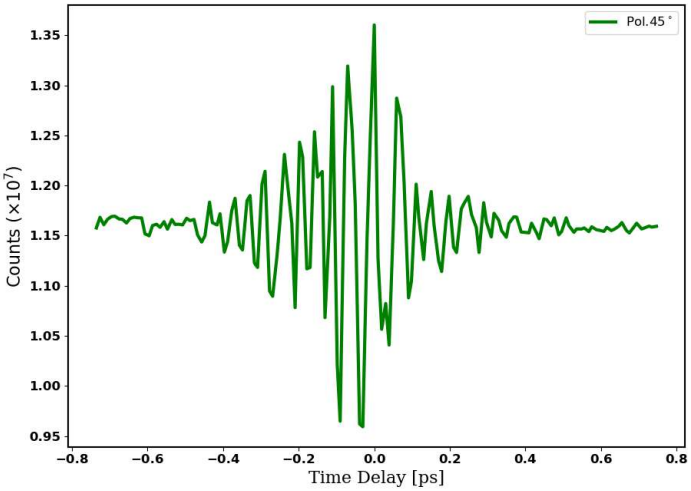


Figure 5.13: Time trace of OKG signal as a function of the time delay $\Delta\tau$ at 10 fs temporal resolution between the pump and probe beams, with 1 s integration time.

It is clear from Fig. 5.13 that with 10 fs temporal step the obtained time trace does not capture all the temporal fine details, in particular the very rapid oscillations, which can only be revealed at 0.66 fs temporal stepsizes. However, this time trace is advantageous, as it is quicker in data acquisition, which is helpful in real applications. The temporal profile was also extracted, presented in Fig. 5.14, and fitted with Gaussian function, whose FWHM $\approx 271 \pm 8$ fs. Given that scanning the pump beam relative to the probe over the same total duration but at larger time stepsizes, such as 10 fs, as shown in Fig. 5.13 yields a smaller number of data points, the Gaussian fitting becomes not perfect. In particular, a single Gaussian function is used in the fitting procedure. That difficulty to use a single Gaussian function for fitting interprets why the single Gaussian function shows asymmetry, where it deviates from a major part of the trailing edge of the temporal profile. Despite this asymmetry, the nonlinear response time can still be estimated to be in fs time scale.

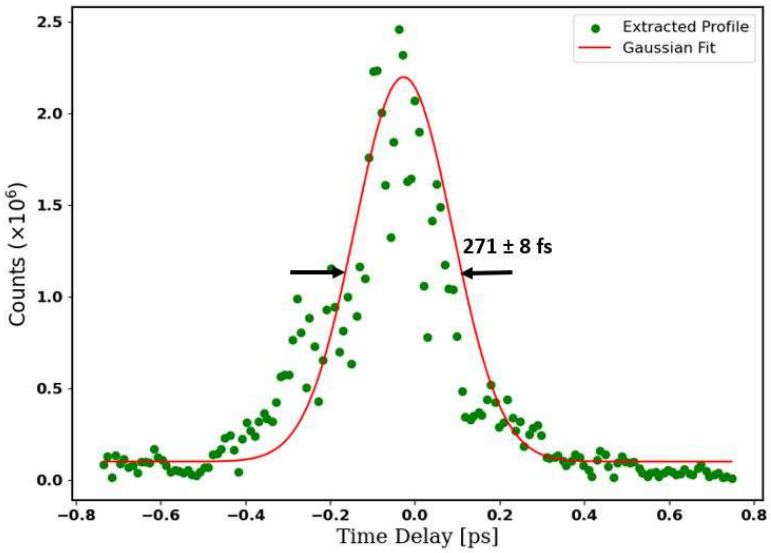


Figure 5.14: Temporal profile of OKG signal of the time trace in Fig. 5.13, fitted with a Gaussian function, whose FWHM $\approx 271 \pm 8$ fs.

For comparison between the nonlinear optical Kerr signal obtained with the BBS glass ($n_2 = 1.6 \times 10^{-18}$ m^2/W), and the liquid that has one order of magnitude less nonlinear refractive index ($n_2 = 3.1 \times 10^{-19}$ m^2/W), two temporal profiles associated with Kerr signal time traces, one of CS_2 and another of BBS were compared to each other. The experimental parameters, such as integration time of 1 s, scanning temporal stepsize of 0.66 fs, and probe and gate beam spot sizes, as well as CS_2probe and gate laser power, were maintained. The result of the optical Kerr signals is provided in Fig. 5.15.

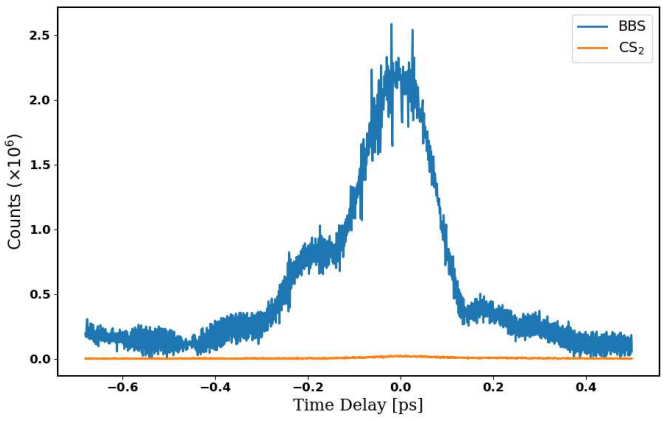


Figure 5.15: Comparison between optical Kerr signal temporal profiles of BBS glass ($n_2 = 1.6 \times 10^{-18}$ m^2/W), and liquid CS_2 ($n_2 = 3.1 \times 10^{-19}$ m^2/W), under similar experimental conditions.

The comparison presented in Fig. 5.15 shows that the optical Kerr signal obtained with the BBS glass specimen is much stronger than the one obtained with liquid CS_2.

For better visibility of CS_2 Kerr signal, this signal was increased by 100×, which renders this signal comparative to the one obtained with the BBS glass, as seen in Fig. 5.16.

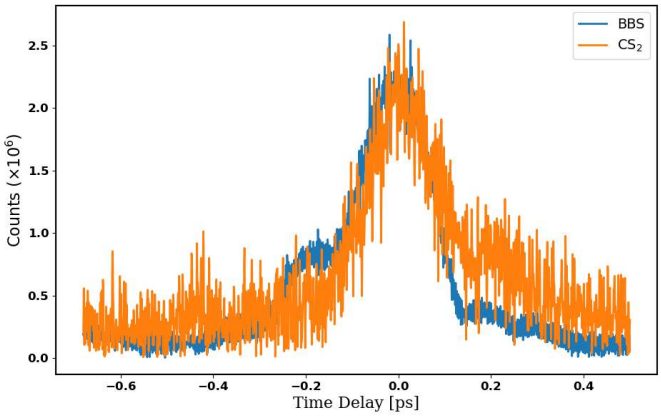


Figure 5.16: Comparison between optical Kerr signal temporal profiles of BBS glass, and liquid CS_2, in which the Kerr signal of liquid CS_2 is increased by 100× for better visibility.

The result shown in Fig. 5.16 coincides with the theoretical prediction of the Kerr signal. We see from Eq. 3.48 in chapter 3, that the induced nonlinear phase shift of the probe, due to the high intensity of the gate beam, scales linearly with n_2 value. However, Eq. 3.49 indicates that the transmitted signal scales quadratically with n_2 value. Given that the n_2 of liquid CS_2 is 10 times smaller than the n_2 of BBS glass, the expected Kerr signal of CS_2 should be 100 times less than the one obtained with BBS glass. That is why increasing the CS_2 Kerr signal 100× for better visibility, yields a comparatively similar Kerr signal to BBS glass, in terms of the signal amplitude. This despite the thickness difference, where BBS signal was obtained by 3 mm material, while the one of CS_2 was 5 mm, which apparently is not the dominant factor in increasing the induced nonlinear phase shift. The gating efficiency of the 3-mm-thick BBS glass specimen has been estimated to be $\sim 3\%$ based on measurements using a 656 nm CW probe and an 820 nm femtosecond gate beam in a degenerate counter-propagating geometry at < 1 nJ gate-pulse energy ($<$ 1.33 GW/cm^2 peak intensity), see the results of Appendix B.

In order to investigate how the optical Kerr signal of BBS glass changes with the polarization angle between the pump and probe beams, the $\lambda/2$ plate was rotated at angles that cover the range between 0° - 360°, with 20° intervals, and the Kerr signal time trace associated with each polarization angle was obtained, from which the Kerr signal time traces at $\theta = 40°$, 90°, 120° and 130° are presented in Fig. 5.17, respectively.

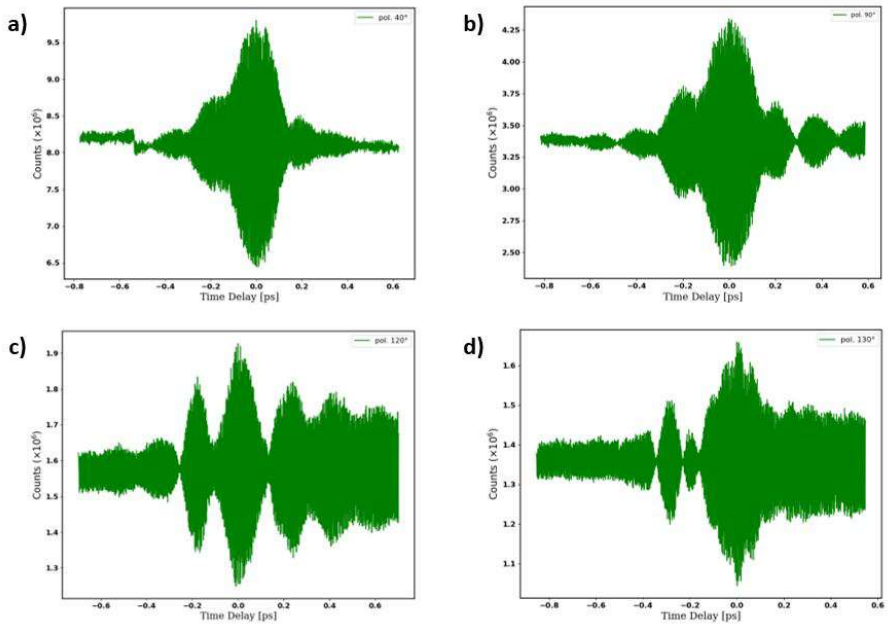


Figure 5.17: Variation of Kerr signal time traces of BBS as the polarization angle between the pump and probe beams changes, for (a) $\theta = 40°$, (b) 90°, (c) 120° and (d) 130°, respectively.

Although changing the polarization angle θ between the gate and probe beam should result in a change of the Kerr signal time trace amplitude, while preserving the temporal profile, it is evident from the time traces shown in Fig, 5.17, that the change of polarization angle affects the temporal profile of Kerr signal time trace, such that the temporal profile contains beats-like structure. These beats-like structures could be arising from a gate beam ellipticity introduced by the short-pass dichroic mirror, which reflects its off toward the Kerr medium. As the $\lambda/2$ plate changes the polarization angle of the gate beam, this might affect the degree of ellipticity introduced by the dichroic mirror. This ellipticity results in having two polarization vectors instead of one, where each vector oscillates along a different axis and has a different amplitude. These two distinct vectors interact with the probe beam differently, which is what creates the observed beats-like structures. Another remark about Fig. 5.17 is that, at $\theta = 90°$ there is a detectable Kerr signal. Given the $\sin^2(2\theta)$ dependence of the transmitted Kerr signal, if the polarization angle θ between the gate and probe is 90°, the Kerr signal will vanish, which is not the case here apparently. This is also attributed to the ellipticity introduced by the short-pass dichroic mirror, but to the probe beam after its polarization vector is being rotated, due to Kerr effect. Without this ellipticity, the linearly polarized probe beam would have been blocked by the analyzer (2nd polarizer), if $\theta = 90°$. But with such introduced ellipticity, still one of the polarization vectors would pass through the analyzer.

From the analysis transmitted Kerr time traces across different polarization angles between the pump and probe, it is clear that the experimental data deviates from the theoretical expected locations, as seen in Fig. 5.18.

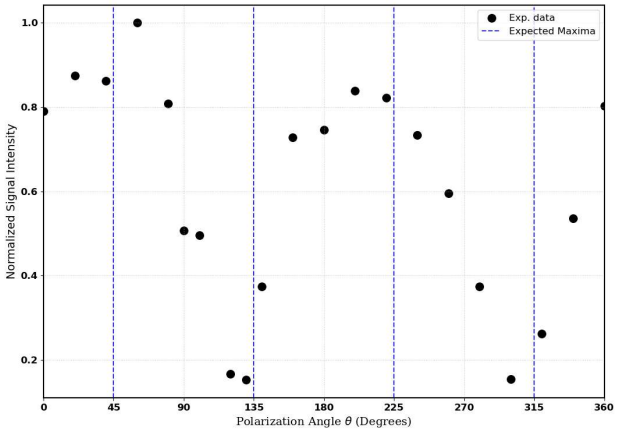


Figure 5.18: Normalized experimental signal as a function of the polarization angle θ (black dots), showing a maximum value at 60°. The theoretical expected maxima locations (dashed blue lines) must appear at 45°, 135°, .., etc.

One remarks also that the maximum transmitted Kerr signal appears at $\sim$ 60°, which deviates by $\sim$ 15° from the expected maxima at 45°, indicated by the dashed blue line. Further, the transmitted Kerr signal is relatively high at both 0° and 360°, which is unexpected from a standard OKG experiment. Again, this might be caused by the ellipticity of one of the beams, or both, especially the gate beam is reflected off by several mirrors, involving the short-pass dichroic mirror. The probe beam also is transmitted through it. In conclusion, an experimental investigation, as well as theoretical modeling will be needed for unveiling the reason for such deviation.

In addition to the potential role of the ellipticity, such a large phase offset could be caused by another effect, i.e., thermal lens effect. Although according to the previous calculation presented earlier of the BBS glass bandgap, the thermal lensing effect was ruled out. However, if there are uncertainties in the experimental parameters that were not taken into account, the thermal lensing effect can be a possible case for the observed phase offset. Another possibility which has been investigated was that the BBS glass might be introducing some degree of depolarization, which ultimately shifts the phase of the experimental time traces, and their associated temporal profiles. To investigate this possibility, the $\lambda/2$ waveplate was placed in the probe beam (λ = 760 nm) path, and initially the BBS glass specimen was removed, then the $\lambda/2$ waveplate was rotated at angles covering the range 0°-360°, with intervals of 30°, and the probe beam counts were recorded by one of the photodetectors (5 times for each polarization angle θ). Then, the BBS glass specimen was placed into

its position, while the $\lambda/2$ waveplate was placed after it before the analyzer, and the same measurements were taken again, for the same number of measurements per angle. A comparison between the probe beam counts, with and without the BBS glass is shown in Fig. 5.19.

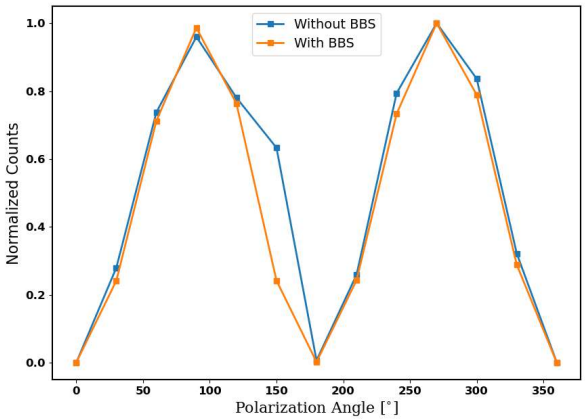


Figure 5.19: Depolarization measurement of the probe beam (λ = 760 nm), with/without BBS glass, over angles range from 0° to 360°, with 30° intervals.

As evidently illustrated in Fig. 5.19, the BBS glass does not introduce any depolarization or phase offset on its own to the probe beam signal, aside from data point located at 150°. It is worth mentioning that the experimental data shown above, were taken with a different experimental configuration, where the short-pass dichroic mirror was removed. Provided that BBS glass is not the cause for the phase offset, and that the gate beam was blocked during those measurements, unblocking the gate beam might be likely inducing thermal lensing. Whereas the heat emanating from depositing the gate pulses' energy accumulates much faster than other lasers, because Taccor fs laser have 10 times higher pulse repetition rate. It is vital to remember that the concern about thermal lensing effect relates particularly to λ = 820 nm, which when its spectral bandwidth is considered, might lie within the optical bandgap of BBS glass, that contains $\sim$ 60 Bi mol. %, as seen in Fig. 5.4. One might think that to completely rule out the possibility that BBS glass is responsible for the phase offset, the depolarization measurement should have been carried out at λ = 820 nm, rather than at λ = 760 nm. Nonetheless, measuring the depolarization at λ = 820 nm, would not have changed the result obtained at λ = 760 nm. In other words, both of them will have the same outcome.

So far, all measurements presented and discussed above were carried out, while the pump and probe beams propagate in opposite directions, with respect to each other. This was intended, as mentioned before, in order to avoid saturation or damaging of the photodetectors. However, there is a caveat with such an experimental scheme.

That is, even though the gate beam temporal overlap is precisely controlled via the delay line, as the two pulses, pump and probe, are counter-propagating, their overlap time will definitely be minimal. Therefore, with such minimal overlap time, between the two pulses, the optical Kerr gate signals will be very small. Thus, the experimental setup was later on reconfigured, in such a way that both the pump and probe beams co-propagate, similar to standard OKG experimental configuration. Also, in this new configuration, the short-pass dichroic mirror was removed, which might have introduced earlier, some degree of ellipticity, to the gate beam before it induces birefringence, and the probe beam after being Kerr-rotated. Another critical reason for removing that dichroic mirror, was that despite its high reflectance ($\sim$ 96 - 100 %) of the pump beam, which is highly desired for maximizing Kerr effect, it was detrimental, as it was reflecting the Kerr-rotated probe beam, at similar reflectance. This means that only $<$ 1-4 % of the Kerr-rotated probe beam signal was reaching the photodetector. This was a consequence of conducting a degenerate OKG experiment. Also, the wavelength degeneracy dictates a stringent constraint in terms of angle turnability, between the pump and probe beam. Ideally, the spatial angle between the two beams must be 0 to ensure maximum spatial overlap, thereby maximizing the transmitted Kerr signals. In practice, there will be a small angle between the two beams. This small spatial angle is acceptable, in case of conducting non-degenerate OKG experiment, whereas the gate beam wavelength can be spectrally filtered. Nevertheless, in degenerate OKG experiments, like ours here, at small spatial angles, the high intensity of the gate beam will bury the Kerr-rotated probe beam signal. Therefore, the gate beam must be at a large angle, so that it can be dumped, or blocked. The spatial angle between the pump and probe beams is $\sim 29^{\circ}$, which is a quite large angle, considering that in standard non-degenerate OKG experiments, the spatial angle does not exceed 3°. Unfortunately, at such a large spatial angle, the optical Kerr signal is drastically reduced, owing to the reduction of the spatial overlap between the pump and probe beam. As a result, the anticipated Kerr signal enhancement, because of the increase of the temporal overlap duration, might not become evident, being partially eliminated, or reduced by the effect of the large spatial angle.

After realigning the pump and probe beams and adjusting their corresponding spot sizes to similar values as previously, and finding the location of the delay line that achieves temporal overlap, the OKG experiment was carried out with the co-propagating scheme. The gate beam power was measured before running the experiment, and it was 902 mW, and the wavelength of the gate beam (hence of the probe beam, due to the degeneracy) was set at 780 nm. This is because as we know from Eq. 3.48 in chapter 3, the induced nonlinear phase shift increases when the probe wavelength decreases. The scanning temporal stepsize was 0.66 fs, and each

data point of the signal was integrated for 1 s. In spite of the large angle of the gate beam, which is ultimately blocked, interference between the gate and probe beams were observed. In fact, imaging of the BBS glass focal plane showed that indeed part of the gate beam was scattered into the BBS glass specimen. This actually poses two challenges, first, the scattered gate light spots were more intense than the probe beam signal itself; second, that scattered light introduced an asymmetric interference pattern. The former, in fact, obscures the Kerr-rotated signal, and makes detecting it cumbersome. The latter yields distorted time traces, hence distorted temporal profiles, from which one can not reliably obtain the nonlinear response time. More interestingly and counter-intuitively, it was observed that the time traces acquired simultaneously by two identical photodetectors (SPADs) showed different time traces, each of which is affected differently by interference between the gate and probe beams, as presented in Fig. 5.20 (a) & (b) of the time traces, and Fig. 5.20 (c) & (d) of their corresponding temporal profiles.

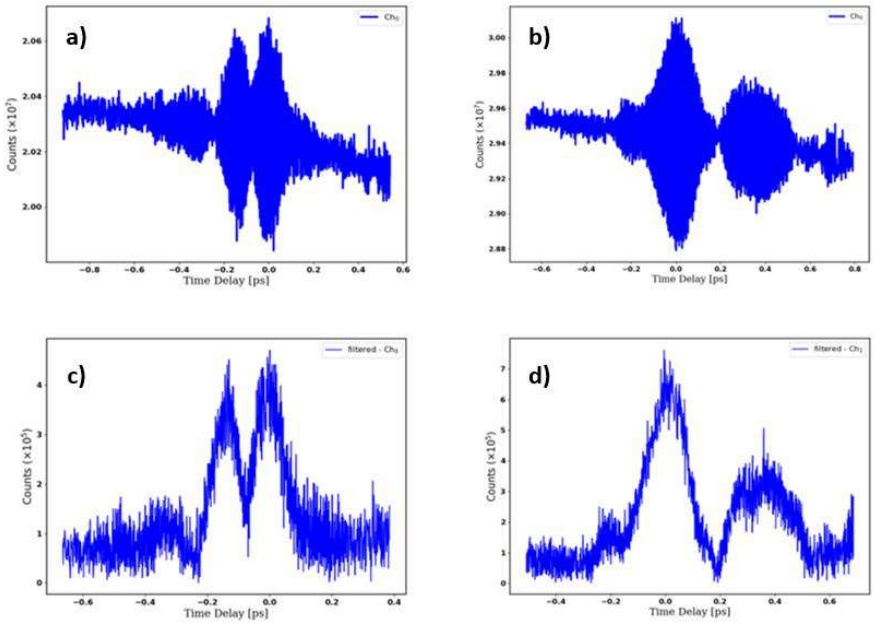


Figure 5.20: Contrast of transmitted signal time trace (λ = 780 nm - co-propagating beams), detected by two identical detectors, (a) Time trace of transmitted signal detected by SPAD connected to Ch_0 of the TCSPC, (b) Time trace of the same transmitted signal detected by SPAD connected to Ch_1 of the TCSPC, (c) Extracted temporal profile from (a) time trace, (d) Extracted temporal profile from (b) time trace.

Similar measurements taken at longer wavelengths (800 and 840 nm), with the same temporal stepsize and integration time, showed similar discrepancy between the two identical photodetectors. Unlike the discrepancy of collected Kerr signals of liquid CS_2, presented in Fig. 4.19 in chapter 4, which were attributed to slightly different probe beam alignment to each detector; the probe misalignment can not interpret

how two identical detectors record different time traces/temporal profiles. This issue necessitates careful investigation, so that the root cause is identified.

Since the thickness of the BBS glass is non-uniform, as seen from Fig. 5.1, taking optical Kerr measurements at different positions across the glass specimen, exhibited different time traces. This is not only due to thickness variations, which will unexpectedly vary the transmitted signals, but also because of the variations of gate beam scattering, which distorts the time traces, as well as their temporal profiles. In order to mitigate the gate beam scattering, different locations were investigated via imaging by the camera to find the locations of the BBS glass that has the least scattering. Furthermore, different irises were utilized to minimize the scattered gate beam signals. Even more, the scattered gate beam signals were recorded separately, and subtracted from transmitted time traces. With such improvements, better signals were obtained, hence their temporal profiles were extracted. For example, at $\lambda =$ 780 nm, temporal stepsizes of 10 fs, and integration time of 3 s, a time trace was obtained, where the polarization angle between the pump and probe beams were 45°, as shown in Fig. 5.21.

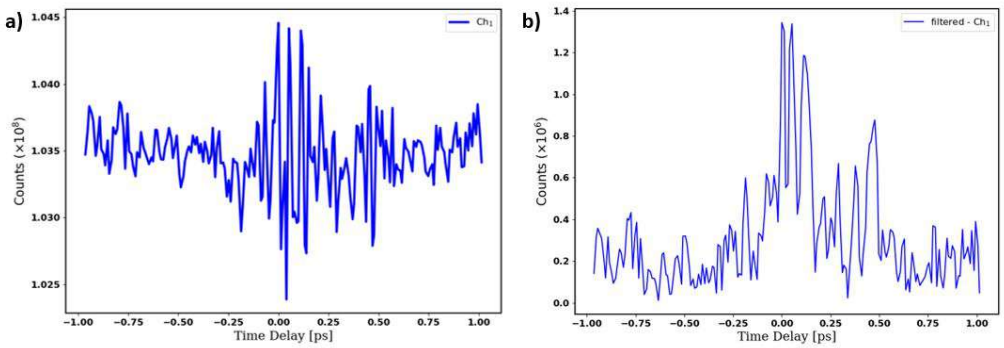


Figure 5.21: (a) Time trace of transmitted signal of co-propagating pump and probe beams, after subtracting scattered gate beam background at $\lambda = 780$ nm, 10 fs temporal stepsize, 3 s integration time, with polarization angle 45°; (b) Temporal profile of the time trace of the transmitted signal.

Fitting the temporal profile of Fig. 5.21 (b), provided in Fig. 5.22 shows that the transmitted signal FWHM $\approx 138 \pm 8$ fs, a value that is comparable with FWHM range, obtained from the OKG experiment, in which the two beams were counter-propagating.

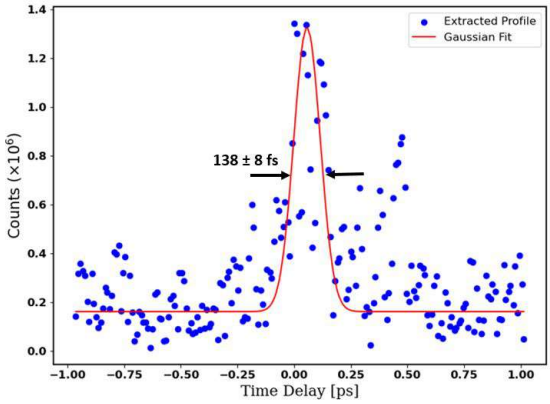


Figure 5.22: Fit of the temporal profile (at $\lambda = 780$ nm), presented in Fig. 5.21 (b), that has a FWHM $\approx 138 \pm 8$ fs.

For further investigation of the measured transmitted signals, firstly the probe beam wavelength was reduced further to be 760 nm, so that a relatively higher Kerr signal can be obtained, secondly a polarization analysis was made. This was performed by rotating the $\lambda/2$ plate, placed in the gate beam optical path, at angles that cover the range from 0° - 200°, with 25 intervals. Since several time traces of the transmitted signals were clearly affected by gate beam scattering background, picking up the peak signals of their associated temporal profiles for polarization angle analysis was not feasible. However, in Fig. 5.23, four traces are provided, owing to their significance to our analysis. Each of the four time traces was taken at $\lambda = 760$ nm (795 mW average gate beam power), with 10 fs temporal timesteps and each data point was integrated for 1 s.

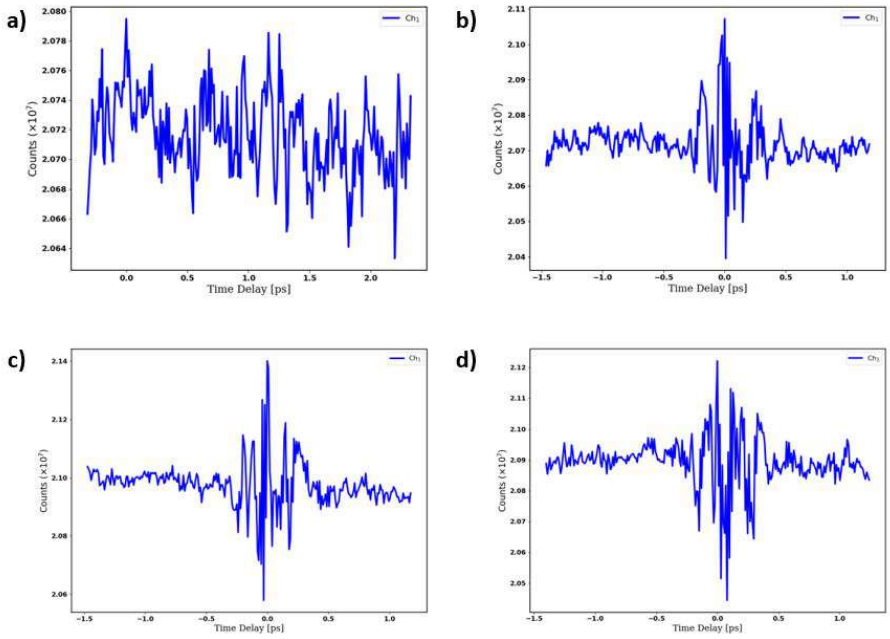


Figure 5.23: Transmitted signal time traces (co-propagating pump and probe beams) at polarization angles (a) 0°, (b) 45°, (c) 75°, (d) 90°, respectively.

Similar to the analysis of the transmitted time traces performed for counter-propagating beams, another analysis was done for the case of co-propagating beams, as a function of the polarization angle. Out of various time traces obtained at different angles, let's consider the four time traces, shown in Fig. 5.23. At the polarization angle 0°, self-diffraction exhibits typically a maxima, at that particular angle. Having merely a background, that can be fitted with a straight line at 2.073×10^7 counts strongly indicate that the previous time traces of the transmitted signals do not correspond to self-diffraction, and belong to optical Kerr expected behavior. This result is in stark contrast to polarization analysis conducted for the counter-propagating beams, whereas at the same polarization angle, the transmitted signal was quite high. Note that in the configuration of co-propagation of the pump and probe beams, some changes were made, such as removing the short-pass dichroic mirror. On the other hand, at $\theta = 45°$, the time trace acquires somewhat symmetric temporal profile, whose peak reaches close to 2.11×10^7 counts. Surprisingly though, the time trace is showing maximum signal at $\theta = 75°$. This result also contradicts both optical Kerr effect, whose maxima appears at either 45° or 135°, and self-diffraction, whose maxima appears either at 0° or 180°. These mysterious results continues with $\theta = 90°$, shown in Fig. 5.23 (d), that exhibits even higher signal than the one recorded at $\theta = 45°$. Whether self-diffraction phenomenon is taking place, or optical Kerr effect, the transmitted signal must vanish, at that particular polarization angle, which is apparently not the case. Since this new experimental setup configuration does not involve the short-pass dichroic mirror, which was introducing some ellipticity, allowing possibly some signals to reach the detector, when $\theta = 90°$, then it can not interpret the detection of high signal, which supposedly must be vanished. On the other hand, because the wavelength of the gate beam (hence the probe beam) is at $\lambda = 760$ nm, whose half its wavelength when considering its spectral bandwidth is far from the BBS glass optical bandgap, the possibility of thermal lensing effect to cause such ambiguity in the results, should be ruled out. For final check, whether the detected transmitted signal belongs to optical Kerr effect or not, the transmitted signal traces were recorded, one time without the analyzer (P_2), and another time with it. For this purpose, the $\lambda/2$ waveplate was reset at 22.5°, so that it rotates the polarization by 45°, and the pump beam was scanned at 10 fs temporal stepsizes, and the integration time was 5 s. At first, the second polarizer remained in the optical setup, crossed with respect to the first polarizers, and the transmitted signal was recorded, as illustrated in Fig. 5.24 (a). Afterwards, the second polarizer was removed, and the transmitted signal was recorded again, as shown in Fig. 5.24 (b). In both cases, the gate beam scattered light signal was separately recorded and later subtracted to mitigate its effect on the recorded time traces.

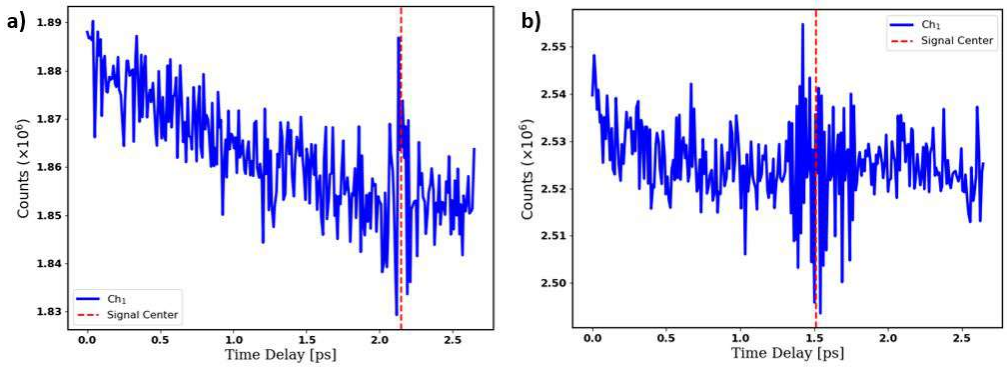


Figure 5.24: Transmitted signal (gate beam background subtracted) (a) With P_2, where the signal is centered around 2.143 $\times$ 10^{-12} s, (b) Without P_2, where the signal is centered around 1.523 $\times$ 10^{-12} s.

In both cases of Fig. 5.24 (a) with P_2 involved in the measurements, and (b) without P_2, time axis was intentionally not centered, so that the difference between the two cases is clarified. We can clearly see that, when the analyzer is removed, some interference-like signal appear, centered around 1.523 $\times$ 10^{-12} s, while with the analyzer involved in the measurement like any standard OKG experiment, there is a signal that appears at different location, specifically at 2.143 $\times$ 10^{-12} s, with $\sim$ 620 fs shift. Unfortunately, such a distinction between these two cases could not have been reproduced, when the experiment was repeated over and over again. This is because the scattered gate beam signals heavily influence the transmitted signals, and manifests itself in peaks that can appear at random locations, whether the second polarizer is used, or not. The same scattering gate beam signals sometimes disappear, or appear with various magnitudes, or at different locations in the time trace, depending upon at which position of the BBS glass specimen it passes through. An example of that is provided in Fig. 5.25, which was taken with similar conditions (wavelength, integration time, and temporal stepsize), to those in Fig. 5.24.

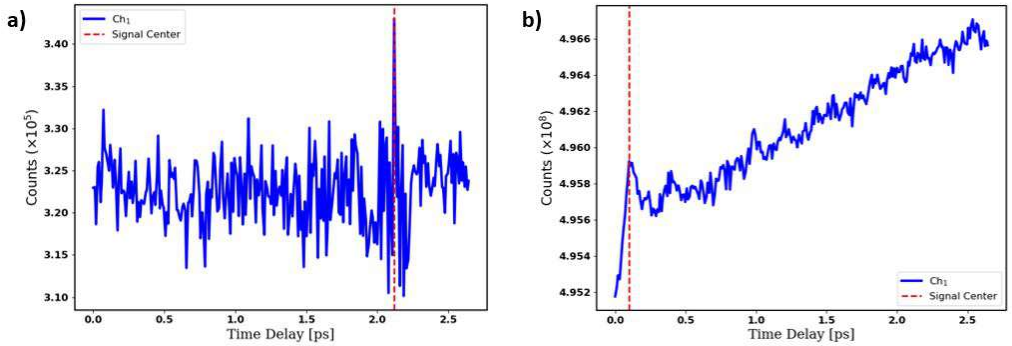


Figure 5.25: Transmitted signal (gate beam background subtracted) (a) With P_2, where the signal is centered around 2.133 $\times$ 10^{-12} s, (b) Without P_2, where the signal is centered around 9.6 $\times$ 10^{-14} s.

Although the repetitive appearance of a signal centered at the same location, when the analyzer is used is a good indication that the signal belongs to optical Kerr effect, it is still yet difficult to handle the gate beam scattered signals, which appear at different locations, and/or different magnitudes. Apparently, the efforts for getting rid of the influence of the gate beam signals on the transmitted time traces, such as subtracting the gate beam scattered signals, or usage of irises, or selecting an optimal position on the BBS glass specimen, were not sufficiently effective. This issue will even represent a greater challenge for measuring optical Kerr signal time traces, as looking for an optimal position on a certain graphene flake would be limited by its small physical dimensions.

Based on the results described above, we conclude that while counter-propagating OKG measurements can be performed in a reproducible manner, they inherently offer only a very limited temporal overlap between the pump and probe beams. The pronounced phase offsets observed in the fitted traces—deviating from the expected peak positions—are most likely due to ellipticity in both the gate and probe beams. For co-propagating, degenerate OKG experiments, a lock-in amplifier becomes indispensable for effectively suppressing scattered light from the gate beam, which otherwise dominates the transmitted traces and compromises their temporal fidelity. We therefore recommend conducting these OKG experiments with non-degenerate pump and probe beams using the OPO. In that configuration, nitrogen must be flushed into the OPO cavity to stabilize the output wavelength. Regardless of the configuration, the use of a lock-in amplifier remains strongly advisable to reduce noise and background contributions.

Chapter 6

Graphene and thin graphite films as a Kerr medium

6.1 Introduction to properties of graphene

Carbon is a fundamental element of life, all of organic molecules contain carbon atoms. In its crystalline form, carbon comes in different allotropes, one is diamond (discussed earlier); the other addressed here is graphene. Graphene is a two-dimensional sheet of carbon atoms arranged in a honeycomb lattice. A single layer is called monolayer graphene; stacking many layers forms bulk graphite. The terminology of "graphene" was coined by the international committee for characterization and terminology of carbon and graphite [332]. The first successful isolation of single-layer of graphene was achieved by Andre Geim and Konstantin Novoselov [333] in 2004, and since then a tremendous interest has been sparked, owing to the unique properties of graphene. It was believed for a long time that isolation of single-layer from the bulky graphite is not possible, according to the common wisdom of the solid-state physics community. This belief originated from a 1930s theoretical argument by Landau and Peierls that truly 2D atomic crystals cannot exist at any finite temperature [334, 335, 336, 337]. According to their theory, low-dimensional materials, i.e., 2D atomic crystals, have thermal fluctuations at any finite temperature and this causes displacement of atoms, comparable to the interatomic distances. As a consequence, the atoms will not be able to maintain their original positions in the crystal lattice, and they can either be decomposed, or segregate [338]. The success attained with isolating a monolayer from graphite by micromechanical cleavage technique encouraged researchers to use the same technique for obtaining 2D atomic crystals from other bulky layered materials, e.g., boron nitride, and several dichalcogenides, etc [339]. These 2D atomic crystals are thermodynamically stable and, in fact, exhibit high crystalline quality.

A monolayer of graphene has a unique structure that gives rise to numerous physical phenomena and applications, such as anomalous quantum Hall effect, Klein tunneling and field-effect transistors (FETs) [340]. The low-dimensionality of graphene, its structural symmetry and the zero-gap it has between the conduction and valence band impart graphene its remarkable optical, electronic, mechanical and thermal properties, such as high mechanical strength [341], superior electrical and thermal conductivities [342, 343]. Unlike traditional semiconductors, the band structure in K-space and the zero-gap point, often described as Dirac point, results in a linear energy-momentum dispersion relationship between the charge carriers. One consequence of that is, around the Dirac point, the behavior of electrons cannot be described by the famous Schrödinger equation. Instead, the appropriate equation in this case is the relativistic Dirac equation since the electrons in this case behave like massless Dirac fermions. If graphene is neutral (not doped), the chemical potential crosses exactly at the Dirac point. The low-energy excitation in graphene is valid solely around Dirac point, which mimics quantum electrodynamics for massless Dirac fermions, with one exception, that is Dirac fermions in graphene move with a speed v_{F} ($\approx 10^6$ m/s) that is 300 times slower than the speed of light c [342]. In fact, in this regard graphene establishes a bridge for studying the quantum relativistic physical phenomena between condensed matter physics and quantum electrodynamics. Another interesting aspect, albeit counterintuitive, of Dirac fermions in graphene is that they exhibit a relativistic trembling motion '*Zitterbewegung*', by which graphene has a minimum conductivity on the order of quantum conductance e^2/h, when it has zero doping [344].

In this chapter, we shall discuss in the first section the crystal structure of graphene, and energy-momentum relationship diagram, as well as the different stacking orders of graphene layers and the Raman spectrum of graphene, which distinguishes single-layer graphene from bilayer graphene and graphite. Then, we go through the various approaches for fabricating graphene, where we focus particularly on the most commonly used techniques for fabricating graphene samples, which are chemical vapor deposition (CVD) and mechanical exfoliation (ME). In the third section, the different methods for determining the number of layers a graphene flake has will be explained. Related to that, the results of using optical microscopy will be presented. Following that section, the thermal transport of graphene layers will be discussed, besides the thermal damage mechanisms induced by intense laser irradiation. Also in this section, we shall show the results of an experiment carried out to study the damage induced by our femtosecond high repetition rate laser. Last but not least, we shall elaborate the nonlinear optical properties of graphene, with particular emphasis on self-phase modulation and optical Kerr effect and our measurements to investigate these two physical phenomena, as those are most relevant to the scope of

our research, hence the scope of this dissertation.

6.2 Structure of graphene

6.2.1 Crystal structure

Graphene is a single atomic layer arranged in a honeycomb lattice that can be viewed as a building block of other dimensionality of carbon atoms. For example, when a sheet of graphene is wrapped up, it creates fullerenes (0D), rolling it produces 1D carbon nanotubes. On the contrary, if many of them are stacked on top of each other, it forms the 3D graphite, as illustrated in Fig. 6.1 [340].

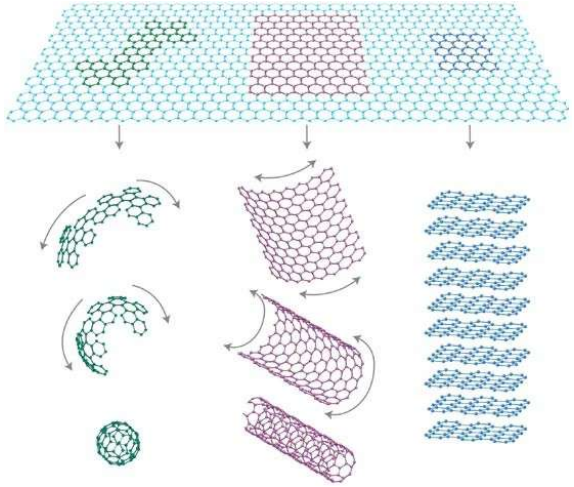


Figure 6.1: Various dimensionality of carbon atoms, represented by 2D graphene as a building block [340].

Graphene is sp^2 hybridized in its hexagonal lattice, and every unit cell in that lattice has a basis of two carbon atoms, as depicted in Fig. 6.2. Each carbon atom has four valence electrons, three of those electrons form covalent tight bonds, which is σ-bond, with its three neighbor atoms, which are located in-plane of the graphene layer, and they do not take part in the electrical conduction of graphene. However, they are responsible for the high thermal conductivity of graphene [345], and its enormous mechanical stiffness [341]. The interatomic distance between each carbon atom and its nearest neighbor is about a ≈ 1.42 Å[346]. The σ-bond electrons are hybridized, whereas the orbital of $2s$ is mixed with the two orbitals p_x and p_y. The fourth electron forms the π-bond, where the π-electrons may move freely between the positive ions of the lattice, and they occupy the p_z orbital that is not hybridized, and oriented along Z-direction, namely out of the plane. The π-bonds form the π and π^* bands, presented in Fig. 6.3, that shows the energy dispersion E(K) along

the high symmetry direction of the triangle Γ M K, which are responsible for most of the interesting properties of graphene [347].

The lattice vectors of graphene can be written as [342]

$$\mathbf{a}_1 = \frac{a}{2}(3, \sqrt{3}), \quad \mathbf{a}_2 = \frac{a}{2}(3, -\sqrt{3}), \tag{6.1}$$

where a is the interatomic distance 1.42 Å. The reciprocal-lattice vectors are given by

$$\mathbf{b}_1 = \frac{2\pi}{3a}(1, \sqrt{3}), \quad \mathbf{b}_2 = \frac{2\pi}{3a}(1, -\sqrt{3}). \tag{6.2}$$

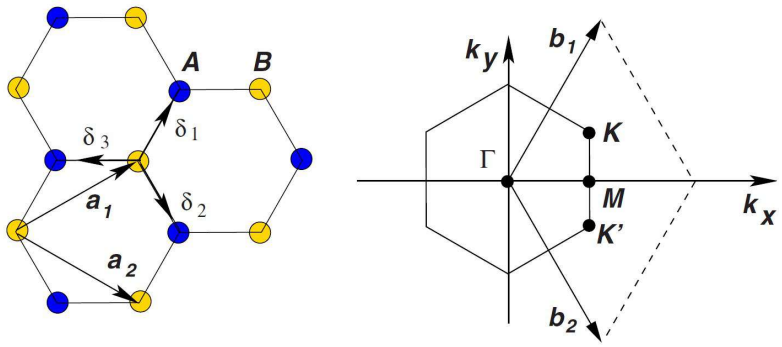


Figure 6.2: Hexagonal lattice and its corresponding Brillouin zone. (a) Lattice structure of graphene, a_1 & a_2 are lattice unit vectors and δ_i, i=1,2,3 are the nearest-neighbor vectors, (b) Brillouin zone, b_1 & b_2 are reciprocal lattice unit vectors in the x-y plane, and K & K′ are locations of Dirac cones [342].

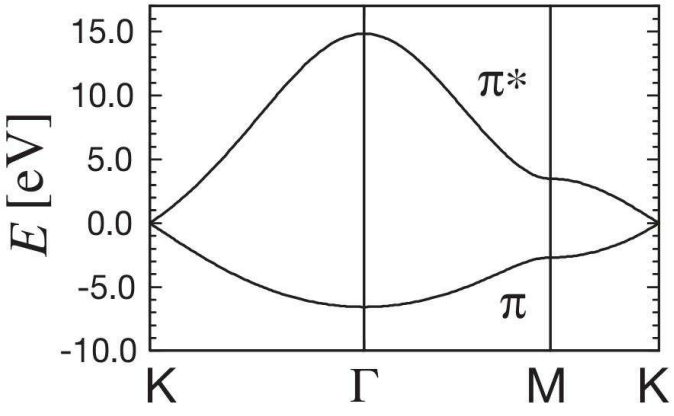


Figure 6.3: Energy dispersion E(K) of π - π^* bands along high symmetry points Γ M K [347].

In the reciprocal lattice, the hexagonal structure represents the Brillouin zone (BZ). The two most significant points in that zone are the K and K′ points, where Dirac

points are located at the corner of the BZ. The momentum space positions of K and K′ are given by

$$\mathbf{K} = \left(\frac{2\pi}{3a}, \frac{2\pi}{3\sqrt{3}a}\right), \quad \mathbf{K}' = \left(\frac{2\pi}{3a}, -\frac{2\pi}{3\sqrt{3}a}\right). \tag{6.3}$$

The three nearest-neighbors vectors in real space are given by

$$\boldsymbol{\delta}_1 = \frac{a}{2}(1, \sqrt{3}) \quad \boldsymbol{\delta}_2 = \frac{a}{2}(1, -\sqrt{3}) \quad \boldsymbol{\delta}_3 = -a(1, 0). \tag{6.4}$$

6.2.2 Band structure

The electronic band structure of graphene can be well-described by tight-binding approximation for π-electrons, whereby the Hamiltonian which considers that electrons can hop to the nearest-neighbor or the next nearest-neighbor is given by

$$H = -t \sum_{\langle i,j\rangle,\sigma} \left(a^\dagger_{\sigma,i} b_{\sigma,j} + \text{H.c.}\right) - t' \sum_{\langle\langle i,j\rangle\rangle,\sigma} \left(a^\dagger_{\sigma,i} a_{\sigma,j} + b^\dagger_{\sigma,i} b_{\sigma,j} + \text{H.c.}\right), \tag{6.5}$$

where $a_{i,\sigma}$ ($a^\dagger_{i,\sigma}$) annihilates (creates) an electron with spin σ ($\sigma = \uparrow, \downarrow$) on site $\mathbf{R}_i$ on sublattice A (an equivalent definition is used for sublattice B), t (≈ 2.8eV) is the nearest-neighbor hopping energy (hopping between different sublattices), and t' is the next nearest-neighbor hopping energy (hopping in the same sublattice).

From that Hamiltonian, Wallace [348] derived the energy bands, which are expressed as

$$E_\pm(\mathbf{k}) = \pm t\sqrt{3 + f(\mathbf{k})} - t' f(\mathbf{k}), \tag{6.6}$$

$$f(\mathbf{k}) = 2\cos(\sqrt{3}k_y a) + 4\cos\left(\frac{\sqrt{3}}{2}k_y a\right)\cos\left(\frac{3}{2}k_x a\right), \tag{6.7}$$

where the plus sign is designated for the upper band π^*, while the negative sign is designated for the lower band π. This expression shows that the energy spectrum as a function of the momentum for an electron-hole pair is symmetric around $E = 0$, provided that $t' = 0$, since for every positive $E_+(\mathbf{K})$ there is $E_-(\mathbf{K}) = -E_+(\mathbf{K})$ corresponding to it. This symmetry is broken when $t' \neq 0$, in turn the two bands π & π^* become asymmetric. The full band structure of graphene based on Eq. 6.6 is depicted in Fig. 6.4, and in the inset a zoom-in of the band structure around Dirac points at K and K′ is shown. It might not be adequately clear in the figure that graphene possesses six pairs of Dirac cones, where at each meeting point between the pair of two cones, there is zero-bandgap.

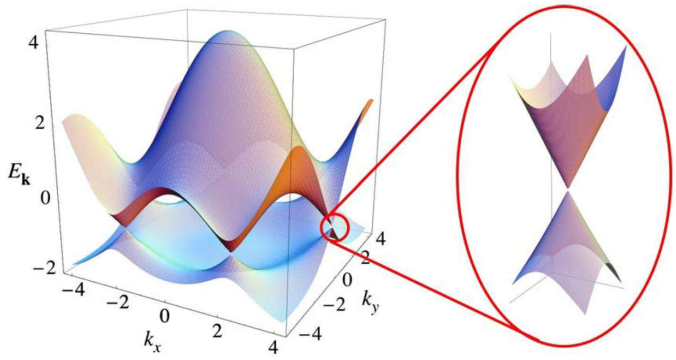


Figure 6.4: 3D representation of electronic dispersion in the honeycomb lattice. (Left) energy spectrum (in units of t) for finite values of t and t', with $t = 2.7$ eV and $t' = -0.2t$. (Right) Close-up on the energy band of one pair of Dirac cones [342].

The dispersion close to Dirac points can be obtained by expanding the full band structure expressed by Eq. 6.6 around the crystal momentum wavevectors of Dirac points $\mathbf{K}$ and $\mathbf{K}'$ given in Eq. 6.3 in the BZ, as $\mathbf{k} = \mathbf{K} + \mathbf{q}$, where the momentum $\mathbf{q} = \mathbf{k} - \mathbf{K}$ measured relative to the Dirac point, assuming $|\mathbf{q}| \ll |\mathbf{K}|$, whereby we can use Taylor expansion of $E(\mathbf{k})$ around $\mathbf{K}$, as follows:

$$E_{\pm}(\mathbf{k}) = E_{\pm}(\mathbf{K} + \mathbf{q}) \approx E(\mathbf{K}) + \mathbf{q} \cdot \nabla_{\mathbf{k}} E(\mathbf{k})|_{\mathbf{k}=\mathbf{K}} + \dots \tag{6.8}$$

Given that $E(\mathbf{K}) = 0$ at Dirac points where the conduction and valence bands meet, the first order expansion becomes

$$E_{\pm}(\mathbf{K} + \mathbf{q}) \approx \mathbf{q} \cdot \nabla_{\mathbf{k}} E(\mathbf{k})|_{\mathbf{k}=\mathbf{K}} \tag{6.9}$$

If we denote $\mathbf{v}_F = \nabla_{\mathbf{k}} E(\mathbf{k})|_{\mathbf{k}=\mathbf{K}}$, then $E_{\pm}(\mathbf{q}) \approx \pm\mathbf{q}\cdot\mathbf{v}_F + O[\mathbf{q}/\mathbf{K}^2]$, where $O[\mathbf{q}/\mathbf{K}^2]$ is a second-order correction term of the approximation, and $\nu_f = 3ta/2$ with $\nu_f \simeq 1 \times 10^6$ m/s.

This tells us that near Dirac points where low-energy excitations occur, the energy spectrum is linear but deviates from linearity as we move farther than Dirac points. This is why electrons near K and K′ points behave similarly to relativistic massless Dirac fermions, in spite of the fact that they are not moving at relativistic speeds. This behavior presents a striking difference between the behavior of electrons in graphene near Dirac points, and Schrödinger electrons in any conventional material. Usually with parabolic energy-momentum dispersion, there is a quadratic relationship between energy and momentum, where $\epsilon(\mathbf{q}) = q^2/2m$, in which m is the electron mass. In this case, the velocity of electrons is $v = \mathrm{dE/dq} = q/m = \sqrt{2E/m}$, and it depends on the energy, meaning the higher the energy, the faster the electron speed. On the contrary, the linear dispersion relationship $E = \pm v_{\mathrm{F}}|\mathbf{q}|$ between

energy and momentum results in a constant velocity, irrespective of how much energy the electron acquires, as we see from $v = \mathrm{dE/dq} = \pm v_{\mathrm{F}}$.

6.2.3 Stacking order of graphene layers

Graphene is strictly defined as a monolayer of 2D crystalline structure, which is zero-gap semiconductor, with a linear Dirac-like spectrum around the Fermi energy, while graphite behaves like a semimetal with a band overlap of about 41 meV. Nonetheless, stacking additional layer of graphene to such single-layer will alter its electronic properties, where it was studied theoretically using tight-binding model that a bilayer of graphene possesses a parabolic energy spectrum like graphite [349] with an extremely small band overlap of 0.16 meV. The electronic structure will keep evolving with further addition of monolayers up to 10 layers, leading to a semimetallic behavior. Another fascinating aspect of stacking two layers of graphene (bilayer), yet extraordinary aspect, is that stacking two layers of graphene at a slight offset called the "magic angle" can paradoxically change the electronic properties of graphene from an insulator to a superconductor [350]. Such a strange phenomenon was quite alluring to researchers to investigate it with tremendous hope and ambition to elicit robust superconductivity at high-temperature one day. Since its discovery, thousands of extensive studies have been carried out in order to understand the cause underpinning the peculiar behavior of twisted graphene layers. For an update about the current progress, and yet open questions, Ref. [351] provides a decent overview.

Two layers of graphene or more are attached together via interlayer coupling through van der Waals force, which is an intramolecular weak force. Three common stacking orders of graphene sheets often exist, those are a simple hexagonal (AAA), hexagonal (ABAB) usually so-called Bernal stacking, and rhombohedral (ABC). The ABA Bernal stacking and the ABC rhombohedral stacking are schematically depicted in Fig. 6.5, for a trilayer graphene.

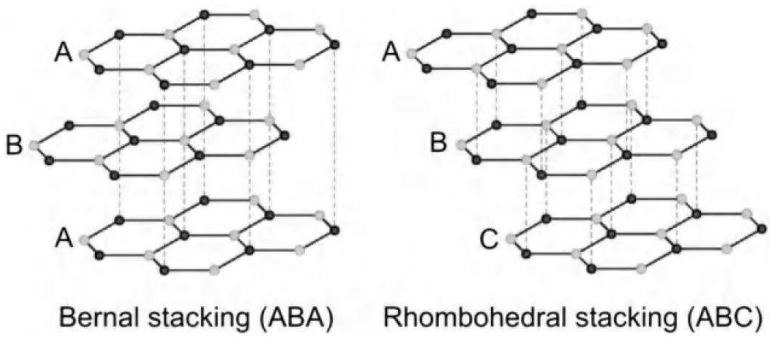


Figure 6.5: Left: ABA Bernal stacking order, Right: ABC rhombohedral stacking order [352].

Noticeably, in ABA Bernal stacking, the third layer of graphene has the same projections on the basal X-Y plane as the first layer, and the interlayer spacing between two layers is 3.35 Å. In the ABC rhombohedral stacking the third layer is shifted relative to the second and first layer. The fourth layer, though, has the same projection on the basal X-Y plane as the first layer, and the interlayer distance is 3.37 Å[352]. In AA stacking order, the second layer of graphene lies directly on top of the first layer, namely it has the exact projection on the basal X-Y plane. On the other hand, disordered graphite, so-called turbostratic graphite, does not exhibit any preferred stacking order. The ABA Bernal stacking order is the most frequently noticed in few-layer graphene (FLG) and graphite, being thermodynamically stable and energy preferable. ABC rhombohedral stacking order has been observed in multilayer graphene epitaxially-grown on silicon-terminated SiC substrate. Moreover, this stacking order is adopted by FLG grown via chemical vapor deposition (CVD).

The stacking order of graphene layers not only alters its electronic properties, but it can also change its optical properties. For example, although a monolayer of graphene is centrosymmetric, which prohibits second-harmonic generation (SHG) in a single-layer of graphene, Shan et al. [353] have observed a strong optical SHG in a Bernal stacked noncentrosymmetric trilayer of graphene, which vanishes in a rhombohedral stacked trilayer. For identification of the stacking orders of graphene layers, Raman spectroscopy has been an effective tool to distinguish them and for counting the number of graphene layers, as well [354], up to some extent, as we shall see. Furthermore, imaging Raman spectrum of graphene has unveiled that different domains on the same graphene sample can possess different stacking orders, which otherwise cannot be recognized by imaging via optical microscopy, as illustrated in Fig. 6.6, for a trilayer graphene prepared by mechanical exfoliation [355].

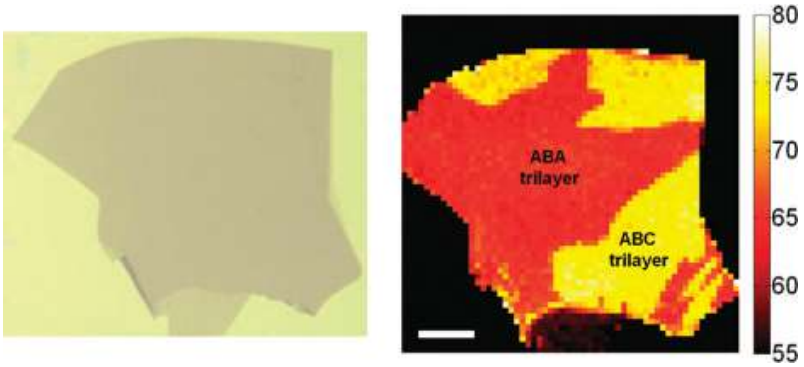


Figure 6.6: Imaging of mechanically exfoliated trilayer graphene. (Left) Optical imaging of the sample, (Right) Spatial Raman imaging of the same sample showing domains of Bernal stacking order, ABA, and other with rhombohedral stacking order ABC [355].

Controlling of the stacking order of graphene layers, owing to its importance, has

been pursued by various methods. For instance, Li et al. [356] investigated how electric fields and carrier doping can globally (across the entire sample) and reversibly control the stacking order in FLG, particularly between ABA and ABC arrangements. In their work, the FLG was encapsulated between hexagonal boron nitride (hBN) and electrically-gated to control the doping level (carrier density). Doping can shift the Fermi level, altering energy balance between the ABA and ABC arrangements, and leading to phase change, since those arrangements acquire different work functions ($\sim$ 10-20 meV). Also, a displacement electric field (D-field) was used to open a bandgap in an ABC stacked graphene, whereas at high D-fields, the rhombedral ABC stacking order becomes energetically favorable. This is a remarkable transition, given that in other situations the ABC arrangement would be rare to occur due to being thermodynamically unstable. Another approach for controlling the stacking order in thin graphite films has been developed by Yang et al. [357], where they modified the van der Waals assembly process by encapsulating the graphite crystals with hBN, and used polydimethylsiloxane (PDMS) coated with polymethyl methacrylate (PMMA) in the transfer process. Interestingly, they found out when the hBN encapsulation is introduced parallel to the graphite zigzag edge, that will preserve the ABC arrangement, while if it is introduced along the armchair direction, it transforms the stacking to ABA. Recently, a new method for precise control of the layer thickness and the stacking sequence has been demonstrated by Nguyen et al. [358] using CVD and a Cu-Si alloy substrate at a wafer scale. In this technique, a Cu-Si surface alloy is firstly created, then a low-concentration CH_4 gas is secondly introduced, which reacts to Si, forming a SiC. Afterwards, by raising the temperature to 1075°C, the Si is sublimated, leaving the C atoms behind that are assembled to form graphene. The key factor to control for obtaining a specific number of layers and a stacking order is the concentration of CH_4 gas. For instance, the following CH_4 concentrations were used to achieve mono-, bi-, tri- and tetralayer graphene were 0.01%, 0.03%, 0.06% and 0.1%, respectively. Subsequent characterization of some grown graphene samples (bilayers and trilayers) has astonishingly shown 100% AB and ABA stacking order without a single sample deviation of that order, while graphene samples of tetralayers have exhibited 80% ABCA order, and 20% ABAB sequence. For a highlight of current efforts and prospect of stacking order engineering of 2D materials, the reader is referred to Ref. [359].

6.2.4 Raman spectrum of graphene

Raman spectroscopy has been a versatile tool in characterization and studying of various properties of graphene [360]. It has been used for counting the number of graphene layers [361], as we shall discuss in subsection 6.4, probing the electric

field effect (EFE) on tuning the electron-phonon coupling of graphene [362], and identifications of charged impurities [363]. Further, it has been used for temperature sensing based on the change of Raman spectrum [364], as well as, measuring the thermal conductivity of graphene [365]. Additionally, the study of structural disorder [366, 367] and variation of stacking order domains of multilayered graphene [355, 357, 368, 369].

Phonon dispersion is the key to understanding graphene's Raman modes. Raman modes are basically vibrational modes (phonons) of the carbon atoms of graphene in the hexagonal lattice. The number of allowed vibrational states is 3 N, where N is the number of atoms in a unit cell. Because graphene has two atoms in its unit cell, this means that it possesses $3\times(2) = 6$ vibrational modes, 3 of which acoustical (A) phonons and the other 3 are optical (O) phonons. Two acoustical (A) phonons, and two optical (O) phonons are in-plane (i) of graphene lattice. The remaining two phonons are located out-of-plane (o). The direction of vibrational modes of the zone-center mode is specified relative to the carbon-carbon (C-C) bond direction, to be either longitudinal (L) or transverse (T) [370]. Therefore, along high symmetry directions ΓM and ΓK, six phonon dispersion curves are assigned for iLO, iTO, oTO, iLA, iTA and oTA in a descending order, as shown in Fig. 6.7.

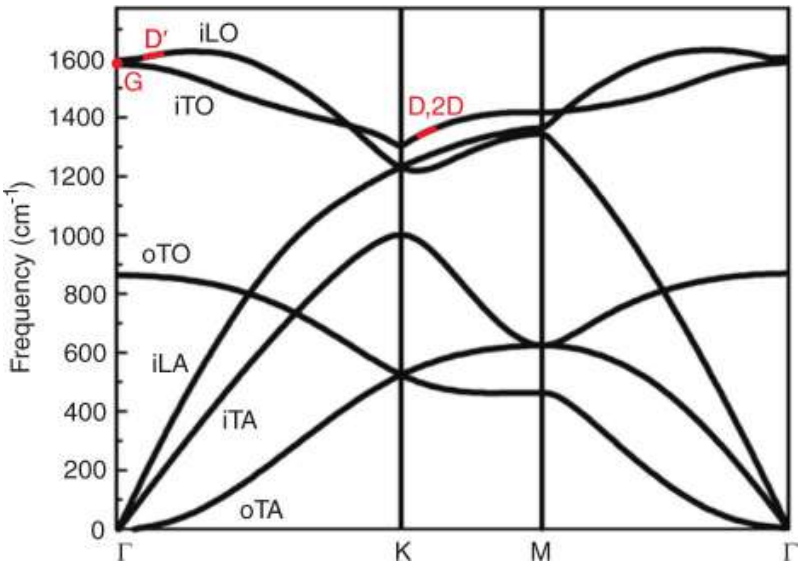


Figure 6.7: Phonon dispersion of graphene. High symmetry points Γ, K, M are represented along the x-axis. Significant Raman bands are highlighted in red [370].

Out of the six phonon dispersion curves, iLO and iTO are mainly responsible for the known Raman bands, and their associated phonon energies are highly dispersive at Γ and K points. At the zone-center mode Γ, a monolayer of graphene has the point group D_{6h}, and this point group changes for N-layer graphene, for example, when the number of graphene layers N is even the point group becomes D_{3d}, and if N is

odd, then the point group becomes D_{3h}. For an infinite number of graphene layers, which represents graphite, the point group will be similar to graphene monolayer, namely D_{6h} [354]. In the framework of group theory [371, 372], the point group D_{6h} at Γ point of a monolayer of graphene has the following corresponding irreducible representations E_{2g}, B_{2g}, A_{2u} and E_{1u} that describe the phonon modes of graphene. Not all those phonon modes are Raman active, whereas some of them are IR active modes [360]. The irreducible representation E_{2g}, in particular, belongs to the only Raman active modes, that are iLO and iTO. Although graphite has the same point group D_{6h}, the total number of vibrational (phonon) modes is larger ($3\times(4) = 12$ modes), since the unit cell contains four atoms unlike graphene, which has only two atoms per unit cell. Accordingly, this point group of graphite has different irreducible representations at zone-center Γ in the BZ, such that $\Gamma_{Opt} = 2E_{2g} + E_{1u} + 2B_{2g} + A_{2u}$, while $\Gamma_{Aco} = A_{2u} + E_{1u}$ [373, 374]. A scheme for the phonon modes for both graphene and graphite along with their irreducible representations, as well as their vibration directions, in-plane and out-of-plane is presented in Fig. 6.8.

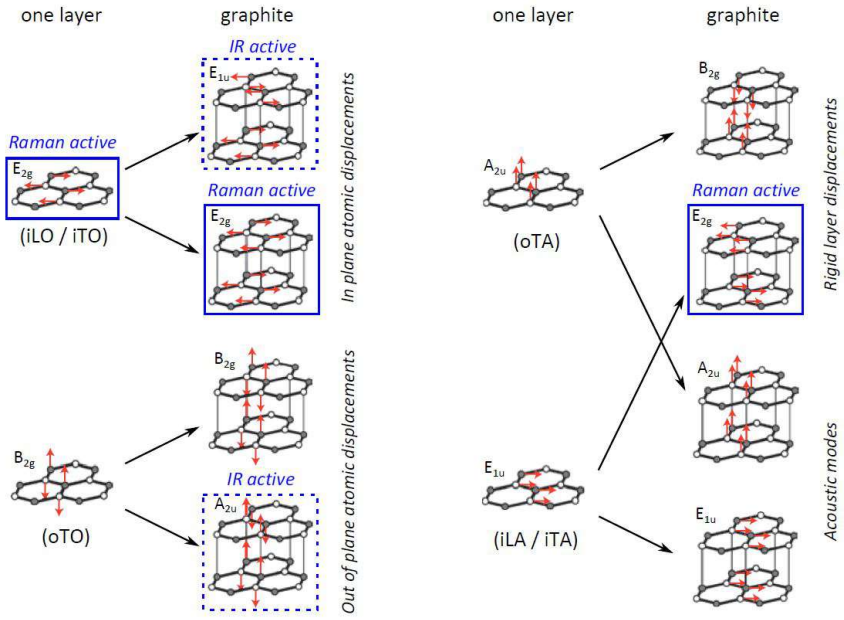


Figure 6.8: Vibrational modes of graphene (left) and graphite (right) at the zone-center Γ [375].

A flake of pristine graphene typically acquires primary Raman bands, such as G, 2D(G′) and 2D′, shown in Fig. 6.9 (a). If the graphene flake is damaged, either through the fabrication process or post-fabrication, some additional Raman bands will appear, such as D, D′, D+D′, as illustrated in Fig. 6.9 (b). The presence of those extra bands, particularly D peak, could be used as an indication, for instance, of defect-induced femtosecond laser irradiation, as we shall discuss in subsection 6.5.3.

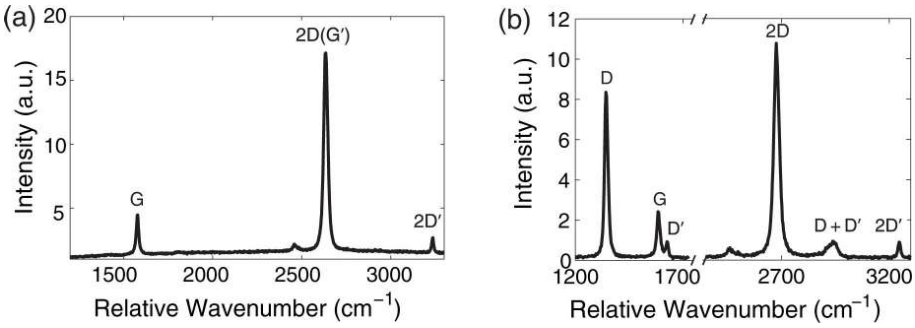


Figure 6.9: Raman spectrum of graphene. (a) Raman spectrum of pristine graphene flake, (b) Raman spectrum of damaged graphene [370].

One of the most important Raman modes is the G band, which is associated with the doubly resonant (iTO and iLO) phonon modes at the center of the first Brillouin zone. The G band appears at ~ 1582 cm^{-1} and it is the only band coming from the first-order Raman scattering process in graphene. The G band has a sharp peak and appears also in graphite, and it corresponds to the irreducible representation of E_{2g} [370, 353]. Further, it dominates all disordered sp^2 carbons along with D band, and involves the in-plane bond-stretching motion of a couple of C atoms in sp^2 atoms [376], as shown in Fig. 6.10 (a). The responsible mechanism for the G band begins with a resonant excitation from an incident photon to a virtual electron-hole pair in graphene, as depicted in Fig. 6.11 (a). Then, one of the zone-center Γ phonons, iTO or iLO, scatter the electron or the hole, and eventually the electron-hole pair will recombine, emitting a radiation at red-shifted wavelength, such that that shift depends on the amount of energy given to the phonons. Clearly, the phonons at Γ point have very little momentum, as we can see from Fig. 6.7. In spite of its distinct presence in graphene and graphite, the Raman peak corresponding to the G band is not the strongest in the entire Raman spectrum. In fact, the strongest peak corresponds to the 2D band of graphene, as evidently observed in Fig. 6.9. The 2D band, formerly called G$'$ band, appears at 2700 cm^{-1}, and takes place as result of a second-order Raman scattering process from an in-plane breathing-like motion of carbon atoms forming the graphene ring, see Fig. 6.10 (b); and belongs to the totally symmetric irreducible group A_1' at K or K$'$ point. The doubly-resonant process of the 2D band formation commences with a creation of an electron-hole pair by an incident photon, similar to the G band, but here near the K point and the electron is inelastically scattered by an iTO phonon to the K$'$ point. This electron must be scattered back to the K point before recombination with a hole, in order to conserve the energy and momentum, which is achieved by another iTO phonon. A similar process can occur to a hole, which is why this process is called doubly-resonant (DR) process, illustrated in Fig. 6.11 (b), because the incident or scattered photon, or the first or second phonons are in resonance with the electronic levels of graphene.

Shown also in Fig. 6.11 (b) is an alternative process, called triple resonance (TR), in which both carriers (an electron & a hole) are scattered by iTO phonons from near K to near K′ and recombine by emitting a photon.

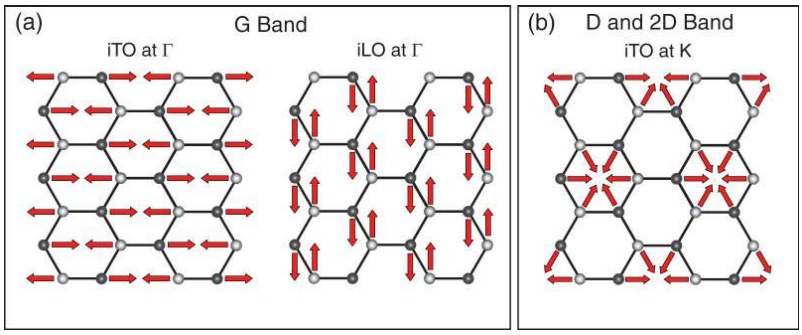


Figure 6.10: Scheme of Raman vibrational modes in graphene. (a) Vibrations of iTO and iLO corresponding to G band at Γ point, (b) Vibrations of iTO corresponding to D & 2D at K point [370].

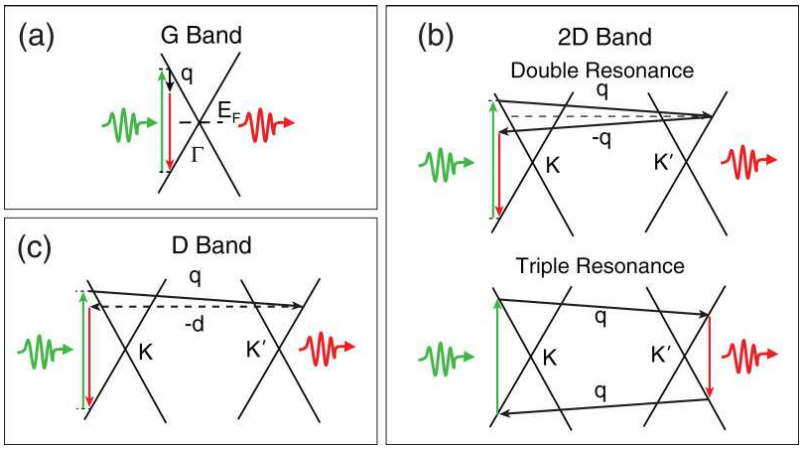


Figure 6.11: Diagram of formation mechanisms of different Raman bands in graphene. (a) First-order Raman scattering process for formation of G band, (b) Doubly-resonant interaction leading to 2D band, (c) Disorder-induced formation of Raman D band [370].

Another significant Raman band, albeit not a primary band, is the disorder-induced D band, which appears at ~ 1350 cm^{-1} at laser excitation energy 2.41 eV (514 nm). This process also requires an iTO phonon, see Fig. 6.11 (C), however it involves a disorder to conserve the momentum, whereas the electron is scattered to the K′ point via an iTO phonon, then it is scattered back to K point by a defect. Since only one phonon is involved in the scattering process, the energy shift of the D band is only half the 2D band. The disorder needed for momentum conservation can emerge from any violation of the symmetry of the graphene lattice, for example, from a vacancy, grain boundaries, sp^3 sites, or a flake's edge. The Raman bands can be dispersive based upon where in the Brillouin zone the scattering happens.

Raman scattering processes, for instance, occurring at the zone-center Γ are not dispersive, meaning the G band energy does not change depending on the energy of the incident photon, depicted in Fig. 6.12 (a). This is actually not the case with Raman scattering processes, occurring at K point, like the DR process responsible for the 2D band, shown in Fig. 6.12 (b) and the scattering process leading to the D band, in which case an increase of the incident photons necessitates phonons farther away from the K point for momentum conservation.

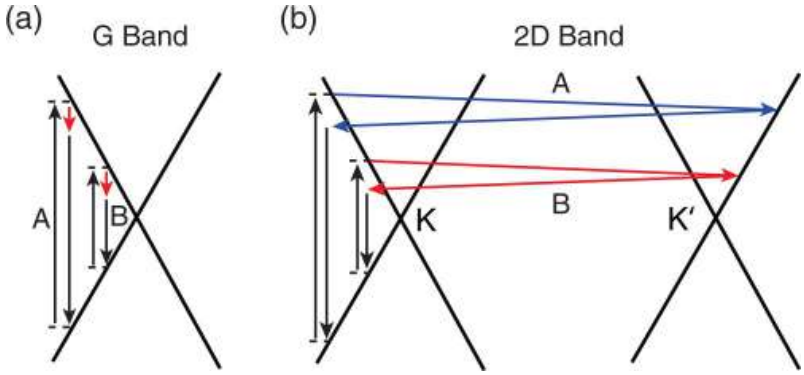


Figure 6.12: Illustration of dispersion of Raman bands at two different excitation energies. (a) For the G band, which is not dispersive based on incident photons [notice red arrows pointed downward], (b) Dispersion of the 2D band [370].

In our work, several samples have been fabricated via mechanical exfoliation technique, which will be discussed in the following section. Typically, the prepared samples contain graphite and thin graphite films, that represent the majority of created flakes, besides graphene, which is a minority onto the substrate. Raman spectroscopy has been used for characterizing those samples, using a PicoQuant CW laser at 656.64 nm. Given that the G band appears at 1587 cm^{-1}, 2D band arises at 2675 cm^{-1}, and D band shows up at 1350 cm^{-1}; with the wavelength of the CW laser, we expect those peaks to appear at the following wavelengths 733.03 nm (G peak), 769.56/797.51 nm for monolayer/graphite (2D peak), and 720.52 nm, respectively. Raman signals are usually very small, moreover, the laser used to characterize Raman spectra will often excite any fluorescent object, i.e., residual of organic molecules at the substrate, and the emitted fluorescence signal is much stronger than Raman, such that it buries most of the Raman peaks. The background created by fluorescence spectrum could be significantly reduced if a confocal pinhole is used to localize the area from which the Raman signal is collected. However, this will not ensure complete elimination of the fluorescence background. Therefore, it needs to be mathematically corrected. In our case, we used the method of asymmetric least squares (ALS) [377], for correcting the baseline of fluorescence.

The Raman spectrum of graphite and graphene in the sample is shown in Fig. 6.13. An image taken by a commercial Zeiss optical microscope of graphite is presented in

Fig. 6.13 (a), and its associated Raman spectrum showing the primary bands, namely G and 2D, in Fig. 6.13 (b). Notice the appearance also of the disorder-induced D band, indicating that the graphite has a defect, not detectable by a simple micrograph. On the same sample, Fig. 6.13 (c) shows a large graphene flake, consisting of 10 - 11 layers, and in Fig. 6.13 (d), its corresponding Raman spectrum is shown. Apparently, this graphene flake was defect-free, as there is no sign of D band (D peak) in its Raman spectrum.

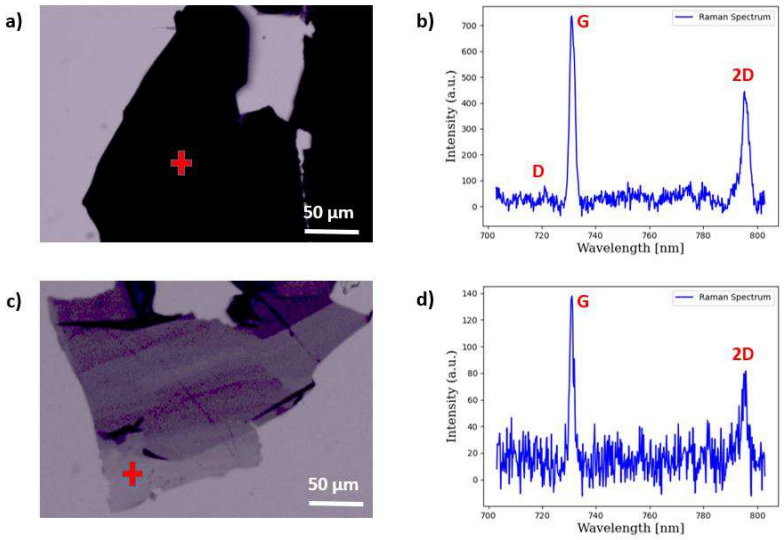


Figure 6.13: Raman spectrum of graphite and graphene. (a) Micrograph of graphite, marked with plus sign (red), (b) its corresponding baseline-corrected Raman spectrum, with 5 s integration time, (c) Micrograph of large graphene, marked with plus sign (red), (d) Graphene's baseline-corrected Raman spectrum, with 1 s integration time.

6.3 Sample preparation

6.3.1 Overview

Graphene has been called the wonder material, owing to its unique physical, thermal, mechanical, optical properties. With the inception of the 2D materials era, propelled by the seminal work of Geim and Novoselov [333], various fabrication techniques for graphene and other 2D lattice crystallines have emerged, each of which has its pros and cons. These techniques can be broadly categorized into two approaches, one is top-down approach, wherein a bulk graphite is segmented into graphene layers; while the other approach is bottom-up approach, where graphene is built-up from a carbon-containing precursor. Generally, each technique varies in terms of scalability, quality of the fabricated flakes, cost, as well as the environmental impact.

The first and simplest top-down approach for fabrication of graphene samples was

introduced by Geim and Novoselov in 2004 [333, 339, 340] as we mentioned before. The technique utilizes merely a scotch-tape to peel graphene layers off a bulk graphite mesa, several times until a monolayer of graphene is isolated. It is technically referred to as mechanical exfoliation (ME), or micromechanical cleavage, and it produces small flakes of graphene at a lab scale. For industrial applications, much larger flake areas are required, which cannot be fabricated via mechanical exfoliation. Besides its simplicity, the advantage of mechanical exfoliation technique is that it produces high quality graphene flakes (pristine graphene), as it does not require chemicals or thermal treatments during fabrication. This also renders it an environmentally-friendly technique, for the same reason. Further details about ME fabrication technique will be provided in subsection 6.3.3. Liquid-phase exfoliation (LPE) is another top-down method for producing graphene that helps to scale-up graphene production [378]. In this method, a graphite powder is dispersed into a solvent, then an energy is applied via ultrasonication to peel graphene layers off. The product is a colloidal suspension, which can be later centrifuged [379], in order to separate single layers of graphene. Although it offers high-yield of graphene flakes, some graphene flakes might have small lateral size, due to being fractured when the rate of interaction between the solvent and graphite is increased, an issue encountered with the same fabrication technique for other 2D materials [380]. Also, a large portion of produced graphene flakes contain multilayers, or few layers. Chemical reduction of graphene oxide (GO) is another route toward mass-production of graphene [381], which belongs to the family of top-down approaches. The process begins firstly with oxidizing graphite by strong oxidants, i.e., sulfuric acid or nitric acid, then the created GO is exfoliated in liquid, e.g., water, to produce single sheets of GO. Afterwards, the GO sheets are reduced to remove their oxygen via a chemical agent, or thermal annealing. This method enables cost-effective fabrication of graphene at large scale. However, graphene obtained by GO reduction suffers from low-quality, as opposed to the very high quality often attained with mechanical exfoliation.

Chemical vapor deposition (CVD) is one of the most commonly used techniques for fabrication of graphene. It is a bottom-up approach that allows synthesis of graphene, particularly single-layer and few-layer graphene at large scale [382]. In this technique, a carbon-containing gas is decomposed at high temperature in presence of a surface catalyst to form graphene. This method truly overcomes the scalability challenge for industrial applications of graphene. Furthermore, graphene layers grown via CVD have uniform, high quality graphene at large areas. Despite these advantages, the quality of CVD graphene is not as high as those fabricated by mechanical exfoliation. Moreover, it requires operation in vacuum chambers and elevated temperatures, which in turn leads to high cost of maintenance, in addition to large energy consumption. CVD grown graphene layers must be transferred from their native substrate, usually

a metal foil, to another substrate that will host graphene for its intended application. The transfer process as such could induce defects into the crystalline lattice of graphene, which would lower its functionality [383]. Epitaxially grown graphene [384] using silicon carbide (SiC) substrates is another fabrication technique, and it offers very high crystalline quality at industrial scale [385]. In this method, a wafer of SiC crystal is decomposed at very high temperature ($\sim$ 1300-1600°C), where Si atoms are sublimated away, leaving the C atoms to be re-organized into graphene. Besides, its major advantage of its wafer-scale mass production, it does not require transfer of graphene layers. Nevertheless, it is extremely costly, because SiC wafers are very expensive, plus the need for operation in vacuum at highly elevated temperatures. The following subsection will give more details about the CVD fabrication process.

6.3.2 Chemical vapor deposition

CVD is a fundamental bottom-up approach that enables wafer-scale fabrication of graphene samples [382]. The CVD technology has rapidly developed and been extended to carbon nanotubes [386], transition metal dichalcogenide (TMD) [387], and heterostructures [388]. In the CVD method, an elevated temperature ($\sim$ 1000°C) is required to decompose a hydrocarbon gas into carbon and hydrogen. On a catalytic substrate, the carbon atoms are rearranging themselves into graphene layers. A thermal CVD is an equipment commonly used in laboratory environments, which necessitates a furnace for controlling thermal energy, temperature controller, vacuum pump, pressure gauge regulator, reaction chamber, and gas flow regulator to control the gas flow rates. The catalytic substrate is often a metal, whose choice is critical as it impacts the solubility of carbon, leading to variations in the number of produced graphene layers [389]. For example, multi-layer graphene is synthesised onto a nickel (Ni) substrate, which has high carbon solubility. It was found that a $\sim$ 300-nm-thick Ni layer on silicon wafer yields large-scale graphene with high mechanical stability [390]. Copper (Cu), which is another commonly used metal as substrate, has low carbon solubility that promotes single-layer graphene production. Whereas a large-area synthesis of predominantly single-layer graphene films onto 25 μm thick Cu foils were demonstrated [391]. If graphene is CVD synthesized onto Ni, as an example, a polycrystalline Ni films are initially electrochemically polished (for cleaning and smoothing the surface), then annealed in Ar/H_2 atmosphere at 900-1000°C to increase the grain size and reduce the nucleation sites, and then exposed to a gas mixture of hydrogen (H_2) and methane (CH_4). A solid solution of carbon atoms dissolved into Ni films after the hydrocarbon is decomposed in this step. Then, samples are cooled down in Ar gas [392]. Graphene films are formed during the cooling down process, where the carbon atoms diffuse out from the Ni-C solid solution and precipitate onto

the Ni surface, as pictorially depicted in Fig. 6.14.

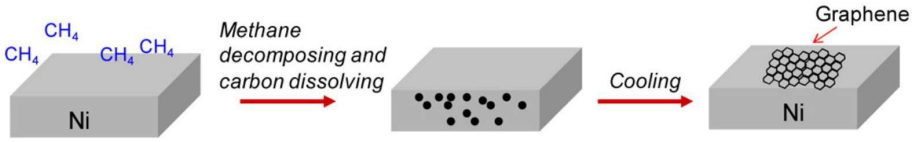


Figure 6.14: Pictorial depiction of CVD growth of graphene onto Ni substrate [392].

The Ni film, in particular Ni(111) plays crucial role in the CVD synthesis as a substrate for graphene growth, due to the similarity of its lattice structure to densely packed hexagonal structure, and the match of lattice constants with graphene. As during the fabrication process, the carbon atoms precipitate and segregate on Ni surface, the segregation behavior will be changed according to the cooling rate, and that has an influence on the thickness and quality of the produced graphene layers. High quality crystalline structure and well-controlled film thicknesses are attained at medium cooling rates [393]. CVD synthesis of graphene without catalytic metal substrate, the so-called non-catalytic CVD process, in which graphene is grown onto a dielectric substrates (e.g., silicon dioxide SiO_2) is also possible [394], and highly desired for electronics and optoelectronics [395, 396]. In practice, growing graphene on dielectric substrates suffers from the issue of inhomogeneity and/or low quality of fabricated graphene layers. However, suppressing the secondary nucleation of graphene (those unwanted graphene nuclei formed after the initial graphene islands formation) can lead to ultrauniform graphene monolayer on dielectric substrates [397].

6.3.3 Mechanical exfoliation

It is one of the widely applied top-down approaches for obtaining single-layers of graphene (SLG) or few-layers graphene (FLG), especially in a research laboratory. The fabrication process begins fundamentally with a graphite mesa, usually obtained either from natural graphite, or from synthetic graphite such as a highly oriented pyrolytic graphite (HOPG). Natural graphite is a mineral extracted from geologic deposits, and it is a pure form of carbon that has normally black crystalline flakes. It has vital properties, like, chemical inertness, thermal stability, and high electrical conductivity. Usually natural graphite is classified according to the crystallinity, grain-size, morphology of its ore, e.g., amorphous graphite (microcrystalline), and crystalline (flakes) [398]. HOPG graphite is a man-made graphite, highly-pure and ordered, covalently-bonded within its layers, and bonded via van der Waals between its graphene sheets due to imperfections in its production. Such type of graphite does not exist in its own in nature, and prepared by similar process to pyrolitic carbon,

which is made by pyrolysis of hydrocarbon (e.g., methane) at elevated temperature, but here for HOPG, during the recrystallization, high tensile stress and pressure are applied along the basal-plane direction to align the crystallites into highly ordered layers [399]. Due to its high conductivity, HOPG is considered as metal, with a shiny glare, as shown in Fig. 6.15. Graphene can also be prepared from the so-called Kish graphite (KG), which is extracted from industrial waste (steel waste) of blast furnace area dust particles, using an effective purification process [400].

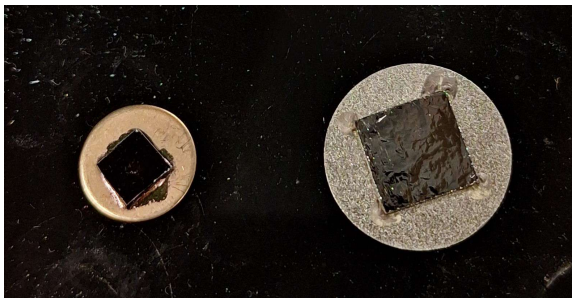


Figure 6.15: Two stacks of HOPG graphite mesa, small (left) and large (right).

Graphene is obtained by peeling off a bulk graphite (similar to the one shown in Fig. 6.15) layer by layer. Overcoming the van der Waals attraction forces adhering the graphite layers requires a mechanical resistance, which is attained by exfoliating graphene by one of two routes, i.e., by applying normal force or lateral force. It is normally possible to obtain graphene by exerting normal force by micromechanical cleavage using a scotch-tape [339, 340]. Exploiting the graphite self-lubricating ability, one can exert lateral force in the lateral direction of graphite, as pictorially depicted in Fig. 6.16. Shown in the same figure also another route for graphene preparation, through force generated during mechanical exfoliation, which leads to fragmentation. This route is like a double-edge sword, where on one hand, it allows easier exfoliation as the graphite is fragmented. On the other hand, graphene produced through this route has small lateral size, not favorable for applications on demand for large-size flakes [401].

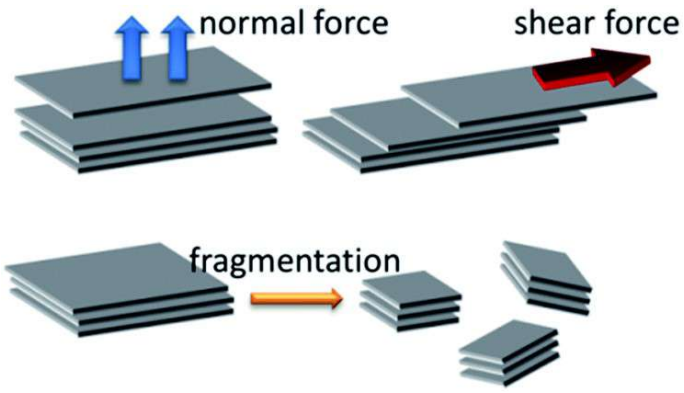


Figure 6.16: Two routes for exfoliating graphene from bulk graphite, along with the fragmentation auxiliary route [401].

For using graphene and thin graphite films as optical Kerr media, we aim for obtaining adequately large flakes, with minimal defects. The reason for that is the laser spot size of pump (gate) beam, even when it is tightly focused is in the range of a few μm. If the flake size is small, the heat dumped into graphene/thin graphite film can readily induce thermal damage, as this heat will not be efficiently dissipated being restricted by the small flake size. If the flake size is large, this ensures reasonable heat dissipation during optical Kerr shutter experiments. Because of this reason, we follow the approach devised by Huag et al. [402] (2015) in which the traditional mechanical exfoliation technique was modified for achieving large-area and high quality graphene. A fundamental difference in our work is that, unlike the paper, we prepare our graphene samples directly onto glass substrates. Additionally, during the preparation of graphene samples, we adapted the technique to suit our available equipment, and achieve more fabrication feasibility.

The preparation steps we carried out began with cleaning the glass substrates with distilled water and isopropanol by rinsing them into a beaker for 10 mins inside an ultrasonic cleaner. After that an UV Ozone cleaner is used for cleaning each side of the glass substrates for 10 mins. The purpose of this step is to destroy any organic molecules remaining on the glass surface. To ensure sufficient cleaning, one can clean the glass substrate for prolonged times in both steps. Once the clean glass substrates are taken out of the UV Ozone cleaner, the exfoliation steps should promptly start to avoid any deposition of any potential pollutants in the lab. It is highly recommended, whenever possible, to prepare graphene samples inside a clean room to avert any contamination. In the mechanical exfoliation step, we use a 19 mm $\times$ 33 m scotch magic tape from 3M company. For successful large-area graphene flake production, the type of the scotch tape, as well as, the glass substrate must be carefully chosen. Out of experience, the best glass substrate that ensures good adhesion to graphene is the one obtained from Menzel Gläser company, with 1 mm

thickness. Throughout our work, we tried other glass substrates, but due to their weak adhesion, no graphene/thin graphite films were attached to them. Processing that kind of glass with O_2 plasma was not absolutely effective to overcome the weak adhesivity. After a sufficiently long piece of scotch-tape was cut by a scissor, the first part of the scotch tape should be applied to the surface of the graphite mesa to pick up a relatively thin sheet of graphite. Then, the scotch tape should be peeled a few times to reduce its thickness, and eventually be pressed against the glass substrate and remain there until the fabrication process is over. It is highly preferable to cut a small piece of scotch tape initially, and exfoliate the upper surface of the graphite mesa, before proceeding with the actual mechanical exfoliation, to avoid using potentially contaminated graphite layers. According to the fragmentation issue we discussed before [401], and the recommendation of the paper [402] we follow, peeling graphene layers from graphite on the scotch tape roughly four times is reasonable for getting graphene flakes with large-area. Further exfoliation will give rise to smaller graphene flakes that are not needed in our application. Once the samples are ready, we heat a laboratory heater at $\sim$ 100 °C and we place our glass substrates containing graphene covered with their scotch tapes for 2 mins. At the end, we take them out and let them cool down to room temperature, and remove the scotch tape by pulling it off quickly from the glass substrate. This sample annealing is performed to remove gas molecules trapped at the interface between the glass substrate and lower surface of graphene flakes. Therefore, the heating increases the pressure of those gas molecules, ejecting them through the edges of graphene flakes. When the sample is cooled down, the pressure on the upper surface of graphene will press it down, which leads to good adhesion between the flake and the substrate with large-yield. Here, our graphene samples are ready for subsequent characterizations. Some examples of our samples we prepared following this approach are shown in Fig. 6.17.

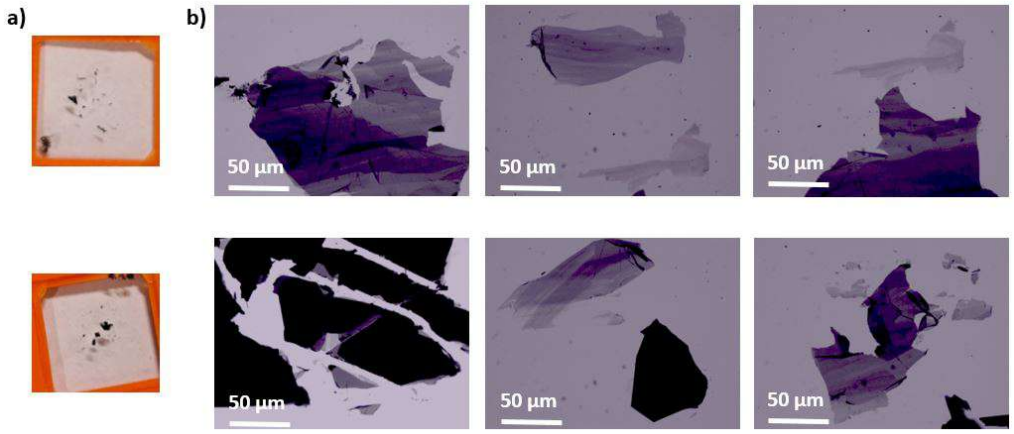


Figure 6.17: Two different samples prepared using mechanical exfoliation technique. (a) Photograph of the two samples, (b) Optical micrographs showcasing graphite, thin graphite films, and graphene contained in those samples.

We see in Fig. 6.17 (a) that this approach is successful for producing large-area flakes, especially for graphite, which is readily seen in the photograph with the naked eye. An optical micrograph taken with Zeiss optical microscope with 20×, 0.25 NA objective lens, showing various thicknesses, are shown in Fig. 6.17 (b), whereas the dark black flakes and strips represent graphite residuals, and thin graphite films, which have greyish color, plus very thin layers that correspond to FLG. Traditionally, for fabrication of graphene electronic devices, either the SLG/FLG layers of interest are transferred to another substrate, or thick graphite flakes are lifted off by, e.g., ultrasonication in isopropanol. In our case, this is an arbitrary choice, which we did not make, since we designed a simple optical microscope into our optical Kerr shutter to target the layers of interest, as we shall explain in section 6.5 and 6.6.

6.4 Identification of number of layers

6.4.1 Optical microscopy

The opacity of a suspended monolayer of graphene is only defined by its fine-structure constant, $\alpha = e^2/\hbar c \approx 1/137$, where c is the speed of light. This parameter describes the coupling between the relativistic electrons of graphene and light, which associates with quantum electrodynamics, not material science. Such an astonishing aspect arises as a consequence of graphene's unique electronic properties [403]. The absorption of this one atom thick layer is $\pi\alpha = 2.3\%$ from the incident white light, which is a universal constant. Optical properties of thin films are described in terms of optical conductivity G. The optical conductivity has a universal constant value $G_0 \equiv e^2/4\hbar$, in case the photon energy E is much larger than both temperature and

Fermi level E_F. The implication in this case is that absorption (P), transmittance (T) and reflectance (R) can be both expressed in terms of universal constant values. Kuzmenko et al. [404] found out that $T = (1+2\pi G_0/c)^{-2} = (1+0.5\pi\alpha)^{-2} \approx 1-\pi\alpha$, from which we get $R \equiv 1/4\pi^2\alpha^2 T$, for normal light incidence. Both T and R are measurable quantities, unlike the optical conductivity G. Using a white light source, the transmittance of different graphene layers have been measured across the visible range, as shown in Fig. 6.18.

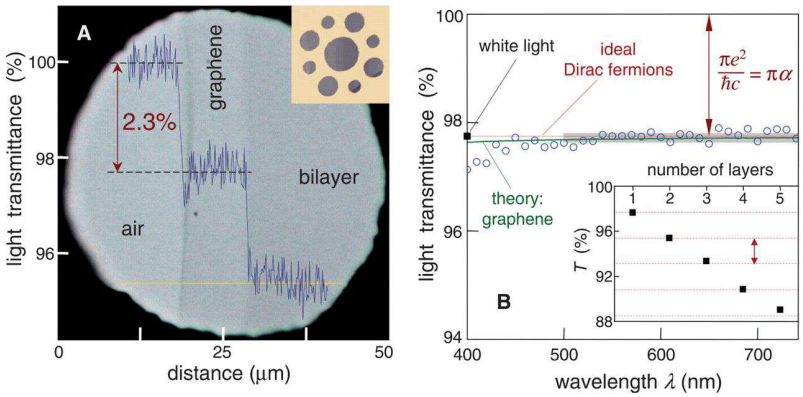


Figure 6.18: Optical vision and transmittance of graphene. (a) Optical vision of monolayer and bilayer graphene, (b) Light transmittance across visible range for monolayer (open circles), ideal behavior of Dirac fermions (red line), expected theoretical behavior (green line). In the inset, reduction of transmission % per graphene layer (black squares) [403].

The light transmittance was measured along a monolayer and bilayer of graphene, Fig. 6.18 (a), and found that the absorption ratio of the monolayer is indeed 2.3%, where transmittance drops with the same ratio from monolayer graphene to bilayer. For a monolayer such absorption was almost constant, see Fig. 6.18 (b) with excellent agreement with theoretical prediction. Needless to say, the transmittance of light decreases as the number of graphene layers increases, as shown in the inset of Fig. 6.18 (b). Optical microscopy has been proven to be a viable tool for visual detection of graphene layers. It evidently overcome the shortcomings of other types of microscopes, i.e., scanning-tunneling, electron and atomic force microscopes (AFM), which are not hindered by their atomic resolution to search and find graphene flakes in large substrates, in addition to being slow, and not able to provide clear signatures to distinguish mononlayer from thick graphite on the sample. Despite its faint visibility, graphene can be seen via an optical microscope, as its opacity (2.3% absorption per layer), which is enough to allow interference between the incident light and that reflected off, e.g., Si substrates through its upper layer of SiO_2, with a reasonable contrast. Blake et al. [405], used a Fresnel's law based model to quantify the reflected intensity of graphene layers onto SiO_2/Si substrate, hence calculate the contrast; which is defined as the relative intensity of reflected light from graphene and the

substrate, normalized by substrate reflected intensity,

$$C = \frac{I_{Graphene} - I_0}{I_0} \tag{6.10}$$

whereas their system was modelled sequentially as air/graphene/SiO_2/Si. It was found out that the oxidized Si layer (SiO_2) thickness on top of Si substrate, along with the wavelength of the monochromatic illumination used are crucial factors for maximizing graphene's visibility. The optimal thickness of SiO_2 was reported to be anywhere between 90 and 280 nm, and the green illumination is appropriate given our eyes sensitivity.

For counting the layers of our graphene samples, we used a somewhat similar model developed by Gaskell et al. [406], but we adapted it for optical transmission, rather than optical reflection. This model allows finding the location and counting of graphene layers on bulk transparent substrates, e.g., soda-lime glass. The model employed in Ref. [405] differs from the one used in Ref. [406] in that the former assumes a certain thickness of graphene monolayer (0.34 nm), and uses a complex refractive index of bulk graphite $n_1 = 2.6 - 1.3\mathrm{i}$, while the latter treats graphene as infinitesimally thin conducting sheet, with universal optical conductance $G = me^2/4\hbar$, where m is the number of graphene layers. Using a commercial Zeiss optical microscope, with the configuration shown in Fig. 6.19, namely glass/graphene/air, where the refractive index of air $n_2 = 1$, and the refractive index of the fused glass substrate $n_1 = 1.4571$ at $\lambda = 630$ nm filtered from a white light source and incident at normal angle. From the model, the transmittance coefficient is

$$t_s = \frac{2n_1 \cos\theta_i}{n_1 \cos\theta_i + n_2 \cos\theta_t + m\pi\alpha}, \tag{6.11}$$

where m is the number of graphene layers, α is the fine structure constant 1/137, θ_i and θ_t are incidence and transmittance angles, equal to 0 (normal incidence), respectively. The transmission T_s is obtained from the following relationship, which reads

$$T_s = \frac{n_2}{n_1}|t_s|^2. \tag{6.12}$$

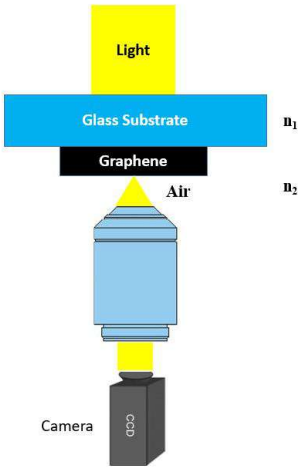


Figure 6.19: Configuration of an optical microscope for counting graphene layers onto fused glass substrates.

From Eq. 6.11, we see that the only quantity that changes is m, depending upon the number of graphene layers, given that other quantities are constant. Thus, only $|t_s|^2$ will be changed in Eq. 6.12. The transmitted light intensity ratio through the glass substrate I_{sub} is determined from T_s, when $m = 0$. Accordingly, I_{sub} is roughly 0.965 ($\sim$ 96.5 %) of the incident intensity I_0. Likewise, the value of T_s for a particular number of graphene layers (m) can be calculated, then the contrast ratio of transmitted light is achieved as follows

$$C = \frac{I_{gr} - I_{sub}}{I_{sub}} \times 100 \tag{6.13}$$

A theoretical calculation of the contrast ratio between the glass substrate and a monolayer, bilayer, trilayer, four-layer, five layer of graphene showed that it is 1.86%, 3.62%, 5.28%, 7.04%, and 8.60%, respectively. This calculation was carried out assuming a light illumination at 630 nm was used. In practice, for finding the number of graphene layers, an image analysis software (i.e. ImagJ) could be used, where a certain area of the substrate is determined by a frame, from which we determine the transmitted light intensity I_{sub} passing through it. Then, we move this frame to the graphene layer of interest, and get the intensity of transmitted light I_{gr}. Subsequently, the contrast ratio is calculated according to the relationship of Eq. 6.13. One can find the number of layers by comparing the experimental C-value to another one calculated theoretically corresponding to the specific number of graphene layers, m.

Using optical microscopy, the distinction of different graphene layers was possible. For example, in Fig. 6.20, we show a micrograph in which a monolayer of graphene was identified, albeit barely visible, as well as a bilayer of graphene. In fact, after roughly 10 layers of graphene, the flake cannot be considered graphene with its

unique properties anymore, and it would be rather considered as thin graphite films. Thin graphite films have demonstrated reasonable optical Kerr signal, as we shall discuss in section 6.6.

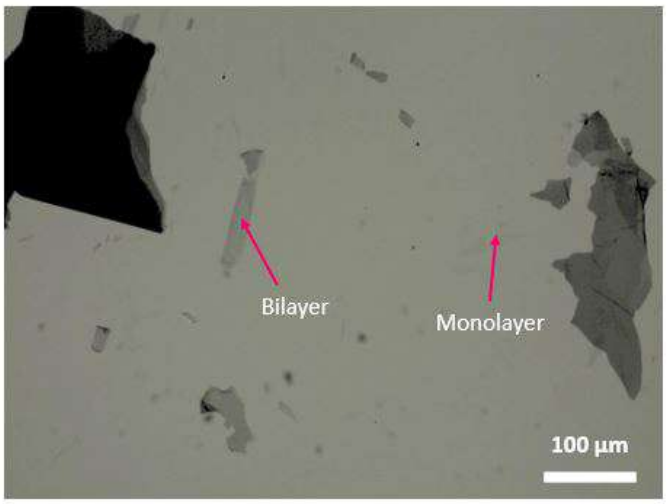


Figure 6.20: Optical micrograph presenting a monolayer (barely seen) and a bilayer of graphene illuminated by a white light.

The same methodology has been utilized in other samples, having different numbers of layers, few of them were graphene, while the rest were thin graphite films, see Fig. 6.21.

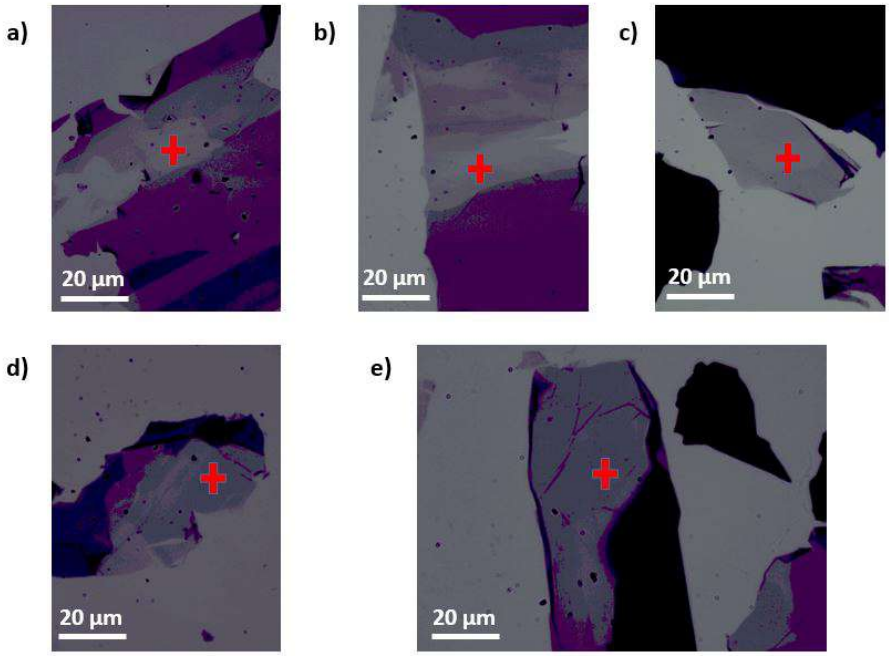


Figure 6.21: Optical micrographs of different graphene and thin graphite films under illumination of light at 630 nm, each of which has a different number of layers. The regions of measurements are marked with a plus sign (red). (a) 3 layers of graphene, (b) 7-8 layers of graphene, (c) Thin graphite film of 13 layers, (d) Thin-graphite film of 17-18 layers, and (e) Thin graphite film of 23-24 layers.

The white light of the microscope was filtered to be at 630 nm for illuminating the samples. The experimentally determined contrast ratio (C-value) of Fig. 6.21 (a) was found to be 4%, and the theoretically calculated C-value (5%) shows that it is a trilayer of graphene. The region selected in Fig. 6.21 (b) has an experimental C-value of 12.5%, while the theoretical C-values are 11.7% and 13.2%, indicating that this flake has 7-8 layers of graphene. Apparently, the region selected in Fig. 6.21 (c) is a thin graphite film, where the experimental C-value is 20 %, and the theoretical C-value is 20.2%, which corresponds to 13 layers. Similarly, Fig. 6.21 (d) is a thin graphite film, with experimental C-value of 26% but the theoretical C-values are 25.2% and 26.4%, indicating that this thin graphite film has 17-18 layers. The thin graphite film of Fig. 6.21 (e) has an experimental C-value of 32.35%, while the theoretical C-values are 32-33%, meaning this film has 23-24 layers.

It is important to emphasize that this technique is highly reliable, given that sufficient contrast is obtained between the substrate and graphene layers. In the work of Ref. [406], the technique was able to count up 9 layers of graphene in the optical reflection microscopy. For thicker flakes (thin graphite films), they avoided modelling graphene layers as infinitesimally thin layers. Instead, they modelled those flakes using a complex refractive index, n_{g}, similar to the approach followed in Ref. [405].

6.4.2 Raman spectrum of graphene layers

Raman microscopy has proven to be a powerful tool to distinguish SLG and FLG samples. It is based on the distinct Raman spectrum exhibited by graphene flakes. Although the initial imaging and recognition of a SLG in the early work of Geim and Novoselov [333] in 2004 was carried out via optical microscopy and AFM, a technique for precise determination of graphene's number of layers was lacking. In 2006, Ferrari et al. [407] used Raman spectrum as a tool to specify the number of graphene layers. Their graphene samples were prepared onto SiO_2/Si substrate via micromechanical cleavage technique, and they contained single, bi-, multi-layers of graphene; some of them were suspended (freely standing), while some others were supported onto substrates. Using a commercial Raman spectrometer, a clear distinction between graphene and graphite can be attained, see Fig. 6.22.

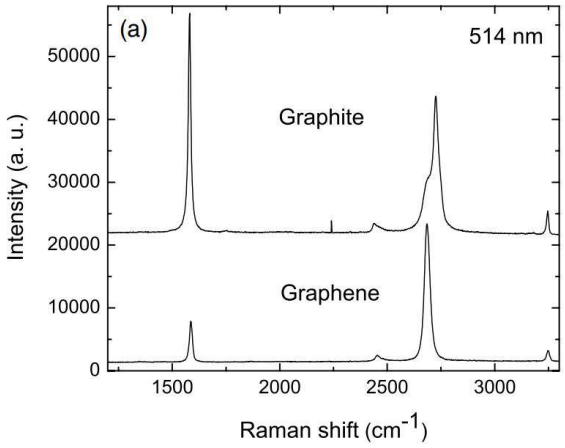


Figure 6.22: Raman spectrum of graphite (top) and graphene (bottom), measured with Raman spectrometer at 514 nm [407]. The 2D peak is rescaled for both to give the same height.

We see in Fig. 6.22 that both graphite and graphene have the well-known G and 2D peaks, appearing at ~ 1580 cm^{-1} and ~ 2700 cm^{-1}, respectively. It can also be seen the absence of the disorder-induced D peak, implying that those samples did not contain any defects, at least within the detection sensitivity of the used Raman spectrometer. Notably, the 2D peak in graphene is higher than its G peak, approximately four times, which is not the case in bulk graphite. One can also observe that the 2D peak in bulk graphite consists of two peaks, $2D_1$ and $2D_2$, roughly 1/4 and 1/2 the height of the G peak. The distinction of a SLG and a large number of graphene layers is identified through the evolution of the Raman spectrum, as the number of layers is increased, see Fig. 6.23, recorded at two excitation wavelengths 514 nm (Fig. 6.23 (a)) and 633 nm (Fig. 6.23 (b)), and notice the changes of the 2D peak. For example, a bilayer of graphene exhibits a much broader 2D peak and

an upshift of its frequency, compared to a SLG. This peak is actually an overlap of four different peaks, $2D_{1B}$, $2D_{1A}$, $2D_{2A}$ and $2D_{2B}$, each of them having different amplitudes, as shown in Fig. 6.23 (c), with $2D_{1A}$ and $2D_{2A}$ having relatively higher intensity than the other two peaks.

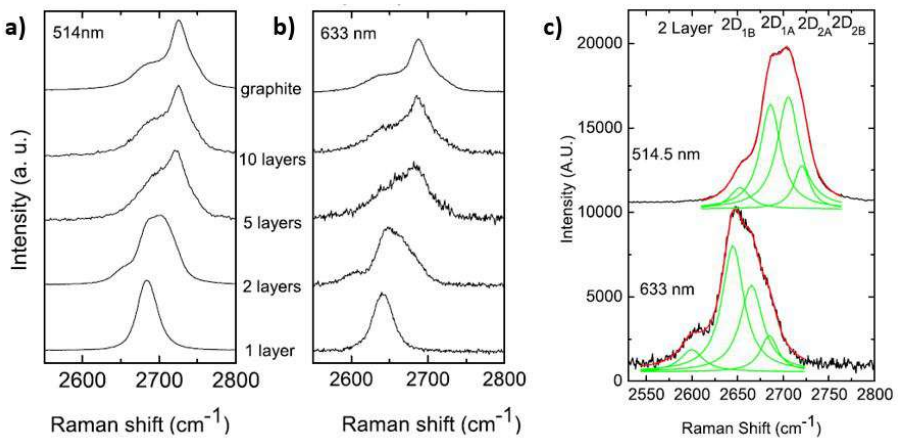


Figure 6.23: Evolution of 2D peak with the increase of the number of graphene layers. (a) Raman spectrum of 2D peak for 1, 2, 5, 10 layers, graphite, respectively excited at 514 nm, (b) The same spectrum excited at 633 nm, (c) Four peaks underlying the 2D peaks, at 514 nm (top), at 633 nm (bottom) [407].

The four Raman 2D peaks of bilayer graphene constituting the main 2D peak originate from four doubly resonant (DR) Raman scattering processes, as a result of the modification of the electronic dispersion curve due to stacking a second layer of graphene on top of the monolayer. Although the conduction and valence bands of the bilayer graphene remains with zero-gap, the electronic bands 1 (corresponds to 1st layer) and 2 (corresponds to the 2nd layer) bend around the points K and K′ [408]. Stacking a third layer of graphene will lead to six DR Raman scattering processes [354].

The measurements of Raman spectrum conducted at the center of graphite and graphene samples did not exhibit D peak, as we point out before. Nonetheless, as this peak arises as a result of any kind of disorder, i.e., by breaking the translation symmetry of the carbon crystalline, it is possible to detect a D peak at the edge of each sample. Fig. 6.24 shows two D peaks, one associated with graphite, measured at its edge, another associated with a SLG measured also at its edge. In addition to the clear distinction between a SLG and graphite in terms of the intensity of both G and 2D peaks, the D peak shown in Fig. 6.24 provides another clear distinction between them. Notably, the D peak associated with SLG is a single sharp peak, while the same peak is much broader and upshifted in frequency, as well as composed of two peaks, D_1 and D_2.

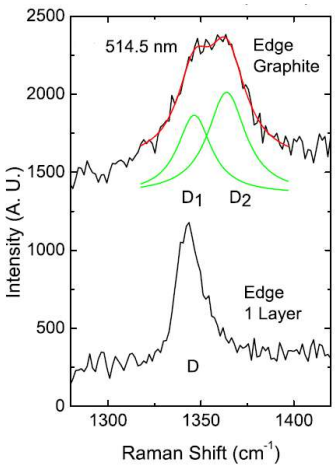


Figure 6.24: Spectrum of Raman D peak measured at the flake's edge at 514 nm illustrating the difference between a SLG (bottom) and graphite (top) [407].

To conclude, Raman spectroscopy has demonstrated that it can uniquely distinguish between a SLG and a bulk graphite. Moreover, for up to five layers of graphene, as noticed from Figs. 6.24 (a) and (b), it shows clear distinction in its Raman spectrum. Unfortunately, beyond five layers, the Raman spectrum does not exhibit any clear change that can enable counting a large number of layers, which poses a limitation on this technique. Throughout our work, we did not use Raman spectroscopy for counting graphene's layer of our samples. Instead, we employed Raman spectroscopy to study the induced damage, due to exposure of our fs laser, as we shall explain in the next section.

6.4.3 Atomic force microscopy

Atomic force microscopes (AFMs) have been an indispensable tool for characterization of thin film qualities, such as morphology, surface roughness, and uniformity. Although AFM is fundamentally used for characterization of those properties, it can also serve for thickness measurements, through determination of height profiles of graphene or other 2D crystals. The number of graphene layers, N, is often estimated by measuring the height of the sample, and dividing it by the interlayer distance, 0.34 nm. For SLG the height estimation via AFM relies quite strongly on the substrate onto which the SLG is deposited [409]. For example, the height of a SLG on SiO_2 substrate is $\sim$ 1 nm [333], while on mica it has a height of $\sim$ 0.4 nm [410]. Such discrepancy of the results concerning the SLG thickness implies that AFM is not a reliable tool for SLG. The discrepancy can be attributed to variation in interactions between the substrate and graphene, and also between the AFM probe and graphene, whereas those interactions rely on the substrate surface energy, graphene structure and sample preparation [411]. For example, water or small organic adlayers between

graphene and mica substrate has been observed when graphene is fabricated in a highly humid environment [412, 413].

The operating principle of an AFM works by measuring the force between a tip and the sample to reconstruct surface topology. It consists of a cantilever made of silicon (Si) or silicon nitride (SiN) with a sharp tip of a nanometer-sized radius used to scan the sample. When this sharp tip approaches the surface of the specimen, the force between the surface of the specimen and the tip deflects the cantilever according to Hooke's law. This deflection is monitored via a laser spot, reflected off the cantilever's surface and detected by a position-sensitive photodiode detector, as schematically shown in Fig. 6.25 [414]. Usually the specimen is moved via a piezoelectric scanner at angstrom scale.

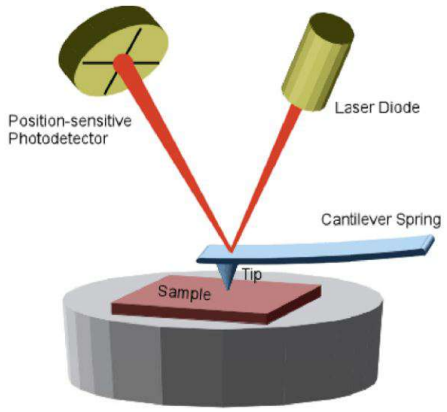


Figure 6.25: Scheme showing the components of a typical AFM and its operating principle [414].

There are commonly three operation modes of AFMs: contact mode, non-contact mode and tapping mode. In contact mode, the tip (probe) of the cantilever touches the surface of the sample. This leads to scratches of the graphene surface, which is why it is regarded as a destructive mode. On the contrary, the tip in non-contact mode scans the surface of the sample at a distance, 1 or 2 nm away from it. The main interaction in this mode is attraction between the tip and the surface of the sample. This requires usage of a fast feedback system to avoid crushing the AFM tip into the sample surface. The most frequently used mode is the tapping mode, in which the cantilever oscillates at a characteristic resonant frequency, whose amplitude is a few hundred nanometers. Despite being highly favored for graphene samples investigation, resolving the substrate-graphene height is challenging with AFM tapping mode. This is because of the strong differences in the tip attraction/repulsion forces between the insulating substrate and the semi-metallic graphene. Actually, this makes it difficult to differentiate between a substrate and the first graphene layer. Theoretically, one can expect a gradual increase of 0.34 nm, as graphene increases by one layer at a

time. Due to the reasons we discussed in case of mica and SiO_2 substrates, e.g., water/organic molecules underneath graphene, the determination of actual surface height is quite difficult. For an example of an attempt to use AFM in the tapping mode, shown in Fig. 6.26, which shows variation of the number of graphene layers of two samples, prepared via mechanical exfoliation from a HOPG graphite [414].

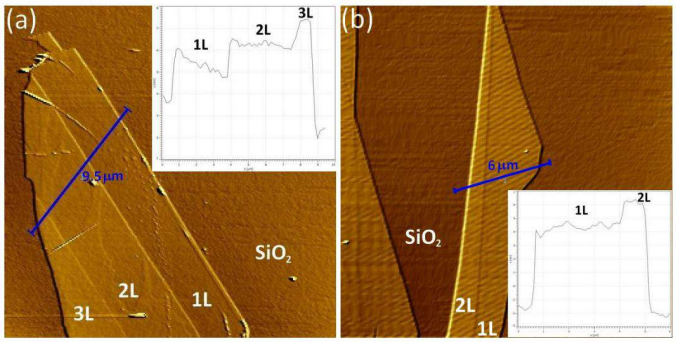


Figure 6.26: Phase image of two graphene samples (in (a) and (b)) deposited onto SiO_2 substrate. The blue lines are cross-sectional profiles across different graphene layers. The inset is the height profile of each sample along the blue line in nm units [414].

Similar to Raman spectroscopy, we did not use AFM to measure the height profile of our graphene and thin graphite film samples. The AFM, though, will be used later for investigating the relationship between the optical Kerr signal strength and the number of graphene layers, particularly for thick flakes (thin graphite films).

6.5 Thermal transport and laser damage of Graphene

6.5.1 Overview of graphene's thermal properties

Thermal properties of graphene are derived from the interesting characteristic of graphite, where there is a clear distinction between bonding characters within and between its planes of carbon atoms. Within a single-sheet of graphite (in-plane), the carbon atoms form hybridized sp^2 orbitals, connecting the carbon atoms together with a covalent bond, leading to stable hexagonal aromatic rings. In contrast, the separate single sheets of graphite are held together with a weak interatomic van der Waals force, giving rise to an anisotropy of its thermal properties. This anisotropy manifests itself in the difference of an *ab initio* calculated bond energies, more than two orders of magnitude, ranging from 50 meV for interplanar bond to 5.9 eV for an intraplanar bond [415]. Besides the low mass of carbon atoms, the thermal anisotropy

gives graphene and its related materials their unique thermal properties.

Understanding the unique thermal properties of graphene requires careful inspection of its phonon dispersion modes. As we mentioned in subsection 6.2.4, there are three optical (O) phonon modes, and three acoustic (A) phonon modes, and that the dispersion of those phonons is described by relationship between the phonon energy (E) (or frequency ω) and the phonon wavevector q. The atomic displacements along the wave propagation direction correspond to longitudinal (L) modes, while the in-plane displacements perpendicular to the propagation direction correspond to transverse (T) modes. In 2D materials like graphene, there are also out-of-plane atomic displacements, known as flexural (Z) phonons. These out-of-plane phonons can also be optical or acoustic phonons [416], see their dispersion curves in Fig. 6.27.

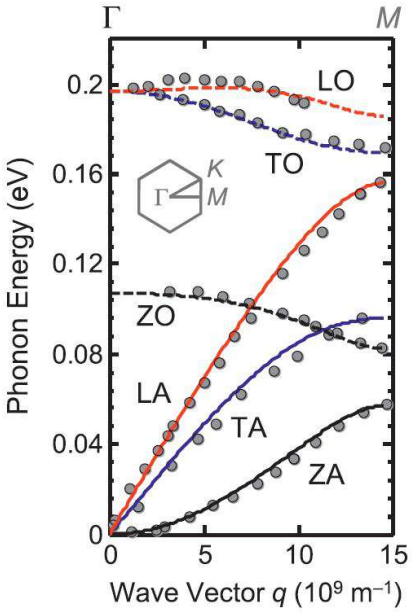


Figure 6.27: Phonon dispersion curves along the high symmetry points Γ-M, for longitudinal (L), Transverse (T), Flexural (Z) phonons modes [416].

We notice from Fig. 6.27, that near point Γ (zone-center in BZ) where q is low, both the transverse acoustic (TA) and longitudinal acoustic (LA) have linear dispersions of $\omega_{\mathrm{TA}} \approx \nu_{\mathrm{TA}} q$ and $\omega_{\mathrm{LA}} \approx \nu_{\mathrm{LA}} q$, respectively. Whereas the group velocities $\nu_{\mathrm{TA}} \approx$ 13.6 km/s and $\nu_{\mathrm{LA}} \approx 21.3$ km/s are 4-6 times higher than those in silicon [417] or germanium [418], which is due to the strong sp^2 in-plane bonds. In contrast, the flexural acoustic (ZA) phonons have approximately quadratic dispersion, $\omega_{\mathrm{ZA}} \approx \alpha q^2$, where $\alpha \approx 6.2 \times 10^{-7}$ m^2/s. The unusual thermal properties of graphene occur owing to the presence and modifications of ZA modes.

The specific heat of a material defined as $C = \mathrm{dU/dT}$ represents the change in energy density U, when the absolute temperature T changes by 1 K. It determines

the thermal energy stored within a body, as well as, how quickly it cools or heats, through the thermal time constant $\tau \approx RCV$, where R is the thermal resistance of heat dissipation, and the volume of the body V. The thermal time constant for a nanoscale object like SLG, or carbon nanotube is $\simeq$ 100 ps [419], and nearly 1 ps for phonon modes relaxation [420]. The specific heat of a material such as graphite or graphene is stored in the lattice vibrations (phonons) and free conducting electrons, $C = C_{\rm ph} + C_{\rm el}$. In graphene, the heat storage is dominated essentially by phonons at any temperature $>$ 1 K, which is different from bulk graphite [421], and the specific heat increases with temperature, as shown in Fig. 6.28. We notice in this figure the classical behavior of solids, where at very high temperatures, the specific heat is nearly constant, due to the excitation of all atomic degrees of freedom (translational and vibrational degrees). For graphite, the $C_{\rm p} \approx 0.7$ J g^{-1}K^{-1} reaches 1/3 of the upper value at room temperature. For an isolated single graphene sheet, similar behavior is expected at room temperature, when all flexural ZA phonons are thermally excited. Nevertheless, the dispersion of ZA phonons of graphene can be altered or suppressed when it is in contact with a substrate (supported graphene) [422], and if it is intercalated [423, 424].

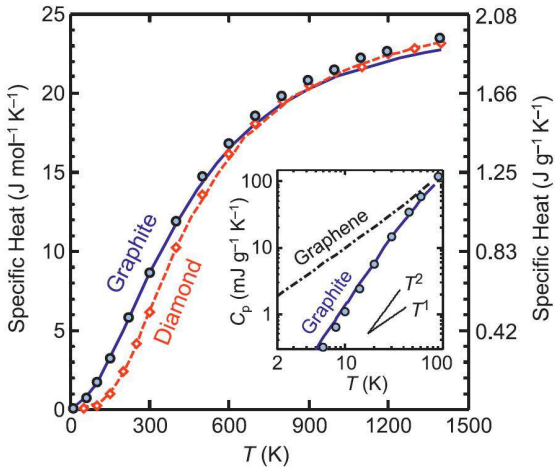


Figure 6.28: Specific heat curves of graphite, diamond and graphene as a function of temperature. The inset shows that specific heat is mostly higher in an isolated single graphene sheet, and dominated by phonons above $\sim$ 1 K[416].

The specific heat at low temperatures ($T \ll \Theta_D$, where Θ_D is Debye temperature) scales as $C_{\rm ph} \sim T^{(d/\alpha)}$ for a phonon dispersion of $\omega \sim q^n$ in d dimensions, which is why the $C_{\rm ph}$ contains significant information about dimensionality of the system, along with its phonon dispersion [425]. Given that an isolated graphene sheet is a 2D material, thus $d = 2$, and the out-of-plane ZA phonons have quadratic dispersion, hence $\alpha = 2$, the behavior of $C_{\rm ph}$ should be linear at very low temperatures, $\propto T$, when ZA phonons dominate, followed by a quadratic behavior, $\propto T^2$, because of

the linear phonon modes, LA and TA, as indicated in the inset of Fig. 6.28. This behavior is in contrast to graphite, whose specific heat rises $\propto T^3$ ($d = 3$, $\alpha = 1$) at very low temperatures (< 10 K), owing to the weak interlayer coupling. This behavior changes at intermediate temperatures (10-100 K), whereas $C_{\rm ph} \propto T^2$, because of the in-plane linear phonons.

6.5.2 Thermal conductivity of graphene

The thermal conductivity of a material κ is the proportionality constant between the heat flux per unit area Q'' (W/m^2), and the temperature gradient ∇T, $Q'' = -\kappa \nabla T$, where the negative sign signifies that the heat flows from high temperature region to low temperature region. The specific heat and thermal conductivity can be related by this relationship $\kappa = \sum C_\nu \lambda$, where ν is the average phonon group velocity, and λ is the mean free path, respectively. This expression is valid under diffusive transport conditions, when the sample dimensions is much greater than the mean free path ($L \gg \lambda$). The anticipation of superior thermal properties of graphene has driven tremendous effort for theoretical and experimental research to calculate and measure the thermal conductivity of graphene. For example, an *ab initio* based calculation has found that the thermal conductivity κ of a suspended single graphene sheet is in the range $\sim$ 2000-5000 W/mK at room-temperature, which depends on flake width, defect concentration, and roughness of graphene edges [426]. This theoretical value is in good agreement with the experimentally measured value of the thermal conductivity of a suspended graphene sheet at room temperature [345]. Such superior thermal conductivity is attributed to the long phonon mean free path that the graphene has, where these phonons are only limited, or scattered by graphene edges. Interestingly, and in contrast to bulk materials at room temperature (300 K), a suspended single graphene sheet exhibits an increasing, logarithmically-divergent thermal conductivity with the sample length, even for those samples with lengths greater than the average mean free path of phonons [427].

Furthermore, graphene layers exhibit a change of the thermal conductivity at room temperature from $\sim$ 2800 to 1300 Wm^{-1}K^{-1}, when the number of graphene layers increases from 2 to 4 layers [428]. This dimensional crossover of thermal conductivity is due to interlayer coupling of the low-energy phonons, and changes of Umklapp scattering. This fascinating result elucidates how the heat conduction evolves from low-dimensional materials, like single graphene sheets, to the 3D bulk material properties, as the number of graphene layers increases. In contrast, a molecular dynamics (MD) simulation in combination of phonon spectral analysis showed that the thermal conductivity of a supported SLG exceeds rapidly, reaching nearly 90 %

of bulk graphite thermal conductivity ($\kappa_{graphite} = 962$ $Wm^{-1}K^{-1}$) at 6 layers only, and saturates at a thickness of 13.4 nm (40 layers), see Fig. 6.29. Furthermore, SLG exhibits insensitivity of to the length-scaling of the flake width, unlike what normally a free standing SLG shows [429]. The reduction of of a supported SLG has been experimentally confirmed, where κ is 600 $Wm^{-1}K^{-1}$ near room temperature [430]. Such reduction of κ for a supported SLG is attributed to graphene-substrate interaction, whereas it blue-shifts the ZA phonons frequencies and broadens their spectral peaks, thereby shortening their lifetimes. The interaction with the substrate is strongly experienced with the first supported graphene layer. Additional graphene layers experience weaker damping from the substrate being shielded by the first layer. Also, those layers experience weaker inter-layer interactions, that is why thermal conductivity of supported graphene increases.

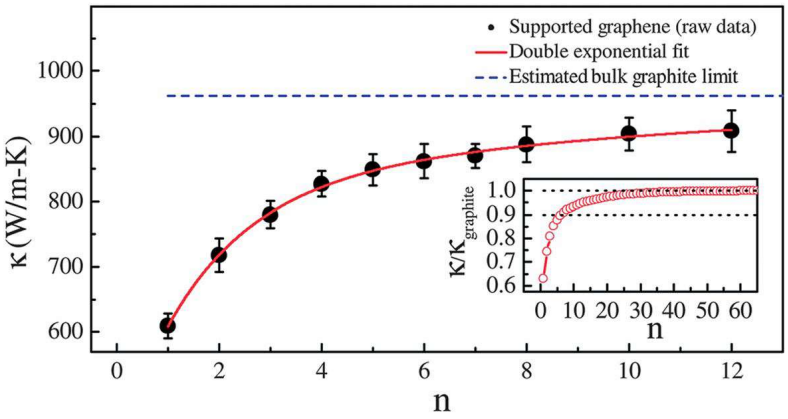


Figure 6.29: Raw data extracted from a MD simulation of thermal conductivity of supported graphene (black dots), with double exponential fit of *kappa* increase (red line). The dashed blue line is an estimated limit of bulk graphite. The inset shows a normalized κ for a large number of layers (open red circles), and the dashed lines are visual guides for saturation limit [429].

There are some techniques that have been developed for measuring the temperature change ΔT and thermal conductivity κ of graphene. The most famous and widely applied of them is a Raman-based spectroscopy technique, developed by Baladin et al. [345], in which a SLG sheet is suspended across a trench created into the SiO_2/Si substrate. This technique has drawn attention due to its relative feasibility as compared to other sophisticated techniques. It is a non-contact optothermal technique, which uses a focused 488 nm laser to create a small hot spot at the center of SLG. The generated heat is mostly dissipated laterally toward the edges, where large graphite layers act as heat sinks, as the air is a poor heat conductor, see Fig. 6.30.

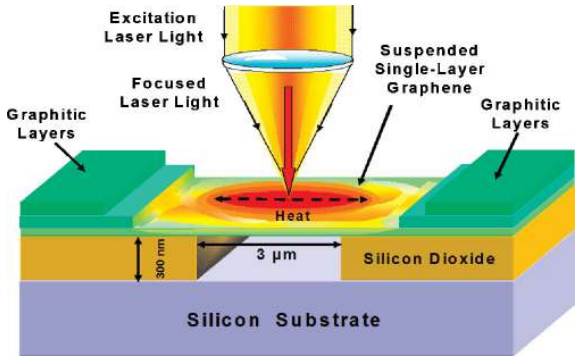


Figure 6.30: Scheme of an optothermal technique for measuring suspended SLG, laying across a trench (underneath), where the focused laser creates a hot spot that dissipates toward the edges [345].

The temperature measurement is carried out based upon the well-defined G peak of Raman spectrum, whose position shifts linearly with temperature, with a slope χ_G (temperature coefficient) that can be separately measured of the sample in a controlled environment [364]. The local temperature of the graphene hot spot increases with increasing the laser power, causing a redshift for the G peak. The temperature rise (ΔT) can be calculated by measuring the change in the G peak frequency ($\delta\omega$) for a known change of laser power (δP), given the knowledge of χ_G. The thermal conductivity κ is extracted using the heat-flow equations for a 2D sheet with plane-wave fronts, using the formula:

$$K = \chi_G \left(\frac{L}{2hW}\right) \left(\frac{\delta\omega}{\delta P}\right)^{-1}, \tag{6.14}$$

where L is the distance to the heat sink, h is graphene thickness, W is the flake width. The measurements showed that a suspended SLG has $\kappa \sim$ 4840 - 5300 $\mathrm{Wm^{-1}K^{-1}}$. The feasibility of this optothermal Raman-based technique, enabled expanding its application to other 2D materials, e.g., transition metal dichalcogenide (TMD), such as molybdenum disulfide (MoS_2) and tungsten disulfide (WS_2) [365].

6.5.3 Mechanisms of laser-induced damage of graphene

The exposure to highly intense light sources, such as fs lasers can cause damage to a bulk graphite, thin graphite films, or graphene. The damage can manifest itself in various forms, i.e., degradation of lattice like defects or cracks; or complete ablation of the carbon layers. Despite being detrimental, those deleterious effects can lead to controllable patterning of graphite or graphene, whenever the appropriate laser parameters are identified. This shows the importance of studying laser-induced damage of graphene or graphite films. For example, the controllable formation of

nanopores in graphene crystal structure [431] could be an alternative way to engineer the electronic properties [432], chemical reactivity [433], and surface interactions [434].

Since graphene layers are isolated from bulk graphite (exfoliated graphene), or accumulated on top of each other (CVD-grown graphene), it is essential to understand the damage mechanisms associated with each physical system that are inter-related to one another. A theoretical analysis of the physical mechanisms of the damage formation induced by fs laser pulses in graphite films was performed by Jeschke et al. [435], using MD calculations based upon a tight-binding (TB) Hamiltonian. This analysis identified a unique property of graphite, that is, it has two distinct laser-induced structural instability mechanisms, one at high laser energy and another at low laser energy. At high energy, e.g. $E_0 \geq 3.3 \pm 0.3$ eV/atom and a flux $F \approx 0.29 \pm 0.03$ J/cm^2, the fs laser excites electrons from occupied states to unoccupied states. Later, these electrons thermalize to a hot Fermi-Dirac distribution within ~ 10 fs, due to electron-electron scattering. This causes a rapid change of the interatomic potential leading to weakening of the in-plane C-C bonds. Within this very short time, the sp^2 in-plane C-C bonds will be broken. At 80 fs from the pulse maximum (pulse width = 20 fs), the disorder inside the in-plane graphite layers evolves with such high absorbed energy, and large volume expansion is observed. Some graphite planes will form strong covalent bonds (cross-linking), rather than being typically attached via the weak van der Waals forces, while some carbon monomers will be evaporated. This mechanism gives rise to melting and evaporation of graphite layers (graphene) from graphite films. The simulation of the time evolution of the ablation process on fs timescale from ordered graphene planes to disordered atoms is displayed in Fig. 6.31.

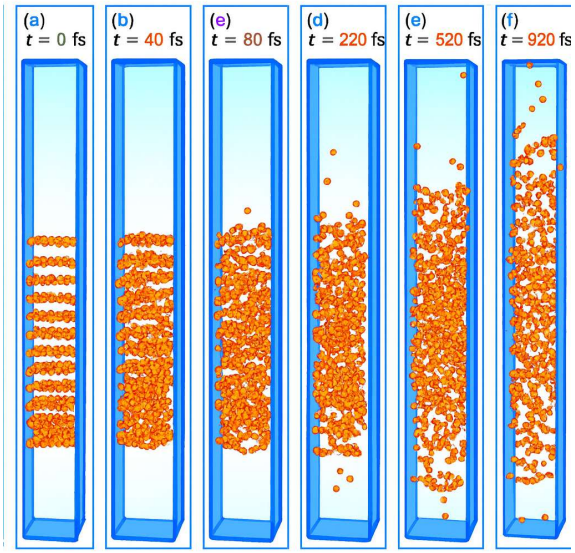


Figure 6.31: Ablation of graphite film with absorbed energy $E_0 = 4.0$ J/atom from a $\tau = 20$ fs laser pulse. Adapted from [435].

At low energy, e.g., $E_0 \geq 2.0 \pm 0.4$ eV/atom and a flux $F \approx 0.17 \pm 0.04$ J/cm^2, the laser pulse excites strongly out-of-plane (c-axis) vibrations in graphene sheets. Typically, the planes of carbon atoms are separated by ~ 3.4 Å. But, due to those vibrations, the graphene layers come close by $\sim$ 1.8-2.0 Å, whereas at such close distance the layers interact strongly with each other, with energy $E \approx 1$ eV, which results in collision and momentum transfer among them. In that situation, the surface layer with initially zero momentum acquires enough kinetic energy to escape the material. We see here that, with this mechanism, the graphene layers of the graphite film remain almost intact, with of course some disorder among layers, and removal of some surface layers. The temporal dynamics of such structural instability is shown in Fig. 6.32. It was also found in this study that the damage mechanisms are irrelevant to the laser pulse duration.

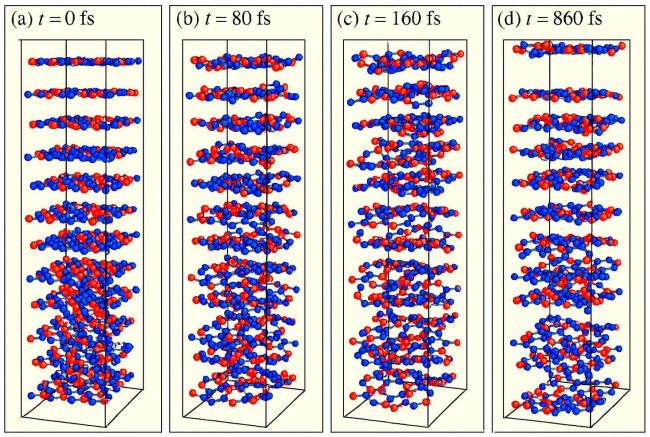


Figure 6.32: Temporal dynamics of vibrations and collisions of graphene layers, induced by an absorbed energy, E_0 =2.0 eV/atom below fragmentation and ablation threshold of surface layers. Adapted from [435].

The collision model presented here coincides with experimental evidence provided by Carbone et al. [436], giving an insight about the preablation mechanism. This experiment was conducted via the technique of ultrafast electron crystallography (UEC) to study the ultrafast structural changes caused by fs laser irradiation to a HOPG graphite crystal, within a range of 3.5-44.5 mJ/cm^2 of laser energy fluences. They showed that within 0-0.5 ps, the laser at 800 nm (1.55 eV) initially excites the electrons from the π bonding band to the antibonding π^* band. It is known that the band of the electronic structure in graphite/graphene is anisotropic, meaning that the excited electrons are not evenly excited in the momentum space. The energy band of graphite/graphene has a saddle point that exists in the vicinity of the M point, which matches the photon energy 1.55 eV of the excitation laser. This implies that the laser energy can be coupled efficiently to this saddle-point, and a large number of electrons can be easily promoted to this point (M point) of the Brillouin zone, as it has a large density of states. An experimental study carried out using femtosecond time-resolved photoemission of the photoexcited electrons, supported by *ab initio* calculations showed that in order for the excited electrons to decay from the M point, those electrons must transfer comparatively large momentum to secondary excitations, i.e., other e-h pairs, in contrast to electrons excited at any other region of the band structure (e.g., K or Γ points) [437]. Because the e-h pair spectrum has negligible overlap with the excited electrons near M-point, meaning that there is no sufficiently large momentum to decay those excited electrons, this transfer is constrained, due to momentum conservation law. Consequently, the excited electrons are expected to have longer lifetimes. However, a study by time-resolved terahertz spectroscopy showed that the majority of the photoexcited electrons at M-point couple efficiently to a certain set of phonons, called strongly coupled optical phonons

(SCOPs) [438]. Those are in-plane high frequency optical phonons to which the photoexcited electrons with high energy can efficiently couple to, and helps them to decay within a characteristic time as fast as 500 fs, depending upon the laser fluence. During that time, when the electrons are excited from the π band to the π^* band, then decay through electron-phonon coupling, the graphite experiences an initial contraction along its c-axis. It is believed that the excited electrons weaken the interlayer bond (van der Waals bond), leading to a situation in which graphene layers in the graphite get closer together along the c-axis. Following this contraction, the graphene layers experience an expansion, and SCOPs transfer their energy into other phonon modes of the graphite lattice within 5-7 ps. This expansion is huge such that it cannot be caused by thermal energy transfer from SCOPs to the overall lattice. That is why this preablation regime of graphite that can lead to damage of the lattice at higher fluences is considered nonthermal.

The damage caused by fs laser irradiation of graphene is commonly characterized by three main techniques: optical microscopy, Raman spectroscopy and atomic force microscope. In the work of Beltaos et al. [439], the damage effect of a Ti:Si laser at 840 nm, $\sim$ 150 fs, with 76 MHz on SLG and multi-layer graphene samples, prepared via mechanical exfoliation was characterized using the three techniques. A laser interaction at $\sim$ 350 mW power for several hours, led to a clear damage of graphite and a complete ablation of the SLG, as shown in Fig. 6.33. This shows that graphite has a higher damage threshold.

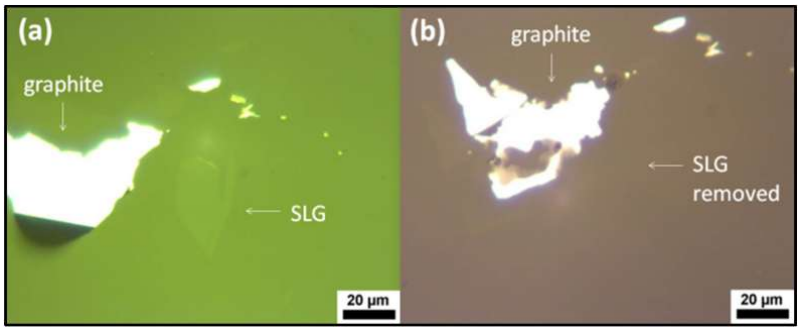


Figure 6.33: Optical micrographs of laser irradiated graphite and SLG, (a) Before and (b) After fs laser exposure [439].

Investigation of another sample of 10-15 layers, in the same work, showed degradation of graphene layers in some regions, while other regions suffered from an ablation with clear edges, see Fig. 6.34 (c) and (d) for images taken by an optical microscope, and Fig. 6.34 (a) & (b) for AFM images corresponding to certain determined regions.

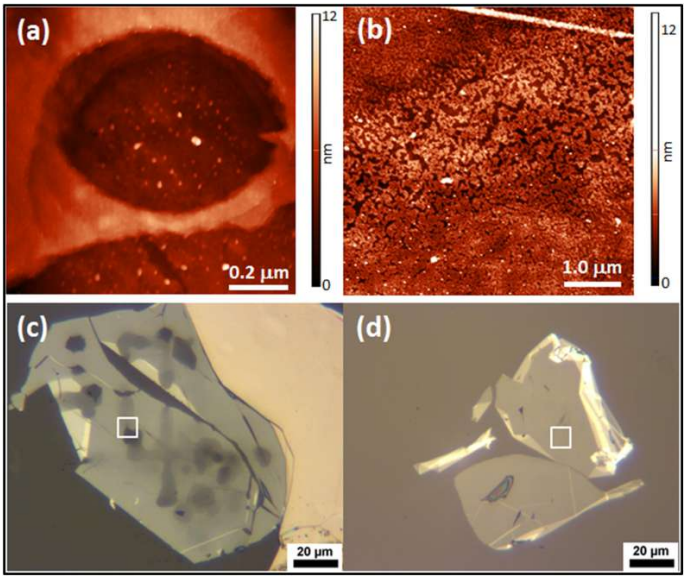


Figure 6.34: Degradation and ablation of 10-15 layers samples. (a) AFM image of an ablation of the region, highlighted in (c) (white square), (b) AFM image of degradation of a region highlighted in (d) [439].

Additional confirmation of the damage and degradation was obtained by taking the Raman spectrum before and after the laser irradiation, where the appearance of D peak is a clear indication of damage occurrence. Investigation of different laser power ranges 50-275 mW and exposure times (1-240 s), showed that the ablation threshold is $\sim$ 4.2 mJ/cm^2 and the ablation power and exposure time can be as little as 250 mW and 2 s, respectively. Roberts et al. [440] studied the effect of very short laser (50 fs) to a SLG fabricated by CVD technique, and found out that the SLG can withstand up to $\sim 3 \times 10^{12}$ W/cm^2 ($\sim$ 200 mJ/cm^2) from a single laser shot before it ablates. Also using 50 fs laser pulses and CVD grown SLG, later transferred to a sapphire substrate, Currie et al. [441] conducted a quantitative study of laser-induced damage, and found that an optical fluence of 14 mJ/cm^2 leads to a local modification of sp^2 carbon bonding structures, with a linear increase in the damaged area when the laser fluence is increased. Further, at laser fluence of 57 mJ/cm^2 (180 mW average power, 1400 GW/cm^2 peak irradiance), the damage caused by laser irradiation, not only induced the D peak in the Raman spectrum, but also caused disappearance of both G and 2D Raman peaks, as shown in Fig. 6.35.

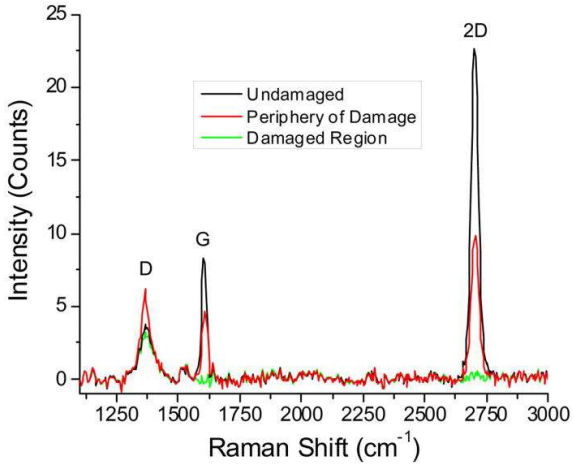


Figure 6.35: Comparison between Raman spectra of undamaged SLG and damaged SLG. (1) Undamaged Raman spectrum (black), (2) Laser irradiated SLG spectrum measured at the damage periphery (red). Notice the increase in D peak intensity, and the prominent reduction of G & 2D peaks. (3) Raman spectrum of the same SLG measured at the damaged region (green), with no discernible peaks [441].

A time-dependent structural modification of single-crystal graphene layers, due to laser irradiation of as little as 1 mW power has been reported by Krauss et al. [442]. The exposure period to such modest power results in different modifications. For example, after 2 hours of 1 mW laser power, the heat removes the adsorbed dopants, like water and O_2, which manifests itself in the form of a redshift of G and 2D peaks, broadening of the G peak, and an increase in the I_{2D}/I_G ratio. Exposure to similar power for hours to ten hours breaks the sp^2 C-C bonds, and results in disassembling the single-crystal into $\sim$ 10 nm interconnected nanocrystallines. The Raman spectrum changes associated with that are strong D peak growth, a blueshift from phonon confinement, and a reduced 2D peak. Surprisingly, although the initial exposure to laser removes adsorbed dopants, the newly created grain boundaries act as docking sites for adsorbates. Additionally, p-type doping is observed for the laser exposed regions. Samples of bilayer graphene samples have shown similar results. Increasing the number of graphene layers weakens substantially this effect. Interestingly, bulk HOPG graphite does not exhibit similar behavior, even at higher laser power of 12 mW.

As far as we see, based upon the different experiments discussed above, seemingly there is no common agreement on an energy fluence value that can be considered the damage threshold for graphene. This might be because the studied graphene samples are fabricated under various conditions, and/or different substrate materials influence graphene samples differently.

6.5.4 Experimental setup and results

Throughout the previous discussions about the thermal properties of graphene, we have shown that the superior thermal conductivity κ of a suspended SLG is drastically reduced when supported by a substrate. Similarly, FLG has reduced κ value approaching a bulk graphite. This implies that the heat deposited by a laser beam will not be efficiently dissipated in those cases, as opposed to a suspended SLG. Although the damage of graphene layers when irradiated by fs laser pulses are essentially caused nonthermally, the accumulated heat into graphene layers should also be taken into account, especially with high repetition rate lasers (e.g., GHz). With 1 GHz repetition rate fs laser, nearly more than one order of magnitude repetition rate compared to the commercial solid-state lasers, the accumulated heat could be a significant issue. Indeed, some of our graphene flakes have been damaged, either in the form of an ablation, or degradation, or sometimes even thinning of graphene and thin graphite film thicknesses. For example, the very first graphene sample, consisting of 10-11 layers, shown in Fig. 6.36 (a) has been completely ablated in some spots, it has also shown some crater-like regions of different sizes in the vicinity of graphite areas, and has been thinned in some other regions, see Fig 6.36 (b).

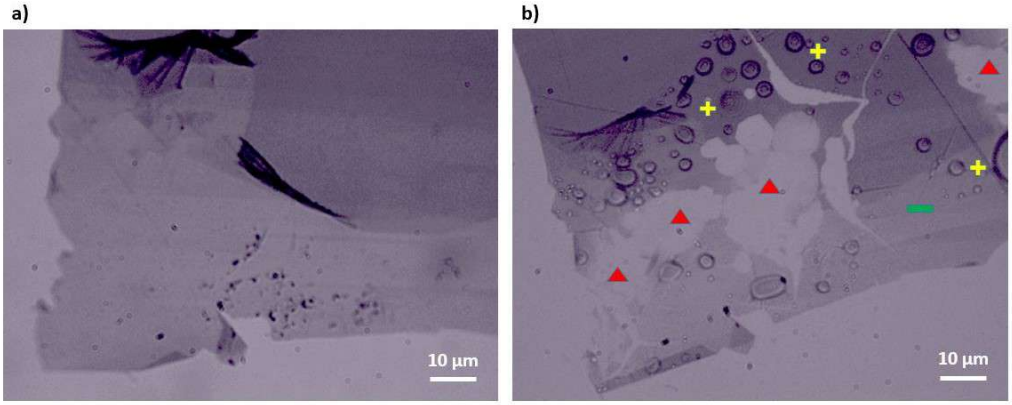


Figure 6.36: Damage of graphene sample of 10-11 layers, owing to fs laser irradiation. (a) Optical micrograph of graphene sample before fs irradiation taken with 100× objective lens (0.95 NA), (b) Optical micrograph of the same sample after fs laser exposure, taken with 50× objective lens (0.4 NA). Red triangles indicate regions of complete ablation, yellow plus sign surrounded by crater-like spots, and the minus green sign indicates a region, where graphene thickness has been thinned.

This damage occurred after exposure to $\sim$ 100 fs laser, 820 nm, 1 GHz repetition rate and 1 W average power. Given the average power and the repetition rate, the laser energy E_{P} was 1 nJ. The beam size D was 20 μm, from which we can calculate the spot area $A = \pi(\mathrm{D}/2)^2$, that is 3.14 $\times$ 10^{-6} cm^2. In order to find the energy fluence F to compare it to other studies, we need to divide the pulse energy E_{P} by the beam spot area A, which gives $\approx$ 0.31 mJ/cm^2. Note that this laser fluence causing damage is nearly more than one order of magnitude lower than the lowest reported laser damage fluence (4 mJ/cm^2) in Ref. [439]. In fact, not only the damage caused by our fs laser extended to far regions on the same area having graphene and graphite, it also extended to other adjacent flakes, as seen in Fig. 6.37. This might have been caused due to scattering of the laser beam.

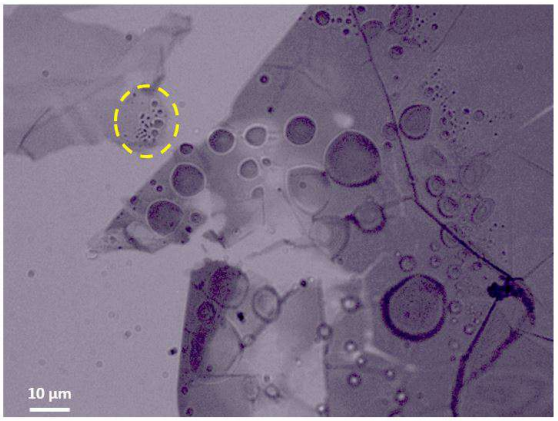


Figure 6.37: Optical micrograph showcasing damage caused by fs laser extended to other flakes, encircled by dashed yellow line.

Provided that the laser damage fluence (0.31 mJ/cm^2) is much smaller than any reported value in literature, and in sake of identifying the safe laser intensity and fluence for working with graphene samples, a new experiment has been carried out to study the damage effect caused, owing to exposure to our fs (1 GHz rate) laser. Similar to the approaches followed in literature to characterize damage in graphene and thin graphite films, we used optical microscopy and Raman spectroscopy as tools in the determination of the safe laser fluence. We excluded AFM from our characterization arsenal, because full scanning of one graphene flake can take a tremendous amount of time, especially since our flake sizes are large. A new setup had been built up using Taccor tune (1 GHz) fs laser, CW laser, camera (pco.pixelfly) and QE pro spectrometer, as shown in the scheme of Fig. 6.38.

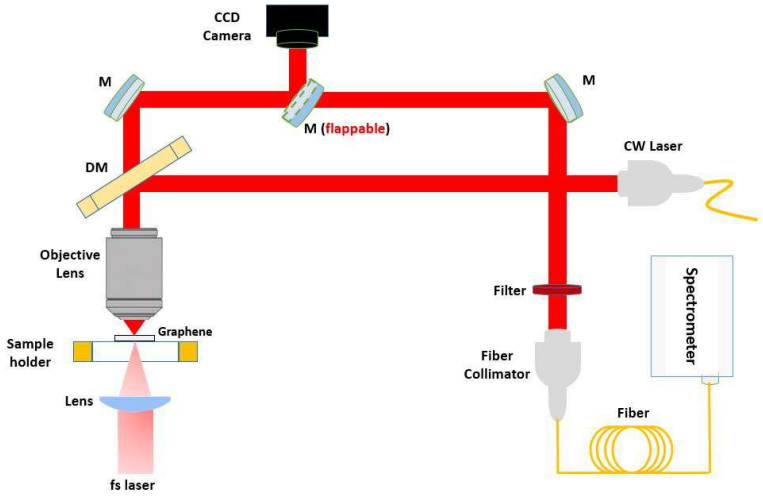


Figure 6.38: Scheme of optical setup for studying damage caused to graphene/thin graphite films samples by Taccor fs laser.

Initially the CW laser was a HeNe laser at 632.8 nm and due to shortage of space on the optical table, it was replaced with a PicoQuant diode laser at 656.64 nm (CW mode). Since this laser is located in another lab, it was coupled to our setup via a long optical fiber attached to a fiber-optic collimator. Although this helped overcome the lack of space problem, the CW laser beam profile could not be well-focused because it shows a granular speckle pattern that spread over a large spot. The speckle pattern arises as multiple modes supported by the fiber interfere with each other, giving rise to an uneven distribution of light at the end of the fiber. Fig. 6.39 exhibits such a granular speckle pattern, reflected when the laser is focused onto gold-coated glass (Fig. 6.39 (a)) and from graphite mesa (6.39 (b)), shown previously in Fig. 6.15.

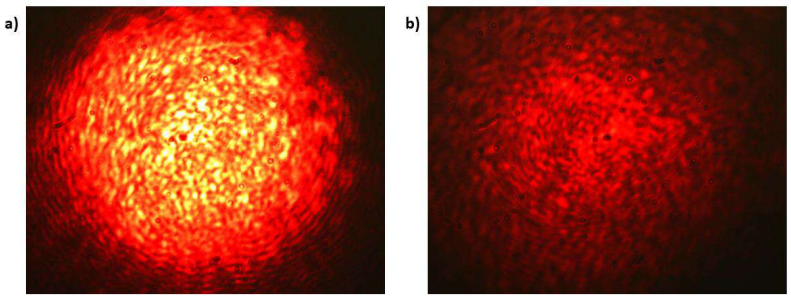


Figure 6.39: Speckle pattern of CW laser transferred through an optical fiber, from reflected light when the laser is focused onto (a) Gold-coated glass, (b) Graphite mesa.

For investigating which fs laser irradiation average power is appropriate to avoid damaging graphene/thin graphite films, a white light was used to image the sample before fs laser irradiation to firstly, determine its location on the sample surface, secondly to check whether or not it has any inherent damage beforehand. Following imaging, the objective lens (40× - 0.65 NA) is flipped and the CW laser, filtered with a 656.64 ± 2 nm bandpass filter, after reflection onto the dichroic mirror (DM), impinge onto the sample for measuring Raman spectrum, whereas the scattered Raman signal passes through the DM, and is guided through mirrors to be recorded by a fiber-coupled spectrometer that has a long-pass F76-667 nm filter in front of it. Then, the Taccor fs laser propagates through the sample, and the objective lens is unflipped to protect it from the intense fs laser. Throughout the experiment various Taccor fs laser powers were used and at different periods of exposure, while different flakes and samples have been studied. The idea here was to detect the presence of the D peak, which often appears whenever a pristine graphene becomes defective. If the initial Raman spectrum before fs laser irradiation indicates already the existence of a D peak, its magnitude is anticipated to increase after more damage occurs, due to fs laser exposure. We know from subsection 6.2.4 that the D peak, given the CW laser wavelength of 656.64 nm, should appear at 720.52 nm. It is important to mention that any data obtained using the fs laser at an average power below 1 W and with an exposure time shorter than 60 minutes will not be considered.. The reason for excluding these data is that during the experiment the CW laser spot size was much bigger than the one of the fs laser used for irradiation. This implies that the smaller fs laser spot was focused onto a small portion of the sample under study, while the Raman spectrum in such a case is collected from a larger area around the potentially damaged small region. This can smear out the D peak in the detected Raman spectrum, taken after Taccor fs laser exposure. Later, the Taccor fs laser spot size was enlarged to be equal to its counterpart of the CW laser. Then, the samples were irradiated at 1 W for 60 minutes. For example, two different thin graphite films on the same sample were investigated, shown in Fig. 6.40. As seen in Fig. 6.40

(a) & (b), this thin graphite film was neither defective before fs laser exposure, nor acquired defects, due to the 1 W of fs laser irradiation for 1 hr. Both imaging and Raman spectrum confirms this conclusion. Fig. 6.40 (c) & (d) are for another thin film. Although the initial Raman spectrum indicates the existence of a D peak, the Raman spectrum taken after fs laser irradiation shows lower magnitude of this peak. Besides, adjacent fluctuations of comparable magnitude have appeared. The D peak of the initial spectrum might have arisen due to a small noise spike, not from a real defect. As known, the induced damage is supposed to increase the D peak, if it is real, which did not take place, and also confirmed from the optical micrograph taken after fs laser irradiation.

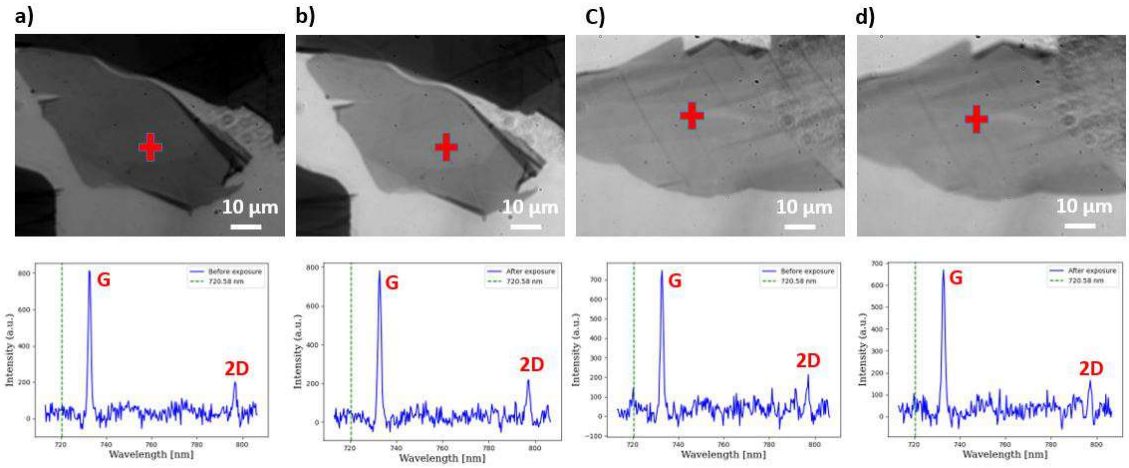


Figure 6.40: Investigation of potential damage caused by Taccor fs laser irradiation for thin graphite films. (a) Optical micrograph before fs laser irradiation, and Raman spectrum acquired via a CW laser (at red plus sign mark). The green dashed line is a visual aid for Raman D peak. (b) Optical micrograph of the same thin film and Raman spectrum after fs laser exposure for 1 hr at 1000 mW. (c) Optical micrograph of another thin film, along with its Raman spectrum before fs laser irradiation. (d) Optical micrograph and Raman spectrum after fs laser irradiation.

With other samples, similar investigations have been carried out but for flakes of graphene layers. For example, a graphene flake consisting of 3 layers (trilayer) and another flake of 7-8 layers shown previously in Fig. 6.21 (a) and (b), have been exposed to similar conditions for studying any potential damage. We see from the optical micrographs before & after fs laser irradiation (7-8 graphene layers) in Fig. 6.41 (a) and (b) that no visual sign of damage exists. However, their Raman spectrum indicates the existence of a defect already before irradiation with Taccor fs laser. Surprisingly, the magnitude of the initial D peak did not increase, owing to fs laser irradiation, which means the exposure of 1 W, fs laser for 1 hr did not cause any further damage. Similar outcome has been obtained with the trilayer of graphene, shown in Fig. 6.41 (c) & (d). Unknowingly, despite each flake of graphene having a

different number of layers, it is observed in both flakes that the 2D peak was almost completely smeared out by background, which was not the case with G peak.

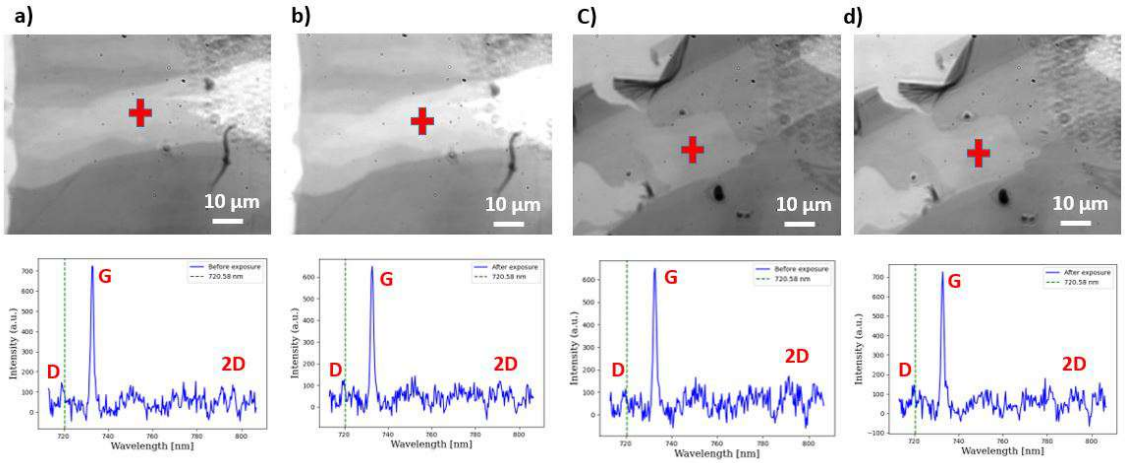


Figure 6.41: Investigation of potential damage caused by fs laser irradiation for flakes of graphene layers. (a) & (b) Optical micrograph of a graphene flake of (7-8) layers, and their corresponding Raman spectra before & after fs laser irradiation, respectively. (c) & (d) Optical micrograph of a graphene flake of (3) layers, and its Raman spectra.

One of the most interesting results was related to the thin graphite film, shown in Fig. 6.42. Before the fs laser irradiation, the image of that film, see Fig. 6.42 (a), shows that it does not contain visible defects. Moreover, its Raman spectrum shows an unclear D peak, because its magnitude is similar to the adjacent background, before G peak. The micrograph of Fig. 6.42 (b) still does not indicate any visible defects, although its Raman spectrum exhibits a bit more prominent D peak, showing that some defect has occurred, albeit until now the film still looks intact. Nonetheless, later imaging after a few days with a commercial optical microscope and a home-built Raman microscope has shown clear damage, in the form of a vertical straight crack, as illustrated in Fig. 6.43.

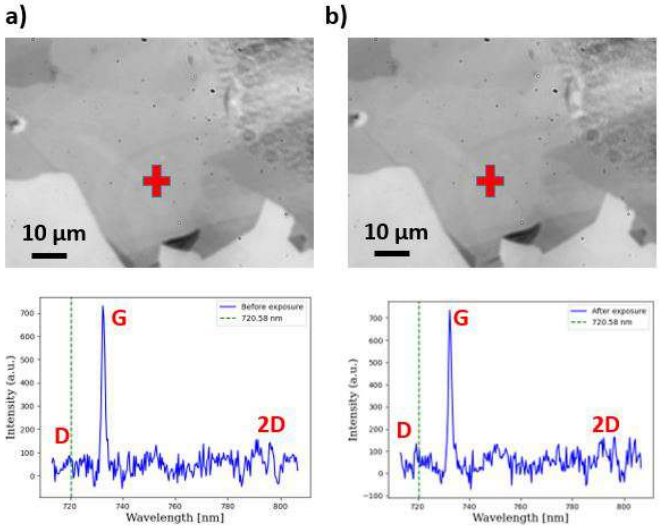


Figure 6.42: Investigation of potential damage for thin graphite film. (a) Optical micrograph of the thin film, and Raman spectrum, before exposure to fs laser, with barely seen D peak in its Raman spectrum, (b) Optical micrograph and Raman spectrum after fs laser (1 W, 1 hr).

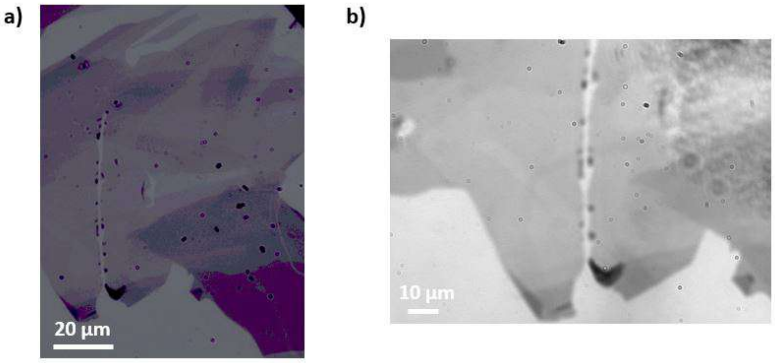


Figure 6.43: Induced crack line, because of fs laser irradiation. (a) Optical micrograph taken by commercial microscope, showing the entire vertical straight crack, (b) Similar optical micrograph, taken by a home-built Raman microscope, showing roughly 3/4 of the crack line.

The outcome of our experiment discussed here, led us to important findings. Firstly, although most of the samples we investigated remained intact, even after one hour of exposure to 1 W fs laser power, some of them showed later cracks, similar to the one in Fig. 6.43. Secondly, utilizing the Taccor fs laser at considerably lower average powers (i.e. 290 mW), in optical Kerr shutter experiments, did not guarantee complete avoidance of damage and/or cracks, even though those samples survived initially much higher laser power. For example, when the fs laser is used at 290 mW, with some thin films, most of the time no visual damage was observed, while using the same power with the same thin films at the same spots, either in the same day, or during other days can damage those films, in a manner similar in ambiguity

to that shown in Fig. 6.43. Thus far, the exact reasons for such vague behavior are yet unclear. However, there are some potential reasons that could be behind it. For instance, it is possible that the variation of laboratory humidity within a day, or several days can influence the damage threshold value of graphene flakes, or thin films. Actually, as those are 2D materials, they have larger surface-to-volume ratio, as compared to their bulky counterparts. Shedin et al. [443] have shown that graphene is capable of sensing individual gas molecules, either being adsorbed onto its surface, or detached from it. Another possibility that can interpret the absurd behavior of graphene and thin graphite films when exposed to fs laser, could be that the fs laser irradiation induces structural modifications in the carbon atoms lattice, which at some point can result in a fracture of the flake/film. In fact, it was shown that an ultrashort laser can pre-weaken the regions covered by its spot size, and induce micro-cracks or voids in glass substrates and subsequent heating can lead to crack propagation, which is a process recently used for glass cleaving and cutting [444, 445]. A similar mechanism could be occurring in our case, but not with the glass substrate, instead with the 2D graphene crystallite. For example, our fs laser pulses could be inducing micro-cracks, and accumulated heat from the high repetition rate (1 GHz) could be playing a role in propagating those cracks. In conclusion, detailed studies are demanded for better understanding of the circumstances and parameters that control the damage caused by fs laser irradiation.

6.6 Nonlinear optical properties of graphene

6.6.1 Overview

Besides the fascinating electronic, optical and thermal properties of graphene, presented in the introduction, it was predicted by Mikhailov [446] that graphene should possess strong nonlinear optical response, over a broad spectral range from microwave to infrared, due to the linear energy-momentum dispersion relationship of the quasi-particles. Such strong nonlinear responses can be achieved by merely moderate electric field values, ranging 5-100 V/m, depending upon the electromagnetic frequency, temperature and doping level. This interesting prediction provoked the nonlinear optics community to investigate the nonlinear optical properties of graphene, such as harmonic generation, four-wave mixing, and other nonlinear optical phenomena, both theoretically and experimentally. Shortly after that, Mikhailov and Ziegler [447] developed a quasi-classical kinetic (Boltzman) theory while ignoring interband transitions to describe the nonlinear behavior of graphene, which takes into account the Fermi-Dirac distribution of electrons, the response of graphene

to continuous and pulsed excitation, as well as the feedback from current-induced electromagnetic (EM) field (self-consistent field effects). Their theory showed that graphene indeed has some interesting nonlinear optical response, such that it can be used as frequency multiplier (harmonic generation) in THz and sub-THz of the EM-field. Bao et al. (2009) [448] used a large area of graphene as a saturable absorber for an ultrafast mode-locked fiber laser. This was achieved via transferring the graphene layer onto the laser fiber, and it was demonstrated that graphene acquires lower absorption saturation intensity as compared to traditional saturable absorbing materials. This feature is attributed to Pauli blocking and the zero-gap graphene has, whereas the interband optical absorption under strong excitation blocks other electrons from occupying the same energy levels, hence saturating them. Graphene can absorb efficiently from IR to visible light, which offers widely tunable saturable absorbers. Hendry et al. (2010) [449] used coherent four-wave mixing for the first time to measure the third-order nonlinear optical susceptibility $\chi^{(3)}$ and found its value remarkably large, weakly wavelength-dependent in near-IR frequency range, where the effective $|\chi^{(3)}_{\text{eff}}| \sim 10^{-7}$ esu ($\sim 10^{-15}\text{m}^2\text{V}^{-2}$). Later on, this value was corrected by Cheng et al. [450], such that $|\chi^{(3)}_{\text{eff}}| \sim 10^{-11}$ esu ($\sim 10^{-19}\text{m}^2\text{V}^{-2}$). Also in 2010, Ishikawa [451] studied the nonlinear optical response of electron dynamics in graphene under intense light pulse in the time-domain. He concluded that the nonlinear optical response of graphene can be neither described solely by intraband dynamics, nor by interband transitions; it is rather an interplay of both. The third harmonic generation was demonstrated by Kumar et al. (2013) [452] in graphene and thin graphite films, where the emission from graphene scaled with the cube of the intensity of incident near-IR beam, and the emitted wavelength was 1/3 of the incident wavelength. Cheng et al. (2014) [450] investigated the linear and third order nonlinear optical conductivity of doped graphene at zero-temperature by performing perturbative calculations around Dirac points using semiconductor Bloch equations. In this work, using approximations valid around Dirac points, and ignoring effects due to scattering and electron-electron interactions, obtaining analytic formulas for those conductivities was possible. Also, they found out that the linear dispersion relationship causes resonances over a wide range of photon energies. Hence, the nonlinearity of graphene can be enhanced via tuning the chemical potential. Later, a quantum theory of the third order nonlinear electrodynamic response of graphene was developed by Mikhailov (2016) [453]. This theory revealed that the nonlinear optical properties of graphene are particularly interesting for low frequency regions (microwave and THz) and for high IR frequencies. The latter is particularly useful for three photon absorption. It also revealed that despite graphene having no inversion symmetry, second harmonic generation can be stimulated by a DC electric current. Different routes have been pursued in order to achieve large enhancement of the

third harmonic generation in graphene, e.g., via coupling it to a cavity [454], or by controlling the doping level by electrical gating [455, 456], which enables the usage of graphene in optoelectronic-based applications.

6.6.2 Self-phase modulation of graphene

It is important to mention that the self-phase modulation referred to in this section is the temporal self-phase modulation, not the spatial self-phase modulation, which is out of the scope of this work. The self-phase modulation of graphene is not less interesting than its other unique properties. In fact, graphene presented a long-standing paradox as theoretical models predicted quite weak third-order susceptibility $\chi^{(3)}$, in contrast to the huge nonlinearity measured experimentally, which led to discrepancy between the measured value of $\chi^{(3)}$ and the theoretically predicted one. For example, experimental measurements of third-order nonlinearity of graphene showed that $|\chi^{(3)}_{\text{eff}}| \sim 10^{-7}$ esu, while the electronic third-order susceptibility predicted theoretically is $|\chi^{(3)}_{\text{th}}| \sim 10^{-9}$ esu. Furthermore, it turns out that the conventional $\chi^{(3)}$-dependent self-phase modulation is not capable of explaining the spectral broadening of graphene, neither quantitatively nor qualitatively. To resolve this paradox, Vermeulen et al. [457] studied SPM of graphene and unveiled a complex phenomenon, so-called saturable photoexcited-carrier refraction (SPCR), which well-interpret the SPM of 2D materials, like graphene. Furthermore, it can also explain an anomalous behavior of graphene, whereas an exponential-like spectral bandwidth growth of picosecond optical pulses was observed, when they propagate along graphene-covered waveguides. The conventional SPM theory fails to explain such behavior, as shown in Fig. 6.44, but the newly introduced SPCR model does not.

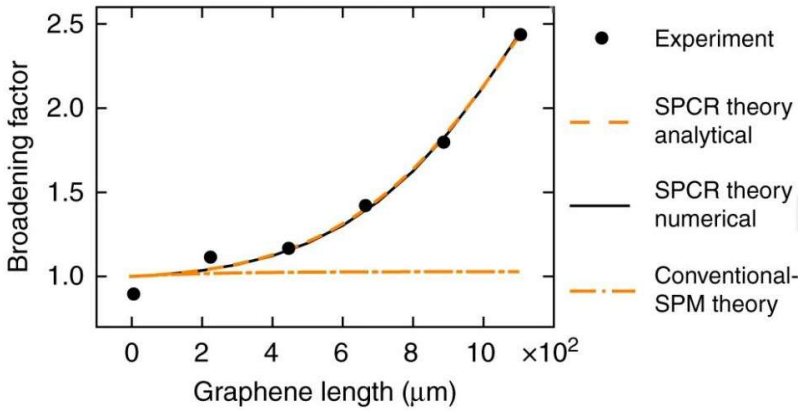


Figure 6.44: Broadening factor of graphene-covered SiO_2 waveguide, exhibiting an exponential-like behavior for graphene length up to 1100 μm, for a waveguide-coupled peak power of 2.7 W [457].

In conventional SPM, the spectral broadening associated with the optical pulses propagating through a nonlinear medium originates from the electronic third-order nonlinear optical susceptibility $\chi^{(3)}$, such that SPM process depends on the induced $\chi^{(3)}$ nonlinear part of refractive index $\Delta n_{(3)}(z,t) \propto \chi^{(3)}|A(z,t)|^2$, where $A(z,t)$ is the pulse amplitude. This affects the pulse chirp and its spectral width through the chirp-index relation $\partial_t \varphi(z,t) \propto \partial_t \int_0^z \Delta n(z',t)\,\mathrm{d}z'$. This spectral width varies linearly with the optical pulse input power, as well as the effective thickness of the nonlinear material. Such dependencies do not apply in graphene as a nonlinear medium. In the SPCR mechanism, the photoexcited carriers in graphene are mainly responsible for its spectral broadening. When optical pulses travel along a graphene-covered waveguide, these pulses experience absorption by graphene, and as a result some free carriers with density $N_\mathrm{c}(z,t)$ are photoexcited. Those photoexcited free carriers change the refractive index $\Delta n_\mathrm{carriers} \propto N_\mathrm{c}(z,t)$ and give rise to pulse chirping, expressed as

$$\partial_t \varphi(z,t) \propto \partial_t \int_0^z \Delta n_\mathrm{carriers}(z',t)\,\mathrm{d}z' \propto \partial_t \int_0^z N_\mathrm{c}(z',t)\,\mathrm{d}z'. \tag{6.15}$$

This phenomenon is already known as free-carrier-refraction (FCR)-induced chirping. However, in graphene-covered waveguides, this phenomenon is much more complex than any 3D system ever studied. Along the optical pulse propagation direction, the time evolution of the density of photoexcited free carriers $N_\mathrm{c}(z,t)$ depends heavily on the saturation of graphene, i.e., $N_\mathrm{c} \sim N_\mathrm{sat}$, that takes place because of Pauli blocking. Pauli blocking in graphene occurs when it is strongly excited, such that the excited charge carriers from the valence band to the conduction band block other carriers to occupy the same level. Meaning that the excited energy-level will be saturated.

When an optical pulse whose pulse width T_0 is close to carrier lifetime τ_c propagates along graphene-covered waveguide, the free carrier density $N_c(z,t)$ builds up following the pulse profile, and due to saturation of graphene, the graphene photoexcited carrier density N_c^gr saturates at the pulse center but keeps exciting carriers at its trailing edge, which yield up-chirping and down-chirping regions around the pulse peak, as indicated in Fig. 6.45 (a), for short propagating distance of 220 μm. As the optical pulse keeps propagating along the graphene-covered waveguide at long propagating distance, i.e., 1100 μm, due to graphene's absorption the pulse power will be reduced, thus it will not undergo saturation, which implies that it remains able to generate free photoexcited carriers. In this particular situation, the instantaneous frequency curve still has up-chirping and down-chirping regions but they get closer toward the pulse center, as shown in Fig. 6.45 (b).

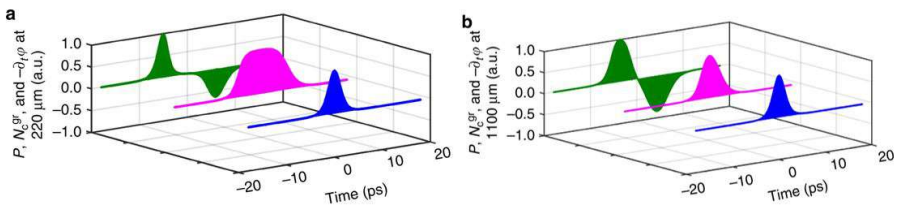


Figure 6.45: 3D illustration of the optical pulse time evolution (blue), and the associated graphene photoexcited carriers density (magenta), and the corresponding instantaneous frequency curves (green), for graphene-covered waveguide at (a) 220 μm propagation distance and (b) 1100 μm [457].

Similar time evolution of the same quantities but with numerically obtained absolute values for 220 and 1100 μm is provided in Fig. 6.46, that clearly shows the effect of long propagation distances in the reduction of the optical pulse power, and the change of the graphene photoexcited carriers N_c^{gr} and the consequence of this dynamic on the instantaneous frequency curves.

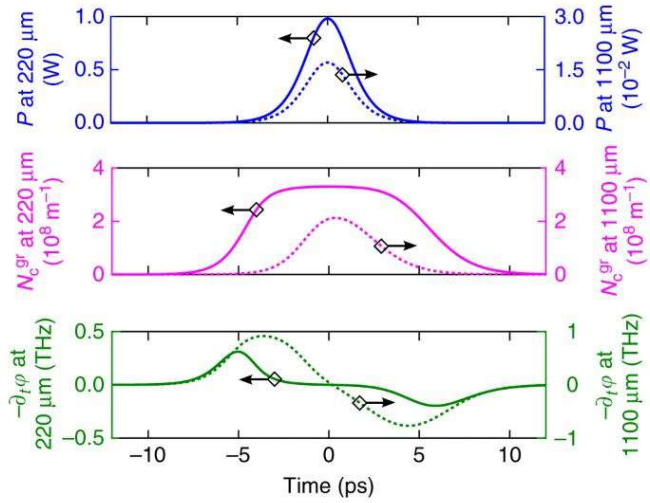


Figure 6.46: Numerically obtained absolute values of the time evolution of the optical pulse propagating along a graphene-covered waveguide, and graphene's photoexcited carriers N_c^{gr} and their corresponding instantaneous frequency profile [457].

For the reasons clarified previously in both chapter 4 and 5, it was necessary to explore SPM of graphene and thin graphite films, for evaluating their ability of causing spectral broadening to the gate laser beam. For this purpose, several thin graphite films, as well as graphene flakes were studied. In each of them, the gate beam spectrum was measured without the sample, then the sample was placed, then the gate beam spectrum was measured again for comparison. It was purposefully chosen to measure the gate beam spectrum without the sample completely (desired flake + substrate), rather than measuring graphene-free spots on the substrate. The reason for that was, it was observed during optical Kerr measurements, that there are

residuals of dissolved carbon, as a result of depositing graphite on not well-dried parts of the glass substrate, distributed in some regions between graphite, thin graphite films, and graphene. These dissolved carbon residuals were giving wrong signals. Thus, to avoid wrong SPM signals, measuring without the entire sample was chosen as an alternative. An example of the several thin graphite films investigated is shown in Fig. 6.47.

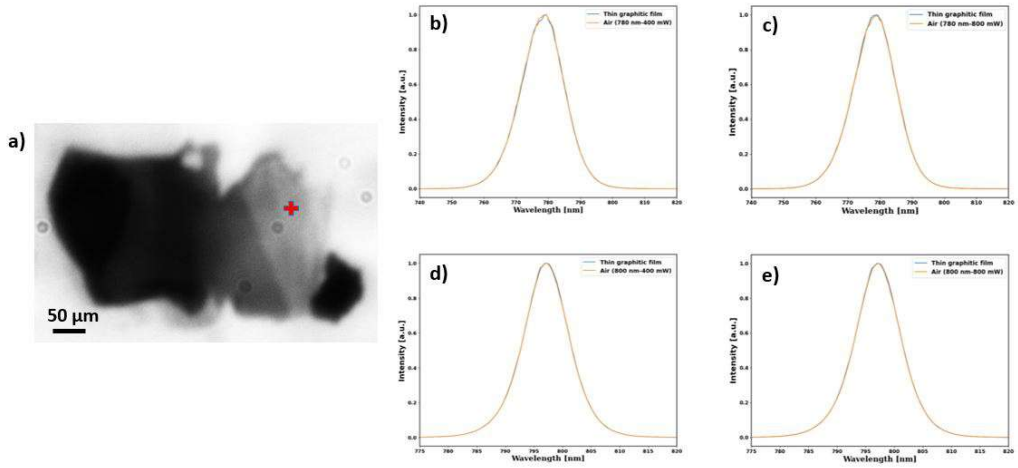


Figure 6.47: Investigation of SPM of thin graphite film. (a) Optical micrograph of the thin film (marked with red plus sign), (b) Gate beam spectrum with (dark blue)/without (orange) the thin film at $\lambda = 780$, at 400 mW average laser power, (c) Gate beam spectrum at $\lambda = 780$, at 800 mW average laser power, (d) Gate beam spectrum with (dark blue)/without (orange) the thin film at $\lambda = 800$, at 400 mW average laser power (pulse peak intensity $I_0 \approx 0.53$ GW/cm^2), and (e) Gate beam spectrum with (dark blue)/without (orange) the thin film at $\lambda = 800$, at 800 mW average laser power (pulse peak intensity $I_0 \approx 1.06$ GW/cm^2).

The exact thickness of the thin graphite films, presented in Fig. 6.47 (a), is not known, as this requires thickness measurement via AFM, and since scanning with AFM is time-consuming, that step was delayed. This thin graphite film was studied at two different wavelengths, 780 and 800 nm, respectively. At each wavelength, it was studied at two different average gate laser power, 400 mW (pulse peak intensity $I_0 \approx 0.53$ GW/cm^2) and 800 mW (pulse peak intensity $I_0 \approx 1.06$ GW/cm^2), where a 1 s integration time was fixed in all cases. As can be seen, regardless of the wavelength of the gate, and/or its average power, no discernible spectral broadening was observed. For an example of the studied graphene flakes, Fig. 6.48 shows an ~ 8 layers graphene flake (identified via the model discussed earlier in subsection 6.4.1), which was presented earlier in Fig. 6.21 (b), but here the image was taken by the incorporated optical microscope into the optical Kerr gate setup.

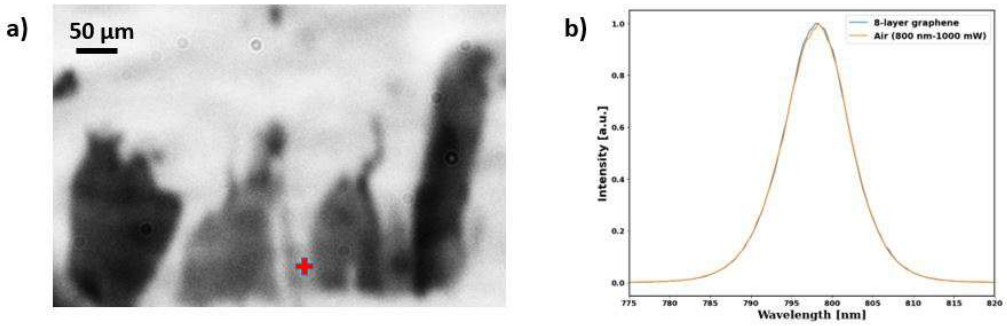


Figure 6.48: Investigation of SPM of graphene. (a) Optical micrograph of the ~ 8 layers graphene flake (marked with red plus sign), (b) Gate beam spectrum with (dark blue) & without (orange) graphene sample, at $\lambda = 800$ nm, at 1000 mW average laser power (pulse peak intensity $I_0 \approx 1.33$ GW/cm^2), 100 ms integration time.

Despite the higher average power of the gate laser (1000 mW), graphene did not exhibit any spectral broadening, similar to thin graphite films. Due to the high average power of the gate, the integration time was reduced to 100 ms to avoid saturation, or damage to the spectrometer's detector.

In view of the SPCR theory presented above, our graphene samples behave in consistency to that theory. The exponential spectral broadening growth observed in Ref. [457] is not expected to be seen in our case. This is because the following reason: for our SPM experiment with graphene to observe similar giant spectral broadening, we need to satisfy two requirements, which are both not fulfilled, one the pulse width of the gate must be comparable to the carriers' relaxation times of graphene; second, the gate laser pulses must propagate through graphene for long distances. As the gate laser has a pulse width of $\sim$ 90-100 fs, which is much shorter than the excited carriers' relaxation time τ_c, our pulse width is not at the time scale of the carrier's relaxation time, where τ_c is $\sim$ 1-2 ps. In principle, our pulse compressor can be used for enlarging the gate laser pulse width, for attaining this requirement. Also, the second requirement is not fulfilled, since the gate laser passes through the thickness of graphene flake, which is only 8 layers thick, as opposed to a graphene waveguide used in the work of Ref. [457], along which their ps laser pulses were propagating.

6.6.3 Kerr nonlinearity of Graphene

The large third order nonlinear optical susceptibility $\chi^{(3)}$ reports of graphene intrigued researchers to study another related quantity, which is the nonlinear refractive index n_2. Early measurement of n_2 value was reported by Zhang et al. (2012) [53], and was carried out by Z-scan technique on few-layer graphene. The measurement was performed using a 10 MHz picosecond laser (FWHM $\sim$ 3.8 ps) centered at 1550 nm.

The reported value was $n_2 \approx 10^{-7}$ cm^2/W, that is almost 9 orders of magnitude larger than bulk dielectric materials. Interestingly, they found that the n_2 value decreases as the excitation flux increases. This result is in stark contrast to nonlinear bulk materials, whose nonlinear index change is independent of laser irradiance. Notice that the n_2 value reported here is positive. Shortly after that, Cheng et al. (2013) [458] measured the nonlinear refractive index n_2, as well as the nonlinear absorption β of a SLG, and found out their values are 1.4 $\times$ 10^{-9} cm^2/W, and 6 $\times$ 10^{-6} cm/W, respectively. Furthermore, they compared the values of these two parameters for various numbers of coupled layers (stacked with order) of CVD-grown graphene versus a similar number of layers of decoupled graphene (randomly stacked), and came out with a surprising result. That is, decoupling of graphene layers can maintain the superior nonlinear optical properties of a SLG. The parameter n_2 was measured in their work via Z-scan technique, with an 80 MHz fs laser (100 fs) at 733 nm. Z-scan technique was again used in the work of Demetriou et al. (2016) [459], where multilayer graphene (5-7 layers) was studied using a 100 fs laser at 1150, 1550, 1900, 2400 nm wavelengths. To avoid any heat accumulation into graphene layers, the experiment was conducted at 1 kHz repetition rate. The nonlinear refractive index n_2 was actually $\sim 10^{-9}$ cm^2/W^{-1} (almost 8 orders of magnitude higher than bulk), and confirmed the irradiance-dependent behavior of graphene. Counter-intuitively, the sign of n_2 was found to be negative. Using degenerate optical Kerr gate ($\lambda_{\text{pump}} = \lambda_{\text{probe}} = 1600$ nm), coupled to optical heterodyne detection (OHD-OKG) to increase the detection sensitivity, the nonlinear refractive index n_2 of a CVD grown SLG was studied by Dremetsika et al. (2016) [239], and found it to be -1.1 $\times$ 10^{-13} m^2/W, a value few orders of magnitude different from what has been reported by other works. A detailed theoretical analysis of the experimental results of this particular work has been presented in Ref. [460, 461]. Ahn et al. (2017) [462] carried out a systematic study to measure the third-order nonlinear optical susceptibility $\chi^{(3)}$, hence n_2 for a mono- and randomly stacked bi- and four-layers across 720, 800, 940, 1230 nm at different fluences. Their measurements were initially performed via Z-scan technique, and further verified using optical Kerr gate method. The outcome of their work showed that a SLG possesses the highest n_2 value, as compared to randomly stacked layers, whereas the n_2 was decreasing with increasing the number of randomly stacked graphene layers, despite the increase of the OKG signal, due to the increased thickness with the number of layers. This is in mismatch with the finding of Ref. [458], showing that randomly stacked graphene layers maintain almost similar SLG n_2 value. For the sake of a systematic study of the Kerr nonlinearity of graphene, Thakur et al. [463] performed an extensive experimental characterization of CVD grown SLG over a wide wavelength range in the near-IR region, 800-1050 nm, and across different pulse widths, using a pump-probe version of the famous Z-scan technique. Due to its

unconventional Kerr nonlinearity and their associated mechanisms, they defined an effective nonlinear refractive index, $n_{2,\text{eff}}$, to distinguish it from the conventional n_2 corresponding to the nonlinear refractive index change $\Delta n = n_2 I$. This is because in graphene the charge carriers are photoexcited, which results in population difference between the conduction and valence band. As pointed out formerly in SPM, the Pauli blocking that is responsible for saturation of absorption plays a significant role in the nonlinear response of graphene, particularly when the pulse duration of the pump laser is comparatively close to the carriers' relaxation time. They figured out that there is a quadratic dependence of $n_{2,\text{eff}}$ on the wavelength, namely $n_{2,\text{eff}} \propto \lambda^2$. Moreover, they found out that $n_{2,\text{eff}}$ increases with increasing the laser pulse width, which is the first confirmation of the finding reported in Ref. [457], which states that the nonlinear refractive index of graphene has a gigantic value as the pulse duration of the laser approaches the relaxation time of the charge carriers, due to SPCR, presented in the previous section.

The discrepancy in reported literature about n_2, in terms of both the magnitude and sign, had remained elusive for a long time. In order to resolve this discrepancy, Castelló-Lurbe et al. [464] introduced a theoretical formalism in 2020 that helps to predict graphene's nonlinear optical properties, and agrees well with the experimentally reported magnitudes and signs of n_2 values. This theoretical formalism considers the perturbative nature of graphene, when it is excited via intense electromagnetic fields, such as lasers, and it shows that the refraction efficiency can be obtained from the instantaneous change in both temperature and chemical potential induced due to laser excitation, as well as the instantaneous change in the linear conductivity of graphene. According to this mathematical formalism, graphene's nonlinear refractive index is directly proportional to the imaginary part of the linear conductivity as follows

$$n_{2,\text{graphene}} \propto -\text{Im}\left(\frac{\Delta\sigma_{yy}^{(1)}(n_{\text{sat}}/2)}{\sigma_0}\right), \tag{6.16}$$

where $\Delta\sigma_{yy}^{(1)}$ is the change of the linear conductivity of graphene as a result of excitation by an electric field of a laser propagating along z-direction and linearly polarized along y-direction, n_{sat} is the saturated photoexcited carriers densities (carriers/m^2), and $\sigma_0 = e^2/4\hbar$ is the universal conductivity. From their work, it turns out that the change of the linear conductivity of graphene, hence its nonlinearity is heavily affected by its temperature change, not its chemical potential, as shown in Fig. 6.49 (a) & (b) for $\lambda_0 = 1550$ nm, and (b) & (c) for $\lambda_0 = 800$ nm, for carrier densities ranging up to $n_{\text{sat}} = 10^{17}$ m^{-2} and assuming an initial hole density $p_0 = 4 \times 10^{12}$ cm^{-2}. Note that Fig. 6.49 (a) and (c) are showing the change of $\text{Im}(\Delta\sigma_{yy}^{(1)}/\sigma_0)$ as a function of the chemical potential for minimum and maximum temperature, and conversely Fig. 6.49 (b) and (d) are showing this change as a function of temperature

T, for minimum and maximum chemical potential μ.

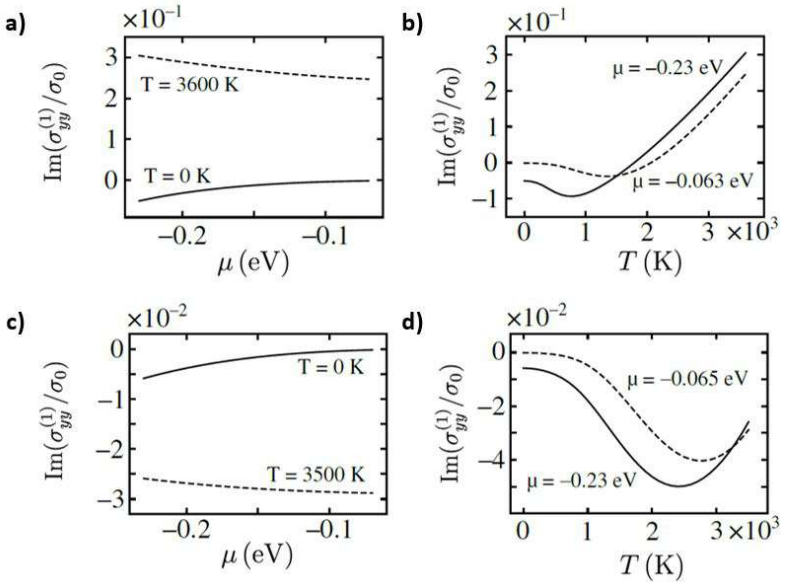


Figure 6.49: Change of the imaginary part of the linear conductivity of graphene as a function of chemical potential μ and temperature T, at $\lambda_0 = 1550$ nm (a) & (b), and at $\lambda_0 = 800$ nm (c) & (d) [464].

The same work has shown that the interplay between the interband transitions and intraband transitions is the key factor that controls the sign and magnitude of the observed $n_{2,\mathrm{gr}}$. For instance, at $\lambda_0 = 1550$ nm, the interband contribution to graphene's linear conductivity, hence its nonlinearity does not depend on the photoexcited carriers concentration, but only on the intraband contribution, i.e., the process of thermalization post-photoexcitation, which is the dominant contribution, as indicated in Fig. 6.50 (a). Since the intraband transition leads to $+ve$ $\mathrm{Im}(\Delta\sigma^{(1)}_{yy}/\sigma_0)$, according to Eq. 6.16, this gives $n_{2,\mathrm{gr}}$ a $-ve$ sign, which is in coincidence with the outcome of the sign of n_2 of graphene typically observed in experiments conducted at telecom wavelength. In contrast, at $\lambda_0 = 800$ nm, both interband and intraband contributions take apart, and as seen in Fig. 6.50 (b), the total contribution results in a $-ve$ $\mathrm{Im}(\Delta\sigma^{(1)}_{yy}/\sigma_0)$, over a large number of photoexcited concentrations, hence gives a $+ve$ $n_{2,\mathrm{gr}}$, which is a result that matches the outcome of experimental studies carried out at that wavelength. It is worth to say that for photoexcited carrier concentrations near saturation n_{sat}, both contributions compete against each other, which leads to smaller magnitudes of $n_{2,\mathrm{gr}}$, compared to the situation when $\lambda_0 = 1550$ nm.

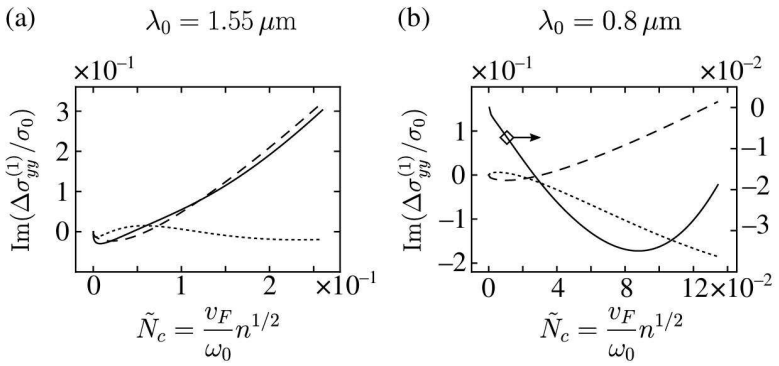


Figure 6.50: Contribution of interband (dotted curve), intraband (dashed curve), and total contribution (solid curves) to the $\mathrm{Im}(\Delta\sigma_{yy}^{(1)}/\sigma_0)$ as carriers concentration increases ranging up to $n_{\mathrm{sat}} = 10^{17}$ m^2 at (a) $\lambda_0 = 1550$ nm and (b) $\lambda_0 = 800$ nm [464].

It is also possible that $n_{2,\mathrm{gr}}$ acquires a $-ve$ sign under different experimental conditions. For example, at higher initial hole densities, i.e., $p_0 = 9 \times 10^{12}$ cm^{-2}, and for carriers concentrations near saturation n_{sat}, the sign of $\mathrm{Im}(\Delta\sigma_{yy}^{(1)}/\sigma_0)$ would be positive, thus the $n_{2,\mathrm{gr}}$ sign will be negative, as depicted in Fig. 6.51 (a), as opposed to the result discussed above related to $p_0 = 4 \times 10^{12}$ cm^{-2} that yields $-ve$ $\mathrm{Im}(\Delta\sigma_{yy}^{(1)}/\sigma_0)$ and $+ve$ $n_{2,\mathrm{gr}}$, clarified in Fig. 6.51 (b).

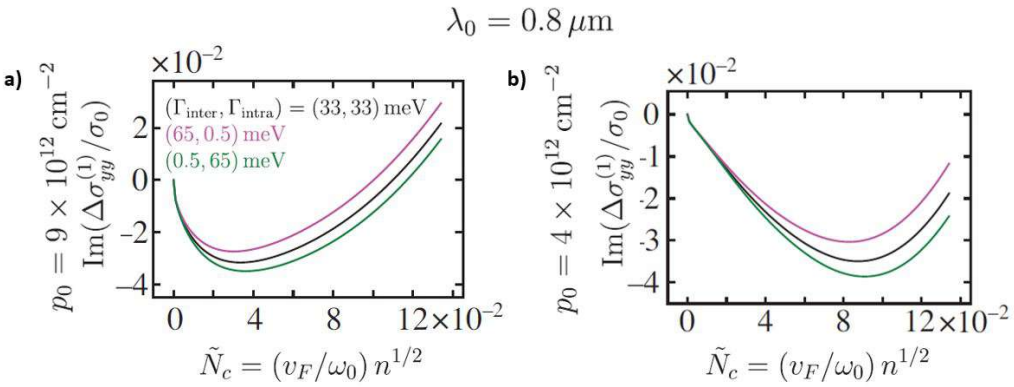


Figure 6.51: Calculated imaginary part of the dynamic conductivity change under different experimental conditions at $\lambda_0 = 800$ nm up to $n_{\mathrm{sat}} = 10^{17}$ m^2, for (a) initial hole density $p_0 = 9 \times 10^{12}$ cm^{-2}, and (b) $p_0 = 4 \times 10^{12}$ cm^{-2} [464].

For understanding optical Kerr signals of graphene, it is essential to grasp an understanding of the underlying mechanism of energy relaxation upon laser irradiation. Such information would give us an idea about the time scale over which graphene layers respond after exposure to intense electric fields from pulsed laser sources. Under strong excitation from intense light pulses, the electrons in graphene are driven into a strongly non-equilibrium state. The conventional perturbation theory often fails in this case to describe the carrier's dynamics. Alternative theoretical models for

elaboration of the transient dynamics of graphene out-of-equilibrium carriers have been developed, see an example in Ref. [465]. Experimentally, ultrafast pump-probe spectroscopy technique has been of paramount importance to provide valuable insight into electron-electron, electron-phonon, and phonon-phonon interactions. The ultrafast (sub-picosecond) non-equilibrium electron dynamics was experimentally studied by Brida et al. [466], combined with a microscopic theory for interpretation of the results. This work identified the mechanisms of the ultrafast dynamics, such as collinear dynamics, which leads to Auger processes, e.g., charge multiplication. Initially, the intense laser pulses excite the electrons of the graphene valence band, promoting them to the conduction band. Those photoexcited electrons have initially a narrow hot-electron distribution, as indicated in Fig. 6.52 (red curve). The amplitude of the peak of this distribution is quite high, but here divided by 3, in sake of comparison with subsequent thermalization stages. Within $\sim$ 10 fs the narrow distribution turns into nonthermal broad distribution (black curve), and subsequently thermalizes into a Fermi-Dirac distribution (green curve), a process that takes 50 fs. Such thermal hot electron populations experience further cooling via emission of optical phonons, over 500 fs. At some point, both electrons and optical phonons thermally equilibrate, whereas in this case the famous hot optical phonons bottleneck takes place, which dramatically slows down the cooling rate. Thereafter, those hot optical phonons undergo anharmonic decay into acoustic phonons [467]. It is also possible for supported graphene onto polar substrates to have direct coupling of the excited charge carriers to the surface optical phonons, which is an additional cooling channel [468].

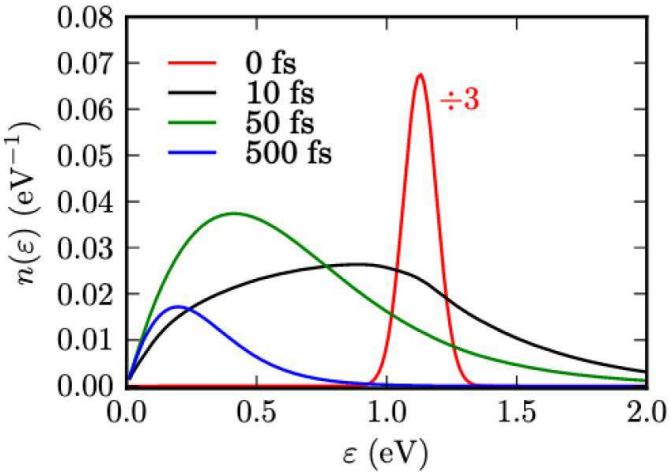


Figure 6.52: Description of the time evolution of electron population per unit cell [in eV^{-1} units]. Red curve depicts the initial hot-electrons, black curve for broadening of the hot-electron peak into nonthermal distribution, green curve shows subsequent thermalization into Fermi-Dirac distribution, blue curve depicts later cooling via phonon emission [469].

Dawlaty et al. [470] measured the ultrafast carrier dynamics using pump-probe spectroscopy for epitaxially-grown graphene samples, on SiC wafers, consisting of 6, 12, 37 layers, respectively. They found two distinct time scales associated with the relaxation of non-equilibrium photoexcited electrons. The first time scale corresponds to an initial fast relaxation transient in the 70-120 fs range, while the second time scale corresponds to a following slower relaxation in the 0.4-0.7 ps range. The fast relaxation time constant belongs to carrier-carrier interactions, and their subsequent carrier-optical phonons transitions. The slower relaxation time constant is for later decay from optical to acoustic phonons. The slower relaxation time, in particular, was found to be inversely proportional to the degree of crystalline disorder. Such that larger crystalline disorder (more defects) results in shorter relaxation times. A similar methodology was used by Newson et al. [471] for studying the ultrafast carrier dynamics of exfoliated graphene and thin graphite films, which are more relevant to our case. Different graphene layers, up to 260 layers, were studied at 295 K on SiO_2/Si substrate. The samples were excited by a 150 fs, 800 nm pump pulses, and probed by a 1300 nm laser. They noticed that as the number of graphene layers increases from 1 to $\sim$ 260 layers, the fast recovery time constant increases from $\sim$ 200 to 300 fs, and the slow recovery time increases from 2.5 to 5 ps. Since the fast recovery time constant of the exfoliated graphene is higher than the fast recovery constant (70-120 fs) observed with epitaxially grown graphene in here [470], it was attributed to the shorter probe wavelength used to study the relaxation of the epitaxially grown graphene, as the photoexcited carriers in this case can couple more efficiently to optical phonons. Additionally, their slow relaxation constant (0.4-0.7 fs) was also faster than its counterpart of exfoliated graphene, which could be due to an increased number of defects in their epitaxially grown graphene samples. Throughout our optical Kerr gate experiments, several flakes and samples, especially thin graphite films have been investigated, both with Taccor fs laser, as well as CW laser. These experiments were carried out in a counter-propagating scheme, explained before in Chapter 4, where both the pump (gate) and probe beams were degenerate, namely at the same wavelength. Unlike solid-state bulky Kerr media, finding the location of a specific number of graphene layers, or a thin graphite film of a certain thickness requires the ability to image graphene samples, in order to point the laser beam spot onto them. For this purpose, a white light source was incorporated into the optical Kerr gate setup, for illuminating the sample of interest, while the 50 mm focal length lens used primarily to focus the gate beam was also employed for imaging graphene/thin graphite films. The experimental configuration is presented in Fig. 6.53.

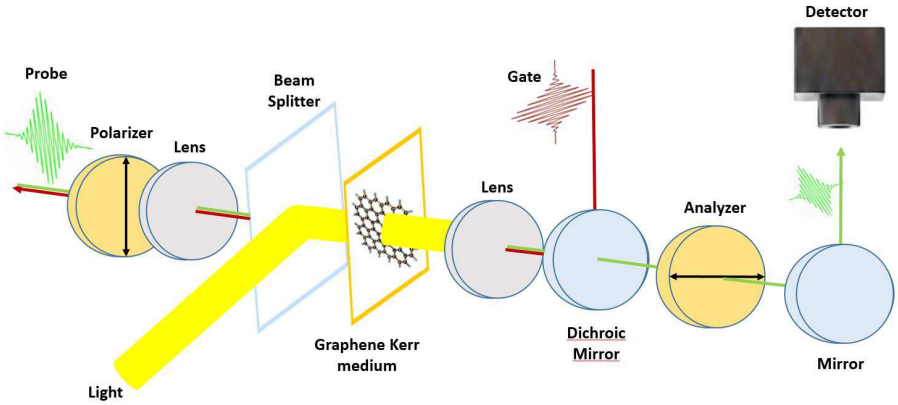


Figure 6.53: Scheme of OKG setup incorporating an improvised home-built microscope into it.

The glass substrate bearing the sample is placed and adhered within a 3D printed frame to protect it. This frame is fixed into a holder attached to an XYZ translation stage, which allows two-dimensional movement control across the X-Y plane, as well as adjusting the focus of the laser onto the sample along Z direction. The 50 mm lens along with the pco.pixelfly camera were evaluated using a resolution target and found that each pixel of the camera sensor has 1.338 μm. Because the 50 mm focal length lens offers small magnification and NA, our samples look apparently smaller in size using this improvised microscope. For a comparison between the images taken by the commercial microscope and our improvised OKG microscope, see Fig. 6.54, in which the commercial microscope images were taken by an objective lens 40× - 0.65 NA, and the OKG microscope images were taken by the 50 mm lens, used for focusing the gate beam.

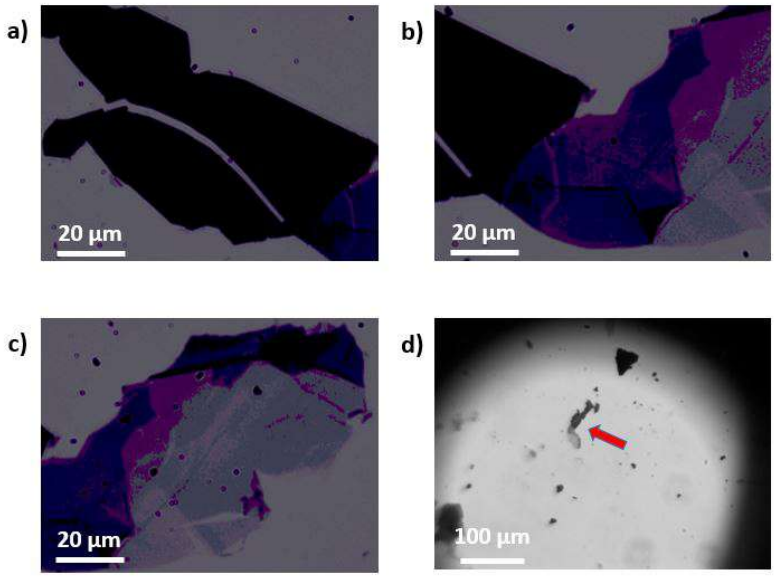


Figure 6.54: Difference between images taken by a commercial microscope (40× - 0.65 NA), and home-built microscope integrated into OKG setup. (a), (b), (c) Optical micrographs obtained by the commercial microscope, for graphite, thick graphite film, thin graphite film, respectively. (d) Optical micrograph of all of them together (pointed at with the red arrow), taken by a home-built OKG microscope.

The OKG experiment performed with graphene and thin graphite films had the pump and probe beams counter-propagating. After the initial alignment, and beam spot size adjustment for both beam (probe beam diameter ≈ 20 μm, and gate beam diameter ≈ 30 μm), as well as specification of the temporal overlap position on the delay line, the OKG began with moving the sample, so that both the gate and probe beams are passing through it. By scanning the gate beam ($\lambda = 820$ nm), whose average power was 1000 mW (pulse peak intensity $I_0 \approx 1.33$ GW/cm^2), with 1 fs temporal stepsizes, similar transmitted time traces to CS_2, were observed with the thin graphite film ($\sim$ 17-18 layers), shown in Fig. 6.54 (c). The transmitted Kerr signal time trace of that thin graphite film was integrated for 5 sec, and it is illustrated in Fig. 6.55 (a), along with its extracted temporal profile, which was not fully scanned up to the end to reduce its exposure time to the 1 W of gate beam laser power.

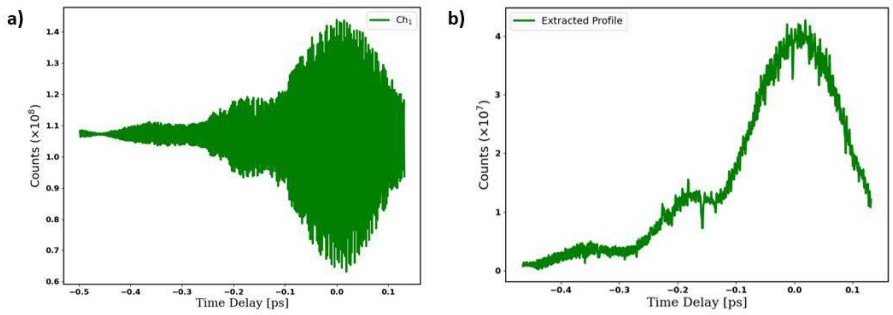


Figure 6.55: (a) Transmitted Kerr signal time trace for degenerate counter-propagating pump and probe beam ($\lambda = 820$ nm) of a thin graphite file ($\sim$ 17-18 layers), at 1 fs temporal stepsizes, and integration time of 5 s, (b) Extracted temporal profile of Kerr signal from its time trace in (a).

Unfortunately, owing to the long exposure time necessary for the 1 fs temporal stepsizes, the relatively long integration time at each point, as well as the high gate power, the irradiated spot of the thin graphite film was damaged, as shown in Fig. 6.56. Because of that damage, later OKG experiments were performed at lower average gate powers, and longer temporal stepsizes.

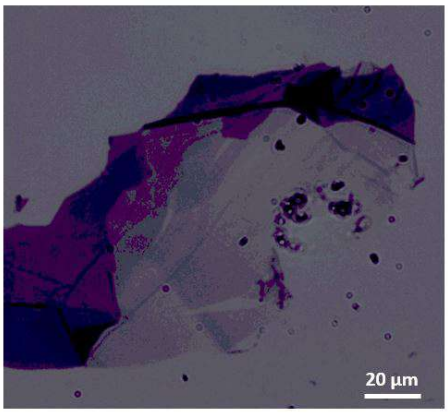


Figure 6.56: Optical micrograph of the damaged thin graphite film after OKG experiment.

To verify that the observed transmitted signal time trace originates from the thin graphite film itself, not any other effect caused by its supporting glass substrate, the same experiment was repeated several times with a bare glass substrate of the same thickness, from the same glass manufacturer, where the pump beam was temporally scanned over the same delay line distance, relative to the probe beam. An example of those measurements is presented in Fig. 6.57, which all of them confirmed that the glass substrate itself does not induce, or cause such a time trace.

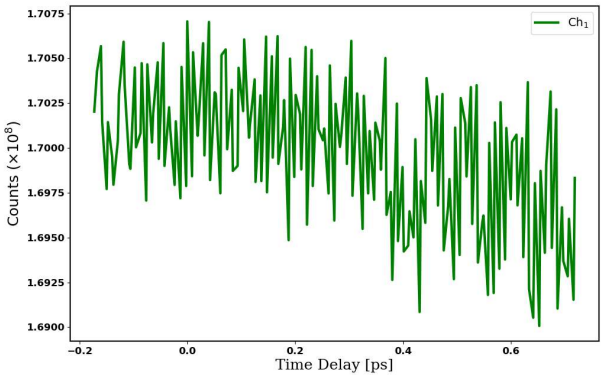


Figure 6.57: Transmitted signal of a bare glass substrate, with a pump beam temporal scan relative to the probe beam of 5 fs temporal stepsizes, and 5 s integration time.

Another graphite film relatively thicker than the one presented in Fig. 6.56 (the exact thickness is unknown, and requires AFM characterization) was used for the OKG experiment. The gate beam average power was reduced to 250 mW (pulse peak intensity $I_0 \approx 0.33$ GW/cm^2) to avoid any damage, larger temporal stepsizes of 25 fs, and 30 s integration time were used for recording the transmitted Kerr signals. This graphite film is shown in Fig. 6.58 (a), along with its transmitted Kerr signal trace, shown in Fig. 6.58 (b).

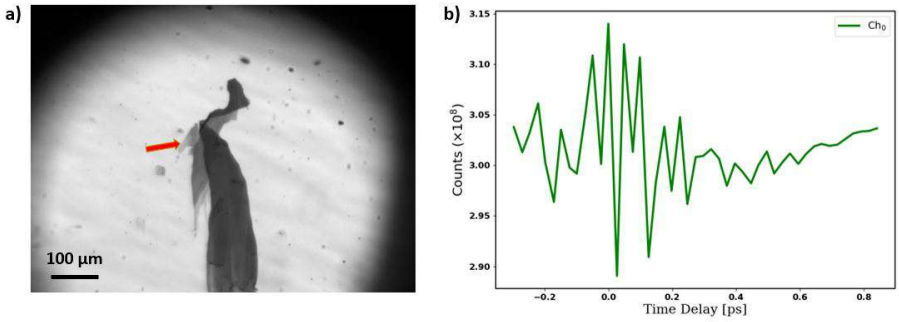


Figure 6.58: (a) Optical micrograph of a graphite film (marked with red arrow), obtained by home-built OKG microscope, (b) Transmitted Kerr signal time trace (pump+probe background subtracted) obtained at gate beam ($\lambda = 820$ nm) average power of 250 mW (pulse peak intensity $I_0 \approx 0.33$ GW/cm^2), 25 fs temporal stepsizes, and 30 s integration time.

The extracted temporal profile of the time trace shown in Fig. 6.58 (b) has been smoothed via the so-called Savitsky-Golay filter, with a window of 7 points, and a polynomial order of 3, which resulted in better temporal profile, as shown in Fig. 6.59, whereas this smoothed temporal profile was used for fitting. Given the nature of the relaxation mechanisms of graphene and thin graphite films, which can be categorized into fast relaxation undergone by the Coulomb-Coulomb interaction

among photoexcited electrons and the later transfer to optical phonons; and a slow relaxation underogne by the slow transfer of energy from the optical phonons to the acoustic phonons, an empirical model of a bi-exponential function convoluted with a Gaussian function for the cross-correlation of the pump and probe pulses was initially used for fitting the experimental data, a model that is often used in transient absorption spectroscopy of graphene/graphite films [469], which is described by the following relationships

$$g(t) = D_1 \exp\left(-\frac{t-t_0}{\tau_1}\right)\left[1-\operatorname{erf}\left(\frac{w}{2\tau_1}-\frac{t-t_0}{w}\right)\right] \tag{6.17}$$

$$+ D_2 \exp\left(-\frac{t-t_0}{\tau_2}\right)\left[1-\operatorname{erf}\left(\frac{w}{2\tau_2}-\frac{t-t_0}{w}\right)\right], \tag{6.18}$$

where $D_1 = C_0 A_1$ and $D_2 = C_0 A_2$ are the relative amplitudes of the fast and slow relaxation, such that A_1 and A_2 are the amplitudes of the fast and slow relaxation, and C_0 is the amplitude of the cross-correlation between the pump and probe beams. The decay time constant for the fast relaxation mechanism is τ_1, while the decay time constant for the slow relaxation mechanism is τ_2, and $w = \sigma\sqrt{2}$ is the cross-correlation width, where σ is the temporal pulse width of the pump and probe pulses. The result of fitting with this model including an offset d, is shown in Fig. 6.59.

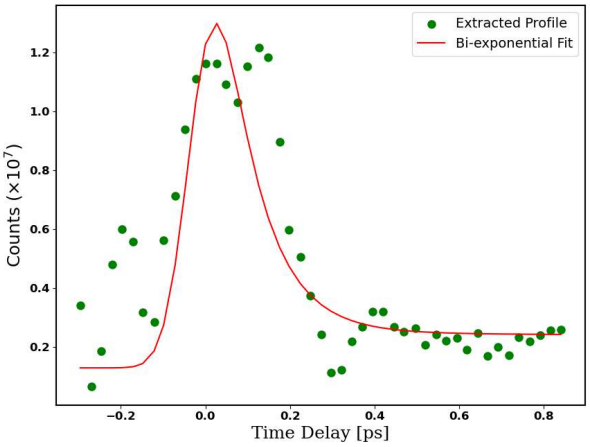


Figure 6.59: Fitting with bi-exponential convoluted with a Gaussian cross-correlation of the pump and probe beams, showing FWHM $\approx 169 \pm 16$ fs.

The fitting parameters gives a fast relaxation time constant $\tau_1 \approx 90 \pm 10$ fs, and a slow relaxation time constant $\tau_2 \approx 18 \pm 7$ ps, which is large uncertainty. Although the bi-exponential function convoluted with a Gaussian function is a valid empirical model to extract the values of τ_1 and τ_2 associated with the fast and slow relaxation mechanisms, in our case it could not reliably extract the relaxation time constants, especially the slow relaxation time constant, which typically has a small amplitude

buried in the noise. In other words, the fitting model fits the slow relaxation constant, along with a relatively large noise, thereby exhibiting huge uncertainty. This noise arises from electronic noise from detectors, stray light getting into the photodetectors, as well as some polarization leakage. However, the FWHM which represents the IRF can be estimated from the bi-exponential model, and its uncertainty is obtained numerically via Monte-Carlo sampling, as the FWHM is not a fitting parameter of the bi-exponential model itself. Based on that, an FWHM $\approx 168 \pm 16$ fs has been obtained.

From the result seen in Fig. 6.59, one can see that the fast relaxation time constant is not comparable to the range of fast relaxation time ($\sim$ 200-300 fs), the slow relaxation time constant does not match the range ($\sim$ 2.5-5 ps), reported in the work of Ref. [471], for exfoliated graphene and thin graphite film. The reason for that could be that, as we see in Fig. 6.59, scanning the gate beam at relatively large temporal stepsize, like 25 fs used here yields few data points. Thus their fitting cannot identify accurately the real relaxation constants. Also, due to the relatively large noise that affects both the fast and slow time constants, a reliable extraction of relaxation constants is not feasible. Moreover, there might be another physical reason for the faster time constant of the fast relaxation process. Since the supporting substrate of the samples is silica glass (SiO_2), which is a polar substrate, there might be an efficient coupling between the surface charges, and photoexcited electrons; as well as efficient coupling between the optical phonons of the graphite film and the surface phonons of the glass substrate. If that is the case, this will enable efficient cooling for the excited carrier, allowing them to acquire faster relaxation times [468].

Another thin graphite film ($\sim$ 13 layers) was studied at relatively higher gate beam average power of 290 mW (pulse peak intensity $I_0 \approx 0.38$ GW/cm^2) and similar integration time, 30 s, which both were increased in order to get better signal. The temporal stepsize of 25 fs was maintained. This thin film is shown in Fig. 6.60 (a), along with its transmitted Kerr signal, Fig. 6.60 (b).

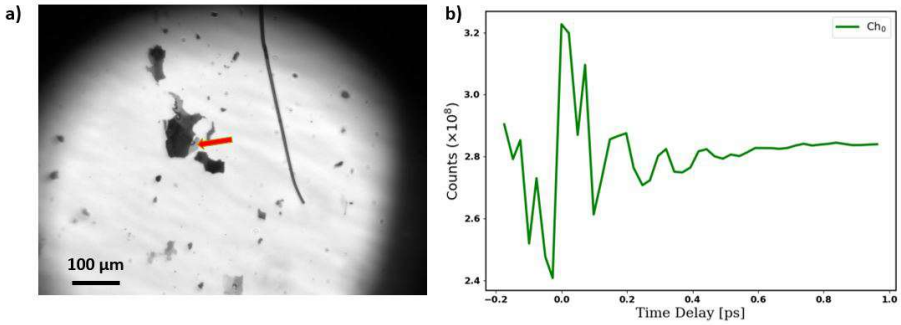


Figure 6.60: (a) Optical micrograph of a graphite film (marked with red arrow), obtained by home-built OKG microscope, (b) Transmitted Kerr signal time trace obtained at gate beam ($\lambda = 820$ nm) average power of 290 mW (pulse peak intensity $I_0 \approx 0.38$ GW/cm^2), 25 fs temporal stepsizes, and 30 s integration time.

This temporal profile of the time trace presented in Fig. 6.60 (b) was extracted, presented in Fig. 6.61 has been also smoothed via Savitsky-Golay filter, with a window of 7 points, and a polynomial order of 3. Similar to what has been done before, an initial attempt was done to use a bi-exponential model to fit the temporal profile, and similar issue with the slow relaxation time constant occured. The result of that fitting attempt is provided in Fig. 6.61, from which a fast relaxation time constant $\tau_1 \approx 58 \pm 3$ fs was obtained, while the slow relaxation time constant $\tau_2 \approx 1 \pm 8$ ps, which is a huge uncertainty, owing to the dominance of noise, and having relatively few number of points.

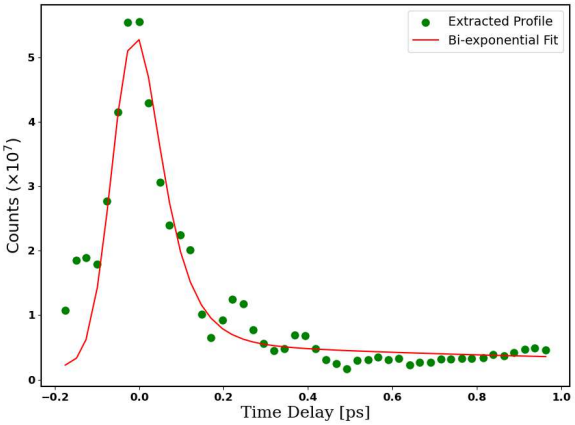


Figure 6.61: Fitting with bi-exponential convoluted with a Gaussian cross-correlation of the pump and probe beams, showing FWHM $\approx 141 \pm 6$ fs.

Also here, the FWHM was estimated similar to before, and found to be $\sim 141 \pm 6$ fs. To estimate the gating efficiency of thin graphite films, measurements using a 656 nm CW probe and an 820 nm femtosecond gate beam in a degenerate counter-propagating geometry at ~ 0.2 nJ gate-pulse energy (pulse peak intensity $I_0 \approx 0.26$

GW/cm^2) were carried out (see Appendix B), which found that the gating efficiency is $\sim 10\%$.

After reconfiguration of the experimental setup, so that the pulsed gate and probe beams co-propagate, where the gate beam was passing through the sample at $\sim 29°$, similar to the BBS glass experiment; several attempts were made to measure the OKG signal time trace. To avoid damaging the graphene and thin graphite films, the maximum gate power used in those measurements was ~ 250 mW. Although the gate beam spatially overlaps at a large angle, with the probe beam, some scattering of it into the sample was noted. Due to the relatively high intensity of the scattered spots of the gate beam, the Kerr-rotated pulsed probe beam signals were obscured by the gate beam scattering.

We have shown that our graphene and thin graphite film samples can be damaged under a gate-laser energy fluence below 0.31 mJ/cm^2—more than an order of magnitude lower than the lowest damage fluences reported in the scientific literature. Although the dominant damage mechanism is a nonthermal interaction between graphite planes occurring on ultrafast timescales, any residual heat accumulation over longer timescales may also induce damage during prolonged exposure. Heat accumulation is a particularly serious concern when using lasers with high repetition rates. As mentioned earlier, our solid-state laser operates at 1 GHz, nearly an order of magnitude higher than most commercial solid-state laser systems.

Unfortunately, the experiment performed to determine the damage threshold—and thereby identify safe average powers or fluences for graphene/thin-graphite OKG measurements—using a home-built Raman microscope was inconclusive. In some cases, graphene or thin graphite films withstood one hour of exposure to 1 W of average power, while in other cases similar samples were damaged at powers as low as 200 mW. One factor that may contribute to this inconsistency is variation in environmental conditions, particularly humidity. A dedicated experiment that tracks heat accumulation at different repetition rates and under controlled environmental conditions is therefore crucial. For any nonlinear-optical application involving graphene—such as OKG or saturable absorption—the damage threshold must be determined unambiguously.

The SPM measurements performed with graphene and thin graphite films were consistent with SPCR theory, since the gate-pulse duration is much shorter than the carrier relaxation time and the pulse traverses only the very small thickness of the film. For OKG experiments with thin graphite films in the counter-propagating configuration, reproducible results were obtained, yielding Kerr-signal time traces exceeding the OKG efficiency of those measured with BBS glass. These signals originate from the 2D material itself and not from the supporting substrate, as

confirmed by measurements on a bare glass coverslip. Unfortunately, the fast and slow relaxation time constants obtained from the data were not reliably extracted, due to the dominance of noise. Hence, both showed a deviation from reported literature values for mechanically exfoliated thin graphite films. However, the IRF values were successfully obtained, exhibiting sub-ps time resolution.

Reconfiguring the experimental setup to resemble the standard co-propagating OKG geometry did not yield reproducible results. This is attributed to scattered gate-beam light entering the probe-beam optical path and severely distorting the transmitted Kerr-signal time trace. A lock-in amplifier will therefore be essential to suppress scattered-light background. Ideally, the OKG experiment should also be performed with non-degenerate pump and probe beams. The OPO can provide an alternative probe wavelength, although the observed wavelength drift presents an additional challenge. This drift may potentially be mitigated by pumping nitrogen gas into the OPO cavity, while the power required to drive the OPO from the Taccor Ti:Sa laser should be minimized.

Chapter 7

Summary and Outlook

In this dissertation, an approach based on using a high-repetition-rate laser (1 GHz) to increase the fluorescence emission rate of single quantum emitters at room temperature has been proposed. This strategy benefits uncoupled emitters by increasing their brightness, thereby making them more suitable for quantum technologies such as quantum computing, quantum cryptography, and quantum information processing. It is even more advantageous for hybrid quantum systems in which emitters are coupled to nanophotonic structures—such as gold nanocones—that yield ultrabright single-photon sources due to Purcell-enhanced radiative decay rates. As the fluorescence lifetime becomes ultrashort in such systems, its measurement exceeds the capabilities of standard detector technologies. To overcome this limitation, an optical Kerr gate (OKG) operating at 1 GHz with sub-picosecond temporal resolution has been demonstrated in this work using two distinct Kerr media: a bulk medium and a two-dimensional material.

The setup was initially characterized using carbon disulfide (CS_2). The measurements revealed the expected ultrafast electronic response arising from bound-electron hyperpolarizability, as well as the fast molecular relaxation component. However, the slow molecular relaxation component could not be clearly resolved, primarily due to the modest gate-pulse intensity and the presence of noise from the SPAD, TCSPC electronics, stray light, probe beam leakage through the cross-polarizers, and incomplete suppression of noise because no lock-in amplifier was used.

The bulk Kerr medium investigated was a 3-mm-thick BBS glass specimen. Using this glass, OKG signals were obtained in a degenerate counter-propagating geometry at < 1 nJ gate-pulse energy (< 1.33 GW/cm^2 peak intensity), achieving an estimated $\sim 3\%$ Kerr-gate efficiency based on measurements using a 656 nm CW probe and an 820 nm femtosecond gate. The resulting instrument response function (IRF) was $\sim 175 \pm 1$ fs. As discussed in Chapter 5, this IRF represents the convolution

of the pump–probe cross-correlation and the intrinsic nonlinear response of the BBS glass; thus, the nonlinear response time of BBS is < 175 fs. To the best of the author's knowledge, this is the first demonstration of a $\chi^{(3)}$ process such as optical Kerr gating (cross-phase modulation) at such modest pulse energies and peak intensities. This is notable because conventional OKG experiments rely on amplified mJ-level pulses—six orders of magnitude higher energy—together with lock-in detection. It is important to note that the IRF is ultimately limited by the cross-correlation of the gate and probe pulses. Therefore, any further reduction in their pulse durations—either through intracavity dispersion compensation, external pulse compression, or improved OPO tuning—would directly translate into an even shorter IRF. In principle, sub-100-fs Kerr-gate resolution is achievable if both pulses are correspondingly shortened.

The second Kerr medium was thin graphite films prepared via mechanical exfoliation. High-quality graphene and thin graphite samples were fabricated, and several exhibited damage thresholds around 0.31 mJ/cm^2—nearly an order of magnitude lower than the lowest reported values in the literature. Self-phase modulation (SPM) measurements did not show any noticeable spectral broadening that could interfere with emitter fluorescence. The results matched the SPCR theory of Vermeulen et al. [457]. The OKG signal obtained with thin graphite films exhibited an IRF of $\sim 141 \pm 6$ fs using < 250 pJ gate-pulse energy (< 0.33 GW/cm^2). An OKG efficiency of $\sim 10\%$ was measured using a 656 nm CW probe. For context, a $\sim 12\%$ efficiency (with ~ 500 fs IRF) was previously reported (Ref. [472]) for a 2-mm-thick Crown-5 glass plate—six orders of magnitude thicker than the graphite films used here—highlighting the exceptional nonlinear potential of graphene-based materials.

Several steps are required to further advance this work. First, achieving reproducible degenerate OKG signals in the co-propagating geometry will necessitate the use of a lock-in amplifier to suppress scattered gate light, which currently distorts the transmitted Kerr-signal time traces. Second, implementing a collinear, non-degenerate OKG represents an important next step. For this, the optical layout must be modified such that part of the Taccor Tune femtosecond laser output is directed to the OKG as the gate (pump), while another portion drives the OPO to generate a probe beam at a different wavelength. This configuration enables effective spectral filtering after the Kerr medium. To address the wavelength instability observed in the OPO, nitrogen gas should be flushed into the OPO cavity, and the required pump power from the Taccor laser must be optimized.

Once this is achieved, the next milestone will be integrating the OKG into the confocal fluorescence microscope currently under construction. In such a configuration, the OPO output would excite the fluorescent sample (providing the probe), while the

high-intensity 1-GHz pulse train from the Ti:Sa laser would act as the gate. For these initial experiments, uncoupled SiV centers are not ideal because their $\sim$ 1-ns lifetime is long compared with the 1-ns pulse separation of the 1-GHz laser. Instead, fast-emitting dyes—such as 4-DASPI, Allura Red AC, Coumarin-30, or Astra Phloxine—are more suitable, as their fluorescence lifetimes lie in the few-picosecond to few-hundred-picosecond range. For ensemble fluorescence detection, BBS glass is appropriate due to its $\sim$ 3% gating efficiency, whereas thin graphite films are expected to yield superior results because of their $\sim$ 10% efficiency.

Although a $\sim$ 10% Kerr-gate efficiency is, in principle, sufficient for detecting single-photon fluorescence above the detector's dark-count rate (DCR), real-world performance is limited by several factors. Stray light and/or probe beam leakage through imperfect crossed-polarizers reaching the SPADs can obscure the Kerr-rotated fluorescence signal. Thermal lensing caused by heat accumulation at 1 GHz can reduce the effective Kerr-gate efficiency. Furthermore, small angular drifts of the polarizers can displace the signal from the SPAD's active area, decreasing detected counts. Therefore, thorough optimization of the optical setup is essential. A major improvement can be obtained by replacing the current economy-grade polarizers with high-extinction-ratio-i.e., Glan–Taylor polarizers, which would greatly reduce probe leakage and increase the signal-to-noise ratio.

The thin graphite films yielding $\sim$ 10% OKG efficiency were produced by exfoliating HOPG, whose graphene layers are highly aligned. This implies that the layers in each thin graphite flake are strongly coupled. The role of interlayer coupling in the Kerr response remains unclear. For example, one study (Ref. [462]) reported that randomly stacked multilayer graphene exhibits a reduced n_2 as the number of layers increases, attributing this to weak interlayer coupling and increased scattering. In contrast, another study (Ref. [458]) found that decoupling the layers preserves the giant n_2 characteristic of monolayer graphene. These contradictory findings indicate that a systematic investigation of stacking order is needed.

Shan et al. [353] showed that second-harmonic generation in trilayer graphene can be enhanced or suppressed depending on stacking order. Cao et al. [350] demonstrated that twisting two graphene layers by 1.1° ("magic angle") produces unconventional superconductivity by modifying the electronic band structure. These findings suggest that stacking order and twist angle may likewise strongly influence $\chi^{(3)}$ nonlinearities such as the OKG response. If certain stacking configurations preserve the monolayer-like nonlinear response, they could significantly enhance the OKG efficiency—an outcome highly desirable for ultrafast single-photon detection.

Beyond graphene-based materials, other platforms may also serve as effective Kerr media. One notable example is photonic crystal fibers (PCFs), which can be engi-

neered to exhibit near-zero dispersion at specific wavelengths—particularly those matching the output of common solid-state lasers. Their extended interaction length dramatically increases the nonlinear phase shift achievable within the medium, offering a potential route toward higher Kerr-gate efficiencies at modest pulse energies. Furthermore, when incorporated into a Sagnac interferometer, PCFs have been shown to detect single photons via Kerr-induced phase modulation [252], demonstrating their suitability for ultrafast measurements in the low-photon-number regime. Such fiber-based Kerr media therefore represent a compelling alternative for future implementations of GHz-rate optical Kerr gating.

Appendix A

Determination of temporal overlap without Kerr medium

With a delay line that is 300 mm long, and a train of pulses, each of which is temporally separated by 1 ns, one can intuitively think that there are three locations on the delay line, where the pump and probe pulses are temporally overlapped. The first location is supposed to be somewhere near 0 mm, the second location somewhere near 150 mm, and the third one is somewhere near 300 mm. Scanning the two pulses at the very edges of the delay line is not possible. Obviously, this is because at these edges the delay line has no space to move anymore. Thus, it is highly likely that the temporal overlap occurs in the vicinity of 150 mm. Needless to say, when a Kerr medium is placed into the OKG, the temporal overlap will be a bit shifted, which will require scanning again in the vicinity of the determined location of the temporal overlap without the Kerr medium to find the new location of temporal overlap. The scan direction and distance to find the new location, depends upon the thickness of the Kerr medium and its linear refractive index. To accurately find the temporal overlap position, it was important to understand how the oscilloscope readout the signal. This signal is a convolution between two trains of pulses (pump and probe) delayed by $\Delta\tau$ relative to each other (see Fig. A.1 (a)) and the IRF of the photodiode detector (see Fig. A.1 (b)).

First, the IRF function of Fig. A.1 (b) was simulated with the function $a \exp\left(-\frac{(x-b)^2}{2c^2}\right)$, with the following parameters, a = -220 $\times$ 10^{-3} V, b = 1.2 $\times$ 10^{-9} s, and from a FWHM IRF = 480 $\times$ 10^{-12}, the value of c = FWHM IRF/$(2\sqrt{2\ln 2})$ was determined. The simulated IRF of the photodiode detector is presented in Fig. A.2.

If we denote the temporal profile of the probe pulse by $g(t)$ and the delayed pump pulse is denoted by $g(t + \Delta\tau)$, then the convolved signal in the time-domain, as

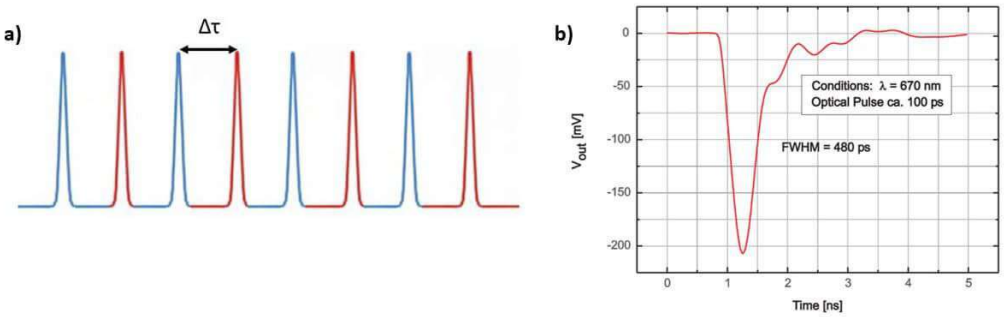


Figure A.1: (a) Pump and probe trains of pulses (different color for visual guide), (b) IRF of TDA200 photodiode detector [473]

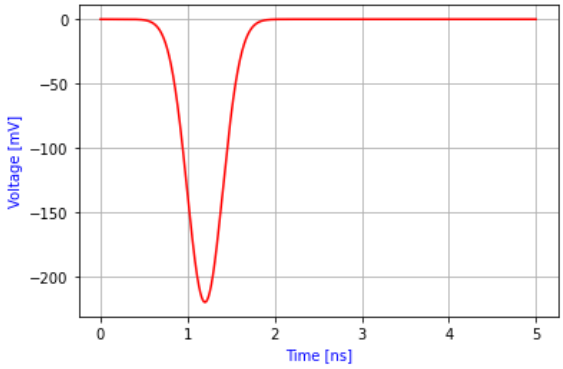


Figure A.2: Simulation of the IRF of TDA200 photodiode detector.

detected by the oscilloscope will be given by the following relationship

$$\text{Osc. Signal} = \mathcal{F}^{-1}\left\{\mathcal{F}\{g(t) + g(t+\tau)\} * \mathcal{F}\{\text{IRF}\}\right\}. \tag{A.1}$$

It is important to clarify that the Equ. A.1 gives the signal for a particular position on the delay line. Meaning that, if we scan a large distance along the delay line to find the accurate location, one needs to collect an oscilloscope signal at each corresponding position. As mentioned before, since the oscilloscope cannot resolve the delays at smaller temporal steps, and because one photodiode detector is used to detect these two trains of pulses together, both pulses are displayed on the oscilloscope screen as one curve, whose voltage amplitude increases or decreases, based on how far apart the two pulses. By subtracting the minima voltages of the curve from the maxima, one can get a single voltage point that represents the degree of the temporal overlap at a specific position on the delay line. Therefore, following this method while scanning the delay line, one will get a voltage amplitude value representing the degree of temporal overlap as a function of delay line position.

A series of measurements had been taken, as described above, and a simulation was made to verify the results, using Equ. A.1. For example, the delay line was scanned from 1-295 mm, with a scan step of 15 mm, which corresponds to delaying

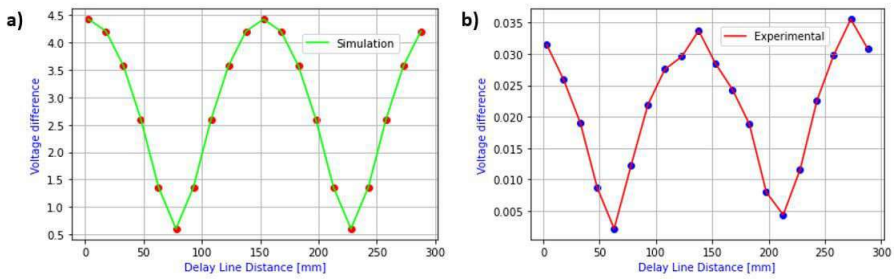


Figure A.3: Comparison between (a) simulation and (b) measurement result of scanning the pump and probe pulses over a distance of 1-295 mm, with 15 mm stepsize (100 ps).

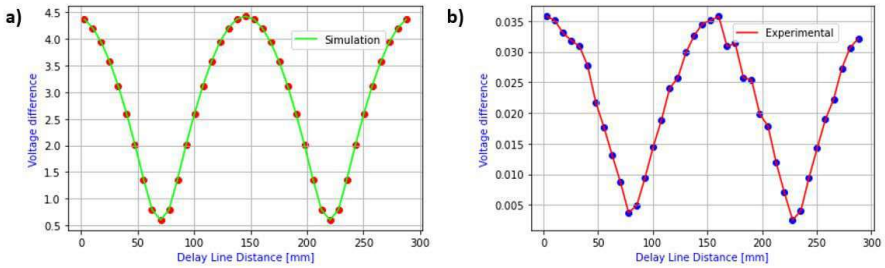


Figure A.4: Comparison between (a) simulation and (b) measurement result of scanning the pump and probe pulses over a distance of 1-295 mm, with 7.5 mm stepsize (50 ps).

the gate and probe pulses by 100 ps. A comparison between the simulation and the experiment is shown in Fig. A3.

The simulation in Fig. A.3 (a) confirms the intuition that the three possible locations, where the pump and probe pulses must temporally overlap is somewhere near 0, 150, 300 mm. Note that the experimental measurement in Fig. A.3 (b) is in excellent agreement with the simulation result, except that the peak at 150 mm is a bit deviated. This deviation could arise from photodiode detector noise, or from the oscilloscope, and/or lack of the necessary precision and step repeatability of the delay line.

Another measurement by scanning the pump and probe trains of pulses over the same distance, but with finer steps, 7.5 mm (50 ps), showed also excellent agreement between the simulation and measurement, as presented in Fig. A.4.

Because of the possible noise sources mentioned above, scanning the pump train of pulses to temporally overlap it, with the probe train of pulses could result in getting different voltage amplitude and/or different peak position. For example, with the same parameters of Fig. A.3, scanning the same distance twice shows that one peak appears at 121 mm of the delay line, while the second scan shows the peak at 136 mm, namely a 15 mm difference, as illustrated in Fig. A.5.

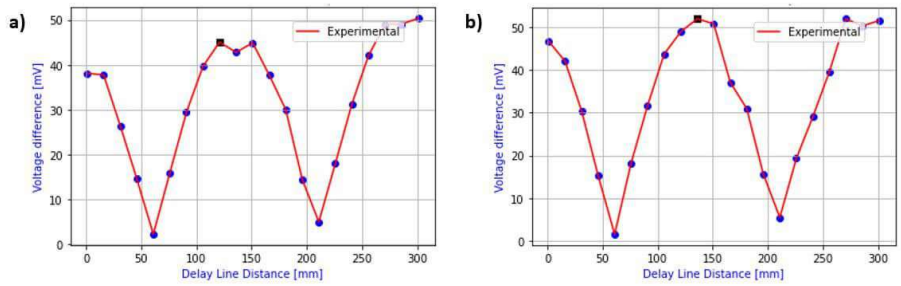


Figure A.5: Two different measurements in which scanning the pump and probe pulses over a distance of 1-295 mm, with 15 mm stepsize (100 ps), gives a peak (a) at 121 mm, and (b) at 136 mm (black square to mark the central peak).

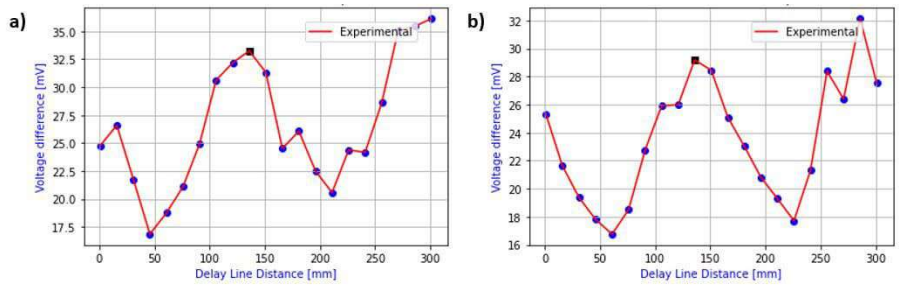


Figure A.6: Two measurements of the voltage amplitude change, when the photodiode detector measures after the second polarizer, taken by scanning over a distance of 1-295 mm, with stepsize of 15 mm (black square to mark the central peak).

Thus far, all the measurements presented previously were taken by placing the Photodiode detector before the second polarizer of the OKS. However, when the same measurements are repeated with the photodiode detector placed after the second polarizer, it is noticed that a significant change, in terms of the voltage amplitude of the measured trace can occur. For example, the measurements presented in Fig. A.5, were investigated with the second polarizer, and the peaks amplitudes are obviously different, as shown in Fig. A.6.

Appendix B

OKG experiment with CW laser as a probe

In the following, the results of an OKG experiment were carried out, where the two beams are counter-propagating, but the gate beam is still the fs laser at 820 nm, while the probe beam is a CW laser at 656.64 nm. This experiment was performed with BBS glass, and thin graphite films. The intention of that experiment was to demonstrate optical Kerr gating at 1 GHz, and was to avoid the difficulty imposed by the degeneracy (the same wavelength) of the pulsed pump and probe beams experiment shown in chapter 5 and 6, in which the Kerr-rotated probe signal was harder to detect. For the detection of the probe beam signals, the QE Pro spectrometer that has high spectral resolution was utilized to detect the Kerr signals via detecting the spectral broadening, which is supposed to occur for the probe beam spectrum, after the gate beam induce the birefringence in the BBS glass. For simplicity, the analysis of the data focused more on the spectral amplitude changes, rather than the spectral broadening. In this regard, the gate beam was initially blocked, and the CW laser spectrum was measured, after passing through the BBS glass, and the analyzer. Then, the gate beam was unblocked, and the CW laser spectrum was measured again for comparison. Whether the gate beam was blocked or not, the CW laser was passing through the BBS glass. The expected outcome from this experiment was that, when the gate beam is unblocked, as it induced birefringence in the BBS glass, the Kerr-rotated signal will be able to pass through the analyzer, the amplitude of the CW laser spectrum is supposed to increase, and becomes broader. The gate laser beam power was maintained at 1 Watt, while the CW laser power was changed to see the effect on the detected signals. For example, at CW laser power of 0.740 mW, the CW laser spectrum was measured and stored in a separate file, when the gate beam was blocked, then it was unblocked and the CW spectrum was measured and stored in a separate file. The spectrum of the CW

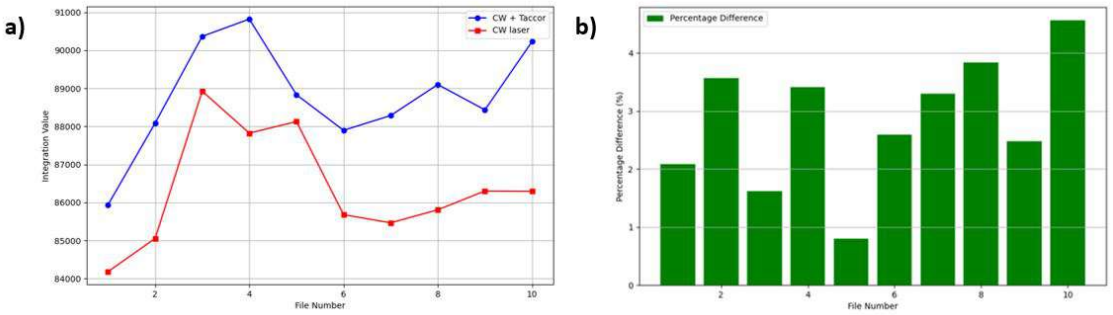


Figure B.1: (a) Integrated CW laser spectrum (at $\lambda = 656.64$ nm - 0.740 mW) of 10 measurements, when the gate beam (Taccor fs laser) was inducing birefringence (blue) versus when it was blocked (red); (b) Percentage increase of CW laser spectrum, when the gate beam is unblocked.

laser in each case was integrated, and 10 measurements were carried out, each of which has its own file number designated for the measurement, as shown in Fig. B.1 (a). Indeed, a rise in the CW laser spectrum was noticed, and the percentage of that increase was calculated, as shown in Fig. B.1 (b).

The maximum percentage increase of the CW laser spectrum observed in Fig. B.1 reaches > 4 %. Such increase cannot be attributed to the normal CW laser fluctuation, which is about 1.22 %. When the average value of the 10 measurements is taken, the OKG efficiency is estimated to be $\sim 3\%$. Interestingly, the CW laser spectrum when the gate beam was blocked has increased after the first measurement when the gate beam was unblocked, which is easily observed through the No. (2-6) measurements. This indicates that the gate beam might be inducing other nonlinear effects of longer relaxation times scale than what Kerr effect typically has. Since the CW laser always passes through the Kerr medium (BBS glass here), it can sense those long time effects, and become affected by them. Over the course of several measurements, the dynamical response of the BBS glass was surprisingly changing. For example, in Fig. B.2 (a), the CW laser spectrum will exhibit different behavior, and it will even decrease, when the gate beam passes through the Kerr medium, which manifests itself in the inverted percentage of the CW laser spectrum, seen in Fig. B.2 (b).

Between the two opposite extremes shown in Fig. B.1 and Fig. B.2, in some measurement sessions, the dynamics can swing between an increase of the CW laser spectrum, after the gate beam unblocked to a decrease in the spectrum, as illustrated in Fig. B.3.

From the previous measurements with CW laser, we can conclude that further study might be required, in order to resolve the other nonlinear dynamical effects, which results in the fluctuation of the CW laser spectrum value. As stated before, the fundamental difference between pulsed mode OKG experiments, wherein the pump

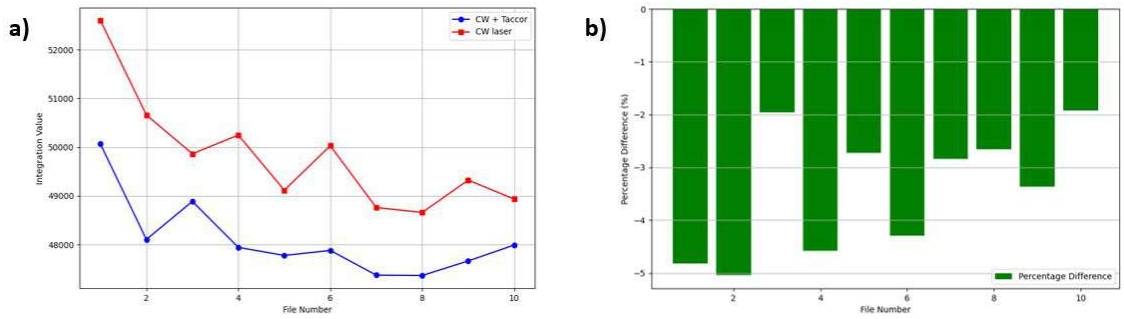


Figure B.2: (a) Integrated CW laser spectrum (at $\lambda = 656.64$ nm - 0.450 mW) of 10 measurements, when the gate beam (Taccor fs laser) was inducing birefringence (blue) versus when it was blocked (red); (b) Percentage decrease of CW laser spectrum, when the gate beam is unblocked.

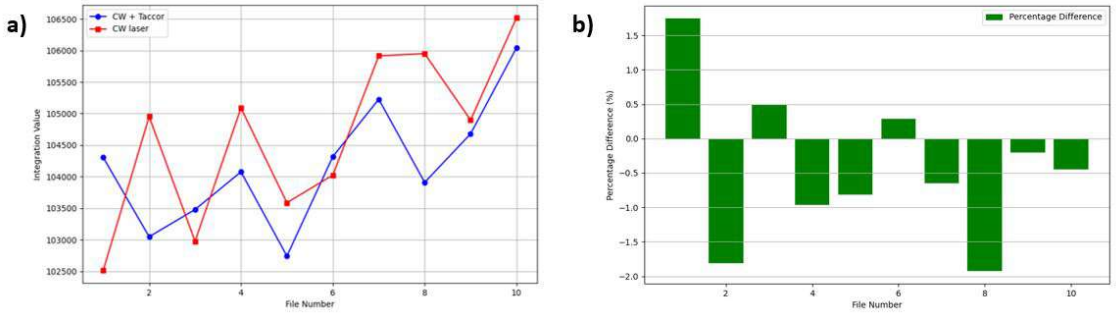


Figure B.3: (a) Integrated CW laser spectrum (at $\lambda = 656.64$ nm - 0.910 mW) of 10 measurements, when the gate beam (Taccor fs laser) was inducing birefringence (blue) versus when it was blocked (red); (b) Percentage increase/decrease of CW laser spectrum, when the gate beam is unblocked.

and probe beams are pulses, and the one in which the probe beam is a CW laser, is that the Kerr signal is obtained, solely, when the two pulses temporally (and of course spatially) overlap. In contrast, as the CW laser beam propagates always through the Kerr medium, any other induced nonlinear effect occurring at longer time scales would affect its spectrum. Having that said, the OKG experiments with probe beams of CW lasers should be carried out with lock-in amplifier detection. This is to achieve fast acquisition of the Kerr signal, which often takes place at very short, or short time scales.

The issue of minimal temporal overlap duration does not exist with the OKG experiment, where the probe beam was a CW laser counter-propagating the pulsed gate beam. This is because the CW laser always propagates through the Kerr medium. On the contrary, this is not fully beneficial, as the CW laser signal can probe any nonlinear effects that happen, over a long time scale. Consequently, this will definitely distort the predicted temporal dynamics, associated with OKG typical response time. That is why for harnessing the signal appropriately, a lock-in amplifier detection would need to be implemented.

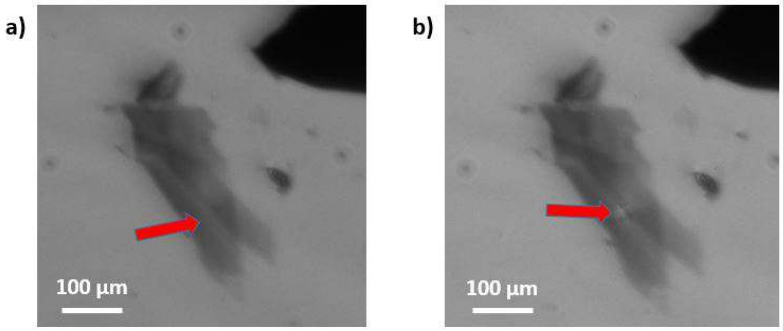


Figure B.4: A graphite film (a) Before and (b) After the OKG experiment with fs pulsed gate beam at 200 mW average power, and CW laser probe at 0.230 mW

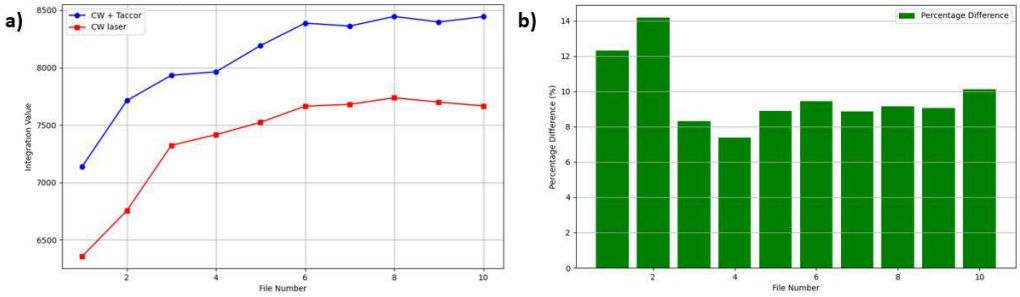


Figure B.5: (a) Integrated CW laser spectrum ($\lambda = 656.64$ nm - avg. power = 0.230 mW), for 10 measurements, when the pulsed gate beam ($\lambda = 820$ nm - avg. power = 200 mW) was blocked (red curve), and when it was unblocked (blue curve); (b) Percentage increase of the CW laser spectrum, as a result of unblocking the gate beam.

Similar OKG experiment with the same parameters was performed with thin graphite films, except that the gate beam average power was 200 mW (pulse peak intensity $I_0 \approx 0.26$ GW/cm^2), and the average power of CW laser ≈ 0.230 mW. The first measurements with a graphite film are presented in Fig. B.4 (a). Although the gate beam power was lower than the values used before with pulsed fs probe, the location on the graphite film that interacted with the laser spot was damaged, as indicated in Fig. B.4 (b). Initially before the OKG experiment begins, the CW laser fluctuation on the sample was found to be ~ 0.7 %. The outcome of the first OKG experiment, showed considerable rise, up to ~ 14 % of the CW laser spectrum, after the gate beam was unblocked, as opposed to when it was blocked, provided in Fig. B.5. As before with BBS glass, the analysis was focused on quantifying the spectral magnitude, rather than spectral width for simplicity. Also, each measurement (gate blocked/unblocked) was taken 10 times.

When the average of the 10 measurements is taken, the average indicate an estimated OKG efficiency of $\sim 10\%$. If we compare the maximum percentage increase in the CW laser spectrum of the graphite film, with the one obtained with BBS glass, we

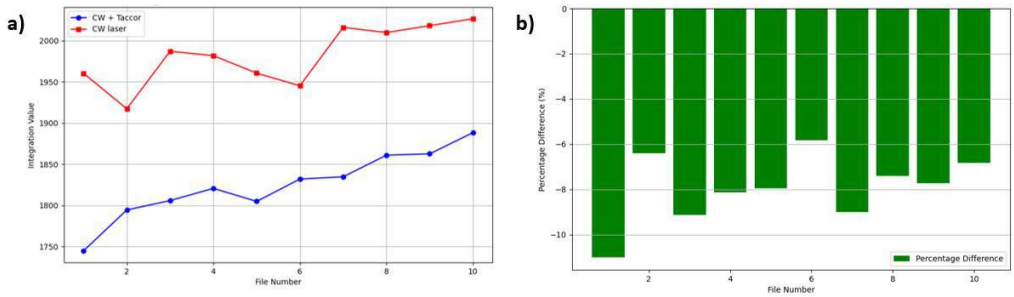


Figure B.6: (a) Integrated CW laser spectrum ($\lambda = 656.64$ nm - avg. power = 0.640 mW), for 10 measurements, when the pulsed gate beam ($\lambda = 820$ nm - avg. power = 200 mW) was blocked (red curve), and when it was unblocked (blue curve); (b) Percentage decrease of the CW laser spectrum, as a result of unblocking the gate beam.

find that it is approximately 10 % higher than the maximum percentage increase of the first measurement of BBS glass. This increase might be related to the relatively higher nonlinear refractive index n_2 that graphene and graphite films have, after considering their much smaller thicknesses, as compared to the BBS glass thickness. Note that the graphite film is capable of changing the magnitude of integrated CW laser spectrum, even when the gate beam is blocked, similar to what has been seen formerly with the BBS glass specimen. The experiment with the graphite film shown in Fig. B.4 (a) was repeated at different undamaged locations. It was noticed that repeating the measurements on any particular location results in the considerable reduction of the percentage increase of the CW laser spectrum. Even worse, the dynamics can change, in the sense that unblocking the gate beam will decrease the CW laser spectrum more than 10 %, when the gate beam average power is increased to 300 mW, as illustrated in Fig. B.6.

In addition to the considerable rise or decline experienced by the CW laser spectrum, when the gate beam is unblocked, abrupt rises and falls were observed in some measurements, when the gate beam is unblocked. An example of these abrupt spectral changes in the spectrum magnitude is seen in Fig. B.7. Such abrupt changes occurring when the gate beam is blocked are larger than the normal fluctuation (0.7 %) of the CW laser spectrum.

The same behavior shown in the previous figures was observed with gate laser average powers as little as 50 mW. Interestingly, upon removing the analyzer, similar behavior was observed, which indicates that the gate beam might be provoking other nonlinear effects, not related directly to the polarization of the CW laser.

With the same propagation scheme, but with replacing the pulse probe by a CW laser at a different wavelength, the OKG experimental results were not conclusive. Another study of the dynamical behavior of the CW laser spectrum upon unblocking the gate

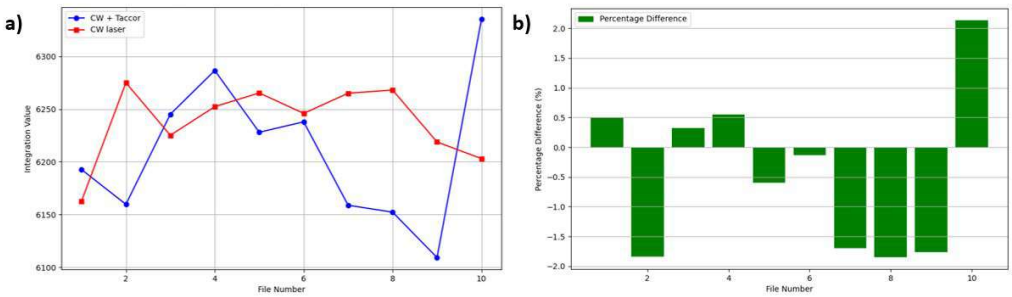


Figure B.7: (a) Integrated CW laser spectrum ($\lambda = 656.64$ nm - avg. power = 0.180 mW), for 10 measurements, when the pulsed gate beam ($\lambda = 820$ nm - avg. power = 200 mW) was blocked (red curve), and when it was unblocked (blue curve); (b) Percentage decrease of the CW laser spectrum, as a result of unblocking the gate beam.

beam, with/without the analyzer can possibly reveal the underlying dynamics.

Bibliography

[1] H. J. Kimble, M. Dagenais, and L. Mandel. „Photon Antibunching in Resonance Fluorescence“. In: *Phys. Rev. Lett.* 39 (11 Sept. 1977), pp. 691–695. DOI: 10.1103/PhysRevLett.39.691. URL: https://link.aps.org/doi/10.1103/PhysRevLett.39.691.

[2] Th. Basché et al. „Photon antibunching in the fluorescence of a single dye molecule trapped in a solid“. In: *Phys. Rev. Lett.* 69 (10 Sept. 1992), pp. 1516–1519. DOI: 10.1103/PhysRevLett.69.1516. URL: https://link.aps.org/doi/10.1103/PhysRevLett.69.1516.

[3] P. Michler et al. „Quantum correlation among photons from a single quantum dot at room temperature“. In: *Nature* 406 (6799 Aug. 2000), pp. 968–970. ISSN: 1476-4687. DOI: 10.1038/35023100. URL: https://doi.org/10.1038/35023100.

[4] Rosa Brouri et al. „Photon antibunching in the fluorescence of individual color centers in diamond“. In: *Opt. Lett.* 25.17 (Sept. 2000), pp. 1294–1296. DOI: 10.1364/OL.25.001294. URL: https://opg.optica.org/ol/abstract.cfm?URI=ol-25-17-1294.

[5] Takayuki Iwasaki et al. „Germanium-Vacancy Single Color Centers in Diamond“. In: *Scientific Reports* 5 (1 Aug. 2015), p. 12882. ISSN: 2045-2322. DOI: 10.1038/srep12882. URL: https://doi.org/10.1038/srep12882.

[6] Masanori Fujiwara et al. „Single tin-vacancy center in nanoscale diamond“. In: *Discover Nano* 20 (1 May 2025), p. 81. ISSN: 2731-9229. DOI: 10.1186/s11671-025-04256-0. URL: https://doi.org/10.1186/s11671-025-04256-0.

[7] Tom Feng and Bradley D. Schwartz. „Characteristics and origin of the 1.681 eV luminescence center in chemical-vapor-deposited diamond films“. In: *Journal of Applied Physics* 73.3 (Feb. 1993), pp. 1415–1425. ISSN: 0021-8979. DOI: 10.1063/1.353239. eprint: https://pubs.aip.org/aip/jap/article-pdf/73/3/1415/18654805/1415_1_online.pdf. URL: https://doi.org/10.1063/1.353239.

[8] Lyle Patrick and W. J. Choyke. „Photoluminescence of Radiation Defects in Ion-Implanted 6*H* SiC“. In: *Phys. Rev. B* 5 (8 Apr. 1972), pp. 3253–3259. DOI: 10.1103/PhysRevB.5.3253. URL: https://link.aps.org/doi/10.1103/PhysRevB.5.3253.

[9] Yu-Ming He et al. „On-demand semiconductor single-photon source with near-unity indistinguishability“. In: *Nature Nanotechnology* 8.3 (2013), pp. 213–217. DOI: 10.1038/nnano.2012.262. URL: https://doi.org/10.1038/nnano.2012.262.

[10] Toan Trong Tran et al. „Quantum emission from hexagonal boron nitride monolayers“. In: *Nature Nanotechnology* 11.1 (Jan. 2016), pp. 37–41. DOI: 10.1038/nnano.2015.242. URL: https://doi.org/10.1038/nnano.2015.242.

[11] M. Koperski et al. „Single photon emitters in exfoliated WSe2 structures“. In: *Nature Nanotechnology* 10.6 (June 2015), pp. 503–506. ISSN: 1748-3395. DOI: 10.1038/nnano.2015.67. URL: https://doi.org/10.1038/nnano.2015.67.

[12] Michael Neumann et al. „Organic Molecules as Origin of Visible-Range Single Photon Emission from Hexagonal Boron Nitride and Mica“. In: *ACS Nano* 17.12 (2023). PMID: 37276077, pp. 11679–11691. DOI: 10.1021/acsnano.3c02348. eprint: https://doi.org/10.1021/acsnano.3c02348. URL: https://doi.org/10.1021/acsnano.3c02348.

[13] A. Mark Fox. „Solid-State Quantum Emitters“. In: *Advanced Quantum Technologies* 8.2 (2025), p. 2300390. DOI: https://doi.org/10.1002/qute.202300390. eprint: https://advanced.onlinelibrary.wiley.com/doi/pdf/10.1002/qute.202300390. URL: https://advanced.onlinelibrary.wiley.com/doi/abs/10.1002/qute.202300390.

[14] Shicheng Yu et al. „A Concise Primer on Solid-State Quantum Emitters“. In: *IEEE Journal of Selected Topics in Quantum Electronics* 31.5 (2025). Quantum Materials and Quantum Devices, pp. 1–16. DOI: 10.1109/JSTQE.2025.3573986.

[15] Navid Soltani et al. „Scanning planar Yagi-Uda antenna for fluorescence detection“. In: *J. Opt. Soc. Am. B* 38.9 (Sept. 2021), pp. 2528–2535. DOI: 10.1364/JOSAB.434980. URL: https://opg.optica.org/josab/abstract.cfm?URI=josab-38-9-2528.

[16] Natasha Tomm et al. „A bright and fast source of coherent single photons“. In: *Nature Nanotechnology* 16 (4 2021), pp. 399–403. ISSN: 1748-3395. DOI: 10.1038/s41565-020-00831-x. URL: https://doi.org/10.1038/s41565-020-00831-x.

[17] Yanik Herrmann et al. „Coherent Coupling of a Diamond Tin-Vacancy Center to a Tunable Open Microcavity“. In: *Phys. Rev. X* 14 (4 Oct. 2024), p. 041013. DOI: 10.1103/PhysRevX.14.041013. URL: https://link.aps.org/doi/10.1103/PhysRevX.14.041013.

[18] Assegid Mengistu Flatae et al. „Plasmon-Assisted Suppression of Surface Trap States and Enhanced Band-Edge Emission in a Bare CdTe Quantum Dot“. In: *The Journal of Physical Chemistry Letters* 10 (11 2019), pp. 2874–2878. DOI: 10.1021/acs.jpclett.9b01083. URL: https://doi.org/10.1021/acs.jpclett.9b01083.

[19] Haritha Kambalathmana. „Nano-optical studies of silicon-vacancy color centers in thin polycrystalline diamond membranes“. URN: urn:nbn:de:hbz:467-118833. PhD Thesis. Siegen, Germany: Universität Siegen, 2024. URL: https://dspace.ub.uni-siegen.de/entities/publication/9cc83cc1-6914-4524-9a18-eeb916c2f055.

[20] V. Manojkumar et al. „Influence of particle size and dielectric environment on radiative lifetimes of colloidal cadmium selenide single photon emitters“. In: *Scientific Reports* 15.1 (Apr. 2025), p. 14639. ISSN: 2045-2322. DOI: 10.1038/s41598-025-99148-9. URL: https://doi.org/10.1038/s41598-025-99148-9.

[21] J. Hours et al. „Exciton radiative lifetime controlled by the lateral confinement energy in a single quantum dot“. In: *Phys. Rev. B* 71 (16 Apr. 2005), p. 161306. DOI: 10.1103/PhysRevB.71.161306. URL: https://link.aps.org/doi/10.1103/PhysRevB.71.161306.

[22] Jelle Storteboom et al. „Lifetime investigation of single nitrogen vacancy centres in nanodiamonds“. In: *Opt. Express* 23.9 (May 2015), pp. 11327–11333. DOI: 10.1364/OE.23.011327. URL: https://opg.optica.org/oe/abstract.cfm?URI=oe-23-9-11327.

[23] Wolfgang Becker. *The bh TCSPC Handbook: for Time-Correlated Single Photon Counting and Fluorescence Lifetime Imaging*. 10th. Available for download on publisher's website. Berlin, Germany: Becker & Hickl GmbH, 2023, approx. 950. URL: https://www.becker-hickl.com/literature/documents/flim/the-bh-tcspc-handbook/.

[24] Yongqing Li et al. „Time-Resolved Photoluminescence Spectroscopy of Exciton–Plasmon Coupling Dynamics“. In: *Plasmonics* 10.2 (Apr. 2015), pp. 271–280. DOI: 10.1007/s11468-014-9805-1. URL: https://doi.org/10.1007/s11468-014-9805-1.

[25] C. Robert et al. „Exciton radiative lifetime in transition metal dichalcogenide monolayers“. In: *Phys. Rev. B* 93 (20 May 2016), p. 205423. DOI: 10.1103/PhysRevB.93.205423. URL: https://link.aps.org/doi/10.1103/PhysRevB.93.205423.

[26] Tengfei Yan et al. „Exciton valley dynamics in monolayer WSe_2 probed by the two-color ultrafast Kerr rotation“. In: *Phys. Chem. Chem. Phys.* 19 (4 2017), pp. 3176–3181. DOI: 10.1039/C6CP07208A. URL: http://dx.doi.org/10.1039/C6CP07208A.

[27] H. Htoon et al. „Effect of Zero- to One-Dimensional Transformation on Multiparticle Auger Recombination in Semiconductor Quantum Rods“. In: *Phys. Rev. Lett.* 91 (22 Nov. 2003), p. 227401. DOI: 10.1103/PhysRevLett.91.227401. URL: https://link.aps.org/doi/10.1103/PhysRevLett.91.227401.

[28] Musa Cadirci et al. „Ultrafast charge dynamics in $CuInS_2$ nanocrystal quantum dots“. In: *Chemical Physics* 438 (2014), pp. 60–65. ISSN: 0301-0104. DOI: https://doi.org/10.1016/j.chemphys.2014.05.001. URL: https://www.sciencedirect.com/science/article/pii/S030101041400130X.

[29] Praket P. Jha and Philippe Guyot-Sionnest. „Trion Decay in Colloidal Quantum Dots“. In: *ACS Nano* 3.4 (2009). PMID: 19341263, pp. 1011–1015. DOI: 10.1021/nn9001177. eprint: https://doi.org/10.1021/nn9001177. URL: https://doi.org/10.1021/nn9001177.

[30] V. I. Klimov et al. „Quantization of Multiparticle Auger Rates in Semiconductor Quantum Dots“. In: *Science* 287.5455 (2000), pp. 1011–1013. DOI: 10.1126/science.287.5455.1011. eprint: https://www.science.org/doi/pdf/10.1126/science.287.5455.1011. URL: https://www.science.org/doi/abs/10.1126/science.287.5455.1011.

[31] Vladimir Pavlenko and Igor Beloussov. „Amplified spontaneous emission from CdSe/CdS/CdZnS quantum dot films“. In: *Journal of Luminescence* 257 (2023), p. 119643. ISSN: 0022-2313. DOI: https://doi.org/10.1016/j.jlumin.2022.119643. URL: https://www.sciencedirect.com/science/article/pii/S0022231322009188.

[32] M. L. Goldman et al. „Phonon-Induced Population Dynamics and Intersystem Crossing in Nitrogen-Vacancy Centers“. In: *Phys. Rev. Lett.* 114 (14 Apr. 2015), p. 145502. DOI: 10.1103/PhysRevLett.114.145502. URL: https://link.aps.org/doi/10.1103/PhysRevLett.114.145502.

[33] V. M. Huxter et al. „Vibrational and electronic dynamics of nitrogen–vacancy centres in diamond revealed by two-dimensional ultrafast spectroscopy“. In: *Nature Physics* 9.11 (2013), pp. 744–749. ISSN: 1745-2481. DOI: 10.1038/nphys2753.

[34] C. Toninelli et al. „Single organic molecules for photonic quantum technologies“. In: *Nature Materials* 20.12 (2021), pp. 1615–1628. ISSN: 1476-4660. DOI: 10.1038/s41563-021-00987-4.

[35] Daniel Fersch et al. „Single-Molecule Ultrafast Fluorescence-Detected Pump-Probe Microscopy“. In: *The Journal of Physical Chemistry Letters* 14.21 (2023). PMID: 37207316, pp. 4923–4932. DOI: 10.1021/acs.jpclett.3c00839. eprint: https://doi.org/10.1021/acs.jpclett.3c00839. URL: https://doi.org/10.1021/acs.jpclett.3c00839.

[36] Haritha Kambalathmana et al. „Plasmonic Nanocone Scanning Antenna: Fabrication and Optical Properties“. In: *Advanced Photonics Research* 5.3 (2024), p. 2300058. DOI: https://doi.org/10.1002/adpr.202300058. eprint: https://advanced.onlinelibrary.wiley.com/doi/pdf/10.1002/adpr.202300058. URL: https://advanced.onlinelibrary.wiley.com/doi/abs/10.1002/adpr.202300058.

[37] Junyang Huang et al. „Plasmon-Induced Trap State Emission from Single Quantum Dots“. In: *Phys. Rev. Lett.* 126 (4 Jan. 2021), p. 047402. DOI: 10.1103/PhysRevLett.126.047402. URL: https://link.aps.org/doi/10.1103/PhysRevLett.126.047402.

[38] V.N. Derepko et al. „Plasmon-exciton nanostructures, based on CdS quantum dots with exciton and trap state luminescence“. In: *Journal of Luminescence* 248 (2022), p. 118874. ISSN: 0022-2313. DOI: https://doi.org/10.1016/j.jlumin.2022.118874. URL: https://www.sciencedirect.com/science/article/pii/S0022231322001491.

[39] *PDM Series - Single Photon Counting Modules*. Product Specification and Overview. Micro Photon Devices (MPD) S.r.l. Bolzano, Italy, 2024. (Visited on 10/16/2025).

[40] Boris Korzh et al. „Demonstration of sub-3 ps temporal resolution with a superconducting nanowire single-photon detector“. In: *Nature Photonics* 14.4 (2020), pp. 250–255. DOI: 10.1038/s41566-020-0589-x. URL: https://doi.org/10.1038/s41566-020-0589-x.

[41] Becker & Hickl GmbH, MIT, and Jet Propulsion Laboratory (JPL). *4.4 ps IRF width of TCSPC with an NbN Superconducting Nanowire Single Photon Detector*. Application Note –. Ultrafast TCSPC setup demonstration. Becker & Hickl GmbH, 2019. URL: https://www.becker-hickl.com/literature/application-notes/4-4-ps-irf-width-of-tcspc-with-an-nbn-superconducting-nanowire-single-photon-detector/.

[42] R. V. Krishnan et al. „Probing subtle fluorescence dynamics in cellular proteins by streak camera based fluorescence lifetime imaging microscopy“. In: *Applied Physics Letters* 83.22 (Dec. 2003), pp. 4658–4660. ISSN: 0003-6951. DOI: 10.1063/1.1630154. URL: https://doi.org/10.1063/1.1630154.

[43] Motoyoshi Baba, Ying Li, and Masahiro Matsuoka. „Intensity Interference of Ultrashort Pulsed Fluorescence“. In: *Phys. Rev. Lett.* 76 (25 June 1996), pp. 4697–4700. DOI: 10.1103/PhysRevLett.76.4697. URL: https://link.aps.org/doi/10.1103/PhysRevLett.76.4697.

[44] Ying Li, M. Baba, and M. Matsuoka. „Femtosecond measurement of fluorescence by two-photon interference“. In: *Phys. Rev. A* 55 (4 Apr. 1997), pp. 3177–3183. DOI: 10.1103/PhysRevA.55.3177. URL: https://link.aps.org/doi/10.1103/PhysRevA.55.3177.

[45] J. Schedlbauer et al. „Ultrafast Single-Molecule Fluorescence Measured by Femtosecond Double-Pulse Excitation Photon Antibunching“. In: *Nano Letters* 20.2 (2020). PMID: 31869232, pp. 1074–1079. DOI: 10.1021/acs.nanolett.9b04354. eprint: https://doi.org/10.1021/acs.nanolett.9b04354. URL: https://doi.org/10.1021/acs.nanolett.9b04354.

[46] Bowen Li et al. „Time-magnified photon counting with 550-fs resolution“. In: *Optica* 8.8 (Aug. 2021), pp. 1109–1112. DOI: 10.1364/OPTICA.420816. URL: https://opg.optica.org/optica/abstract.cfm?URI=optica-8-8-1109.

[47] Ashley Lyons et al. „Fluorescence lifetime Hong-Ou-Mandel sensing“. In: *Nature Communications* 14 (1 2023), p. 8005. ISSN: 2041-1723. DOI: 10.1038/s41467-023-43868-x. URL: https://doi.org/10.1038/s41467-023-43868-x.

[48] Marius A. Albota and Franco N. C. Wong. „Efficient single-photon counting at 1.55 μm by means of frequency upconversion“. In: *Opt. Lett.* 29.13 (July 2004), pp. 1449–1451. DOI: 10.1364/OL.29.001449. URL: https://opg.optica.org/ol/abstract.cfm?URI=ol-29-13-1449.

[49] Rostislav V. Roussev et al. „Periodically poled lithium niobate waveguide sum-frequency generator for efficient single-photon detection at communication wavelengths“. In: *Opt. Lett.* 29.13 (July 2004), pp. 1518–1520. DOI: 10.1364/OL.29.001518. URL: https://opg.optica.org/ol/abstract.cfm?URI=ol-29-13-1518.

[50] S. Kinoshita et al. „Efficient optical Kerr shutter for femtosecond time-resolved luminescence spectroscopy“. In: *Review of Scientific Instruments* 71.9 (Sept. 2000), pp. 3317–3322. ISSN: 0034-6748. DOI: 10.1063/1.1287043. URL: https://doi.org/10.1063/1.1287043.

[51] Naoki Sugimoto et al. „Ultrafast response of third-order optical nonlinearity in glasses containing Bi_2O_3“. In: *Opt. Lett.* 21.20 (Oct. 1996), pp. 1637–1639. DOI: 10.1364/OL.21.001637. URL: https://opg.optica.org/ol/abstract.cfm?URI=ol-21-20-1637.

[52] Naoki Sugimoto et al. „Third-order optical nonlinearities and their ultrafast response in Bi_2O_3–B_2O_3–SiO_2 glasses“. In: *J. Opt. Soc. Am. B* 16.11 (Nov. 1999), pp. 1904–1908. DOI: 10.1364/JOSAB.16.001904. URL: https://opg.optica.org/josab/abstract.cfm?URI=josab-16-11-1904.

[53] Han Zhang et al. „Z-scan measurement of the nonlinear refractive index of graphene“. In: *Opt. Lett.* 37.11 (June 2012), pp. 1856–1858. DOI: 10.1364/OL.37.001856. URL: https://opg.optica.org/ol/abstract.cfm?URI=ol-37-11-1856.

[54] Abdul-Hamid Fattah et al. „Ultrafast single-photon detection at high repetition rates based on optical Kerr gates under focusing“. In: *Opt. Lett.* 46.3 (Feb. 2021), pp. 560–563. DOI: 10.1364/OL.414895. URL: https://opg.optica.org/ol/abstract.cfm?URI=ol-46-3-560.

[55] Joseph R. Lakowicz. *Principles of Fluorescence Spectroscopy*. 3rd. New York: Springer, 2006. ISBN: 978-0-387-31278-1. DOI: 10.1007/978-0-387-46312-4. URL: https://link.springer.com/book/10.1007/978-0-387-46312-4.

[56] B. Valeur. „Introduction: On the Origin of the Terms Fluorescence, Phosphorescence, and Luminescence“. In: *New Trends in Fluorescence Spectroscopy: Applications to Chemical and Life Sciences*. Ed. by Bernard Valeur and Jean-Claude Brochon. Berlin, Heidelberg: Springer Berlin Heidelberg, 2001, pp. 3–

6. ISBN: 978-3-642-56853-4. DOI: 10.1007/978-3-642-56853-4_1. URL: https://doi.org/10.1007/978-3-642-56853-4_1.

[57] Francis Perrin. „La fluorescence des solutions - Induction moléculaire. – Polarisation et durée d'émission. – Photochimie“. In: *Ann. Phys.* 10.12 (1929), pp. 169–275. DOI: 10.1051/anphys/192910120169. URL: https://doi.org/10.1051/anphys/192910120169.

[58] Thorsten Schweizer, Heiko Kubach, and Thomas Koch. „Investigations to characterize the interactions of light radiation, engine operating media and fluorescence tracers for the use of qualitative light-induced fluorescence in engine systems“. In: *Automotive and Engine Technology* 6.3 (Dec. 2021), pp. 275–287. ISSN: 2365-5135. DOI: 10.1007/s41104-021-00092-3. URL: https://doi.org/10.1007/s41104-021-00092-3.

[59] HandWiki Contributor or File Creator. *File:Stokes shift diagram.svg*. https://handwiki.org/wiki/File:Stokes_shift_diagram.svg. Accessed: 10 October 2025. 2024. URL: https://handwiki.org/wiki/File:Stokes_shift_diagram.svg.

[60] Michael Kasha. „Characterization of electronic transitions in complex molecules“. In: *Discuss. Faraday Soc.* 9 (0 1950), pp. 14–19. DOI: 10.1039/DF9500900014. URL: http://dx.doi.org/10.1039/DF9500900014.

[61] Kenneth Willeford. „The Luminescence Hypothesis of Olfaction“. In: *Sensors* 23.3 (2023). ISSN: 1424-8220. DOI: 10.3390/s23031333. URL: https://www.mdpi.com/1424-8220/23/3/1333.

[62] LibreTexts. *Selection rules and transition moment integral*. Accessed: 10 October 2025. URL: https://chem.libretexts.org/Bookshelves/Physical_and_Theoretical_Chemistry_Textbook_Maps/Supplemental_Modules_(Physical_and_Theoretical_Chemistry)/Spectroscopy/Fundamentals_of_Spectroscopy/Selection_rules_and_transition_moment_integral.

[63] Vlastimil Fidler and Peter Kapusta. „Fluorescence Kinetics and Time-Resolved Measurement“. In: *Fluorescence Spectroscopy and Microscopy in Biology*. Ed. by Radek Šachl and Mariana Amaro. Cham: Springer International Publishing, 2023, pp. 53–86. ISBN: 978-3-031-30362-3. DOI: 10.1007/4243_2022_31. URL: https://doi.org/10.1007/4243_2022_31.

[64] Jacob M. Goldberg et al. „Thioamide Quenching of Fluorescent Probes through Photoinduced Electron Transfer: Mechanistic Studies and Applications“. In: *Journal of the American Chemical Society* 135.49 (2013), pp. 18651–18658.

DOI: 10.1021/ja409709x. eprint: https://doi.org/10.1021/ja409709x. URL: https://doi.org/10.1021/ja409709x.

[65] Raymond Chang. *Physical Chemistry for the Biosciences*. Sausalito, California: University Science Books, 2005.

[66] Alan Migdall et al., eds. *Single-Photon Generation and Detection: Physics and Applications*. Vol. 45. Experimental Methods in the Physical Sciences. Waltham, MA: Academic Press, 2013. ISBN: 978-0-12-387695-9. DOI: 10.1016/C2011-0-06900-1.

[67] R. Hanbury Brown and R.Q. Twiss. „LXXIV. A new type of interferometer for use in radio astronomy". In: *The London, Edinburgh, and Dublin Philosophical Magazine and Journal of Science* 45.366 (1954), pp. 663–682. DOI: 10.1080/14786440708520475. eprint: https://doi.org/10.1080/14786440708520475. URL: https://doi.org/10.1080/14786440708520475.

[68] R. Hanbury Brown and R. Q. Twiss. „Correlation between Photons in two Coherent Beams of Light". In: *Nature* 177.4497 (1956), pp. 27–29. DOI: 10.1038/177027a0.

[69] E. Murray et al. „Quantum photonics hybrid integration platform". In: *Applied Physics Letters* 107.17 (2015), p. 171108. DOI: 10.1063/1.4935029.

[70] Mark Fox. *Quantum Optics: An Introduction*. Oxford University Press, Apr. 2006. ISBN: 9780198566724. DOI: 10.1093/oso/9780198566724.001.0001. URL: https://doi.org/10.1093/oso/9780198566724.001.0001.

[71] Ray Horak. *Webster's New World Telecom Dictionary*. John Wiley & Sons, 2007. ISBN: 978-0471774570.

[72] COMSOL AB. *Wi-Fi Booster Yagi-Uda Antenna (COMSOL Application ID: 99891)*. https://doc.comsol.com/6.1/doc/com.comsol.help.models.rf.yagi_uda_antenna/yagi_uda_antenna.html. COMSOL Multiphysics ® Version 6.1 Documentation. 2022. URL: https://doc.comsol.com/6.1/doc/com.comsol.help.models.rf.yagi_uda_antenna/yagi_uda_antenna.html (visited on 10/11/2025).

[73] Lukas Novotny and Niek van Hulst. „Antennas for light". In: *Nature Photonics* 5.2 (2011), pp. 83–90. DOI: 10.1038/nphoton.2010.237. URL: https://doi.org/10.1038/nphoton.2010.237.

[74] Palash Bharadwaj, Bradley Deutsch, and Lukas Novotny. „Optical Antennas". In: *Adv. Opt. Photon.* 1.3 (Nov. 2009), pp. 438–483. DOI: 10.1364/AOP.1.000438. URL: https://opg.optica.org/aop/abstract.cfm?URI=aop-1-3-438.

[75] Mario Agio. „Optical antennas as nanoscale resonators“. In: *Nanoscale* 4 (3 2012), pp. 692–706. DOI: 10.1039/C1NR11116G. URL: http://dx.doi.org/10.1039/C1NR11116G.

[76] Alexander L. Efros and Louis E. Brus. „Nanocrystal Quantum Dots: From Discovery to Modern Development“. In: *ACS Nano* 15.4 (2021), pp. 6192–6210. DOI: 10.1021/acsnano.1c01399.

[77] Nobel Prize Outreach AB. *The Nobel Prize in Chemistry 2023 - Summary*. Accessed on [12.10.2025]. 2023. URL: https://www.nobelprize.org/prizes/chemistry/2023/summary/.

[78] A. I. Ekimov and A. A. Onushchenko. „Quantum Size Effect in Three-Dimensional Microscopic Semiconductor Crystals“. In: *JETP Letters* 118.1 (2023), S15–S17. DOI: 10.1134/S0021364023130040.

[79] L. E. Brus. „A simple model for the ionization potential, electron affinity, and aqueous redox potentials of small semiconductor crystallites“. In: *The Journal of Chemical Physics* 79.11 (1983), pp. 5566–5571. DOI: 10.1063/1.445676.

[80] A. I. Ekimov and A. A. Onushchenko. „Size Quantization of the Electron Energy Spectrum in a Microscopic Semiconductor Crystal“. In: *JETP Letters* 118.1 (2023), S12–S14. DOI: 10.1134/S0021364023130027.

[81] L. E. Brus. „Electron–electron and electron-hole interactions in small semiconductor crystallites: The size dependence of the lowest excited electronic state“. In: *The Journal of Chemical Physics* 80.9 (1984), pp. 4403–4409. DOI: 10.1063/1.447218.

[82] F. Pelayo García de Arquer et al. „Semiconductor quantum dots: Technological progress and future challenges“. In: *Science* 373.6555 (2021), eaaz8541. DOI: 10.1126/science.aaz8541. eprint: https://www.science.org/doi/pdf/10.1126/science.aaz8541. URL: https://www.science.org/doi/abs/10.1126/science.aaz8541.

[83] Young-Shin Park et al. „Auger Recombination of Biexcitons and Negative and Positive Trions in Individual Quantum Dots“. In: *ACS Nano* 8.7 (2014), pp. 7288–7296. ISSN: 1936-0851. DOI: 10.1021/nn5023473. URL: https://doi.org/10.1021/nn5023473.

[84] Victor I. Klimov. „Multicarrier Interactions in Semiconductor Nanocrystals in Relation to the Phenomena of Auger Recombination and Carrier Multiplication“. In: *Annual Review of Condensed Matter Physics* 5.Volume 5, 2014 (2014), pp. 285–316. ISSN: 1947-5462. DOI: https://doi.org/10.1146/annurev-conmatphys-031113-133900. URL: https://www.annualreviews.org/content/journals/10.1146/annurev-conmatphys-031113-133900.

[85] Graham H. Carey et al. „Colloidal Quantum Dot Solar Cells“. In: *Chemical Reviews* 115.23 (2015), pp. 12732–12763. ISSN: 0009-2665. DOI: 10.1021/acs.chemrev.5b00063. URL: https://doi.org/10.1021/acs.chemrev.5b00063.

[86] Yufei Shu et al. „Quantum Dots for Display Applications“. In: *Angewandte Chemie International Edition* 59.50 (2020), pp. 22312–22323. DOI: https://doi.org/10.1002/anie.202004857. eprint: https://onlinelibrary.wiley.com/doi/pdf/10.1002/anie.202004857. URL: https://onlinelibrary.wiley.com/doi/abs/10.1002/anie.202004857.

[87] Hélio M. Gil et al. „NIR-quantum dots in biomedical imaging and their future“. In: *iScience* 24.3 (2021), p. 102189. ISSN: 2589-0042. DOI: https://doi.org/10.1016/j.isci.2021.102189. URL: https://www.sciencedirect.com/science/article/pii/S2589004221001577.

[88] Cherie R. Kagan et al. „Colloidal Quantum Dots as Platforms for Quantum Information Science“. In: *Chemical Reviews* 121.5 (2021), pp. 3186–3233. ISSN: 0009-2665. DOI: 10.1021/acs.chemrev.0c00831. URL: https://doi.org/10.1021/acs.chemrev.0c00831.

[89] M. Nirmal et al. „Fluorescence intermittency in single cadmium selenide nanocrystals“. In: *Nature* 383.6603 (1996), pp. 802–804. ISSN: 1476-4687. DOI: 10.1038/383802a0. URL: https://doi.org/10.1038/383802a0.

[90] Alexander L. Efros and David J. Nesbitt. „Origin and control of blinking in quantum dots“. In: *Nature Nanotechnology* 11.8 (2016), pp. 661–671. ISSN: 1748-3395. DOI: 10.1038/nnano.2016.140. URL: https://doi.org/10.1038/nnano.2016.140.

[91] Benoit Mahler et al. „Towards non-blinking colloidal quantum dots“. In: *Nature Materials* 7.8 (2008), pp. 659–664. ISSN: 1476-4660. DOI: 10.1038/nmat2222. URL: https://doi.org/10.1038/nmat2222.

[92] Jiaojian Shi et al. „All-optical fluorescence blinking control in quantum dots with ultrafast mid-infrared pulses“. In: *Nature Nanotechnology* 16.12 (2021), pp. 1355–1361. ISSN: 1748-3395. DOI: 10.1038/s41565-021-01016-w. URL: https://doi.org/10.1038/s41565-021-01016-w.

[93] S. Bounouar et al. „Ultrafast Room Temperature Single-Photon Source from Nanowire-Quantum Dots“. In: *Nano Letters* 12.6 (2012), pp. 2977–2981. ISSN: 1530-6984. DOI: 10.1021/nl300733f. URL: https://doi.org/10.1021/nl300733f.

[94] Vigneshwaran Chandrasekaran et al. „Nearly Blinking-Free, High-Purity Single-Photon Emission by Colloidal InP/ZnSe Quantum Dots“. In: *Nano Letters* 17.10 (2017), pp. 6104–6109. ISSN: 1530-6984. DOI: 10.1021/acs.nanolett.7b02634. URL: https://doi.org/10.1021/acs.nanolett.7b02634.

[95] Bo Wang et al. „Weakly Confined Organic–Inorganic Halide Perovskite Quantum Dots as High-Purity Room-Temperature Single Photon Sources“. In: *ACS Nano* 18.16 (2024), pp. 10807–10817. ISSN: 1936-0851. DOI: 10.1021/acsnano.3c12311. URL: https://doi.org/10.1021/acsnano.3c12311.

[96] Xing Lin et al. „Electrically-driven single-photon sources based on colloidal quantum dots with near-optimal antibunching at room temperature“. In: *Nature Communications* 8.1 (2017), p. 1132. ISSN: 2041-1723. DOI: 10.1038/s41467-017-01379-6. URL: https://doi.org/10.1038/s41467-017-01379-6.

[97] T. Miyazawa et al. „Single-photon emission at 1.5 µm from an InAs/InP quantum dot with highly suppressed multi-photon emission probabilities“. In: *Applied Physics Letters* 109.13 (Sept. 2016), p. 132106. ISSN: 0003-6951. DOI: 10.1063/1.4961888. URL: https://doi.org/10.1063/1.4961888.

[98] Matthias Paul et al. „Single-photon emission at 1.55 μm from MOVPE-grown InAs quantum dots on InGaAs/GaAs metamorphic buffers“. In: *Applied Physics Letters* 111 (3 July 2017), p. 033102. DOI: 10.1063/1.4993935. URL: https://doi.org/10.1063/1.4993935.

[99] T. Müller et al. „A quantum light-emitting diode for the standard telecom window around 1,550 nm“. In: *Nature Communications* 9 (1 2018), p. 862. ISSN: 2041-1723. DOI: 10.1038/s41467-018-03251-7. URL: https://doi.org/10.1038/s41467-018-03251-7.

[100] Johannes Michl et al. „Strain-Free GaSb Quantum Dots as Single-Photon Sources in the Telecom S-Band“. In: *Advanced Quantum Technologies* 6.12 (2023), p. 2300180. DOI: https://doi.org/10.1002/qute.202300180. eprint: https://advanced.onlinelibrary.wiley.com/doi/pdf/10.1002/qute.202300180. URL: https://advanced.onlinelibrary.wiley.com/doi/abs/10.1002/qute.202300180.

[101] Dev Kumar Thapa and Soumava Biswas. „Single photon generation from quantum dots: recent advances, challenges and prospects“. In: *Nanoscale* 7 (17 2015), pp. 7489–7517. DOI: 10.1039/D5NR00091B. URL: http://dx.doi.org/10.1039/D5NR00091B.

[102] Nianjun Yang, ed. *Novel Aspects of Diamond: From Growth to Applications*. Vol. 131. Topics in Applied Physics. Springer, Cham, 2019. ISBN: 978-3-030-12469-4. DOI: 10.1007/978-3-030-12469-4.

[103] B. Lounis and W. E. Moerner. „Single photons on demand from a single molecule at room temperature“. In: *Nature* 407.6803 (Sept. 2000), pp. 491–493. DOI: 10.1038/35035032. URL: https://doi.org/10.1038/35035032.

[104] Lawrence S. Pan and Don R. Kania, eds. *Diamond: Electronic Properties and Applications*. Electronic Materials: Science & Technology. Springer New York, NY, 1995. ISBN: 978-0-7923-9524-9. DOI: 10.1007/978-1-4615-2257-7.

[105] Alexander M. Zaitsev. *Optical Properties of Diamond. A Data Handbook*. Berlin, Heidelberg: Springer Berlin, Heidelberg, 2001. ISBN: 978-3-540-66582-3. DOI: 10.1007/978-3-662-04548-0.

[106] Steven Prawer and Igor Aharonovich, eds. *Quantum Information Processing with Diamond: Principles and Applications*. 1st ed. Cambridge: Woodhead Publishing, 2014. ISBN: 978-0-85709-656-2.

[107] W. Kaiser and W. L. Bond. „Nitrogen, A Major Impurity in Common Type I Diamond“. In: *Phys. Rev.* 115 (4 Aug. 1959), pp. 857–863. DOI: 10.1103/PhysRev.115.857. URL: https://link.aps.org/doi/10.1103/PhysRev.115.857.

[108] A. Gruber et al. „Scanning Confocal Optical Microscopy and Magnetic Resonance on Single Defect Centers“. In: *Science* 276.5321 (1997), pp. 2012–2014. DOI: 10.1126/science.276.5321.2012. eprint: https://www.science.org/doi/pdf/10.1126/science.276.5321.2012. URL: https://www.science.org/doi/abs/10.1126/science.276.5321.2012.

[109] Christian Kurtsiefer et al. „Stable Solid-State Source of Single Photons“. In: *Phys. Rev. Lett.* 85 (2 July 2000), pp. 290–293. DOI: 10.1103/PhysRevLett.85.290. URL: https://link.aps.org/doi/10.1103/PhysRevLett.85.290.

[110] L. Rondin et al. „Surface-induced charge state conversion of nitrogen-vacancy defects in nanodiamonds“. In: *Phys. Rev. B* 82 (11 Sept. 2010), p. 115449. DOI: 10.1103/PhysRevB.82.115449. URL: https://link.aps.org/doi/10.1103/PhysRevB.82.115449.

[111] T. Gaebel et al. „Photochromism in single nitrogen-vacancy defect in diamond“. In: *Applied Physics B* 82.2 (2006), pp. 243–246. ISSN: 1432-0649. DOI: 10.1007/s00340-005-2056-2. URL: https://doi.org/10.1007/s00340-005-2056-2.

[112] Hannes Bernien et al. „Two-Photon Quantum Interference from Separate Nitrogen Vacancy Centers in Diamond“. In: *Phys. Rev. Lett.* 108 (4 Jan. 2012), p. 043604. DOI: 10.1103/PhysRevLett.108.043604. URL: https://link.aps.org/doi/10.1103/PhysRevLett.108.043604.

[113] Gopalakrishnan Balasubramanian et al. „Ultralong spin coherence time in isotopically engineered diamond“. In: *Nature Materials* 8.5 (2009), pp. 383–387. ISSN: 1476-4660. DOI: 10.1038/nmat2420. URL: https://doi.org/10.1038/nmat2420.

[114] E. D. Herbschleb et al. „Ultra-long coherence times amongst room-temperature solid-state spins“. In: *Nature Communications* 10.1 (2019), p. 3766. ISSN: 2041-1723. DOI: 10.1038/s41467-019-11776-8. URL: https://doi.org/10.1038/s41467-019-11776-8.

[115] Alexios Beveratos et al. „Nonclassical radiation from diamond nanocrystals“. In: *Phys. Rev. A* 64 (6 Nov. 2001), p. 061802. DOI: 10.1103/PhysRevA.64.061802. URL: https://link.aps.org/doi/10.1103/PhysRevA.64.061802.

[116] Tina Müller et al. „Optical signatures of silicon-vacancy spins in diamond“. In: *Nature Communications* 5.1 (2014), p. 3328. ISSN: 2041-1723. DOI: 10.1038/ncomms4328. URL: https://doi.org/10.1038/ncomms4328.

[117] U. F. S. D'Haenens-Johansson et al. „EPR of a defect in CVD diamond involving both silicon and hydrogen that shows preferential alignment“. In: *Phys. Rev. B* 82 (15 Oct. 2010), p. 155205. DOI: 10.1103/PhysRevB.82.155205. URL: https://link.aps.org/doi/10.1103/PhysRevB.82.155205.

[118] Elke Neu et al. „Fluorescence and polarization spectroscopy of single silicon vacancy centers in heteroepitaxial nanodiamonds on iridium“. In: *Phys. Rev. B* 84 (20 Nov. 2011), p. 205211. DOI: 10.1103/PhysRevB.84.205211. URL: https://link.aps.org/doi/10.1103/PhysRevB.84.205211.

[119] I Aharonovich et al. „Diamond-based single-photon emitters“. In: *Reports on Progress in Physics* 74.7 (June 2011), p. 076501. DOI: 10.1088/0034-4885/74/7/076501. URL: https://doi.org/10.1088/0034-4885/74/7/076501.

[120] Elke Neu et al. „Single photon emission from silicon-vacancy colour centres in chemical vapour deposition nano-diamonds on iridium“. In: *New Journal of Physics* 13.2 (Feb. 2011), p. 025012. DOI: 10.1088/1367-2630/13/2/025012. URL: https://doi.org/10.1088/1367-2630/13/2/025012.

[121] Kay D Jahnke et al. „Electron–phonon processes of the silicon-vacancy centre in diamond“. In: *New Journal of Physics* 17.4 (Apr. 2015), p. 043011. DOI: 10.1088/1367-2630/17/4/043011. URL: https://doi.org/10.1088/1367-2630/17/4/043011.

[122] M. J. Crane et al. „High-pressure, high-temperature molecular doping of nanodiamond“. In: *Science Advances* 5.5 (2019), eaau6073. DOI: 10.1126/sciadv.aau6073. eprint: https://www.science.org/doi/pdf/10.1126/sciadv.aau6073. URL: https://www.science.org/doi/abs/10.1126/sciadv.aau6073.

[123] Yuri N. Palyanov et al. „High-Pressure Synthesis and Characterization of Ge-Doped Single Crystal Diamond“. In: *Crystal Growth & Design* 16.6 (2016), pp. 3510–3518. DOI: 10.1021/acs.cgd.6b00481. eprint: https://doi.org/10.1021/acs.cgd.6b00481. URL: https://doi.org/10.1021/acs.cgd.6b00481.

[124] Yan-Kai Tzeng et al. „Improving the creation of SiV centers in diamond via sub-μs pulsed annealing treatment“. In: *Nature Communications* 15 (1 Aug. 2024), p. 7251. DOI: 10.1038/s41467-024-51523-2. URL: https://doi.org/10.1038/s41467-024-51523-2.

[125] Matthew J. Crane et al. „Photothermal effects during nanodiamond synthesis from a carbon aerogel in a laser-heated diamond anvil cell“. In: *Diamond and Related Materials* 87 (2018), pp. 134–142. ISSN: 0925-9635. DOI: https://doi.org/10.1016/j.diamond.2018.05.013. URL: https://www.sciencedirect.com/science/article/pii/S0925963518302310.

[126] Valeri Sonin et al. „The composition of the fluid phase in inclusions in synthetic HPHT diamonds grown in system Fe–Ni–Ti–C“. In: *Scientific Reports* 12 (1 Jan. 2022), p. 1246. DOI: 10.1038/s41598-022-05153-7. URL: https://doi.org/10.1038/s41598-022-05153-7.

[127] Andrey Bolshakov et al. „Photoluminescence of SiV centers in single crystal CVD diamond in situ doped with Si from silane“. In: *physica status solidi (a)* 212.11 (2015), pp. 2525–2532. DOI: https://doi.org/10.1002/pssa.201532174. eprint: https://onlinelibrary.wiley.com/doi/pdf/10.1002/pssa.201532174. URL: https://onlinelibrary.wiley.com/doi/abs/10.1002/pssa.201532174.

[128] S Pezzagna et al. „Creation efficiency of nitrogen-vacancy centres in diamond“. In: *New Journal of Physics* 12.6 (June 2010), p. 065017. DOI: 10.1088/1367-2630/12/6/065017. URL: https://doi.org/10.1088/1367-2630/12/6/065017.

[129] Lukas Hunold et al. „Scalable Creation of Deep Silicon-Vacancy Color Centers in Diamond by Ion Implantation through a 1-μm Pinhole“. In: *Advanced Quantum Technologies* 4.12 (2021), p. 2100079. DOI: https://doi.org/10.1002/qute.202100079. eprint: https://advanced.onlinelibrary.wiley.c

om/doi/pdf/10.1002/qute.202100079. URL: https://advanced.onlinelibrary.wiley.com/doi/abs/10.1002/qute.202100079.

[130] Christoph E. Nebel. „CVD diamond: a review on options and reality“. In: *Functional Diamond* 3.1 (2023), p. 2201592. DOI: 10.1080/26941112.2023.2201592. eprint: https://doi.org/10.1080/26941112.2023.2201592. URL: https://doi.org/10.1080/26941112.2023.2201592.

[131] J.O. Orwa et al. „Fabrication of single optical centres in diamond—a review“. In: *Journal of Luminescence* 130.9 (2010). Special Issue based on the Proceedings of the Tenth International Meeting on Hole Burning, Single Molecule, and Related Spectroscopies: Science and Applications (HBSM 2009) - Issue dedicated to Ivan Lorgere and Oliver Guillot-Noel, pp. 1646–1654. ISSN: 0022-2313. DOI: https://doi.org/10.1016/j.jlumin.2009.12.028. URL: https://www.sciencedirect.com/science/article/pii/S0022231309006309.

[132] Chengke Chen, Bo Jiang, and Xiaojun Hu. „Research Progress on Silicon Vacancy Color Centers in Diamond“. In: *Functional Diamond* 4.1 (2024), p. 2332346. DOI: 10.1080/26941112.2024.2332346. eprint: https://doi.org/10.1080/26941112.2024.2332346. URL: https://doi.org/10.1080/26941112.2024.2332346.

[133] Bogumil Zelent et al. „Photophysical Properties of Allura Red for Monitoring Quality of Foods and Pharmaceuticals“. In: *Biophysical Journal* 112 (3 2017), 585a. ISSN: 0006-3495. DOI: 10.1016/j.bpj.2016.11.3148. URL: https://doi.org/10.1016/j.bpj.2016.11.3148.

[134] Richard Ludescher, Jennifer Komaiko, and Maria Corradini. „Monoazo dyes as probes for bulk and local viscosity: Potential applications in semi-solid foods“. In: *Agro Food Industry Hi-Tech* 23 (May 2012), pp. 12–14.

[135] G.Corradini Maria et al. „Identifying and selecting edible luminescent probes as sensors of food quality“. In: *AIMS Biophysics* 3.2 (2016), pp. 319–339. ISSN: 2377-9098. DOI: 10.3934/biophy.2016.2.319. URL: https://www.aimspress.com/article/doi/10.3934/biophy.2016.2.319.

[136] Hideki Kandori, Hiroyuki Sasabe, and Mamoru Mimuro. „Direct Determination of a Lifetime of the S_2 State of β-Carotene by Femtosecond Time-Resolved Fluorescence Spectroscopy“. In: *Journal of the American Chemical Society* 116 (6 Mar. 1994), pp. 2671–2672. ISSN: 0002-7863. DOI: 10.1021/ja00085a078. URL: https://doi.org/10.1021/ja00085a078.

[137] Sergei M. Bachilo and Tomas Gillbro. „Beta-carotene S1 fluorescence“. In: *5th International Conference on Laser Applications in Life Sciences*. Ed. by Pavel A. Apanasevich et al. Vol. 2370. International Society for Optics and Photonics. SPIE, 1995, pp. 719–723. DOI: 10.1117/12.197418. URL: https://doi.org/10.1117/12.197418.

[138] Per Ola Andersson et al. „Solvent and Temperature Effects on Dual Fluorescence in a Series of Carotenes. Energy Gap Dependence of the Internal Conversion Rate“. In: *The Journal of Physical Chemistry* 99.44 (1995), pp. 16199–16209. DOI: 10.1021/j100044a002. eprint: https://doi.org/10.1021/j100044a002. URL: https://doi.org/10.1021/j100044a002.

[139] R. F. Dallinger, W. H. Woodruff, and M. A. J. Rodgers. „The lifetime of the excited singlet state of β–carotene: consequences to photosynthetic light harvesting“. In: *Photochemistry and Photobiology* 33.2 (1981), pp. 275–277. DOI: https://doi.org/10.1111/j.1751-1097.1981.tb05339.x. eprint: https://onlinelibrary.wiley.com/doi/pdf/10.1111/j.1751-1097.1981.tb05339.x. URL: https://onlinelibrary.wiley.com/doi/abs/10.1111/j.1751-1097.1981.tb05339.x.

[140] Jiho Kim and Minyung Lee. „Excited-State Photophysics and Dynamics of a Hemicyanine Dye in AOT Reverse Micelles“. In: *The Journal of Physical Chemistry A* 103 (18 1999), pp. 3378–3382. DOI: 10.1021/jp984167e. URL: https://doi.org/10.1021/jp984167e.

[141] W. Sibbett and J.R. Taylor. „Passive mode locking in the blue spectral region“. In: *Optics Communications* 46.1 (1983), pp. 32–36. ISSN: 0030-4018. DOI: https://doi.org/10.1016/0030-4018(83)90025-1. URL: https://www.sciencedirect.com/science/article/pii/0030401883900251.

[142] Thang B. Hoang, Gleb M. Akselrod, and Maiken H. Mikkelsen. „Ultrafast Room-Temperature Single Photon Emission from Quantum Dots Coupled to Plasmonic Nanocavities“. In: *Nano Letters* 16 (1 2016), pp. 270–275. ISSN: 1530-6984. DOI: 10.1021/acs.nanolett.5b03724. URL: https://doi.org/10.1021/acs.nanolett.5b03724.

[143] Gleb M. Akselrod et al. „Efficient Nanosecond Photoluminescence from Infrared PbS Quantum Dots Coupled to Plasmonic Nanoantennas“. In: *ACS Photonics* 3 (10 2016), pp. 1741–1746. DOI: 10.1021/acsphotonics.6b00357. URL: https://doi.org/10.1021/acsphotonics.6b00357.

[144] Shailesh Kumar, Alexander Huck, and Ulrik L. Andersen. „Efficient Coupling of a Single Diamond Color Center to Propagating Plasmonic Gap Modes“. In: *Nano Letters* 13.3 (2013). PMID: 23414581, pp. 1221–1225. DOI: 10.1

021/nl304682r. eprint: https://doi.org/10.1021/nl304682r. URL: https://doi.org/10.1021/nl304682r.

[145] Daniel Riedel et al. „Deterministic Enhancement of Coherent Photon Generation from a Nitrogen-Vacancy Center in Ultrapure Diamond“. In: *Phys. Rev. X* 7 (3 Sept. 2017), p. 031040. DOI: 10.1103/PhysRevX.7.031040. URL: https://link.aps.org/doi/10.1103/PhysRevX.7.031040.

[146] Julia Benedikter et al. „Cavity-Enhanced Single-Photon Source Based on the Silicon-Vacancy Center in Diamond“. In: *Phys. Rev. Appl.* 7 (2 Feb. 2017), p. 024031. DOI: 10.1103/PhysRevApplied.7.024031. URL: https://link.aps.org/doi/10.1103/PhysRevApplied.7.024031.

[147] Simeon I. Bogdanov et al. „Ultrabright Room-Temperature Sub-Nanosecond Emission from Single Nitrogen-Vacancy Centers Coupled to Nanopatch Antennas“. In: *Nano Letters* 18.8 (2018). PMID: 29969274, pp. 4837–4844. DOI: 10.1021/acs.nanolett.8b01415. eprint: https://doi.org/10.1021/acs.nanolett.8b01415. URL: https://doi.org/10.1021/acs.nanolett.8b01415.

[148] H. Kambalathmana et al. „Exploring ultrafast single-photon emission of silicon-vacancy color centers in diamond nano-membranes coupled with gold nano-cones“. In: *Quantum Nanophotonic Materials, Devices, and Systems 2019*. Ed. by Cesare Soci, Matthew T. Sheldon, and Mario Agio. Vol. 11091. International Society for Optics and Photonics. SPIE, 2019, p. 1109108. DOI: 10.1117/12.2528749. URL: https://doi.org/10.1117/12.2528749.

[149] Andrew M. Boyce et al. „Plasmonic Diamond Membranes for Ultrafast Silicon Vacancy Emission“. In: *Nano Letters* 24.12 (2024). PMID: 38478720, pp. 3575–3580. DOI: 10.1021/acs.nanolett.3c04002. eprint: https://doi.org/10.1021/acs.nanolett.3c04002. URL: https://doi.org/10.1021/acs.nanolett.3c04002.

[150] Hengming Li et al. „Room-Temperature Picosecond Single-Photon Emission from a Silicon Vacancy Center in Diamond“. In: *ACS Nano* 19.20 (2025). PMID: 40373269, pp. 19310–19317. DOI: 10.1021/acsnano.5c02273. eprint: https://doi.org/10.1021/acsnano.5c02273. URL: https://doi.org/10.1021/acsnano.5c02273.

[151] S. Ditalia Tchernij et al. „Fluorine-based color centers in diamond“. In: *Scientific Reports* 10 (1 2020), p. 21537. ISSN: 2045-2322. DOI: 10.1038/s41598-020-78436-6. URL: https://doi.org/10.1038/s41598-020-78436-6.

[152] E. Nieto Hernandez et al. „Efficient Fabrication of High-Density Ensembles of Color Centers via Ion Implantation on a Hot Diamond Substrate“. In: *Advanced Physics Research* 3.12 (2024), p. 2400067. DOI: https://doi.org/10.1002/apxr.202400067. eprint: https://advanced.onlinelibrary.wiley.com/doi/pdf/10.1002/apxr.202400067. URL: https://advanced.onlinelibrary.wiley.com/doi/abs/10.1002/apxr.202400067.

[153] P. Michler et al. „A Quantum Dot Single-Photon Turnstile Device“. In: *Science* 290.5500 (2000), pp. 2282–2285. DOI: 10.1126/science.290.5500.2282. eprint: https://www.science.org/doi/pdf/10.1126/science.290.5500.2282. URL: https://www.science.org/doi/abs/10.1126/science.290.5500.2282.

[154] Jin Liu et al. „A solid-state source of strongly entangled photon pairs with high brightness and indistinguishability“. In: *Nature Nanotechnology* 14 (6 2019), pp. 586–593. ISSN: 1748-3395. DOI: 10.1038/s41565-019-0435-9. URL: https://doi.org/10.1038/s41565-019-0435-9.

[155] Liang Zhai et al. „Quantum interference of identical photons from remote GaAs quantum dots“. In: *Nature Nanotechnology* 17 (8 2022), pp. 829–833. ISSN: 1748-3395. DOI: 10.1038/s41565-022-01131-2. URL: https://doi.org/10.1038/s41565-022-01131-2.

[156] Alexios Beveratos et al. „Single Photon Quantum Cryptography“. In: *Phys. Rev. Lett.* 89 (18 Oct. 2002), p. 187901. DOI: 10.1103/PhysRevLett.89.187901. URL: https://link.aps.org/doi/10.1103/PhysRevLett.89.187901.

[157] A. Sipahigil et al. „An integrated diamond nanophotonics platform for quantum-optical networks“. In: *Science* 354.6314 (2016), pp. 847–850. DOI: 10.1126/science.aah6875. eprint: https://www.science.org/doi/pdf/10.1126/science.aah6875. URL: https://www.science.org/doi/abs/10.1126/science.aah6875.

[158] Jan Jeske et al. „Stimulated emission from nitrogen-vacancy centres in diamond“. In: *Nature Communications* 8 (1 2017), p. 14000. ISSN: 2041-1723. DOI: 10.1038/ncomms14000. URL: https://doi.org/10.1038/ncomms14000.

[159] S. Lagomarsino et al. „Creation of Silicon-Vacancy Color Centers in Diamond by Ion Implantation“. In: *Frontiers in Physics* Volume 8 - 2020 (2021). ISSN: 2296-424X. DOI: 10.3389/fphy.2020.601362. URL: https://www.frontiersin.org/journals/physics/articles/10.3389/fphy.2020.601362.

[160] Andrei Faraon et al. „Coupling of Nitrogen-Vacancy Centers to Photonic Crystal Cavities in Monocrystalline Diamond“. In: *Phys. Rev. Lett.* 109 (3 July 2012), p. 033604. DOI: 10.1103/PhysRevLett.109.033604. URL: https://link.aps.org/doi/10.1103/PhysRevLett.109.033604.

[161] Pietro Aprà et al. „Creation, Control, and Modeling of NV Centers in Nanodiamonds“. In: *Advanced Functional Materials* 34.39 (2024), p. 2404831. DOI: https://doi.org/10.1002/adfm.202404831. eprint: https://advanced.onlinelibrary.wiley.com/doi/pdf/10.1002/adfm.202404831. URL: https://advanced.onlinelibrary.wiley.com/doi/abs/10.1002/adfm.202404831.

[162] Julie A. Smyder et al. „The influence of continuous vs. pulsed laser excitation on single quantum dot photophysics“. In: *Phys. Chem. Chem. Phys.* 16 (47 2014), pp. 25723–25728. DOI: 10.1039/C4CP01395F. URL: http://dx.doi.org/10.1039/C4CP01395F.

[163] Mattias Jönsson and Gunnar Björk. „Evaluating the performance of photon-number-resolving detectors“. In: *Phys. Rev. A* 99 (4 Apr. 2019), p. 043822. DOI: 10.1103/PhysRevA.99.043822. URL: https://link.aps.org/doi/10.1103/PhysRevA.99.043822.

[164] Jan Provazník et al. „Benchmarking photon number resolving detectors“. In: *Opt. Express* 28.10 (May 2020), pp. 14839–14849. DOI: 10.1364/OE.389619. URL: https://opg.optica.org/oe/abstract.cfm?URI=oe-28-10-14839.

[165] Aleksandr Verevkin. „Photon number-resolved detectors: prospects and applications“. In: *Nanoscale Imaging, Spectroscopy, Sensing, and Actuation for Biomedical Applications IV*. Ed. by Alexander N. Cartwright and Dan V. Nicolau. Vol. 6447. International Society for Optics and Photonics. SPIE, 2007, p. 644706. DOI: 10.1117/12.695002. URL: https://doi.org/10.1117/12.695002.

[166] Robert H. Hadfield. „Single-photon detectors for optical quantum information applications“. In: *Nature Photonics* 3 (12 2009), pp. 696–705. ISSN: 1749-4893. DOI: 10.1038/nphoton.2009.230. URL: https://doi.org/10.1038/nphoton.2009.230.

[167] M. D. Eisaman et al. „Invited Review Article: Single-photon sources and detectors“. In: *Review of Scientific Instruments* 82.7 (2011), p. 071101. ISSN: 0034-6748. DOI: 10.1063/1.3610677. URL: https://doi.org/10.1063/1.3610677.

[168] G A Morton. „Photomultipliers for Scintillation Counting“. In: *R C A Rev.* Vol: 10 (Nov. 1949). URL: https://www.osti.gov/biblio/4434191.

[169] G. A. Morton. „Photon Counting“. In: *Appl. Opt.* 7.1 (Jan. 1968), pp. 1–10. DOI: 10.1364/AO.7.000001. URL: https://opg.optica.org/ao/abstract.cfm?URI=ao-7-1-1.

[170] G.A. Morton. „The Scintillation Counter“. In: ed. by L. Marton. Vol. 4. Advances in Electronics and Electron Physics. Academic Press, 1952, pp. 69–107. DOI: https://doi.org/10.1016/S0065-2539(08)61076-8. URL: https://www.sciencedirect.com/science/article/pii/S0065253908610768.

[171] Hamamatsu Photonics K.K. *Photomultiplier Tubes*. Hamamatsu Learning Center, Florida State University. URL: http://hamamatsu.magnet.fsu.edu/articles/photomultipliers.html (visited on 10/15/2025).

[172] Guang-Zhao Xu et al. „Superconducting microstrip single-photon detector with system detection efficiency over 90% at 1550 nm“. In: *Photon. Res.* 9.6 (June 2021), pp. 958–967. DOI: 10.1364/PRJ.419514. URL: https://opg.optica.org/prj/abstract.cfm?URI=prj-9-6-958.

[173] Hiroyuki Shibata et al. „SNSPD With Ultimate Low System Dark Count Rate Using Various Cold Filters“. In: *IEEE Transactions on Applied Superconductivity* 27.4 (2017), pp. 1–4. DOI: 10.1109/TASC.2016.2631947.

[174] Andreas Vetter et al. „Cavity-Enhanced and Ultrafast Superconducting Single-Photon Detectors“. In: *Nano Letters* 16.11 (2016). PMID: 27759401, pp. 7085–7092. DOI: 10.1021/acs.nanolett.6b03344. eprint: https://doi.org/10.1021/acs.nanolett.6b03344. URL: https://doi.org/10.1021/acs.nanolett.6b03344.

[175] Lixing You. In: *Nanophotonics* 9.9 (2020), pp. 2673–2692. DOI: doi:10.1515/nanoph-2020-0186. URL: https://doi.org/10.1515/nanoph-2020-0186.

[176] D Salvoni et al. „Lidar techniques for a SNSPD-based measurement“. In: *Journal of Physics: Conference Series* 1182.1 (Feb. 2019), p. 012014. DOI: 10.1088/1742-6596/1182/1/012014. URL: https://doi.org/10.1088/1742-6596/1182/1/012014.

[177] Michele Sclafani et al. „Sensitivity of a superconducting nanowire detector for single ions at low energy“. In: *Nanotechnology* 23.6 (Jan. 2012), p. 065501. DOI: 10.1088/0957-4484/23/6/065501. URL: https://doi.org/10.1088/0957-4484/23/6/065501.

[178] Davide Tamborini et al. „Superconducting nanowire single-photon detectors for Diffuse Correlation Spectroscopy“. In: *Biophotonics Congress: Optics in the Life Sciences Congress 2019 (BODA,BRAIN,NTM,OMA,OMP)*. Optica Publishing Group, 2019, BW1A.5. DOI: 10.1364/BRAIN.2019.BW1A.5. URL: https://opg.optica.org/abstract.cfm?URI=BRAIN-2019-BW1A.5.

[179] Sangita Tripathy, Kriti Tyagi, and Pratiksha Pratap. „A comprehensive study of various superconductors for superconducting nanowire single photon detectors applications“. In: *iScience* 27.10 (Oct. 2024). ISSN: 2589-0042. DOI: 10.1016/j.isci.2024.110779. URL: https://doi.org/10.1016/j.isci.2024.110779.

[180] Iman Esmaeil Zadeh et al. „Superconducting nanowire single-photon detectors: A perspective on evolution, state-of-the-art, future developments, and applications“. In: *Applied Physics Letters* 118.19 (May 2021), p. 190502. ISSN: 0003-6951. DOI: 10.1063/5.0045990. eprint: https://pubs.aip.org/aip/apl/article-pdf/doi/10.1063/5.0045990/20021815/190502_1_5.0045990.pdf. URL: https://doi.org/10.1063/5.0045990.

[181] Chandra M Natarajan, Michael G Tanner, and Robert H Hadfield. „Superconducting nanowire single-photon detectors: physics and applications“. In: *Superconductor Science and Technology* 25.6 (Apr. 2012), p. 063001. DOI: 10.1088/0953-2048/25/6/063001. URL: https://doi.org/10.1088/0953-2048/25/6/063001.

[182] Itamar Holzman and Yachin Ivry. „Superconducting Nanowires for Single-Photon Detection: Progress, Challenges, and Opportunities“. In: *Advanced Quantum Technologies* 2.3-4 (2019), p. 1800058. DOI: https://doi.org/10.1002/qute.201800058. eprint: https://advanced.onlinelibrary.wiley.com/doi/pdf/10.1002/qute.201800058. URL: https://advanced.onlinelibrary.wiley.com/doi/abs/10.1002/qute.201800058.

[183] A. M. Kadin and M. W. Johnson. „Nonequilibrium photon-induced hotspot: A new mechanism for photodetection in ultrathin metallic films“. In: *Applied Physics Letters* 69.25 (Dec. 1996), pp. 3938–3940. ISSN: 0003-6951. DOI: 10.1063/1.117576. eprint: https://pubs.aip.org/aip/apl/article-pdf/69/25/3938/18523641/3938_1_10.1063_1.117576.pdf. URL: https://doi.org/10.1063/1.117576.

[184] Hiroyuki Shibata. „Superconducting Single-photon Detectors“. In: *NTT Technical Review* 9.9 (Sept. 2011). Feature Articles: State-of-the-Art Single-photon Technologies, pp. 43–47. URL: https://www.ntt-review.jp/archive/ntttechnical.php?contents=ntr201109fa9.html.

[185] Yifan Liu et al. „Superconducting nanowire single-photon detector enhanced near-infrared II portable confocal microscopy for tissue imaging with indocyanine green“. In: *Opt. Lett.* 49.22 (Nov. 2024), pp. 6349–6352. DOI: 10.1364/OL.537612. URL: https://opg.optica.org/ol/abstract.cfm?URI=ol-49-22-6349.

[186] Orit Skorka and Dileepan Joseph. „CMOS digital pixel sensors: technology and applications“. In: *Nanosensors, Biosensors, and Info-Tech Sensors and Systems 2014*. Ed. by Vijay K. Varadan. Vol. 9060. International Society for Optics and Photonics. SPIE, 2014, 90600G. DOI: 10.1117/12.2044808. URL: https://doi.org/10.1117/12.2044808.

[187] Wolfgang Becker. *Advanced Time-Correlated Single Photon Counting Techniques*. Vol. 81. Springer Series in Chemical Physics. Springer-Verlag, 2005. ISBN: 978-3-540-28882-4. DOI: 10.1007/3-540-28882-1.

[188] Desmond V. O'Connor and David Phillips. *Time-Correlated Single Photon Counting*. London: Academic Press, 1984. ISBN: 978-0-12-524140-3.

[189] PicoQuant GmbH. *PicoHarp 300 User's Manual and Technical Data: Time-Correlated Single Photon Counting System with USB Interface*. Software Version 2.3. User's Manual and Technical Data for PicoHarp 300 TCSPC Module and Picosecond Event Timer. PicoQuant GmbH. Berlin, Germany, 2009.

[190] PicoQuant GmbH. *Time-Correlated Single Photon Counting*. Technical Note. Accessed from https://www.picoquant.com/images/uploads/page/files/7253/technote_tcspc.pdf. Berlin, Germany: PicoQuant GmbH. URL: https://www.picoquant.com/images/uploads/page/files/7253/technote_tcspc.pdf.

[191] J S Courtney-Pratt. „A review of the methods of high-speed photography“. In: *Reports on Progress in Physics* 20.1 (Jan. 1957), p. 379. DOI: 10.1088/0034-4885/20/1/307. URL: https://doi.org/10.1088/0034-4885/20/1/307.

[192] J S Courtney-Pratt. „A new method for the photographic study of fast transient phenomena.“ eng. In: *Research; a journal of science and its applications* 2.6 (June 1949), pp. 287–94.

[193] D.J. Bradley and G.H.C. New. „Ultrashort pulse measurements“. In: *Proceedings of the IEEE* 62.3 (1974), pp. 313–345. DOI: 10.1109/PROC.1974.9427.

[194] P. Gallant et al. „Characterization of a subpicosecond x-ray streak camera for ultrashort laser-produced plasmas experiments“. In: *Review of Scientific Instruments* 71.10 (Oct. 2000), pp. 3627–3633. ISSN: 0034-6748. DOI: 10.1063/1.1310347. URL: https://doi.org/10.1063/1.1310347.

[195] Y.K. Zhao et al. „Application and Development of the Streak Camera Measurement System at HLS-II“. In: *Proc. IPAC'21* (Campinas, SP, Brazil). International Particle Accelerator Conference 12. https://doi.org/10.18429/JACoW-IPAC2021-TUPAB222. JACoW Publishing, Geneva, Switzerland, Aug. 2021, TUPAB222, pp. 1942–1944. ISBN: 978-3-95450-214-1. DOI: 10.18429/JACoW-

IPAC2021-TUPAB222. URL: https://jacow.org/ipac2021/papers/tupab222.pdf.

[196] Ivo H. M. Van Stokkum et al. „(Sub)-Picosecond Spectral Evolution of Fluorescence Studied with a Synchroscan Streak-Camera System and Target Analysis“. In: *Biophysical Techniques in Photosynthesis*. Ed. by Thijs J. Aartsma and Jörg Matysik. Dordrecht: Springer Netherlands, 2008, pp. 223–240.

[197] Jayanta Mondal, Narayan Chandra Maity, and Ranjit Biswas. „Detection of ultrafast solvent dynamics employing a streak camera“. In: *Journal of Chemical Sciences* 135.3 (Aug. 2023), p. 84. ISSN: 0973-7103. DOI: 10.1007/s12039-023-02208-8. URL: https://doi.org/10.1007/s12039-023-02208-8.

[198] J. Itatani et al. „Attosecond Streak Camera“. In: *Phys. Rev. Lett.* 88 (17 Apr. 2002), p. 173903. DOI: 10.1103/PhysRevLett.88.173903. URL: https://link.aps.org/doi/10.1103/PhysRevLett.88.173903.

[199] E. Goulielmakis et al. „Direct Measurement of Light Waves“. In: *Science* 305.5688 (2004), pp. 1267–1269. DOI: 10.1126/science.1100866. eprint: https://www.science.org/doi/pdf/10.1126/science.1100866. URL: https://www.science.org/doi/abs/10.1126/science.1100866.

[200] Hamamatsu Photonics K.K. *Streak Tube: Operating Principle, Applications, and Selection Guide*. Technical Information, Catalog/Booklet. Document Number: SHSS0006E. Hamamatsu Photonics K.K. Hamamatsu City, Japan, 2022. URL: https://www.hamamatsu.com/content/dam/hamamatsu-photonics/sites/documents/99_SALES_LIBRARY/sys/SHSS0006E_STREAK.pdf.

[201] Masayuki Komura and Shigeru Itoh. „Fluorescence measurement by a streak camera in a single-photon-counting mode“. In: *Photosynthesis Research* 101.2 (Sept. 2009), pp. 119–133. ISSN: 1573-5079. DOI: 10.1007/s11120-009-9463-x. URL: https://doi.org/10.1007/s11120-009-9463-x.

[202] Markus Allgaier et al. „Streak camera imaging of single photons at telecom wavelength“. In: *Applied Physics Letters* 112.3 (Jan. 2018), p. 031110. ISSN: 0003-6951. DOI: 10.1063/1.5004110. URL: https://doi.org/10.1063/1.5004110.

[203] Thomas M. Nordlund. „Streak Cameras for Time-Domain Fluorescence“. In: *Topics in Fluorescence Spectroscopy: Techniques*. Ed. by Joseph R. Lakowicz. Boston, MA: Springer US, 1999, pp. 183–260. ISBN: 978-0-306-47057-8. DOI: 10.1007/0-306-47057-8_3. URL: https://doi.org/10.1007/0-306-47057-8_3.

[204] Vassily Kornienko et al. „The Space-Charge Problem in Ultrafast Diagnostics: An All-Optical Solution for Streak Cameras“. In: *Ultrafast Science* 4 (2024), p. 0055. DOI: 10.34133/ultrafastscience.0055. eprint: https://spj.science.org/doi/pdf/10.34133/ultrafastscience.0055. URL: https://spj.science.org/doi/abs/10.34133/ultrafastscience.0055.

[205] Z. Y. Ou et al. „Fourth-order interference technique for determining the coherence time of a light beam“. In: *J. Opt. Soc. Am. B* 6.1 (Jan. 1989), pp. 100–103. DOI: 10.1364/JOSAB.6.000100. URL: https://opg.optica.org/josab/abstract.cfm?URI=josab-6-1-100.

[206] Z.Y. Ou et al. „Observation of beating between blue and green light“. In: *Optics Communications* 69.1 (1988), pp. 1–5. ISSN: 0030-4018. DOI: https://doi.org/10.1016/0030-4018(88)90058-2. URL: https://www.sciencedirect.com/science/article/pii/0030401888900582.

[207] Y. Miyamoto et al. „Measurement of ultrafast optical pulses with two-photon interference“. In: *Opt. Lett.* 18.11 (June 1993), pp. 900–902. DOI: 10.1364/OL.18.000900. URL: https://opg.optica.org/ol/abstract.cfm?URI=ol-18-11-900.

[208] Tohru Kobayashi et al. „Femtosecond intermolecular electron transfer in diffusionless, weakly polar systems: nile blue in aniline and N,N-dimethylaniline“. In: *Chemical Physics Letters* 180.5 (1991), pp. 416–422. ISSN: 0009-2614. DOI: https://doi.org/10.1016/0009-2614(91)85142-J. URL: https://www.sciencedirect.com/science/article/pii/000926149185142J.

[209] A. J. Devaney. „The inverse problem for random sources“. In: *Journal of Mathematical Physics* 20.8 (Aug. 1979), pp. 1687–1691. ISSN: 0022-2488. DOI: 10.1063/1.524277. URL: https://doi.org/10.1063/1.524277.

[210] Gordon J. Hedley et al. „Picosecond time-resolved photon antibunching measures nanoscale exciton motion and the true number of chromophores“. In: *Nature Communications* 12.1 (Feb. 2021), p. 1327. ISSN: 2041-1723. DOI: 10.1038/s41467-021-21474-z. URL: https://doi.org/10.1038/s41467-021-21474-z.

[211] K. Uesaka et al. „Wavelength exchange in a highly nonlinear dispersion-shifted fiber: theory and experiments“. In: *IEEE Journal of Selected Topics in Quantum Electronics* 8.3 (2002), pp. 560–568. DOI: 10.1109/JSTQE.2002.1016359.

[212] Bowen Li et al. „Parametric spectrotemporal analyzer based on four-wave mixing Bragg scattering“. In: *Opt. Lett.* 43.8 (Apr. 2018), pp. 1922–1925. DOI: 10.1364/OL.43.001922. URL: https://opg.optica.org/ol/abstract.cfm?URI=ol-43-8-1922.

[213] J G Rarity, P R Tapster, and R Loudon. „Non-classical interference between independent sources“. In: *Journal of Optics B: Quantum and Semiclassical Optics* 7.7 (June 2005), S171. DOI: 10.1088/1464-4266/7/7/007. URL: https://doi.org/10.1088/1464-4266/7/7/007.

[214] Yu-Hao Deng et al. „Quantum Interference between Light Sources Separated by 150 Million Kilometers“. In: *Phys. Rev. Lett.* 123 (8 Aug. 2019), p. 080401. DOI: 10.1103/PhysRevLett.123.080401. URL: https://link.aps.org/doi/10.1103/PhysRevLett.123.080401.

[215] R. R. Alfano, ed. *Semiconductors Probed by Ultrafast Laser Spectroscopy*. Vol. II. Orlando, FL: Academic Press, Inc. (Harcourt Brace Jovanovich, Publishers), 1984. ISBN: 0-12-049902-9.

[216] Bernard Valeur and M. N. Berberan-Santos. *Molecular Fluorescence: Principles and Applications*. Second. Wiley-VCH, 2012. DOI: 10.1002/9783527650002. URL: https://onlinelibrary.wiley.com/doi/book/10.1002/9783527650002.

[217] LightCon GmbH & Co. KG. *Time-Resolved Fluorescence Spectroscopy*. LightCon GmbH & Co. KG. 2024. URL: https://lightcon.com/applications/time-resolved-fluorescence-spectroscopy/ (visited on 10/17/2025).

[218] Valentin G. Dmitriev, Gagik G. Gurzadyan, and David N. Nikogosyan. *Handbook of Nonlinear Optical Crystals*. 3rd ed. Vol. 64. Springer Series in Optical Sciences. Berlin, Heidelberg: Springer, 1999. ISBN: 978-3-540-65394-3. DOI: 10.1007/978-3-540-46793-9.

[219] Hans Roland Schanz. „Femtosecond Broadbandfluorescence Upconversion“. Dissertation zur Erlangung des akademischen Grades doctor rerum naturalium (dr. rer. nat.) Berlin: Humboldt-Universität zu Berlin, 2002.

[220] Youying Rong et al. „Excited-state lifetime measurement of silicon vacancy centers in diamond by single-photon frequency upconversion“. In: *Laser Physics* 28.5 (Apr. 2018), p. 055401. DOI: 10.1088/1555-6611/aaa02f. URL: https://doi.org/10.1088/1555-6611/aaa02f.

[221] Aaron P. VanDevender and Paul G. Kwiat. „Quantum transduction via frequency upconversion (Invited)“. In: *J. Opt. Soc. Am. B* 24.2 (Feb. 2007), pp. 295–299. DOI: 10.1364/JOSAB.24.000295. URL: https://opg.optica.org/josab/abstract.cfm?URI=josab-24-2-295.

[222] Xiaorong Gu et al. „High-Speed Single-Photon Frequency Upconversion With Synchronous Pump Pulses“. In: *IEEE Journal of Selected Topics in Quantum Electronics* 15.6 (2009), pp. 1748–1752. DOI: 10.1109/JSTQE.2009.2024329.

[223] Kun Huang et al. „Wide-field mid-infrared single-photon upconversion imaging“. In: *Nature Communications* 13.1 (2022), p. 1077. DOI: 10.1038/s41467-022-28716-8. URL: https://doi.org/10.1038/s41467-022-28716-8.

[224] Joseph M. Beechem and Ludwig Brand. „Time-resolved fluorescence of proteins“. In: *Annual Review of Biochemistry* 54.Volume 54, 1985 (1985), pp. 43–71. ISSN: 1545-4509. DOI: https://doi.org/10.1146/annurev.bi.54.070185.000355. URL: https://www.annualreviews.org/content/journals/10.1146/annurev.bi.54.070185.000355.

[225] Jianhua Xu and Jay R. Knutson. „Chapter 8 Ultrafast Fluorescence Spectroscopy via Upconversion: Applications to Biophysics“. In: *Fluorescence Spectroscopy*. Vol. 450. Methods in Enzymology. Academic Press, 2008, pp. 159–183. DOI: https://doi.org/10.1016/S0076-6879(08)03408-3. URL: https://www.sciencedirect.com/science/article/pii/S0076687908034083.

[226] Simin Cao et al. „Ultrafast Fluorescence Spectroscopy via Upconversion and Its Applications in Biophysics“. In: *Molecules* 26.1 (2021), p. 211. DOI: 10.3390/molecules26010211. URL: https://doi.org/10.3390/molecules26010211.

[227] T. H. Maiman. „Stimulated Optical Radiation in Ruby“. In: *Nature* 187 (4736 Aug. 1, 1960), pp. 493–494. ISSN: 1476-4687. DOI: 10.1038/187493a0. URL: https://doi.org/10.1038/187493a0.

[228] M. A. Duguay and J. W. Hansen. „An ultrafast light gate“. In: *Applied Physics Letters* 15.6 (Sept. 1969), pp. 192–194. ISSN: 0003-6951. DOI: 10.1063/1.1652962. URL: https://doi.org/10.1063/1.1652962.

[229] K. Sala and M. C. Richardson. „Optical Kerr effect induced by ultrashort laser pulses“. In: *Phys. Rev. A* 12 (3 Sept. 1975), pp. 1036–1047. DOI: 10.1103/PhysRevA.12.1036. URL: https://link.aps.org/doi/10.1103/PhysRevA.12.1036.

[230] R. L. Fork, B. I. Greene, and C. V. Shank. „Generation of optical pulses shorter than 0.1 psec by colliding pulse mode locking“. In: *Applied Physics Letters* 38.9 (May 1981), pp. 671–672. ISSN: 0003-6951. DOI: 10.1063/1.92500. URL: https://doi.org/10.1063/1.92500.

[231] B. I. Greene and R. C. Farrow. „Direct measurement of a subpicosecond birefringent response in CS_2“. In: *The Journal of Chemical Physics* 77.9 (Nov. 1982), pp. 4779–4780. ISSN: 0021-9606. DOI: 10.1063/1.444384. URL: https://doi.org/10.1063/1.444384.

[232] B.I. Greene and R.C. Farrow. „The subpicosecond Kerr effect in CS_2“. In: *Chemical Physics Letters* 98.3 (1983), pp. 273–276. ISSN: 0009-2614. DOI: https://doi.org/10.1016/0009-2614(83)87164-4. URL: https://www.sciencedirect.com/science/article/pii/0009261483871644.

[233] P. P. Ho and R. R. Alfano. „Optical Kerr effect in liquids“. In: *Phys. Rev. A* 20 (5 Nov. 1979), pp. 2170–2187. DOI: 10.1103/PhysRevA.20.2170. URL: https://link.aps.org/doi/10.1103/PhysRevA.20.2170.

[234] S. A. Myers and E. J. Robinson. „Kerr effect in CS_2, C_6H_6, and CCl_4“. In: *The Journal of Chemical Physics* 58.8 (Apr. 1973), pp. 3526–3527. ISSN: 0021-9606. DOI: 10.1063/1.1679688. URL: https://doi.org/10.1063/1.1679688.

[235] J. M. Dziedzic, R. H. Stolen, and A. Ashkin. „Optical Kerr effect in long fibers“. In: *Appl. Opt.* 20.8 (Apr. 1981), pp. 1403–1406. DOI: 10.1364/AO.20.001403. URL: https://opg.optica.org/ao/abstract.cfm?URI=ao-20-8-1403.

[236] Roberto Righini. „Ultrafast Optical Kerr Effect in Liquids and Solids“. In: *Science* 262.5138 (1993), pp. 1386–1390. DOI: 10.1126/science.262.5138.1386. eprint: https://www.science.org/doi/pdf/10.1126/science.262.5138.1386. URL: https://www.science.org/doi/abs/10.1126/science.262.5138.1386.

[237] Yaobing Xiong et al. „Efficient optical Kerr gating property of fluorotellurite glass“. In: *Optik* 125 (Feb. 2014), pp. 1444–1447. DOI: 10.1016/j.ijleo.2013.09.016.

[238] X. Wang et al. „Large and ultrafast third-order optical nonlinearity of GeS_2–Ga_2 S_3–CdS chalcogenide glass“. In: *Chemical Physics Letters - CHEM PHYS LETT* 399 (Nov. 2004), pp. 230–233. DOI: 10.1016/j.cplett.2004.10.024.

[239] Evdokia Dremetsika et al. „Measuring the nonlinear refractive index of graphene using the optical Kerr effect method“. In: *Opt. Lett.* 41.14 (July 2016), pp. 3281–3284. DOI: 10.1364/OL.41.003281. URL: https://opg.optica.org/ol/abstract.cfm?URI=ol-41-14-3281.

[240] Alyson J. A. Carvalho et al. „Near-infrared ultrafast third-order nonlinear optical response of 2D NbS_2, $NbSe_2$, $ZrTe_2$, and MoS_2“. In: *Opt. Lett.* 48.9 (May 2023), pp. 2297–2300. DOI: 10.1364/OL.487443. URL: https://opg.optica.org/ol/abstract.cfm?URI=ol-48-9-2297.

[241] J. Takeda et al. „Time-resolved luminescence spectroscopy by the optical Kerr-gate method applicable to ultrafast relaxation processes“. In: *Phys. Rev. B* 62 (15 Oct. 2000), pp. 10083–10087. DOI: 10.1103/PhysRevB.62.10083. URL: https://link.aps.org/doi/10.1103/PhysRevB.62.10083.

[242] Wenjiang Tan et al. „Control of the gated spectra with narrow bandwidth from a supercontinuum using ultrafast optical Kerr gate of bismuth glass“. In: *Applied Physics Letters* 93.5 (Aug. 2008), p. 051109. ISSN: 0003-6951. DOI: 10.1063/1.2968202. URL: https://doi.org/10.1063/1.2968202.

[243] B. Schmidt et al. „A broadband Kerr shutter for femtosecond fluorescence spectroscopy“. In: *Applied Physics B* 76.8 (July 2003), pp. 809–814. DOI: 10.1007/s00340-003-1230-7. URL: https://doi.org/10.1007/s00340-003-1230-7.

[244] S. Arzhantsev and M. Maroncelli. „Design and Characterization of a Femtosecond Fluorescence Spectrometer Based on Optical Kerr Gating“. In: *Applied Spectroscopy* 59.2 (2005). PMID: 15720762, pp. 206–220. DOI: 10.1366/0003702053085007. eprint: https://doi.org/10.1366/0003702053085007. URL: https://doi.org/10.1366/0003702053085007.

[245] Lars Gundlach and Piotr Piotrowiak. „Femtosecond Kerr-gated wide-field fluorescence microscopy“. In: *Opt. Lett.* 33.9 (May 2008), pp. 992–994. DOI: 10.1364/OL.33.000992. URL: https://opg.optica.org/ol/abstract.cfm?URI=ol-33-9-992.

[246] Jolie C. Blake et al. „Ultraviolet femtosecond Kerr-gated wide-field fluorescence microscopy“. In: *Opt. Lett.* 41.11 (June 2016), pp. 2462–2465. DOI: 10.1364/OL.41.002462. URL: https://opg.optica.org/ol/abstract.cfm?URI=ol-41-11-2462.

[247] Tatsuya Fujino, Takuya Fujima, and Tahei Tahara. „Picosecond time-resolved imaging by nonscanning fluorescence Kerr gate microscope“. In: *Applied Physics Letters* 87.13 (Sept. 2005), p. 131105. ISSN: 0003-6951. DOI: 10.1063/1.2067694. URL: https://doi.org/10.1063/1.2067694.

[248] Wenjiang Tan et al. „High Time-Resolved Three-Dimensional Imaging Using Ultrafast Optical Kerr Gate of Bismuth Glass“. In: *IEEE Photonics Technology Letters* 23.8 (2011), pp. 471–473. DOI: 10.1109/LPT.2011.2109704.

[249] Yuhu Ren et al. „Microscopic Imaging Through a Turbid Medium by Use of a Differential Optical Kerr Gate“. In: *IEEE Photonics Technology Letters* 28.4 (2016), pp. 394–397. DOI: 10.1109/LPT.2015.2496618.

[250] Connor Kupchak et al. „Terahertz-bandwidth switching of heralded single photons“. In: *Opt. Lett.* 44.6 (Mar. 2019), pp. 1427–1430. DOI: 10.1364/OL.44.001427. URL: https://opg.optica.org/ol/abstract.cfm?URI=ol-44-6-1427.

[251] Peter S. Eldridge, Jolie C. Blake, and Lars Gundlach. „Ultrafast Probe of Carrier Diffusion and Nongeminate Processes in a Single CdSSe Nanowire“. In: *Journal of Spectroscopy* 2015.1 (2015), p. 574754. DOI: https://doi.org/10.1155/2015/574754. eprint: https://onlinelibrary.wiley.com/doi/pdf/10.1155/2015/574754. URL: https://onlinelibrary.wiley.com/doi/abs/10.1155/2015/574754.

[252] Masahiro Yabuno et al. „Ultrafast measurement of a single-photon wave packet using an optical Kerr gate“. In: *Opt. Express* 30.4 (Feb. 2022), pp. 4999–5007. DOI: 10.1364/OE.446010. URL: https://opg.optica.org/oe/abstract.cfm?URI=oe-30-4-4999.

[253] Robert W. Boyd. *Nonlinear Optics*. 4th ed. San Diego, CA (Imprint of Elsevier): Academic Press, 2020. ISBN: 978-0-12-811002-7. DOI: 10.1016/C2015-0-05510-1.

[254] D. E. Spence, P. N. Kean, and W. Sibbett. „60-fsec pulse generation from a self-mode-locked Ti:sapphire laser“. In: *Opt. Lett.* 16.1 (Jan. 1991), pp. 42–44. DOI: 10.1364/OL.16.000042. URL: https://opg.optica.org/ol/abstract.cfm?URI=ol-16-1-42.

[255] U. Morgner et al. „Sub-two-cycle pulses from a Kerr-lens mode-locked Ti:sapphire laser“. In: *Opt. Lett.* 24.6 (Mar. 1999), pp. 411–413. DOI: 10.1364/OL.24.000411. URL: https://opg.optica.org/ol/abstract.cfm?URI=ol-24-6-411.

[256] D. H. Sutter et al. „Semiconductor saturable-absorber mirror–assisted Kerr-lens mode-locked Ti:sapphire laser producing pulses in the two-cycle regime“. In: *Opt. Lett.* 24.9 (May 1999), pp. 631–633. DOI: 10.1364/OL.24.000631. URL: https://opg.optica.org/ol/abstract.cfm?URI=ol-24-9-631.

[257] Matthew A. Hall, Joseph B. Altepeter, and Prem Kumar. „Ultrafast Switching of Photonic Entanglement“. In: *Phys. Rev. Lett.* 106 (5 Feb. 2011), p. 053901. DOI: 10.1103/PhysRevLett.106.053901. URL: https://link.aps.org/doi/10.1103/PhysRevLett.106.053901.

[258] Kate Lauren Fenwick. „Exploiting Ultrafast Optical Pulses: Probing Excitonic Properties of 2D Materials and Utilizing the Kerr Effect for All-Optical Switching“. A thesis submitted to the Department of Physics, Engineering

Physics and Astronomy. Master of Science Thesis. Kingston, Ontario, Canada: Queen's University, Aug. 2019.

[259] Naoki Sugimoto et al. „Femtosecond and terahertz optical Kerr shutter switching in glass containing high concentration of Bi_2O_3". In: *Optics Communications* 161.1 (1999), pp. 47–50. ISSN: 0030-4018. DOI: https://doi.org/10.1016/S0030-4018(99)00018-8. URL: https://www.sciencedirect.com/science/article/pii/S0030401899000188.

[260] Henry J. Meyer, Sandra Mamani, and Robert R. Alfano. „Femtosecond Optical Kerr Gate in tissues". In: *Journal of Biophotonics* 16.12 (2023), e202300099. DOI: https://doi.org/10.1002/jbio.202300099. eprint: https://onlinelibrary.wiley.com/doi/pdf/10.1002/jbio.202300099. URL: https://onlinelibrary.wiley.com/doi/abs/10.1002/jbio.202300099.

[261] Henry J. Meyer et al. „Femtosecond optical Kerr effect in normal and grades of cancerous breast tissues as a new optical biopsy method". In: *Journal of Biophotonics* 17.2 (2024), e202300344. DOI: https://doi.org/10.1002/jbio.202300344. eprint: https://onlinelibrary.wiley.com/doi/pdf/10.1002/jbio.202300344. URL: https://onlinelibrary.wiley.com/doi/abs/10.1002/jbio.202300344.

[262] Robert R. Alfano, Shah Faisal B. Mazhar, and Lingyan Shi. „Higher harmonic and supercontinuum generation arising from electronic self-phase modulation under ultrafast laser pulses for various states of matter". In: *Optik* 247 (2021), p. 167872. ISSN: 0030-4026. DOI: https://doi.org/10.1016/j.ijleo.2021.167872. URL: https://www.sciencedirect.com/science/article/pii/S0030402621014522.

[263] Robert R. Alfano and Shah Faisal B. Mazhar. „Higher harmonics and supercontinuum generated from the Kerr response time in different states of matter from a universal electromagnetic model". In: *Scientific Reports* 13.1 (Sept. 2023), p. 15467. DOI: 10.1038/s41598-023-42579-z. URL: https://doi.org/10.1038/s41598-023-42579-z.

[264] John E. Beetar et al. „Multioctave supercontinuum generation and frequency conversion based on rotational nonlinearity". In: *Science Advances* 6.34 (2020), eabb5375. DOI: 10.1126/sciadv.abb5375. eprint: https://www.science.org/doi/pdf/10.1126/sciadv.abb5375. URL: https://www.science.org/doi/abs/10.1126/sciadv.abb5375.

[265] Adrea R. Johnson et al. „Octave-spanning coherent supercontinuum generation in a silicon nitride waveguide". In: *Opt. Lett.* 40.21 (Nov. 2015), pp. 5117–5120.

DOI: 10.1364/OL.40.005117. URL: https://opg.optica.org/ol/abstract.cfm?URI=ol-40-21-5117.

[266] M. N. Islam et al. „Cross-phase modulation in optical fibers“. In: *Opt. Lett.* 12.8 (Aug. 1987), pp. 625–627. DOI: 10.1364/OL.12.000625. URL: https://opg.optica.org/ol/abstract.cfm?URI=ol-12-8-625.

[267] J. David Musgraves, Juejun Hu, and Laurent Calvez, eds. *Springer Handbook of Glass*. 1st ed. Springer Handbooks. Cham: Springer Cham, 2019. ISBN: 978-3-319-93726-7. DOI: 10.1007/978-3-319-93728-1.

[268] John Kerr. „XLIII. On rotation of the plane of polarization by reflection from the pole of a magnet“. In: *The London, Edinburgh, and Dublin Philosophical Magazine and Journal of Science* 3.19 (1877), pp. 321–343. DOI: 10.1080/14786447708639245. eprint: https://doi.org/10.1080/14786447708639245. URL: https://doi.org/10.1080/14786447708639245.

[269] John Kerr. „XXIV. On reflection of polarized light from the equatorial surface of a magnet“. In: *The London, Edinburgh, and Dublin Philosophical Magazine and Journal of Science* 5.30 (1878), pp. 161–177. DOI: 10.1080/14786447808639407. eprint: https://doi.org/10.1080/14786447808639407. URL: https://doi.org/10.1080/14786447808639407.

[270] John Kerr. „XL. A new relation between electricity and light: Dielectrified media birefringent“. In: *The London, Edinburgh, and Dublin Philosophical Magazine and Journal of Science* 50.332 (1875), pp. 337–348. DOI: 10.1080/14786447508641302. eprint: https://doi.org/10.1080/14786447508641302. URL: https://doi.org/10.1080/14786447508641302.

[271] A. D. Buckingham. „Birefringence Resulting from the Application of an Intense Beam of Light to an Isotropic Medium“. In: *Proceedings of the Physical Society. Section B* 69.3 (Mar. 1956), p. 344. DOI: 10.1088/0370-1301/69/3/309. URL: https://doi.org/10.1088/0370-1301/69/3/309.

[272] Fujio Shimizu. „Frequency Broadening in Liquids by a Short Light Pulse“. In: *Phys. Rev. Lett.* 19 (19 Nov. 1967), pp. 1097–1100. DOI: 10.1103/PhysRevLett.19.1097. URL: https://link.aps.org/doi/10.1103/PhysRevLett.19.1097.

[273] R. R. Alfano and S. L. Shapiro. „Observation of Self-Phase Modulation and Small-Scale Filaments in Crystals and Glasses“. In: *Phys. Rev. Lett.* 24 (11 Mar. 1970), pp. 592–594. DOI: 10.1103/PhysRevLett.24.592. URL: https://link.aps.org/doi/10.1103/PhysRevLett.24.592.

[274] R. R. Alfano and S. L. Shapiro. „Emission in the Region 4000 to 7000 Å Via Four-Photon Coupling in Glass“. In: *Phys. Rev. Lett.* 24 (11 Mar. 1970), pp. 584–587. DOI: 10.1103/PhysRevLett.24.584. URL: https://link.aps.org/doi/10.1103/PhysRevLett.24.584.

[275] Robert R. Alfano, ed. *The Supercontinuum Laser Source: The Ultimate White Light*. 4th ed. Springer Cham, 2023. ISBN: 978-3-031-06197-4. DOI: 10.1007/978-3-031-06197-4. URL: https://link.springer.com/book/10.1007/978-3-031-06197-4.

[276] Andrew M. Weiner. *Ultrafast Optics*. 1st ed. John Wiley & Sons, Inc., 2008. ISBN: 978-0-471-41539-8. DOI: 10.1002/9780470473467. URL: https://onlinelibrary.wiley.com/doi/book/10.1002/9780470473467.

[277] P. P. Ho, P. Y. Lu, and R. R. Alfano. „Observation of broadened and oscillatory optically induced Kerr kinetics in neat liquids“. In: *Phys. Rev. A* 21 (5 May 1980), pp. 1730–1734. DOI: 10.1103/PhysRevA.21.1730. URL: https://link.aps.org/doi/10.1103/PhysRevA.21.1730.

[278] W. Kaiser and C. G. B. Garrett. „Two-Photon Excitation in CaF_2: Eu^{2+}“. In: *Phys. Rev. Lett.* 7 (6 Sept. 1961), pp. 229–231. DOI: 10.1103/PhysRevLett.7.229. URL: https://link.aps.org/doi/10.1103/PhysRevLett.7.229.

[279] Giancarlo C. Righini and Luigi Sirleto, eds. *Advances in Nonlinear Photonics*. 1st ed. An imprint of Elsevier. Woodhead Publishing, 2023. ISBN: 978-0-323-98384-6.

[280] National Institute of Standards and Technology (NIST). *NIST Chemistry WebBook, SRD 69: Carbon disulfide (CS_2)*. Permanent link for CAS No. 75-15-0. 2024. URL: https://webbook.nist.gov/cgi/cbook.cgi?ID=C75150&Mask=205 (visited on 10/28/2025).

[281] K. D. Dorkenoo et al. „Stimulated Rayleigh-wing scattering with two-beam coupling in CS_2“. In: *J. Opt. Soc. Am. B* 12.1 (Jan. 1995), pp. 37–42. DOI: 10.1364/JOSAB.12.000037. URL: https://opg.optica.org/josab/abstract.cfm?URI=josab-12-1-37.

[282] V. Besse, H. Leblond, and G. Boudebs. „Filamentation of light in carbon disulfide“. In: *Phys. Rev. A* 89 (4 Apr. 2014), p. 043840. DOI: 10.1103/PhysRevA.89.043840. URL: https://link.aps.org/doi/10.1103/PhysRevA.89.043840.

[283] R.A. Ganeev et al. „Nonlinear refraction in CS_2“. In: *Applied Physics B* 78 (3 Feb. 2004), pp. 433–438. ISSN: 1432-0649. DOI: 10.1007/s00340-003-1389-y. URL: https://doi.org/10.1007/s00340-003-1389-y.

[284] K. D. Dorkenoo, A. J. van Wonderen, and G. Rivoire. „Interplay between the optical Kerr effect and stimulated light scattering in bulk carbon disulfide“. In: *J. Opt. Soc. Am. B* 15.6 (June 1998), pp. 1762–1772. DOI: 10.1364/JOSAB.15.001762. URL: https://opg.optica.org/josab/abstract.cfm?URI=josab-15-6-1762.

[285] De Gui Kong et al. „The fifth-order nonlinearity of CS_2“. In: *Journal of Physics B: Atomic, Molecular and Optical Physics* 42.6 (Mar. 2009), p. 065401. DOI: 10.1088/0953-4075/42/6/065401. URL: https://doi.org/10.1088/0953-4075/42/6/065401.

[286] M. Sheik-Bahae, A. A. Said, and E. W. Van Stryland. „High-sensitivity, single-beam n_2 measurements“. In: *Opt. Lett.* 14.17 (Sept. 1989), pp. 955–957. DOI: 10.1364/OL.14.000955. URL: https://opg.optica.org/ol/abstract.cfm?URI=ol-14-17-955.

[287] M. Sheik-Bahae et al. „Sensitive measurement of optical nonlinearities using a single beam“. In: *IEEE Journal of Quantum Electronics* 26.4 (1990), pp. 760–769. DOI: 10.1109/3.53394.

[288] Andrea Gnoli, Luca Razzari, and Marcofabio Righini. „Z-scan measurements using high repetition rate lasers: how to manage thermal effects“. In: *Opt. Express* 13.20 (Oct. 2005), pp. 7976–7981. DOI: 10.1364/OPEX.13.007976. URL: https://opg.optica.org/oe/abstract.cfm?URI=oe-13-20-7976.

[289] J. Wang et al. „Time-resolved Z-scan measurements of optical nonlinearities“. In: *J. Opt. Soc. Am. B* 11.6 (June 1994), pp. 1009–1017. DOI: 10.1364/JOSAB.11.001009. URL: https://opg.optica.org/josab/abstract.cfm?URI=josab-11-6-1009.

[290] Y. M. Cheung and S. K. Gayen. „Optical nonlinearities of tea studied by Z-scan and four-wave mixing techniques“. In: *J. Opt. Soc. Am. B* 11.4 (Apr. 1994), pp. 636–643. DOI: 10.1364/JOSAB.11.000636. URL: https://opg.optica.org/josab/abstract.cfm?URI=josab-11-4-636.

[291] Hang Zhang et al. „Efficient optical Kerr gate of tellurite glass for acquiring ultrafast fluorescence“. In: *Journal of Optics* 14.6 (May 2012), p. 065201. DOI: 10.1088/2040-8978/14/6/065201. URL: https://doi.org/10.1088/2040-8978/14/6/065201.

[292] Wenjiang Tan et al. „Femtosecond optical Kerr gate with double gate pulses: Simulation and experiment“. In: *Optics & Laser Technology* 145 (2022), p. 107531. ISSN: 0030-3992. DOI: https://doi.org/10.1016/j.optlastec.2021.107531. URL: https://www.sciencedirect.com/science/article/pii/S0030399221006198.

[293] V. V. Kim et al. „Variation of the sign of nonlinear refraction of carbon disulfide in the short-wavelength region“. In: *Opt. Mater. Express* 12.5 (May 2022), pp. 2053–2062. DOI: 10.1364/OME.451733. URL: https://opg.optica.org/ome/abstract.cfm?URI=ome-12-5-2053.

[294] Sumit Singhal, Sirshendu Dinda, and Debabrata Goswami. „Measurement of pure optical nonlinearity in carbon disulfide with a high-repetition-rate femtosecond laser“. In: *Appl. Opt.* 56.3 (Jan. 2017), pp. 644–648. DOI: 10.1364/AO.56.000644. URL: https://opg.optica.org/ao/abstract.cfm?URI=ao-56-3-644.

[295] Sandra Mamani et al. „Optical Kerr effect for underlying the orientational and translational fluctuations of molecular interactions in non-polar CS_2 vapor and liquid states“. In: *Optics Communications* 569 (2024), p. 130773. ISSN: 0030-4018. DOI: https://doi.org/10.1016/j.optcom.2024.130773. URL: https://www.sciencedirect.com/science/article/pii/S0030401824005108.

[296] Henry J. Meyer, Mikhail Sharonov, and Robert R. Alfano. „Ultra-high intensity temporally oscillatory optical Kerr effect in Carbon Disulfide arising from electronic and molecular distortions“. In: *Optics Communications* 524 (2022), p. 128806. ISSN: 0030-4018. DOI: https://doi.org/10.1016/j.optcom.2022.128806. URL: https://www.sciencedirect.com/science/article/pii/S0030401822005156.

[297] Constantinos Kalpouzos et al. „Femtosecond laser-induced optical kerr dynamics in CS_2/alkane binary solutions“. In: *Chemical Physics Letters* 150.1 (1988), pp. 138–146. ISSN: 0009-2614. DOI: https://doi.org/10.1016/0009-2614(88)80411-1. URL: https://www.sciencedirect.com/science/article/pii/0009261488804111.

[298] D. McMorrow, W.T. Lotshaw, and G.A. Kenney-Wallace. „Femtosecond optical Kerr studies on the origin of the nonlinear responses in simple liquids“. In: *IEEE Journal of Quantum Electronics* 24.2 (1988), pp. 443–454. DOI: 10.1109/3.144.

[299] Tzer-Hsiang Huang et al. „Coherent coupling and transient optical Kerr effect in liquids“. In: *Nonlinear Optics '98. Materials, Fundamentals and Applications Topical Meeting (Cat. No.98CH36244)*. 1998, pp. 84–86. DOI: 10.1109/NLO.1998.710189.

[300] Govind P. Agrawal. *Nonlinear Fiber Optics*. English. Third. San Diego: Academic Press, 2001. ISBN: 978-0-12-045144-9. DOI: 10.1016/B978-0-12-045144-9.X5000-0.

[301] Matthew A. Hall, Joseph B. Altepeter, and Prem Kumar. „Ultrafast Switching of Photonic Entanglement“. In: *Phys. Rev. Lett.* 106 (5 Feb. 2011), p. 053901. DOI: 10.1103/PhysRevLett.106.053901. URL: https://link.aps.org/doi/10.1103/PhysRevLett.106.053901.

[302] John M. Donohue, Jonathan Lavoie, and Kevin J. Resch. „Ultrafast Time-Division Demultiplexing of Polarization-Entangled Photons“. In: *Phys. Rev. Lett.* 113 (16 Oct. 2014), p. 163602. DOI: 10.1103/PhysRevLett.113.163602. URL: https://link.aps.org/doi/10.1103/PhysRevLett.113.163602.

[303] Akito Kawasaki et al. „Real-time observation of picosecond-timescale optical quantum entanglement towards ultrafast quantum information processing“. In: *Nature Photonics* 19 (3 Mar. 2025), pp. 271–276. ISSN: 1749-4893. DOI: 10.1038/s41566-024-01589-7.

[304] Kate L. Fenwick et al. „Carving out configurable ultrafast pulses from a continuous wave source via the optical Kerr effect“. In: *Opt. Express* 28.17 (Aug. 2020), pp. 24845–24853. DOI: 10.1364/OE.399878. URL: https://opg.optica.org/oe/abstract.cfm?URI=oe-28-17-24845.

[305] Gaurov Shikari. „Study of Non-linear Effects Using Single Mode Fiber“. Master's thesis. University of Siegen, 2022.

[306] Liang Dong. „Thermal lensing in optical fibers“. In: *Opt. Express* 24.17 (Aug. 2016), pp. 19841–19852. DOI: 10.1364/OE.24.019841. URL: https://opg.optica.org/oe/abstract.cfm?URI=oe-24-17-19841.

[307] Kate L. Fenwick. „Exploiting ultrafast optical pulses: probing excitonic properties of 2D materials and utilizing the Kerr effect for all-optical switching“. Master's thesis. Queen's University, 2019.

[308] Safa Kasap and Peter Capper, eds. *Springer Handbook of Electronic and Photonic Materials*. 2nd ed. Springer Handbooks. Springer Cham, 2017. ISBN: 978-3-319-48931-5. DOI: 10.1007/978-3-319-48933-9.

[309] J.S Sanghera and I.D Aggarwal. „Active and passive chalcogenide glass optical fibers for IR applications: a review“. In: *Journal of Non-Crystalline Solids* 256-257 (1999), pp. 6–16. ISSN: 0022-3093. DOI: https://doi.org/10.1016/S0022-3093(99)00484-6. URL: https://www.sciencedirect.com/science/article/pii/S0022309399004846.

[310] „A critical review of infrared transparent oxide glasses“. In: *Optical Materials: X* 20 (2023), p. 100258. ISSN: 2590-1478. DOI: https://doi.org/10.1016/j.omx.2023.100258. URL: https://www.sciencedirect.com/science/article/pii/S2590147823000323.

[311] F Smektala et al. „Chalcogenide glasses with large non-linear refractive indices“. In: *Journal of Non-Crystalline Solids* 239.1 (1998), pp. 139–142. ISSN: 0022-3093. DOI: https://doi.org/10.1016/S0022-3093(98)00730-3. URL: https://www.sciencedirect.com/science/article/pii/S0022309398007303.

[312] „Non-linear optical properties of chalcogenide glasses measured by Z-scan“. In: *Journal of Non-Crystalline Solids* 274.1 (2000). Physics of Non-Crystalline Solids 9, pp. 232–237. ISSN: 0022-3093. DOI: https://doi.org/10.1016/S0022-3093(00)00215-5. URL: https://www.sciencedirect.com/science/article/pii/S0022309300002155.

[313] „Optical non-linearity in oxide glasses“. In: *Journal of Non-Crystalline Solids* 203 (1996). Optical and Electrical Propertias of Glasses, pp. 96–101. ISSN: 0022-3093. DOI: https://doi.org/10.1016/0022-3093(96)00338-9. URL: https://www.sciencedirect.com/science/article/pii/0022309396003389.

[314] R. Rangel-Rojo et al. „Near-infrared optical nonlinearities in amorphous chalcogenides“. In: *Optics Communications* 109.1 (1994), pp. 145–150. ISSN: 0030-4018. DOI: https://doi.org/10.1016/0030-4018(94)90752-8. URL: https://www.sciencedirect.com/science/article/pii/0030401894907528.

[315] Isabella-Ioana Oprea, Hartmut Hesse, and Klaus Betzler. „Optical properties of bismuth borate glasses“. In: *Optical Materials* 26.3 (2004), pp. 235–237. ISSN: 0925-3467. DOI: https://doi.org/10.1016/j.optmat.2003.10.006. URL: https://www.sciencedirect.com/science/article/pii/S0925346704000266.

[316] Hiroyuki Nasu, Jun Matsuoka, and Kanichi Kamiya. „Second- and third-order optical non-linearity of homogeneous glasses“. In: *Journal of Non-Crystalline Solids* 178 (1994). Proceding of the First PAC RIM Metting on Glass and Optical Materials, pp. 23–30. ISSN: 0022-3093. DOI: https://doi.org/10.1016/0022-3093(94)90260-7. URL: https://www.sciencedirect.com/science/article/pii/0022309394902607.

[317] Hiroyuki Nasu et al. „Nonresonant-Type Third-order Nonlinearity of (PbO, Nb_2O_5)-TiO_2-TeO_2 Glass Measured by Third-Harmonic Generation“. In: *Japanese Journal of Applied Physics* 31.12R (Dec. 1992), p. 3899. DOI: 10.1143/JJAP.31.3899. URL: https://doi.org/10.1143/JJAP.31.3899.

[318] Pierre Van Rysselberghe. „Remarks concerning the Clausius-Mossotti Law“. In: *The Journal of Physical Chemistry* 36.4 (1932), pp. 1152–1155. DOI: 10.1021/j150334a007. eprint: https://doi.org/10.1021/j150334a007. URL: https://doi.org/10.1021/j150334a007.

[319] Kwan-Chi Kao. *Dielectric Phenomena in Solids: With Emphasis on Physical Concepts of Electronic Processes*. 1st ed. San Diego, CA: Academic Press, 2004. ISBN: 978-0-12-396561-5. DOI: 10.1016/B978-0-12-396561-5.X5010-5. URL: https://www.sciencedirect.com/book/9780123965615/dielectric-phenomena-in-solids.

[320] Tomoharu Hasegawa, Tatsuo Nagashima, and Naoki Sugimoto. „Z-scan study of third-order optical nonlinearities in bismuth-based glasses“. In: *Optics Communications* 250.4 (2005), pp. 411–415. ISSN: 0030-4018. DOI: https://doi.org/10.1016/j.optcom.2005.02.022. URL: https://www.sciencedirect.com/science/article/pii/S0030401805001239.

[321] Jianliang Zhang et al. „Nonlinear optical properties in bismuth-based glasses“. In: *Journal of Wuhan University of Technology-Mater. Sci. Ed.* 26.1 (Feb. 2011), pp. 61–64. ISSN: 1993-0437. DOI: 10.1007/s11595-011-0168-6. URL: https://doi.org/10.1007/s11595-011-0168-6.

[322] J. Tauc, R. Grigorovici, and A. Vancu. „Optical Properties and Electronic Structure of Amorphous Germanium“. In: *physica status solidi (b)* 15.2 (1966), pp. 627–637. DOI: https://doi.org/10.1002/pssb.19660150224. eprint: https://onlinelibrary.wiley.com/doi/pdf/10.1002/pssb.19660150224. URL: https://onlinelibrary.wiley.com/doi/abs/10.1002/pssb.19660150224.

[323] J. Tauc. „Optical properties and electronic structure of amorphous Ge and Si“. In: *Materials Research Bulletin* 3.1 (1968), pp. 37–46. ISSN: 0025-5408. DOI: https://doi.org/10.1016/0025-5408(68)90023-8. URL: https://www.sciencedirect.com/science/article/pii/0025540868900238.

[324] Yuan Gao et al. „Effect of Bi_2O_3 on the structure and thermal properties of Bi_2O_3-SiO_2-B_2O_3 glasses prepared by sol-gel method“. In: *Journal of Sol-Gel Science and Technology* 103.3 (Sept. 2022), pp. 713–721. ISSN: 1573-4846. DOI: 10.1007/s10971-022-05895-w. URL: https://doi.org/10.1007/s10971-022-05895-w.

[325] A. R. Zanatta. „Revisiting the optical bandgap of semiconductors and the proposal of a unified methodology to its determination“. In: *Scientific Reports* 9.1 (Aug. 2019), p. 11225. ISSN: 2045-2322. DOI: 10.1038/s41598-019-47670-y. URL: https://doi.org/10.1038/s41598-019-47670-y.

[326] Doris Möncke and Doris Ehrt. „Charge transfer transitions in glasses - Attempt of a systematic review“. In: *Optical Materials: X* 12 (2021), p. 100092. ISSN: 2590-1478. DOI: https://doi.org/10.1016/j.omx.2021.100092. URL: https://www.sciencedirect.com/science/article/pii/S259014782100022X.

[327] L. B. Fu et al. „Investigation of self-phase modulation based optical regeneration in single mode As_2Se_3 chalcogenide glass fiber“. In: *Opt. Express* 13.19 (Sept. 2005), pp. 7637–7644. DOI: 10.1364/OPEX.13.007637. URL: https://opg.optica.org/oe/abstract.cfm?URI=oe-13-19-7637.

[328] Robert Hellwarth, Joel Cherlow, and Tien-Tsai Yang. „Origin and frequency dependence of nonlinear optical susceptibilities of glasses“. In: *Phys. Rev. B* 11 (2 Jan. 1975), pp. 964–967. DOI: 10.1103/PhysRevB.11.964. URL: https://link.aps.org/doi/10.1103/PhysRevB.11.964.

[329] Inuk Kang et al. „Time-domain observation of nuclear contributions to the optical nonlinearities of glasses“. In: *Phys. Rev. B* 54 (18 Nov. 1996), R12641–R12644. DOI: 10.1103/PhysRevB.54.R12641. URL: https://link.aps.org/doi/10.1103/PhysRevB.54.R12641.

[330] Tianxing Lin et al. „Ultrafast nonlinear optical properties of Bi_2O_3–B_2O_3–SiO_2 oxide glass“. In: *Optics Communications* 275.1 (2007), pp. 230–233. ISSN: 0030-4018. DOI: https://doi.org/10.1016/j.optcom.2007.03.011. URL: https://www.sciencedirect.com/science/article/pii/S0030401807002702.

[331] Lihe Yan et al. „Pump power dependence of Kerr signals in femtosecond cross pump-probe optical Kerr measurements“. In: *Opt. Express* 17.24 (Nov. 2009), pp. 21509–21514. DOI: 10.1364/OE.17.021509. URL: https://opg.optica.org/oe/abstract.cfm?URI=oe-17-24-21509.

[332] H. P. Boehm, R. Setton, and E. Stumpp. In: *Pure and Applied Chemistry* 66.9 (1994), pp. 1893–1901. DOI: doi:10.1351/pac199466091893. URL: https://doi.org/10.1351/pac199466091893.

[333] K. S. Novoselov et al. „Electric Field Effect in Atomically Thin Carbon Films“. In: *Science* 306.5696 (2004), pp. 666–669. DOI: 10.1126/science.1102896. eprint: https://www.science.org/doi/pdf/10.1126/science.1102896. URL: https://www.science.org/doi/abs/10.1126/science.1102896.

[334] Rudolf E. Peierls. „Bemerkungen über Umwandlungstemperaturen“. In: *Helvetica Physica Acta* 7 (1934), pp. 81–83.

[335] Rudolf E. Peierls. „Quelques proprietes typiques des corps solides“. In: *Annales de l'Institut Henri Poincaré* 5 (1935), pp. 177–222.

[336] Lev D. Landau. „Zur Theorie der Phasenumwandlungen II“. In: *Physikalische Zeitschrift der Sowjetunion* 11 (1937), pp. 26–35.

[337] Lev D. Landau and Evgeny M. Lifshitz. *Statistical Physics, Part I*. 3rd ed. Sections 137 and 138. Oxford: Pergamon, 1980.

[338] Mikhail I. Katsnelson. „Graphene: carbon in two dimensions“. In: *Materials Today* 10.1 (2007), pp. 20–27. ISSN: 1369-7021. DOI: https://doi.org/10.1016/S1369-7021(06)71788-6. URL: https://www.sciencedirect.com/science/article/pii/S1369702106717886.

[339] K. S. Novoselov et al. „Two-dimensional atomic crystals“. In: *Proceedings of the National Academy of Sciences* 102.30 (2005), pp. 10451–10453. DOI: 10.1073/pnas.0502848102. eprint: https://www.pnas.org/doi/pdf/10.1073/pnas.0502848102. URL: https://www.pnas.org/doi/abs/10.1073/pnas.0502848102.

[340] Andre K. Geim and Konstantin S. Novoselov. „The rise of graphene“. In: *Nature Materials* 6.3 (2007), pp. 183–191. DOI: 10.1038/nmat1849. URL: https://doi.org/10.1038/nmat1849.

[341] Changgu Lee et al. „Measurement of the Elastic Properties and Intrinsic Strength of Monolayer Graphene“. In: *Science* 321.5887 (2008), pp. 385–388. DOI: 10.1126/science.1157996. eprint: https://www.science.org/doi/pdf/10.1126/science.1157996. URL: https://www.science.org/doi/abs/10.1126/science.1157996.

[342] A. H. Castro Neto et al. „The electronic properties of graphene“. In: *Rev. Mod. Phys.* 81 (1 Jan. 2009), pp. 109–162. DOI: 10.1103/RevModPhys.81.109. URL: https://link.aps.org/doi/10.1103/RevModPhys.81.109.

[343] Ravi Prasher. „Graphene Spreads the Heat“. In: *Science* 328.5975 (2010), pp. 185–186. DOI: 10.1126/science.1188998. eprint: https://www.science.org/doi/pdf/10.1126/science.1188998. URL: https://www.science.org/doi/abs/10.1126/science.1188998.

[344] M.I. Katsnelson and K.S. Novoselov. „Graphene: New bridge between condensed matter physics and quantum electrodynamics“. In: *Solid State Communications* 143.1 (2007). Exploring graphene, pp. 3–13. ISSN: 0038-1098. DOI: https://doi.org/10.1016/j.ssc.2007.02.043. URL: https://www.sciencedirect.com/science/article/pii/S0038109807003043.

[345] Alexander A. Balandin et al. „Superior Thermal Conductivity of Single-Layer Graphene“. In: *Nano Letters* 8.3 (2008). PMID: 18284217, pp. 902–907. DOI: 10.1021/nl0731872. eprint: https://doi.org/10.1021/nl0731872. URL: https://doi.org/10.1021/nl0731872.

[346] Daniel R. Cooper et al. „Experimental Review of Graphene“. In: *International Scholarly Research Notices* 2012.1 (2012), p. 501686. DOI: https://doi.org/10.5402/2012/501686. eprint: https://onlinelibrary.wiley.com/doi/pdf/10.5402/2012/501686. URL: https://onlinelibrary.wiley.com/doi/abs/10.5402/2012/501686.

[347] Ado Jorio et al. *Raman Spectroscopy in Graphene Related Systems*. Wiley-VCH, 2011. ISBN: 978-3-527-40811-5. DOI: 10.1002/9783527632695. URL: https://onlinelibrary.wiley.com/doi/book/10.1002/9783527632695.

[348] P. R. Wallace. „The Band Theory of Graphite“. In: *Phys. Rev.* 71 (9 May 1947), pp. 622–634. DOI: 10.1103/PhysRev.71.622. URL: https://link.aps.org/doi/10.1103/PhysRev.71.622.

[349] B. Partoens and F. M. Peeters. „From graphene to graphite: Electronic structure around the K point“. In: *Phys. Rev. B* 74 (7 Aug. 2006), p. 075404. DOI: 10.1103/PhysRevB.74.075404. URL: https://link.aps.org/doi/10.1103/PhysRevB.74.075404.

[350] Yuan Cao et al. „Unconventional superconductivity in magic-angle graphene superlattices“. In: *Nature* 556 (7699 Apr. 1, 2018), pp. 43–50. ISSN: 1476-4687. DOI: 10.1038/nature26160. URL: https://doi.org/10.1038/nature26160.

[351] Eva Y. Andrei and Allan H. MacDonald. „Graphene bilayers with a twist“. In: *Nature Materials* 19 (12 Dec. 1, 2020), pp. 1265–1275. ISSN: 1476-4660. DOI: 10.1038/s41563-020-00840-0. URL: https://doi.org/10.1038/s41563-020-00840-0.

[352] Jamie H. Warner et al. *Graphene: Fundamentals and Emergent Applications*. 1st ed. Elsevier, 2012. ISBN: 978-0123945938.

[353] Yuwei Shan et al. „Stacking symmetry governed second harmonic generation in graphene trilayers“. In: *Science Advances* 4.6 (2018), eaat0074. DOI: 10.1126/sciadv.aat0074. eprint: https://www.science.org/doi/pdf/10.1126/sciadv.aat0074. URL: https://www.science.org/doi/abs/10.1126/sciadv.aat0074.

[354] L.M. Malard et al. „Raman spectroscopy in graphene“. In: *Physics Reports* 473.5 (2009), pp. 51–87. ISSN: 0370-1573. DOI: https://doi.org/10.1016/j.physrep.2009.02.003. URL: https://www.sciencedirect.com/science/article/pii/S0370157309000520.

[355] Chun Hung Lui et al. „Imaging Stacking Order in Few-Layer Graphene“. In: *Nano Letters* 11.1 (2011). PMID: 21121668, pp. 164–169. DOI: 10.1021/nl1032827. eprint: https://doi.org/10.1021/nl1032827. URL: https://doi.org/10.1021/nl1032827.

[356] Hongyuan Li et al. „Global Control of Stacking-Order Phase Transition by Doping and Electric Field in Few-Layer Graphene“. In: *Nano Letters* 20.5 (2020). PMID: 32286843, pp. 3106–3112. DOI: 10.1021/acs.nanolett.9b05092. eprint: https://doi.org/10.1021/acs.nanolett.9b05092. URL: https://doi.org/10.1021/acs.nanolett.9b05092.

[357] Yaping Yang et al. „Stacking Order in Graphite Films Controlled by van der Waals Technology“. In: *Nano Letters* 19.12 (2019). PMID: 31664847, pp. 8526–8532. DOI: 10.1021/acs.nanolett.9b03014. eprint: https://doi.org/10.1021/acs.nanolett.9b03014. URL: https://doi.org/10.1021/acs.nanolett.9b03014.

[358] Van Luan Nguyen et al. „Layer-controlled Single-crystalline Graphene Film with Stacking Order via Cu–Si Alloy Formation“. In: *Nature Nanotechnology* 15.10 (Oct. 2020), pp. 861–867. DOI: 10.1038/s41565-020-0743-0.

[359] Carter Fox et al. „Stacking Order Engineering of Two-Dimensional Materials and Device Applications“. In: *Chemical Reviews* 124.4 (2024). PMID: 38150266, pp. 1862–1898. DOI: 10.1021/acs.chemrev.3c00618. eprint: https://doi.org/10.1021/acs.chemrev.3c00618. URL: https://doi.org/10.1021/acs.chemrev.3c00618.

[360] Andrea C. Ferrari and Denis M. Basko. „Raman Spectroscopy as a Versatile Tool for Studying the Properties of Graphene“. In: *Nature Nanotechnology* 8.4 (Apr. 2013), pp. 235–246. DOI: 10.1038/nnano.2013.46.

[361] A. C. Ferrari et al. „Raman Spectrum of Graphene and Graphene Layers“. In: *Phys. Rev. Lett.* 97 (18 Oct. 2006), p. 187401. DOI: 10.1103/PhysRevLett.97.187401. URL: https://link.aps.org/doi/10.1103/PhysRevLett.97.187401.

[362] Jun Yan et al. „Electric Field Effect Tuning of Electron-Phonon Coupling in Graphene“. In: *Phys. Rev. Lett.* 98 (16 Apr. 2007), p. 166802. DOI: 10.1103/PhysRevLett.98.166802. URL: https://link.aps.org/doi/10.1103/PhysRevLett.98.166802.

[363] C. Casiraghi et al. „Raman fingerprint of charged impurities in graphene“. In: *Applied Physics Letters* 91.23 (Dec. 2007), p. 233108. ISSN: 0003-6951. DOI: 10.1063/1.2818692. eprint: https://pubs.aip.org/aip/apl/artic

le-pdf/doi/10.1063/1.2818692/14386026/233108_1_online.pdf. URL: https://doi.org/10.1063/1.2818692.

[364] I. Calizo et al. „Temperature Dependence of the Raman Spectra of Graphene and Graphene Multilayers“. In: *Nano Letters* 7.9 (2007). PMID: 17718584, pp. 2645–2649. DOI: 10.1021/nl071033g. eprint: https://doi.org/10.1021/nl071033g. URL: https://doi.org/10.1021/nl071033g.

[365] Hoda Malekpour and Alexander A. Balandin. „Raman-based technique for measuring thermal conductivity of graphene and related materials“. In: *Journal of Raman Spectroscopy* 49.1 (2018), pp. 106–120. DOI: https://doi.org/10.1002/jrs.5230. eprint: https://analyticalsciencejournals.onlinelibrary.wiley.com/doi/pdf/10.1002/jrs.5230. URL: https://analyticalsciencejournals.onlinelibrary.wiley.com/doi/abs/10.1002/jrs.5230.

[366] A. C. Ferrari, S. E. Rodil, and J. Robertson. „Interpretation of infrared and Raman spectra of amorphous carbon nitrides“. In: *Phys. Rev. B* 67 (15 Apr. 2003), p. 155306. DOI: 10.1103/PhysRevB.67.155306. URL: https://link.aps.org/doi/10.1103/PhysRevB.67.155306.

[367] Andrea C. Ferrari. „Raman spectroscopy of graphene and graphite: Disorder, electron–phonon coupling, doping and nonadiabatic effects“. In: *Solid State Communications* 143.1 (2007). Exploring graphene, pp. 47–57. ISSN: 0038-1098. DOI: https://doi.org/10.1016/j.ssc.2007.03.052. URL: https://www.sciencedirect.com/science/article/pii/S0038109807002967.

[368] Chunxiao Cong et al. „Raman Characterization of ABA- and ABC-Stacked Trilayer Graphene“. In: *ACS Nano* 5.11 (2011). PMID: 21962035, pp. 8760–8768. DOI: 10.1021/nn203472f. eprint: https://doi.org/10.1021/nn203472f. URL: https://doi.org/10.1021/nn203472f.

[369] Konstantin G. Wirth et al. „Experimental Observation of ABCB Stacked Tetralayer Graphene“. In: *ACS Nano* 16.10 (2022). PMID: 36205460, pp. 16617–16623. DOI: 10.1021/acsnano.2c06053. eprint: https://doi.org/10.1021/acsnano.2c06053. URL: https://doi.org/10.1021/acsnano.2c06053.

[370] Ryan Beams, Luiz Gustavo Cançado, and Lukas Novotny. „Raman characterization of defects and dopants in graphene“. In: *Journal of Physics: Condensed Matter* 27.8 (Jan. 2015), p. 083002. DOI: 10.1088/0953-8984/27/8/083002. URL: https://doi.org/10.1088/0953-8984/27/8/083002.

[371] E. Kogan and V. U. Nazarov. „Symmetry classification of energy bands in graphene“. In: *Phys. Rev. B* 85 (11 Mar. 2012), p. 115418. DOI: 10.1103/PhysRevB.85.115418. URL: https://link.aps.org/doi/10.1103/PhysRevB.85.115418.

[372] L. M. Malard et al. „Group-theory analysis of electrons and phonons in N-layer graphene systems“. In: *Phys. Rev. B* 79 (12 Mar. 2009), p. 125426. DOI: 10.1103/PhysRevB.79.125426. URL: https://link.aps.org/doi/10.1103/PhysRevB.79.125426.

[373] Andrea Ferrari et al. „Raman spectroscopy of graphite“. In: *Philosophical Transactions of the Royal Society of London. Series A: Mathematical, Physical and Engineering Sciences* 362.1824 (2004), pp. 2271–2288. DOI: 10.1098/rsta.2004.1454. eprint: https://royalsocietypublishing.org/doi/pdf/10.1098/rsta.2004.1454. URL: https://royalsocietypublishing.org/doi/abs/10.1098/rsta.2004.1454.

[374] R.J. Nemanich, G. Lucovsky, and S.A. Solin. „Infrared active optical vibrations of graphite“. In: *Solid State Communications* 23.2 (1977), pp. 117–120. ISSN: 0038-1098. DOI: https://doi.org/10.1016/0038-1098(77)90663-9. URL: https://www.sciencedirect.com/science/article/pii/0038109877906639.

[375] Dominik Metten. „Probing the opto-electronic and mechanical properties of suspended graphene membranes by Raman spectroscopy“. PhD thesis. Université de Strasbourg, 2016. URL: https://theses.fr/2016STRAE002.

[376] A. C. Ferrari and J. Robertson. „Interpretation of Raman spectra of disordered and amorphous carbon“. In: *Phys. Rev. B* 61 (20 May 2000), pp. 14095–14107. DOI: 10.1103/PhysRevB.61.14095. URL: https://link.aps.org/doi/10.1103/PhysRevB.61.14095.

[377] P. H. C. Eilers and H. F. M. Boelens. *Baseline Correction with Asymmetric Least Squares Smoothing*. Report 1. Leiden University Medical Centre, 2005, p. 5.

[378] Yenny Hernandez et al. „High-yield production of graphene by liquid-phase exfoliation of graphite“. In: *Nature Nanotechnology* 3.9 (Sept. 2008), pp. 563–568. ISSN: 1748-3395. DOI: 10.1038/nnano.2008.215. URL: https://doi.org/10.1038/nnano.2008.215.

[379] Artur Ciesielski and Paolo Samorì. „Graphene via sonication assisted liquid-phase exfoliation“. In: *Chem. Soc. Rev.* 43 (1 2014), pp. 381–398. DOI: 10.1039/C3CS60217F. URL: http://dx.doi.org/10.1039/C3CS60217F.

[380] Yi Lin et al. „Aqueous Dispersions of Few-Layered and Monolayered Hexagonal Boron Nitride Nanosheets from Sonication-Assisted Hydrolysis: Critical Role of Water“. In: *The Journal of Physical Chemistry C* 115.6 (2011), pp. 2679–2685. DOI: 10.1021/jp110985w. eprint: https://doi.org/10.1021/jp110985w. URL: https://doi.org/10.1021/jp110985w.

[381] Goki Eda and Manish Chhowalla. „Chemically Derived Graphene Oxide: Towards Large-Area Thin-Film Electronics and Optoelectronics“. In: *Advanced Materials* 22.22 (2010), pp. 2392–2415. DOI: https://doi.org/10.1002/adma.200903689. eprint: https://advanced.onlinelibrary.wiley.com/doi/pdf/10.1002/adma.200903689. URL: https://advanced.onlinelibrary.wiley.com/doi/abs/10.1002/adma.200903689.

[382] Johann Coraux et al. „Structural Coherency of Graphene on Ir(111)“. In: *Nano Letters* 8.2 (2008). PMID: 18189442, pp. 565–570. DOI: 10.1021/nl0728874. eprint: https://doi.org/10.1021/nl0728874. URL: https://doi.org/10.1021/nl0728874.

[383] Dongliang Zhang et al. „Defects Produced during Wet Transfer Affect the Electrical Properties of Graphene“. In: *Micromachines* 13.2 (2022). ISSN: 2072-666X. URL: https://www.mdpi.com/2072-666X/13/2/227.

[384] Th. Seyller et al. „Epitaxial graphene: a new material“. In: *physica status solidi (b)* 245.7 (2008), pp. 1436–1446. DOI: https://doi.org/10.1002/pssb.200844143. eprint: https://onlinelibrary.wiley.com/doi/pdf/10.1002/pssb.200844143. URL: https://onlinelibrary.wiley.com/doi/abs/10.1002/pssb.200844143.

[385] Victor Yu. Aristov et al. „Graphene Synthesis on Cubic SiC/Si Wafers. Perspectives for Mass Production of Graphene-Based Electronic Devices“. In: *Nano Letters* 10.3 (2010). PMID: 20141155, pp. 992–995. DOI: 10.1021/nl904115h. eprint: https://doi.org/10.1021/nl904115h. URL: https://doi.org/10.1021/nl904115h.

[386] Y. Xia et al. „One-Dimensional Nanostructures: Synthesis, Characterization, and Applications“. In: *Advanced Materials* 15.5 (2003), pp. 353–389. DOI: https://doi.org/10.1002/adma.200390087. eprint: https://advanced.onlinelibrary.wiley.com/doi/pdf/10.1002/adma.200390087. URL: https://advanced.onlinelibrary.wiley.com/doi/abs/10.1002/adma.200390087.

[387] Lei Tang et al. „Chemical Vapor Deposition Growth of Two-Dimensional Compound Materials: Controllability, Material Quality, and Growth Mechanism“. In: *Accounts of Materials Research* 2.1 (2021), pp. 36–47. DOI: 10.1021/acco

untsmr.0c00063. eprint: https://doi.org/10.1021/accountsmr.0c00063. URL: https://doi.org/10.1021/accountsmr.0c00063.

[388] Zhengyang Cai et al. „Chemical Vapor Deposition Growth and Applications of Two-Dimensional Materials and Their Heterostructures“. In: *Chemical Reviews* 118.13 (2018). PMID: 29384374, pp. 6091–6133. DOI: 10.1021/acs.chemrev.7b00536. eprint: https://doi.org/10.1021/acs.chemrev.7b00536. URL: https://doi.org/10.1021/acs.chemrev.7b00536.

[389] Jungtae Nam et al. „Chemical vapor deposition of graphene and its characterizations and applications“. In: *Current Applied Physics* 61 (2024), pp. 55–70. ISSN: 1567-1739. DOI: https://doi.org/10.1016/j.cap.2024.02.010. URL: https://www.sciencedirect.com/science/article/pii/S1567173924000403.

[390] Keun Soo Kim et al. „Large-scale pattern growth of graphene films for stretchable transparent electrodes“. In: *Nature* 457.7230 (Feb. 2009), pp. 706–710. ISSN: 1476-4687. DOI: 10.1038/nature07719. URL: https://doi.org/10.1038/nature07719.

[391] Xuesong Li et al. „Large-Area Synthesis of High-Quality and Uniform Graphene Films on Copper Foils“. In: *Science* 324.5932 (2009), pp. 1312–1314. DOI: 10.1126/science.1171245. eprint: https://www.science.org/doi/pdf/10.1126/science.1171245. URL: https://www.science.org/doi/abs/10.1126/science.1171245.

[392] Yi Zhang, Luyao Zhang, and Chongwu Zhou. „Review of Chemical Vapor Deposition of Graphene and Related Applications“. In: *Accounts of Chemical Research* 46.10 (2013). PMID: 23480816, pp. 2329–2339. DOI: 10.1021/ar300203n. eprint: https://doi.org/10.1021/ar300203n. URL: https://doi.org/10.1021/ar300203n.

[393] Qingkai Yu et al. „Graphene segregated on Ni surfaces and transferred to insulators“. In: *Applied Physics Letters* 93.11 (Sept. 2008), p. 113103. ISSN: 0003-6951. DOI: 10.1063/1.2982585. eprint: https://pubs.aip.org/aip/apl/article-pdf/doi/10.1063/1.2982585/14402630/113103_1_online.pdf. URL: https://doi.org/10.1063/1.2982585.

[394] Zheng Yan et al. „Growth of Bilayer Graphene on Insulating Substrates“. In: *ACS Nano* 5.10 (2011). PMID: 21888396, pp. 8187–8192. DOI: 10.1021/nn202829y. eprint: https://doi.org/10.1021/nn202829y. URL: https://doi.org/10.1021/nn202829y.

[395] Jianyi Chen et al. „Oxygen-Aided Synthesis of Polycrystalline Graphene on Silicon Dioxide Substrates“. In: *Journal of the American Chemical Society* 133.44 (2011). PMID: 21988639, pp. 17548–17551. DOI: 10.1021/ja2063633. eprint: https://doi.org/10.1021/ja2063633. URL: https://doi.org/10.1021/ja2063633.

[396] Jingyu Sun et al. „Direct Growth of High-Quality Graphene on High-κ Dielectric $SrTiO_3$ Substrates“. In: *Journal of the American Chemical Society* 136.18 (2014). PMID: 24746139, pp. 6574–6577. DOI: 10.1021/ja5022602. eprint: https://doi.org/10.1021/ja5022602. URL: https://doi.org/10.1021/ja5022602.

[397] Huaping Wang et al. „Primary Nucleation-Dominated Chemical Vapor Deposition Growth for Uniform Graphene Monolayers on Dielectric Substrate“. In: *Journal of the American Chemical Society* 141.28 (2019). PMID: 31265267, pp. 11004–11008. DOI: 10.1021/jacs.9b05705. eprint: https://doi.org/10.1021/jacs.9b05705. URL: https://doi.org/10.1021/jacs.9b05705.

[398] Gilpin Robinson Jr. et al. *Graphite*. Professional Paper 1802J. Reston, VA: U.S. Geological Survey, 2017, p. 36. DOI: 10.3133/pp1802J. URL: https://pubs.usgs.gov/publication/pp1802J.

[399] L. C. F. Blackman and Alfred Rene Jean Paul Ubbelohde. „Stress recrystallization of graphite“. In: *Proceedings of the Royal Society of London. Series A. Mathematical and Physical Sciences* 266.1324 (1962), pp. 20–32. DOI: 10.1098/rspa.1962.0044. eprint: https://royalsocietypublishing.org/doi/pdf/10.1098/rspa.1962.0044. URL: https://royalsocietypublishing.org/doi/abs/10.1098/rspa.1962.0044.

[400] Ankitha Rao et al. „From steel waste to energy storage: kish graphite derived graphene electrodes for high performance supercapacitors“. In: *Mater. Adv.* 6 (16 2025), pp. 5486–5505. DOI: 10.1039/D5MA00399G. URL: http://dx.doi.org/10.1039/D5MA00399G.

[401] Min Yi and Zhigang Shen. „A review on mechanical exfoliation for the scalable production of graphene“. In: *J. Mater. Chem. A* 3 (22 2015), pp. 11700–11715. DOI: 10.1039/C5TA00252D. URL: http://dx.doi.org/10.1039/C5TA00252D.

[402] Yuan Huang et al. „Reliable Exfoliation of Large-Area High-Quality Flakes of Graphene and Other Two-Dimensional Materials“. In: *ACS Nano* 9.11 (2015). PMID: 26336975, pp. 10612–10620. DOI: 10.1021/acsnano.5b04258. eprint: https://doi.org/10.1021/acsnano.5b04258. URL: https://doi.org/10.1021/acsnano.5b04258.

[403] R. R. Nair et al. „Fine Structure Constant Defines Visual Transparency of Graphene“. In: *Science* 320.5881 (2008), pp. 1308–1308. DOI: 10.1126/science.1156965. eprint: https://www.science.org/doi/pdf/10.1126/science.1156965. URL: https://www.science.org/doi/abs/10.1126/science.1156965.

[404] A. B. Kuzmenko et al. „Universal Optical Conductance of Graphite“. In: *Phys. Rev. Lett.* 100 (11 Mar. 2008), p. 117401. DOI: 10.1103/PhysRevLett.100.117401. URL: https://link.aps.org/doi/10.1103/PhysRevLett.100.117401.

[405] P. Blake et al. „Making graphene visible“. In: *Applied Physics Letters* 91.6 (Aug. 2007), p. 063124. ISSN: 0003-6951. DOI: 10.1063/1.2768624. eprint: https://pubs.aip.org/aip/apl/article-pdf/doi/10.1063/1.2768624/13197090/063124_1_online.pdf. URL: https://doi.org/10.1063/1.2768624.

[406] P. E. Gaskell et al. „Counting graphene layers on glass via optical reflection microscopy“. In: *Applied Physics Letters* 94.14 (Apr. 2009), p. 143101. ISSN: 0003-6951. DOI: 10.1063/1.3115026. eprint: https://pubs.aip.org/aip/apl/article-pdf/doi/10.1063/1.3115026/14410823/143101_1_online.pdf. URL: https://doi.org/10.1063/1.3115026.

[407] A. C. Ferrari et al. „Raman Spectrum of Graphene and Graphene Layers“. In: *Phys. Rev. Lett.* 97 (18 Oct. 2006), p. 187401. DOI: 10.1103/PhysRevLett.97.187401. URL: https://link.aps.org/doi/10.1103/PhysRevLett.97.187401.

[408] L. M. Malard et al. „Probing the electronic structure of bilayer graphene by Raman scattering“. In: *Phys. Rev. B* 76 (20 Nov. 2007), p. 201401. DOI: 10.1103/PhysRevB.76.201401. URL: https://link.aps.org/doi/10.1103/PhysRevB.76.201401.

[409] „Production and processing of graphene and 2d crystals“. In: *Materials Today* 15.12 (2012), pp. 564–589. ISSN: 1369-7021. DOI: https://doi.org/10.1016/S1369-7021(13)70014-2. URL: https://www.sciencedirect.com/science/article/pii/S1369702113700142.

[410] Cristina Vallés et al. „Solutions of Negatively Charged Graphene Sheets and Ribbons“. In: *Journal of the American Chemical Society* 130.47 (2008). PMID: 18975900, pp. 15802–15804. DOI: 10.1021/ja808001a. eprint: https://doi.org/10.1021/ja808001a. URL: https://doi.org/10.1021/ja808001a.

[411] Cameron J Shearer et al. „Accurate thickness measurement of graphene“. In: *Nanotechnology* 27.12 (Feb. 2016), p. 125704. DOI: 10.1088/0957-4484/27/12/125704. URL: https://doi.org/10.1088/0957-4484/27/12/125704.

[412] O. Ochedowski, B. Kleine Bussmann, and M. Schleberger. „Graphene on Mica - Intercalated Water Trapped for Life“. In: *Scientific Reports* 4.1 (Aug. 2014), p. 6003. ISSN: 2045-2322. DOI: 10.1038/srep06003. URL: https://doi.org/10.1038/srep06003.

[413] Peigen Cao et al. „Atomic Force Microscopy Characterization of Room-Temperature Adlayers of Small Organic Molecules through Graphene Templating“. In: *Journal of the American Chemical Society* 133.8 (2011). PMID: 21294575, pp. 2334–2337. DOI: 10.1021/ja108554p. eprint: https://doi.org/10.1021/ja108554p. URL: https://doi.org/10.1021/ja108554p.

[414] Víctor Manuel Freire Soler. „Fabrication and Characterization of Macroscopic Graphene Layers on Metallic Substrates“. PhD Thesis. Barcelona, Spain: Universitat de Barcelona, 2014. URL: https://diposit.ub.edu/dspace/bitstream/2445/60843/1/VMFS_PhD_THESIS.pdf.

[415] Matthias C. Schabel and José Luís Martins. „Energetics of interplanar binding in graphite“. In: *Phys. Rev. B* 46 (11 Sept. 1992), pp. 7185–7188. DOI: 10.1103/PhysRevB.46.7185. URL: https://link.aps.org/doi/10.1103/PhysRevB.46.7185.

[416] Eric Pop, Vikas Varshney, and Ajit K. Roy. „Thermal properties of graphene: Fundamentals and applications“. In: *MRS Bulletin* 37.12 (Dec. 2012), pp. 1273–1281. ISSN: 1938-1425. DOI: 10.1557/mrs.2012.203. URL: https://doi.org/10.1557/mrs.2012.203.

[417] D. Lacroix et al. „Phonon transport in silicon, influence of the dispersion properties choice on the description of the anharmonic resistive mechanisms“. In: *The European Physical Journal B* 67.1 (Jan. 2009), pp. 15–25. ISSN: 1434-6036. DOI: 10.1140/epjb/e2008-00464-6. URL: https://doi.org/10.1140/epjb/e2008-00464-6.

[418] V. S. Bagaev et al. „Propagation of high-frequency acoustic phonons in germanium and their interaction with electron-hole drops“. In: *Soviet Physics JETP* 50.5 (1979), pp. 1013–1017.

[419] Zhun-Yong Ong and Eric Pop. „Frequency and polarization dependence of thermal coupling between carbon nanotubes and SiO2“. In: *Journal of Applied Physics* 108.10 (Nov. 2010), p. 103502. ISSN: 0021-8979. DOI: 10.1063/1.3484494. URL: https://doi.org/10.1063/1.3484494.

[420] Zhun-Yong Ong, Eric Pop, and Junichiro Shiomi. „Reduction of phonon lifetimes and thermal conductivity of a carbon nanotube on amorphous silica“. In: *Phys. Rev. B* 84 (16 Oct. 2011), p. 165418. DOI: 10.1103/PhysRevB.84.165418. URL: https://link.aps.org/doi/10.1103/PhysRevB.84.165418.

[421] Lorin X. Benedict, Steven G. Louie, and Marvin L. Cohen. „Heat capacity of carbon nanotubes“. In: *Solid State Communications* 100.3 (1996), pp. 177–180. ISSN: 0038-1098. DOI: https://doi.org/10.1016/0038-1098(96)00386-9. URL: https://www.sciencedirect.com/science/article/pii/0038109896003869.

[422] Zhun-Yong Ong and Eric Pop. „Effect of substrate modes on thermal transport in supported graphene“. In: *Phys. Rev. B* 84 (7 Aug. 2011), p. 075471. DOI: 10.1103/PhysRevB.84.075471. URL: https://link.aps.org/doi/10.1103/PhysRevB.84.075471.

[423] A. M. Shikin et al. „Graphene: Synthesis and features of electronic structure“. In: *Nanotechnologies in Russia* 6.9 (Oct. 2011), p. 625. ISSN: 1995-0799. DOI: 10.1134/S1995078011050132. URL: https://doi.org/10.1134/S1995078011050132.

[424] D. Farías et al. „Modification of the surface phonon dispersion of a graphite monolayer adsorbed on Ni(111) caused by intercalation of Yb, Cu and Ag“. In: *Surface Science* 454-456 (2000), pp. 437–441. ISSN: 0039-6028. DOI: https://doi.org/10.1016/S0039-6028(00)00253-3. URL: https://www.sciencedirect.com/science/article/pii/S0039602800002533.

[425] James Hone. „Phonons and Thermal Properties of Carbon Nanotubes“. In: *Carbon Nanotubes: Synthesis, Structure, Properties, and Applications*. Ed. by Mildred S. Dresselhaus, Gene Dresselhaus, and Phaedon Avouris. Berlin, Heidelberg: Springer Berlin Heidelberg, 2001, pp. 273–286. ISBN: 978-3-540-39947-6. DOI: 10.1007/3-540-39947-X_11. URL: https://doi.org/10.1007/3-540-39947-X_11.

[426] D. L. Nika et al. „Phonon thermal conduction in graphene: Role of Umklapp and edge roughness scattering“. In: *Phys. Rev. B* 79 (15 Apr. 2009), p. 155413. DOI: 10.1103/PhysRevB.79.155413. URL: https://link.aps.org/doi/10.1103/PhysRevB.79.155413.

[427] Xiangfan Xu et al. „Length-dependent thermal conductivity in suspended single-layer graphene“. In: *Nature Communications* 5.1 (Apr. 2014), p. 3689. ISSN: 2041-1723. DOI: 10.1038/ncomms4689. URL: https://doi.org/10.1038/ncomms4689.

[428] Suchismita Ghosh et al. „Dimensional crossover of thermal transport in few-layer graphene“. In: *Nature Materials* 9.7 (July 2010), pp. 555–558. ISSN: 1476-4660. DOI: 10.1038/nmat2753. URL: https://doi.org/10.1038/nmat2753.

[429] Jie Chen, Gang Zhang, and Baowen Li. „Substrate coupling suppresses size dependence of thermal conductivity in supported graphene“. In: *Nanoscale* 5 (2 2013), pp. 532–536. DOI: 10.1039/C2NR32949B. URL: http://dx.doi.org/10.1039/C2NR32949B.

[430] Jae Hun Seol et al. „Two-Dimensional Phonon Transport in Supported Graphene“. In: *Science* 328.5975 (2010), pp. 213–216. DOI: 10.1126/science.1184014. eprint: https://www.science.org/doi/pdf/10.1126/science.1184014. URL: https://www.science.org/doi/abs/10.1126/science.1184014.

[431] S Katsiaounis et al. „Graphene nano-sieves by femtosecond laser irradiation“. In: *Nanotechnology* 34.10 (Dec. 2022), p. 105302. DOI: 10.1088/1361-6528/aca7cb. URL: https://doi.org/10.1088/1361-6528/aca7cb.

[432] Claire Berger et al. „Electronic Confinement and Coherence in Patterned Epitaxial Graphene“. In: *Science* 312.5777 (2006), pp. 1191–1196. DOI: 10.1126/science.1125925. eprint: https://www.science.org/doi/pdf/10.1126/science.1125925. URL: https://www.science.org/doi/abs/10.1126/science.1125925.

[433] Xiaobin Fan, Guoliang Zhang, and Fengbao Zhang. „Multiple roles of graphene in heterogeneous catalysis“. In: *Chem. Soc. Rev.* 44 (10 2015), pp. 3023–3035. DOI: 10.1039/C5CS00094G. URL: http://dx.doi.org/10.1039/C5CS00094G.

[434] Wenjing Yuan and Gaoquan Shi. „Graphene-based gas sensors“. In: *J. Mater. Chem. A* 1 (35 2013), pp. 10078–10091. DOI: 10.1039/C3TA11774J. URL: http://dx.doi.org/10.1039/C3TA11774J.

[435] Harald O. Jeschke, Martin E. Garcia, and K. H. Bennemann. „Theory for the Ultrafast Ablation of Graphite Films“. In: *Phys. Rev. Lett.* 87 (1 June 2001), p. 015003. DOI: 10.1103/PhysRevLett.87.015003. URL: https://link.aps.org/doi/10.1103/PhysRevLett.87.015003.

[436] Fabrizio Carbone et al. „Structural Preablation Dynamics of Graphite Observed by Ultrafast Electron Crystallography“. In: *Phys. Rev. Lett.* 100 (3 Jan. 2008), p. 035501. DOI: 10.1103/PhysRevLett.100.035501. URL: https://link.aps.org/doi/10.1103/PhysRevLett.100.035501.

[437] Gunnar Moos et al. „Anisotropy of Quasiparticle Lifetimes and the Role of Disorder in Graphite from Ultrafast Time-Resolved Photoemission Spectroscopy“. In: *Phys. Rev. Lett.* 87 (26 Dec. 2001), p. 267402. DOI: 10.1103/PhysRevLett.87.267402. URL: https://link.aps.org/doi/10.1103/PhysRevLett.87.267402.

[438] Tobias Kampfrath et al. „Strongly Coupled Optical Phonons in the Ultrafast Dynamics of the Electronic Energy and Current Relaxation in Graphite“. In: *Phys. Rev. Lett.* 95 (18 Oct. 2005), p. 187403. DOI: 10.1103/PhysRevLett.95.187403. URL: https://link.aps.org/doi/10.1103/PhysRevLett.95.187403.

[439] A Beltaos et al. „Damage effects on multi-layer graphene from femtosecond laser interaction“. In: *Physica Scripta* 2014.T162 (Sept. 2014), p. 014015. DOI: 10.1088/0031-8949/2014/T162/014015. URL: https://doi.org/10.1088/0031-8949/2014/T162/014015.

[440] Adam Roberts et al. „Response of graphene to femtosecond high-intensity laser irradiation“. In: *Applied Physics Letters* 99.5 (Aug. 2011), p. 051912. ISSN: 0003-6951. DOI: 10.1063/1.3623760. eprint: https://pubs.aip.org/aip/apl/article-pdf/doi/10.1063/1.3623760/14455279/051912_1_online.pdf. URL: https://doi.org/10.1063/1.3623760.

[441] Marc Currie et al. „Quantifying pulsed laser induced damage to graphene“. In: *Applied Physics Letters* 99.21 (Nov. 2011), p. 211909. ISSN: 0003-6951. DOI: 10.1063/1.3663875. URL: https://doi.org/10.1063/1.3663875.

[442] B. Krauss et al. „Laser-induced disassembly of a graphene single crystal into a nanocrystalline network“. In: *Phys. Rev. B* 79 (16 Apr. 2009), p. 165428. DOI: 10.1103/PhysRevB.79.165428. URL: https://link.aps.org/doi/10.1103/PhysRevB.79.165428.

[443] F. Schedin et al. „Detection of individual gas molecules adsorbed on graphene“. In: *Nature Materials* 6.9 (Sept. 2007), pp. 652–655. ISSN: 1476-4660. DOI: 10.1038/nmat1967. URL: https://doi.org/10.1038/nmat1967.

[444] Myriam Kaiser et al. „Tailored-edge laser glass cleaving supported by thermal separation“. In: *Laser Applications in Microelectronic and Optoelectronic Manufacturing (LAMOM) XXVIII*. Ed. by Aiko Narazaki, Laura Gemini, and Jan Kleinert. Vol. 12408. International Society for Optics and Photonics. SPIE, 2023, p. 124080C. DOI: 10.1117/12.2649794. URL: https://doi.org/10.1117/12.2649794.

[445] Myriam Kaiser et al. „Customized edge cutting of display glass with laser-only machining“. In: *Frontiers in Ultrafast Optics: Biomedical, Scientific, and Industrial Applications XXIV*. Ed. by Peter R. Herman, Roberto Osellame, and Adela Ben-Yakar. Vol. 12875. International Society for Optics and Photonics. SPIE, 2024, 128750E. DOI: 10.1117/12.3000909. URL: https://doi.org/10.1117/12.3000909.

[446] S. A. Mikhailov. „Non-linear electromagnetic response of graphene“. In: *Europhysics Letters* 79.2 (June 2007), p. 27002. DOI: 10.1209/0295-5075/79/27002. URL: https://doi.org/10.1209/0295-5075/79/27002.

[447] S A Mikhailov and K Ziegler. „Nonlinear electromagnetic response of graphene: frequency multiplication and the self-consistent-field effects“. In: *Journal of Physics: Condensed Matter* 20.38 (Aug. 2008), p. 384204. DOI: 10.1088/0953-8984/20/38/384204. URL: https://doi.org/10.1088/0953-8984/20/38/384204.

[448] Qiaoliang Bao et al. „Atomic-Layer Graphene as a Saturable Absorber for Ultrafast Pulsed Lasers“. In: *Advanced Functional Materials* 19.19 (2009), pp. 3077–3083. DOI: https://doi.org/10.1002/adfm.200901007. eprint: https://advanced.onlinelibrary.wiley.com/doi/pdf/10.1002/adfm.200901007. URL: https://advanced.onlinelibrary.wiley.com/doi/abs/10.1002/adfm.200901007.

[449] E. Hendry et al. „Coherent Nonlinear Optical Response of Graphene“. In: *Phys. Rev. Lett.* 105 (9 Aug. 2010), p. 097401. DOI: 10.1103/PhysRevLett.105.097401. URL: https://link.aps.org/doi/10.1103/PhysRevLett.105.097401.

[450] J L Cheng, N Vermeulen, and J E Sipe. „Third order optical nonlinearity of graphene“. In: *New Journal of Physics* 16.5 (May 2014), p. 053014. DOI: 10.1088/1367-2630/16/5/053014. URL: https://doi.org/10.1088/1367-2630/16/5/053014.

[451] Kenichi L. Ishikawa. „Nonlinear optical response of graphene in time domain“. In: *Phys. Rev. B* 82 (20 Nov. 2010), p. 201402. DOI: 10.1103/PhysRevB.82.201402. URL: https://link.aps.org/doi/10.1103/PhysRevB.82.201402.

[452] Nardeep Kumar et al. „Third harmonic generation in graphene and few-layer graphite films“. In: *Phys. Rev. B* 87 (12 Mar. 2013), p. 121406. DOI: 10.1103/PhysRevB.87.121406. URL: https://link.aps.org/doi/10.1103/PhysRevB.87.121406.

[453] S. A. Mikhailov. „Quantum theory of the third-order nonlinear electrodynamic effects of graphene“. In: *Phys. Rev. B* 93 (8 Feb. 2016), p. 085403. DOI: 10.1103/PhysRevB.93.085403. URL: https://link.aps.org/doi/10.1103/PhysRevB.93.085403.

[454] Chris Beckerleg et al. „Cavity enhanced third harmonic generation in graphene“. In: *Applied Physics Letters* 112.1 (Jan. 2018), p. 011102. ISSN: 0003-6951. DOI: 10.1063/1.4999054. eprint: https://pubs.aip.org/aip/apl/article-pdf/doi/10.1063/1.4999054/14506311/011102_1_online.pdf. URL: https://doi.org/10.1063/1.4999054.

[455] Tao Jiang et al. „Gate-tunable third-order nonlinear optical response of massless Dirac fermions in graphene“. In: *Nature Photonics* 12.7 (July 2018), pp. 430–436. ISSN: 1749-4893. DOI: 10.1038/s41566-018-0175-7. URL: https://doi.org/10.1038/s41566-018-0175-7.

[456] Giancarlo Soavi et al. „Broadband, electrically tunable third-harmonic generation in graphene“. In: *Nature Nanotechnology* 13.7 (July 2018), pp. 583–588. ISSN: 1748-3395. DOI: 10.1038/s41565-018-0145-8. URL: https://doi.org/10.1038/s41565-018-0145-8.

[457] Nathalie Vermeulen et al. „Graphene's nonlinear-optical physics revealed through exponentially growing self-phase modulation“. In: *Nature Communications* 9 (1 July 11, 2018), p. 2675. ISSN: 2041-1723. DOI: 10.1038/s41467-018-05081-z. URL: https://doi.org/10.1038/s41467-018-05081-z.

[458] Wei Chen et al. „The nonlinear optical properties of coupling and decoupling graphene layers“. In: *AIP Advances* 3.4 (Apr. 2013), p. 042123. ISSN: 2158-3226. DOI: 10.1063/1.4802889. eprint: https://pubs.aip.org/aip/adv/article-pdf/doi/10.1063/1.4802889/13000039/042123_1_online.pdf. URL: https://doi.org/10.1063/1.4802889.

[459] Giorgos Demetriou et al. „Nonlinear optical properties of multilayer graphene in the infrared“. In: *Opt. Express* 24.12 (June 2016), pp. 13033–13043. DOI: 10.1364/OE.24.013033. URL: https://opg.optica.org/oe/abstract.cfm?URI=oe-24-12-13033.

[460] Evdokia Dremetsika and Pascal Kockaert. „Enhanced optical Kerr effect method for a detailed characterization of the third-order nonlinearity of two-dimensional materials applied to graphene“. In: *Phys. Rev. B* 96 (23 Dec. 2017), p. 235422. DOI: 10.1103/PhysRevB.96.235422. URL: https://link.aps.org/doi/10.1103/PhysRevB.96.235422.

[461] N. A. Savostianova and S. A. Mikhailov. „Optical Kerr effect in graphene: Theoretical analysis of the optical heterodyne detection technique“. In: *Phys. Rev. B* 97 (16 Apr. 2018), p. 165424. DOI: 10.1103/PhysRevB.97.165424. URL: https://link.aps.org/doi/10.1103/PhysRevB.97.165424.

[462] Kwang Jun Ahn et al. „Wavelength and fluence-dependent third-order optical nonlinearity of mono- and multi-layer graphene“. In: *Appl. Opt.* 56.36 (Dec. 2017), pp. 9920–9924. DOI: 10.1364/AO.56.009920. URL: https://opg.optica.org/ao/abstract.cfm?URI=ao-56-36-9920.

[463] Siddharatha Thakur et al. „Experimental Characterization of the Ultrafast, Tunable and Broadband Optical Kerr Nonlinearity in Graphene“. In: *Scientific Reports* 9 (1 July 2019), p. 10540. ISSN: 2045-2322. DOI: 10.1038/s41598-019-46710-x. URL: https://doi.org/10.1038/s41598-019-46710-x.

[464] David Castelló-Lurbe, Hugo Thienpont, and Nathalie Vermeulen. „Predicting Graphene's Nonlinear-Optical Refractive Response for Propagating Pulses“. In: *Laser & Photonics Reviews* 14.6 (2020), p. 1900402. DOI: https://doi.org/10.1002/lpor.201900402. eprint: https://onlinelibrary.wiley.com/doi/pdf/10.1002/lpor.201900402. URL: https://onlinelibrary.wiley.com/doi/abs/10.1002/lpor.201900402.

[465] Diogo F. P. Cunha et al. „Two-Step Relaxation of Non-Equilibrium Electrons in Graphene: The Key to Understanding Pump–Probe Experiments“. In: *Applied Sciences* 14.3 (2024). ISSN: 2076-3417. DOI: 10.3390/app14031250. URL: https://www.mdpi.com/2076-3417/14/3/1250.

[466] D. Brida et al. „Ultrafast collinear scattering and carrier multiplication in graphene“. In: *Nature Communications* 4.1 (June 2013), p. 1987. ISSN: 2041-1723. DOI: 10.1038/ncomms2987. URL: https://doi.org/10.1038/ncomms2987.

[467] J. M. Iglesias et al. „Hot carrier and hot phonon coupling during ultrafast relaxation of photoexcited electrons in graphene“. In: *Applied Physics Letters* 108.4 (Jan. 2016), p. 043105. ISSN: 0003-6951. DOI: 10.1063/1.4940902. eprint: https://pubs.aip.org/aip/apl/article-pdf/doi/10.1063/1.4940902/14477594/043105_1_online.pdf. URL: https://doi.org/10.1063/1.4940902.

[468] Bo Gao et al. „Studies of Intrinsic Hot Phonon Dynamics in Suspended Graphene by Transient Absorption Microscopy“. In: *Nano Letters* 11.8 (2011). PMID: 21696177, pp. 3184–3189. DOI: 10.1021/nl201397a. eprint: https://doi.org/10.1021/nl201397a. URL: https://doi.org/10.1021/nl201397a.

[469] Rustam Gatamov. „Ultrafast pump-probe fluence and wavelength dependent relaxation dynamics in graphene“. Submitted to the Faculty of the Graduate School of Vanderbilt University. PhD thesis. Nashville, Tennessee: Vanderbilt University, Dec. 2020.

[470] Jahan M. Dawlaty et al. „Measurement of ultrafast carrier dynamics in epitaxial graphene“. In: *Applied Physics Letters* 92.4 (Jan. 2008), p. 042116. ISSN: 0003-6951. DOI: 10.1063/1.2837539. eprint: https://pubs.aip.org/aip/apl/article-pdf/doi/10.1063/1.2837539/14386809/042116_1_online.pdf. URL: https://doi.org/10.1063/1.2837539.

[471] Ryan W. Newson et al. „Ultrafast carrier kinetics in exfoliated graphene and thin graphite films“. In: *Opt. Express* 17.4 (Feb. 2009), pp. 2326–2333. DOI: 10.1364/OE.17.002326. URL: https://opg.optica.org/oe/abstract.cfm?URI=oe-17-4-2326.

[472] I Dmitruk et al. „Efficiency estimates and practical aspects of an optical Kerr gate for time-resolved luminescence spectroscopy“. In: *Methods and Applications in Fluorescence* 4.4 (Oct. 2016), p. 044007. DOI: 10.1088/2050-6120/4/4/044007. URL: https://doi.org/10.1088/2050-6120/4/4/044007.

[473] PicoQuant GmbH. *TDA-200 Trigger Diode Assembly*. Product Webpage. 2018. URL: https://www.picoquant.com/products/category/accessories/tda-200-trigger-diode-assembly (visited on 11/10/2025).

List of Publications

A. Journal Articles

- **Farrag, A.**, Flatae, A. M., Agio, M. (2025). *Graphene and thin graphite films for ultrafast optical Kerr gating at 1 GHz repetition rate under focused illumination. arXiv.* https://doi.org/10.48550/arXiv.2511.17713
- **Farrag, A.**, Flatae, A. M., Stott, L. M., Lagatti, A., Lapini, A., Möncke, D., Agio, M. (2025). *Ultrafast optical Kerr Gate at 1 GHz repetition rate by focusing on BBS glass. arXiv.* https://doi.org/10.48550/arXiv.2511.17493
- Fattah, A., Flatae, A., **Farrag, A.**, and Agio, M. (2021). *Ultrafast single-photon detection at high repetition rates based on optical Kerr gates under focusing. Opt. Lett., 46*, 560-563. doi:10.1364/OL.414895

B. Book Chapters

- Mario Agio, Duncan England, Assegid M. Flatae, **Amr Farrag**, Abdul A. Fattah, 14 - *Nonlinear optics for ultrafast single-photon detection*, Editor(s): Giancarlo C. Righini, Luigi Sirleto, In Woodhead Publishing Series in Electronic and Optical Materials, Advances in Nonlinear Photonics, Woodhead Publishing, 2023, Pages 413-437, ISBN 9780323983846, https://doi.org/10.1016/B978-0-32-398384-6.00021-8

C. Conferences and Proceedings

- **Farrag, A.**, Flatae, A. M., Ashjari, A., Möncke, D., Agio, M. (2025). Ultrafast Detection of Quantum Emitters at High Repetition Rates. In *DPG Spring Meeting Bonn 2025.* https://www.dpg-verhandlungen.de/year/2025/conference/bonn/part/k/session/6/contribution/5

- **Farrag, A.**, Fattah, A.-H., Flatae, A. M., Agio, M. (2024). Ultrafast single-photon detection at high repetition rates based on optical Kerr gates under focusing. In *DPG Spring Meeting Freiburg 2024*. https://www.dpg-verhandlungen.de/year/2024/conference/freiburg/part/q/session/55/contribution/30

- **Farrag, A.**, Fattah, A.-H., Flatae, A. M., Agio, M. (2022). Ultrafast single-photon detection at high repetition rates based on optical Kerr gates under focusing. In *DPG Spring Meeting Erlangen 2022 (online)*. https://www.dpg-verhandlungen.de/year/2022/conference/erlangen/part/k/session/7/contribution/5

- Agio, M., **Farrag, A.**, Kambalathmana, H. , Fattah, A., Flatae, A. M. (2022). *Ultrafast detection of quantum emitters*. In *Proceedings of SPIE* PC1199904. https://doi.org/10.1117/12.2608088

- Flatae, A. M., Fattah, A., **Farrag, A.**, Agio, M. (2021). Ultrafast Single-Photon Detection based on Optical Kerr Gates. In *OSA Technical Digest*. Optica Publishing Group.